Disks in close Binary Stars

Dissertation

der Mathematisch-Naturwissenschaftlichen Fakultät

der Eberhard Karls Universität Tübingen

zur Erlangung des Grades eines

Doktors der Naturwissenschaften

(Dr. rer. nat.)

vorgelegt von

Lucas Marius Jordan

aus Tübingen

Tübingen

2024

Gedruckt mit Genehmigung der Mathematisch-Naturwissenschaftlichen Fakultät der Eberhard Karls Universität Tübingen.

Tag der mündlichen Qualifikation:	09.05.2025
Dekan:	Prof. Dr. Thilo Stehle
1. Berichterstatter/-in:	Prof. Dr. Rolf Kuiper
2. Berichterstatter/-in:	Prof. Dr. Klaus Werner

Gewidmet an
Willy Kley

This work is licensed under a CC BY-NC 4.0 license.
https://creativecommons.org/licenses/by-nc/4.0/

Kurzfassung

Scheiben in engen Doppelsternsystemen bieten optimale Möglichkeiten, astrophysikalische Modelle zu testen und zu verbessern. In dieser Arbeit werden solche Systeme im Zusammenhang mit Zwergnovae sowie Planetenentstehung untersucht. Zwergnovae sind eine Unterklasse der kataklysmischen Veränderlichen (CV), bei denen es sich um enge Doppelsternsysteme mit einem Abstand von etwa einem Sonnenradius handelt. Diese bestehen aus einem Weißen Zwerg, der von einem leichteren Sekundärstern umkreist wird, von dem Masse auf den Weißen Zwerg übertragen wird. Durch den Massentransfer entsteht eine Scheibe um den Weißen Zwerg. In dieser Akkretionsscheibe treten sich wiederholende Zwergnova Ausbrüche auf.

Bei SU UMa-Sternen, einer Unterklasse der Zwergnovae benannt nach dem repräsentativen System SU Ursae Majoris, entwickeln sich einige Ausbrüche zu Superausbrüchen. Bei diesen Ausbrüchen treten Helligkeitsschwankungen auf, die als Superhumps bezeichnet werden und deren Periodizität etwas länger ist als die Umlaufzeit des Doppelsternsystems. Superhumps können durch eine exzentrische Scheibe erklärt werden, die langsam in prograder Richtung präzediert. Die sehr kurzen Zeitskalen, auf denen sich diese Zyklen wiederholen, mit Ausbrüchen von wenigen Tagen Dauer und Abständen von wenigen Wochen, machen diese Systeme zu idealen Testobjekten für Modelle der Akkretionsscheibe und der Wechselwirkung zwischen Scheibe und Doppelsternsystem.

In größeren Systemen von Hauptreihensternen wurden Planeten um den Primärstern eines Doppelsternsystems entdeckt, die einander näher als 40 au sind. Bei so geringen Abständen werden die Scheiben um den Primärstern dynamisch gestört. Dadurch sind diese Scheiben kleiner, haben eine geringere Masse und haben eine kürzere Lebensdauer als Scheiben um Einzelsterne. Dennoch wurden einige Dutzend Planeten in engen Doppelsternsystemen entdeckt. Sollten diese Systeme die gleiche Konfiguration haben wie zur Zeit der Planetenentstehung, würde dies darauf hindeuten, dass die Planetenentstehung robust ist und schnell verläuft. Die Wachstumsphase von Planetesimalen ist ein kritischer Schritt in der Planetenentstehung. Nach heutigen Modellen kann dieses Wachstum nur gelingen, wenn die Scheibe trotz der Störungen durch den Sekundärstern dynamisch ruhig bleibt. Da diese Systeme zu klein sind, um sie in Beobachtungen aufzulösen, und zu komplex sind, um sie analytisch zu beschreiben, können sie derzeit nur mit Hilfe von numerischen Methoden untersucht werden.

In dieser Arbeit habe ich neue zweidimensionale numerische hydrodynamische Modelle entwickelt, um Scheiben in engen Doppelsternsystemen zu simulieren. Anschließend habe ich diese Modelle verwendet, um sowohl die Ausbruchszyklen von SU UMa-Systemen als auch die Umgebung von engen Doppelsternsystemen, in denen sich Planeten bilden könnten, zu untersuchen.

Abstract

Disks in close binaries offer great opportunities for testing and refining astrophysical models and are studied in this thesis in the context of dwarf novae and planet formation. Dwarf novae are a subclass of cataclysmic variables (CVs), which are close binary systems with separations on the order of one solar radius, consisting of a white dwarf orbited by a mass transferring low-mass secondary star. The mass transfer forms a disk around the white dwarf, and it is this accretion disk that repeatedly undergoes dwarf nova outbursts.

In SU UMa stars, a subclass of dwarf novae named after the prototype SU Ursae Majoris, some outbursts evolve into superoutbursts that exhibit brightness variations called superhumps, which typically have a slightly longer periods than the binary. The superhumps can be explained by an eccentric disk with a slow prograde precession. The extremely fast timescales on which these cycles evolve, with outbursts lasting a few days occurring every other week, make these systems ideal testbeds for probing disk models and studying binary disk interactions.

On a different scale, planets have been discovered around primary stars in main sequence binary systems with separations of less than 40 au. At such close distances, the disks around the primary are dynamically perturbed and are smaller, have reduced masses, and have shorter lifetimes compared to disks around single stars. Despite this, a few dozen planets are known in close binary systems, suggesting that the planet formation process is robust and fast if they were formed at the positions currently observed. Current models predict that planetesimal growth, a critical step in the planet formation process, can only succeed if the disk remains dynamically calm despite the perturbations of the secondary. Because these systems are too small to resolve in observations and too complex to study analytically, they can currently only be studied using numerical simulations.

In this thesis, I developed new two-dimensional numerical hydrodynamical models to simulate disks in close binaries. I then used these models to study both, SU UMa outburst cycles, and the environment around close binaries in which planets might form.

Contents

1 Publications

In this chapter I list the publications I have been involved with in chronological order by publication date and describe my contributions to them. The motivations and explanations for the publications, as well as the publications themselves are given in the main body of this thesis.

Jordan et al. 2021:
Lucas M. Jordan, Wilhelm Kley, Giovanni Picogna and Francesco Marzari
Disks in close binary stars. γ-Cephei revisited
Astronomy & Astrophysics, 654, A54, October 2021
After planning the project and detailing the goals with the collaborators, I ran the simulations, made the evaluations, created the plots, and wrote the paper.

Joseph et al. 2023:
Jibin Joseph, Alexandros Ziampras, Lucas Jordan, George A. Turpin and Richard P. Nelson
Measuring the numerical viscosity in simulations of protoplanetary disks in Cartesian grids. The viscously spreading ring revisited
Astronomy & Astrophysics, 678, A134, October 2023
I was invited to this project to provide comparison simulations after it was already planned and underway. I ran all the FARGO code simulations for the paper (not to be confused with the PLUTO simulations using the FARGO method) and used the FARGO code to reproduce and explain the results from Speith & Kley (2003). In addition, I wrote the initial versions of Appendix B, most of the text in Sections 2, 3, and 4, and contributed to Sections 1 and 5. In addition, I was involved in proofreading and discussions throughout the writing process, except for the parts involving the ATHENA code.

Rometsch et al. 2024:
Thomas Rometsch, Lucas M. Jordan, Tobias W. Moldenhauer, Dennis Wehner, Steven Rendon Restrepo, Tobias W. A. Müller, Giovanni Picogna, Wilhelm Kley, and Cornelis P. Dullemond
FARGOCPT: 2D Multiphysics code for simulating disk interactions with stars, planets, and particles
Astronomy & Astrophysics, 684, A192, April 2024
Most of the paper was written by Thomas and me, with me writing most of the sections relevant to this thesis. Additionally, I was involved in proofreading and discussions throughout the writing process.

Jordan et al. 2024:

Lucas M. Jordan, D. Wehner and R. Kuiper

Two-dimensional simulations of disks in close binaries. Simulating outburst cycles in cataclysmic variables.

Astronomy & Astrophysics, 689, A354, September 2024

After the topic was brought to us by Willy Kley, I provided Dennis Wehner, then a master's student, with an initial isothermal setup and helped and mentored him to develop the code and run the simulations for the paper. Major steps during the project, such as the new equation of state, were planned together with Rolf Kuiper. I then performed an evaluation of the simulations starting from the scripts by D. Wehner, created the plots, and wrote the paper while, the collaborators provided advice and proofreading.

Jordan & Rometsch 2025:

Lucas M. Jordan and Thomas Rometsch

Hydrodynamical simulations with strong indirect terms in Fargo-like codes. Numerical aspects of non-inertial frame and artificial viscosity

Astronomy & Astrophysics, 693, A177, January 2025

I ran all the simulations for the project and wrote almost all the text, while Thomas provided me with an initial setup for planet-disk interaction, lots of advice, useful discussions, and proofreading throughout the project.

2 Introduction

One of the brightest stars in the night sky and closest to Earth is Alpha Centauri A. Like more than half of all stars, Alpha Centauri A is not alone, but is in a multiple system with a close companion and an additional third companion far away from the two inner stars.

The majority of stars form in groups within the dense regions of a giant molecular cloud, called embedded clusters (Lada & Lada 2003). Observations of nearby field stars (stars that are not part of a stellar cluster) find that nearly half (46%) of solar-type stars reside in binary (33%) or multiple systems consisting of three or more stars (13%) (Raghavan et al. 2010). The mean binary separation for Sun-like stars is 40 au (where 1 au is the distance between the Earth and the Sun) with a broad log-normal distribution and their mass ratios are uniformly distributed (Offner et al. 2023, July; Raghavan et al. 2010). The multiplicity fraction increases with the stellar mass (Duchêne & Kraus 2013) and is higher in star-forming regions. Overall 58% of the main sequence stars are estimated to be in multiple systems (Offner et al. 2023, July).

Multiple-star systems are in most cases hierarchically structured, meaning that, for example, triple systems consist of a close binary system and a distant third star (Tokovinin 2014). Due to the hierarchical structure, these systems can often be approximated as binary systems. Evidently, binary systems are common and are also known to harbor planets[1,2] which makes them interesting objects to study.

Binary stars don't just form together and remain bound in the main sequence phase, they continue to evolve. In the late stages of evolution, when the primary star first inflates into a red giant, it can tidally interact with and engulf its companion star to reduce the binary orbit and eject the shell around its white dwarf core. A special case of such a late-stage configuration is a white dwarf star that accretes the outer envelope of its companion star (Belloni & Schreiber 2023). The mass transfer to the white dwarf can lead to various instabilities in the system that cause drastic changes in its brightness, hence these systems are called a cataclysmic variable (CV).

In this chapter, I will give an overview of how binary systems form in Section 2.1, planet formation in general in Section 2.2, the challenges of forming planets in binary systems in Section 2.3, how binaries turn into cataclysmic variables in Section 2.4, different types of cataclysmic variables in Section 2.5 and finally the dwarf novae zoo and how it is modeled in Section 2.6.

[1] For an up-to-date list of circumbinary planets, see https://exoplanet.eu/planets_binary_circum
[2] For an up-to-date list of S-type planets in close binaries, see https://exoplanet.eu/planets_binary

2.1 Binary formation

Stars form inside molecular clouds. The formation of multiple star systems is influenced by the initial conditions such as mass, density, temperature, and metallicity of the cloud (e.g. Bate 2019). And even after the stars are formed, the stellar system can be drastically altered by encounters with other stars. Although the cloud collapse is a chaotic event, the majority of binaries are expected to form via two different scenarios, disk instability, and core fragmentation, which are depicted in Fig. 2.1.1.

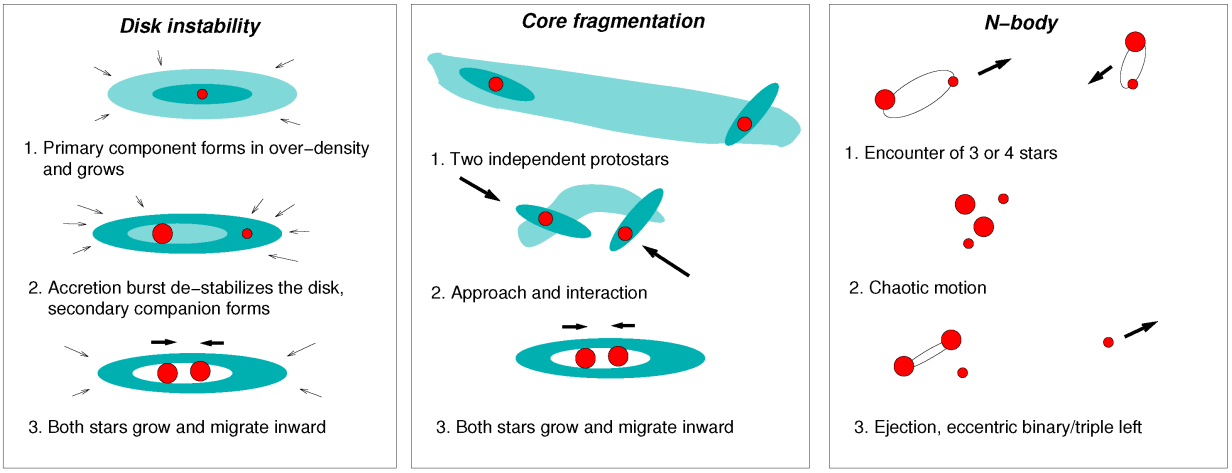

Figure 2.1.1. *Image taken from: Tokovinin (2021). Sketch of binary star formation scenarios.*

Summarized from Tokovinin (2021): in the disk instability scenario, the primary star is formed first and companions are formed by the gravitational instability of the disk around the primary star. As stellar and disk masses are correlated, this typically occurs around massive stars. But less massive disks can also become unstable due to accretion bursts from the collapsing cloud (Kratter et al. 2010). Binary systems formed by disk instability start with low mass ratios (i.e., the primary is much more massive than the companion). Depending on how long the disk remains, the binary separation shrinks due to interaction with the circumbinary disk (Heath & Nixon 2020; Penzlin et al. 2022; Tiede et al. 2020) and the mass ratio grows towards unity because the lighter star accretes more material from the disk (Lai & Muñoz 2023, Fig. 11). This formation channel is therefore more efficient at producing massive, compact binaries with smaller mass ratios and less inclined circumstellar and circumbinary disks than the core fragmentation scenario (Tokovinin 2021).

In the core fragmentation scenario, the protostars form independently in the same region of the molecular cloud. They become gravitationally bound and form a binary system by dissipating excess kinetic energy through star-disk interactions (Bate 2019). This formation channel is more efficient at producing wide binaries with misaligned orbits and high eccentricities. Simulations find that the majority of binary systems are formed by core fragmentation (Bate 2019).

After the stars formed a binary system, further evolution of the system is the same for both formation scenarios. Disk-binary interactions tend to drive the circumbinary disk to coplanar

configurations when the initial inclination is below a critical value ($i_{\rm crit} \approx 40°$) and to polar orbits when it is above (Martin & Lubow 2017; 2018; Zanazzi & Lai 2018). The stellar disks are driven to coplanar orbits by the binary disk interaction (Foucart & Lai 2013; Fragner & Nelson 2010), although accretion from a polar circumbinary disk can cause stellar disks to be stable in a polar configuration (Smallwood et al. 2023). Binary systems in which one or more planets orbit one of the stars have low inclinations, suggesting either efficient alignment of the circumstellar disks with the binary through disk-binary interactions or that these systems were formed with low inclinations via disk fragmentation (Christian et al. 2022; Dupuy et al. 2022).

Observations of circumbinary disks, on the other hand, find that the disks have large inclinations $i > 40°$ when the binary separations are larger than 0.6 au (Czekala et al. 2019) with only a slight preference for aligned disks (Ceppi et al. 2024). Whereas simulations of star cluster formation also find a slightly higher preference for alignment with a mean inclination of 34° (Elsender et al. 2023).

While inclined disks are common and currently of growing interest in the scientific astronomical community, I will only focus on coplanar disks in this thesis. On the one hand, planet formation in binary systems is complicated enough in the coplanar case, and on the other hand, two-dimensional simulations are already limited by computational cost without the additional complexity of a third dimension needed to model inclinations.

2.2 Planet formation

Before discussing the difficulties of planet formation within the stellar disks of close binary systems, I present an overview of planet formation as it is thought to occur around a single, isolated star. For a more in-depth review of planet formation, I recommend the reviews by Armitage & Kley (2019); Drążkowska et al. (2023).

There are two main paths for planets to form, gravitational instability and core accretion. If the disk around a star becomes gravitationally unstable, the outcome could also be a planet instead of a star (Boss 1997). The disk instability model produces only massive gas giants far from the central star (Boss 2010), 30 to 70 au. The model is invoked to explain a handful of observed far-out planets (Nero & Bjorkman 2009) such as the 4 super Jupiter planets beyond 16 au in the HR 8799 system (Marois et al. 2008). But it fails to explain the majority of observed planets that are less massive and closer to their star. Earth-like planets and gas giants closer to the star, such as Jupiter and Saturn, are thought to form by core accretion, which is described as a multi-step process, as depicted in Fig. 2.2.1.

The dust from which planets form is already present in the interstellar clouds, which have a dust-to-gas mass ratio of about $\approx 1\%$ (Li & Draine 2001). Dust in interstellar clouds is small $< 1\ \mu$m (Mathis et al. 1977; Weingartner & Draine 2001) and its growth is prevented by the long growth timescales due to low densities and repeated destruction of dust grains by interstellar shock waves caused by nearby supernovae (Draine 1995; Jones et al. 1994).

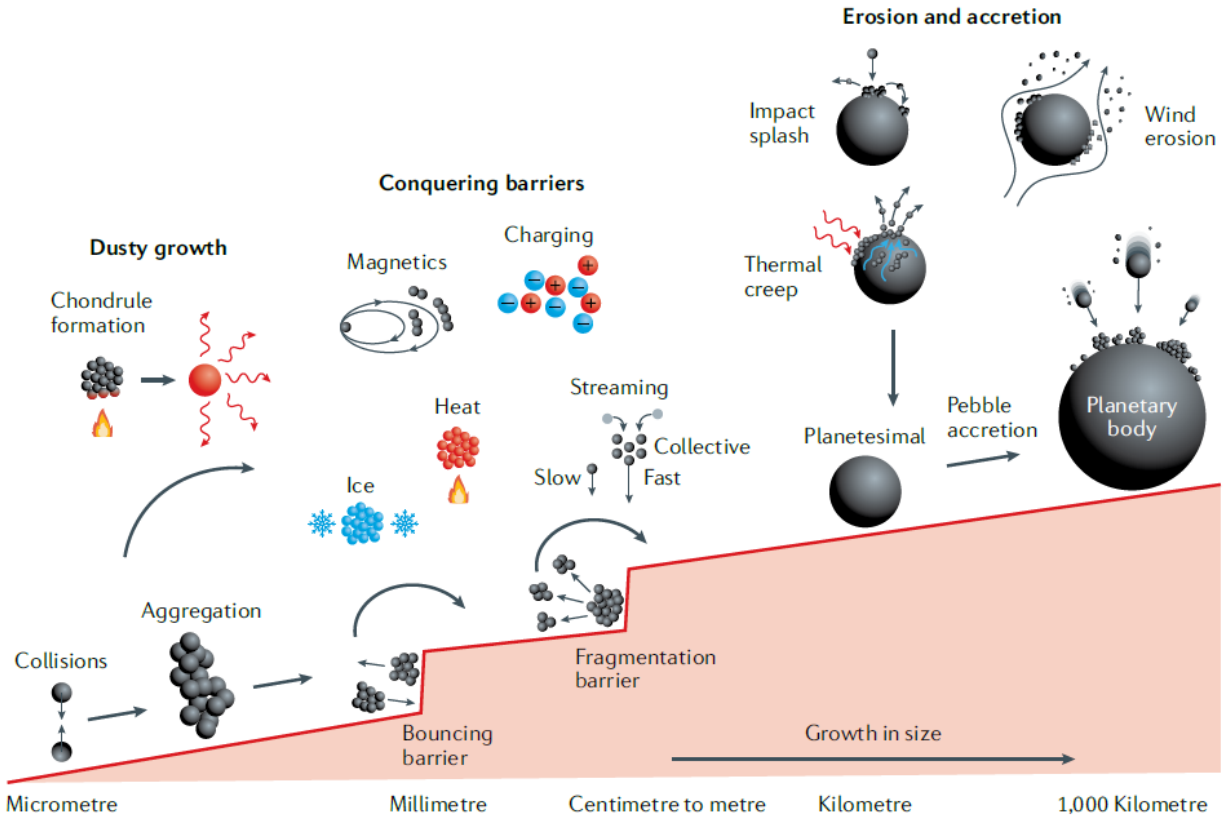

Figure 2.2.1. *Image taken from: Wurm & Teiser (2021). Sketch of the core-accretion scenario for planet formation. It describes the different growth stages from dust to protoplanets.*

From dust to aggregates

When regions of the interstellar cloud collapse to form a star, the dust growth times decrease with increasing density and the dust starts to grow by hitting and sticking together with other dust grains in the earliest stage of planet formation (Bate 2022; Vorobyov et al. 2024). This growth is also confirmed from observations by the detection of infrared and millimeter wavelength emissions from the dust particles (Miotello et al. 2014).

By the time the cloud core collapses to form a pre-stellar disk (Bate 2011), the dust particles in the inner regions of the pre-stellar disk might grow to sizes of 0.1 mm (Bate 2022). From then on, the protostar forms and continues its evolution to a pre-main sequence star, dispersing its gaseous envelope, at which point the pre-stellar disk is reclassified as a protoplanetary disk with typical masses of a few percent of the central star (Williams & Cieza 2011, Sect. 4).

In the protoplanetary disk, the small dust particles are strongly coupled with the gas. They continue to grow through hit-and-stick with low collision velocities determined by Brownian motion (Blum & Wurm 2008). The growth process itself has been emulated in numerical experiments (Dominik & Tielens 1997; Paszun & Dominik 2009; Seizinger & Kley 2013; Wada et al. 2008) and laboratory experiments (Brisset et al. 2016; Kothe et al. 2013): the sub-micron sized dust particles form fluffy, fractal aggregates. As they grow to millimeter or centimeter sizes, their motion starts to decouple from the surrounding gas, increasing the collision velocities and leading to deformation and compaction of the aggregates. The compacted

aggregates are more likely to bounce off each other, stopping further growth at the so-called bouncing barrier (Zsom et al. 2010).

These compacted aggregates can be baked into *mm-cm* sized compact pebbles, called chondrules, by heating events around the young star (Krot et al. 2009). Chondrules are small *mm* sizes spherical grains, which are readily found in meteorites today.

From aggregates to pebbles

How *mm* sized aggregates continue their growth beyond the bouncing barrier is still an active field of research. Should the aggregates grow beyond the bouncing barrier, they further decouple from the gas, leading to higher collision velocities and fragmentation of the aggregates (Schräpler et al. 2012) at the fragmentation barrier.

A popular model for growth beyond the bouncing barrier is the evaporation of water-ice particles and following recondensation on the surface of dust particles (Drążkowska & Alibert 2017). This allows the dust particles to grow to larger sizes through hit-and-stick due to the enhanced sticking properties caused by their icy mantle. However, this effect is temperature dependent and is only effective near the water condensation temperature (Musiolik & Wurm 2019). Because the temperature decreases with the distance to the star, a narrow temperature range translates to a narrow ring in the protoplanetary disk.

A similar model was proposed with enhanced sticking properties near the dust evaporation temperature 1000 K (Demirci et al. 2019) which could explain planet formation closer to the star. Another mechanism, which is not dependent on the distance to the star, is the electrical charging of the dust aggregates through collisions which then can lead to additional attractive forces (Steinpilz et al. 2020).

While it is not clear how the dust grows beyond the bouncing barrier, the existence of planetesimals and planets is proof that it does succeed. More direct evidence of dust growth is found in meteorites, which contain chondrules of several *cm* in size (Simon et al. 2018). And also from observations of large particles in the dust rings of TW Hydrae (Macías et al. 2021).

Another challenge of this growth phase is the fast radial drift of meter-sized pebbles toward the star due to the gas drag (Weidenschilling 1977) which is called the drift barrier or meter-size barrier (even though it also applies to *cm* sized dust pebbles). Either this drift must be slowed down, or the growth to kilometer-sized planetesimals, which are less affected by the gas drag, must be fast.

From pebbles to planetesimals

As the pebbles grow to several centimeters in size, they decouple further from the gas and settle to the midplane more efficiently (Fromang & Nelson 2009) and they can be trapped in pressure bumps or vortices, as was observed in the DSHARP survey (Dullemond et al. 2018; Pérez et al. 2018; Rosotti et al. 2020). If the concentration of dust is high, then the feedback from the drag between gas and dust can accelerate the gas which reduces the drift of the pebbles. The slower drift at the radii of high pebble concentration leads to further accumulation of pebbles that drift inwards from larger radii. This leads to a self-amplifying

process of increasing dust density, until eventually the dust density becomes high enough to gravitationally collapse and form kilometer-sized planetesimals. This process is called the streaming instability (Li & Youdin 2021; Youdin & Goodman 2005) and it efficiently solves the drift barrier problem by stopping the drift and quickly turning the pebbles into planetesimals which are less affected by gas drag.

Streaming instability requires an initial increase in dust density and large grains to be effective. These conditions do not require a pressure bump, but are more easily found at pressure bumps. Pressure bumps occur around ice or dust evaporation temperatures (also called snow lines or ice lines), which together with the enhanced sticking properties of dust particles at these temperatures make them the ideal sites for the formation of planetesimals (Drążkowska & Alibert 2017).

Determining the features of streaming instability and how to detect them in observations is still in its infancy. But attempts by Zagaria et al. (2023), who combined observational measurements of the dust size and dust density in the rings of HD 163296 with dust fragmentation and diffusivity models, found that the results are in agreement with the expected features of ongoing streaming instability.

The comet 67P/Churyumov-Gerasimenko has been visited and studied by the Rosetta mission in 2014. The fluffy, low filling factor of the comet together with the monodisperse millimeter size distribution of the pebbles on its surface, is consistent with the gentle gravitational collapse of pebbles via the streaming instability (Blum et al. 2017). Additionally, the population of binary comets in the Kuiper belt that consist of two asteroids of similar size and similar composition with prograde binary orbits is also in agreement with the formation of these objects via streaming instability (Nesvorný et al. 2019).

From planetesimals to planets

Streaming instability is found to produce planetesimals of $10 - 200$ km in size (Polak & Klahr 2023) which is also the observed size range for primordial asteroids in our asteroid belt (Ferrone et al. 2023). Unlike pebbles and dust particles, planetesimals are held together by self-gravity rather than material strength. They are only weakly coupled to the gas which reduces their radial drift and relative velocities. This allows planetary embryos to grow through mutual collisions, which is sped up by gravitational focusing. This phase is called the runaway growth phase (Wetherill & Stewart 1989) because the planetary embryos grow faster the heavier they are ($\dot{m}/m \propto m^{1/3}$, where m is the mass of the embryo (Ida & Makino 1993).

The runaway growth slows down to $\dot{m}/m \propto m^{-1/3}$ when the mass of the planetary embryos becomes comparable to the total mass of the smaller planetesimals in the disk (Ida & Makino 1993), at what is called the planetesimal isolation mass, which is roughly equal to the weight of the Moon or Mars. The growth slows down because the planetary embryos have accreted a significant portion of the nearby planetesimals and they are massive enough to stir up the remaining planetesimals which weakens the effect of the gravitational focusing. Since the growth rate now decreases with the planetary embryo mass, the masses and growth rates of the planetary embryos start to equalize while preventing small planetesimals from growing

further. Due to the even growth of a small group of embryos and suppression of planetesimals, this phase is called the oligarchic growth phase (Kokubo & Ida 1998).

During the oligarchic growth phase, the planetary embryos start to accrete pebbles once they reach a size of 1000 km (Ormel & Klahr 2010). At that size they are massive enough to form an atmosphere which then captures the pebbles from the surrounding gas, allowing them to rapidly grow beyond the planetesimal isolation mass (Lambrechts & Johansen 2012). The now protoplanets grow by pebble accretion until they become massive enough to open a partial gap in the gas disk, creating a pressure bump near the planet that stops the inward drift of the pebbles and thus their own growth (Lambrechts et al. 2014; Morbidelli & Nesvorny 2012). This pebble isolation mass is equal to several Earth masses depending on the disk parameters (Bitsch et al. 2018).

When the pebble accretion stops, the envelope of the protoplanet is no longer supported by the accretional heat and starts to contract (Lambrechts & Johansen 2014). If the protoplanet is massive enough, the envelope is not hydrostatically stable and rapidly grows via runaway gas accretion (Perri & Cameron 1974). The critical mass for runaway gas accretion is estimated to be around ten Earth masses (Bodenheimer & Pollack 1986; Mizuno 1980) and depends on the distance to the star, the heating of the envelope, and its cooling efficiency (Piso & Youdin 2014).

Observational evidence of this growth phase is limited as planetesimals and their collisions are hidden inside the disk. Observations find that the dust disks are significantly smaller than the gas disks, implying inward dust drift which is a prerequisite for pebble accretion (Long et al. 2022; Trapman et al. 2020). The next observable phase of planet formation can be obtained by assuming that the gaps and asymmetric features in the dust and gas disks are created by a planet. The mass of the planet can then be estimated from the gap width using hydrodynamical models (Dipierro et al. 2015; Kanagawa et al. 2021; Paardekooper & Mellema 2004). When planet has grown to $\gtrapprox$ 1 Jupiter mass, it will open a gap in the gas disk. The high amount of gravitational energy released by gas being accreted onto the gas giant is bright enough to be directly observed, as was done for the gas giants in the system PDS 70 (Haffert et al. 2019).

Forming a planetary system

The final shape of the planetary system is determined by the lifetime of the disk, the growth rate of the protoplanets, and their interaction with the gas giants that are thought to have formed first. Rocky planets do not grow to gas giants because the critical mass for runaway growth is higher closer to the star (Ormel et al. 2021) and therefore cannot be reached within the lifetime of the gas disk ($\approx$ 3 Myr, Ribas et al. 2015). Instead, if the pebble flux is high enough, the planetary embryos reach the pebble isolation mass, migrate inward, and merge into super-earths of 5 – 10 Earth masses (Lambrechts et al. 2019).

If the pebble flux is low, either due to a low amount of dust in the disk or due to pebbles being trapped in pressure bumps outside the snowline or by the gap of a gas giant (Morbidelli et al. 2015), then the planetary embryos will not grow beyond the planetesimal isolation

mass (Moon to Mars size), see Lambrechts et al. (2019). After the gas disk dissipates and no longer stabilizes the orbits of the embryos they merge into Earth-like planets (less than 5 Earth masses). The final planet system emerges after this giant-impact phase, which lasts for a few 100 Myr (Chambers 2001). Due to the release of gravitational energy during accretion and radioactive heating, protoplanets are initially born as hot magma worlds which makes studying the growth process beyond the planetesimal accretion phase in our solar system more complicated, see Lichtenberg et al. (2023) for a review.

2.3 Planet formation in close binaries

In binary systems, planets are found on two different types of orbits, S-type (satellite type) orbits, in which the planet orbits one of the stars, and P-type (planetary type) orbits, in which the planet orbits both stars (Dvorak 1982). Both orbit types are illustrated in Fig. 2.3.1. Most P-type planets are detected near the stability limit (Holman & Wiegert 1999), meaning their orbits would be unstable if they were closer to the binary. The emerging picture is that P-type planets form at larger distances and migrate inwards to their current positions, see Penzlin et al. (2021) and references therein.

At the time of this writing, there are less than three dozen known circumbinary (P-type) planets[3]. Due to the small number of detections, the current statistics are inconclusive. However, observations suggest that giant planets occur at rates similar to those around single stars (Martin et al. 2019), while the occurrence rate of Earth-like planets is lower. The dearth of Earth-like planets may be caused by the ejection due to gravitational interactions with gas giants (Fitzmaurice et al. 2022) or the binary system (Martin & Fitzmaurice 2022). Therefore, it is believed that beyond the stability limit the planet formation process is unaffected by the perturbations of the binary and proceeds as it does around single stars (Bromley & Kenyon 2015).

For S-type planets, on the other hand, there is a clear observable suppression of planet occurrence rates in close binary systems (Kraus et al. 2016). The red histogram in Fig. 2.3.2 shows the distribution of planet-hosting binary stars, while the blue line shows the distribution of binary systems in general. The suppression of planet formation can be inferred from the deficit of systems with separations of less than 200 au. The efficiency of planet formation drastically declines for separations around 47 au, which is why in the context of planet formation, binaries closer than 40 au are called *c*lose binary systems (Kraus et al. 2016).

Disks in close binaries

Circumstellar disks are believed to be the birthplace of planets in close binaries. These disks are observed to have shorter lifetimes (Cieza et al. 2009; Kraus et al. 2012) and to be less massive (Andrews & Williams 2005; Harris et al. 2012) than disks around wide binaries or single stars. They are also expected to be truncated in size by tidal interaction with the

[3]For an up-to-date list of confirmed circumbinary planets, see https://exoplanet.eu/planets_binary_circum

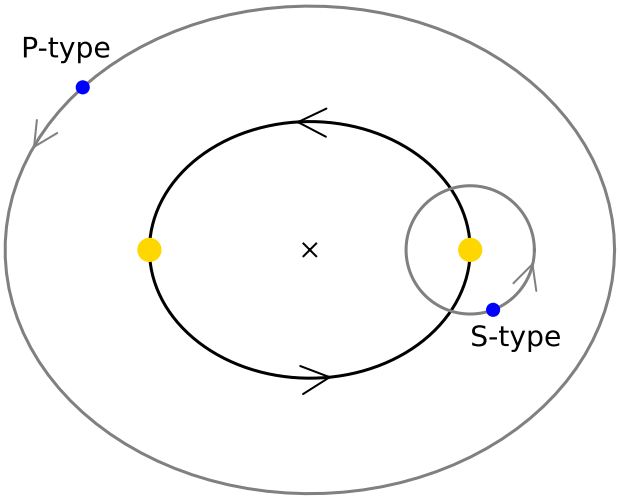

Figure 2.3.1. *Sketch of a planet-type orbit (P-type, orbits both stars) and a satellite-type orbit (S-type, orbits one of the stars) in binary systems.*

companion star (Artymowicz & Lubow 1994). More recently it became possible to observe the sizes of the dust disks (Cox et al. 2017; Manara et al. 2019; Zurlo et al. 2023) and gaseous disks (Rota et al. 2022). The gas disks are found to be in agreement with the theoretical, predictions while the dust disks are found to be smaller than expected for single stars, which can be explained by dust growth and the faster radial drift in close binaries (Zagaria et al. 2021a; b).

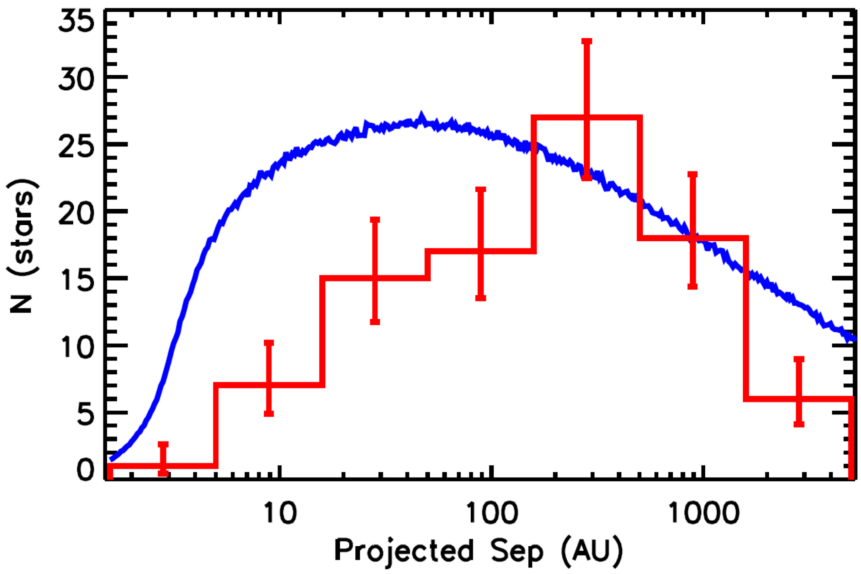

Figure 2.3.2. *Image credit: Kraus et al. 2016. The red histogram presents the distribution of planet-hosting binary stars. It shows a clear deficit of systems with separations less than* 200 au *compared to the expected distribution of binary systems from Raghavan et al. (2010), shown as the blue line.*

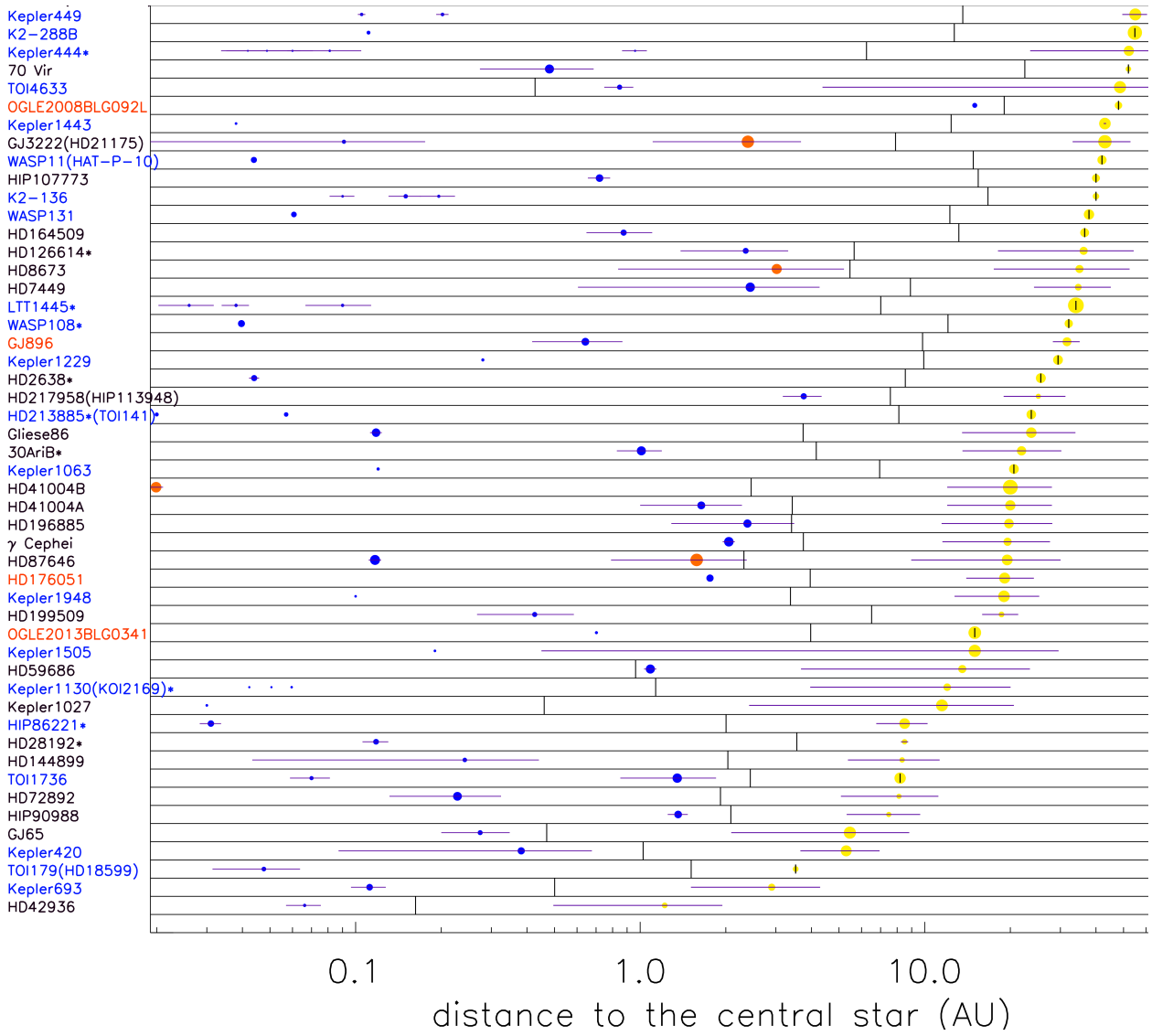

Figure 2.3.3. *Image credit: Philippe Thebault*[4] *(Thebault & Haghighipour 2015). List of detected S-type planets in close binaries.*

Challenges for planet formation in close binaries

Despite the unfavorable conditions for planet formation in close binaries, there are a growing number of detected planets in close binary systems (Thebault & Haghighipour 2015) which are shown in Fig. 2.3.3. Especially the observations of coplanar multi-planet systems such as Kepler-444 are taken as evidence that planet formation can succeed in close binaries (Dupuy et al. 2016).

The Kepler-444 system is a binary with a semi-major axis of 52 au and an eccentricity of 0.55, leading to a minimum distance during periastron of 23.5 au (Zhang et al. 2023). The system also hosts 5 tightly packed, coplanar planets orbiting the primary (Dupuy et al. 2016). The coplanarity of the system makes it unlikely that the binary semi-major axis has shrunk via a flyby event after the planets had already formed or that the planets were formed somewhere else and captured by the primary star after a scattering event, indicating that the

[4] See https://exoplanet.eu/planets_binary for an up to date list of confirmed S-type planets in close binaries.

planets have formed in the disk of the primary star. Planets forming in the short-lived disks of close binaries under the perturbing influence of the companion star implies that the planet formation process is both efficient and robust which makes close binaries an interesting target for planet formation studies.

The presence of a companion affects all stages of planet formation inside the disk around the primary, as discussed in detail in Thebault & Haghighipour (2015). The microscopic dust particles follow the gas and collide due to their Brownian motion, allowing them to hit and stick together. While this process itself is identical to that around single stars, the companion star perturbs the gas, launching spiral waves that move through the disk and heat the gas, potentially evaporating ice particles and moving the snow line with the binary period (Picogna & Marzari 2013).

The pressure maxima inside the spiral waves can trap dust pebbles, but they also cause hydraulic jumps that prevent dust from settling to the midplane (Picogna & Marzari 2013). While the streaming instability has not been explicitly studied in the context of binaries, externally driven turbulence is expected to weaken the streaming instability (Lim et al. 2024). The vertical mixing of dust by spiral waves can also be expected to weaken pebble accretion of planetary embryos, as was shown for spiral waves caused by giant planets in Bae et al. (2016).

Studies on planet formation in close binaries focused on the planetesimal accretion phase because that phase is better understood and easier to model. The issues that planet accretion faces inside a close binary system are illustrated in Fig. 2.3.4. It shows the eccentricity and longitude of pericenter of an initially circular planetesimals cloud around the primary star of a close binary system after 400 binary orbits while the gas drag was ignored.

The gravitational interaction between the planetesimals and the companion star excites the eccentricities of the planetesimals and forces them into an anti-aligned orbit with the binary. The eccentricities of the planetesimals oscillate with the distance to the primary star and these oscillations become narrower with time, eventually leading to orbital crossing (Marzari & Scholl 2000). Orbital crossing due to different eccentricities is illustrated in Fig. 2.3.5(a). At the locations of orbital crossing, the collision velocities are high, leading to destructive collisions that can grind planetesimals down to dust (Thébault et al. 2004). These studies also found that gas drag can dampen the eccentricities and align the planetesimals with the gas disk, reducing the collision velocities of equal-sized planetesimals.

Shortly after that, it was realized that the efficiency of the gas drag depends on the size of the planetesimals (Paardekooper et al. 2008; Thébault et al. 2006; 2008). Small planetesimals are more affected by the gas and are damped more efficiently than large planetesimals, as illustrated in Fig. 2.3.6. The figure shows the eccentricity and longitude of pericenter of the planetesimals cloud and the gas disk under the influence of gas drag in an eccentric, precessing disk. The small planetesimals (blue dots) have damping timescales that are shorter than the precession timescale of the disk, which causes the planetesimals to align with the disk. Larger planetesimals (red dots) are less affected by the gas. The eccentricities oscillations caused

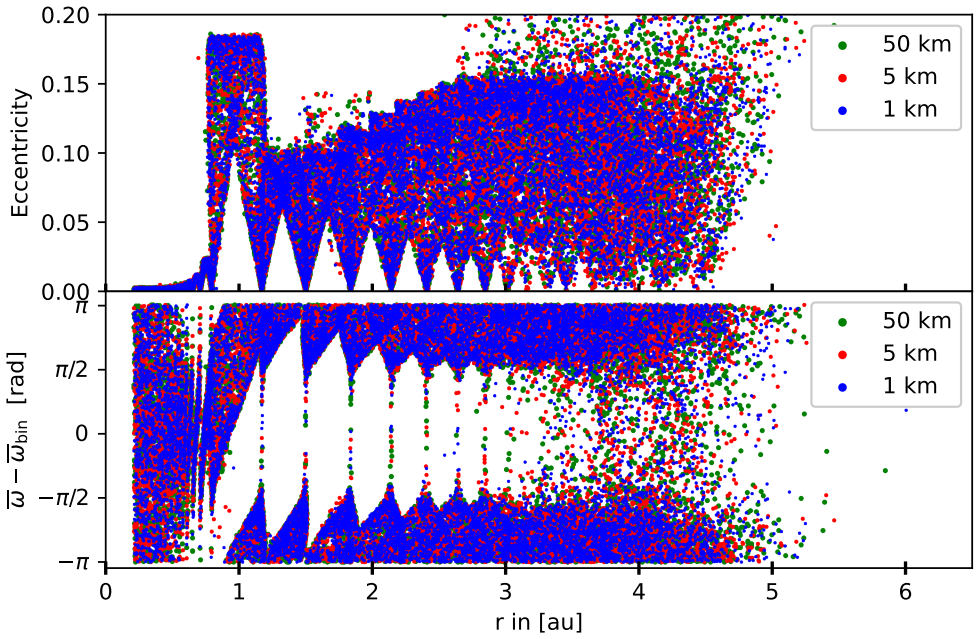

Figure 2.3.4. *Planetesimal eccentricity and longitude of pericenter in a binary system after 400 binary orbits without gas drag. The particles were initially on circular orbits.*

by the companion are damped but their damping timescales are longer than the precession timescale of the disk. Therefore, they are not aligned with the disk but rather oscillate around the alignment and forced eccentricity caused by the companion star (Paardekooper et al. 2008). The even larger planetesimal (green dots) still display the eccentricity oscillations caused by the companion star but with damped oscillation amplitudes.

The different eccentricities and longitudes of pericenter of the planetesimals lead to orbital crossings due to eccentricities Fig. 2.3.5(a) and misaligned orbits Fig. 2.3.5(b) between planetesimal populations of different sizes, preventing planetesimal growth.

Rafikov (2013) noted that the gravity of the disk should be considered, as it is independent of size and therefore affects all planetesimals equally. The effects of the disk gravity have been studied in detail by Rafikov & Silsbee (2015) and used to develop a framework to follow planetesimal growth in a global simulation in Silsbee & Rafikov (2021). They found that if the disk eccentricity is low, apsidally aligned to the binary, and sufficiently massive then planetesimal growth can succeed in close binaries. Under these conditions, there are radii inside the disk where the forced eccentricity of the large planetesimals is equal to the disk eccentricity of the small planetesimals, allowing for low collision velocities of different-sized planetesimals and thus for planetesimal growth.

The current understanding whether planet formation can succeed in close binaries is therefore hinging on the dynamic of the circumstellar disks. This has led to a number of studies that focus on the dynamics of the primary disk in close binaries (Fragner & Nelson 2010; Kley et al. 2008; Martin et al. 2020; Marzari et al. 2009; 2012; Müller & Kley 2012; Paardekooper et al. 2008).

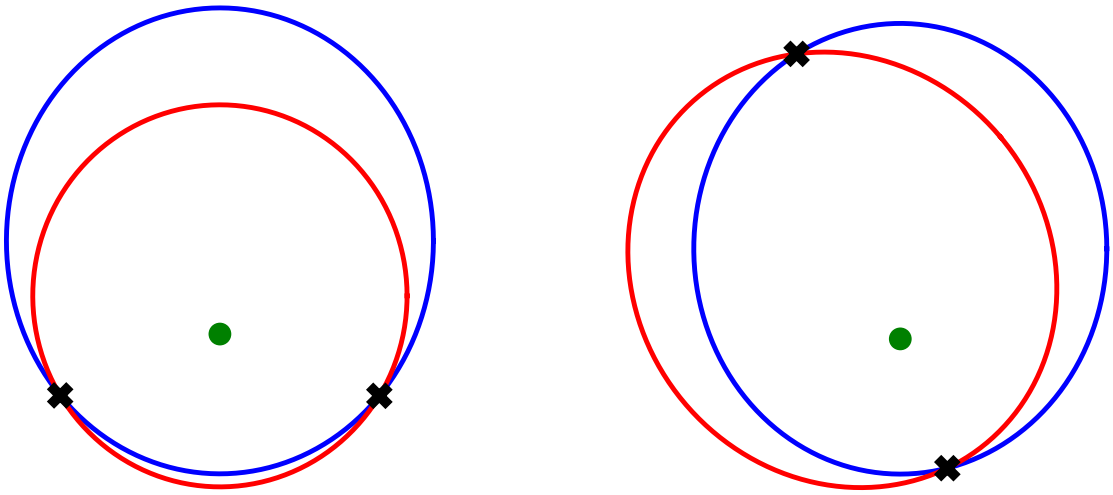

(a): *Different eccentricities.* **(b):** *Different longitudes of periastron.*

Figure 2.3.5. *Sketch of orbital crossing between two planetesimals with different eccentricities* **(a)** *or misaligned orbits* **(b)**.

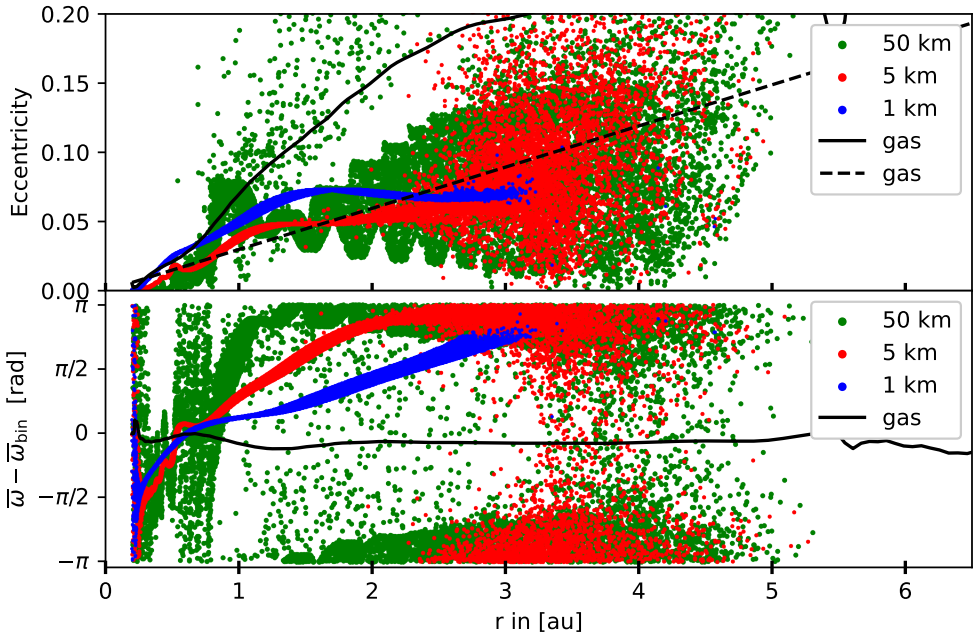

Figure 2.3.6. *Planetesimal eccentricity and longitude of pericenter in a binary system after 400 binary orbits. The particles are embedded in an eccentric, precessing disk around the primary star and were initially on circular orbits.*

Fig. 2.3.7(a) shows an artistic illustration of the hierarchical triple system GG Tau A, which is a hierarchical triple system with a massive circumbinary disk and a circumstellar disk around the primary star. The semi-major axis between the primary star and the spectroscopic binary companion is 34 au with an eccentricity of 0.28 (Cazzoletti et al. 2017). Detected signatures that hint at ongoing planet formation (Phuong et al. 2020) make this system a prime target for planet formation studies in close binaries.

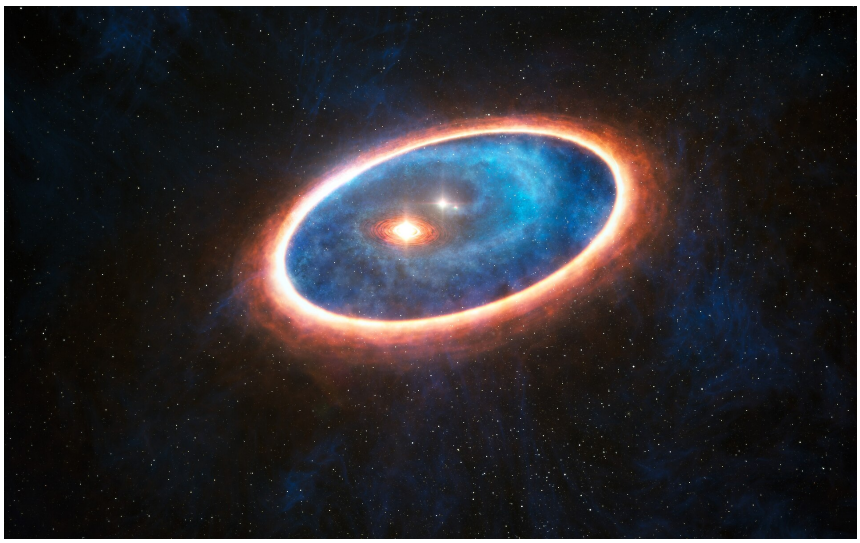

(a): *Image credit: ESO/L. Calçada*[5]*. Artistic illustration of GG Tau A, a hierarchical triple system surrounded by a massive circumbinary disk.*

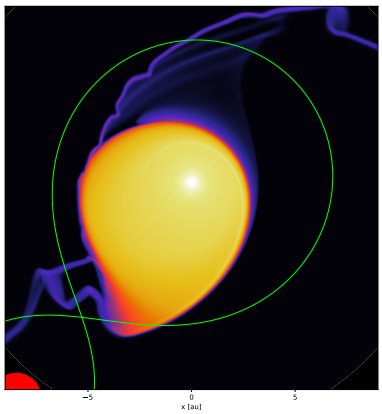

(b): *Simulation of the primary disk in the binary system Gamma Cephei. The companion star is marked with a red dot and the green line indicates the Roche lobe.*

Figure 2.3.7. *Sketch of how disks in close binary systems might look like* **(a)** *and how they appear in two-dimensional simulations* **(b)**.

Fig. 2.3.7(b) shows a simulation of the primary disk in the binary system Gamma Cephei (Jordan et al. 2021). The system is often used as a test bed for planet formation in close binaries, due to the detection of a planet around the primary by Hatzes et al. (2003). The green line indicates the Roche lobe of the binary, inside which objects are gravitationally bound to the respective star. As can be seen in the figure, during the periastron passage the disk overflows the Roche lobe and spiral arms are launched due to the perturbation of the companion. This, together with the asymmetry of the disk, makes it currently seem unlikely that planet formation could succeed in this system. I will go into more detail about the dynamics of the disk in this system and discuss the implications for planet formation in Chapter 4 and Chapter 5.

2.4 Cataclysmic variable formation

For all stars, the hydrogen-burning phase eventually comes to an end. In a binary star system, the primary star will leave the hydrogen-burning phase first, because more massive stars evolve faster than lighter stars. The primary then expands and becomes a red giant, a transformation that can change the entire binary system.

There is a large variety of different close binary systems that can emerge when the stars in binary systems evolve past their main sequence phase. I refer to Belloni & Schreiber (2023) for an overview of compact accreting systems and their formation channels.

One kind of compact accreting systems are cataclysmic variables (CVs), which consist of a white dwarf and a Roche lobe-filling companion star, and are known for their large variations

[5]Source: https://www.eso.org/public/news/eso1434/

in brightness over time. From the family of CVs, I will discuss only the non-magnetic subset of CVs that undergo nova outbursts, in order to introduce the SU UMa dwarf novae that I have studied in detail. A comprehensive overview of the zoo of CVs and their outbursts can be found in Warner (1995).

CVs most likely originate from binary systems with primary masses between 1.5 and $6M_{\odot}$, mass ratios between $m_2/m_1 = 0 - 0.4$ (Zorotovic et al. 2011), and binary separations of $1 - 10$ au (Ritter 2010). Due to the higher mass, the primary star will evolve much faster than the secondary star and reach the end of its main sequence phase first. The primary then expands and evolves into a red giant and starts to overflow its Roche lobe (Ritter 2010). A sketch of this process and the events that follow are shown in Figure 2.4.1. The Roche lobe overflow causes mass to be transferred from the red giant to its main sequence companion. As the mass moves away from the center of mass, the binary separation and thus the Roche lobes of the stars shrink (Ritter 2010).

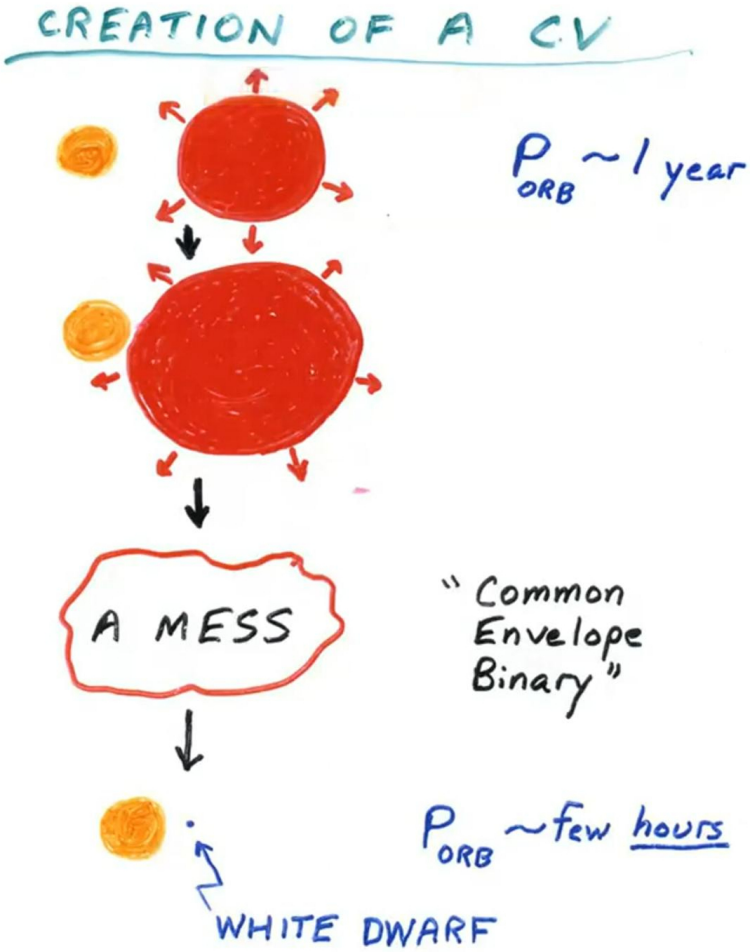

Figure 2.4.1. *Image Credit: Joseph Patterson, AAVSO Webinar 2020. Cartoon of the formation of a cataclysmic variable.*

A red giant has a degenerate core, meaning that the core is not supported by thermal pressure generated by fusion but rather by the electron degeneracy pressure. This causes the red giant to expand when losing mass, leading to more mass loss and binary shrinkage.

The accretional heating by the transferred mass causes the companion to expand to giant dimensions itself leading to a deep contact of the two stars (Ritter 2010).

Due to the shrinking binary separation, the companion star will enter the shell of the red giant eventually, leading to a common envelope phase between the companion and the core of the primary. This leads to a plunge-in phase, see Ivanova & Nandez (2016) for insights from numerical simulations, where the orbit rapidly shrinks and the envelope is ejected. The entire common envelope phase is still poorly understood. Estimates for its duration range from a few hundred days from numerical simulations (Ivanova & Nandez 2016) to a few hundred years from theoretical estimates (Ritter 2010). Due to the brevity of the common envelope phase, the mass of the companion star remains effectively unchanged, while the system ejects $50 - 80\%$ of the mass and up to 99% of the angular momentum (Ritter 2010).

If the envelope does not disperse quickly enough, the two stars will merge, leaving behind a single white dwarf. Otherwise, a cataclysmic variable emerges, consisting of a white dwarf and a main sequence star with orbital periods of a few hours. The system will slowly lose angular momentum due to gravitational radiation and, if the companion is massive enough to have a radiative core ($m_2 \gtrsim 0.2\ M_\odot$), also due to magnetic braking (compare Ritter 2010). This causes the binary separation to shrink until the companion fills its Roche lobe and mass transfer starts, pushing the binary apart and compensating for the loss of angular momentum.

2.5 Cataclysmic variables

Fig. 2.5.1 shows an artistic illustration of a cataclysmic variable system (CVs). It depicts the white dwarf on the left side of the figure and the Roche lobe-filling companion star on the right side. The companion pushes gas over the Lagrange L_1 point into the Roche lobe of the white dwarf (Lubow & Shu 1975). Due to the conservation of angular momentum, the gas does not hit the white dwarf directly, but instead begins to orbit it, forming an accretion disk. The location where the gas stream impacts the accretion disk is called the "hotspot" and is seen as a bright spot near the center of the image.

The average white dwarf mass in CVs is $0.8\ M_\odot$ which is significantly higher than the average white dwarf mass of single stars of $0.6\ M_\odot$. This discrepancy itself is an active field of research, see Zorotovic & Schreiber (2020). The white dwarf is accompanied by an M dwarf or sub-stellar companion with masses between 0 and $0.3\ M_\odot$ (Patterson et al. 2005). Both the white dwarf and the companion are faint, making the accretion disk the dominant light source of the system even during the non-outburst phases called quiescence (Patterson et al. 2005). Typical quiescent luminosities of CVs are a few percent of the solar luminosity (Coppejans et al. 2016).

However, CVs do undergo outbursts that cause large increases in brightness over time, called novae, which is Latin for "new" because they were first observed as new stars in the sky. They are classified into different classes according to the magnitude of their brightness variations caused by the different mechanisms that lead to the outburst.

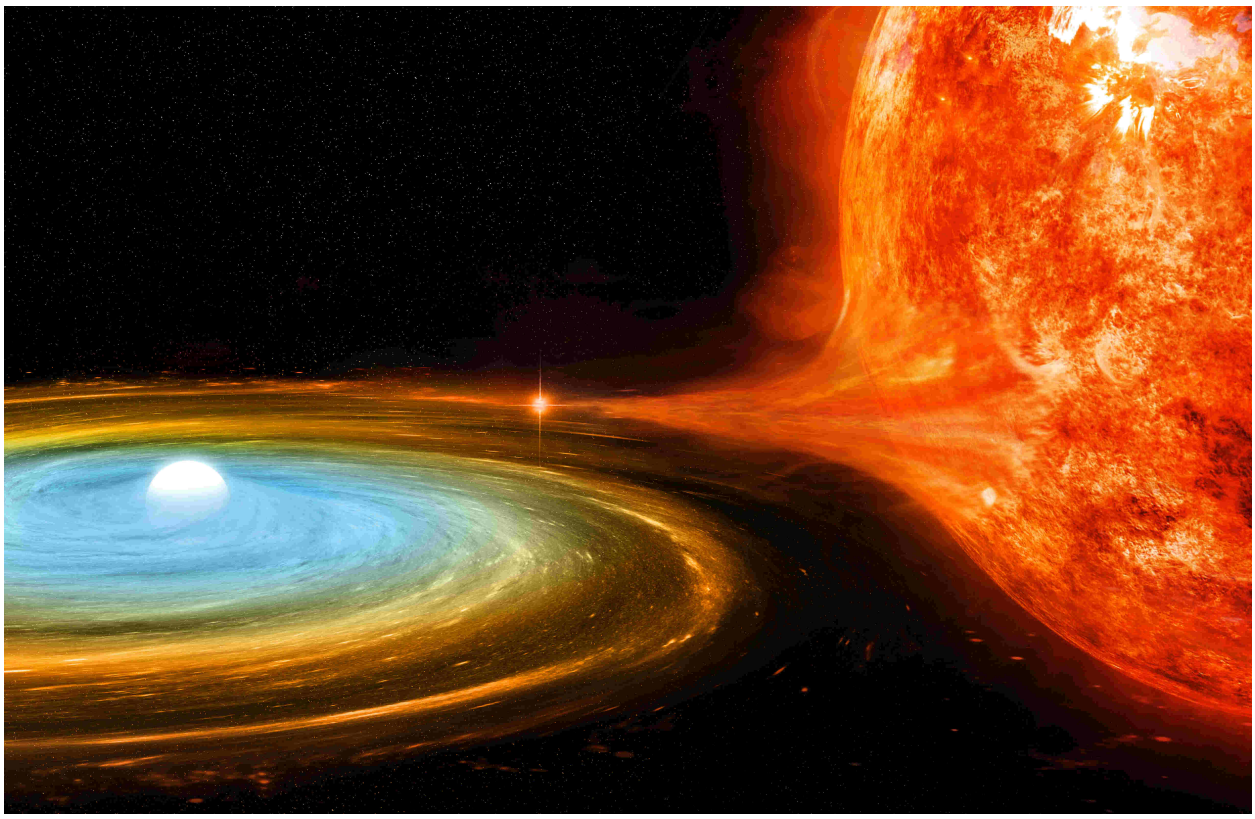

Figure 2.5.1. *Image credit: NASA/CXC/M.Weiss*[6]*. Artistic illustration of a cataclysmic binary. The companion star is pushing gas towards the white dwarf. The hotspot, i.e. the location where the mass stream impacts the accretion disk, is seen as a bright spot near the center of the image.*

Supernovae

The largest brightness variations that can occur in CVs are Type Ia supernovae (Wang & Han 2012, Sect. 4.2). These occur when the mass of the white dwarf grows above the Chandrasekhar limit of 1.4 $M_\odot$ (Rotondo et al. 2011). At this mass the white dwarf will ignite a rapid fusion of carbon and oxygen to iron, leading to a thermonuclear explosion that destroys the white dwarf and releases a large amount of energy (Hoyle & Fowler 1960). Type Ia supernovae have peak luminosities of 5.5 billion times the luminosity of the Sun (Hamuy et al. 1996) and their homogeneous brightness evolution due to the specific white dwarf mass required to start the explosion makes them useful tools as standard candles for measuring extragalactic distances (Branch & Tammann 1992). Supernovae are no longer part of the cataclysmic variable family because there are other sources of supernovae, but I listed them anyway because of the common origin of the name.

Novae

The next smaller outburst are called classical novae or just novae. These are caused when the accumulated hydrogen on the surface of the white dwarf reaches a critical mass and starts to burn in an unstable manner, leading to thermonuclear runaway (Chomiuk et al. 2021). The accumulation of hydrogen and subsequent nova only occurs if the accretion rate is below a

[6]Source: https://www.nasa.gov/mission_pages/chandra/images/double-trouble-a-white-dwarf-surprises-astronomers.html

critical level ($\dot{m}_{\rm acc} > 10^{-7} {\rm M}_\odot/{\rm yr}$). Above the critical accretion rate, the accreted hydrogen is continuously and stably burned into helium (Chomiuk et al. 2021).

Novae outbursts do not destroy the white dwarf, but only eject a shell of the white dwarf from the system. Their recurrence time is inversely correlated with mass accretion rate and white dwarf mass, with typical recurrence rates of 10^4 to 10^7 years (Chomiuk et al. 2021). There are also extreme cases of novae that host a massive white dwarf near the Chandrasekhar limit and an accretion rate near the critical limit which outburst every couple of years and are therefore called recurrent novae (Chomiuk et al. 2021).

The critical mass for an outburst and the outburst brightness also scale inversely with the white dwarf mass, leading to fainter outbursts for recurrent novae compared to classical novae. Overall, the outburst luminosities range from 1 to 10^6 $L_\odot$ with a mean of 10^5 $L_\odot$ (Özdönmez et al. 2018), where $L_\odot$ is one solar luminosity. For classical novae, the outbursts are expected to lead to a net mass loss due to the observed enhancement of heavy elements from the white dwarf in the ejected material, leaving only recurrent novae as potential progenitors for Type Ia supernovae (Chomiuk et al. 2021; Wang & Han 2012).

2.6 Dwarf novae

The third and faintest brightness variation in non-magnetic CVs are dwarf novae, caused by a change in the brightness of the accretion disk around the white dwarf. The outbursts reach peak luminosities of about 1 $L_\odot$, last for a few days to weeks (Patterson 2011), and have fast recurrence times ranging from a few days to a few years (Coppejans et al. 2016; Lasota 2001). The mass-transfer rates of dwarf novae are well below the critical accretion rate for classical novae (Dubus et al. 2018), dwarf novae could therefore simultaneously be classical novae that are building up a hydrogen shell on the surface of the white dwarf (Shara et al. 1986).

Dwarf novae period gap

Dwarf novae (DN) are categorized into three groups based on their outburst properties, each named after a representative system: U Gem, Z Cam, and SU UMa. The different DN groups are separated by a period gap, with U Gem and Z Cam systems having periods in the range of 3 – 16 h and are separated by a dearth of systems with periods between 2 – 3 h from the SU UMa systems, which have periods between 80 min – 2 h (Ritter 2010). The currently favored model for the period gap is the disruption of magnetic braking due to the transition from a radiative to a convective core in the companion star (Belloni & Schreiber 2023). While this hypothesis was proposed by Spruit & Ritter (1983), the reason for the reduced angular momentum loss has since changed and is now attributed to an increase in the complexity of the magnetic field on the surface of the companion star, which reduces the efficiency of magnetic braking (Garraffo et al. 2018; Taam & Spruit 1989).

Using a mass-radius relation, the period gap can be translated to a critical mass ratio of $q = 0.35$ or to a critical companion mass (Patterson et al. 2005). Above the gap, the companion star has a high mass $m_2 \geq 0.2\ M_\odot$ with a radiative core. The high angular momentum loss

due to magnetic braking leads to a high mass transfer rate, which drives the secondary out of thermal equilibrium and increases its size (Spruit & Ritter 1983). When the mass transfer stops due to the disruption of magnetic braking, the companion star will shrink and the system becomes detached (Spruit & Ritter 1983). The binary separation, and thus the orbital period, will then shrink due to gravitational radiation (Paczynski & Sienkiewicz 1981), which is an order of magnitude weaker than magnetic braking, until they come into contact again below the period gap and with a lower mass transfer rate.

Dwarf novae zoo

Due to the period gap, U Gem and Z Cam systems have larger binary separations, higher mass ratios, and higher mass transfer rates than SU UMa systems. These parameters, together with other effects such as the magnetic field strength of the white dwarf, the possible inclination of the disk, and the physical processes in the disk, will shape the outburst properties.

In some cases, the dwarf novae systems are observed edge-on as eclipsing binaries as depicted in Fig. 2.6.1. In that case, the companion star occults the accretion disk, which allows for precise measurements of disk quantities like the size and the radial temperature profile even though the system itself cannot be resolved.

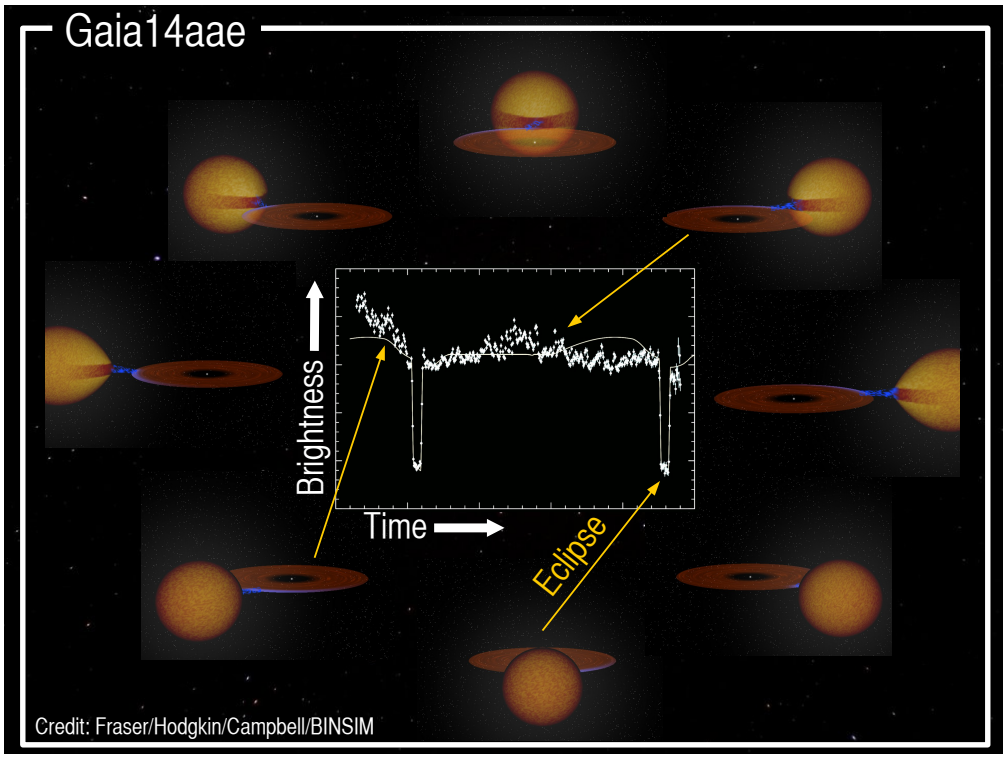

Figure 2.6.1. *Image credits: M. Fraser, S. Hodgkin, H. Campbell and the BinSim software*[7]*. The central plot shows the light curve of the cataclysmic variable Gaia14aae during one orbit. The plot is surrounded by sketches of the expected orientation of the system to explain the light curve.*

This, together with the observable friendly timescales of the systems, makes dwarf novae ideal laboratories for testing accretion disk models and disk-binary interactions. An overview

[7] Source: https://www.skyatnightmagazine.com/news/unique-cannibalising-binary-system-discovered

of the different models for dwarf novae can be found in Hameury (2020); Lasota (2001); Warner (1995).

Fig. 2.6.2 shows the light curves of different classes of dwarf novae, the data has been taken from AAVSO and from the Kepler mission via *Lightkurve* (Astropy Collaboration et al. 2022; Lightkurve Collaboration et al. 2018, December). The first panel shows the U Gem system SS Cyg, which is characterized by normal dwarf novae outbursts, with every other outburst being a long outburst with a flat top. The middle panel shows the Z Cam system Z Cam, which in addition to normal and long outbursts also has standstills. Standstills occur when the system does not return to quiescence after an outburst, but remains at an elevated brightness level, which can last from a few days to a few years (Simonsen et al. 2014). The bottom panel shows the SU UMa system V1504 Cygni. In these systems, every other normal outburst turns into a superoutburst, which is brighter and longer than normal outbursts. During the slow decline of the superoutburst, small brightness variations called superhumps appear, which have a slightly longer period than the orbital period of the system.

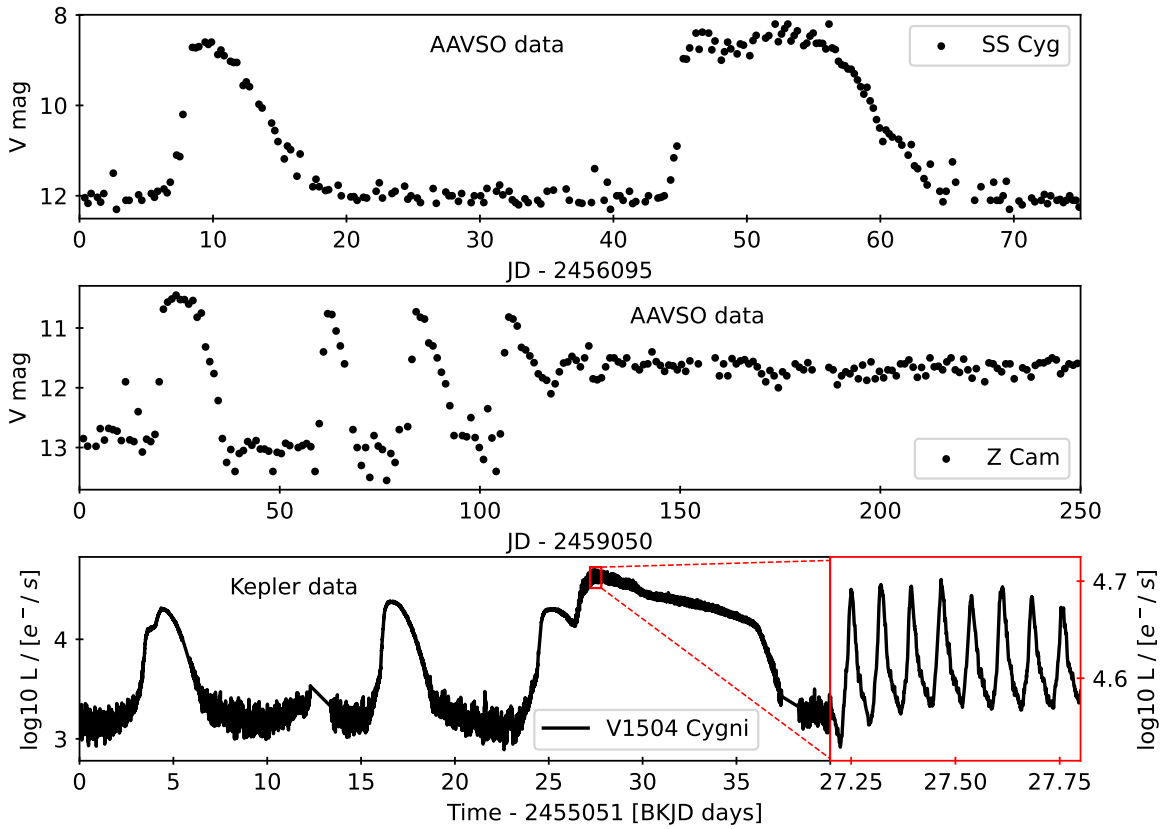

Figure 2.6.2. *Example light curves of the different classes of dwarf novae. Top: SS Cyg, which is a U Gem system. Middle: Z Cam, which is a Z Cam system. Bottom: V1504 Cygni, which is a SU UMa system, the lower left corner shows a zoom in on the superhumps. These systems are observed face on, meaning the companion does not eclipse the accretion disk.*

There are two main models to explain the outbursts. In both models, the normal outbursts are caused by a thermal instability in the accretion disk. The disk mass increases with time due to the mass transfer from the companion star, which increases the disk temperature due to viscous heating. When the temperature in the disk reaches the hydrogen ionization

temperature, the opacity of the gas increases drastically, making the disk more opaque and reducing its cooling efficiency. The reduction in cooling efficiency as the temperature rises then leads to runaway heating of the disk, causing an outburst. The high disk temperature during the outburst leads to a high mass transfer rate through the disk, causing the disk to lose mass and return to quiescence after falling below the hydrogen ionization temperature (Hōshi 1979).

In addition to the thermal instability, the disk instability model (DIM) assumes that the transition from an optically thin to an optically thick disk also changes the disk structure from radiative to convective, increasing the angular momentum transport in the disk and enhancing the outburst (Meyer & Meyer-Hofmeister 1981; Mineshige & Osaki 1983). The DI model has been extended to the thermal-tidal instability model (TTIM) by including tidal interactions with the companion (Osaki 1989; Whitehurst 1988). During normal outbursts, the disk grows in size until it reaches the 3:1 resonance radius (where the gas orbits the white dwarf three times for each orbit of the companion star). Near this radius, the companion exerts strong tidal torques on the gas (Lubow 1991), driving angular momentum transport and eccentricity growth. The higher angular momentum transport explains the longer duration of superoutbursts, and the disk eccentricity explains the superhumps (Osaki 1989). Above the period gap, the disk does not reach the 3:1 resonance radius and remains circular, which can explain the long outbursts (Buat-Ménard et al. 2001).

The difference between U Gem and Z Cam systems is explained by a critical mass transfer rate, where the transfer rate from the secondary is greater than the mass loss from the disk during the outburst (e.g. Simonsen et al. 2014). Above the critical mass transfer rate are the nova-like systems, where the disk is permanently in an outburst state. U Gem systems are well below the critical mass transfer rate while Z Cam systems are close to it (Dubus et al. 2018), such that a small increase (factor of two) in the mass transfer rate can lead to a standstill (Simonsen et al. 2014).

An alternative to the DIM is the mass transfer instability model (Bath & Pringle 1981), which explains the outbursts by a large increase (factor of ~ 100, e.g. Schlindwein & Baptista 2024) in mass transfer caused by an instability in the companion. Similarly, as an alternative to the TTI, superoutbursts and superhumps can be explained by an additional enhancement and modulation of the mass transfer rate due to the irradiation of the companion star by either the accretion disk (Smak 2009a) or the boundary layer where the disk is accreting on the white dwarf (Osaki 1985).

These models are not exclusive and the described effects can be active simultaneously. It remains to be discerned to which degree each effect contributes to the observed events and whether additional mechanisms are needed.

I refer to Baptista & Schlindwein (2022) for a recent study arguing in favor of the mass transfer instability model, and to my own work (Jordan et al. 2024), presented in Chapter 6, in which we argue in favor of the TTI model based on the results of our non-isothermal, two-dimensional hydrodynamic simulations.

3 Theoretical background and code implementation

During my PhD, my colleague Thomas Rometsch and I have used a version of the FARGO code (Baruteau 2008; Masset 2000) which was maintained by the computational physics group at the University of Tübingen (CPT). We have both debugged, modernized, and extended the code to match the requirements of our research. After ~5 years of development and many exciting simulations, we, with the help of friends and colleagues, had revised the entire code and added so many new features and tests that we decided to publish our code as the FARGOCPT code (Rometsch et al. 2024) which is freely available under https://github.com/rometsch/fargocpt.

The paper starting on the following page, explains the code and documents all the physical equations that are needed to study the interaction between stars, planets, gas, and dust in an astrophysical context.

The changes to the code that are required to simulate the circumbinary disk in the frame of one of the stars are described in detail in Appendix A. And my thoughts and concerns about how to approximate the effects of vertical stratification of astrophysical disks in two-dimensional, polar coordinate, hydrodynamical codes are described in Appendix B.

A&A, 684, A192 (2024)
https://doi.org/10.1051/0004-6361/202348687
© The Authors 2024

Astronomy & Astrophysics

FargoCPT: 2D Multiphysics code for simulating disk interactions with stars, planets, and particles⋆

Thomas Rometsch[1], Lucas M. Jordan[2], Tobias W. Moldenhauer[2], Dennis Wehner[3], Steven Rendon Restrepo[4], Tobias W. A. Müller[2], Giovanni Picogna[5], Wilhelm Kley[2,†], and Cornelis P. Dullemond[1]

[1] Institut für Theoretische Astrophysik, Zentrum für Astronomie (ZAH), Universität Heidelberg, Albert-Ueberle-Str. 2, 69120 Heidelberg, Germany
e-mail: rometsch@uni-heidelberg.de
[2] Institut für Astronomie und Astrophysik, Universität Tübingen, Auf der Morgenstelle 10, 72076 Tübingen, Germany
[3] Fakultät für Physik, Universität Duisburg-Essen, Lotharstraße 1, 47057 Duisburg, Germany
[4] Leibniz-Institut für Astrophysik Potsdam (AIP), An der Sternwarte 16, 14482 Potsdam, Germany
[5] Universitäts-Sternwarte, Fakultät für Physik, Ludwig-Maximilians-Universität München, Scheinerstr. 1, 81679 München, Germany

Received 21 November 2023 / Accepted 29 January 2024

ABSTRACT

Context. Planet-disk interactions play a crucial role in the understanding of planet formation and disk evolution. There are multiple numerical tools available to simulate these interactions, including the commonly used FARGO code and its variants. Many of the codes have been extended over time to include additional physical processes, with a focus on their accurate modeling.
Aims. We introduce FargoCPT, an updated version of FARGO that incorporates other previous enhancements to the code, to provide a simulation environment tailored to studies of the interactions between stars, planets, and disks. It is meant to ensure an accurate representation of planet systems, hydrodynamics, and dust dynamics, with a focus on usability.
Methods. The radiation-hydrodynamics part of FargoCPT uses a second-order upwind scheme in 2D polar coordinates, supporting multiple equations of state, radiation transport, heating and cooling, and self-gravity. Shocks are considered using artificial viscosity. The integration of the N-body system is achieved by leveraging the REBOUND code. The dust module utilizes massless tracer particles, adapted to drag laws for the Stokes and Epstein regimes. Moreover, FargoCPT provides mechanisms to simulate accretion onto stars and planets.
Results. The code has been tested in practice in the context of multiple studies. Additionally, it comes with an automated test suite for checking the physics modules. It is available online.
Conclusions. FargoCPT offers a unique set of simulation capabilities within the current landscape of publicly available planet–disk interaction simulation tools. Its structured interface and underlying technical updates are intended to assist researchers in ongoing explorations of planet formation.

Key words. hydrodynamics – methods: numerical – protoplanetary disks – planet–disk interactions – binaries: close – novae, cataclysmic variables

1. Introduction

Planet migration is a crucial component of our understanding of planet formation. Besides analytical or semi-analytical calculations, one way to study it is via hydrodynamic calculations coupled with gravitational N-body simulations. Specifically, in the context of planet formation, the shape of the hydrodynamic object resembles a thin, flared disk. The computer program FARGO (Masset 2000) is meant to simulate these protoplanetary disks by numerically solving the hydrodynamics equations on a staggered grid using a second-order upwind scheme. It includes a special algorithm, with the same name, which can relax the time step constraint by making use of the axial symmetry of the disk flow, thereby reducing the computational cost of simulations. The specific form of the hydrodynamic equations solved by the program is stated later in Sect. 2.

Because FARGO is tailored to the study of protoplanetary disks, the code uses a cylindrical grid, reflecting the major symmetry of the system. One main assumption used in the code is that the simulated disks are thin in the sense that their vertical extent is small compared to the radial distance from the central star. This is the justification for approximating the three-dimensional (3D) disk with a two-dimensional (2D) representation. Using this approximation significantly reduces the required time for simulations of protoplanetary disks and enables the long-term study of these systems. In its original form, the code employed the (locally) isothermal assumption, in which the temperature is assumed to be fixed in time and only dependent on the distance from the central start. This allows for the energy equation to be solved analytically, while additionally reducing the computational cost of the simulation.

Over the past two decades, studies have shown that additional effects play an important role in the evolution of protoplanetary disks and their interaction with embedded planets (for overviews, see Kley & Nelson 2012; Baruteau et al. 2014; Paardekooper et al. 2023). The relevant physical processes include the heating and cooling of the gas (e.g., Baruteau & Masset 2008a; Kley & Crida 2008; Paardekooper & Papaloizou 2008; Lega et al. 2014; Masset 2017), self-gravity (e.g., Pierens & Huré 2005; Baruteau & Masset 2008b), and radiation transport (e.g., Morohoshi & Tanaka 2003; Paardekooper & Mellema 2006). We have added

⋆ The code is available at https://github.com/rometsch/fargocpt.
† Deceased.

Open Access article, published by EDP Sciences, under the terms of the Creative Commons Attribution License (https://creativecommons.org/licenses/by/4.0), which permits unrestricted use, distribution, and reproduction in any medium, provided the original work is properly cited.
This article is published in open access under the Subscribe to Open model. Subscribe to A&A to support open access publication.

all of these effects to our version of the FARGO code and made them fully controllable from the input file and verified their correctness through extensive testing. We also extended the number of physical quantities that are evaluated during the simulation and written to output files.

While there are multiple options to run planet–disk interaction simulations including the aforementioned effects, we have recognized a need for a simulation code that is not only able to simulate the relevant physical processes accurately, but is also easy to use. This is especially important for students and researchers who are not experts in modifying and compiling C/C++ or FORTRAN codes in a typical Linux environment. These skills can pose a significant hurdle when running simulations.

The primary aim behind publishing this code is to provide a comprehensive simulation tool for planet–disk interactions that remains accessible and useful to both students and more senior researchers. To this end, the testing suite for the physical modules is fully automated with pass-fail tests so it can be run after every future modification of the code to ensure that it is still working as intended.

On the physics side, a significant enhancement is the incorporation of radiation physics. Furthermore, the introduction of a particle module enables in-depth studies on the impact of embedded planet systems on the structure and dust distribution of planet-forming disks, a task that is currently often performed to model disk observations. We also added cooling and mass inflow functions and an updated equation of state specifically tailored to study cataclysmic variable systems. Additionally, the code can simulate the disk centered around any combination of N-body objects. This enables, for instance, simulations of circumbinary disks in the center of mass-frame or simulations of a circumsecondary disk in a binary star system.

Simulation programs for planet–disk interaction can, broadly speaking be organized into two main categories: Lagrangian and Eulerian methods. Lagrangian methods trace the dynamics of the disk by following the motion of a large number of particles. The most common example of this is the Smoothed Particle Hydrodynamics (SPH) method with a prominent example being the PHANTOM code (Price et al. 2018).

The Eulerian methods solve the hydrodynamics equations on a grid, which can either be fixed or dynamic. In this category, again, we can distinguish between two main approaches used in astrophysics: methods that require artificial viscosity and Godunov methods (Woodward & Colella 1984). Either of these methods can be implemented as a finite-volume or finite-difference method. Godunov methods solve the Riemann problem at the cell interfaces to compute the fluxes through the interfaces. This approach allows for an accurate treatment of shocks and an approximate treatment of smooth flows. Prominent examples include the PLUTO code Mignone et al. (2007) and the Athena++ code (Stone et al. 2020).

Schemes based on artificial viscosity can be derived as a finite-difference scheme from Taylor series expansions of the Euler equations (Woodward & Colella 1984). This technique assumes that the solution is smooth, which is not the case at discontinuities such as shocks. It approximates shocks by smearing out discontinuities into smooth regions of strong gradients via artificial viscosity. The ZEUS code (Stone & Norman 1992) and the FARGO code (which is based on the ZEUS code) are prominent examples of this approach. While these codes were classified as finite-difference schemes, they employed a staggered grid and implemented their advection step by splitting the domain into cells and computing the fluxes through the cell interfaces. The cell as a basic geometrical unit and the sharing of fluxes among adjacent cells, which ensures the conservation of the advected quantities to machine-precision by construction, warrant the classification of the advection scheme as "finite-volume" (Anderson et al. 2020). We lean towards this classification because it rests on an intrinsic property of the scheme. However, the crucial distinction seems to be the one between Godunov methods and methods that require artificial viscosity and the FARGO code family falls into the latter category.

While Godunov methods are (formally) more accurate when handling discontinuities such as shocks, the artificial viscosity methods are better at modeling smooth flows and, in practice, they are often more robust and easier to use. Both approaches have their advantages and disadvantages and the choice of which method to use depends on the specific problem at hand. For a specific example, see Ziampras et al. (2023b) who used both PLUTO and FARGO3D to investigate the buoyancy waves in the coorbital region of small-mass planets.

The original FARGO code was introduced by Masset (2000). Based on this code, other groups developed their version of the FARGO code. Examples include FARGO2D1D (Crida et al. 2007), GFARGO (Regály et al. 2012; Masset 2015), FARGOCA (Lega et al. 2014), FARGO_THORIN (Chrenko et al. 2017), the official successor FARGO3D (Benítez-Llambay & Masset 2016), as well as FARGOADSG (Baruteau & Masset 2008a,b; Baruteau & Zhu 2016), which is the predecessor of our code.

In this work, we present FARGOCPT, the FARGO version developed by members of the Computational Physics group at the University of Tübingen since 2012. Publications from this group, using the code, include Müller & Kley (2012, 2013), Picogna & Kley (2015), Rometsch et al. (2020, 2021), and Jordan et al. (2021).

Furthermore, we present novel approaches for handling challenging aspects of planet–disk interaction simulations. We introduce a new method for handling the indirect term suitable for simulations centered on individual stars in binary systems (Sect. 3.5), a local viscosity stabilizer for use in the context of cataclysmic variables (Sect. 3.9.2), and a correction for dust diffusion treated by stochastic kicks (Sect. 3.12.2).

This document is structured as follows. First, the physical problem at hand is sketched out in Sect. 2. Then, the newly introduced physics modules are described in Sect. 3. Software engineering and usability aspects of the code are discussed in Sect. 4. Finally, we present our conclusions in Sect. 5 with a discussion of the code. The appendix includes a presentation of various test cases included in the automatic test suite.

2. Physical system

The FARGOCPT code is a computer program that numerically solves the vertically integrated radiation-hydrodynamics equations in the one-temperature approximation coupled with an N-body system. They are expressed as:

$$\frac{\partial \Sigma}{\partial t} + \nabla \cdot (\Sigma \boldsymbol{u}) = 0, \tag{1}$$

$$\frac{\partial \Sigma \boldsymbol{u}}{\partial t} + \nabla \cdot (\Sigma \boldsymbol{u} \otimes \boldsymbol{u}) = -\nabla P + \Sigma \boldsymbol{k} + \nabla \tau, \tag{2}$$

$$\frac{\partial e}{\partial t} + \nabla \cdot (e \boldsymbol{u}) = -P \nabla \boldsymbol{u} + \mathcal{S} + \mathcal{R}\mathcal{T}, \tag{3}$$

with the surface density, $\Sigma = \int_{-\infty}^{\infty} \rho \, \mathrm{d}z$, as the vertically integrated gas volume density, ρ, the gas velocity, $\boldsymbol{u}$, the vertically integrated internal energy density, $e = \Sigma\epsilon$, with the specific internal energy, ϵ, the vertically integrated pressure, $P = \int_{-\infty}^{\infty} p \, \mathrm{d}z$, accelerations, $\boldsymbol{k}$, due to external forces (e.g., due to gravity), the viscous stress tensor, τ, and heat sinks and sources, $\mathcal{S}$ (see Sect. 3.8). The last term represents the radiation transport:

$$\mathcal{RT} = -\int_{-\infty}^{\infty} \nabla \boldsymbol{F} \mathrm{d}z \tag{4}$$

with the radiation flux, $\boldsymbol{F}$, in three dimensions. In the code, the vertical component of the radiation flux is split off and treated with an effective model, see Sect. 3.8. The code handles radiation hydrodynamics using the one-temperature approach which is discussed in more detail in Sect. 3.8.5.

In polar coordinates (r, ϕ), to which the code is tailored, the equations are expressed as (e.g., Masset 2002):

$$\frac{\partial \Sigma}{\partial t} + \frac{1}{r}\frac{\partial (r u_r \Sigma)}{\partial r} + \frac{1}{r}\frac{\partial \left(u_\phi \Sigma\right)}{\partial \phi} = 0, \tag{5}$$

$$\frac{\partial u_r}{\partial t} + u_r \frac{\partial u_r}{\partial r} + \frac{u_\phi}{r}\frac{\partial u_r}{\partial \phi} - \frac{u_\phi^2}{r} = -\frac{1}{\Sigma}\frac{\partial P}{\partial r} + k_r + \frac{f_r}{\Sigma}, \tag{6}$$

$$\frac{\partial u_\phi}{\partial t} + u_r \frac{\partial u_\phi}{\partial r} + \frac{u_\phi}{r}\frac{\partial u_\phi}{\partial \phi} + \frac{u_r u_\phi}{r} = -\frac{1}{\Sigma r}\frac{\partial P}{\partial \phi} + k_\phi + \frac{f_\phi}{\Sigma}, \tag{7}$$

$$\frac{\partial e}{\partial t} + \frac{1}{r}\frac{\partial (r u_r e)}{\partial r} + \frac{1}{r}\frac{\partial \left(u_\phi e\right)}{\partial \phi} = -\frac{P}{r}\frac{\partial (r u_r)}{\partial r} - \frac{P}{r}\frac{\partial u_\phi}{\partial \phi} + \mathcal{S} + \mathcal{RT}, \tag{8}$$

where f_r and f_ϕ are the radial and azimuthal forces per unit area due to viscosity (see Eqs. (82) and (83)). For a rotating coordinate system, we follow the conservative formulation of Kley (1998) and add the respective terms to the two momentum equations.

The left-hand sides of these equations are the transport step and the right-hand sides are the source terms. Following the scheme of the ZEUS code (Stone & Norman 1992), the transport step is solved by a finite-volume method based on an upwind scheme with a second-order slope limiter (van Leer 1977) and the code can make use of the FARGO algorithm (Masset 2000) to speed up the simulation. The source terms are updated as described in Sect. 3.1 using first-order Euler steps or implicit updates. The definitions for the heating and cooling term, $\mathcal{S}$, and the radiation transport term, $\mathcal{RT}$, are given in Sect. 3.8.

The external accelerations $\boldsymbol{k}$ are due to the gravitational forces from the star(s) and planets, correction terms in case of a non-inertial frame, and the self-gravity of the disk:

$$\boldsymbol{k} = -\nabla(\Phi_{\mathrm{Nb}} + \Phi_{\mathrm{Ind}}) - a_{\mathrm{SG}}. \tag{9}$$

The interaction of the disk with the N-body objects is considered via the gravitational potential, as expressed in Eq. (15). Self-gravity of the gas is considered as an acceleration (see Sect. 3.7).

The N-body objects feel the gravitational acceleration $\boldsymbol{a}$ exerted by the gas. This is computed by summation of the smoothed gravitational acceleration over all grid cells. We refer to Sect. 3.6 for formulas and details about the smoothing. Because the simulation can be run in a non-inertial frame of reference, the correction terms are applied as detailed in Sect. 3.5.

Finally, FARGOCPT features a particle module based on Lagrangian super-particles, where a single particle might represent any number of physical dust particles or solid bodies. The particles feel the gravity from the N-bodies and interact with the gas through a gas-drag law. Additionally, the dust diffusion was modeled to consider the effects of gas turbulence. The particle module is described in detail in Sect. 3.12. The next section describes the various physics modules that were added to the code.

3. Improvements of the physics modules

We built upon the original FARGO code by Masset (2000) and its improved version FARGOADSG. It already included treatment of the energy equation (Baruteau & Masset 2008a), self-gravity (Baruteau & Masset 2008b), and a Lagrangian particle module (Baruteau & Zhu 2016). We advanced these modules, added new physics modules, and added features to improve the usability of the code. For a detailed description of the FARGOADSG code, and with it of the underlying hydrodynamics part of the code presented here, we recommend Chap. 3 of Baruteau (2008). This section starts with outlining the order of operations in the operator splitting approach and then describes the various new features and changes.

3.1. Order of operations and interaction of subsystems

This section details the order in which the physical processes are considered during one iteration in the code and how they interact. For the update step, we used the sequential operator splitting (also known as Lie-Trotter splitting) where possible, meaning that we always use the most up-to-date quantities from the previous operators when applying the current operator. This is the simplest and oldest splitting scheme and has better accuracy than applying all operators using the quantities at the beginning of the step. This scheme is known as additive splitting (e.g., Geiser et al. 2017). Each time step starts with accretion onto the planets. Conceptually, this is the same as performing planet accretion at the end of the time step, except for the first and last iteration of the simulation.

Then, the code computes the gravitational forces between the N-body objects and the gas, between the N-body objects and the dust particles, and the self-gravity of the disk. At this stage, the indirect term, namely, the corrections for the non-inertial frame, is computed and added to the gravitational interaction. These are then applied to the subsystems by updating the velocities of the N-body objects, updating the acceleration of the dust particles, and updating the potential of the gas. Experience shows that for the interaction between N-body and gas the positions of the N-body objects have to be at the same time as the gas. From this point on, the N-body system and the particle system evolve independently in time until the end of the time step.

The gas velocities are first updated by the self-gravity acceleration and then by the N-body gravity potential, the pressure gradient, and, in the case of the radial update, also the centrifugal acceleration. At this step, the code updates the internal energy of the gas with compression heating. It is important to perform the energy update at this step before the viscosity is applied to avoid instabilities. Then, the code sequentially updates the velocities and the internal energy further by artificial viscosity, viscosity (both of which depend on the gas velocities), as well as heating and cooling terms. The heating and cooling steps are

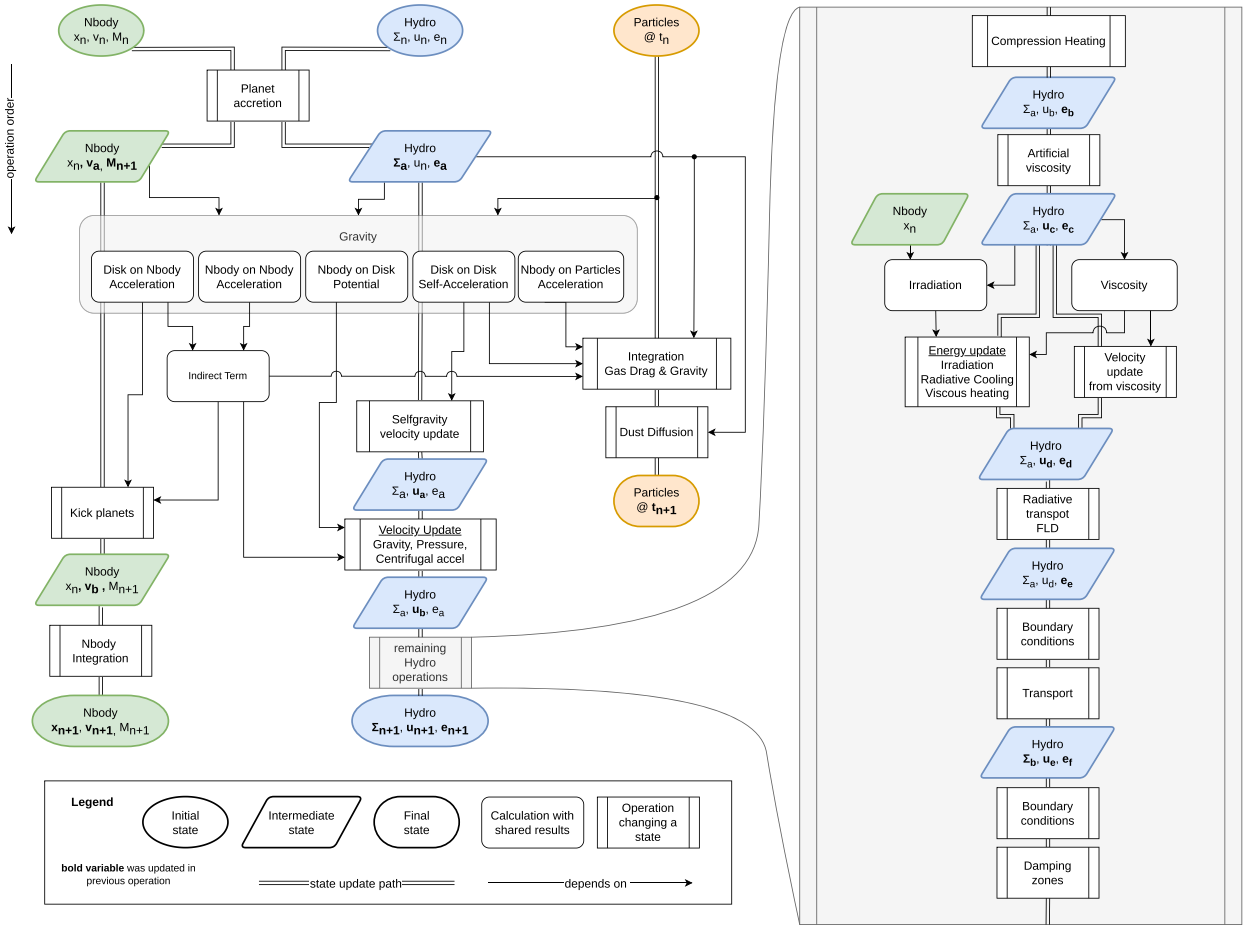

Fig. 1. Order of operations in the operator splitting scheme showing the evolution of the N-body, hydro, and particle subsystems throughout one iteration step. Single-line arrows mean that the originating object is used in the calculation of the destination. Double lines indicated the evolution of one of the subsystems from the initial state (ellipse) over intermediate states (parallelogram) to the final state (round shape). Each rectangle with rounded corners is a computation of an intermediate quantity using the state of the subsystem to which it is connected. The rectangles with bars on the sides indicate an operation that changes the state of a system. The variables that were changed by an operation are indicated in boldface in the intermediate states.

applied simultaneously for numerical stability. Finally, the internal energy is updated by radiation transport. Once all the forces and source terms were applied, the transport step is conducted. Boundary conditions and the wave-damping zone are applied at the appropriate sub-steps throughout the hydrodynamics step.

A detailed diagram of the order of the operations during each time step and the interactions between the subsystems is shown in Fig. 1. The diagram illustrates how each of the subsystems is advanced in time and between which sub-steps information is exchanged between the subsystems. The next paragraphs guide through the diagram starting from the top, explaining the meaning of the differently shaped patches, arrows, and lines. Each of the three subsystems is colored differently: the N-body system is shown in green, the hydrodynamics in blue, and the dust particles in orange. A colored patch represents the "state" of a subsystem. Elliptical patches indicate the initial state at the beginning of a time step, parallelograms indicate the intermediate states and colored rectangles with rounded corners indicate the final state at the end of the time step. Each state is labeled with variable names. The respective subscript indicates the sub-step during the operator splitting. For example, the energy is updated from e_n, first to e_a, then to e_b and after additional steps finally to e_{n+1}. These variables will be used in Sect. 3.8 to refer to the sub-steps. A variable printed in bold text indicates that the variable was changed by the last operation.

A white rectangle with rounded corners indicates an "intermediate calculation", the result of which is subsequently used in multiple operations. For example, the calculation of the indirect term is used in all three subsystems. Finally, the rectangles with bars on the sides indicate an "operation" that changes the state of a system.

Double lines trace the change of a subsystem throughout the time step. Lines with arrows attached at the end emerge from a state patch or an intermediate calculation and end in an operation or intermediate calculation patch. The large rectangle with bars shaded in grey at the right side of the diagram illustrates the sub-steps involved in the hydrodynamics part of the simulation. Except for the irradiation operation which requires the position of the N-bodies, this part of the simulation is independent of the N-body system.

Table 1. Possible cases for the disk gravity.

Case	N-body	Particles	Disk	"DiskFeedback"	"SelfGravity"
Massless	No	No	No	No	No
Massive w/o sg	Yes	No	No	Yes	No
Massive	Yes	Yes	Yes	Yes	Yes

Notes. The first group of columns indicates whether or not gravity from the disk is applied to the respective system (N-body, particles, and disk) in the simulation. The second group shows the configuration of the code parameters.

The shaded rectangle with rounded corners in the upper third of the diagram illustrates the various gravitational interactions between the subsystems. The information indicated by arrows that end at the borders of this patch can be applied in any of the contained intermediate calculations.

The operations are ordered from the top to bottom in the order they are applied during the time step. This means that an operation or a state is generally only influenced by states above it or at the same level. Please follow the arrows to get a sense of the order of operations.

3.2. N-body module

The original FARGO code includes a Runge-Kutta fifth-order N-body integrator, which was used with the same time step as the hydro simulations. This could lead to some situations in which the time step was too large for the N-body simulation, for instance, during close encounters in simulations of multiple migrating planets. Instead of implementing our N-body code with adaptive time-stepping, we incorporated the well-established and well-tested REBOUND code (Rein & Liu 2012) with its 15th order IAS15 integrator (Rein & Spiegel 2015) into FARGOCPT. REBOUND is called during every integration step of the hydro system to advance the N-body system for the length of the CFL time step. During this time, multiple N-body steps might be performed as needed. The interaction with the gas is incorporated by adding $\Delta t\, \boldsymbol{a}$ to the velocities of the bodies before the N-body integration.

We changed the central object from an implicit object, which was assumed to be of mass 1 in code units placed at the origin, to a moving point mass. It is now treated exactly like any other N-body object, notably including gravitational smoothing, which was not applied to the star before. This solves an inconsistency between the interaction of disk and planets and of the disk and star. This is necessary as the smoothing simulates the effect of the disk being stratified in the vertical direction and makes the potential behave more like it would in 3D (Müller et al. 2012).

Changing the star from being an implicit object to an explicit one, we changed all the relevant equations, which now include the mass of the central object and the distance to it.

3.3. Gravitational interactions

The dominant physical interaction between planets and a disk is gravity. In principle, any object that has mass causes a gravitational acceleration on any other object. In our simulation, N-body objects are considered to have a mass and particles are considered to be massless. The gas disk can be configured in one of three states. First, it can be massless and not accelerate the N-bodies. Second, the disk can massive, accelerate the N-bodies, the particles and itself (self-gravity included). Third, it can massive, accelerate the N-bodies, but not itself or the particles (self-gravity ignored).

The first two cases are consistent whereas the third case is inconsistent. However, it is a commonly used approximation. The reason for this is that the computation of the (self)gravity of the gas disk is computationally expensive.

In the third case, when the forces on the N-bodies due to the gas are computed using the full surface density, the N-bodies feel the full mass of the disk interior to their orbit, while gas on the same orbit does not feel this mass. Consequently, their respective equilibrium state angular velocities differ which causes a non-physical shift in resonance locations and, thus, in the torque and migration rate experienced by the planets (Baruteau & Masset 2008b). This mismatch can be alleviated by simply subtracting the azimuthal average of the surface density in the calculation of the force. This is done in the code in the case that self-gravity is disabled.

Our code does not support a configuration in which only one of the N-bodies feels the disk, such as a situation in which the planet feels the disk but the star does not. This is done intentionally to avoid nonphysical systems. Likewise, the indirect term caused by the disk is always included if the disk has mass (cases 2 and 3).

Whether the disk is considered to have mass is configured by the "DiskFeedback" option. If this is set to "yes", the disk is considered to have mass and vice-versa. The three cases and the value of the code parameters are summarized in Table 1.

3.4. Coordinate center

Because the star is treated like any other N-body object and it is able to move, we need to define the coordinate center of the hydro domain. In principle, we can choose an arbitrary reference point. However, because the N-body system dominates the gravity, we choose the center of mass of any combination of N-bodies as the coordinate center.

With the N-body objects located at $\boldsymbol{r}_i$, with $i = 1, 2, \ldots, N_p$, the coordinate center, $\boldsymbol{R}$, can now be set as:

$$\boldsymbol{R} = \frac{1}{\sum_{i=1}^{N_c} M_i} \sum_{i=1}^{N_c} M_i\, \boldsymbol{r}_i, \tag{10}$$

where N_c is the number of point masses whose center of mass is chosen to be the coordinate center. For example, $N_c = N_p$ selects the full N-body system as a reference, $N_c = 1$ selects the primary as a center and $N_c = 2$ selects a stellar binary or the center of mass of a star-planet system.

The center of mass of the full N-body system is likely the most desirable of such choices because it can be an inertial frame that does not require considering fictitious forces. This eliminates the need for an extra acceleration term to correct for the non-inertial frame, the so-called indirect term, which can be the

source of numerical instabilities. At least it eliminates the need for the indirect term resulting from the N-body system, which generally dominates the indirect term, although contributions from the disk gravity might still need to be considered. One application is the simulation of circumbinary disks, in which the natural coordinate center is the center of mass of the binary stars.

3.5. Shift-based indirect term

The correction forces needed because of a non-inertial frame are typically called the indirect term in the context of planet–disk interaction simulations. Based on the definition of the coordinate center in Eq. (10), the corresponding acceleration can formally be written as:

$$\boldsymbol{a}_{\rm Ind} = -\frac{\mathrm{d}^2}{\mathrm{d}t^2}\boldsymbol{R} = -\frac{1}{M_c}\sum_{i=1}^{N_c} M_i\,\boldsymbol{a}_i, \tag{11}$$

where we used $\boldsymbol{a}_i = \ddot{\boldsymbol{r}}_i$, defined $M_c = \sum_{i=1}^{N_c} M_i$, and assumed that the derivatives of the masses are negligible. The individual $\boldsymbol{a}_i$ should include all accelerations from forces acting on a specific N-body i, including gravity from all sources, other N-bodies or the disk.

Usually, this correction term is evaluated at the start of a time step, yielding a vector $\boldsymbol{a}^t_{\rm Ind}$. As outlined in Sect. 2, this is then added to the velocities of the N-bodies as a sort of Euler step $\boldsymbol{v}_i^{t\prime} = \boldsymbol{v}_i + \Delta t \boldsymbol{a}^t_{\rm Ind}$ before integration of the N-body system. For the disk, the indirect term is applied through the potential. This update is first-order in time. As long as the magnitude of the indirect term is small compared to direct gravity, this choice appears to be good enough.

Using an Euler step as above is not sufficient in simulations in which the indirect term becomes stronger than the direct gravity. This can be the case in simulations of circumbinary disks centered on one of the stars that are useful for the study of circumstellar disks in binary star systems. In such simulations, the disk can become unstable with the Euler method.

As a solution, we compute the indirect term as the average acceleration felt by the coordinate center during the whole time step. The average acceleration is computed from the actual shift needed to keep the coordinate center put. Therefore we call this method the "shift-based indirect term". In our code, this is achieved by making a copy of the N-body system after the N-body velocities have been updated by disk gravity, integrating the copy in time and computing the net acceleration from the velocities as:

$$\boldsymbol{a}_{\rm Ind} = -\frac{\boldsymbol{v}_c^{t+\Delta t} - \boldsymbol{v}_c^t}{\Delta t}. \tag{12}$$

where $\boldsymbol{v}_c = \frac{\mathrm{d}}{\mathrm{d}t}\boldsymbol{R}$ is the velocity of the coordinate center. The code then discards the N-body system copy, applies this indirect term to the N-body, hydro, and particle systems, and integrates them. In this way, the acceleration of the center and the indirect term cancel out and the system stays put much better compared to the old method. The computation of the acceleration is handled this way because the IAS15 integrator is a predictor-corrector scheme that does not produce an effective acceleration that would be accessible from the outside. Using the acceleration from an explicit Runge-Kutta scheme would produce the same results.

We tested, both, the old and the shift-based indirect term implementations and could not find any discernable difference in the dynamics of systems with embedded planets as massive as 10 Jupiter masses around a solar mass star. However, the shift-based indirect term enables simulations of circumbinary disks centered on one of the stars which was previously not possible. Even resolved simulations of circumsecondary disks (centered on the secondary star) when the latter is less massive than the primary star are possible. For the impact of this new scheme on the simulation of circumbinary disks, we refer to Jordan et al. (in prep.).

3.6. Gravity and smoothing

For modeling the gravity, we used the common scale-height-dependent smoothing approach. This approach accounts for the fact that a gas cell in 2D, which represents a vertically extended disk, experiences a weaker gravitational pull from an N-body object compared to the same cell for a truly razor-thin 2D disk (Müller et al. 2012). The potential due to a point mass, k, with mass, M_k, at a distance, d_{ik}, from the center of a cell, i, is then given by:

$$\Phi_k = -\frac{\mathrm{G}M_k}{\sqrt{d_{ik}^2 + \epsilon_i^2}}, \tag{13}$$

where G is the gravitational constant, d_{ij} is the distance between the point mass and the cell, and $\epsilon_i = \alpha_{\rm sm} H_i$ is the smoothing length with the smoothing parameter, $\alpha_{\rm sm}$, and the cell scale height, H_i. According to Müller et al. (2012), $\alpha_{\rm sm}$ should be between 0.6 and 0.7 to accurately describe gravitational forces and torques, which is why we apply it to all N-bodies, even the central star. Masset (2002) found that a factor of 0.76 most closely reproduces type I migration rates of 3D simulations. We note that ϵ_i has to be evaluated with the scale height at the location of the cell, not the location of the N-body object (Müller et al. 2012).

When the gravity of planets inside the disk is also considered for computing the scale height (Sect. 3.11), the scale height and the smoothing length in Eq. (13) become smaller in the vicinity of the planet. There, the smoothing can then become too small such that numerical instabilities occur.

To remedy this issue, we added an additional smoothing adapted from Klahr & Kley (2006). We found this to be a necessity when simulating binaries where one component enters the simulation domain due to an eccentric orbit or small inner domain radius. It is applied as a factor to the potential in Eq. (13) and is given by:

$$\Phi_k^{\rm sm} = \Phi_k \begin{cases} \left[\left(\frac{s_{ik}}{\epsilon_i}\right)^4 - 2\left(\frac{s_{ik}}{\epsilon_i}\right)^3 + 2\left(\frac{s_{ik}}{\epsilon_i}\right)\right] & \text{if } s_{ik} < d_{{\rm sm},k} \\ 1 & \text{otherwise;} \end{cases} \tag{14}$$

where $s_{ik} = \sqrt{d_{ik}^2 + \epsilon_i^2}$ is the ϵ-smoothed distance and $d_{{\rm sm},k}$ is another smoothing length, separate from ϵ_i. This smoothing is purely numerically motivated and guarantees numerical stability close to the planet. It has no effect outside $d_{{\rm sm},k}$. The smoothing length, $d_{{\rm sm},k}$, is a fraction of the Roche radius, $R_{\rm Roche}$, which is the distance from the point mass to its L1 point with respect to point mass, $k = 1$. For the case that the mass of the N-body particles changes, for example, with planet accretion, we compute $R_{\rm Roche}$ using one Newton-Raphson iteration to calculate the dimensionless Roche radius, starting from its value during the

last iteration. For low planet masses, $R_{\rm Roche}$ reduces to the Hill radius.

In many Fargo code variants, the gravity of the central star is not smoothed. However, the smoothing is required because the disk is vertically extended. The gravitational potential of the central star should therefore also be smoothed, otherwise, it is overestimated. This results in a deviation of order 10^{-4} for the azimuthal velocity compared to a non-smoothed stellar potential. Although this deviation is small, we believe that the stellar potential should be smoothed for consistency. A downside of this choice is that there exists no known analytical solution for the equilibrium state of a disk around a central star with a smoothed potential.

The full N-body system with $N_{\rm NB}$ members then has the total potential:

$$\Phi_{\rm NB} = \sum_{k=1}^{N_{\rm NB}} \Phi_k^{\rm sm}. \tag{15}$$

Having covered how the point masses affect the gas, the following paragraphs describe how the planets are affected by the gas. For a given point mass, k, at position, $\boldsymbol{r}_k$, the gravitational acceleration exerted onto the point mass by the disk is:

$$\boldsymbol{a}_k^{\rm gas} = -{\rm G} \sum_{i=1}^{N_{\rm cell}} f_{\rm sm} \frac{m_i}{s_{ik}^3} \boldsymbol{d}_{ik}, \tag{16}$$

where $\boldsymbol{d}_{ik} = \boldsymbol{r}_k - \boldsymbol{r}_i$ is the distance vector between the planet and the cell, m_i is the mass of a grid-cell, i, and s_{ik} is the smoothed distance between the cell and the point mass. It is given by $s_{ik} = \sqrt{d_{ik}^2 + \epsilon_i^2}$ with $d_{ik} = |\boldsymbol{d}_{ik}|$.

Again, the acceleration includes ϵ_i to account for the finite vertical extent of the disk. The same coefficient is used for the potential. The additional factor is the analog to Eq. (14) and is given by:

$$f_{\rm sm} = \begin{cases} 4\left(\frac{s_{ik}}{l_1}\right)^3 - 3\left(\frac{s_{ik}}{l_1}\right)^4, & s_{ik} \le l_1 \\ 1 & s_{ik} > l_1 \end{cases}. \tag{17}$$

We note that the interaction is not symmetric. The acceleration of N-body objects due to the gas is computed using direct summation while the gravitational potential in Eq. (15) enters into the momentum expressions in Eqs. (6) and (7) via a numerical differentiation. Because we computed the smoothing length using the scale height at the location of the cell (as we argue should be done on physical grounds, e.g., Müller et al. 2012), the differentiation causes extra terms that depend on the smoothing length.

To alleviate this issue, we implemented computing the acceleration of the gas due to the N-body objects by direct summation, which has negligible computational overhead. In this way, the interaction is fully symmetric and no additional terms are introduced. As of now, we are unaware of how much this asymmetry affects the results of simulations of planet–disk interaction and the issue is left for future work.

3.7. Self-gravity

Calculating the gravitational potential of a thin (2D) disk is a complex task. Indeed, it requires the vertical averaging of Poisson's equation, which in general is not feasible. Due to this limitation, in thin disk simulations, we often resort to a Plummer potential approximation for the gas, taking the following form:

$$\Psi_{\rm sg}(\boldsymbol{r}) = -{\rm G} \iint \frac{\Sigma(\boldsymbol{r}')}{s^2 + \epsilon_{\rm sg}^2} \, {\rm d}\boldsymbol{r}' \tag{18}$$

with $s = \|\boldsymbol{r} - \boldsymbol{r}'\|$, the gravitational constant, G, and a smoothing length, $\epsilon_{\rm sg}$. Contrary to a common belief, the role of this smoothing length is not to avoid numerical divergences at the singularity, $s = 0$. While it indeed fulfills this function, its main purpose is to account for the vertical stratification of the disk. In other terms, it permits gathering the combined effects of all disk vertical layers in the midplane. Without such a smoothing length, the magnitude of the self-gravity (SG) acceleration would be overestimated. In this context, many smoothing-lengths have been proposed but the most widely used is the one proposed by Müller et al. (2012). Based on an analytic approach, they suggested that the softening should be proportional to the gas scale height, $\epsilon_{sg} = 1.2 H_g$, to correctly capture SG at large distances.

Direct computation of the potential according to Eq. (18) is prohibitive since it requires N^2 operations. Fortunately, assuming a logarithmic spacing in the radial direction and a constant disk aspect ratio, $h = H/r = $ const., the potential can be recast as a convolution product, which can be efficiently computed in order $N \log(N)$ operations (Binney & Tremaine 1987) thanks to fast Fourier methods (Frigo & Johnson 2005). Such a method was implemented for the SG accelerations by Baruteau (2008). We use the same method and the module used in FargoCPT is based on the implementation in FargoADSG (Baruteau & Masset 2008b).

The traditional choice for the smoothing length is $\epsilon_{\rm sg}^2 = B\, r^2$, where B is a constant. This choice, however, has two drawbacks. First, it breaks the $r - r'$ symmetry of the gravitational interaction, which violates Newton's third law of motion. As a consequence, a nonphysical acceleration in the radial direction is manifested (Baruteau 2008). Second, even if the choice of $B = 1.2\, h$ minimizes the errors at large distances (Müller et al. 2012) this, nonetheless, results in SG underestimation at small distances, independent of the value of B (Rendon Restrepo & Barge 2023). This underestimation can quench gravitational collapse.

FargoCPT includes two improvements to alleviate those problems. The asymmetry problem can be alleviated by choosing a smoothing length that fulfills the symmetry requirement $\epsilon_{\rm sg}^2(\boldsymbol{r}, \boldsymbol{r}') = \epsilon_{\rm sg}^2(\boldsymbol{r}', \boldsymbol{r})$. Additionally, it can be shown that the Fourier scheme is still applicable for a more general form of the smoothing length $\epsilon_{\rm sg}^2(\boldsymbol{r}, \boldsymbol{r}') = rr'\, f(r/r', \phi - \phi')$. This is fulfilled if the smoothing length is a Laurent series in the ratio $\frac{r}{r'}$ and a Fourier series in $\phi - \phi'$ (which additionally captures the 2π periodicity in ϕ). Testing has shown, that the azimuthal dependence is negligible, so we only consider the constant term from the Fourier series. Furthermore, the radial dependence is only weak, so we only consider the first two terms of the Laurent series. This leads to the following form of the smoothing length:

$$\epsilon_{\rm sg}^2(\boldsymbol{r}, \boldsymbol{r}') = \chi^2 rr' + \lambda^2 (r - r')^2, \tag{19}$$

with two positively defined coefficients χ and λ. These two parameters depend on the aspect ratio h and can be precomputed for a given grid size by numerically minimizing the error between the 2D approximation and the full 3D summation of the gravitational acceleration. This requires specifying the vertical stratification of the disk. Assuming that the gravity from the

central object is negligible compared to the disk SG, the vertical stratification is a *Spitzer* profile:

$$\rho(z) = \frac{\Sigma}{2H_{\rm sp}} \frac{1}{\cosh^2(z/H_{\rm sp})}, \qquad H_{\rm sp} = \frac{c_{\rm iso}^2}{\pi G \Sigma} \approx QH = Qhr, \tag{20}$$

with the Toomre parameter

$$Q = \frac{c_s \kappa_e}{\pi G \Sigma} \approx \frac{c_s \Omega_{\rm K}}{\pi G \Sigma}, \tag{21}$$

with the epicycle frequency κ_e. Furthermore assuming a grid with $r_{\rm max}/r_{\rm min} = 250/20$, the fit formula for the coefficients are $\chi(h) = -0.7543h^2 + 0.6472h$ and $\lambda(h) = 0.4571h + 0.6737\sqrt{h}$. This is the formula used in FARGOCPT. For grids with substantially different ratios of outer to inner boundary radius, the minimization procedure has to be repeated and the constants changed. This smoothing length leads to a symmetric self-gravity force and has reduced errors for both small and large distances.

In the case of a non-constant aspect ratio, we use the mass-averaged aspect ratio which is recomputed after several time-steps. An additional benefit of the symmetric formulation is improved conservation of angular momentum by way of removing the self-acceleration present when using the old smoothing length.

In the limit of weak self-gravity, $Q \geq 20$, Rendon Restrepo & Barge (2023) corrected the underestimation of SG at small distances introducing a space-dependent smoothing length, which matches the exact 3D SG force with an accuracy of 0.5%. However, they did not correct the symmetry issue. Despite, this oversight they showed that their correction can lead to the gravitational collapse of a dust clump trapped inside a gaseous vortex (Rendon Restrepo & Gressel 2023) or maintain a fragment bound by gravity (Rendon Restrepo et al. 2022). In their latest work, (Rendon Restrepo et al., in prep.) found the exact kernel for all SG regimes which makes the use of a smoothing length obsolete:

$$K = \frac{1}{\sqrt{\pi}} \langle H \rangle^{-2} \frac{d}{8} \exp\left(\frac{d^2}{8}\right) \left[K_1\left(\frac{d^2}{8}\right) - K_0\left(\frac{d^2}{8}\right) \right], \tag{22}$$

where K_0 and K_1 are modified Bessel functions of the second kind, $d = \|\boldsymbol{r} - \boldsymbol{r}'\|/\langle H \rangle(r, r')$ and $\langle H \rangle(\boldsymbol{r}, \boldsymbol{r}') = \sqrt{\frac{H_{\rm sg}^2(\boldsymbol{r}') + H_{\rm sg}^2(\boldsymbol{r})}{2}}$ with $H_{\rm sg}$ defined in Eq. (23). This Kernel remains compatible with the aforementioned convolution product and fast Fourier methods. Although it is computationally expensive to compute the kernel using Bessel functions, it can be precomputed for locally isothermal simulations, thus, it has to be computed only once. For radiative simulations in which the aspect ratio changes, it can be updated only every so often making the method computationally feasible. Finally, this solution shares the properties of the solution presented above making the SG acceleration symmetric and removing the self-acceleration.

When considering SG, the balance between vertical gravity and pressure that sets the scale height needs to include the SG component as well. This effect can be included in the standard vertical density stratification $\rho(z) = \Sigma/(2\pi H) \exp\left(-1/2(z/H)^2\right)$ to good approximation by adjusting the definition of the scale height (Bertin & Lodato 1999, see their Appendix A). In the case that the SG option is turned on, the standard scale height is replaced by:

$$H_{\rm sg} = \sqrt{\frac{2}{\pi}} H f(Q), \tag{23}$$

$$f(Q) = \frac{\pi}{4Q} \left[\sqrt{1 + \frac{8Q^2}{\pi}} - 1 \right], \tag{24}$$

with the Toomre Q parameter from Eq. (21). In the code, we multiply the result of the standard scale height computation by the factor $\sqrt{2/\pi} f(Q)$. The epicycle frequency κ_e in the Toomre parameter in Eq. (21) is calculated as $\kappa_e^2 = 1/r^3 \mathrm{d}((r^2\Omega)^2)/\mathrm{d}r$ (e.g., Binney & Tremaine 1987) with the angular velocity of the gas Ω.

For simulations of collapse in self-gravitating disks, we added the OpenSimplex algorithm to our code to initialize noise in the density distribution. The noise is intended to break the axial symmetry of the disk and thereby help gravitational instabilities to develop.

3.8. Energy equation and radiative processes

The original FARGO (Masset 2000) code did not include treatment of the energy equation. This was added in various later incarnations of the FARGO code, including FargoADSG (Baruteau & Masset 2008a) on which this code is based. In this section, we outline the procedure of how the energy update is performed in FARGOCPT. Refer to the grey box on the right in Fig. 1 for a visual representation. The subscripts of the variables in this section refer to the ones in Fig. 1, intended to help the reader in locating the sub-steps.

The energy update step due to compression or expansion, shock heating, viscosity, irradiation, and radiative cooling or β-cooling is implemented using operator splitting. Our scheme consists of a mix of implicit update steps.

In principle, we perform the energy update on the sum of internal energy density e and the radiation energy density $e_{\rm rad} = aT^4$, thus assuming a perfect coupling between the ideal and the photon gas, the so-called one-temperature approximation (see Sect. 3.8.5 for more detail). Separately, these quantities change according to:

$$\frac{\partial e}{\partial t} = -p\nabla \boldsymbol{u} + Q_{\rm shock} + Q_{\rm visc}, \tag{25}$$

$$\frac{\partial e_{\rm rad}}{\partial t} = Q_{\rm irr} - \int_{-\infty}^{\infty} \nabla \cdot \boldsymbol{F} \mathrm{d}z, \tag{26}$$

$$= Q_{\rm irr} - Q_{\rm cool} - \int_{-\infty}^{\infty} \left(\nabla \cdot \boldsymbol{F} - \frac{\partial F_z}{\partial z} \right) \mathrm{d}z, \tag{27}$$

with the 3D radiation energy flux $\boldsymbol{F}$, viscous heating $Q_{\rm visc}$, shock-heating as captured by artificial viscosity $Q_{\rm shock}$, irradiation $Q_{\rm irr}$, and radiative losses at the disk surfaces $Q_{\rm cool} = \int_{-\infty}^{\infty} \frac{\partial F_z}{\partial z} \mathrm{d}z$. Note, that the vertical cooling part $Q_{\rm cool}$ is split off from the integral over $\nabla \cdot \boldsymbol{F}$.

In principle, the total energy update is then:

$$\begin{aligned} \frac{\partial (e + e_{\rm rad})}{\partial t} = &- p\nabla \boldsymbol{u} + Q_{\rm shock} \\ &+ Q_{\rm visc} + Q_{\rm irr} - Q_{\rm cool} \\ &- \int_{-\infty}^{\infty} \left(\nabla \cdot \boldsymbol{F} - \frac{\partial F_z}{\partial z} \right) \mathrm{d}z. \end{aligned} \tag{28}$$

We split this update into three main parts applied in the following order. The first line represents shock heating and compression heating (see Sect. 3.8.1), the second line represents heating and cooling (see Sect. 3.8.2), and the third line represents the radiation transport (see Sect. 3.8.5).

The following subsections review the details of this process.

3.8.1. Compression heating and shock heating

The pressure term is updated first following D'Angelo et al. (2003) with an implicit step using an exponential decay ensuring stability (see their Eq. (24)). The update is expressed as:

$$e_b = e_a \exp\left[-(\gamma-1)\Delta t \nabla \cdot \boldsymbol{u}_n\right], \tag{29}$$

with the adiabatic index, γ. As a next step, shock heating is treated in the form of heating from artificial viscosity:

$$e_c = e_b + Q_{\text{shock}}\,\Delta t, \tag{30}$$

with Q_{shock} being the right-hand-side of Eq. (88) where $\Sigma = \Sigma_a$ and $\boldsymbol{u} = \boldsymbol{u}_b$.

3.8.2. Heating and cooling

This step considers the update due to viscosity, irradiation, and cooling. The relevant part from Eq. (28) is

$$\frac{\partial(e + e_{\text{rad}})}{\partial t} = Q_{\text{visc}} + Q_{\text{irr}} - Q_{\text{cool}}. \tag{31}$$

To arrive at the expression for this update step, we first insert explicit expressions for the two energies. The internal energy density is $e = \rho c_V T$ with the specific heat capacity $c_V = \frac{\mathrm{k_B}}{\mathrm{m_H}\mu(\gamma-1)}$, where $\mathrm{k_B}$ is the Boltzmann constant, $\mathrm{m_H}$ is the mass of a hydrogen atom, and μ is the mean molecular weight. The radiation energy density is given by $e_{\text{rad}} = \frac{4\sigma_{\text{SB}}}{c}T^4$ with the Stefan-Boltzmann constant σ_{SB} and the speed of light c. Then, we use a first-order discretization for the time derivative and rearrange it according to the time index of T. Finally, we convert to an expression for the internal energy e arriving at:

$$e_d = e_c + \Delta t \frac{Q_{\text{visc}} + Q_{\text{irr}} - Q_{\text{cool}}}{\alpha} \tag{32}$$

with

$$\alpha = 1 + 8H\Big|_{e=e_b} \frac{\sigma_{\text{SB}}}{c}\left(\frac{m_\mu(\gamma-1)}{R\Sigma_a}\right)^4 e_b^3. \tag{33}$$

This implicit energy update is stable in our testing. The heating and cooling rates are calculated as described in the following sections. Each of the terms is optional and can be configured by the user. Cooling rates are discussed in Sects. 3.8.3 and 3.8.4, irradiation is discussed in Sect. 3.8.6. and viscous heating is discussed in Sect. 3.9.

3.8.3. Radiative Cooling

For radiative cooling, we take the same approach as (Müller & Kley 2012) where energy can escape through the disk surfaces and the energy transport from the disk midplane to the surfaces is modeled using an effective opacity. The associated cooling term is

$$Q_{\text{cool}} = 2\sigma_{\text{SB}} \frac{T^4 - T_{\text{min}}^4}{\tau_{\text{eff}}}. \tag{34}$$

The minimum temperature T_{min}, defaulting to 4 K, is set to take into account that the disk does not cool towards a zero Kelvin region but rather towards a cold environment slightly warmer than the cosmic microwave background. This can be important in the outer regions of the disk and effectively sets a temperature floor. For the effective opacity we used (Hubeny 1990; Müller & Kley 2012; D'Angelo & Marzari 2012):

$$\tau_{\text{eff}} = \frac{3}{8}\tau + \frac{k}{4} + \frac{1}{4\tau + \tau_{\text{min}}}, \tag{35}$$

where $k = 2$ for an irradiated disk and $k = \sqrt{3}$ for a non-irradiated disk (D'Angelo & Marzari 2012) , $\tau = \kappa\Sigma/\sqrt{8\pi}$ is the optical depth calculated from the Rosseland mean opacity κ, and $\tau_{\text{min}} = 0.01$ is a floor value to capture optically very thin cases in which line opacities become dominant (Hubeny 1990).

There are three options to compute the opacity in the code: `lin` (Lin & Papaloizou 1985), `bell` (Bell & Lin 1994), and `constant` for a constant opacity. For the first two, see Müller & Kley (2012) for more details. Additional opacity laws can be easily implemented by expanding the code by a function that returns the opacity $\kappa(\rho, T)$ as a function of the temperature and volume density.

In case of β-cooling (Gammie 2001), we have:

$$Q_\beta = (e - e_{\text{ref}})\frac{\Omega_K}{\beta} \tag{36}$$

is added to Q_{cool} where e_{ref} is the reference energy to which the energy is relaxed. This reference can either be the initial value or prescribed by a locally isothermal temperature profile. We note that β-cooling is a misnomer as it is not exclusively a cooling process but rather a relaxation process towards a reference state. If the temperature is lower than in the reference state, the energy is increased, that is, heating occurs.

3.8.4. S-curve cooling

For the specific case of simulating cataclysmic variables, we also included the option to compute Q_{cool} according to Ichikawa & Osaki (1992) and Kimura et al. (2020). Their model splits the cooling function into a cold, radiative branch and a hot, convective branch. They used opacities based on Cox & Stewart (1969) and a vertical radiative flux, namely, the radiative loss from one surface of the disk, of:

$$F = \tau\sigma T^4, \tag{37}$$

for the optically thin regime to derive the radiative flux of the cold branch:

$$\begin{aligned}\log F_{\text{cool,cgs}} = {} & 9.49\log T_{\text{cgs}} + 0.62\log\Omega_{\text{cgs}} \\ & + 1.62\log\Sigma_{\text{cgs}} + 0.31\log\mu - 25.48,\end{aligned} \tag{38}$$

where the subscript cgs indicates the value of the respective quantity in cgs units. The cold branch is valid for temperatures, $T < T_A$, where T_A is the temperature at which:

$$\tau\sigma T_A^4 = F_{\text{cool}}(T_A) = F_A. \tag{39}$$

The radiative flux of the hot branch is derived by assuming that disk quantities do not vary in the vertical direction (one-zone model) for an optically thick disk:

$$F = \frac{16\sigma T^4}{3\kappa\rho H}. \tag{40}$$

Using Kramer's law for the opacity of ionized gas, the radiative flux can be approximated as:

$$\log F_{\rm hot,cgs} = 8\log T_{\rm cgs} + \log\Omega_{\rm cgs} + 2\log\Sigma_{\rm cgs} + 0.5\log\mu - {\rm c_{hot}}, \tag{41}$$

where the constant $c_{\rm hot} = 25.49$ was used in Ichikawa & Osaki (1992) and $c_{\rm hot} = 23.405$ in Kimura et al. (2020). The difference between the two constants is that the first leads to weaker cooling compared to the latter. The hot branch is valid for temperatures $T > T_B$, where T_B is the temperature at which:

$$F_{\rm hot,cgs}(T_B) = F_B, \tag{42}$$

where $\log F_B = \max(K, \log F_A)$ with (based on Fig. 3 in Mineshige & Osaki 1983)

$$K = 11 + 0.4\log\left[\frac{2\times10^{10}}{r_{\rm cm}}\right]. \tag{43}$$

The radiative flux in the intermediate branch is given by an interpolation between the cold and hot branches:

$$\log {\rm F_{int}} = (\log F_A - \log F_B)\log\frac{T}{T_B}/\log\frac{T_A}{T_B} + \log F_B. \tag{44}$$

The cooling term is then given by $Q_{\rm cool}^{\rm scurve} = 2F$ due to the radiation from both sides of the disk where F is the radiative flux pieced together from the cool, intermediate, and hot branches as described above. These prescriptions were developed for the conditions inside an accretion disk, and we found that it leads to numerical issues when applied to the low-density regions outside a truncated disk. We therefore opted to modulate the radiative flux with a square root function for densities below $\Sigma_{\rm thresh} < 2\,{\rm g\,cm^{-2}}$ and a square function for temperatures below $T_{\rm thresh} < 1200\,{\rm K}$:

$$Q_{\rm cool}^{\rm scurve} = 2F(T_{\rm tmp}, \Sigma_{\rm tmp})\cdot\sqrt{\frac{\Sigma}{\Sigma_{\rm tmp}}}\cdot\left(\frac{T}{T_{\rm tmp}}\right)^2, \tag{45}$$

$$\Sigma_{\rm tmp} = \max\left(\Sigma, 2\,{\rm g\,cm^{-2}}\right), \tag{46}$$

$$T_{\rm tmp} = \max\left(T, 1200\,{\rm K}\right). \tag{47}$$

3.8.5. In-plane radiation transport using FLD

The last term in Eqs. (3) and (28), the in-plane radiation transport, is treated using the flux-limited diffusion (FLD) approach (Levermore & Pomraning 1981; Levermore 1984). The method allows us to treat radiation transport as a diffusion process, both, in the optically thick and optically thin regime. Our implementation builds upon Kley (1989), Kley & Crida (2008), Müller (2013) and uses the successive over-relaxation (SOR) method to solve the linear equation system involved in the implicit energy update.

In principle, the process of radiation transport is described by the evolution of a two-component gas consisting of an ideal gas and a photon gas which have thermal energy densities $e = e_{\rm gas}$ and $e_{\rm rad}$, respectively (Mihalas & Mihalas 1984). In the flux-limited diffusion approximation, their coupled evolution is given by (Kley 1989; Commerçon et al. 2011; Kolb et al. 2013):

$$\frac{\partial e_{\rm rad}}{\partial t} - \nabla\cdot\left(\frac{c\lambda}{\kappa_{\rm R}\rho}\nabla e_{\rm rad}\right) = \kappa_{\rm P}\rho c\left(a_{\rm R}T^4 - e_{\rm rad}\right), \tag{48}$$

$$\frac{\partial e}{\partial t} = -\kappa_{\rm P}\rho c\left(a_{\rm R}T^4 - e_{\rm rad}\right), \tag{49}$$

where λ is the flux limiter. We use the flux limiter presented in Kley (1989, see this reference for alternatives) which is given by:

$$\lambda = \begin{cases} 2/(3+\sqrt{9+10R^2}), & 0\le R\le 2, \\ 10/(10R+9+\sqrt{180R+81}), & R>2 \end{cases} \tag{50}$$

with the dimensionless quantity

$$R = \frac{1}{\rho\kappa}\frac{|\nabla e|}{e}. \tag{51}$$

In FARGOCPT, we use the one-temperature approximation, meaning that we assume that the photon gas and the ideal gas instantaneously equilibrate their temperatures, $T_{\rm gas} = T$ and $T_{\rm rad}$. This approximation allows us to reduce Eqs. (48) and (49) into a single equation for the total thermal energy, $e + e_{\rm rad}$. We further assume that $e_{\rm rad}$ is negligible against e (and the same for their time derivatives) yielding:

$$\frac{\partial e}{\partial t} \approx \frac{\partial(e+e_{\rm rad})}{\partial t} = \nabla\cdot\frac{\lambda c}{\rho\kappa}\nabla e_{\rm rad} = \nabla\cdot\frac{\lambda\,16\,\sigma_{\rm SB}}{\rho\kappa}T_{\rm rad}^3\,\nabla T_{\rm rad}, \tag{52}$$

where we used $e_{\rm rad} = 4\,\sigma_{\rm SB}T_{\rm rad}^4/c$. To see that $e_{\rm rad}$ is indeed negligible against e, we assume that the gas is a perfect gas and consider the ratio of energy densities:

$$\frac{e_{\rm rad}}{e} = \frac{a_{\rm R}T^4}{\rho c_V T} = 2.15\times10^{-23}\left(\frac{T}{1\,{\rm K}}\right)^3\left(\frac{\rho}{{\rm g/cm^3}}\right)^{-1}, \tag{53}$$

where we used $\mu = 2.35$ and $\gamma = 1.4$. Assuming further a minimum mass solar nebula (MMSN; Hayashi 1981) density with $\Sigma(r) = 1700\,{\rm g/cm^2}\,(r/{\rm au})^{-3/2}$, the ratio becomes:

$$\frac{e_{\rm rad}}{e} = 4.46\times10^{-16}\left(\frac{T}{1\,{\rm K}}\right)^{3.5}. \tag{54}$$

The dependence on the radius cancels out in the calculation of ρ from Σ because of the specific exponent of $-3/2$ of the MMSN. Now, we can see that $e_{\rm rad}/e$ ranges from 4.7×10^{-9} at $T = 100\,{\rm K}$ to 1.6×10^{-4} at $T = 2000\,{\rm K}$. Thus, the approximation is justified in the context of planet-forming disks.

Then, we again make use of the assumption that the gas and the photon gas equilibrate their temperatures instantaneously, namely, $T = T_{\rm rad}$, and use the fact that ρ can be considered constant during the radiation transport part of the operator splitting scheme. Furthermore, we assume the opacity κ to be constant during the radiation transport step, although in principle it depends on T. Equation (52) can then be recast into an equation for T yielding:

$$\frac{\partial T}{\partial t} = -\frac{1}{\rho c_V}\nabla\cdot\frac{\lambda\,16\,\sigma_{\rm SB}}{\rho\kappa}T^3\,\nabla T = \frac{1}{\rho c_V}\nabla\cdot K\,\nabla T \tag{55}$$

with $K = \lambda\frac{16\sigma_{\rm SB}}{\rho\kappa}$. This diffusion equation is then discretized and the resulting linear equation system is solved using the SOR method resulting in an updated temperature T'. Details of the discretization and implementation of the SOR solver can be found in Appendix 1 of Müller (2013). Finally, we assume that the gas is a perfect gas and update its internal energy density by using the new temperature,

$$e_e = \Sigma c_V T'. \tag{56}$$

Here, e_e is an energy surface density again (also see Fig. 1), as opposed to the energy volume densities in the rest of the section above.

We note that our implementation uses the 3D formulation. Other implementations of midplane radiation transport (also the one described in Müller 2013) use the surface density instead and have to introduce a factor $\sqrt{2\pi}H$ (sometimes also chosen as $2H$) to link the surface density to the volume density which depends on the vertical stratification of the disk. However, if we assume ρ (or equivalently H) to be constant throughout the radiative transport step, this factor cancels out in the end and the two approaches are equivalent. For the sake of simplicity, we use the 3D version and assume that all horizontal radiation transport is confined to the midplane. Before the radiation transport step, we compute $\rho = \Sigma/(\sqrt{2\pi}H)$.

The FLD implementation is tested with two separate tests. The first test, presented in Appendix D.8, shows a test for the physical part in which a disk equilibrates to two different temperatures enforced at the inner and outer boundaries. The second test, presented in Appendix D.9, shows a test for the SOR diffusion solver which compares the numerical results of a 2D diffusion process against the available analytical solution. We note that the current implementation of the FLD module only considers a perfect gas so it should not be used together with the non-constant adiabatic index (see Sect. 3.8.7) without further testing or modifications.

3.8.6. Irradiation

The irradiation term is computed as the sum of the irradiation from all N-body objects. This allows for simulations in which planets or a secondary star irradiate the disk. An N-body object is considered to be irradiating, if it is assigned a temperature and radius in the config file.

For each single source with index k, the heating rate due to irradiation is computed following Menou & Goodman (2004) and D'Angelo & Marzari (2012) as:

$$Q^k_{\rm irr} = 2(1-\epsilon)\frac{L_k}{4\pi d_k^2} W_G \frac{1}{\tau_{\rm eff}}, \tag{57}$$

with the disk albedo ϵ which is set to $1/2$, the luminosity of the source, L_k, the distance to the source, d_k, and the effective optical depth, $\tau_{\rm eff}$. The luminosity is calculated as $L_k = 4\pi R_k \sigma_{\rm SB} T_k^4$ with the radius, R_k, and the temperature, T_k, of the source, and the effective opacity, $\tau_{\rm eff}$, as given in Eq. (35). The remaining factor W_G is a geometrical factor that accounts for the disk geometry in the case of a central star (Chiang & Goldreich 1997) and includes terms for close to the source (first term) and far from the source (second term). It is given by:

$$W_G = 0.4\left(\frac{R_k}{r}\right) + h\left(\frac{{\rm d}\log H}{{\rm d}\log r} - 1\right). \tag{58}$$

We assume the flaring of the disk, $F = \frac{{\rm d}\log H}{{\rm d}\log r} - 1$, is constant in time and has the value of the free parameter specified for the initial conditions. Properly accounting for the disk geometry would require ray-tracing from all sources to all grid cells which is computationally expensive. Finally, the total irradiation heating rate is given by:

$$Q_{\rm irr} = \sum_k Q^k_{\rm irr}, \tag{59}$$

where the sum runs over all irradiating objects.

3.8.7. Non-constant adiabatic Index

In astrophysics, it is very common to treat matter as ideal gas, for which the following equation, also known as the ideal gas law, holds:

$$p = \frac{k_{\rm B}}{\mu {\rm m_u}}\rho T, \tag{60}$$

with the pressure p, the Boltzmann constant, $k_{\rm B}$, the mean molecular weight, μ, the density, ρ, the temperature, T, and the atomic mass unit $\rm m_u$. In the case of an ideal gas, the assumption is that there are no interactions between the gas particles and the pressure is only exerted by interactions with the boundary of a volume, containing the gas. This is very often a good approximation, especially in the case of accretion disks where densities are low.

A further assumption that is commonly made is that of a perfect gas, for which the pressure and sound speed are related to ρ and T by the same constant adiabatic index:

$$\gamma = \frac{c_p}{c_V}, \tag{61}$$

which is the ratio of the specific heat capacity at constant pressure with the one at constant volume, with $\gamma = 5/3$ for a monatomic gas and $\gamma = 7/5$ for a diatomic gas (e.g., Vaidya et al. 2015). The pressure and sound speed of a perfect gas are:

$$p = (\gamma - 1)\rho\epsilon \tag{62}$$

and

$$c_s = \sqrt{\gamma\frac{p}{\rho}}. \tag{63}$$

The assumption of a perfect gas is a good approximation at $300 \lesssim T \lesssim 1000$–$2000$ K, with some density dependence (see Fig. 1 of D'Angelo & Bodenheimer 2013). At lower or higher temperatures, contributions by rotational and vibrational degrees of freedom, or changes in the chemical composition such as the dissociation and ionization of hydrogen, would need to be taken into account. Confusingly, the perfect gas is often referred to as the ideal gas in the literature.

In the following, we outline the case of a general ideal gas in which the single constant adiabatic index is replaced with two other quantities. Hence, in Eqs. (62) and (63) the constant γ will be replaced by the effective adiabatic index $\gamma_{\rm eff}$ and the first adiabatic exponent Γ_1, respectively.

With these changes, the equation of state can account for the dissociation and ionization processes of hydrogen, as well as rotational and translational degrees of freedom at lower temperatures. Such an equation of state was already implemented in PLUTO by Vaidya et al. (2015) which serves as a basis for the changes in our code. In the PLUTO code, this equation of state is called the "PVTE" equation of state which stands for pressure-volume-temperature-energy. We adopted the same name for the equation of state in FargoCPT.

We start by writing the total internal energy density $\rho\epsilon$ of an ideal gas as a summation of several contributions:

$$\rho\epsilon = (\varepsilon_{\rm H_2} + \varepsilon_{\rm H,I} + \varepsilon_{\rm H,II} + \varepsilon_{\rm H+H} + \varepsilon_{\rm He})R\rho T = \sum_i \varepsilon_i R\rho T, \tag{64}$$

with $R = k_B/m_H$. These contributions are given by (compare Table 1 from Vaidya et al. 2015):

$$\begin{aligned}
\varepsilon_{\mathrm{H,I}} &= \frac{3}{2}X(1+x)y \text{ (translational energy for hydrogen)},\\
\varepsilon_{\mathrm{He}} &= \frac{3}{8}Y \text{ (translational energy for helium)},\\
\varepsilon_{\mathrm{H+H}} &= 4.48\mathrm{eV}\, Xy/(2k_BT) \text{ (dissociation energy for molecular hydrogen)},\\
\varepsilon_{\mathrm{H,II}} &= 13.6\mathrm{eV}\, Xxy/(k_BT) \text{ (ionization energy for atomic hydrogen)},\\
\varepsilon_{\mathrm{H_2}} &= \frac{X(1-y)}{2}\left[\frac{3}{2}+\frac{T}{\zeta_v}\frac{\mathrm{d}\zeta_v}{\mathrm{d}T}+\frac{T}{\zeta_r}\frac{\mathrm{d}\zeta_r}{\mathrm{d}T}\right] \text{ (internal energy for molecular hydrogen)},
\end{aligned}$$

where X (defaulting to 0.75 in the code) and $Y = 1 - X$ are the hydrogen and helium mass fractions and y and x are the hydrogen dissociation and ionization fractions, defined as:

$$y = \frac{\rho_{\mathrm{H,I}}}{\rho_{\mathrm{H,I}} + \rho_{\mathrm{H_2}}}, \tag{65}$$

and

$$x = \frac{\rho_{\mathrm{H,I}}}{\rho_{\mathrm{H,I}} + \rho_{\mathrm{H,II}}}, \tag{66}$$

ζ_v and ζ_r are the partition functions of vibration and rotation of the hydrogen molecule and are described in D'Angelo & Bodenheimer (2013). If we assume local thermodynamic equilibrium, then y and x can be computed by using the following two Saha equations:

$$\frac{x^2}{1-x} = \frac{m_H}{X\rho}\left(\frac{m_e k_B T}{2\pi\hbar^2}\right)^{3/2}\exp\left(\frac{-13.60\,\mathrm{eV}}{k_B T}\right), \tag{67}$$

$$\frac{y^2}{1-y} = \frac{m_H}{2X\rho}\left(\frac{m_H k_B T}{4\pi\hbar^2}\right)^{3/2}\exp\left(\frac{-4.48\,\mathrm{eV}}{k_B T}\right). \tag{68}$$

After applying the ideal gas law and inserting Eq. (64), the pressure-internal energy relation becomes:

$$p = \frac{R\rho T}{\mu} = \frac{\rho\epsilon}{\mu(\sum_i \varepsilon_i)} = (\gamma_{\mathrm{eff}} - 1)\rho\epsilon, \tag{69}$$

where $\gamma_{\mathrm{eff}} = 1 + \frac{1}{\mu(\sum_i \varepsilon_i)}$ is the effective adiabatic index and μ is the mean molecular weight, given by:

$$\mu = 4\left[2X\left(1 + y + 2xy\right) + Y\right]. \tag{70}$$

Now, by using the relation from Eq. (69) an equation for the temperature can be derived:

$$T = \frac{\mu p}{R\rho} = \frac{\mu\left(\gamma_{\mathrm{eff}} - 1\right)\rho\epsilon}{R\rho}, \tag{71}$$

which can be solved for a given internal energy and density as a root-finding problem:

$$\frac{\mu\left(\gamma_{\mathrm{eff}} - 1\right)\rho\epsilon}{R\rho} - T = 0. \tag{72}$$

The sound speed is given by:

$$c_s = \sqrt{\Gamma_1 \frac{p}{\rho}}, \tag{73}$$

where Γ_1 is the first adiabatic exponent, which is defined as:

$$\Gamma_1 = \frac{1}{c_V}\left(\frac{p}{\rho T}\right)\chi_T^2 + \chi_\rho, \tag{74}$$

where the temperature and density exponents are defined by:

$$\begin{aligned}
\chi_T &= \left(\frac{\partial \ln P}{\partial \ln T}\right)_\rho = 1 - \frac{\partial \ln \mu}{\partial \ln T},\\
\chi_\rho &= \left(\frac{\partial \ln P}{\partial \ln \rho}\right)_T = 1 - \frac{\partial \ln \mu}{\partial \ln \rho}.
\end{aligned} \tag{75}$$

Since the computational effort to compute γ_{eff}, Γ_1, and μ for every cell at every time step is very high, we precompute them to create lookup tables. During the simulation, the values of γ_{eff}, Γ_1, and μ are interpolated from the lookup tables for given densities and internal energies. How these tables can be implemented is also explained in Vaidya et al. (2015).

As our code is 2D, we require the scale height to compute the densities used for reading the adiabatic indices from the lookup table. To compute the scale height, our method requires the adiabatic indices. This results in a cyclic dependency. We found that this is not an issue, as successive time-steps naturally act as an iterative solver for this problem. We additionally always compute the scale height twice, before and after updating the adiabatic indices and we perform this iteration twice per time step. We tested our implementation using the shock tube test. Because there is no analytical solution for the shock tube test with non-constant adiabatic indices, we compared our results against results generated with the PLUTO code. The test is shown in Fig. D.3 under the label 'PVTE' and we find good agreement between our implementation and the implementation by Vaidya et al. (2015).

3.9. Viscosity

Viscosity is implemented as an operator splitting step (see Fig. 1 for its context). The full viscous stress tensor reads (see, e.g., Shu 1992):

$$\sigma_{ij} = 2\mu\left[\frac{1}{2}\left(\frac{\partial u_i}{\partial x_j} + \frac{\partial u_j}{\partial x_i}\right) - \frac{\delta_{ij}}{3}\nabla\cdot\boldsymbol{u}\right] + \zeta\delta_{ij}\nabla\cdot\boldsymbol{u}, \tag{76}$$

where $i, j \in \{1, 2\}$ indicate the spatial directions, μ and ζ are the shear and bulk viscosity, respectively, and δ_{ij} is the Kronecker δ. The shear viscosity is given by $\mu = \nu\Sigma$ with the kinematic viscosity denoted by ν. In our case, ζ is neglected, although artificial viscosity (see Sect. 3.9.1) reintroduces a bulk viscosity. The kinematic viscosity is either given by a constant value or the α-prescription (Shakura & Sunyaev 1973) for which:

$$\nu = \alpha c_s H, \tag{77}$$

with the disk scale height, H.

The relevant elements in polar coordinates of the viscous stress tensor are:

$$\sigma_{rr} = 2\nu\Sigma\left(\frac{\partial u_r}{\partial r} - \frac{1}{3}\nabla\cdot\boldsymbol{u}\right), \tag{78}$$

$$\sigma_{\phi\phi} = 2\nu\Sigma\left(\frac{1}{r}\frac{\partial u_\phi}{\partial \phi} + \frac{u_r}{r} - \frac{1}{3}\nabla\cdot\boldsymbol{u}\right), \tag{79}$$

$$\sigma_{r\phi} = \nu\Sigma\left(\frac{\partial u_\phi}{\partial r} + \frac{1}{r}\frac{\partial u_r}{\partial \phi}\right), \tag{80}$$

$$\nabla\cdot\boldsymbol{u} = \frac{\partial u_r}{\partial r} + \frac{1}{r}\frac{\partial u_\phi}{\partial \phi} + \frac{u_r}{r}. \tag{81}$$

The momentum update is then performed according to Kley (1999; see also D'Angelo et al. 2002) as:

$$\Sigma\frac{\partial u_r}{\partial t} = \frac{1}{r}\frac{\partial (r\sigma_{rr})}{\partial r} + \frac{1}{r}\frac{\partial \sigma_{r\phi}}{\partial \phi} - \frac{\sigma_{\phi\phi}}{r}, \tag{82}$$

$$\Sigma\frac{\partial u_\phi}{\partial t} = \frac{1}{r^2}\frac{\partial (r^2\sigma_{r\phi})}{\partial r} + \frac{1}{r}\frac{\partial \sigma_{\phi\phi}}{\partial \phi}. \tag{83}$$

Finally, the energy update due to viscosity (D'Angelo et al. 2003) is given by:

$$\frac{\partial e}{\partial t} = \frac{Q_{\rm visc}}{\Delta t} = \frac{1}{2\nu\Sigma}\left[\sigma_{rr}^2 + 2\sigma_{r\phi}^2 + \sigma_{\phi\phi}^2\right] + \frac{2\nu\Sigma}{9}(\nabla\cdot\boldsymbol{u})^2, \tag{84}$$

where $Q_{\rm visc}$ is to be used in the energy update in Eq. (32).

3.9.1. Tscharnuter and Winkler artificial viscosity

The role of artificial viscosity is to handle (discontinuous) shock fronts in finite-difference schemes. This is achieved by smoothing the shock front over several grid cells by adding a bulk viscosity term. Tscharnuter & Winkler (1979) raised concerns about the formulation of artificial viscosity introduced by Von Neumann & Richtmyer (1950), as it can produce artificial pressure even if there are no shocks (e.g., Bodenheimer et al. 2006, Sect. 6.1.4). Tscharnuter & Winkler (1979) then proposed a tensor artificial viscosity, analogous to the viscous stress tensor, that is independent of the coordinate system and frame of reference. For our implementation of this artificial viscosity, we follow Stone & Norman (1992, Appendix B) who added two additional constraints on the artificial viscosity: the artificial viscosity constant must be the same in all directions and the off-diagonal elements of the tensor must be zero to prevent artificial angular momentum transport. We note that there is also an artificial viscosity described in the main text of Stone & Norman (1992), sometimes referred to as the "Stone and Norman" artificial viscosity, which does not have these properties and is only applicable in Cartesian coordinates. Nonetheless, it is sometimes used in cylindrical and spherical coordinates.

In our case, we use the version suited for curve-linear coordinates and the artificial viscosity pressure tensor is given by:

$$\mathbf{Q} = \begin{cases} l^2\Sigma\,(\nabla\cdot\boldsymbol{u})\left[\nabla\otimes\boldsymbol{u} - \frac{1}{3}(\nabla\cdot\boldsymbol{u})\,\mathbf{I}\right] & \text{if } \nabla\cdot\mathbf{u} < 0 \\ 0 & \text{otherwise} \end{cases}, \tag{85}$$

where $l = q\,\Delta x$ is the distance over which shocks are smoothed with the dimensionless parameter q near unity and the cells size Δx. It is given by $\Delta x = \max(\Delta x_{\rm a}, \Delta x_{\rm b})$ where a and b indicate the grid of cell centers and interfaces, respectively. The contribution to the momentum equation is:

$$\Sigma\frac{\partial u_\phi}{\partial t} = \frac{\partial Q^\phi_{\ \phi}}{r\partial\phi}, \tag{86}$$

$$\Sigma\frac{\partial u_r}{\partial t} = \frac{\partial Q^r_{\ r}}{\partial r} + \frac{Q^r_{\ r}}{r} - \frac{Q^\phi_{\ \phi}}{r}. \tag{87}$$

Finally, the shock heating caused by the artificial viscosity is given by:

$$\frac{\partial e}{\partial t} = -l^2\Sigma\,(\nabla\cdot\boldsymbol{u})\,\frac{1}{3}\left[\left(\frac{\partial u_r}{\partial r}\right)^2 + \left(\frac{\partial u_\phi}{r\partial\phi} + \frac{u_r}{r}\right)^2 + \left(\frac{\partial u_\phi}{r\partial\phi} + \frac{u_r}{r} - \frac{\partial u_r}{\partial r}\right)^2\right]. \tag{88}$$

To ensure the stability of these updates, we use a CFL constraint analogous to the one in (Stone & Norman 1992, see their Sect. 4.6):

$$\Delta t_{\rm art} = \frac{\Delta x^2}{4l^2\,\nabla\cdot\boldsymbol{u}} = \frac{1}{4q^2\,\nabla\cdot\boldsymbol{u}}. \tag{89}$$

3.9.2. Local viscosity stabilizer

We found numerical instabilities in simulations of disks in close binary systems. In these systems, the disk is truncated by tidal forces (e.g., Artymowicz & Lubow 1994). At this truncation radius, the strong density gradients can cause numerical instabilities in the viscosity update step which drastically reduces the time step.

To prevent these instabilities, we designed a damping method that checks whether the viscosity update is too large and unstable and then reduces the update to a stable size. This method has the advantage that it is a local per-cell update that can be dropped into the existing code with only one modification to the update step. An alternative solution would be to implement a full implicit viscosity update step based on solving a linear system of equations which would have required substantial changes to our code in the viscosity update step. Furthermore, this implicit update would be computationally more expensive whereas the overhead of the local damping method is negligible. Because the instability is numerical and confined to only a small region, we argue that the damping method is a valid solution.

For our method, we interpret the viscosity update as a diffusion process. As we are only looking at a single cell, we treat the velocities of the neighboring cells as constant. We then can write the velocity update due to viscosity in the form of:

$$u^{t+\Delta t} = u^t + \Delta t\left(c_1\cdot u^t + c_2\right), \tag{90}$$

where in the nomenclature of Fig. 1, $u^{t+\Delta t} = u_d$ and $u^t = u_c$. The analytical solution to this equation is an exponential relaxation to the equilibrium velocity of $u_{\rm eq} = -\frac{c_2}{c_1}$. When the explicit update overshoots the equilibrium velocity, the method becomes unstable. One option to avoid the instability is to add $\Delta t\cdot c_1 > -1$ to the CFL criteria but this effectively freezes the simulation. Instead, the code can now be configured to:

$$u_d = u_c + \Delta t\frac{c_1\cdot u_c + c_2}{\max(0,\ 1 + \Delta t\cdot c_1) - \Delta t\cdot c_1}. \tag{91}$$

for the velocity update due to viscosity (see Sect. 3.9). For $\Delta t\cdot c_1 > -1$, the update reverts to Eq. (90), while for $\Delta t\cdot c_1 < -1$, the new velocity is set to the equilibrium velocity, $u_{\rm eq}$.

Compared to the other solution for overly large time steps (which typically allow for overshooting), we argue that an exponential decay to the equilibrium velocity is a physically more

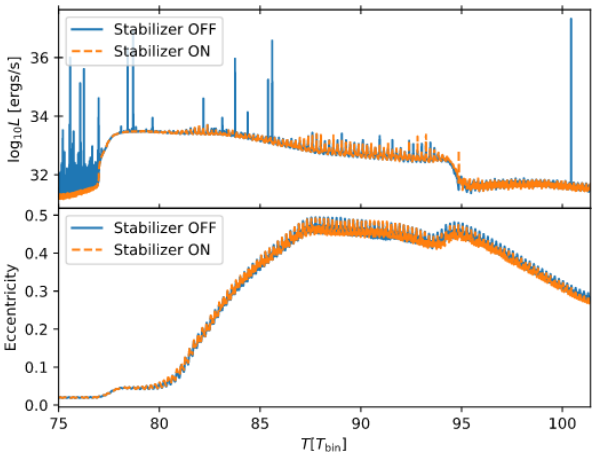

Fig. 2. Luminosity and mass-weighted eccentricity during a super-outburst in a cataclysmic variable system with and without our viscosity stabilizer. The simulation without the stabilizer required 3.8 times more time-steps during the shown time frame.

plausible choice. However, we should keep in mind that this method violates angular momentum conservation. In our tests, we found that only a few, low-density cells are unstable that have little influence on the whole simulation.

In Fig. 2, we show two simulations of a cataclysmic variable during a super-outburst, with the only difference being the stabilizing method turned on (blue line) or off (red line). The top and bottom panels show the time evolution of luminosity and mass-weighted eccentricity, respectively. The numerical instabilities that are dominating the luminosity (red line) are prevented by this method. Yet, the overall time evolution of the eccentricity is similar. Using the eccentricity as a proxy for the dynamical evolution of the disk, we can conclude that the stabilizing method only has a negligible impact on the physics.

3.10. CFL criterion for heating and cooling

A heating and cooling time step criterion was added similar to the cooling CFL criteria used in the PLUTO code (Mignone et al. 2007). We found the additional CFL criteria beneficial to simulations of disks in close binaries that have truncated disks with strong density gradients (Wehner et al., in prep.). The time step must be smaller than:

$$\Delta t_{\mathrm{heatcool}} = f \frac{e}{|Q_p - Q_-|}, \tag{92}$$

where f is a fudge factor to set the maximum energy change per time step. We found that a factor of $f = 10$ by trial-and-error to improve stability while not impacting the overall time step too much.

3.11. Scale-height dependent on all point masses

The scale height is determined by the balance between vertical gravity and pressure forces. Realistically, the gravity of all N-body objects, including planets, should contribute to the gravitational force. Including these contributions, the scale height can be computed as (Günther et al. 2004):

$$H = \left[\sum_i^{N_b} \frac{1}{H_i^2}\right]^{-1/2}, \quad H_i = \frac{c_s^{\mathrm{iso}}}{\Omega_{\mathrm{K},i}}, \tag{93}$$

where $c_s^{\mathrm{iso}} = c_s/\sqrt{\gamma}$ is the isothermal sound speed and $\Omega_{\mathrm{K},i}$ is the Keplerian frequency with respect to the ith N-body object.

For the computation of self-gravity presented in Sect. 3.7, we need a value for the aspect ratio. In the case that the full N-body system influences the scale height, we compute the aspect ratio in an analog way:

$$h = \left[\sum_i^{N_b} \frac{1}{h_i^2}\right]^{-1/2}, \quad h_i = \frac{c_s^{\mathrm{iso}}}{v_{\mathrm{K},i}}. \tag{94}$$

3.12. Particle system

FARGOCPT can simulate solid particles of any size in a protoplanetary disk. A collection of solid particles is represented as Lagrangian super-particles. This means that a bunch of identical physical particles, with the same size and same density, are represented by one super-particle. These super-particles are then evolved in the simulation according to the forces acting on them: a drag force due to the gas and gravity from the N-body objects and the disk if self-gravity of the gas is enabled.

These super-particles do not react back on the gas. As such, the mass of each super-particle can be changed freely even after the simulation. The number of super-particles determines how well the dynamics of solid particles are resolved or sampled in the simulation. The first implementation of these Lagrangian super-particles in FARGOCPT was used in Picogna & Kley (2015).

The particle system is synchronized to the N-body and hydro simulation once every iteration, namely, at time t^n, and then integrated for a time equal to the time step resulting from the CFL criterion Δt, that is, until $t^{n+1} = t^n + \Delta t$. The code supports two different integrators for particle motion. The first one is an implicit exponential midpoint integrator as described in Mignone et al. (2019, Appendix B.2.1) that combines two regimes of particle sizes ranging from micrometer-sized dust (St $\ll 1$) to meter-sized boulders (St ≥ 1). The second choice is an explicit fifth order Runge-Kutta integrator with adaptive time stepping (Cash & Karp 1990) to integrate very large particles with St $\gg 1$ such as planetesimals.

In both integrators, the integration step can be performed in polar coordinates while the explicit integrator also supports Cartesian coordinates. The polar formulation conserves angular momentum better in the case of circular particle orbits. We found, however, that as soon as the orbits become eccentric, this advantage disappears.

3.12.1. Drag force

The friction force for the gas drag is calculated as a smooth interpolation between the Epstein and Stokes regimes. We use a model that follows Picogna et al. (2018) but with the Epstein drag calculated according to Woitke & Helling (2003).

The drag model depends on three dimensionless numbers: Knudsen number Kn, Mach number Ma, and Reynolds number Re. Those are given by:

$$\mathrm{Kn} = \frac{l}{2a}, \tag{95}$$

$$\mathrm{Ma} = \frac{v_{\mathrm{rel}}}{c_s}, \tag{96}$$

$$\mathrm{Re} = \frac{2a\rho_s v_{\mathrm{rel}}}{\nu}, \tag{97}$$

where a is the radius of the solid particle, l is the mean free path of the gas molecules, c_s is the sound speed, ρ_s is the material density of the particle, $v_{\rm rel}$ is the relative velocity between the particle and the gas, and ν is the kinematic viscosity coefficient of the gas. We note that the latter is different from the kinematic viscosity coefficient used to model turbulent accretion with the α model.

The mean free path of the gas molecules is given by (Haghighipour & Boss 2003):

$$l = \frac{m_0}{\pi a_0 \rho_g} = 4.72 \times 10^{-9}\,\mathrm{cm}\,\frac{\mathrm{g/cm^3}}{\rho_g}. \tag{98}$$

with $a_0 = 1.5 \times 10^{-8}$ cm, assuming the gas consists primarily of H_2 molecules, and the mass volume density of the gas ρ_g. The kinematic viscosity coefficient is given by:

$$\nu = \frac{1}{3} m_0 \frac{v_{\rm thermal}}{\sigma}, \tag{99}$$

with the thermal velocity $v_{\rm thermal} = \sqrt{8/\pi}\, c_s^{\rm iso}$ and the collisional cross-section between the gas molecules $\sigma = \pi a_0^2$.

The drag force $\boldsymbol{F}_{\rm drag}$, a particle in the disk is subjected to, is related to the stopping time $t_{\rm stop}$ via:

$$\boldsymbol{F}_{\rm drag} = -\frac{m_{\rm s}}{t_{\rm stop}} \boldsymbol{v}_{\rm rel}, \tag{100}$$

with the mass of a solid particle $m_{\rm s}$. The stopping time is given by:

$$t_{\rm stop} = \frac{4}{3} \frac{l \rho_{\rm s}}{\rho_g C_{\rm d} c_s\, \mathrm{Kn}}. \tag{101}$$

The total drag coefficient results from a quadratic interpolation between the free molecular flow (Epstein) and viscous regime (Stokes) and is given by (Woitke & Helling 2003, see their Eq. (18)):

$$C_{\rm d} = \frac{9\,\mathrm{Kn}^2\, C_{\rm E} + C_{\rm S}}{(3\,\mathrm{Kn} + 1)^2}. \tag{102}$$

The Epstein drag coefficient is a smooth interpolation of the sub- and supersonic regimes of the Stokes drag (Woitke & Helling 2003, see their Eq. (13)):

$$C_{\rm E} = 2\sqrt{\mathrm{Ma}^2 + \frac{128}{9\pi}}. \tag{103}$$

The Stokes drag coefficient is given by (Eq. (15) in Woitke & Helling 2003):

$$C_{\rm S} = \begin{cases} \frac{24\,\mathrm{Ma}}{\mathrm{Re}} + 3.6\,\mathrm{Ma}\,\mathrm{Re}^{-0.313}, & \mathrm{Re} \le 500, \\ 9.5 \times 10^{-5}\,\mathrm{Ma}\,\mathrm{Re}^{1.397}, & 500 < \mathrm{Re} \le 1500, \\ 2.61\,\mathrm{Ma}, & 1500 < \mathrm{Re}, \end{cases} \tag{104}$$

We note that the expressions here differ from the ones in Picogna et al. (2018) and Woitke & Helling (2003) because ours are formulated for computing $t_{\rm stop}$ in Eq. (101), while the others are formulated for computing $\boldsymbol{F}_{\rm drag}$ directly. In Appendix D.6, we present a test of the radial dust drift velocity resulting from the gas drag.

3.12.2. Dust diffusion

Simulating dust with Stokes numbers around unity requires treating dust diffusion due to unresolved small-scale turbulent motion of the gas. Otherwise, this dust accumulates nonphysically in a single point at a pressure maximum, such as the centers of large-scale vortices. Our code includes dust diffusion modeled with stochastic kicks in analogy to Charnoz et al. (2011). In this model, the Lagrangian super-particles receive a kick at every time step. The kick is only applied in the radial direction such that:

$$r^{\rm new} = r^{\rm old} + \delta r, \tag{105}$$

and the azimuthal velocity is corrected to conserve angular momentum:

$$\dot{\phi}^{\rm new} = \dot{\phi}^{\rm old} \frac{r^{\rm old}}{r^{\rm new}}. \tag{106}$$

The correction of the azimuthal velocity is required to avoid a nonphysical drift due to the changed angular momentum.

The kick strength is:

$$\delta r = \langle \delta r \rangle \Delta t \Omega_{\rm K} + W\sigma + \delta_{\rm 2D}, \tag{107}$$

where we the symbols carry the same meaning as in Charnoz et al. (2011, see their Eq. (17)). $\langle \delta r \rangle = \Delta t\, D_d / \rho_g\, \partial \rho_g / \partial r$ is the mean and $\sigma^2 = 2 D_d \Delta t$ is the variance of a random Gaussian variable, W is a standard normal random variable, and $\delta_{\rm 2D}$ is an additional displacement to take into account the second dimension, namely, the diffusion in the ϕ direction. The dust diffusion coefficient is $D_d = \nu/\mathrm{Sc} = \alpha c_s H/\mathrm{Sc}$ with the Schmidt number, $\mathrm{Sc} = (1 + \mathrm{St}^2)^2/(1 + 4\mathrm{St}^2)$ (Youdin & Lithwick 2007). The factor $\Delta t \Omega_{\rm K}$ takes into account the time correlation in the kicks due to the gas turbulence (see Sect. 2.7 in Charnoz et al. 2011).

The 2D correction,

$$\delta_{\rm 2D} = \sqrt{r^2 + (W\sigma)^2} - r, \tag{108}$$

can be derived by a geometrical argument taking into account the diffusive spread in the azimuthal direction. We consider a dust particle on a circular orbit that is displaced by a turbulent kick in the azimuthal direction. Its final location will be radially further out from where it started, independent of whether it was kicked in the direction of the orbit or opposite to it. This positive radial change is taken into account by $\delta_{\rm 2D}$.

To save computational costs, we use the same standard random number, W, in Eq. (107) and in Eq. (108). This introduces correlations between two contributions to the kick. However, the factor $W\sigma$ is a small number compared to the relevant length scales and the 2D correction is quadratic in $W\sigma$ which can be seen by a Taylor expansion of Eq. (108): $\delta_{\rm 2D} \approx \frac{1}{2} (W\sigma)^2 / r$. Additionally, the direction of the radial kick and the 2D correction are not correlated, because the latter is always positive. Thus the effect of the correlations should be negligible.

To our knowledge, this correction has not been used before when kicks were only applied in the radial direction. However, we found it to be necessary to match the solutions of the radial advection-diffusion equation, see Appendix D.5.

For generating the random numbers for these steps, we added the small non-cryptographic random generator by Bob Jenkins (JSF) which is fast and well-tested. The implementation of the generator as well as tests are shown in O'Neill (2018).

A test of this procedure is presented in Appendix D.6 in the form of a comparison of simulations of the spread of a

thin dust ring simulated in FARGOCPT against a solution of the radial advection-diffusion equation. We find excellent agreement between the two approaches.

3.13. Accretion onto point masses

When accretion is enabled, mass is removed from the disk and added to the N-body object. The mass is removed from the vicinity of the N-body object similar to Kley (1999) with a fixed half-emptying time. The momentum of the accreted mass is added to the N-body object. The radius around the N-body object from which mass is removed, $R_{\rm acc}$, is given by a fraction of the Roche lobe radius $R_{\rm Roche}$, which we calculate as described in Sect. 3.6. The accretion radius is given by:

$$R_{\rm acc} = c \cdot R_{\rm Roche}. \tag{109}$$

For a cell with mass m_i and distance d_i to the accreting object, the rate of mass removal is given by:

$$\dot{m}_i = -f_i m_i \frac{\log(2)}{T_{\rm P}}, \tag{110}$$

where f_i is the accretion fraction for cell i. Close to the planet, it is higher and decreases with distance. We use a simple two-step function such that:

$$f_i = \begin{cases} 2f_{\rm acc} & \text{if } R_{\rm acc}/2 < d_i \leq R_{\rm acc}, \\ f_{\rm acc} & \text{if } d_i > R_{\rm acc}/2, \\ 0 & \text{if } d_i > R_{\rm acc}, \end{cases} \tag{111}$$

with the accretion parameter, $f_{\rm acc}$, which can be chosen individually for each N-body object. f_i is additionally limited by the mass in the cell m_i such that $f_i = \min(f_i, (m_i - A_i\Sigma_{\rm floor})T_{\rm P}/(\log(2)\Delta t))$, where A_i is the area of cell i and $\Sigma_{\rm floor}$ is the density floor. This scheme effectively takes away mass from the cells with a half-emptying time of $T_{\rm P}/f_i$. Summation over the cells in the vicinity of the body yields the accretion rate and momentum transfer onto it:

$$\dot{M} = -\sum_{i\in\mathcal{V}} \dot{m}_i, \tag{112}$$

$$\dot{\boldsymbol{P}} = -\sum_{i\in\mathcal{V}} \dot{m}_i \boldsymbol{u}_i. \tag{113}$$

where $\mathcal{V}$ is the set of indices of cells that are located within $R_{\rm acc}$ of the accreting object.

For accretion onto binary stars from a circumbinary disk, we can use a more sophisticated model of accretion. Assume that, within the cavity of the circumbinary disk, both stars are surrounded by their own disks which are tidally truncated, keeping them small. Assume further that within these disks the accretion happens according to a simple 1D viscous accretion-disk model and that the stars accrete at the same rate as the mass flows through these disks. Then, the accretion rate onto the stars is given by (Lynden-Bell & Pringle 1974):

$$\dot{M}_{\rm acc} = 3\pi\nu\Sigma s. \tag{114}$$

The free parameter s accounts for the increase in accretion close to an object due to gas friction at the boundary layer. The idea is analogous to the viscous inflow boundary condition (Sect. 3.14.2). For our purposes, we assume ν and Σ to be constant and equal to the average values within $R_{\rm acc}$.

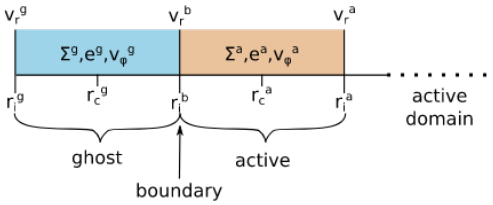

Fig. 3. Schematic of the location of the quantities for the boundary conditions. The first active cell is shown in beige and the ghost cells are in blue. The ghost cells are not updated by the source terms and transport steps. Their values are used to apply the boundary conditions.

With this model of accretion, we can modify the scheme above in such a way that the rate of mass removed from the disk in the vicinity of the object is equal to the 1D viscous accretion rate given by Eq. (114). To achieve this, we choose f_i such, that

$$\sum_{i\in\mathcal{V}} \dot{m}_i = \sum_{i\in\mathcal{V}} f_i m_i = \Delta t \dot{M}_{\rm acc}. \tag{115}$$

Again, we want $f(d)$ to vary with the distance d to the accreting object and we want $f(d)$ to be zero for $d > R_{\rm acc}$. Now, instead of a step function, we choose a smooth power law function for $f(d)$ such that

$$f(d) = f_0\left(1 - \left(\frac{d}{R_{\rm acc}}\right)^q\right), \tag{116}$$

with the understanding that $f(d > R_{\rm acc}) = 0$. With this choice, the physical model from above, and assuming $q > 0$, we find:

$$f_0 = 3\frac{q+2}{q} s \frac{\nu}{R_{\rm acc}}. \tag{117}$$

In the code, we use $q = 1$. This enables the physically motivated computation of an accretion rate onto a secondary star which is located within the computational domain.

3.14. Boundary conditions

This section describes the boundary conditions (BCs) that are implemented in the code. We start by stating the most basic BCs and then describe the more complex ones. In the code, BCs are applied by setting the value of Σ, e, u_ϕ in the center of the ghost cells and u_r on its two interfaces.

The nomenclature used in this section is as follows. The superscripts a and g denote the last cell in the active domain and the ghost cell, respectively. The location of the cell centers are r^a and r^g. Additionally, the superscript b denotes the boundary at $R_{\rm min}$ and $R_{\rm max}$. The locations of the interfaces are r_i^a for the interface between the first and second active cell, r_i^b for the boundary interface, and r_i^g for the interface of the ghost cell facing away from the active domain. Values in the center of the ghost cells are Σ^g, e^g and u_ϕ^g. The two values on the ghost cell interfaces are u_r^b, at the interface between the active domain and the ghost cell and u_r^g. The values in the first cell of the active domain are Σ^a, e^a, u_ϕ^a and the radial velocity at the interface between the first and second active cell is u_r^a. See Fig. 3 for a schematic of the location of these quantities.

In the code, BCs can either be set for each variable individually or for all variables at once. We call the latter case a composite BC. Here, we start by introducing the individual BCs.

Table 2. Boundary conditions available on all variables of $x \in \{\Sigma, e, u_r, u_\phi\}$.

Condition	Formula
Zero-gradient	$x^{g,b} = x^a$
Disk model	$x^{g,b} = x_{\rm dm}(r^{g,b})$
Reference	$x^{g,b} = x_{\rm ref}(r^{g,b})$

Notes. The superscript g, b indicates that the same formula is used for variables in the center of the ghost cell and on the interfaces. The radii are understood to be at the respective locations.

3.14.1. Boundary conditions applicable to all variables

Several BCs are available for each variable. These are summarized in Table 2.

The "zero-gradient" BC enforces a radial derivative of zero at the boundary. It copies the value from the last active cell into the ghost cell for cell-centered variables and from the last active cell interface into the ghost cell interface for interface variables.

The "disk model" BC is used to set the boundaries according to a specific disk model. The code currently supports a power law disk as a model. The functions $x_{\rm dm}(r)$ specify the disk model for each variable x. An example is the surface density $\Sigma_{\rm dm}(r) = \Sigma_0 (r/r_0)^{-p}$.

Another choice to set the boundaries to a specific model is the "reference" BC. In this case, the reference values $x_{\rm ref}(r)$ are loaded from a special simulation snapshot. The same snapshot is used for the damping zones (see Sect. 3.14.6). This snapshot is generated at the beginning of the simulation and contains the initial conditions by default. To specify a custom model, the user can run the simulation for zero time steps (using the `-N 0` command line flag) and then replace the reference values with the desired arbitrary model using an external tool. Then, the simulation can be continued from snapshot number 0.

3.14.2. Radial velocity boundary conditions

Several BCs apply only to the radial velocity u_r, see Table 3. They are mostly connected to the flow through the boundary.

By mirroring the flow, we can simulate a "reflective" boundary. This is achieved by setting the radial velocity to zero on the boundary and to the negative value of the radial velocity in the last active cell at the other interface of the ghost cell. This keeps mass from flowing out of the domain but also reflects waves back into the domain and can cause wave interference patterns and instabilities in the worst case. Usually, the reflective boundary is used together with damping zones (see Sect. 3.14.6) to prevent these issues.

The opposite behavior is achieved by the "outflow" BC. It lets mass flow out of the domain but does not allow mass to flow into the domain. This is achieved by using a zero-gradient condition if the velocity vector is pointing outwards at the boundary and by setting the radial velocity to zero otherwise. Pointing outwards means that the radial velocity is positive at the outer boundary and negative at the inner boundary. Despite being an outflow condition for mass, this prescription can still reflect waves back into the domain, but it is less of an issue as the boundary tends to form an empty area between the disk and the boundary.

At the inner boundary, it can be advantageous to more closely control the flow through the boundary to model a certain accretion rate onto the star. There are currently two options to influence this flow. The first option is the "viscous outflow" BC. This BC assumes a steady-state accretion disk at the inner boundary. Then, analogous to the viscous accretion model presented in Sect. 3.13, the accretion rate through the boundary is given by (Lynden-Bell & Pringle 1974):

$$\dot{M} = 3\pi\nu\Sigma s, \tag{118}$$

with the free parameter s for which 5 is a suitable value for accretion onto a solar-type star (Pierens & Nelson 2008). The BC is implemented by setting the radial velocity at the boundary $u_r^{g/b} = v_{\rm visc}(r_i^{g/b})$ with the viscous inflow speed:

$$v_{\rm visc} = -\frac{3}{2}\frac{s\nu}{r}. \tag{119}$$

Another choice is to set the radial velocity to a fraction of the Keplerian velocity at the inner boundary. This is done by the "Keplerian" BC for the radial direction. It sets the radial velocity to the negative of the fraction of the Keplerian velocity at the inner boundary. This BC can also be applied at the outer boundary.

Table 3. Boundary conditions for the radial velocity, u_r.

Condition	Formula
Reflective	$u_r^g = -u_r^a$, $u_r^b = 0$
Outflow	$\begin{cases} u_r^{g/b} = u_r^a & \text{if } \boldsymbol{u}^a \text{ points outwards} \\ u_r^{g/b} = 0 & \text{otherwise} \end{cases}$
Viscous outflow	$u_r^{g/b} = -c\, v_{\rm visc}(r_i^{g/b})$, at $R_{\rm min}$
Keplerian	$u_r^{g/b} = c\, v_{\rm K}(r_i^b)$

Notes. The factors c are different for each boundary condition and can be selected by the user in the config file. The boundary conditions from Table 2 are also available for u_r.

Table 4. Boundary conditions for the azimuthal velocity u_ϕ.

Condition	Formula
Keplerian	$u_\phi^g = c\, v_{\rm K}(r_c^g) - r\Omega_F$
Zero-shear	$u_\phi^g = r_c^g\, \Omega^a$ with $\Omega^a = u_\phi^a / r_c^a$
Balanced	$u_\phi^g = \sqrt{v_{\rm K}^2\,(\mathcal{S} + \mathcal{P} + \mathcal{Q}) - r g_r} - r\Omega_F$

Notes. The boundary conditions from Table 2 are also available for u_ϕ.

3.14.3. Azimuthal velocity boundary conditions

Table 4 summarizes the BCs that are available for the azimuthal velocity. The most basic condition is the "Keplerian" BC which sets the azimuthal velocity to a fraction of the Keplerian velocity at the boundary, corrected for the frame rotation. The fraction can be chosen to be sub- or super-Keplerian to reflect additional pressure support or other effects. It can be used to model boundary layers where the disk connects to the star. Then the fraction is chosen such that u_ϕ is the surface rotation velocity of the star.

Depending on the flow close to the boundary, the Keplerian or any of the basic BCs might lead to shear at the boundary. This results in torques at the boundary which might be nonphysical or undesirable. To avoid this, we can use the "zero-shear" BC which removes the shear at the boundary by scaling the

azimuthal velocity in the last active cell to the ghost cell such that both have the same angular velocity.

Finally, the code supports the "balanced" BC which sets the azimuthal velocity such that the centrifugal force is in equilibrium with all other forces. This is especially useful for equilibrium disk models, see also Appendix B. In addition to the gravity of the central object, this takes into account pressure, the quadrupole moment from a central binary, smoothing, and self-gravity. It is expressed as:

$$u_\phi^g = \sqrt{v_\mathrm{K}^2 (\mathcal{S} + \mathcal{P} + \mathcal{Q}) - r g_r} - r\Omega_F, \tag{120}$$

where g_r is the radial component of the self-gravity acceleration (see Sect. 3.7) and $\mathcal{P}$, $\mathcal{S}$, and $\mathcal{Q}$ represent pressure, smoothing, and quadrupole moment, respectively, and the last term accounts for the rotating frame. This equation can be derived (see Appendix B) from the radial force balance starting from the radial momentum conservation Eq. (6).

Usually, the term $\mathcal{S}$ equals 1 in other instances of this formula in the literature. However, when the gravitational potential (Eq. (13)) is differentiated to calculate the external forces acting on the disk, additional terms that depend on the smoothing length appear, because the smoothing length depends on the location in the disk. These terms are accounted for in the centrifugal balance by:

$$\mathcal{S} = \frac{1 + (h\alpha_\mathrm{sm})^2 \left(1 + \frac{\mathrm{d}\log h}{\mathrm{d}\log r}\right)}{(1 + (h\alpha_\mathrm{sm})^2)^{3/2}}, \tag{121}$$

where α_sm is the smoothing parameter (see Sect. 3.6). See Appendix B for more detail. The pressure term is as usual given by (e.g., Baruteau 2008, Eq. (3.4)):

$$\mathcal{P} = h^2 \frac{\mathrm{d}\log \mathrm{P}}{\mathrm{d}\log r} = h^2 \left(2\frac{\mathrm{d}\log h}{\mathrm{d}\log r} + \frac{\mathrm{d}\log \Sigma}{\mathrm{d}\log r} - 1\right), \tag{122}$$

where where the last equality follows from $P = c_{s,\mathrm{iso}}^2 \Sigma$ and $c_{s,\mathrm{iso}} = h\, v_\mathrm{K}$. For simulations of circumbinary disks, it can be advantageous to account for the quadrupole term of the gravitation potential of the binary. The inclusion of this term can be turned on by the user. The term reads (Muñoz et al. 2019, Eq. (23)):

$$\mathcal{Q} = \frac{3Q}{r^2}, \tag{123}$$

with the quadrupole moment of the binary (Muñoz et al. 2019, Eq. (24)):

$$Q = \frac{a_b^2}{4} \frac{q_b}{(1+q_b)^2} \left(1 + \frac{3}{2} e_b^2\right). \tag{124}$$

Here, a_b is the binary separation, q_b is the binary mass ratio q_b, and e_b is the binary eccentricity.

3.14.4. Radiative transfer boundary conditions

The radiative transfer module solves a diffusion equation. In the azimuthal boundary, the periodicity is built in, but on the radial boundaries, a BC is required. If the module is enabled, the user must specify such conditions. The BC is applied right before the SOR solver is called.

There are three options available. First, a "zero-gradient" conditions for the diffusion coefficient K (see Eq. (52)). Second, a "zero-flux" condition which sets the diffusion coefficient to zero at the boundary (r_i^b). Third, an "outflow" condition which allows for the flux to leave the domain, implemented by setting $T = T_\mathrm{floor}$ in the ghost cell.

Table 5. Composite boundaries and their descriptions

Condition	Description
Center of mass	Calculate a disk model centered around the center of mass and shift it to the primary frame.
Roche lobe overflow	Simulates mass overflow through the L1 point between binary stars.
Outflow	$\{\Sigma, e\}$ = zero-gradient, v_r = outflow
Reflecting	$\{\Sigma, e\}$ = zero-gradient, v_r = reflecting
Reference	$\{\Sigma, e, u_r, u_\phi\}$ = reference
Custom	Template for the user to modify.

3.14.5. Composite boundary conditions

The BCs presented above apply to single variables. This subsection introduces the composite BCs, collections of BCs which apply to the variables, Σ, e, and u_r. The BC for u_ϕ still needs to be set individually, except for the "reference" case.

The "outflow", "reflecting", and "zero-gradient" composite BCs are simply shorthands to set the individual BCs as described in Table 5. These BCs reflect what is commonly used in other codes.

The "center of mass" BC is intended for the special case of simulating infinite circumbinary disks in the center of one of the stars. It enforces the initial power law profile for density and temperature, the equilibrium for azimuthal velocity according to Eq. (120), and the viscous speed for the radial velocity at the boundary and the outer damping region with respect to the center of mass of the N-body system instead of the coordinate center. In a second step, the gas velocities are transformed from polar to cartesian coordinates, shifted by the velocity of the coordinate center and transformed back to polar coordinates in the frame of the central object.

For simulations of cataclysmic variables, we implemented a "Roche lobe overflow" BC that models the mass flow through the L1 point between binary stars when one of the stars is overflowing its Roche lobe. While the function is implemented generally, it only works as intended if the primary is at the coordinate center and the outer edge of the domain has the size of the Lagrangian L_1 point.

We compute the width of the mass stream using the approximate function in Warner (2003) Sect. 2.4.1 which is a simplified version of the isothermal model for a Roche lobe overflow from Meyer & Meyer-Hofmeister (1983):

$$W \approx \sqrt{\frac{2.4 \times 10^{13}}{\pi} \left(\frac{T_s}{\mathrm{K}}\right) T_\mathrm{orb}^2(h)\,\mathrm{cm}^2}. \tag{125}$$

We then select the cell in the outer boundary, which is closest to the secondary and smooth the mass stream with a Gaussian profile over three times its width. We found that the initial stream width and temperature are of little importance as it quickly reaches a new equilibrium upon entering the simulation domain and that the width is mostly determined by the grid resolution.

The initial radial velocity of the stream is computed, the same as in Kley et al. (2008), as a small fraction binary's orbital frequency:

$$u_{r,\mathrm{stream}} = -2 \times 10^{-3} \Omega_\mathrm{bin} r_\mathrm{cell}, \tag{126}$$

however, again, the exact value of $u_{r,\mathrm{stream}}$ does not make a difference as long it is small compared to the orbital velocity. For

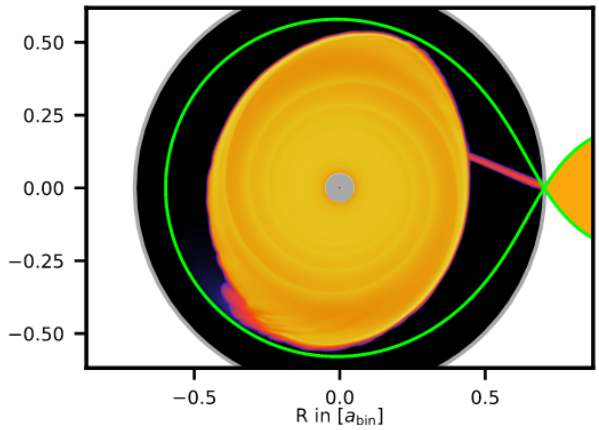

Fig. 4. Logarithmic density plot of a simulation with the "Roche lobe overflow" boundary condition showing the stream of material emerging from the L_1 point. The green line indicates the Roche lobe of the binary system and the grey circle is the outer boundary of the simulation domain. Outside the small region around the Lagrangian L_1 point the boundary condition is set to "outflow".

this localized infall condition, the described boundary values are set inside the transport step to ensure the chosen mass flux. We note that the Roche lobe overflow condition is only applied to the cells within the width of the stream. The rest of the ghost cells are unaffected. Thus, when using the Roche lobe overflow BC, additional individual BCs have to be specified for all variables. A demonstration of the "Roche lobe overflow" BC is presented in Fig. 4. Note that is up to the user to ensure that the outer boundary is located at the Lagrangian L_1 point.

3.14.6. Damping zones

FARGOCPT supports damping zones (DZ) at the inner and outer boundary as presented in de Val-Borro et al. (2006). The DZs are used to damp waves that are reflected at the boundaries. We choose to use the words "damping zone" instead of "damping boundary condition" because they are, strictly speaking, not a boundary condition in the context of partial differential equations. They behave more akin to a heat bath in thermodynamics.

The DZs are implemented as an exponential relaxation of any of the quantities $X \in \{\Sigma, e, u_r, u_\phi\}$. The damping is given by:

$$\frac{\partial X}{\partial t} = -\frac{X - X_{\rm ref}(\boldsymbol{r})}{\tau_{\rm damp}} a(r), \tag{127}$$

with the damping timescale $\tau_{\rm damp}$ and the damping function, $a(r)$.

The reference value, $X_{\rm ref}$, is saved as a separate snapshot at the beginning of the simulation and by default contains the initial values. It can also be manually changed by the user to support arbitrary damping fields in 2D. Other choices for $X_{\rm ref}$ include 0, the azimuthal average of the ring, or for the case of inner radial velocity, the viscous speed according to Eq. (119). This relaxation step is applied at the end of each time step as the last update of the hydro system, see Fig. 1.

The regions of the DZs are defined by two separate parameters $c_{\rm di}$ and $c_{\rm do}$ for the inner and outer zone, respectively. The inner damping zone reaches from $R_{\rm min}$ to $R_{\rm di} = c_{\rm di} R_{\rm min}$ and the outer damping zone reaches from $R_{\rm do} = c_{\rm do} R_{\rm max}$ to $R_{\rm max}$.

The damping timescale $\tau_{\rm damp}$ is given by:

$$\tau_{\rm damp} = \beta \frac{2\pi}{\Omega_{\rm K}(R_{\rm ref})}, \tag{128}$$

where β is a free parameter to configure the damping strength. The reference radius, $R_{\rm ref}$, can be chosen by the user for each zone separately and defaults to inner and outer boundary radius.

The damping function $a(r)$ is used to smoothly reduce the damping from one at the boundary to zero towards the active computational domain. We use a second-order polynomial with the condition that its first derivative vanishes at the transition from the damping zone to the active domain located at $R_{\rm di/do}$. This is fulfilled by the choice of:

$$a(r) = \begin{cases} \left(\frac{R_{\rm di} - r}{R_{\rm di} - R_{\rm min}}\right)^2 & \text{if } R_{\rm min} \le r \le R_{\rm di}, \\ \left(\frac{r - R_{\rm do}}{R_{\rm max} - R_{\rm do}}\right)^2 & \text{if } R_{\rm do} \le r \le R_{\rm max}, \\ 0 & \text{otherwise.} \end{cases} \tag{129}$$

The update step is discretized using the analytical solution of Eq. (127) to avoid overshooting and is given by:

$$X^{t+\Delta t} = X_{\rm ref} + (X^t - X_{\rm ref}) \exp\left(-\frac{\Delta t a(r)}{\tau_{\rm damp}}\right). \tag{130}$$

The DZ can be enabled for each quantity and in each zone individually. We note that the DZ creates and removes mass, energy and momentum in the simulation domain and, thus, breaks conservation of these quantities. The change of mass due to the DZ can be monitored.

4. Software features

4.1. Hybrid parallelization

FARGOCPT has been parallelized using a hybrid MPI + OpenMP approach. This is currently the most efficient way to make use of the underlying CPU and memory structure of most supercomputers. A scaling test can be found in Appendix A which shows that the code reasonably scales at least up to 500 CPU cores.

Modern computers often have multiple NUMA (non-uniform memory access) nodes per processor package. As a result, a specific CPU core can access a part of the system memory with lower latency than the rest of the memory. Because hydrodynamics simulations rely heavily on memory access, it is important to instruct the operating system to take this into account.

This is automatically attempted by default when using the launcher (see Sect. 4.3), but can be done manually and the automatic mapping should be checked. In practice, one MPI process is launched per NUMA node and OpenMP threads are launched as many as there are cores per NUMA node. It is usually worthwhile to tune the execution settings (number of processes and threads) to the architecture of the computer used to run the simulation. To find out the number of NUMA nodes and cores per NUMA node on a Linux system, one can use the lstopo or lscpu utilities. For consumer PCs, one might need to enable a setting in the bios for the operating system to be aware of the NUMA topology.

4.2. Interactivity via signals

Planet-disk interaction simulations with any of the available codes typically run in a non-interactive mode, and only provide feedback through logs and monitor files once a predefined time step has been covered by the simulation. For example, in the case that the CFL time step tends to zero, this can lead to simulations freezing without any indication of the cause.

To address issues such as frozen simulations, we have introduced UNIX signal handling with three signals. One can interact with the simulation using the kill command, for example, using kill -SIGUSR1 <fargo pid>.

`SIGUSR1` allows users to request a status report, including current simulation time and details on CFL time step constraints, aiding in identifying freeze causes. `SIGUSR2` enables immediate stack trace printing, useful in development for locating algorithmic issues or runtime issues, for instance, when a cluster filesystem hangs. Finally, `SIGTERM` allows for a graceful shutdown, saving a snapshot for later resumption, beneficial in cluster environments or when simulations must be paused due to resource sharing.

4.3. Usability

We aimed to make using the code as straightforward as possible to encourage students to perform numerical experiments. This includes changes to the command line interface as well as the restructuring of the config files discussed later in Sect. 4.6.

The command line interface traditionally included the selection of a mode, either to start or restart a simulation and the specification of the path to a config file. A common task is to restart an existing simulation to extend it after its initially targeted time was reached or after the allocated wall time on a shared computing resource has elapsed.

Traditionally, this required specifying the output number of the snapshot that was last written to disk. In our experience, this manual task can be error-prone, sometimes resulting in the loss of parts of the simulation data. We added the "automatic" mode, which starts the simulation if no simulation output has been written yet and restarts the simulation from the latest snapshot present. This has proven to essentially eliminate errors during routine restarting of simulations, saving duplicate spending of computational resources.

Furthermore, the compiled executable is launched through a Python launcher to handle the setup for parallel execution. This launcher guesses an appropriate selection of the OpenMP thread and MPI process numbers under several different workload managers and MPI implementations. Again, this is aimed to enable straightforward access to the code without specific knowledge about OpenMP and MPI, which can initially be a substantial hurdle. Experienced users can skip this launcher, write their own or manually specify the parameters, to achieve a potentially more optimal configuration.

Installing all required libraries and compiling the code can be a substantial hurdle, especially for someone not familiar with Linux operating systems. To this end, we made FARGOCPT seamlessly available inside the virtual computers provided by GitHub called "codespaces"[1]. Using this service, one can start a virtual machine with the code ready to go from within the FARGOCPT GitHub repository[2] with the click of a button. Then one can get familiar with or use the code with the integrated Jupyter notebooks, all in the browser and without needing to use the command line or compile the code. Although these codespaces have runtime restrictions, the freely available resources are enough, at the time of writing, for learning to use the code, prototyping setups and even low-resolution scientific simulations. When this free service should no longer be available, the FARGOCPT code can still be used in a similar fashion using the `docker` container provided in the GitHub repository.

[1] https://github.com/features/codespaces
[2] https://github.com/rometsch/fargocpt

4.4. Python interface

We created a Python module that comes with the code to facilitate starting the code from within a Jupyter Notebook or Python scripts, loading data from output directories and creating an interactive overview plot. It comes with a command line interface that can be used to start simulations with an automatically determined suitable CPU allocation and to inspect output data.

The GitHub repository of the code includes multiple Jupyter notebooks with example cases that illustrate how to build and use the code. Additionally, there are examples of how to load and visualize the output data and some common simulation scenarios.

4.5. C++ port and code restructuring

FargoADSG (Baruteau 2008) was converted from a C code to a C++ object-oriented by Müller et al. (2012). Notably, the data structure was converted to be object-oriented, a data class holding a number of other structures for the storage of physical quantities defined on a polar grid. Functionalities of these classes include the tracking of units with pre- and post-hooks for input and output.

Later, functionally separate parts of the code were split up (into C++ namespaces). Examples include software aspects such as the parsing and storage of parameters, units and output, and physics modules such as the N-body system, boundary conditions or radiative transport. This was done to highlight the structure of the code to make it easier to maintain and extend, and to make it easier to understand for new users.

4.6. Config files

Config files have been changed from a custom flavor of the `ini` file format to the well-defined and documented `yaml` format. The advantage of this is twofold. First, the config files can be easily processed and generated using scripts, for example, with any of the `yaml` packages in the Python ecosystem. This can help avoid errors in preparing simulations for parameter studies. Along the same lines, the parsing of the config files in the actual C++ simulation code is off-loaded to an existing and tested library which can handle and report syntax errors in the config files and handle type conversions. The latter two are examples in which the authors experienced time-consuming errors with other codes in the past.

Second, `yaml` supports structured data which enables setting the parameters and initial conditions of the N-body objects within the config file. This change removes the column-based and unchecked planet file in favor of a structured entry in the main configuration file.

An aspect that sets FARGOCPT apart from other versions of the code is that the config file is the only place that is changed to configure the simulations. No compile time parameters are used. In our opinion, this makes the code easier to use for first-time users.

4.7. Output format

Originally, all simulation output files were stored in one single output folder for all snapshots. Depending on the simulation, several thousand snapshots can be written to disk resulting in several thousand to several tens of thousands of files in a single folder. This makes working with these simulations cumbersome because simply listing the contents of this output directory can take multiple tens of seconds on cluster file systems which are optimized for parallel throughput rather than metadata access.

Furthermore, extracting a single snapshot from a simulation directory included the error-prone manual extraction of various state variables from different text files.

In FARGO-like codes, time series data is usually written to tab-separated-value text files. However, the contents of the columns are often not described, neither the content of a column nor its unit. This lack of description of the data is made worse by the fact that the structure of these files can change between different versions of the same code or be modified by the user to track any quantity of interest that is not already present in the standard output leading to confusion and necessitating the knowledge of which particular version of the code was used to generate a particular set out output data. While we generally encourage saving which exact version of the code was used (e.g., the git commit id), even storing the source code of the simulation with the output data, reading the values from a text file should not necessitate the study of the accompanying source code.

In addition, the input files for the simulation were required to infer the unit system used in the simulation because the base units of length, mass and time can be set in the configuration file. Hence, the outputs were not self-descriptive.

We remedied these issues with the following changes. The output directory was restructured such that each snapshot was saved into a separate directory within the `snapshot` subdirectory. Such a directory contains all binary data about density, energy and velocity fields, all scalar quantities such as the time, the rotation angle of the frame and intermediate integration variables and all information about the state of the N-body and particle systems. Additionally, a copy of the input file is saved for each snapshot to save the history of parameters should they change during a restart.

Additionally, yaml info files are written to the output directory containing information about the units used in the simulation and the quantities that were written as parts of the snapshots to unambiguously specify the physical quantities. This grounds these code units on a physical scale. A rescaling of the results can still be done as long as the set of physical assumptions allow it.

The files containing time series data are now collected in one single sub-directory called `monitor`. Each such text file includes a header that describes the content of each column in the text file and specifies its unit in a string readable by the `astropy` Python library in an automated fashion.

Furthermore, the output directory now contains an empty text file with the name `fargocpt_output_vx_y`, where `x_y` specifies the major and minor version of the code. This helps with the automation of postprocessing when multiple versions of the same code or even different codes are used in a single project.

4.8. Unit system

Because we carry out numerical simulations of physical processes, we necessarily need to choose a system of units. This unit system, often called "code units", can be specified using two or four parameters in the config file. The base length L_0 and the base mass M_0 are required and the base time T_0 and the base temperature Θ_0 are optional. If the base time T_0 is not chosen explicitly, it is computed such that G = 1 in code units. This is equivalent to one Keplerian orbit at distance L_0 around an object of mass M_0 having a period of 2π, thus:

$$T_0 = \sqrt{\frac{L_0^3}{GM_0}} = \frac{1}{\Omega_K\big|_{M_0,L_0}}, \tag{131}$$

with the gravitational constant G and the Keplerian angular velocity, $\Omega_K = \sqrt{GM/R^3}$. If the temperature unit is not specified, it is calculated such that the specific gas constant $R = \frac{k_B}{\mu}$ is unity in code units, thus:

$$\Theta_0 = \frac{G\,\mu\,M_0}{k_B\,L_0}, \tag{132}$$

with the mean molecular weight μ and the Boltzmann constant k_B. Internally, all calculations are carried out and all output is written in the code unit system $\mathcal{U} = (L_0, M_0, T_0, \Theta_0)$.

In the config file, the user can specify physical parameters either as a number without units, in which case they are interpreted to be in code units, or they can be specified with a number and a unit symbol. This number and unit are then automatically converted to code units. As an example, consider a unit system with $L_0 = 1$ au and $M_0 = 1\,M_\odot$. The reference surface density, Σ_0, which has the key `Sigma0` in the config file can then either be specified in code units using

```
Sigma0: 1e-5,
```

in which case, $\Sigma_0 = 10^{-5}\,\frac{M_0}{L_0^2} = 10^{-5}\,\frac{M_\odot}{\mathrm{au}^2} \approx 88.85\,\frac{\mathrm{g}}{\mathrm{cm}^2}$. Alternatively, the same could be specified using:

```
Sigma0: 88.85 g/cm^2.
```

The former version is more informative in simulations of a scale-free problem while the latter version is more informative in simulations aimed at simulating existing protoplanetary disk systems. This flexibility in terms of units combines the usefulness of a unit system adapted to the physical problem at hand (code units) with the necessity to specify certain physical parameters in physical units, such as parameters inferred from observations or experiments. We hope that this feature helps to avoid common conversion errors in setting up simulations.

The implementation of the unit parsing is based on the C++ units runtime library (LLNL 2022). All conversions are performed in the initialization step, so variables during the actual simulations do not carry any units.

Unit symbols supported in the config file are specified by the LLNL (2022) library[3], they include all SI units with prefixes, and the convenience units: `au`, `solMass`, `solRadius`, `jupiterMass`, `jupiterRadius`, `earthMass`, and `earthRadius`. Usually, most unit strings that work with the Python `astropy` package also work here. Furthermore, combinations of powers of units are supported, as in the example above.

In addition to the definition of units, (LLNL 2022) is also the source for the definition of physical constant[4], namely the

[3] See https://units.readthedocs.io/en/latest/user-guide/from_string.html for more details.

[4] https://units.readthedocs.io/en/latest/user-guide/Physical_constants.html

Table 6. Automated test cases and references to their descriptions in Appendix D.

App.	Test
D.1	Steady state accretion disk
D.2	Shocktube
D.3	Viscous heating-cooling equilibrium temperature
D.4	Viscous spreading ring
D.5	Dust diffusion
D.6	Dust drift
D.7	Type I migration torque
D.8	Flux-limited diffusion 1D
D.9	Flux-limited diffusion 2D
D.10	Self-gravity solver
	Cold disk with the perfect equation of state
	Irradiation-cooling equilibrium temperature
	N-body integration
	Planet orbiting a disk

gravitational constant, G, the Boltzmann constant, k_B, the atomic mass units u, the Planck constant, h, and the speed of light, c. These are based on the 2019 redefinition of the SI units[5] and the NIST 2018 CODATA[6] physical constants table.

4.9. Test suite

Having a test suite is crucial to illustrate that the code is working as intended and that the various physical modules of the code actually provide approximations to the underlying equations. This is an essential part of any simulation code.

FARGOCPT comes with an automatic test suite. The test suite can be run by executing the `run_tests.sh` script within the `tests` directory. This automatically executes multiple test cases and compares the results to reference data or theoretical expectations. The result of the test is then either "passed" or "failed". Each test case therefore includes threshold values for deviations from the reference data. The test suite is designed to be run on a local computer in a matter of minutes and does not require a supercomputer. This makes testing the code base relatively straightforward and cheap. Currently, the automatic tests include tests for most of the major physical modules. The tests are are listed in Table 6. See Appendix D for more details.

5. Discussion

5.1. Leapfrog-like scheme

In addition to the integration schedule presented in Fig. 1, we also implemented a leapfrog-like schedule presented in Appendix C. This scheme performs the source term step twice with half of the time step size and the transport step once with the full time step size. The transport step is performed in between the two source term steps.

This allows for larger simulation time steps by relaxing the CFL criteria of the source step but it also becomes more expensive because the source term is evaluated twice. This is prohibitive when self-gravity or radiative transport is enabled. Without these enabled, the scheme still runs around 7% slower than the Euler scheme.

While in theory, a leapfrog scheme has higher accuracy than an Euler scheme, and it is advantageous to conduct the transport step less often and with larger time steps due to numerical diffusion, we found that the benefits are negligible for typical planet disk interaction simulations. We found the leapfrog scheme only to be beneficial for simulations where the source terms dominate the numerical errors and not the transport step, for instance, in test simulations of an equilibrium disk. An example of such a simulation is the heating and cooling test presented in Appendix D.3. In this model, the transport step is effectively only an advection along the azimuthal direction, which is trivial in the polar coordinate system.

Because of these reasons, we see no benefit in using the leapfrog scheme as implemented in the current version of the code over the default scheme for typical planet–disk interaction simulations. The operator splitting scheme we use is formally only accurate up to first-order in time (worst case). Therefore, we suspect that more substantial improvements to accuracy can be made by implementing higher-order time stepping such as a second-order Runge-Kutta scheme. This is left for future work.

5.2. Considering why another FARGO code would be useful

FARGOCPT is another addition to the family of FARGO codes. This raises the question of why the community needs another FARGO code when FARGO3D or FARGOCA exist which even support 3D simulations. Our answer to this question is twofold. First, to the knowledge of the authors, the collection of physics modules implemented in FARGOCPT is unique compared to other publicly available versions of codes for the study of planet–disk interaction. At present, the FARGOCPT code includes different equations of state, viscous heating and irradiation, local β-cooling, cooling through the disk surfaces, midplane energy transport, self-gravity, high-order N-body integration, accretion onto N-body objects, and a particle module which includes gas drag laws for a wide range of particle sizes and dust diffusion, all while making use of the FARGO speedup. For example, the public version of FARGO3D does not support self-gravity, while FARGOADSG and Athena++ do not support radiation transport. Both are processes that are important in current problems of planet–disk interaction (e.g., Ziampras et al. 2023a) and protoplanetary disks (e.g., Rendon Restrepo & Barge 2022). FARGOCPT also includes many of the typically used effective models for planet–disk interaction, such as β-cooling. While these effective models can be implemented in other codes with relative ease by an experienced programmer, these implementations still have to be manually validated by the user. Hence, having a tested implementation is nearly always preferable (Wilson et al. 2012), even if they are only taken as a starting point and modified for a specific problem.

Second, we believe that the code presented here is easier to use, understand and modify than other versions of FARGO. This is especially important for students who are new to the field and want to perform numerical experiments. We anticipate that this will lead to a more efficient learning process and a more efficient use of the time of the students. Additionally, features such as the support for physical units in the config files and a self-contained output reduce the chance of human error in the simulation workflow. This leads to a more efficient use of the attention of the user to the physical model behind the simulation and the scientific problem at hand.

[5] https://www.nist.gov/si-redefinition/meet-constants
[6] https://physics.nist.gov/cuu/Constants/Table/allascii.txt

Furthermore, we are not aware of any other hydrodynamics code for the study of planet–disk interactions that can be used in the browser. This property can make FARGOCPT a valuable tool for teaching and learning about planet–disk interactions. Indeed, it was already successfully used to teach hydrodynamics and planet migration at the SPP 1992 summer school on planet formation in Rauenberg, Germany, in August of 2023.

5.3. Future development

As with any software project, many possible improvements can be made to the code base. Here, we outline some of the potential improvements that we believe might be worthwhile to be incorporated into future iterations of the code:

More general self-gravity solver. One of the foundational assumptions of our current self-gravity module is that the aspect ratio needs to be assumed constant for the Fourier Method to work. This limits the accuracy of simulations with the combination of self-gravity and radiation physics, the latter of which generally leads to a non-uniform aspect ratio. Removing this limitation would, for example, allow for more accurate studies of gravitational collapse within the disk, which includes a balance between pressure, built up by compression heating and reduced by radiation transport, and self-gravity. This could be achieved using tree-based or multigrid methods.

Higher-order time-stepping. By integrating higher-order time-stepping techniques, we can potentially achieve better temporal resolution and improved simulation stability, thus ensuring more accurate representations of physical systems over time. The groundwork for such a change has already been laid in the leapfrog-like scheme presented in Appendix C and a second-order Runge-Kutta scheme could be implemented in a similar fashion.

Matrix solvers for heating, cooling and viscosity. Currently, the heating and cooling terms, as well as the viscosity update rely on either a simple implicit but local update step and the viscosity update uses a simple explicit update step (see Sect. 2 for resulting issues). These updates can be replaced by fully implicit updates which rely on a matrix or linear system solver to increase accuracy and stability (see also Sect. 3.9.2). To this end, the SOR linear system solver used in the flux-limited diffusion model could be adapted to the heating, cooling and viscosity update steps.

Irradiation Using Ray-tracing. For studying scenarios such as accretion onto planets, where the impact of radiation sources can dominate the local evolution, introducing a ray-tracing mechanism for irradiation can be beneficial. Currently, the irradiation is computed using a simple distance-based approximation, formally only valid for a single star in the center of a flaring disk. While it is computationally expensive, ray tracing can provide a more precise depiction of the dynamics of the disk when it is heated by accreting planets including influences of shadows.

In this paper, we introduce FARGOCPT, a new and publicly available[7] version of the FARGO code. We present the new and improved physics modules, such as radiation physics, self-gravity, and the particle module, and the new features of the code, such as the hybrid parallelization, the Python interface, and the new test suite. The paper is intended as a reference for students and researchers who want to use the code and as a starting point for future development of this and other FARGO-like codes. We hope that the code will be useful for the community and that it will be used to study the complex and fascinating physics of planet–disk interactions and protoplanetary disks.

[7] Available at `https://github.com/rometsch/fargocpt`.

Acknowledgements. TR and LJ would like to express their gratitude to Alex Ziampras for the numerous insightful and productive discussions and Gabriel-Dominique Marleau for helpful comments on the thermodynamics aspects of the manuscript. T.R., G.P., W.K. and C.D. acknowledge funding from the Deutsche Forschungsgemeinschaft (DFG) research group FOR 2634 "Planet Formation Witnesses and Probes: Transition Disks" under grants DU 414/22-1, and KL 650/29-1, 650/29-2, 650/30-1, and 650/30-2. SRR acknowledges funding from the European Union (ERC, Epoch-of-Taurus, 101043302). Views and opinions expressed are however those of the authors only and do not necessarily reflect those of the European Union or the European Research Council. Neither the European Union nor the granting authority can be held responsible for them. The authors acknowledge support by the High Performance and Cloud Computing Group at the Zentrum für Datenverarbeitung of the University of Tübingen, the state of Baden-Württemberg through bwHPC and the German Research Foundation (DFG) through grant INST 37/935-z1 FUGG. Plots in this paper were made using the Python library `matplotlib` (Hunter 2007).

References

Anderson, D. A., Tannehill, J. C., & Pletcher, R. H. 2020, Computational Fluid Mechanics and Heat Transfer, 4th edn., Computational and Physical Processes in Mechanics and Thermal Sciences (Boca Raton, FL: CRC Press)
Artymowicz, P., & Lubow, S. H. 1994, ApJ, 421, 651
Baruteau, C. 2008, PhD thesis, Observatoire de Paris
Baruteau, C., & Masset, F. 2008a, ApJ, 672, 1054
Baruteau, C., & Masset, F. 2008b, ApJ, 678, 483
Baruteau, C., & Zhu, Z. 2016, MNRAS, 458, 3927
Baruteau, C., Crida, A., Paardekooper, S. J., et al. 2014, Protostars and Planets VI, eds. H. Beuther, R. S. Klessen, C. P. Dullemond, & T. Henning (University of Arizona Press), 667
Bell, K. R., & Lin, D. N. C. 1994, ApJ, 427, 987
Benítez-Llambay, P., & Masset, F. 2016, ApJS, 223, 11
Bertin, G., & Lodato, G. 1999, A&A, 350, 694
Binney, J., & Tremaine, S. 1987, Galactic Dynamics (Princeton University Press)
Bodenheimer, P., Laughlin, G., Rozyczka, M., et al. 2006, Numerical Methods in Astrophysics: An Introduction, Series in Astronomy and Astrophysics (Taylor & Francis)
Cash, J. R., & Karp, A. H. 1990, ACM Trans. Math. Softw., 16, 201
Charnoz, S., Fouchet, L., Aleon, J., & Moreira, M. 2011, ApJ, 737, 33
Chiang, E. I., & Goldreich, P. 1997, ApJ, 490, 368
Chrenko, O., Brož, M., & Lambrechts, M. 2017, A&A, 606, A114
Commerçon, B., Teyssier, R., Audit, E., Hennebelle, P., & Chabrier, G. 2011, A&A, 529, A35
Cox, A. N., & Stewart, J. N. 1969, Nauchnye Informatsii, 15, 1
Crida, A., Morbidelli, A., & Masset, F. 2007, A&A, 461, 1173
D'Angelo, G., & Marzari, F. 2012, ApJ, 757, 50
D'Angelo, G., & Bodenheimer, P. 2013, ApJ, 778, 77
D'Angelo, G., Henning, T., & Kley, W. 2002, A&A, 385, 647
D'Angelo, G., Henning, T., & Kley, W. 2003, ApJ, 599, 548
de Val-Borro, M., Edgar, R. G., Artymowicz, P., et al. 2006, MNRAS, 370, 529
Frigo, M., & Johnson, S. G. 2005, Proc. IEEE, 93, 216
Gammie, C. F. 2001, ApJ, 553, 174
Geiser, J., Hueso, J. L., & Martinez, E. 2017, J. Comput. Appl. Math., 309, 359
Günther, R., Schäfer, C., & Kley, W. 2004, A&A, 423, 559
Haghighipour, N., & Boss, A. P. 2003, ApJ, 583, 996
Hawley, J. F., Smarr, L. L., & Wilson, J. R. 1984, ApJ, 277, 296
Hayashi, C. 1981, Progr. Theor. Phys. Suppl., 70, 35
Hubeny, I. 1990, ApJ, 351, 632
Hunter, J. D. 2007, Comput. Sci. Eng., 9, 90
Ichikawa, S., & Osaki, Y. 1992, PASJ, 44, 15
Jordan, L. M., Kley, W., Picogna, G., & Marzari, F. 2021, A&A, 654, A54
Joseph, J., Ziampras, A., Jordan, L., Turpin, G. A., & Nelson, R. P. 2023, A&A, 678, A134
Kimura, M., Osaki, Y., Kato, T., & Mineshige, S. 2020, PASJ, 72, 22
Klahr, H., & Kley, W. 2006, A&A, 445, 747
Kley, W. 1989, A&A, 208, 98
Kley, W. 1998, A&A, 338, L37
Kley, W. 1999, MNRAS, 303, 696

Kley, W., & Crida, A. 2008, A&A, 487, L9
Kley, W., & Nelson, R. P. 2012, ARA&A, 50, 211
Kley, W., Papaloizou, J. C. B., & Ogilvie, G. I. 2008, A&A, 487, 671
Kolb, S. M., Stute, M., Kley, W., & Mignone, A. 2013, A&A, 559, A80
Lega, E., Crida, A., Bitsch, B., & Morbidelli, A. 2014, MNRAS, 440, 683
Levermore, C. D. 1984, J. Quant. Spec. Radiat. Transf., 31, 149
Levermore, C. D., & Pomraning, G. C. 1981, ApJ, 248, 321
Lin, D. N. C., & Papaloizou, J. 1985, On the Dynamical Origin of the Solar System (University of Arizona Press)
LLNL 2022, Units C++ runtime library, https://github.com/LLNL
Lodato, G. 2008, New Astron. Rev, 52, 21
Lust, R. 1952, Zeitsch. Naturfor. A, 7, 87
Lynden-Bell, D., & Pringle, J. E. 1974, MNRAS, 168, 603
Masset, F. 2000, A&AS, 141, 165
Masset, F. 2002, A&A, 387, 605
Masset, F. 2015, Astrophysics Source Code Library [record ascl:1509.008]
Masset, F. 2017, MNRAS, 472, 4204
Menou, K., & Goodman, J. 2004, ApJ, 606, 520
Meyer, F., & Meyer-Hofmeister, E. 1983, A&A, 121, 29
Mignone, A., Bodo, G., Massaglia, S., et al. 2007, ApJS, 170, 228
Mignone, A., Flock, M., & Vaidya, B. 2019, ApJS, 244, 38
Mihalas, D., & Mihalas, B. W. 1984, Foundations of Radiation Hydrodynamics (Oxford University Press)
Mineshige, S., & Osaki, Y. 1983, PASJ, 35, 377
Morohoshi, K., & Tanaka, H. 2003, MNRAS, 346, 915
Muñoz, D. J., Miranda, R., & Lai, D. 2019, ApJ, 871, 84
Müller, T. W. A. 2013, Dissertation, Universität Tübingen
Müller, T. W. A., & Kley, W. 2012, A&A, 539, A18
Müller, T. W. A., & Kley, W. 2013, A&A, 560, A40
Müller, T. W. A., Kley, W., & Meru, F. 2012, A&A, 541, A123
Nakagawa, Y., Sekiya, M., & Hayashi, C. 1986, Icarus, 67, 375
O'Neill, M. 2018, Bob Jenkins's Small PRNG Passes PractRand (And More!), https://www.pcg-random.org/posts/bob-jenkins-small-prng-passes-practrand.html
Paardekooper, S. J., & Mellema, G. 2006, A&A, 459, L17
Paardekooper, S. J., & Papaloizou, J. C. B. 2008, A&A, 485, 877
Paardekooper, S.-J., Baruteau, C., & Kley, W. 2011, MNRAS, 410, 293
Paardekooper, S., Dong, R., Duffell, P., et al. 2023, Astron. Soc. Pac., 534, 685
Picogna, G., & Kley, W. 2015, A&A, 584, A110
Picogna, G., Stoll, M. H. R., & Kley, W. 2018, A&A, 616, A116
Pierens, A., & Huré, J. M. 2005, A&A, 433, L37
Pierens, A., & Nelson, R. P. 2008, A&A, 482, 333
Price, D. J., Wurster, J., Tricco, T. S., et al. 2018, PASA, 35, e031
Pringle, J. E. 1981, ARA&A, 19, 137
Regály, Z., Juhász, A., Sándor, Z., & Dullemond, C. P. 2012, MNRAS, 419, 1701
Rein, H., & Liu, S.-F. 2012, A&A, 537, A128
Rein, H., & Spiegel, D. S. 2015, MNRAS, 446, 1424
Rendon Restrepo, S., & Barge, P. 2022, A&A, 666, A92
Rendon Restrepo, S., & Barge, P. 2023, A&A, 675, A96
Rendon Restrepo, S., & Gressel, O. 2023, 2D simulations of dust trapping by self-gravitating vortices, Protostars and Planets VII, poster PF-07-003
Rendon Restrepo, S., Barge, P., & Vavrik, R. 2022, arXiv e-prints [arXiv:2207.04252]
Rometsch, T., Rodenkirch, P. J., Kley, W., & Dullemond, C. P. 2020, A&A, 643, A87
Rometsch, T., Ziampras, A., Kley, W., & Béthune, W. 2021, A&A, 656, A130
Sauer, T. 2012, Numerical Analysis (Pearson Education)
Shakura, N. I., & Sunyaev, R. A. 1973, A&A, 500, 33
Shu, F. H. 1992, The Physics of Astrophysics, II: Gas Dynamics (University Science Books)
Sod, G. A. 1978, J. Comput. Phys., 27, 1
Speith, R., & Kley, W. 2003, A&A, 399, 395
Stone, J. M., & Norman, M. L. 1992, ApJS, 80, 753
Stone, J. M., Tomida, K., White, C. J., & Felker, K. G. 2020, ApJS, 249, 4
Tscharnuter, W. M., & Winkler, K. H. A. 1979, Comput. Phys. Commun., 18, 171
Vaidya, B., Mignone, A., Bodo, G., & Massaglia, S. 2015, A&A, 580, A110
van Leer, B. 1977, J. Comput. Phys., 23, 276
Von Neumann, J., & Richtmyer, R. D. 1950, J. Appl. Phys., 21, 232
Warner, B. 2003, Cataclysmic Variable Stars (Cambridge University Press)
Wilson, G., Aruliah, D. A., Titus Brown, C., et al. 2012, arXiv e-prints [arXiv:1210.0530]
Woitke, P., & Helling, C. 2003, A&A, 399, 297
Woodward, P., & Colella, P. 1984, J. Comput. Phys., 54, 115
Youdin, A. N., & Lithwick, Y. 2007, Icarus, 192, 588
Zhu, Z., Stone, J. M., Rafikov, R. R., & Bai, X.-n. 2014, ApJ, 785, 122
Ziampras, A., Nelson, R. P., & Rafikov, R. R. 2023a, MNRAS, 524, 3930
Ziampras, A., Paardekooper, S.-J., & Nelson, R. P. 2023b, MNRAS, 525, 5893

Appendix A: Parallel scaling

This section presents the scaling of the code with the number of cores used in the simulation. The scaling was measured on the Tübingen compute cluster BINAC on 1 to 16 nodes with 28 cores each of an Intel Xeon E5-2630v4 CPU connected via an InfiniBand network.

The test was performed using a locally isothermal disk with an embedded Saturn-mass planet and a grid size of $N_r \times N_\phi = 1024 \times 2048$. The strong scaling speed-up, namely, the time required for a constant workload (same grid size) divided by the number of cores, is nearly perfect up to 224 cores, see Fig. A.1.

For 112 cores, there appears to be a super-linear speed-up. The code is parallelized by dividing the disk up into radial subdomains, each assigned to an MPI process (one for each NUMA node used). Each subdomain consists of several consecutive rings. These domains are then processed by several OpenMP threads (7 in the case of this test). The case of 112 cores might be a sweet spot where the CPU cache is utilized more efficiently for this specific size of the subdomain, resulting in the super-linear speed up. For higher core counts, the speed-up declines, which might be due to the increased communication overhead or because the grid size is not large enough to keep the cores busy.

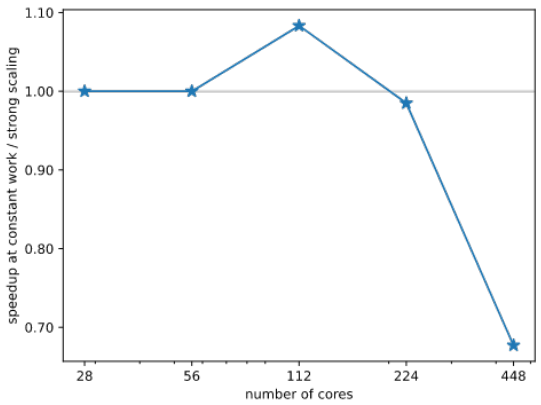

Fig. A.1. Speedup factor with number of cores on the Tübingen compute cluster BINAC.

Appendix B: Simulations of equilibrium disks

To simulate a steady-state accretion disk, we prescribe the densities and velocities of a locally isothermal model at the outer boundary with an additional wave-killing zone where we damp to only the velocities of the isothermal mode. To achieve a steady state, we need to consider all forces in the centrifugal balance.

The model disk is described by the following equations. The scale height is given by:

$$H = h\,r = h_0\,r\left(\frac{r}{R_0}\right)^F, \tag{B.1}$$

where r is the distance to the central star, F is the flaring index, and R_0 the radius where $h = h_0$. The surface density is:

$$\Sigma = \Sigma_0\left(\frac{r}{R_0}\right)^{-S}, \tag{B.2}$$

with the free parameter, S. The sound speed is:

$$c_s^{\rm iso} = h v_{\rm K}, \tag{B.3}$$

where $v_{\rm K}$ and $\Omega_{\rm K}$ denote the Keplerian orbital velocity and frequency. Assuming an perfect equation of state, the pressure is:

$$P = {c_s^{\rm iso}}^2\,\Sigma. \tag{B.4}$$

The gravitational interaction between the central star and the disk is computed using a smoothed gravitational potential of a point mass:

$$\Phi = -\frac{GM}{\sqrt{r^2+\epsilon^2}} = -\frac{GM}{r}\frac{1}{\sqrt{1+(\frac{\epsilon}{r})^2}}, \tag{B.5}$$

with the smoothing length, $\epsilon = \alpha_{\rm sm} H$. Note that this smoothing length also has a radial dependence. Its radial derivative is given by:

$$\frac{\partial \epsilon}{\partial r} = (F+1)\frac{\epsilon}{r}. \tag{B.6}$$

With that in mind, we can compute the radial derivative of the smoothed potential:

$$\frac{\partial \Phi}{\partial r} = -\frac{GM}{r^2}\frac{1+(F+1)(\frac{\epsilon}{r})^2}{\sqrt{1+(\frac{\epsilon}{r})^2}^3}, \tag{B.7}$$

where we identify the second term on the r.h.s as the effect of the gravitational force due to smoothing.

Following is a derivation of the equilibrium azimuthal velocity of the disk. Assume, that the disk is axially symmetric and in a steady state, thus, in the radial momentum equation Eq. (6) we have $\partial/\partial t = 0$ and $\partial/\partial\phi = 0$. Additionally, assume, that u_r is much smaller than u_ϕ and that radial changes of u_r are small, so $u_r \partial u_r/\partial r$ can be neglected. Furthermore, assume that viscous effects can be neglected, $f_r = 0$. Equation (6) is then reduced to:

$$-\frac{u_\phi^2}{r} = -\frac{1}{\Sigma}\frac{\partial P}{\partial r} + k_r + \frac{f_r}{\Sigma}, \tag{B.8}$$

We now assume that the gravitational forces are the only external force, $k_r = -\partial\Phi/\partial r + g_r$, with the gravitational potential due to point masses, Φ, and the radial acceleration due to the gravity of the disk, g_r. Then, multiply by $-r$ to arrive at:

$$u_\phi^2 = \frac{r}{\Sigma}\frac{\partial P}{\partial r} + r\frac{\partial \Phi}{\partial r} - r g_r = \frac{r\,c_s^2}{P}\frac{\partial P}{\partial r} + r\frac{GM_*}{r^2} f_g - r g_r \tag{B.9}$$

$$= c_s^2 \frac{\partial \log P}{\partial \log r} + v_{\rm K}\, f_g - r g_r. \tag{B.10}$$

In the second step, we used $P = c_s^2\Sigma$ and factored out the squared Keplerian velocity, $v_K^2 = GM_*/r$, from the gravitational potential term. The new factor f_g contains the information about the spatial dependence of the smoothing length and of higher multipole moments of the gravitational potential (for the quadrupole term see Eq. (123)). For a non-smoothed gravitational potential of a point mass or one with a smoothing length without spacial dependence $f_g = 1$. Typically, f_g is close to unity. Now we divide by r^2, take the square root, and use $c_s = h\,v_{\rm K}$ to obtain the angular velocity,

$$\Omega = \sqrt{\Omega_{\rm K}\left[h^2\frac{\partial \log P}{\partial \log r} + f_g\right] - r\,g_r}. \tag{B.11}$$

Finally, we insert the expressions for h (Eq. (B.1)) and Σ (Eq. (B.2)), and differentiate the smoothed gravitational potential (see Eq. (B.7)) to obtain:

$$\Omega = \sqrt{\Omega_\mathrm{K}^2 \left[(2F - S - 1)\, h^2 + \frac{1 + (F+1) h^2 \alpha_\mathrm{sm}^2}{(1 + h^2 \alpha_\mathrm{sm}^2)^{(3/2)}} + Q \right] - \frac{g_r}{r}}. \tag{B.12}$$

The second term in square brackets would be equal to 1 if the effect of the gravitational smoothing is neglected and the formula would then be the common solution for a pressure-supported disk.

The quadrupole term, Q, (see Eq. (123)) is only needed for a disk around binary stars. In this case, the approximation used for computing the quadrupole term is linearly independent of the other contribution to the centrifugal balance Eq. (B.8). Therefore the contribution of the quadrupole moment can simply be added to the term inside the square brackets.

The radial velocity in a steady-state viscous accretion disk is given by (e.g., Lodato 2008):

$$\Sigma u_r \frac{\partial (r^2 \omega)}{\partial r} = \frac{1}{r} \frac{\partial}{\partial r} \left(\nu \Sigma r^3 \frac{\mathrm{d}\omega}{\mathrm{d}r} \right). \tag{B.13}$$

where ν is given by the α-viscosity (Shakura & Sunyaev 1973) prescription:

$$\nu = \alpha H c_s^\mathrm{iso} \sqrt{\gamma}. \tag{B.14}$$

Here, α is the viscosity parameter. While analytical solutions exist to Eq. (B.13), we found them to be impractical and chose to solve the equation numerically for u_r, using a five-point stencil derivative (Sauer 2012, p. 250) to generate a lookup table that is evaluated with linear interpolation. To ensure that the infalling mass rate has the exact prescribed value the density must only be created at the outer boundary. Beware of using the wave-damping zones at the same time, because they can also create mass.

Appendix C: Leapfrog-like scheme

We implemented a leapfrog-like scheme for the time-stepping, trying to solve a numeric instability that arose in the simulation of circum-binary disk simulations. It increases the accuracy of the source terms step by splitting it into two halves, one before and one after the transport step. This corresponds to a kick-drift-kick leapfrog scheme known from N-body integrators.

During testing, we found that the biggest source of errors is in the transport step and improving the source terms step brings little improvement in most cases. The gas feedback on the N-body system is already accurate with a single kick because the hydro time step is significantly smaller than the N-body time step would allow. The scheme only noticeably improves the accuracy of the code for simulations where the transport step is not important, such as the heating and cooling test presented in Appendix. D.3. There, the simulation benefits from the higher temporal resolution of the source terms step. However, this scenario would be identical to using a smaller time step for the whole simulation. The rough outline of this scheme is that a kick-drift-kick scheme is used for the gas (when identifying the source terms as kick and transport as drift) and a drift-kick-drift scheme for the N-body system.

First, we advance the N-body system and the dust particles by half a time step from t_0 to $t_0 + 1/2dt$ and use them at this position to update their velocities and compute their interaction with the gas. We then apply the source terms with half a time step and perform the transport step with a full time step. After transport, we compute the second half of the source terms and N-body-gas interactions and with the fully updated velocities evolve the N-body system and gas particles to the full time step. The steps in the scheme are as follows:

- advance N-body by $\Delta t/2$ to $t + \Delta t/2$
- update N-body velocities by $\Delta t/2$ from disk feedback
- advance particles to $t + \Delta t/2$ from interactions with N-body and gas
- gas source terms with $\Delta t/2$
- gas transport gas by Δt
- update N-body velocities by $\Delta t/2$ from disk feedback
- gas source terms with $\Delta t/2$
- advance particles to $t + \Delta t$ from interactions with N-body and gas
- advance N-body with previously calculated accelerations by $\Delta t/2$ to $t + \Delta t$

The N-body advance steps include accretion onto the N-body objects. Ultimately, we found that the benefits of using this scheme are only minor. The transport step is the largest source of error except in artificial test cases where the source terms are the only relevant part of the simulation.

The only noteworthy difference we could find is that the scheme needs fewer hydro steps compared to the default scheme because the CFL conditions for the source terms can be relaxed. This can lead to less numerical diffusion but at slightly longer runtimes. For example, for a typical simulation of a circumstellar disk in a close binary, the leapfrog scheme needed 25% fewer iterations compared to the default scheme at 5% increased runtime.

Appendix D: Test suite

This section describes some of the tests that are included in the test suite of FargoCPT. The test suite can be run by executing the `run_tests.sh` script within the `tests` directory. For a list of the tests, please refer to Sect. 4.9.

Appendix D.1: Steady-state accretion test

To test our boundary conditions (BCs), we initialize an infinite disk with a constant mass flow rate throughout the whole domain. We use a simple locally isothermal model without any gravitational potential smoothing ($\Phi = \sqrt{GM/r}$) to simplify the equations in Sect. B. Using $\Sigma(r) = 600.55 (\frac{r}{1\,\mathrm{au}})^{-1/2} \mathrm{g\,cm^{-2}}$, $h = 0.05$, $\alpha = 10^{-3}$, $F = 0$ around a $1\,\mathrm{M}_\odot$ star should result in $\dot{M} = 10^{-8} \mathrm{M}_\odot/\mathrm{yr}$. At the outer edge, we set the surface density and velocities of the model in the ghost cells and damp to the velocities of the model near the boundaries (from 100 to 64 au, with a damping time factor of $\beta = 3$, see Eq. (128)). By only setting the density in the ghost cells and not damping to it, we keep precise control over the amount of mass flowing into the domain. In Fig. D.1 we showcase the model on a domain from 1 to 100 au and $\mathrm{N_r} \times \mathrm{N}_\phi = 192 \times 270$ resolution (square cells), the plot is taken after a time of $5 \cdot 10^5$ orbits at $r = 1$. At the outer boundary, our inflow condition deviates from the analytical model by 3% for the mass flow rate and 0.4% for the surface density. At the inner boundary, a simple open boundary (blue line in Fig. D.1) leads to a larger radial velocity (and thereby mass flow

rate) than the viscous speeds. This causes the disk to be drained of mass inwards to outwards. Setting a no torque condition for the azimuthal velocity ($\mathrm{d}\Omega/\mathrm{d}r = 0$, orange line) increases the radial velocity and mass drain at the inner boundary. We do not recommend this option, as it has also caused problems in other simulations. When we damp the radial velocity and surface density to the initial values from 1 to 2 au (green line), the mass rate is constant throughout the whole domain, except the few cells at the inner boundary; but those are well within the damping zone and do not affect the inner domain.

In Fig. D.2 we test our viscous outflow boundary (see Sect. 3.14.2) and our viscous accretion function (see Sect. 3.13), each with a viscous enhancement factor of $s = 1$. The viscous accretion function removes mass from 1 to 5 au, which is not measured in the mass flow rate inside the domain, the mass piles up near the inner boundary due to the reflective BCs used. Note that the accretion function is not intended as a BC but for accreting objects inside the simulation domain. Both functions keep the surface density and mass flow rate relatively close to the analytical model inside the domain. These functions utilize the viscosity of the gas to remove mass from the domain. Other mechanisms can drive accretion but are not measured by our α viscosity, such as angular momentum transfer by spirals due to a massive planet. These have to be accounted for in the accretion enhancement factor s. This factor is an approximation for the increased accretion due to shearing at the boundary layer between the disk and the star (compare eq. 46 in Lodato (2008)):

$$\dot{M} = \frac{3\pi\nu\Sigma}{1 - \sqrt{R_{\mathrm{in}}/R}} \approx 3\pi\nu\Sigma s. \tag{D.1}$$

Using the viscous outflow condition allows us to change the influence on the disk from a reflective-like boundary $s \lessapprox 3$ to an open like boundary $s \gtrapprox 10$. A value of $s = 5$ was found to be suitable for accretion on a star with Jupiter-type companion Pierens & Nelson (2008).

Generally, all our tests show deviations from the analytical solution, which we suspect is due to the numerical errors when the equations are solved on the grid. Even small discrepancies in the velocity on the grid and analytical solution can then lead to larger density pile-ups that we find in our tests. To test this, we repeated our viscous inflow simulation with half the resolution ($\mathrm{N_r} \times \mathrm{N}_\phi = 96 \times 135$), which is the green line in Fig. D.2. This run shows slightly larger errors in the mass flow rate and significantly larger errors in the density profile close to the inner boundary.

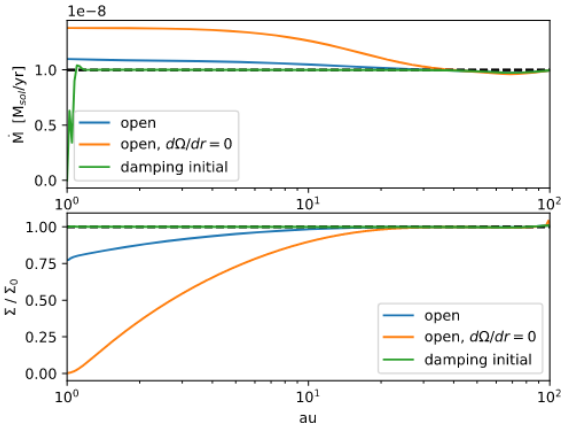

Fig. D.1. Outflow boundary removes more mass than supplied by the disk. The figure shows the accretion rate through the disk and surface density for different choices of boundary conditions. The top and bottom panels show the mass per unit of time flowing through a ring of a given radius and the ratio of surface density to its initial value, respectively.

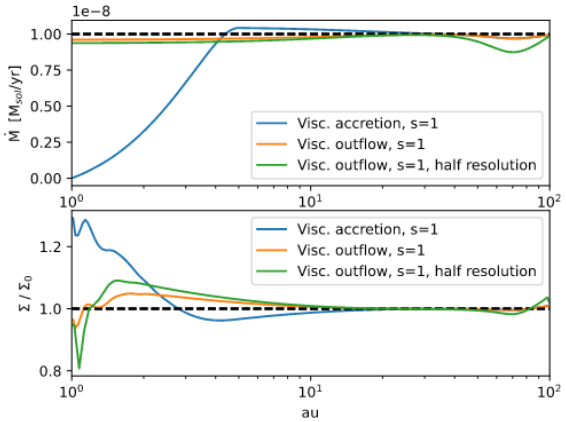

Fig. D.2. Viscous accretion through and at the inner boundary for different resolutions and methods. The panels are analogous to Fig. D.1. The dip in mass flow rate for the blue line in the inner region is due to the method removing mass from the domain and thus disturbing the equilibrium state.

Appendix D.2: Shock tube

We added the Sod shock tube test by Sod (1978) to our code, see Fig. D.3, which is a classic test for the transport step, updated due to pressure forces and artificial viscosity. The test is split into two parts, the first part is the classical shock tube with a perfect gas, meaning that the adiabatic index for the sound speed and pressure are equal and constant and the second part is for an ideal gas with the caloric equation of state (PVTE) by Vaidya et al. (2015). For these tests, we approximate a Cartesian grid by spacing the radial cells arithmetically between $R_{\mathrm{min}} = 1000$ and $R_{\mathrm{max}} = 1001$. As the setup is axisymmetric and the viscosity is zero, there is no interaction due to the azimuthal dimension. All units are set to 1 for this test. For the classical shock tube, we follow Stone & Norman (1992) and initialize the right half of the domain with $\Sigma_0 = 1$ and $e_0 = 2.5$ and the left half with $\Sigma_0 = 0.125$ and $e = 0.25$. How to analytically solve the setup at $t > 0$ is described in Hawley et al. (1984). The analytical solution as well as the results from our code with 100 cells for different combinations of integrator schemes and artificial viscosity is shown in Fig D.3. For space reasons, we only show the results for the densities. The full results can be viewed by executing the Python script of the test case in our code. All four combinations of integration schemes and artificial viscosity reproduce the analytical solution and converge to it for higher resolutions without meaningful differences in quality and performance.

We used the same initial conditions for the caloric equation of state shock tube test. But in this case, the units used are important and there is no known analytical solution. We copied the units from the shock tube test in Vaidya et al. (2015) and used it as a reference to our results. Both, the setup and the units are supplied with the official PLUTO code inside the HD test problems and 1000 radial cells are used. The results are shown as the second set of lines in Fig. D.3 where our FARGO run used the

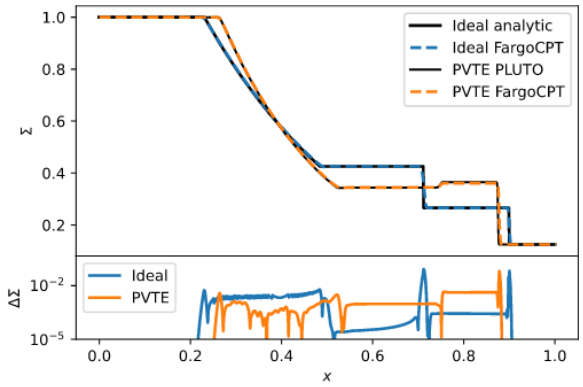

Fig. D.3. Gas surface densities of the shock tube test with 100 cells for different combinations of artificial viscosity and integration schemes as well as for the caloric equation of state (PVTE) by Vaidya et al. (2015) with 1000 cells. The simulation time is $t = 0.228$ in both cases. The top and bottom panels show the surface density and the deviations from the reference case respectively, respectively.

TW artificial viscosity and the standard integration scheme and agrees with the PLUTO results.

Appendix D.3: Heating and cooling test

To evaluate our viscous heating and radiative cooling modules, we used the setup and model presented in D'Angelo et al. (2003), see their Sect. 3.1. The model simplifies the radiative cooling module such that an analytical formula for the density and temperature profile for a disk in hydrostatic equilibrium can be derived. The formula for the effective opacity in (35) is changed to:

$$\tau_{\rm eff} = \frac{3}{8}\tau, \tag{D.2}$$

with $\tau = 1/2\kappa\Sigma$. The opacity of the material in the disk is computed as:

$$\kappa = 2 \times 10^{-6}\, T^2 \ {\rm cm^2\ g^{-1}\ K^{-2}}. \tag{D.3}$$

The kinematic viscosity is set to a constant $\nu = 5 \times 10^{16}\ {\rm cm^2\ s^{-1}}$. The setup consists of a central star $M = 1 M_\odot$ and a domain ranging from 1 to 20 au with reflective boundaries. To reach the equilibrium state faster, the radial velocities at the boundaries are damped to zero. The initial surface density and temperature are set as constant $\Sigma = 197\ {\rm g\,cm^{-2}}$ and $T = 352\,{\rm K}$. The simulation is then evolved to 10^4 orbital periods at $r = 1$ au. The expected equilibrium profiles for this specific setup are given by (D'Angelo et al. 2003):

$$\Sigma(r) = 300 \sqrt{\frac{5\ {\rm au}}{r}}\ {\rm g\,cm^{-2}}, \tag{D.4}$$

$$T(r) = 104 \left(\frac{5\ {\rm au}}{r}\right)^2\ {\rm K}, \tag{D.5}$$

and are plotted alongside the results from our code in Fig. D.4. Apart from deviations at the boundaries, the theoretical profiles are reproduced by the code well.

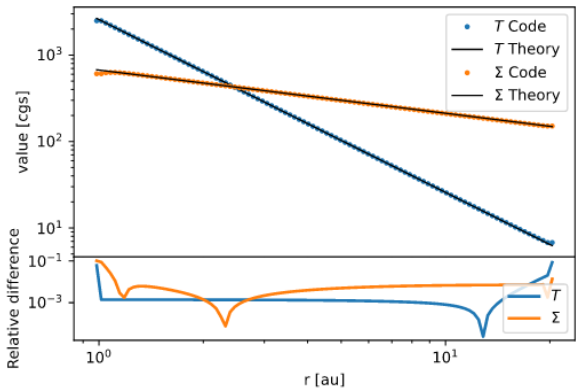

Fig. D.4. Gas surface density and temperature profile in the hydrostatic equilibrium for the model from D'Angelo et al. (2003) together with the expected theoretical profiles.

Appendix D.4: Viscous spreading ring test

The viscous spreading ring is suited to test the ability of the code to transport angular momentum due to the radial shearing inside disks. A pressure-less ring is initialized and then evolved in time. Such a setup has been studied and solved analytically by Lust (1952); Pringle (1981) among others. A gas ring of mass m at radius R_0 from the central star evolves in terms of dimensionless radius $x = R/R_0$ and time $\tau = 12\nu t R_0^{-2}$ as:

$$\Sigma(x,\tau) = \frac{m}{\pi R_0^2}\tau^{-1}x^{-1/4}\exp\left[-(1+x^2)/\tau\right] I_{1/4}(2x/\tau), \tag{D.6}$$

where $I_{1/4}$ is the modified Bessel function of the first kind. The ring is also subject to a viscous instability developing on top of the ring (Speith & Kley 2003). We initialized a spreading ring according to (D.6) at $\tau_0 = 0.16$ in a setup where $GM_c = R_0 = 1$ on a logarithmic grid with $N_r \times N_\phi = 512 \times 256$ in a domain ranging from 0.2 to 1.8 with a constant kinematic viscosity of $\nu = 4.77 \cdot 10^{-5}$. Figure D.5 shows the azimuthally averaged surface density at $\tau = 439.82$ and it agrees well with the analytical model from (D.6). There are clear deviations from the analytical model close to the inner boundary, which is due to the strict outflow boundaries used in the simulation. The viscous instability becomes visible as density waves when taking a slice along the x axis (magenta line). This instability was studied numerically in detail by Joseph et al. (2023), where it was found that it should always develop as a one-armed trailing spiral spanning the whole domain.

Appendix D.5: Dust diffusion test

This section presents the test case for the dust diffusion module. We compare our stochastic implementation against a numerical solution of the 1D advection-diffusion equation. The setup is inspired by the test case in Charnoz et al. (2011, see their Eq. (28) for the 1D advection-diffusion equation). We tried to exactly replicate their setup as described in their Sect. 3.3 with the goal of replicating their Fig. 5. However, using the parameters available in their text and using educated guesses for the remaining model parameters we could not match the curves in their Figure. Thus, we changed our reference to a 1D simulation with the DISKLAB code developed by Cornelis Dullemond and Til Birnstiel which can be used to solve the 1D advection-diffusion

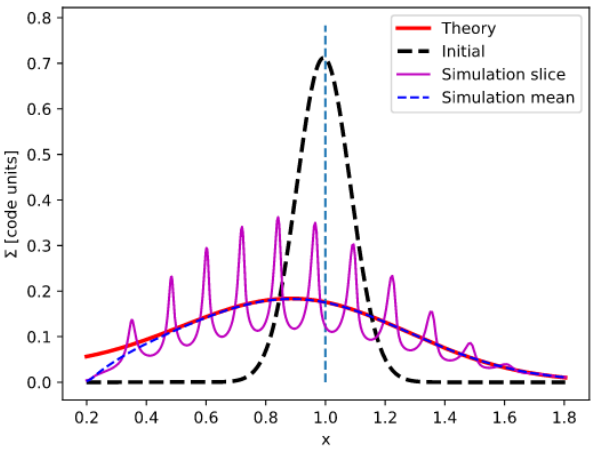

Fig. D.5. Viscous spreading ring test from Speith & Kley (2003) on a logarithmic grid $N_r \times N_\phi = 512 \times 256$. The ring is initialized with $\Sigma(x, \tau = 0.016)$ (black line) and then evolved to $\tau = 439.82$. The vertical dashed cyan line marks the position of the initial ring at time $\tau = 0$. The blue line is the azimuthal averaged surface density, which matches the analytical formula (red line) well. The viscous instability can be seen as waves in a density slice along the x axis (magenta line).

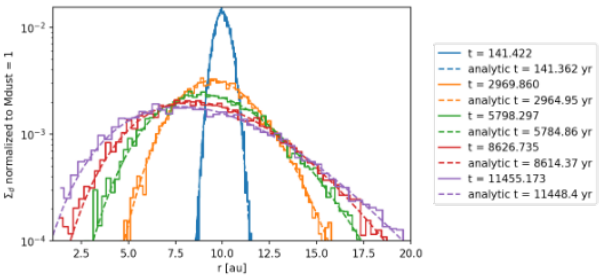

Fig. D.6. Dust diffusion test. Comparison of dust diffusion with Lagrangian super-particles in FARGOCPT with numerical integration of the 1D advection-diffusion equation using an implicit method.

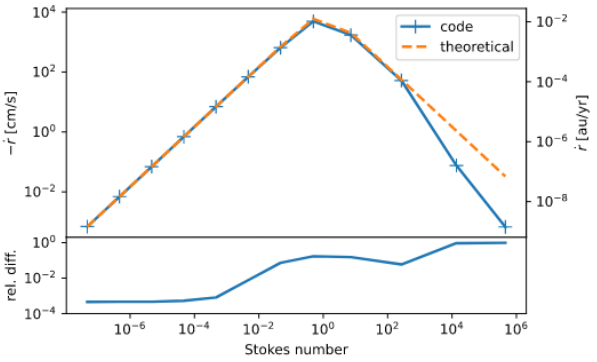

Fig. D.7. Results of the dust drift test. The top and bottom panel shows the value and deviation from the theoretical prediction of the drift speed as a function of the Stokes number, respectively. The large deviations for Stokes numbers around and larger than unity are due to oscillations in the integration. See Fig. D.8.

equation using an implicit method. The comparison of the dust surface density calculated from the dust particle location histogram with the surface density from the DISKLAB simulation is shown in Fig. D.6. The dust surface density is normalized such that the total dust mass equals 1. There is an excellent agreement between the results of the two approaches.

Notably, the 2D correction from Eq. (108) to account for kicks in the azimuthal direction is needed to match the results from the advection-diffusion equation.

The parameters for the setup are as follows. The simulation tracks 10.000 particles with a physical particle size of 10^{-5} cm and a material density of 2.65 g/cm^2 on their orbit around a 0.5 solar-mass star. Turbulence is parameterized by a viscous $\alpha = 0.01$. The surface density of the gas follows $\Sigma(r) = 20\,\mathrm{g/cm^2}\ (\mathrm{r/1au})^{-1}$. At $r = 10$ au, where the particles are initially launched on circular orbits, the Stokes number is $\mathrm{St} = 2.08 \times 10^{-5}$. The grid spans from 1 au to 40 au with 1235 radial cells spaces logarithmically and 726 equally spaced azimuthal cells. The time step is fixed at 0.1 in code units which corresponds to 5.81 days.

Appendix D.6: Dust drift test

This test repeats the test from Picogna & Kley (2015) Appendix C.1, first suggested by Zhu et al. (2014), by comparing the dust drift velocity of individual particles with different stokes numbers to an analytical prediction.

The equilibrium radial dust drift velocity is expected to be (Picogna & Kley 2015, Eq. (C.1)):

$$v_{\mathrm{drift}} = \frac{\mathrm{St} v_{r,\mathrm{gas}} - \eta v_K}{\mathrm{St} + \mathrm{St}^{-1}}, \quad \eta = -h^2 \left(\frac{\mathrm{dlog}\Sigma}{\mathrm{dlog}r} + \frac{\mathrm{dlog}T}{\mathrm{dlog}r} \right). \tag{D.7}$$

In this case, the gas is not evolved and its radial velocity $u_{r,\mathrm{gas}}$ is kept zero in the whole domain, such that only the second term contributes to the drift velocity. Note that this definition of η follows from Nakagawa et al. (1986) Eq. (1) for a locally isothermal disk by correcting for a missing '/' in their formula, such that $r\Omega_K^2$ is in the denominator.

The resulting comparison of particle drift velocities is compared to the analytical predictions for the exponential midpoint integrator in Fig. D.7. The time evolution of these velocities is shown in Fig. D.8 where the oscillations of the velocity around the mean value can be observed for particles with $\mathrm{St} > 1$, in line with the findings of Picogna & Kley (2015) Fig. C.2 and Zhu et al. (2014) Fig. 23.

The simulation models a protoplanetary disk around a $1\,\mathrm{M}_\odot$ star, with an initial surface density of $\Sigma(r) = 88.872\,\mathrm{g/cm^2}\ (\mathrm{r/1au})^{-1}$ at $r = 1$ au. The disk, with zero explicit viscosity and a constant aspect ratio of $h = 0.05$, extends from 0.5 au to 3 au, and is governed by an isothermal equation of state. Dust particles with material density 2.65 g/cm^3 and sizes from 10^{-8} to 10^2 m are initialized on circular orbits at $r = 1$ au.

Appendix D.7: Planet torque

This test case evaluates the torque exerted onto a low-mass planet by the disk. We compare the torque from a simulation to the theoretical expression for the linear Lindblad torque from Paardekooper et al. (2011, their Eq. (14)). The torque, Γ_L, is given

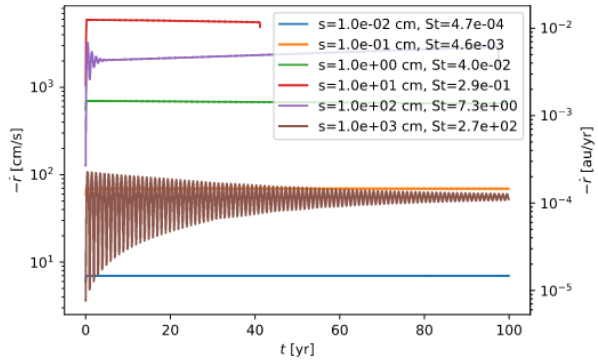

Fig. D.8. Selected dust particle trajectories from the dust drift test. The panel shows the drift velocity as a function of time with the particle size and Stokes number encoded by color. The black lines show the expected value from Eq. (D.7). For larger dust particles with Stokes equal or greater than unity, oscillations occur due to the integration method. The particles represented by the red and purple lines leave the domain at the inner boundary during the simulation.

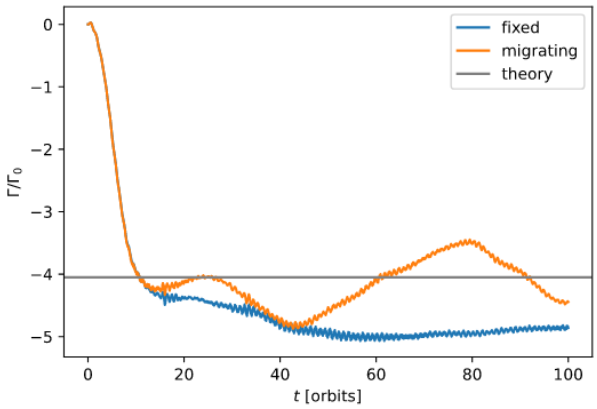

Fig. D.9. Torque of a small mass planet compared to theoretical prediction. The torque needs some time to build while the initially smooth disk adjusts to the presence of the planet.

by:

$$\frac{\Gamma_\mathrm{L}}{\Gamma_0} = -\frac{1}{\gamma}(2.5 + 1.7\beta - 0.1\alpha)\left(\frac{0.4}{b/h}\right), \tag{D.8}$$

with the adiabatic index γ, $\beta = \frac{\mathrm{dlog}T}{\mathrm{dlog}r}$, $\alpha = \frac{\mathrm{dlog}\Sigma}{\mathrm{dlog}r}$, aspect ratio h, and the smoothing length factor $b = r_\mathrm{sm}/r$. The torque normalization is $\Gamma_0 = (q/h)^2\Sigma_p r_p^4\Omega_p^2$ with the planet-to-star mass ratio q, the surface density at the planet location Σ_p, the planetary orbital radius r_p and the planetary orbital angular velocity Ω_p.

Figure D.9 shows a comparison of the torque as measured in two simulations and the theoretical prediction. One simulation calculates the torques for a planet that is on a fixed orbit, while in the other simulation, the planet is allowed to move. For the fixed planet, the resulting torque is overestimated while the torque for the moving planet oscillates around the expected value.

We note that the boundary conditions can have a substantial impact on the torque in this test. Here, reflective boundary conditions in combination with wave-damping zones towards the inner and outer boundaries had to be used.

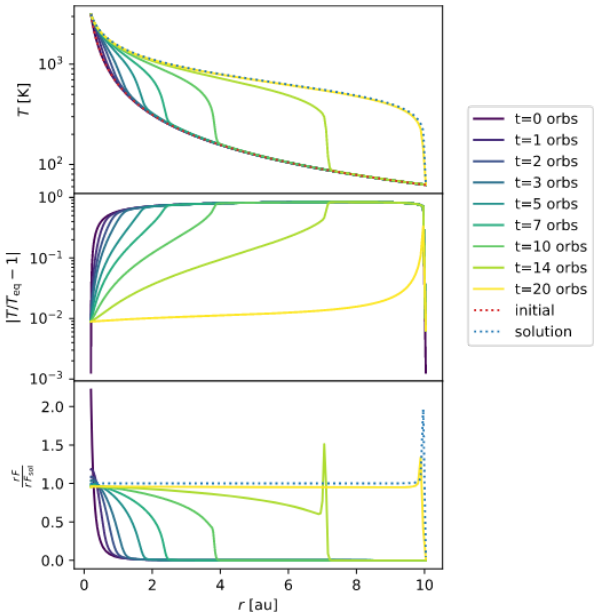

Fig. D.10. Equilibration of a radial temperature profile due to radiation transport in the midplane with a constant opacity. This is used to test the FLD module. The panels show, from top to bottom, the radial temperature profile, the deviation from the equilibrium solution, and the azimuthally integrated flux through a ring at the respective radius, normalized by the equilibrium flux. Time is indicated by the color of the lines.

The simulation features a $2 \cdot 10^{-5}\,\mathrm{M}_\odot$ planet at $r = 1\,\mathrm{au}$ around a $1\,\mathrm{M}_\odot$ star. The locally isothermal disk is initialized with $\Sigma(r) = 0.000376\,(\mathrm{r/1au})^{-1.5} = 3340.84\,\mathrm{g/cm^2}\ (\mathrm{r/1au})^{-1.5}$ with zero explicit viscosity and a constant aspect ratio of $h = 0.05$. The resolution is such that the scale height is resolved by 6 cells at the location of the planet which corresponds to 219 x 753 cells.

Appendix D.8: Flux-limited-diffusion test

This section describes the test of the flux-limited diffusion (FLD) module. This test is a simple 1D diffusion test with constant opacity and two different temperatures at the inner and outer boundaries.

Figure D.10 shows the results of this test. The panels show, from top to bottom, the radial temperature profile, the deviation from the equilibrium solution, and the azimuthally integrated flux through a ring at the respective radius, normalized by the equilibrium flux. Time is indicated by the color of the lines. The azimuthally integrated flux is expected to be constant for an equilibrium disk.

The numerical criterion for passing this test is that the maximum deviation from the equilibrium solution is smaller than 0.1 inside of $r < 9.5$ au. The numerical solution shows boundary effects, because of which the pass criterion is relatively loose. Please see the center panel of Fig. D.10 for the radial profile and time evolution of the deviation.

Appendix D.9: Diffusion equation solver test

This test is aimed at the 2D diffusion part of the FLD solver and tests the solution of the diffusion equation with a constant diffusion coefficient. The diffusion equation with a constant coefficient,

$$\frac{\partial x}{\partial t} = K\Delta x, \tag{D.9}$$

has an analytical solution in 2D in the form of a Gaussian profile with a prefactor containing the time. We use this analytical solution both as an initial condition and as the solution to compare. In this test, we treat the temperature as an arbitrary variable and manually set the diffusion coefficient to a constant value. The usual schedule for the time stepping is ignored and the initial condition is loaded from a file at the start of the diffusion test and the result is written out directly after the test. We perform a specified number of iterations with a fixed time step.

With an infinite domain and a δ distribution as an initial condition, the analytical solution in two dimensions is:

$$x(\boldsymbol{r}, t) = \frac{x_0}{4\pi t K} \exp\left(-\frac{|\boldsymbol{r} - \boldsymbol{r_0}|^2}{4Kt}\right) + c, \tag{D.10}$$

where c is a constant offset.

We use a domain size of $r \in \{0.01, 2\}$ cm with 1000 uniformly spaced radial cells and 1500 azimuthal cells, a constant diffusion coefficient of $K = 1\,\mathrm{cm}^2/\mathrm{s}$, the center of the Gaussian profile $\boldsymbol{r}_0 = (1\,\mathrm{cm}, 0)$, an offset $c = 0.1$, and an initial time of $t_0 = 10^{-3}$ s. We then evolve the diffusion equation until $t = 2 \times 10^{-3}$ s, with 10 steps of $\Delta t = 10^{-4}$ s.

A radial cut through the center of the Gaussian profiles and the deviation from the analytical solution is shown in Fig. D.11. The top panel shows the radial cut minus the offset and the bottom panel shows the relative deviation from the analytical solution.

The criterion for passing the test is that the integrated absolute deviation: $\Delta = \sum_i^{N_\mathrm{cells}} A_i \left| f_i^\mathrm{code} - f_i^\mathrm{analytical} \right|$, with the cell area A_i is smaller than the threshold of 4×10^{-2} at the given resolution.

There are deviations from the analytical solution at the center of the numerical solution. It tends to be slightly higher than the analytical solution. We suspect that this is due to boundary effects. Increasing the resolution helps to reduce the deviation at the center, but it stays up to the resolution of 1000 radial and 1500 azimuthal cells, for which $\delta = 1.5 \times 10^{-2}$. For runtime reasons, the resolution for the test suite is chosen lower at 100 times 150 cells, for which $\delta = 3.73 \times 10^{-2}$ and the threshold is chosen just above this value at 4×10^{-2}.

Appendix D.10: Self-gravity solver test

This test is aimed at verifying the self-gravity solver based on the Fourier method, as described in Sect. 3.7. It is separated into two parts: a test of the solver in the radial direction and one in the azimuthal direction. We test the implementation with the symmetric smoothing length given in Eq. (19).

As a comparison, we recompute the gravitational acceleration from the surface density by direct summation according to:

$$\boldsymbol{a}(\boldsymbol{r}) = -\sum_{n=1}^{N_\mathrm{rad}} \sum_{k=1}^{N_\mathrm{az}} \frac{\mathrm{G}\, A_{nk}\, \Sigma_{nk}}{\left(d^2 + \epsilon(r, r_{nk}, h)^2\right)^{3/2}} \boldsymbol{d}, \tag{D.11}$$

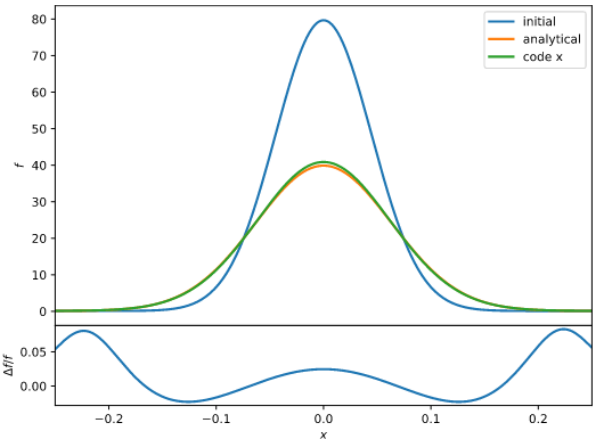

Fig. D.11. 2D diffusion of the analytical solution to the diffusion equation with constant diffusion coefficient. The top panel shows radial cuts through the center of the 2D distributions: the initial condition and the analytical and numerical solutions. The bottom panel shows the relative deviation between the numerical and the analytical solution.

where $\boldsymbol{d} = \boldsymbol{r}_{nk} - \boldsymbol{r}$, $d = |\boldsymbol{d}|$, and A_nk is the cell area. The quantities with subscript are the cell center values loaded from the simulation output. These recomputed values are then compared to the output from the Fourier-method-based SG solver in the code.

In both cases, the test is performed on a 2D grid with $N_\mathrm{rad} \times N_\mathrm{az} = 128 \times 256$ cells, with a logarithmic radial grid spanning from 1 to 12.5 au.

For the radial test, the surface density is axisymmetric and given by $\Sigma(r) = 200\,\mathrm{g/cm^2}\,(\mathrm{r}/1\mathrm{au})^{-1}$ and the aspect ratio is constant throughout the disk with $h = 0.05$. Fig. D.12 shows the radial acceleration of the disk due to the self-gravity of the disk. The top panel shows the radial SG acceleration as a function of radius for the direct summation, g_r^ds, and the Fourier method, g_r^F. The bottom panel shows their relative difference, $|g_r^\mathrm{F}/g_r^\mathrm{ds} - 1|$, and absolute difference, $|g_r^\mathrm{F} - g_r^\mathrm{ds}|$. The two methods agree well which illustrates that the Fourier method works as intended. The relative difference is below 0.0014 for $r > 2$ au. This value is used as a threshold in the pass-fail test. We exclude the zone inwards of 2 au because the acceleration has a crossing of zero there which enlarges the relative difference at this location.

For the azimuthal case, we initialize the surface density with two Gaussian peaks at $r_0 = 4$ au at two different azimuths:

$$\Sigma(r, \phi) = \Sigma_0 \sum_{i \in \{1,2\}} \exp\left(-\frac{(r - r_0)^2}{2\sigma_r^2} - \frac{(\phi - \phi_i)^2}{2\sigma_\phi^2}\right), \tag{D.12}$$

with $\sigma_r = 1$ au, $\sigma_\phi = 0.3$ rad, $\phi_1 = \pi$, $\phi_2 = \pi/2$ and $\Sigma_0 = 50\,\mathrm{g/cm^2}$.

Fig. D.13 shows the azimuthal acceleration due to the self-gravity of the disk as a function of azimuth at $r = 4$ au. In this case, the match is even better than in the radial case and relative deviations are constant and smaller.

The difference between the radial and azimuthal direction might stem from a subtle difference in the implementation of the Fourier-based SG solver. A property of this solver is that it implicitly treats all directions as periodic. In the azimuthal direction, our simulation grid is periodic which makes the Fourier method directly applicable. In the radial direction, however, a trick has to be used and the grid needs to be enlarged at the outer

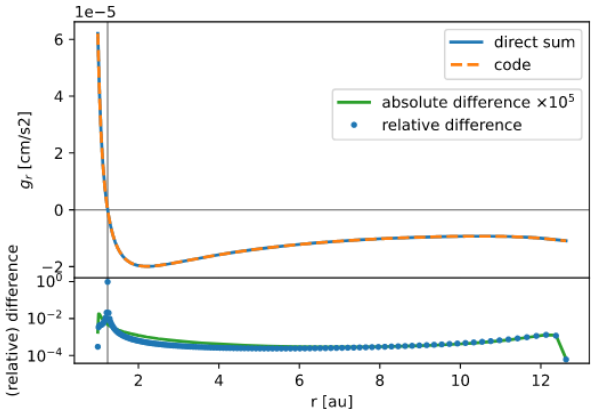

Fig. D.12. Comparison of the radial SG acceleration against results from direct summation. The top and bottom panels show the radial SG acceleration as a function of radius obtained with the Fourier method (code) and direct summation, and the relative and absolute differences between both curves, respectively. The horizontal gray line marks the zero value of acceleration and the vertical gray line indicates the crossing of zero.

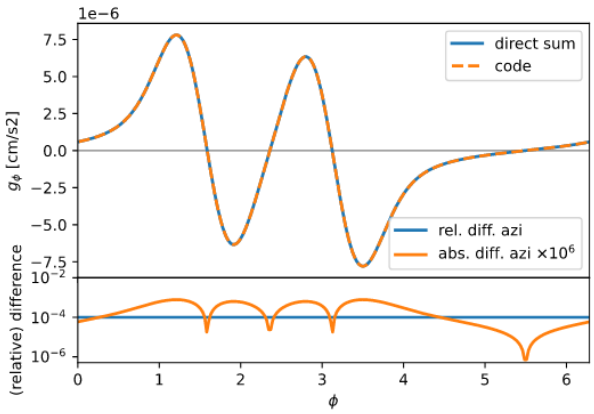

Fig. D.13. Same as Fig. D.12, but showing the azimuthal SG acceleration as a function of azimuth at $r = 4$ au.

radial boundary to twice the size with cells containing zero density. We suspect that this trick causes the radial acceleration to be less accurate than the azimuthal acceleration.

4 Parameter study of protoplanetary disks in close binaries

Whether the planetesimal growth phase of planet formation can succeed inside the primary disk of a close binary depends on the dynamics of the disk (Silsbee & Rafikov 2021). The conditions for successful planetesimal growth, a primary disk with low eccentricity, no precession, and alignment with the binary, were met in the non-isothermal simulations of Müller & Kley (2012) and Marzari et al. (2012). Their simulations, like those of similar studies, simulated only a small domain around the primary star, ignoring the secondary disk and the circumbinary disk.

My first project was to repeat their simulations using more recent disk parameters. Müller & Kley (2012) used a α viscosity parameter of 0.01 which was derived from disk models of cataclysmic variables (e.g. Mineshige & Osaki 1983) while Marzari et al. (2012) used a constant kinematic shear viscosity of $\nu = 10^{-5}$, which corresponds to a slightly lower α parameter of $5 \cdot 10^{-3}$. More recent estimates of the effective viscosity of protoplanetary disks, on the other hand, find that they are less turbulent than disks in cataclysmic variables, and instead have α parameters in the range of $3 \cdot 10^{-4}$ to $3 \cdot 10^{-3}$ (Rosotti 2023).

After running a few test simulations, I found that the disk in the simulations of Müller & Kley (2012) and Marzari et al. (2012) were strongly influenced by numerical parameters such as the domain size and grid resolution. Therefore, we decided to conduct a parameter study with an appropriate numerical setup to study the effects of different physical parameters on the disk dynamics. We found that the conditions for planet formation are less favorable than suggested by previous studies, and published our results in Jordan et al. (2021), presented on the following page.

A&A 654, A54 (2021)
https://doi.org/10.1051/0004-6361/202141248
© ESO 2021

Astronomy & Astrophysics

Disks in close binary stars

γ-Cephei revisited

Lucas M. Jordan[1], Wilhelm Kley[1], Giovanni Picogna[2], and Francesco Marzari[3]

[1] Institut für Astronomie und Astrophysik, Universität Tübingen, Auf der Morgenstelle 10, 72076 Tübingen, Germany
e-mail: lucas.jordan@uni-tuebingen.de
[2] Universitäts-Sternwarte, Fakultät für Physik, Ludwig-Maximilians-Universität München, Scheinerstr 1, 81679 München, Germany
[3] Dipartimento di Fisica, University of Padova, via Marzolo 8, 35131 Padova, Italy

Received 4 May 2021 / Accepted 28 July 2021

ABSTRACT

Context. Close binaries ($a_{\rm bin} \leq 20$ au) are known to harbor planets, yet planet formation is unlikely to succeed in such systems. Studying the dynamics of disks in close binaries can help to understand how those planets could have formed.
Aims. We study the impact that numerical and physical parameters have on the dynamics of disks in close binaries. We use the γ-Cephei system as an example and focus on disk quantities such as disk eccentricity and the precession rate as indicators for the dynamical state of the disks.
Methods. We simulate disks in close binaries by performing two-dimensional radiative hydrodynamical simulations using a modified version of the FARGO code. First, we perform a parameter study for different numerical parameters to confirm that our results are robust. In the second part, we study the effects of different masses and different viscosities on the disks' dynamics.
Results. Previous studies on radiative disks in close binaries used too low resolutions and too small simulation domains, which impacted the disk's dynamics. We find that radiative disks in close binaries, after an initialization phase, become eccentric with mean eccentricities between 0.06 and 0.27 and display a slow retrograde precession with periods ranging from $4{-}40 T_{\rm bin}$ which depends quadratically on the disk's mean aspect ratio. In general, the disks show a coherent, rigid precession which can be broken, however, by changes in the opacity law reducing the overall eccentricity of the disk.

Key words. hydrodynamics – protoplanetary disks – accretion, accretion disks – planets and satellites: formation – methods: numerical

1. Introduction

Up to now, about a dozen known planets have been detected that reside inside a close binary system ($a_{\rm bin} \lessapprox 20$ au) orbiting one of the stars in the system, in an S-type orbit (Thebault & Haghighipour 2015). One well-studied example is the γ-Cephei system, which is a close binary system with a semi-major axis of 20 au and eccentricity of 0.4 (Endl et al. 2011). It harbors a giant planetary companion (Hatzes et al. 2003) with a mass of $m \sin i = 1.85\, M_{\rm Jup}$ distanced 2 au from the more massive companion (Endl et al. 2011). This minimum planet mass was determined via radial velocity measurements, but recently Benedict et al. (2018) claimed a much larger actual mass of $\sim$9.4 $M_{\rm Jup}$ and a non-coplanar system using *Hubble* Space Telescope astrometry data. The origin of planets in these close binaries incites many questions, as previous studies have shown that the standard planet formation process is highly problematic at the observed positions of the planets due to the presence of a close stellar companion (see Thebault & Haghighipour 2015; Marzari & Thebault 2019 for a full discussion).

The position of the planet in γ-Cephei is not too far from the orbital stability limit of $\sim$4 au (Holman & Wiegert 1999; Pichardo et al. 2005). At this position, the companion plays an important role in the planet formation process. The planetesimal accretion phase was found to be the phase that is most sensitive to gravitational disturbances. The eccentricity of the planetesimals is excited by the companion star and damped by the gas disk. The size dependency of the gas drag causes misalignment in the pericenters for different-sized planetesimals. This leads to orbit-crossings that cause destructive collisions and prevent further growth (Thébault et al. 2006, 2008). The relative velocities between the planetesimals become even larger if the hosting disk is eccentric (Paardekooper et al. 2008). Later, Rafikov (2013) noted that the disk gravity has a dominant effect on the planetesimal's dynamics and concluded in Rafikov & Silsbee (2015) that planetesimal growth could succeed in close binaries given that the disk is apsidally aligned to the binary and has a very small eccentricity ($e_{\rm d} \leq 0.02$). Therefore, precise modeling of disks in close binaries is necessary to understand how planet formation can succeed.

Within the context of superhumps in cataclysmic variables (Pearson 2006), the importance of tidal effects by the secondary star was demonstrated in the simulations by Whitehurst (1988). Later, eccentric disks in circular close binaries were studied by Lubow (1991a) who found, using linear analysis, that the $m = 3$ eccentric inner Lindblad resonance can drive the growth of disk eccentricity in such systems. This was also confirmed numerically in Lubow (1991b) and Artymowicz & Lubow (1994). Though later it was shown that the $m = 3$ resonance is not the only cause for eccentricity growth in disks in close binaries either by removing the resonance from the potential or by using a larger mass ratio of the binary that truncates the disk

to sizes such that the $m = 3$ resonance is not contained in the disk anymore (Kley et al. 2008; Marzari et al. 2009). Generally, hydrodynamical simulations have shown that in close binary star systems, either circular or eccentric, the disks regularly develop large eccentricities $e_d \geq 0.2$ and start precessing (Paardekooper et al. 2008; Kley et al. 2008; Marzari et al. 2009, 2012; Müller & Kley 2012). In those simulations, it has been seen that the size of the disk is an important indicator for the final disk eccentricity. Disks that are more exposed to the perturbations of the companion tend to develop larger eccentricities. The size of the disk is determined by the viscosity of the gas with higher viscosity leading to larger disks, and by the tidal effect of the secondary star that leads to disk truncation.

Concerning numerical considerations, Paardekooper et al. (2008) noted that the numerical methods used in the simulations can drastically affect the dynamics of the disk. They found that their simulations, which used the RODEO code (Paardekooper & Mellema 2006) with the diffusive minmod limiter, produced disks in a quiet state that have low eccentricity and show no precession. This quiet state was not affected by changes to resolution or boundary conditions. When the less diffusive superbee flux limiter was used, the disks entered an excited state with precession and high eccentricity that strongly depended on the resolution and boundary condition used. Disks in this low eccentric state have also been observed in locally isothermal simulations that include self-gravity (Marzari et al. 2009), or in radiative simulations (Müller & Kley 2012; Marzari et al. 2012), or SPH simulations (Martin et al. 2020).

After all, it is currently not clear how numerical considerations and physical parameters impact the dynamics of circumstellar disks in close binary stars. To better understand the process of planet formation in binary stars and gain more insight into the subgroup of superhump systems in cataclysmic variables, further development in theoretical and numerical models of disk dynamics in binary star systems is warranted. Additionally, there have been massive advances in computational resources since those studies were performed, and we decided to revisit the problem of disks in close binaries and continue the studies presented in Müller & Kley (2012). The focus of this paper lies again on the system γ-Cephei, being one of the outstanding sample systems, with the first planet discovered in a close binary star (Hatzes et al. 2003). In our study, we treat physically realistic disks by including internal heating and radiative cooling.

This paper is structured as follows. In Sect. 2, we present our model used for the simulations and the methods for analysis. We briefly explain our standard model in Sect. 3. Tests of different grid resolutions, domain-sizes and boundary condition are presented in Sect. 4, and the results from simulations with different disk masses and viscosities are shown in Sect. 5. We discuss global trends of the disks in detail in Sect. 6, highlight difficulties when simulating disks in close binaries in Sect. 7, and finally summarize our results in Sect. 8.

2. Model

In this work, we simulated two-dimensional, radiative disks, using a modified version of the FARGO code including the energy equation. The code solves the vertically integrated hydrodynamical equations on a polar coordinate system $(r - \phi)$, centered on the primary star. It uses an upwind scheme with a second-order flux limiter (van Leer 1977), linear interpolation to reconstruct variables, and the fast advection in rotating gaseous objects (FARGO) method for the azimuthal advection,

Table 1. Physical and numerical parameters for initializing the standard model.

Primary star mass	$1.4\,M_\odot$
Secondary star mass	$0.4\,M_\odot$
Semi-major axis	20 au
Eccentricity	0.4
Orbital period	66.7 a
Disk mass	$0.01\,M_\odot$
α viscosity	10^{-3}
Adiabatic index	7/5
Initial density profile	$\propto r^{-1}$
Initial temperature profile	$\propto r^{-1}$
$R_{\rm min} - R_{\rm max}$	0.2–12 au
Grid ($N_r \times N_\varphi$)	760×1162

Notes. Since there is no gravitational feedback from the disk onto the stars, the binary orbital parameters do not change during the simulation. The disk mass of $10^{-2}\,M_\odot$ equates to $\Sigma(1\,\text{au}) = 2570\,\text{g cm}^{-2}$.

for details, see Masset (2000). For shock smoothing, artificial viscosity is used as described in Stone & Norman (1992). The simulated disks are non-self-gravitating and the gravitational back-reaction from the disks onto the binary stars is neglected. The orbit of the binary is integrated with a fifth-order Runge–Kutta method. The source terms for the energy equation include viscous heating and radiative cooling alongside compressive heating. For the Rosseland mean opacity, we used the piecewise power-laws as put forward in Lin & Papaloizou (1985). The full equations and physical assumptions are specified in detail in Müller & Kley (2012), and we do refer to that work for more information.

2.1. Initialization

The physical and numerical parameters of our fiducial model are presented in Table 1. For the initial temperature, we use a power-law with $T(r) \propto r^{-1}$, which leads to a disk with constant aspect ratio, h, see Eq. (5). The reference temperature is chosen such that $h = 0.05$. Since viscous heating and radiative cooling are explicitly included in the models, the actual disk temperature will change quickly during the simulations. For the initial density, we chose the same power-law $\Sigma(r) \propto r^{-1}$. Because the disk around the primary is truncated by the tidal forces of the secondary, the initial disk surface density is smoothly reduced beyond 6 au to start the disk closer to the equilibrium size. The total initial disk mass of our fiducial model (including this tapering) is $10^{-2}\,M_\odot$ which equates to $\Sigma(1\,\text{au}) = 2570\,\text{g cm}^{-2}$. The initial radial velocity is set to zero, and the initial angular velocity is set to the Keplerian angular velocity.

2.2. Boundary conditions

We use outflow boundaries at the outer edge of the computational domain for all our simulations. At the inner edge of the domain, reflective boundaries are used, unless stated otherwise. The implementation of the boundaries is identical to Müller & Kley (2012) (it is important to note that the reflective boundary condition in their Sect. 2.2 is missing a minus sign, and it should read $v_{0j} = -v_{2j}$, for the radial velocity). We added wave damping zones at the inner edge to prevent waves from being reflected into the domain by damping the radial velocity v_r to zero and the

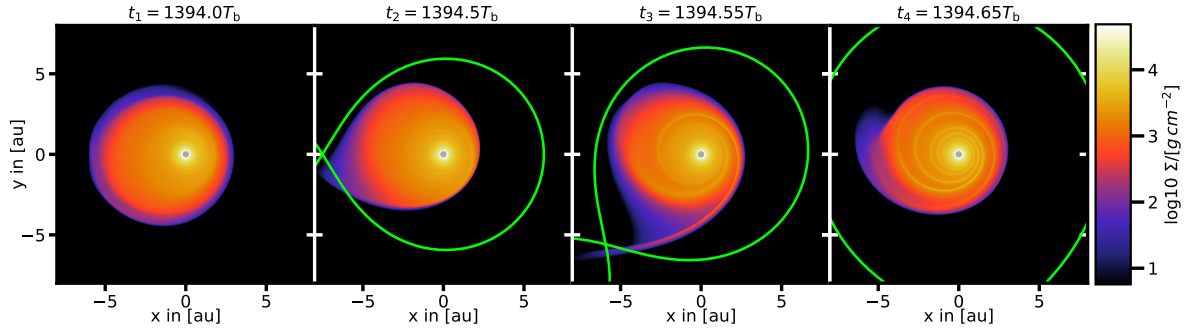

Fig. 1. Disk surface density during one binary orbit for the standard parameters, see Table 1, after the equilibrium has been reached. The green line indicates the Roche lobes of the stars. In the *leftmost image* (t_1) the binary is at apastron and the disk is unperturbed. At the binary's periastron (t_2) the disk is maximally distorted and has the highest eccentricity. After the periastron passage (t_3) two spiral arms are launched that wind inward and dissipate again (t_4). Most of the disk's mass loss happens in the time frame between t_2 and t_4 that spans 15% of the binary's period.

surface density Σ and internal energy e to the azimuthal average by using the damping mechanism as described by de Val-Borro et al. (2006)

$$\frac{\mathrm{d}x}{\mathrm{d}t} = \frac{x - x_0}{\tau} f(r), \tag{1}$$

where $x \in \{v_r, \Sigma, e\}$, x_0 is the desired value, τ is the damping timescale and $f(r)$ is a quadratic ramp-up function that rises from 0 to 1 from the start to the end of the damping zone. The wave damping zone ranges from $1.1\,R_{\min}$ to $R_{\min}$. For the damping timescale we used $\tau = 10^{-3} 2\pi\Omega_k(R_{\min})^{-1}$ where Ω_k is the Keplerian angular velocity around the primary. We also tested slower wave damping and no wave damping and found that it has little effect on the disk's dynamics.

2.3. Numerical considerations

To avoid numerical instabilities from too low density or energy values at the outer border of the disk, we used a density floor of $\Sigma_{\text{floor}} = 10^{-7} \cdot \Sigma_0$ where $\Sigma_0 = \Sigma(1\,\text{au})|_{t=0}$ and a temperature floor of $T_{\text{floor}} = 10\,\text{K}$. We use the α-prescription by Shakura & Sunyaev (1973) to model the viscosity and name simulations for our viscosity study by their α value. Inside plots, we compare the simulations by their kinematic viscosity, as it is the relevant quantity that affects the disk's dynamics. The coefficient of the kinematic viscosity is defined as

$$\nu = \alpha c_s^2 \Omega_k^{-1}, \tag{2}$$

where c_s is the adiabatic sound speed.

We also tested the disk dynamics of our standard case using additionally the PLUTO code (Mignone et al. 2007). These results, presented in Appendix A, showed similar behavior.

2.4. Analysis

We describe the disk's dynamics by its global eccentricity e_d and longitude of pericenter, ω_d. These are calculated from the mass-weighted average over all cells as has been used in previous studies (Kley et al. 2008). The desired quantity is calculated for each cell by assuming that the gas parcel moves on a 2-body Keplerian orbit around the primary star, then the average over the whole disk is calculated as

$$f_d = \frac{\iint f_d(r,\varphi)\Sigma(r,\varphi) r \mathrm{d}r\mathrm{d}\varphi}{M_{\text{Disk}}}, \tag{3}$$

where $f_d \in \{e_d, \omega_d, h, \nu\}$. Similarly, the radial profile of a disk quantity is calculated as

$$f_d(r) = \frac{\int f_d(r,\varphi)\Sigma(r,\varphi)\,\mathrm{d}\varphi}{\int \Sigma(r,\varphi)\,\mathrm{d}\varphi}. \tag{4}$$

In the presentation of our results we refer to the disk temperature mostly through the aspect ratio, h, which is the ratio of the vertical pressure scale height of the disk, H, over the radius. It is given by

$$h = \frac{H}{r} = \frac{c_{s,\text{iso}}}{r\Omega_K}, \tag{5}$$

where the second equality follows for standard thin accretion disks.

Before engaging in our parameter studies, we first checked if resolution and domain size is sufficient to resolve the disk dynamics. These studies are presented in Sect. 4 below. Afterward, we varied the mass of the disk between $2 \times 10^{-3}\,M_\odot$ to $5 \times 10^{-2}\,M_\odot$ the α-viscosity parameter from 10^{-4} to 10^{-2}, and document the effects that these variations have on the disks' dynamics.

3. Standard model

We present the physical and numerical parameters of our fiducial model in Table 1. In deviation from the standard model used in Müller & Kley (2012), which was also based on the γ-Cephei system, we reduced the viscosity parameter from $\alpha = 10^{-2}$ to $\alpha = 10^{-3}$, because this better represents the average viscosity found in recent disk observations (e.g., Rafikov 2017; Sellek et al. 2020; Trapman et al. 2020). Additionally, we increased the numerical resolution of the grid and the extent of the simulation domain.

The general behavior of the disk during a binary revolution is displayed in Fig. 1. During the binary apastron, the disk is eccentric but the overall density is smooth, without any spiral features. Just before periapse, the disk becomes visibly affected by the companion and is extended toward the secondary in a shape that follows the Roche lobe of the primary. Mass loss occurs shortly after the periapse, during the same time, two spiral arms develop that wind toward the disk's center and dissipate.

The radial disk structure is displayed in Fig. 2 using the time-averaged radial surface density and temperature profiles. The

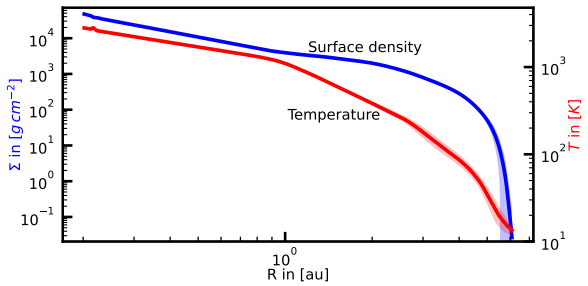

Fig. 2. Time-averaged radial profile of the surface density and gas temperature of our fiducial model. Solid lines are averaged over 200 snapshots taken at the binary apastron during the simulation time from 1300 $T_{\rm bin}$ to 1500 $T_{\rm bin}$. The shaded areas show the 1σ variations.

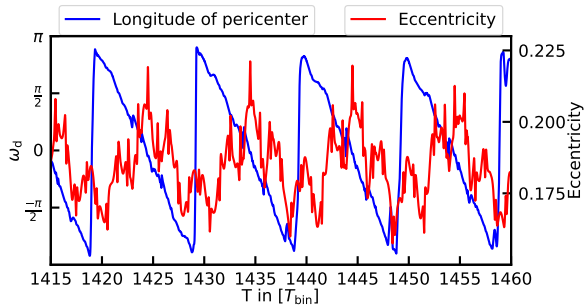

Fig. 3. Time evolution of the mass-weighted disk eccentricity and the mass weighted longitude of pericenter for the fiducial model. The disk has the lowest eccentricity and has the least variation during one binary orbit when the longitude of pericenter is aligned with the binary periastron ($\omega_{\rm d} = \pm\pi$). From that point the disk's eccentricity and variation during one binary orbit increases and reaches a maximum when the longitude of pericenter is aligned with the binary apastron ($\omega_{\rm d} = 0$).

transition between opacity power-laws are visible as bends in the temperature profile, such as the bend at 1 au caused by the sublimation of dust at 1100 K. Inside the dust sublimation region, the temperature gradient becomes shallower due to the lower opacity, and the surface density gradient becomes steeper due to the disk being in a viscous equilibrium. Beyond 4.5 au, surface density drops rapidly because of the tidal truncation of the binary. The kink in temperature close to the inner edge is caused by the wave damping region.

All of our simulations produced retrograde precessing disks with one precession period, lasting between 4–40 $T_{\rm bin}$, depending on their temperature. The effects of the precession on the disk eccentricity are shown for the standard model in Fig. 3. When the disk's apocenter is aligned with the binary's periastron, the disk is most affected by the binary's periastron passage, resulting in the largest perturbations (seen as the largest spikes in Fig. 3). At this point, the disk's eccentricity is also the largest. When the disk's longitude of pericenter is moving toward the binary's periastron, it becomes less affected by the companion, resulting in weaker perturbations during the binary's periastron passage and a waning disk eccentricity.

4. Numerical convergence

Before we present our studies on the influence of the physical parameter, we first showcase in this section the impact of the numerical parameters on the disk's behavior in a close binary star. Starting from our standard model in Table 1, we varied one numerical parameter at a time and studied their effect on the dynamical evolution on the disk. A suitable indicator for the dynamical state of the disk is the mass averaged global disk eccentricity, $e_{\rm d}$, calculated according to Eq. (3), and we present our finding in terms of $e_{\rm d}$.

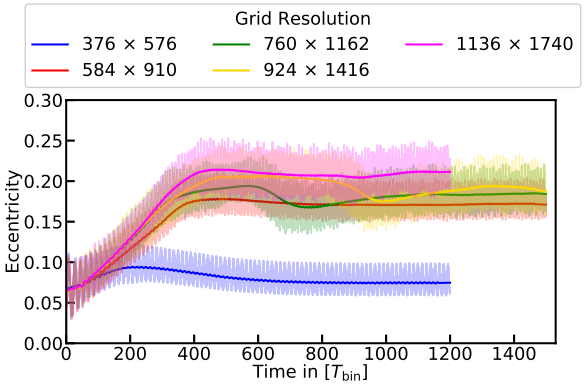

Fig. 4. Time evolution of the mass-weighted disk eccentricity (see Eq. (3)) for different resolutions for a logarithmic grid. Solid lines are time averaged values while the transparent lines are the simulation data.

4.1. Grid resolution

In Fig. 4 the disk's eccentricity is shown for different resolutions of the logarithmic grid. For our standard model (green line in Fig. 4) it takes the disk around 400 orbits to reach an equilibrium state (similar values were found in Kley et al. 2008 and Müller & Kley 2012 for locally isothermal simulations). The final eccentricity reached in this equilibrium state depends on the numerical resolution. A too low resolution can damp the disk's eccentricity significantly, as seen clearly in the lowest resolution case, 376 × 576, in Fig. 4, which ends up in a different, low eccentric state compared to higher resolution cases. In simulations with higher resolutions (with more than six cells per radial pressure scale height) $e_{\rm d}$ grows until a new equilibrium state is reached with $e_{\rm d} \approx 0.17$–0.22 for the various resolutions. Our fiducial model has a resolution of eight cells per radial pressure scale height to leave enough headroom to conduct simulations with colder disks (and therefore fewer cells per scale height) on the same grid. Other works, which conducted numerical convergence studies, also found that resolutions of around eight cells per scale height are required to reach convergence, for example, Thun et al. (2017) and Oliva & Kuiper (2020). In the high eccentric state, the disks show a retrograde precession with a period of (9.5–10.2) $T_{\rm bin}$, which is always identical to the corresponding oscillation period of $e_{\rm d}$, as shown in Fig. 3 for the standard case.

We repeated the resolution test with an arithmetic grid and found the same behavior with comparable final disk eccentricity. Although, a significantly higher resolution of 1846 × 1800 on an arithmetic grid was required to match the simulation using a 760 × 1162 resolution on a logarithmic grid. This is caused by the fact that the arithmetic grid has a lower resolution (cells per pressure scale height) in the inner disk region and instead has a higher resolution at the periphery than the logarithmic grid. Reaching convergence between the two grids indicates that our disk is sufficiently resolved throughout the whole domain and that the numerical viscosity should be negligible.

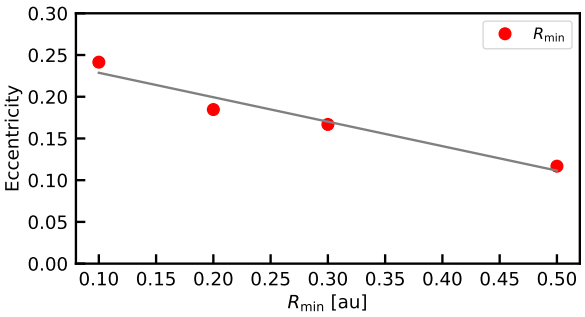

Fig. 5. Time-averaged mass-weighted disk eccentricity plotted against the location of the inner domain boundary.

We take these resolution studies as a sign that the excited, eccentric disk state is physical and that the low eccentric state at lower grid resolutions is only numerical. Since increasing the resolution further above our standard model, has little effect on the dynamics, and for computational reasons, we choose the 760×1162 resolution as our standard. Considering our new results, it turns out that previous studies of radiative disks (e.g., Müller & Kley 2012) may have suffered from too low grid resolution.

4.2. Location of the outer boundary

Previous studies on γ-Cephei used domain-sizes of 0.5–8 au, equivalent to 0.025–0.4 a_{bin}, (Kley & Nelson 2008; Müller & Kley 2012; Paardekooper et al. 2008), while Marzari et al. (2009) used 0.5–15 au but with a larger $a_{bin} = 30$ au, instead of our $a_{bin} = 20$. To check the impact of the chosen value of the outer boundary on the disk dynamics, we ran simulations using different values for R_{max}. We found that the outer radius R_{max} has little effect on the dynamics of the disk, but does change the mass loss rate across the outer boundary. When the companion passes periastron, mass is ejected from the primary disk. If R_{max} is too small, mass ejected from the disk is removed from the simulation before it can be re-accreted onto the primary disk. Increasing R_{max} further than 12 au (binary distance at periastron) leads to the same mass loss rates once the disk has reached equilibrium. Hence, the simulation domain should therefore at least contain the whole Roche lobe of the primary in apocenter, as in our standard case.

4.3. Location of the inner boundary

The location of the inner domain radius, R_{min}, directly influences the dynamics of the disks. The further out the position of the inner boundary, the lower the disk eccentricity with an approximately linear dependency, see Fig. 5. For reflective boundaries, the radial velocity and hence eccentricity is forced to zero at the boundary. If the boundary is closer to the star, it has less influence on the rest of the disk, allowing it to develop higher eccentricity, see Fig. 6. This increase in eccentricity for smaller R_{min} could also be explained by additional higher-order resonances still being captured inside the domain (Marzari et al. 2009). Similar to the disk eccentricity, the precession rate increases for decreasing R_{min}, from $0.09\, T_{bin}^{-1}$ at $R_{min} = 0.5$ au to $0.12\, T_{bin}^{-1}$ at $R_{min} = 0.1$ au. Therefore, adding an inner disk region influences the eccentricity and precession rate of the whole disk while the radial temperature and the surface density profile remain unchanged (image not shown).

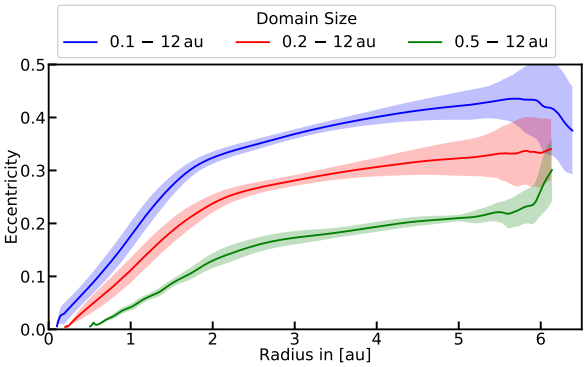

Fig. 6. Azimuthally averaged disk eccentricity (see Eq. (4)) for different locations of the inner radius. Solid lines are averaged over 200 snapshots taken at the binary apastron during the simulation time from $1000\, T_{bin}$ to $1200\, T_{bin}$. The shaded areas show the 1σ variations. The disk has a radius of $\approx$5 au, eccentricities at radii beyond that do not contribute to the disks eccentricity.

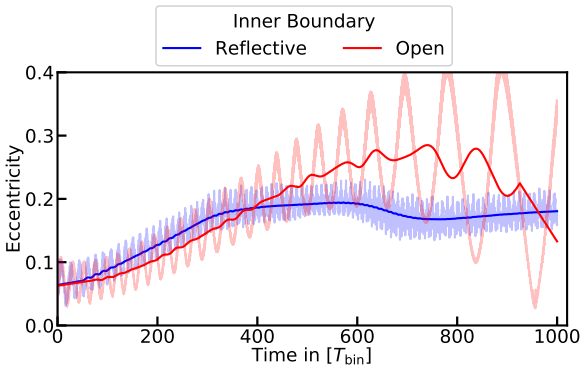

Fig. 7. Time evolution of the mass-weighted disk eccentricity for different inner boundary conditions. Solid lines are averaged values while the transparent lines are the simulation data. The simulation with an open boundary at the inner domain does not reach an equilibrium state due to the rapid mass loss. The lower temperatures from losing mass slow down the precession rate.

For open boundaries, a smaller R_{min} reduces the artificial mass loss at the inner boundary. Due to the high computational cost of reducing the inner radius of the domain, we limit R_{min} to 0.2 au for the rest of our simulations.

4.4. Inner boundary condition

We also ran a test using an open inner boundary condition without damping at the inner boundary. The simulation develops a similar eccentricity compared to the standard case with a reflective inner boundary condition (Fig. 7). Since any mass that crosses the inner boundary is removed from the simulation, the disk loses mass very fast and forms an elliptic inner hole (Fig. 8). This behavior is in agreement with the simulations shown in Kley et al. (2008) and Marzari et al. (2012). This rapid mass loss prevents the disk from reaching an equilibrium state as the disk continuously becomes colder, which causes the precession rate to slow down (compare Fig. 17 below). The disk's eccentricity profile behaves differently. Throughout the whole disk, the

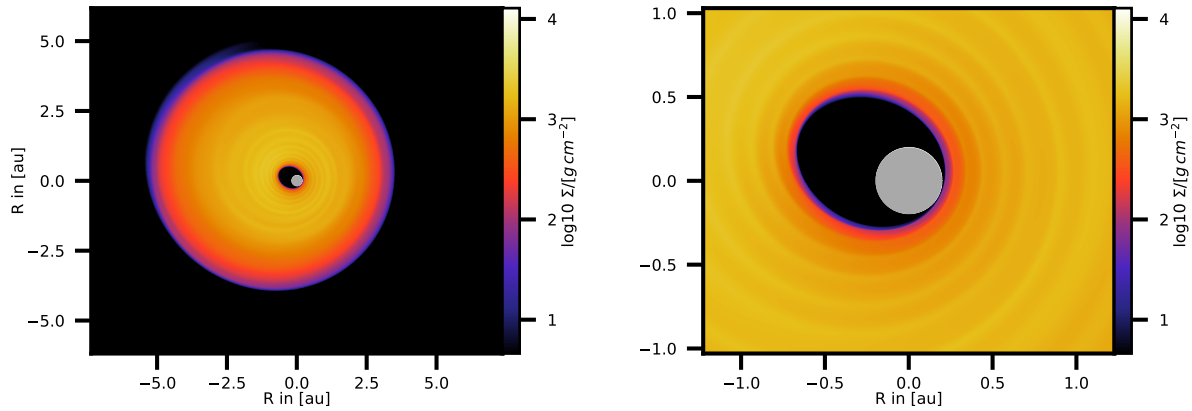

Fig. 8. Snapshot of the disks surface density after 481 orbital periods at the binary apastron. The simulation used an open inner boundary condition. *Right*: zoom in on the inner 1 au. Mass being removed at the inner boundary (gray area) causes the development of an eccentric hole.

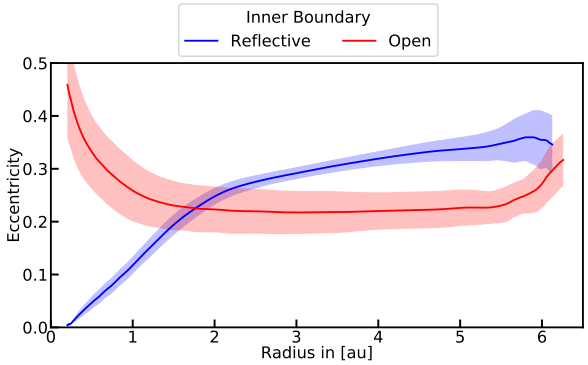

Fig. 9. Radial profiles of the time averaged mass-weighted disk eccentricity for different inner boundary conditions. Solid lines are averaged over 200 snapshots taken at binary apastron between $T = 400$ and $600T_{\rm bin}$. The shaded areas show the $1\,\sigma$ variations. Eccentricity as well as precession are more uniform throughout the disk when open boundaries are used. The radial profiles are cut at a radius where the time averaged surface density drops below 100 times the floor value.

eccentricity is constant, whereas in the simulation with reflective boundaries, the eccentricity is forced to zero at the inner boundary and grows outward (Fig. 9). Similarly, the disk precesses as a solid body at all times, while for simulation with reflective boundary, we find deviations from solid body precession, see Sect. 6 for more details. The gas at the edge of the inner eccentric hole develops high radial velocities and variations in the azimuthal velocity that severely limit the timestep, making these simulations computationally too expensive for a full parameter study in this work.

5. Dependence on physical parameters

Having analyzed the impact of purely numerical parameters, we conclude, that the computational setup of the standard model (see Table 1) seems to be sufficient to capture all relevant physical properties of the disks. We shall use it throughout this section to study the effects of physical parameters on the disk's dynamics. The α-parameters and initial disk masses tested in this section are listed above in Table 2.

Table 2. All the simulations for the parameter study.

α-parameter	1×10^{-4}	3×10^{-4}	$\underline{1 \times 10^{-3}}$	3×10^{-3}
	5×10^{-3}	6×10^{-3}	7×10^{-3}	1×10^{-2}
Initial disk mass	2×10^{-3}	5×10^{-3}	$\underline{1 \times 10^{-2}}$	2×10^{-2}
in $[M_\odot]$	3×10^{-2}	4×10^{-2}	5×10^{-2}	

Notes. The simulations use the same parameters as the fiducial model in Table 1, but have one disk parameter changed. Each number represents one simulation. The default parameters are underlined in blue.

5.1. Disk mass

The disk's mass density has a direct influence on its temperature, first by increasing the heating through the viscous stress tensor and secondly by increasing the optical depth thereby reducing the radiative cooling efficiency. Thus, increasing the disk mass should directly increase the disk temperature and subsequently impact the disk dynamics, that is, its eccentricity. We tested this by varying the initial disk masses, ranging from 2×10^{-3} to $5 \times 10^{-2}\,M_\odot$, while keeping the other parameters unchanged from the standard model.

5.1.1. Temperature profile

The radial disk temperature (here given as the relative disk thickness) resulting from different disk masses is displayed in Fig. 10, and it clearly shows a monotonic increase in aspect ratio with disk mass within the disk proper, that is, inside of about 6 au. But the individual curves show some substructures. For the lowest mass ($2 \times 10^{-3} M_\odot$) case (the blue line in Fig. 10), a drop-off in aspect ratio is visible for radii inside of ~2 au. Inside of this radius, the disk temperature surpasses the ice sublimation temperature ~160 K. This trend reverses when all the ices are sublimated at ~220 K (at around 1.2au) and the opacity increases with temperature again.

Not considering, for now, the strong increase in h close to the inner boundary, all models show a drop in aspect ratio toward

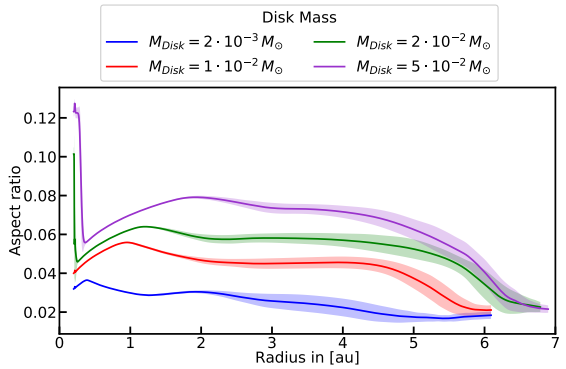

Fig. 10. Radial profiles of the time averaged mass-weighted disk scale height, here $h = H/r$, for different initial disk masses. Solid lines are averaged over 200 snapshots taken at binary apastron during the simulation time from 1300 $T_{\rm bin}$ to 1500 $T_{\rm bin}$. The shaded areas show the 1 σ variations. The radial profiles are cut at a radius where the time averaged surface density drops below 100 times the floor value.

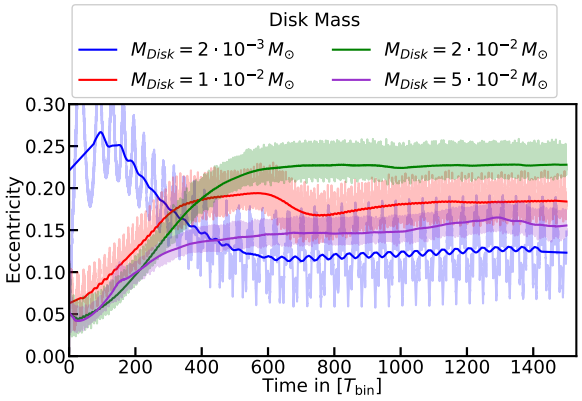

Fig. 11. Time evolution of the mass-weighted disk eccentricity for different initial disk masses.

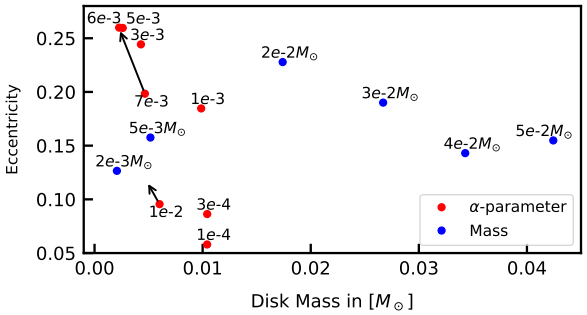

Fig. 12. Time-averaged mass-weighted disk eccentricity plotted against the mass-weighted disk temperature. The arrows indicate the state after 2000 $T_{\rm bin}$. At that time the $\alpha = 10^{-2}$ case has not reached an equilibrium yet.

the inner edge, which indicates the sublimation of dust grains at about 1100 K and a lowering of the opacity. With increasing mass, this transition moves further out, as does the maximum of h. The standard model with $M_{\rm d} = 10^{-2}\, M_\odot$ reaches the threshold at ∼1 au while for the highest disk mass it lies at about 2 au. At the very inner edge, the models with larger disk mass show a strong increase in temperature up to over 3300 K. This is caused by the dissociation of hydrogen, which drastically increases the opacity, leading to high aspect ratios.

We also tested the effect stellar irradiation from the central star would have on our disks using the irradiation model from Menou & Goodman (2004). Following the procedure described in Ziampras et al. (2020), we took a time-averaged radial density profile of our disks and calculated its temperature in thermal equilibrium under the influence of viscous heating, stellar irradiation, and radiative cooling. We found that stellar irradiation does not affect on the optically thick, dense inner half of the disk ($r \lesssim 2$–4 au depending on model) and only becomes relevant at the outer parts. However, due to the existence of a maximum in the aspect ratio in this region (see Fig. 10), the outer parts would be shadowed by the inner regions (from the star or hot inner disk) if a more realistic irradiation model was used. We conclude that stellar irradiation has no effect on the dynamics of our disks and can be neglected.

5.1.2. Time evolution of the eccentricity

The time evolution of the global disk eccentricity is displayed in Fig. 11 for four different disk masses. After about 600 to 800 $T_{\rm bin}$ all models settle to a quasi-stationary state. The simulations show that the small eccentricity for the low mass case is accompanied by larger deviations from solid body precession. Deviations from solid body precession appear as varying precession rates at different radii inside the disk. In our simulations, we observe that the disk's eccentricity is suppressed, when neighboring gas rings precess independently of each other. From Fig. 11 it can also be seen, that the oscillation period of the eccentricity becomes shorter with higher disk mass, which implies a faster retrograde precession rate. We discuss these effects in more detail in Sect. 6.

The low mass case $2 \times 10^{-2}\, M_\odot$ (blue line in Fig. 11) has a peculiar eccentricity evolution because it is the one farthest away from an equilibrium profile during initialization. It is too cold to precess for the first 20 binary orbits; because the longitude of pericenter is positive in the beginning, this results in a rapid eccentricity growth (compare the eccentricity growth for $\omega_{\rm d} > 0$ in Fig. 3). The disk becomes more compacted by the tidal forces of the companion and starts precessing, resulting in a hot inner region and cold outer rim with a large temperature gradient across the disk. Due to the strong temperature gradient, the disk precesses at different speeds at different radii, resulting in strong damping of the eccentricity, as mentioned above.

The resulting disk eccentricities in the equilibrium state are shown in Fig. 12, which includes additionally the results for different viscosities. We find that the simulation with a disk mass of $2 \times 10^{-2}\, M_\odot$ (resulting in an aspect ratio of $h = 0.057$) develops the largest eccentricity. More massive and less massive disks develop a smaller eccentricity (see blue points in Fig. 12). This finding is in agreement with Marzari et al. (2012) who found their eccentricities peaking at $h = 0.05$ in their locally isothermal runs (compare their Fig. 1). Their explanation states that for cold disks, the perturbations (spiral arms) move inward more slowly and get tightly wound up. They are then more affected by viscous damping and become less efficient at depositing angular momentum in the inner parts of the disk. In hot disks, radiative damping dissipates the perturbations faster, leading to an overall lower disk eccentricity. The drop-off in eccentricity when deviating from the optimal h with the highest $e_{\rm d}$ is much smaller in our simulations, with the time-averaged eccentricity never dropping below $e_{\rm d} \sim 0.12$.

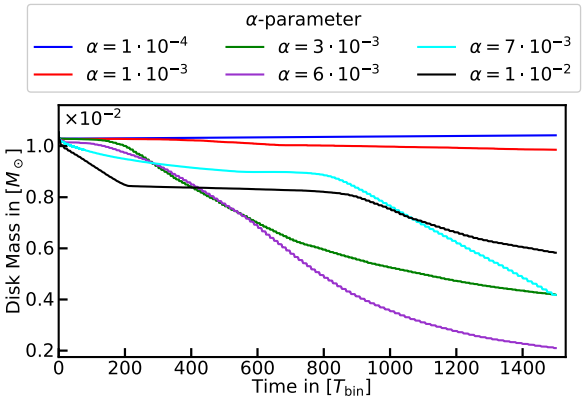

Fig. 13. Time evolution of the disk mass for different α values.

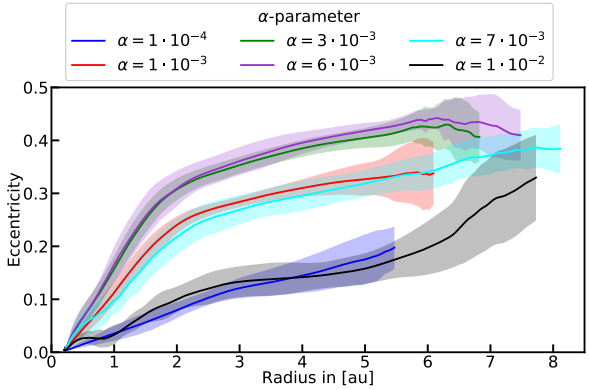

Fig. 14. Radial profiles of the time averaged mass-weighted disk eccentricity for different α values. Solid lines are averaged over 200 snapshots taken at the binary apastron during the simulation time from 1300 $T_{\rm bin}$ to 1500 $T_{\rm bin}$. The shaded areas show the 1 σ variations. The radial profiles are cut at a radius where the time averaged surface density drops below 100 times the floor value.

5.1.3. Mass loss

As explained above, the disks lose mass across the outer boundary of the computational domain. Starting from the initial setup, all models typically lose about 2.5% of their mass during the first few orbits. Ignoring this mass loss at the beginning, the disks lose mass on a longer timescale which is mostly ejected during the binary periastron passage when the disk's longitude of pericenter is aligned to the binary apastron, see Fig. 1 above. Mass outflow only occurs if the disks are large and eccentric enough to overflow the primary's Roche lobe during the periapse. It regulates itself because at some point, the disks become small enough to fit entirely inside the primary's Roche lobe and mass loss during pericenter passage becomes negligible. The mass-loss rate increases during the growth of the disk's eccentricity and then settles to a stationary value. For the standard case, this quasi-equilibrium is reached at around $600T_{\rm bin}$. After that, the disk loses mass at a rate of about $3.6 \times 10^{-9}\,M_\odot\,{\rm yr}^{-1}$ for the standard case, and $1.4 \times 10^{-7}\,M_\odot\,{\rm yr}^{-1}$ for the more viscous $\alpha = 6 \times 10^{-3}$ case. Disks with a viscosity smaller than our standard case do lose even less mass to outflow, while our most viscous disks lose 80% of their mass within our simulation time of 1500 binary orbits, see Fig. 13.

In the simulation with an open inner boundary, the disk loses 80% of the initial mass within 900 binary orbits. Due to its low viscosity of $\alpha = 10^{-3}$, very little mass is lost by outflow, and most of the mass is lost through the inner boundary. This mass loss might be enhanced by our artificial large inner boundary. The mass loss through the inner boundary can be described as an exponential decay, as would be expected from the viscous accretion around a single star, and starts at $2.1 \times 10^{-7}\,M_\odot\,{\rm yr}^{-1}$ when the disk still has its full mass and drops to $6.5 \times 10^{-8}\,M_\odot\,{\rm yr}^{-1}$ at $900\,T_{\rm bin}$ when the disk mass is at $2.5 \times 10^{-3}\,M_\odot$.

5.2. Viscosity

We tested α values ranging from 10^{-4} to 10^{-2}. The resulting eccentricities as a function of radius are displayed in Fig. 14. For smaller viscosities, from $\alpha = 10^{-4}$ to 6×10^{-3}, we confirm the trend found in Kley et al. (2008) and Müller & Kley (2012) that higher viscosity leads to more eccentric disks.

For even higher α, the disk dynamics evolve differently, and eccentricity drops again, as indicated by the cyan and black curves in Fig. 14. For these two highest α-values ($\alpha = 7 \times 10^{-3}$ and 10^{-2}) the disks first enter a quiet state that is steady, low-eccentric and non-precessing. Only after several hundreds of orbits do the disks start to precess and become more eccentric. At the time of $2000\,T_{\rm bin}$ the $\alpha = 7 \times 10^{-3}$ simulation reaches the same final eccentricity of $\bar{e}_{\rm d} \approx 0.25$ as the $\alpha = 6 \times 10^{-3}$ case, while the simulation with $\alpha = 10^{-2}$ continues to grow its eccentricity at a slow but constant rate.

Higher α values result in stronger viscous torques, causing the disk to spread further outward. A larger disk is more affected by the companion and thus develops a larger eccentricity. The gas at the outer rim of the disk also has the largest eccentricity. Because of that, it is ejected from the disk during periastron passage which prevents further growth of eccentricity and limits the disk radius. The evolution of disk mass for the different disk viscosities is shown in Fig. 13, which shows a clear trend for the lower viscosity cases that the mass loss increases with viscosity, as expected. At first, the two high viscosity cases show relatively small mass loss against the initial expectation. This is due to the disks initially remaining much more circular and only start losing mass after becoming excited, in the same way as described above.

6. Global trends

In this section, we look for global trends in the simulations from the previous section. We vary simultaneously, mass and viscosity of the disks and we present the data in different forms to better visualize the connection between the physical state of the disk and its dynamical behavior.

6.1. Eccentricity

Figures 15 and 16 show the averaged disk eccentricity and disk radius plotted against the global averaged disk viscosity. The data is first mass-averaged, see Eq. (3), and then time-averaged over the final ten precession periods, at simulation times between 1200 and $1500\,T_{\rm bin}$. We measure the precession periods as the time between two adjacent peaks of the longitude of pericenter (see Fig. 3). The blue dots always represent data from simulations with different disk masses and red dots data from those with different viscosity. Figure 15 shows a positive correlation

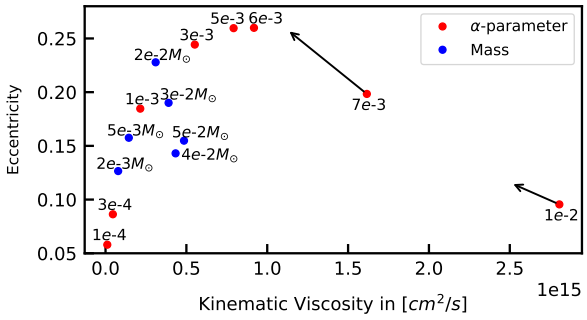

Fig. 15. Time-averaged mass-weighted eccentricity plotted against the time averaged mass-weighted viscosity. The arrows indicate the state after 2000 $T_{\rm bin}$. At that time the $\alpha = 10^{-2}$ case has not reached an equilibrium yet.

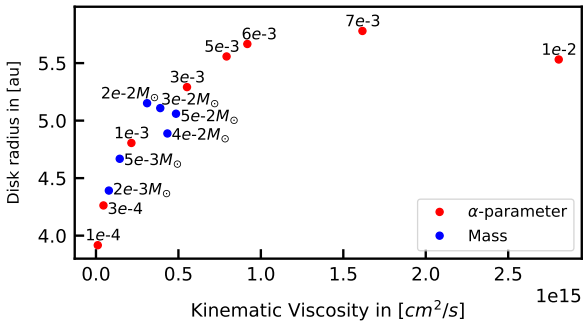

Fig. 16. Time-averaged disk radius plotted against mass-weighted kinematic viscosity.

between viscosity and eccentricity, except for the high viscosity simulations. These start in a quiet state and retain a smaller eccentricity for the whole run time. In the following discussion, we ignore those two simulations because they have not reached an equilibrium state at the end of our standard simulation time of 1500 $T_{\rm bin}$. The positive correlation between eccentricity and viscosity is in agreement with earlier studies (Kley et al. 2008; Müller & Kley 2012). It can be explained by larger viscous torques increasing the disk's size, making it more susceptible to perturbations of the companion and causes a higher eccentricity. The simulations with different disk masses follow the same trend, except for the higher mass simulations, see Fig. 12 above. We attribute the lower eccentricity in high mass simulation to radiative damping of the perturbations.

Similarly, diffusive action of viscosity is reflected in Fig. 16 which shows a positive correlation between disk size and viscosity. The disk expansion due to viscosity stops at an average disk radius of ~5.7 au, equivalent to 0.28 $a_{\rm bin}$, see Fig. 16, and a mass-weighted eccentricity of 0.25, Fig. 15. It is important to note that since we keep the number of grid cells constant, simulations with a low aspect ratio are less resolved. This could enhance the drop-off in eccentricity for simulations with low viscosity or low mass.

We find that the disk's eccentricity increases linearly with its radius, which has been noted by Marzari et al. (2009), who changed the disk size by varying the binary's eccentricity. We note that the linear correlation between size and eccentricity could also partly be explained by our method of determining the

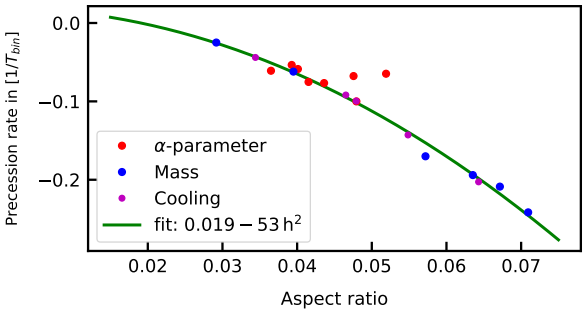

Fig. 17. Precession rate plotted against the mass-weighted disk aspect ratio. Red dots mark the simulations with different α values, blue dots with different disk masses and magenta dots with different cooling factors and lower resolution. The green line is a quadratic fit through the data points. The precession rate depends linearly on the disk Temperature with $T \propto h^2$.

disk's radius as the distance from the primary that contains 99% of the disk mass.

6.2. Precession rate

The precession rate was determined as described in the previous section. We find a slow retrograde precession for all disks, with one precession period lasting between 5 to 40 binary orbital periods. The precession rates are shown in Fig. 17 as a function of the global disk aspect ratio. The models for different disk masses and viscosities show a unique quadratic relation, fitted approximately by

$$\dot{\omega}_{\rm d} = (0.019 - 53\,h^2) T_{\rm bin}^{-1}. \quad (6)$$

In general, the disk's precession rate depends on the balance of gravitational and pressure forces (Goodchild & Ogilvie 2006). The gravitational forces induce a prograde precession while the pressure forces result in retrograde precession. We find retrograde precession for all our simulations, indicating that the disks are hot enough to be pressure-dominated. Our values for the precession rate and, in particular, the quadratic dependence with the mean scale height h are in excellent agreement with the locally isothermal simulations in Kley et al. (2008), obtained for circular binaries.

Since in our model $T \propto h^2$, this implies a linear relation between disk temperature and precession rate. We restarted our standard case with a modified heating and cooling rate to test the linear relation between precession rate and temperature. The heating and cooling rate were directly multiplied by factors of either 0.1 or 10. After that, the precession rates adjusted themselves on the thermal timescale, which is only a few (~3) binary orbits. The resulting precession rates are shown as purple dots in Fig. 17, and they lie on the same curve. For the simulations with varying α-values, the relation between the precession rate and the temperature is not as pronounced, and simulations that start in the low eccentric disk state do not fit the model anymore (two rightmost big red points in the plot). In Fig. 3, it can be seen that the disks build up eccentricity when the longitude of pericenter is shifting toward the binary's periastron and reduce their eccentricity when the longitude of pericenter is shifting away from the binary periastron position. This causes disks with lower precession rates to have more time to increase their eccentricity and have therefore a larger variance in eccentricity oscillations.

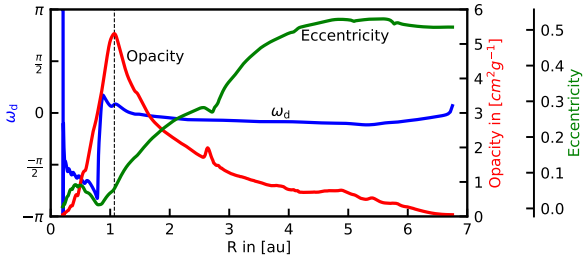

Fig. 18. Snapshot at $T = 662.74\,T_{\rm bin}$ of the radial profile of the longitude of pericenter, opacity and eccentricity of the fiducial model. The dashed vertical black line indicates the position of the change in the opacity power-law at $T = 1100$ K. The longitude of pericenter becomes undefined for $e = 0$ at the inner boundary.

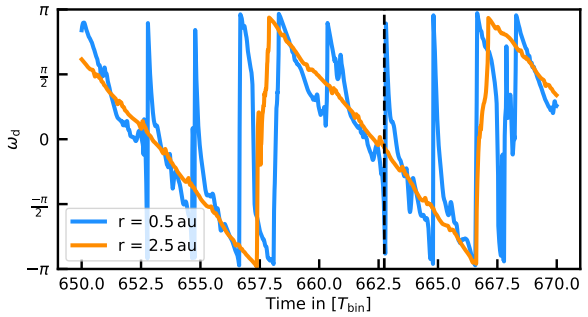

Fig. 19. Time evolution of the azimuthally mass-weighted average of the longitude of pericenter at two different radii for the fiducial model. The dotted line indicates the time the snapshot used in Fig. 18.

6.3. Solid body precession

Typically, in our simulations, the disks precess as a solid body, that is, the radial profile of the longitude of pericenter is constant across the whole disk. In some simulations, however, we observe deviations from the solid body precession. These mostly appear as jumps in the longitude of pericenter, at radii at which the opacity changes due to the temperature gradient in the disk. In our opacity models, the variation with temperature is given by different power-laws. Abrupt changes in these split the disk into regions with different temperature gradients, which affects the propagation of the perturbations in the disk as sound waves are partially reflected at these discontinuities. This can cause the disk to split into two regions at the power-law transition that precess independent of each other.

An example of this effect is displayed in Fig. 18 which shows a snapshot of the disk longitude of pericenter, opacity, and eccentricity of the fiducial model just after the binary periastron passage when the spiral arms had propagated to the inner parts of the disk. The change in wave propagation induced by the opacity law splits the disk's longitude of pericenter at ∼1 au where the temperature in the disk surpasses the dust sublimation temperature of $T \approx 1100$ K and the temperature dependence of the opacity changes from $\kappa \sim T^1$ to $\kappa \sim T^{-9}$. Figure 19 shows that the precession at the inner region of the disk (blue line) becomes irregular and independent of the outer disk region (red line). By the time the binary reaches apastron, the perturbations have dissipated, and the inner region of the disk starts to realign to the outer region of the disk. While the region's precession is disconnected, the eccentricity of the disk is reduced at the boundary between the two regions, lowering the eccentricity throughout the whole disk. For our low mass simulation $M_{\rm disk} = 2 \times 10^{-3} M_\odot$, the longitude of pericenter breaking happens when the temperature surpasses 155 K and the power-law changes from $\kappa \sim T^2$ to $\kappa \sim T^{-7}$. This transition happens further outward at 2 au, causing the eccentricity damping of the differential precession to be more effective (compare the onset of longitude of pericenter breaking for the low mass simulation (blue line) at $t = 100\,T_{\rm bin}$ versus the onset of breaking for the fiducial model (red line) at $t = 600\,T_{\rm bin}$ in Fig. 11).

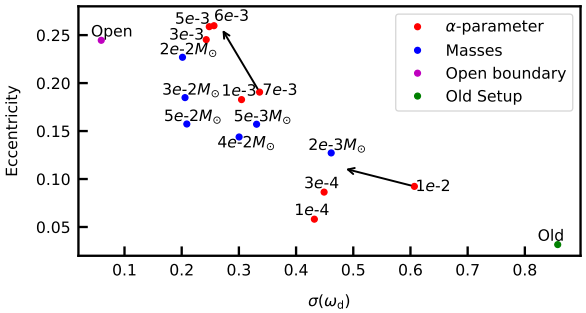

Fig. 20. Disk eccentricity plotted against the standard deviation of the longitude of pericenter of all cells. The values mass averaged and time averaged over 200 snapshots at binary periastron from $T = 1300\,T_{\rm bin}$ to $T = 1500\,T_{\rm bin}$. The old setup is using the standard parameters presented in Müller & Kley (2012). The arrows indicate the state after $2000\,T_{\rm bin}$.

We calculated the mass-weighted standard deviation of the longitude of pericenter $\sigma(\omega_d)$ for all cells in the disk and found an anticorrelation between $\sigma(\omega_d)$ and disk eccentricity, see Fig. 20. This effect acts on top of the other effects that influence the disk eccentricity that we discussed in this work. For the high mass simulations in Fig. 20, the drop in eccentricity without an increase in $\sigma(\omega_d)$ is caused by radiative damping. Simulations with a low α-value develop a lower eccentricity than other simulations with comparable $\sigma(\omega_d)$, indicating that the drop is due to their smaller size rather than differential precession.

Disks that enter a quiet state do not precess and have a highly varying longitude of pericenter; but due to their very low eccentricity, it is not clear whether their high $\sigma(\omega_d)$ is damping their eccentricity or their low eccentricity makes determining the longitude of pericenter less precise. Additionally, this effect depends on the inner boundary condition. An open inner boundary condition removes mass and reduces the temperature gradient across the disk, reducing the influence of power-law changes in the opacity table. This again highlights the importance the inner boundary has in our simulations.

7. Discussion

7.1. Comparison to previous work

Previous studies about radiative disks in the system of γ-Cephei (Müller & Kley 2012; Marzari et al. 2012) found only low disk eccentricities of $e_d \sim 0.05$, which is in contrast to our new simulations presented here. We attribute the differences to a combination of the high viscosity values used for their fiducial models of $\alpha \approx 10^{-2}$, a too low resolution, and a too-small simulation domain. For such a high viscosity, the disks stay in a quiet state with low eccentricity and no precession. This

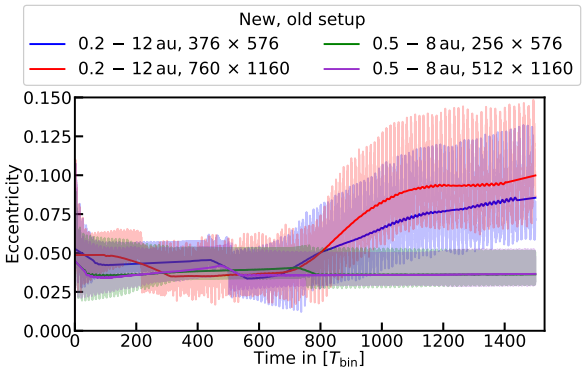

Fig. 21. Time evolution of the mass-weighted disk eccentricity for the parameters of the standard case of Müller & Kley (2012) that is shown in green, and the parameters given in Table 1 but with $\alpha = 10^{-2}$.

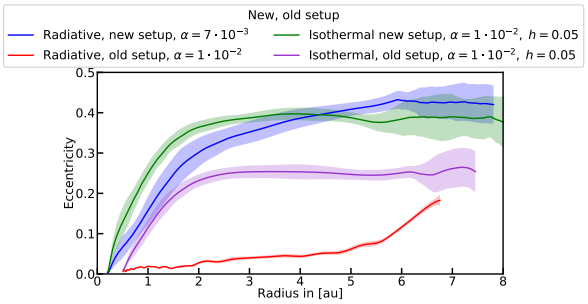

Fig. 22. Radial profiles of the time averaged mass-weighted disk eccentricity for our new setup and the standard models from Müller & Kley (2012). Solid lines are averaged over 200 snapshots taken at binary apastron. The shaded areas show the 1 σ variations.

quiet state is robust to changes in numerical parameters, giving a false sense that lower resolutions and smaller domains have converged. Figure 21 shows simulations for the standard parameters from Müller & Kley (2012) (green curve) and their convergence test (purple line) and simulations with the domain size of our standard model Table 1 (red and blue lines). After we increased the domain size, the disks started to develop eccentricity and precession after 700 T_{bin} of simulation time, which is longer than the simulation time of the convergence tests in Müller & Kley (2012). The difference in disk structure for the setups is shown in Fig. 22. The plot compares the radial eccentricity profile of radiative and locally isothermal models for the new and old setup, averaged over 200 snapshots taken at binary apastron. The curves for the old model (red and purple) use the original data from Müller & Kley (2012) with their standard viscosity parameter of $\alpha = 10^{-2}$. The radiative simulation on the new setup uses a lower viscosity of $\alpha = 7 \times 10^{-3}$ because the $\alpha = 1 \times 10^{-2}$ simulation has not reached an equilibrium state at the end of the simulation time of 2000 T_{bin}. Figure 22 highlights the drastic difference between a quiet state and an excited state. The eccentricity of the disk in the quiet state is very low ($e_d \leq 0.05$), and it does not precess. This means that the disk is always in the same state when the binary reaches apastron, as indicated by the vanishing standard deviation of the eccentricity. On the other hand, the dynamics of an excited disk also depend on the disk's own orientation inside the binary and oscillates with the disk's precession rate. It can be seen that the dynamics of our radiative simulations are closer to the dynamics of locally isothermal simulations rather than to the radiative simulations performed in previous studies. It is still not clear why radiative simulations perform worse than locally isothermal simulations at low resolutions. Despite locally isothermal and radiative simulations being similar at high resolutions, we recommend performing fully radiative simulations as locally isothermal simulations are overestimating the disk's eccentricity as they are missing effects like radiative damping and breaking of the solid body precession that can damp perturbations in the disk.

7.2. Mass loss

The mass-loss rates we found from mass ejection, are negligible compared to the mass accretion rates we found in our simulation with an outflow inner boundary condition. Allowing mass to leave through the inner boundary limits the disk's lifetime in our simulations to $\lessapprox 10^5$ yr for $\alpha = 10^{-3}$. This represents a lower estimate for the disk's lifetime as the mass loss is overestimated by our boundary condition. In realistic systems, the circumprimary disk will be accompanied by a circumsecondary disk and a circumbinary disk that all exchange mass between each other, as shown in numerical simulations (e.g., Günther & Kley 2002; Kaigorodov et al. 2010; Nelson & Marzari 2016; Muñoz & Lai 2016). The circumstellar disks could then be replenished with material from the circumbinary disk, which increases their lifetime (Monin et al. 2007). Observations of GG Tau A, which is a triple star system with a comparable configuration to γ-Cephei that hosts a disk around the primary star and a massive circumbinary disk of ~0.15 $M_\odot$, find mass accretion rates from the circumbinary disk onto the circumstellar disks of $\dot{M} \approx 6.4 \times 10^{-8}\, M_\odot\, \mathrm{yr}^{-1}$ (Phuong et al. 2020). The infalling mass is expected to be accreted in an approximately equal ratio onto the circumstellar disks (Dittmann & Ryan 2021). Extrapolating the mass loss rate from our open inner boundary condition simulation to the point it would be balanced out by a mass accretion rate of $3.2 \times 10^{-8} M_\odot\, \mathrm{yr}^{-1}$ results in a disk mass of $M_d \approx 8 \times 10^{-4}\, M_\odot$. Since our inner outflow boundary condition likely leads to an artificially enhanced mass accretion, circumstellar disks with masses of a few $10^{-3}\, M_\odot$ could have the same lifetime as the circumbinary disk that feeds them. A similar mass has been estimated from observations for the disk around GG Tau Aa (Dutrey et al. 2014). This indicates that the circumstellar disk lifetime inside binaries is not necessarily a constraint for planet formation as they are fed by circumbinary disks that have been observed to have similar lifetimes as disks around single stars (Kuruwita et al. 2018)

7.3. Accretion shocks

The mass infalling onto the circumprimary disk is accreted in pulses (Muñoz & Lai 2016), leading to shocks and shock heating in the disk (Nelson & Marzari 2016) and could cause the disk to develop a third spiral arm (Picogna & Marzari 2013). Since those studies did not resolve the circumstellar disks at a high enough resolution or evolved the system long enough to build up eccentricity, the effects of pulsed accretion on the disk dynamics are poorly understood. We conclude from these studies that the perturbations of the infalling material onto the circumprimary disk are minor compared to the gravitational perturbations of the companion. Therefore, we expect the trends we found to hold even if a mass accretion onto the disk is added.

All our simulations are two-dimensional. Running the same setup with three dimensions will affect the disk dynamics. Due to an extra degree of freedom for the gas motion, shock heating is less effective in 3D than in 2D Bate et al. (2003). As the companion excites strong shocks inside the disk that produce significant heat, our 2D approach likely overestimates the disk's temperatures. Additionally, density wave propagation and their deposition of angular momentum into the disk could be different in three dimensions Lubow & Ogilvie (1998); Lee & Gu (2015) which could affect the disk dynamics. While comparable 3D simulations did find differences to 2D simulations Picogna & Marzari (2013); Zhu et al. (2015), these were located at the disk's surface. Thus, we expect our 2D simulations to be comparable to the dynamics found in a 3D simulation at the mid-plane, where most of the mass resides.

8. Summary

We revisited the γ-Cephei system by performing grid-based, two-dimensional hydrodynamical simulations to study the dynamics of the disk around the primary star in an eccentric binary star. All of our simulations include viscous heating and radiative cooling. The disk dynamics are analyzed in terms of eccentricity and precession rate. We carefully separated physical from numerical behavior by investigating first the effects of numerical parameters before looking into the impact of physical conditions such as disk mass and viscosity.

We found that previous studies on radiative disks in close binaries used a too low resolution and too small simulation domain to properly resolve the disk dynamics. When using appropriate resolution and domain size, we observe considerably higher disk eccentricities. To reach the higher eccentric state, a resolution of at least six grid cells per scale height is required. Also, the simulation domain should contain the whole Roche lobe of the primary at phases of its orbit to avoid artificial mass loss through the outer boundary. The disk eccentricity linearly declines with increasing inner domain radius. This could imply that the disk becomes more circular as the inner region is cleared by photoevaporation.

It was already noted in Paardekooper et al. (2008) that the numerical methods used can change the outcome of the simulations. These effects were not observed in later studies such as Müller & Kley (2012) due to their fiducial model being caught in a quiet state that is robust to numerical changes. This quiet state is characterized by a low eccentricity and no disk precession. These occur in the initial phase of the simulations for viscosities larger than $\alpha \geq 7 \times 10^{-3}$, and they can last for over $\approx 700\, T_{\rm bin}$. Eventually, the disks do become eccentric and start precessing. We found all of our disks become excited across different numerical and physical parameters as well as different codes (additionally to our FARGO code, we tested the PLUTO code). We are therefore confident that the excited state is physical and that the very low eccentricities reported for radiative disks in Müller & Kley (2012); Marzari et al. (2012) are inaccurate.

In agreement with Müller & Kley (2012) and Marzari et al. (2012), we find that it is important to perform more realistic simulations that include viscous heating and radiative cooling. Locally isothermal models overestimate the disk's eccentricity because they are missing effects like radiative damping or breaking of the solid body precession of the disk which can dissipate perturbations and damp the disk's eccentricity.

We used reflective boundaries at the inner radius for our simulations so that the disks can reach an equilibrium state. This boundary can physically be interpreted as the disk extending to the star's surface. We also ran a test simulation with an outflow inner boundary condition which coarsely resembles a cavity with perfect accretion, possibly created by a stellar magnetosphere. Despite these being two opposite extremes for the inner boundary condition, they lead to a similar early development of the disks. The disk evolution diverges over time as the open inner boundary simulation rapidly loses mass. We conclude that the trends we find would also apply to a more realistic boundary condition.

For the mass-weighted and time-averaged disk eccentricity, we found values from 0.06 to 0.27 (Fig. 15). The disk's size is given by a balance of viscous versus gravitational torques. In our simulations, we found values from 4 au for disks with low viscosities, which is identical to the orbital stability limit for massless test particles (Holman & Wiegert 1999; Pichardo et al. 2005), up to a maximum disk size of 5.8 au for higher viscosities (Fig. 16). The disk size, or indirectly the viscosity, is an important factor for the disk eccentricity. Smaller disks are less affected by the perturbations of the secondary and become less eccentric. The disks' eccentricity can also be reduced by radiative damping. In our simulations, radiative damping becomes effective for hot disks with $h \geq 0.06$. The eccentricity of the disk oscillates with the same period as the longitude of pericenter, and we found that the amplitude of the oscillation increases with the precession period. Our simulations did not include the effects of self-gravity, which can change the radial alignment of the longitude of pericenter and can damp the disk's eccentricity Marzari et al. (2009).

In all our simulations, we observed a slow retrograde precession of the disk. The precession rate depends linearly on the mean disk temperature, or equivalently, quadratically on the aspect ratio, as given by Eq. (6). This relation is in good agreement with the values found in Kley et al. (2008), who performed locally isothermal simulations for disks in circular binaries in the context of the superhump phenomenon in cataclysmic variables. From Eq. (6), we can expect that disks with low temperature will change to a prograde precession which might occur for disks with small disk masses during the dissipation phase.

We noticed in our simulations that the disk needs to precess as a solid body to be able to develop high eccentricities. Changes in the opacity power-law can break the longitude of pericenter alignment inside the disk, splitting the disk into an inner and outer region that precess independently of each other, reducing the overall disk eccentricity (see Fig. 18). We correlate the disk eccentricity to the standard deviation of the longitude of pericenter across all cells and find a downward trend in Fig. 20. We suspect that the low disk eccentricities found in Martin et al. (2020) could be explained similarly. In their isothermal SPH simulations, they observed that particles at different radii have different precession rates (see their Fig. 1). This could have prevented their disks from reaching higher eccentricities.

Concerning the impact on the planet formation process, the temperatures in our models with realistic masses ($M_{\rm d} \leq 10^{-2} M_{\odot}$) are cold enough for silicate to be present in a solid-state throughout most of the disk. For our coldest model $M_{\rm d} = 2 \times 10^{-3} M_{\odot}$ the snowline (160 K) is located in the middle of the disk at 2 au and the dust sublimation temperature (1100 K) is reached near the inner boundary at 0.5 au. Due to the low disk mass, the heating of the shocks is also weak. The spiral wave heats the outer parts of the disk to 200 K while the heating strength is reduced in parts where the disk temperature is already higher than 200 K from viscous heating. While the ices are repeatedly sublimated and recondensed by the spiral waves, silicate dust particles are mostly unaffected by the shock heating from the

companion. However, we find high eccentricities and a retrograde precession for disks in close binaries over a wide range of parameters. High gas eccentricities have been found to increase the collision velocities between particles inside the disk, which slows down dust coagulation (Zsom et al. 2011) and makes planetesimal accretion less likely to succeed (Paardekooper et al. 2008). Therefore, our results support previous studies that found that the standard planet formation channel is unlikely to succeed in the γ-Cephei system as it is currently observed.

Alternative formation scenarios have been proposed to explain the increasing number of planets detected in close binary stars (see Schwarz et al. 2016 or Fig. 1 in Marzari & Thebault 2019 for a complete list of systems). Instead of in situ formation, the planets could also have formed inside a circumbinary disk and then be scattered and captured on a circumstellar orbit (Gong & Ji 2018). Additionally, they could have formed in a less hostile environment and end up in a close binary through a variety of different star-star scattering scenarios (e.g., Marzari & Barbieri 2007; Malmberg et al. 2007; Fragione 2019). Nevertheless, there are multi-planet systems observed in close binaries, such as the Kepler-444 system (Lillo-Box et al. 2014) which hosts five small, coplanar planets around the primary star. It is unlikely that they formed via scattering events suggesting that planet formation can indeed succeed in close binaries after all (Dupuy et al. 2016).

Acknowledgments. We would like to thank Alexandros Ziampras for helping to utilize the PLUTO code and for helpful discussions about the disk's thermodynamics. The authors acknowledge support by the High Performance and Cloud Computing Group at the Zentrum für Datenverarbeitung of the University of Tübingen, the state of Baden-Württemberg through bwHPC, and the German Research Foundation (DFG) through grant INST 37/935-1 FUGG. All plots in this paper were made with the Python library matplotlib Hunter (2007).

References

Artymowicz, P., & Lubow, S. H. 1994, ApJ, 421, 651
Bate, M. R., Lubow, S. H., Ogilvie, G. I., & Miller, K. A. 2003, MNRAS, 341, 213
Benedict, G. F., Harrison, T. E., Endl, M., & Torres, G. 2018, RNAAS, 2, 7
de Val-Borro, M., Edgar, R. G., Artymowicz, P., et al. 2006, MNRAS, 370, 529
Dittmann, A., & Ryan, G. 2021, ApJ, submitted [arXiv:2102.05684]
Dupuy, T. J., Kratter, K. M., Kraus, A. L., et al. 2016, ApJ, 817, 80
Dutrey, A., di Folco, E., Guilloteau, S., et al. 2014, Nature, 514, 600
Endl, M., Cochran, W. D., Hatzes, A. P., & Wittenmyer, R. A. 2011, in American Institute of Physics Conference Series, 1331, Planetary Systems Beyond the Main Sequence, eds. S. Schuh, H. Drechsel, & U. Heber, 88
Fragione, G. 2019, MNRAS, 483, 3465
Gong, Y.-X., & Ji, J. 2018, MNRAS, 478, 4565
Goodchild, S., & Ogilvie, G. 2006, MNRAS, 368, 1123
Günther, R., & Kley, W. 2002, A&A, 387, 550
Hatzes, A. P., Cochran, W. D., Endl, M., et al. 2003, ApJ, 599, 1383
Holman, M. J., & Wiegert, P. A. 1999, AJ, 117, 621
Hunter, J. D. 2007, Comput. Sci. Eng., 9, 90
Kaigorodov, P. V., Bisikalo, D. V., Fateeva, A. M., & Sytov, A. Y. 2010, Astron. Rep., 54, 1078
Kley, W., & Nelson, R. P. 2008, A&A, 486, 617
Kley, W., Papaloizou, J. C. B., & Ogilvie, G. I. 2008, A&A, 487, 671
Kuruwita, R. L., Ireland, M., Rizzuto, A., Bento, J., & Federrath, C. 2018, MNRAS, 480, 5099
Lee, W.-K., & Gu, P.-G. 2015, ApJ, 814, 72
Lillo-Box, J., Barrado, D., & Bouy, H. 2014, A&A, 566, A103
Lin, D. N. C., & Papaloizou, J. 1985, in Protostars and Planets II, eds. D. C. Black, & M. S. Matthews, 981
Lubow, S. H. 1991a, ApJ, 381, 259
Lubow, S. H. 1991b, ApJ, 381, 268
Lubow, S. H., & Ogilvie, G. I. 1998, ApJ, 504, 983
Malmberg, D., de Angeli, F., Davies, M. B., et al. 2007, MNRAS, 378, 1207
Martin, R. G., Lissauer, J. J., & Quarles, B. 2020, MNRAS, 496, 2436
Marzari, F., & Barbieri, M. 2007, A&A, 467, 347
Marzari, F., & Thebault, P. 2019, Galaxies, 7, 84
Marzari, F., Scholl, H., Thébault, P., & Baruteau, C. 2009, A&A, 508, 1493
Marzari, F., Baruteau, C., Scholl, H., & Thebault, P. 2012, A&A, 539, A98
Masset, F. 2000, A&AS, 141, 165
Menou, K., & Goodman, J. 2004, ApJ, 606, 520
Mignone, A., Bodo, G., Massaglia, S., et al. 2007, ApJS, 170, 228
Monin, J. L., Clarke, C. J., Prato, L., & McCabe, C. 2007, in Protostars and Planets V, eds. B. Reipurth, D. Jewitt, & K. Keil, 395
Muñoz, D. J., & Lai, D. 2016, ApJ, 827, 43
Müller, T. W. A., & Kley, W. 2012, A&A, 539, A18
Nelson, A. F., & Marzari, F. 2016, ApJ, 827, 93
Oliva, G. A., & Kuiper, R. 2020, A&A, 644, A41
Paardekooper, S. J., & Mellema, G. 2006, A&A, 450, 1203
Paardekooper, S. J., Thébault, P., & Mellema, G. 2008, MNRAS, 386, 973
Pearson, K. J. 2006, MNRAS, 371, 235
Phuong, N. T., Dutrey, A., Diep, P. N., et al. 2020, A&A, 635, A12
Pichardo, B., Sparke, L. S., & Aguilar, L. A. 2005, MNRAS, 359, 521
Picogna, G., & Marzari, F. 2013, A&A, 556, A148
Rafikov, R. R. 2013, ApJ, 765, L8
Rafikov, R. R. 2017, ApJ, 837, 163
Rafikov, R. R., & Silsbee, K. 2015, ApJ, 798, 70
Schwarz, R., Bazso, A., Zechner, R., & Funk, B. 2016, in International Conference on the Astrophysics of Planetary Habitability
Sellek, A. D., Booth, R. A., & Clarke, C. J. 2020, MNRAS, 498, 2845
Shakura, N. I., & Sunyaev, R. A. 1973, A&A, 24, 337
Stone, J. M., & Norman, M. L. 1992, ApJS, 80, 753
Thebault, P., & Haghighipour, N. 2015, Planet Formation in Binaries, 309
Thébault, P., Marzari, F., & Scholl, H. 2006, Icarus, 183, 193
Thébault, P., Marzari, F., & Scholl, H. 2008, MNRAS, 388, 1528
Thun, D., Kley, W., & Picogna, G. 2017, A&A, 604, A102
Trapman, L., Rosotti, G., Bosman, A. D., Hogerheijde, M. R., & van Dishoeck, E. F. 2020, A&A, 640, A5
van Leer, B. 1977, J. Comput. Phys., 23, 276
Whitehurst, R. 1988, MNRAS, 232, 35
Zhu, Z., Dong, R., Stone, J. M., & Rafikov, R. R. 2015, ApJ, 813, 88
Ziampras, A., Ataiee, S., Kley, W., Dullemond, C. P., & Baruteau, C. 2020, A&A, 633, A29
Zsom, A., Sándor, Z., & Dullemond, C. P. 2011, A&A, 527, A10

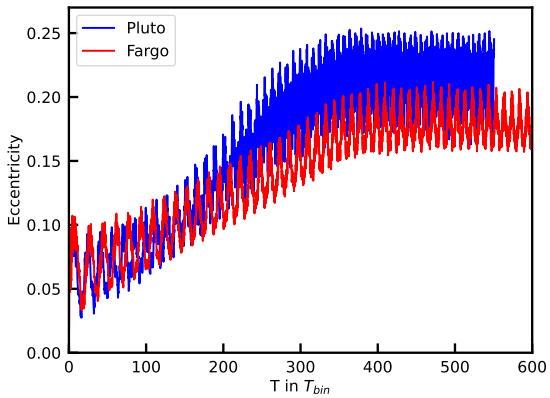

Fig. A.1: Time evolution of the disk eccentricity using the physical setup of the standard model. Displayed are the results of two different codes that differ slightly in their resolution and domain size, see text for details.

Appendix A: Test of different codes

To corroborate and validate our findings, we performed supplementarily simulations for the standard model using two different codes. Our results are presented in Fig. A.1. All simulations use the physical setup of the standard model. The FARGO run uses 760×1160 active cells on a domain ranging from $0.2 - 12$ au. The PLUTO run uses the 648×1160 cells but has its domain size reduced from $0.3 - 10$ au to produce the same cell size as in the FARGO simulation. The inner boundary is larger to reduce computation time, and the outer boundary is smaller for numerical stability. The FARGO simulation utilizes the Fargo method to speed up the simulations while the PLUTO run does not apply the Fargo method and therefore requires approximately ten times more timesteps due to the smaller Δt. The PLUTO code also uses a slightly different definition of the coefficient of the kinematic viscosity of $\nu = \alpha H c_s$, which is a factor $\gamma^{-1/2}$ smaller than in our FARGO code, where γ is the adiabatic index.

For both codes, the disks enter an excited state with comparable eccentricity evolution. The differences between the simulations can be explained primarily by the different numerical methods used in the codes. The PLUTO code utilizes a Riemann-solver-based method that conserves total energy, at least in the hydrodynamic part. In contrast, FARGO uses a second-order upwind scheme that is not energy conserving and utilizes artificial viscosity to stabilize discontinuities. This energy-conserving property makes shock heating more effective and causes the PLUTO simulation to develop a higher disk temperature in the outer regions ($r > 1$ au). Due to the higher temperature, PLUTO produces a faster precessing disk which is in agreement with our predictions. The PLUTO simulation has a steeper eccentricity increase from the inner boundary, which results in an overall higher disk eccentricity. The overall similar dynamical evolution of the disk for the different codes lends strong support to our conclusion that the eccentric disk state is physical.

5 Interaction between circumbinary and circumstellar protoplanetary disks

The results for the circumprimary disk in Jordan et al. (2021) suggest that the conditions required for planet formation to succeed as given by Silsbee & Rafikov (2021), are not met inside the circumprimary disk. The disk eccentricities were too high, and the disk lifetimes too short.

However, the circumprimary disk does not exist in isolation. The secondary star also has a circumstellar disk, and both stars are surrounded by a circumbinary disk. Depending on the physical parameters (Penzlin et al. 2022), the gravitational interaction transfers the angular momentum from the binary to the circumbinary disk. Which leads to reduced mass accretion and longer lifetimes of the disk (Vartanyan et al. 2016).

Observations find that two-thirds of close binary systems lose their disks quickly within $\lessapprox 1$ Myr, while the rest evolves on timescales similar to disks around single stars. The oldest disks (≈ 10 Myr) are found in binary systems such as HD 98800 B and η Cha 9 (Kraus et al. 2012).

As long as the circumbinary disk exists, mass will be accreted on both stars, potentially feeding the circumstellar disks around them. In this chapter, I want to study the circumstellar disks that result from mass accretion from a circumbinary disk. The model of the circumbinary disk is based on the observations of GG Tau A (Keppler et al. 2020), see Fig. 5.0.1. GG Tau A is a 1.5 Myr old hierarchical quintuple consisting of a central binary system with a binary separation of 35 au, where the companion itself is a spectroscopic binary with a separation of less than 5 au (Di Folco et al. 2014). The system also hosts a second binary at a distance of 1500 au (Keppler et al. 2020). The central binary is surrounded by a massive disk of 0.15 $M_\odot$ (which is 10% of the total mass of the stars) and extends from 180 to 850 au. At a distance of 150 pc, the system is close enough to observe gas streams inside the cavity, from which mass accretion rates of $6.4 \cdot 10^{-8}\ M_\odot$/yr onto the binary are estimated (Phuong et al. 2020).

The setup in this chapter is based on the γ-Cephei system, which has been the focus of hydrodynamical simulations (Jordan et al. 2021; Kley & Nelson 2008; Müller & Kley 2012; Paardekooper et al. 2008) since the discovery of a planet (Hatzes et al. 2003) around the primary. While all the gas has been expelled from the system, it has comparable binary parameters to GG Tau A. I will therefore probe whether planet formation in the circumprimary disk of γ-Cephei would be feasible if it did not have a planet but a circumbinary disk similar to GG Tau A instead.

More recent observations of γ-Cephei by Benedict et al. (2018) have shown that the planet around the primary star has a high mass of 9 M_J and a high inclination $i = 70°$ with respect to the plane of the binary. Modeling systems with high inclinations is not possible with the 2D

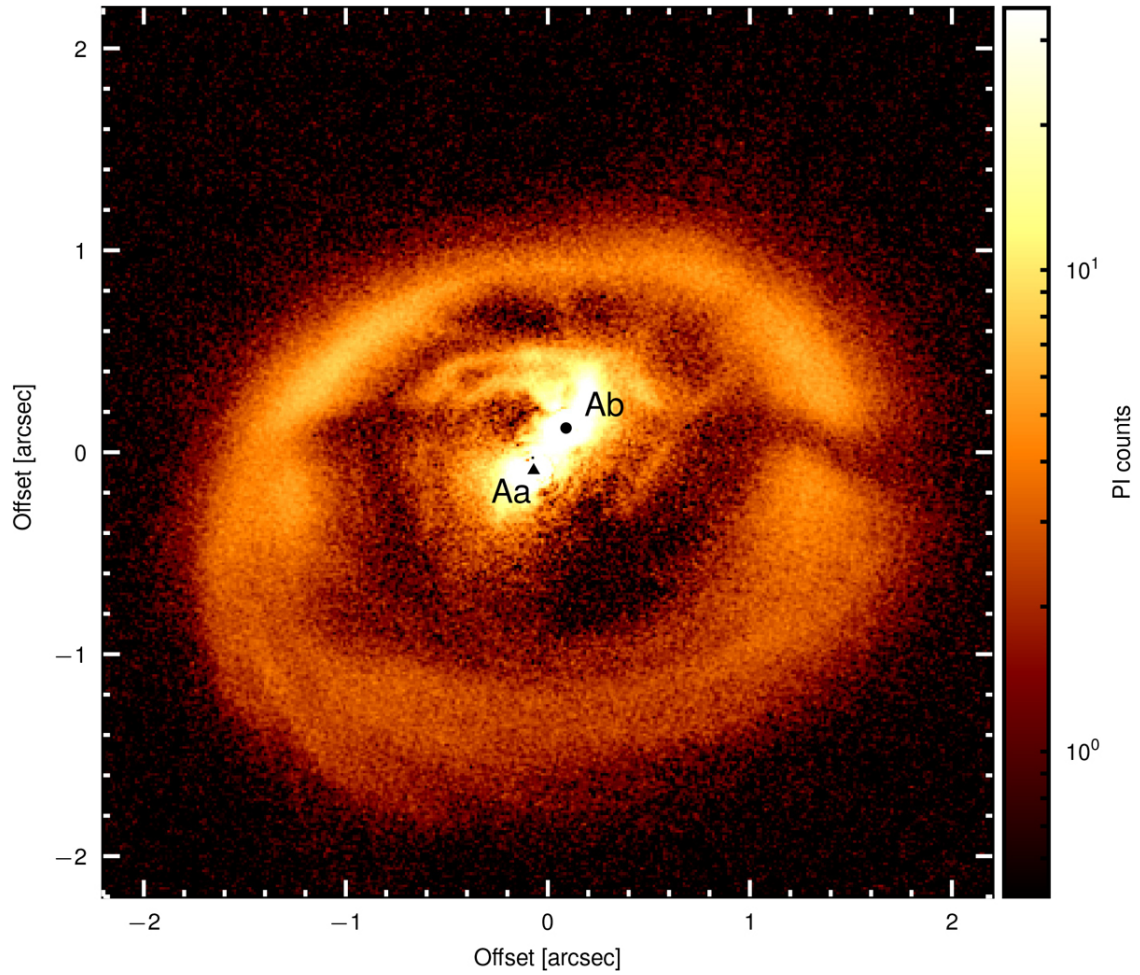

Figure 5.0.1. *Observation of the circumbinary disk of GG Tau A. Image taken from Keppler et al. (2020).*

hydrodynamical code used in this study, instead, 3D SPH codes are used (e.g. Smallwood et al. 2023).

While polar orbits seem to be common for giant planets in close binaries (Behmard et al. 2022), Earth-like planets tend to be coplanar with the binary (Dupuy et al. 2022). Coplanar, multiplanet system configurations, such as in the Kepler-444 system (2016), are seen as a sign of in situ planet formation in such systems. Resonant planetary systems make it unlikely that the planets have formed elsewhere and scattered to their current positions, and the coplanar configuration makes it unlikely that the binary system has moved closer together through gravitational interactions with other stars after the planets had already formed. This study aims to help understand the environments in which these systems form.

In the rest of this chapter, I will present a series of simulations based on the γ-Cephei system with a circumbinary disk that produces a mass accretion rate similar to that observed in GG Tau A. I will then study the circumstellar disks around both stars that are sustained by the mass accretion from the circumbinary disk. An overview of the different simulations is given in Fig. 5.1.1. In Section 5.1 I search for a locally isothermal profile that describes a steady-state accretion disk far from the binary. This profile is then used to create a damping

region in the outer simulation domain (see the blue dashed ring in plot (a) in Fig. 5.1.1), which together with the inflow conditions create an infinite disk.

In Section 5.3 the infinite disk is evolved for a long time until an equilibrium state is reached where the mass accretion through the inner boundary is equal to the mass injection rate through the outer boundary (see plot (b) in Fig. 5.1.1). This equilibrium state is then used to initialize the following simulations.

I then reduce the inner radius so that it fits inside the Roche lobe of the primary star and place sinkholes around both stars, see plot (c) in Fig. 5.1.1. This setup allows me to measure the mass accretion rates to each star, which is done in Section 5.4.

Starting from the same initial conditions, the simulation is repeated in the frame of the secondary star (see plot (d) in Fig. 5.1.1). By comparing the accretion rates between the two simulations, I measure the effects of the non-inertial frame on the mass accretion rates in Section 5.4.

In Section 5.6, I first initialize a disk around the secondary that loses mass at the same rate as the mass accretion rate from the circumbinary disk to the secondary found in the previous section. Then the secondary disk is combined with the circumbinary disk, see plot (e) in Fig. 5.1.1. The setup is then evolved for one precession period of the binary disk, while the secondary disk is monitored and its properties are evaluated afterwards.

In Section 5.7 this process is repeated for the primary star. First the primary disk is initialized, as well as the secondary disk in the frame of the primary, with mass loss rates equal to the mass accretion rates from the circumbinary disk. Then all three disks are combined in one simulation, see plots (f, g) in Fig. 5.1.1, while the properties of the primary disk are monitored and evaluated afterwards. I then summarize the results in Section 5.8, discuss the implications of my results for planet formation in the primary disk in Section 5.9, and give a conclusion and outlook in Section 5.10.

5.1 Finding the steady-state profile of a circumbinary disk

The difference between an infinite and a finite toroidal circumbinary disk was studied in Muñoz et al. (2020). They found that after an initial transient phase, the finite disk entered a pseudo-stationary state that behaved similarly to an infinite disk in a steady state. The only relevant difference they mentioned was the decaying disk mass and mass accretion to the binary. The initial transient phase depends on the chosen initial conditions, which are unknown. Therefore, I create a locally isothermal model that reproduces the equilibrium state of the circumbinary disk far from the binary in our non-isothermal simulation. This profile is then used to simulate an infinite disk that is independent of the initial conditions and interacts with the binary due to the physical properties of the system.

The non-isothermal model uses the standard advection equations together with radiative surface cooling with the opacity table from Lin & Papaloizou (1985), the artificial viscosity by Tscharnuter & Winkler (1979), the stellar irradiation model from Menou & Goodman (2004), and the α viscosity model by Shakura & Sunyaev (1973). How these models are implemented in the simulation is explained in detail in Rometsch et al. (2024), and the isothermal model used in this study is explained in Rometsch et al. (2024), Appendix B.

The binary parameters are based on the γ-Cephei system using the parameters from Endl et al. (2011). The temperatures and radii of the stars were estimated from observed values of young pre-main sequence stars (Pecaut & Mamajek 2013)[1]. The binary parameters are listed in Table 5.1. The initial disk conditions and grid parameters are listed in Table 5.2.

The disk parameters are based on observations of GG Tau A by Keppler et al. (2020) and Phuong et al. (2020), which is a system that can be approximated with parameters comparable to γ-Cephei, which also contains a massive circumbinary disk and stellar disks. Based on the simulations in Keppler et al. (2020), I assume that the gap size is about $3.8\,a_{\mathrm{bin}}$ and initialize the surface density as

$$\Sigma(r) = \Sigma_0 \cdot (r/[a_{\mathrm{bin}}])^{-S} \cdot \frac{1}{1+\exp(3.8\,a_{\mathrm{bin}} - r)/(0.38\,a_{\mathrm{bin}})}, \tag{5.1.1}$$

where Σ_0 is a reference surface density at $r = 1\,a_{\mathrm{bin}}$, r is the radial distance to the center of mass of the binary, and S is the power-law index of the surface density. I assume that our circumbinary disk has a size of $10\,a_{\mathrm{bin}} = 200\,\mathrm{au}$, which is a typical size for a protoplanetary disk (e.g. Ansdell et al. 2018). This means that only the gas within $r < 10\,a_{\mathrm{bin}}$ is considered when calculating the disk mass, even though the disk is as large as the simulation domain with an outer radius of $R_{\mathrm{max}} = 60\,a_{\mathrm{bin}}$.

[1] The stellar parameters were taken from https://www.pas.rochester.edu/~emamajek/EEM_dwarf_UBVIJHK_colors_Teff.txt, which is an updated version of Table 5 from Pecaut & Mamajek (2013)

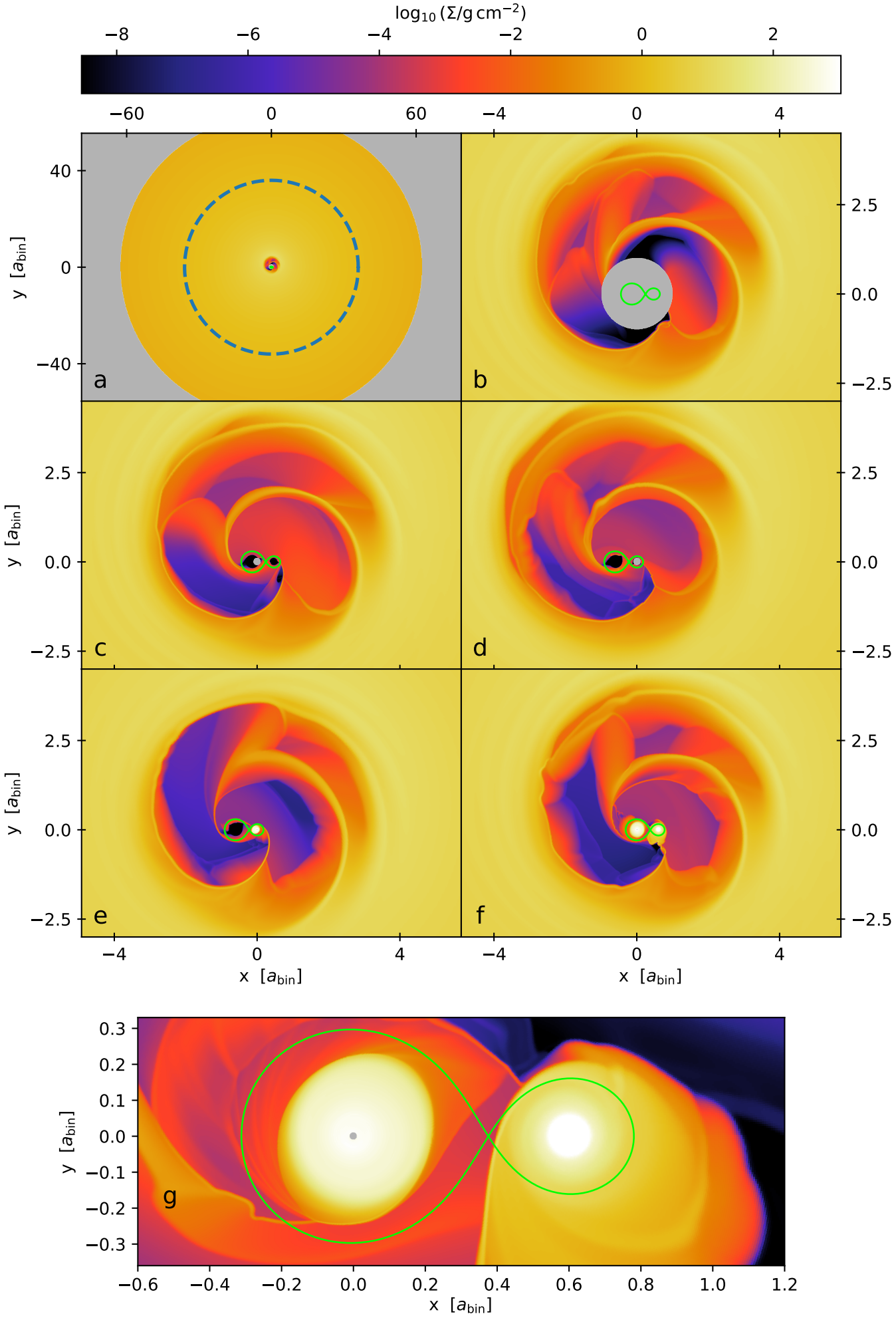

Figure 5.1.1. *Logarithmic surface densities of the different simulations used in the evaluation. See text for details.*

Beyond $r > 15\ a_{\rm bin}$, the effects of the binary are negligible (Muñoz et al. 2019), and the disk can be estimated by the equation for a Keplerian disk around the center of mass. The mass transfer rate through a steady-state accretion disk is given by (Lodato 2008):

$$\dot{M} = -2\pi r \Sigma v_r, \tag{5.1.2}$$

where v_r is the radial velocity of the gas.

Because the density far from the binary is low, the disk becomes passive, meaning that the gas is heated by irradiation from the binary stars and not by viscous heating. For passive disks, the flaring index, which is a measure for the vertical thickness of the disk H, is given by $F = 2/7$ (Chiang & Goldreich 1997). The α viscosity model, together with the condition for steady-state accretion $\dot{M} = \text{const}$, results in a surface density power law index of $S = 2F + 1/2$. At the inner boundary I applied strict outflow conditions, and at the outer boundary the disk is fixed to the initial isothermal profile. I used a high α parameter of 10^{-2} to reduce the simulation time needed to reach an equilibrium state and chose three different disk masses of $M_{\rm CBD} = 0.2\%, 1\%$, and $5\%\ M_\odot$.

The temperatures and surface densities of the non-isothermal disk are initialized from the locally isothermal model whose parameters are listed in Table 5.3. The disk is then evolved for 200 binary orbits. Afterwards, the locally isothermal model is fitted to the azimuthally averaged energy profile from the simulation, yielding an aspect ratio h_0 and a flaring index F. With the fitted temperature profile, the radial velocity was calculated, via the viscosity, which was then used to fit the surface density parameters (Σ_0 and S) using the steady-state accretion condition. Finally, Σ_0 is adjusted to reproduce the desired disk mass. Since I am interested in a steady-state far from the binary, I only used cells between $35 - 50\ a_{\rm bin}$ for the fitting procedure. Using this new locally isothermal model, a new simulation was initialized and evolved for 200 binary orbits. The entire procedure was repeated until the locally isothermal model converged to the temperature profile of the irradiated disk, while simultaneously describing a steady-state accretion disk.

The final parameters are listed in Table 5.3, all parameters except Σ_0 do not change with the disk mass (they have relative differences around 10^{-4}, which I neglect here), confirming that the outer disk is passive.

Table 5.1: *Binary parameters*

	Primary	Secondary
Stellar mass	$1.4\,M_\odot$	$0.4\,M_\odot$
Effective temperature	6670 K	3470 K
Stellar radius	$1.533\,R_\odot$	$0.421\,R_\odot$
Luminosity	$4.17\,L_\odot$	$0.02\,L_\odot$
Semi-major axis	20 au	
Eccentricity	0.4	
Orbital period	66.7 a	

Note: The binary parameters and stellar masses are taken from Endl et al. (2011). The stellar temperature and radius are adopted from Pecaut & Mamajek (2013), who provide a mass-temperature-size relation for young pre-main sequence stars[1].

Table 5.2: *Physical and numerical parameters for initializing the standard disk model.*

Binary disk mass	$0.002\,M_\odot - 0.05\,M_\odot$
Binary disk α	10^{-2}
Adiabatic index	$7/5$
Mean molecular weight m_μ	2.35
Initial density profile	$\propto r^{-1.1}$
Initial aspect ratio	0.05
Initial Flaring index	$2/7$
$R_{min} - R_{max}$	$10 - 60\,a_{bin}$
Grid ($N_r \times N_\varphi$)	339×1160

Table 5.3: *Locally isothermal model parameters of the steady-state profile.*

$M_d\,[M_\odot]$	$2 \cdot 10^{-3}$	$1 \cdot 10^{-2}$	$5 \cdot 10^{-2}$
h_0	0.038	0.038	0.038
F	0.294	0.294	0.294
Σ_0	$6 \cdot 10^{-5}$	$3 \cdot 10^{-4}$	$1.5 \cdot 10^{-3}$
S	1.097	1.097	1.097

Note: h_0, is the reference aspect ratio at $r = 1\ a_{bin}$, F is the flaring index, which together describe the aspect ratio $h = h_0 \cdot (r/1\ a_{bin})$ where r is the distance to the center of mass. And Σ_0 is the reference surface density and S is the density slope: $\Sigma = \Sigma_0 \cdot (r/a_{bin})^{-S}$.

5.2 Boundary conditions

In later simulations, the simulation is centered on one of the stars. This causes the circumbinary disk in the system to be in a non-inertial frame and to be rocked around. Unless the indirect term is treated with very high precision, which it is not, it would prevent a steady flow from forming at the outer boundary.

[1]The stellar parameters were taken from https://www.pas.rochester.edu/~emamajek/EEM_dwarf_UBVIJHK_colors_Teff.txt, which is an updated version of the Table 5 from Pecaut & Mamajek (2013)

To try to achieve a steady flow at the outer boundary, I use a damping region from $0.6R_{\mathrm{max}}$ to R_{max} (see the blue dashed ring in plot (a) in Fig. 5.1.1), where the energy and velocities are relaxed to the initial profile from the previous section. How the velocities are calculated is described in Appendix B.4 and the energy is given by:

$$e(r) = \frac{1}{\gamma - 1} \cdot \Sigma c_{s,\mathrm{iso}}^2 \,, \tag{5.2.1}$$

where $c_{s,\mathrm{iso}}$ is the isothermal sound speed as defined in Appendix B.1.

The relaxation method is taken from de Val-Borro et al. (2006):

$$\frac{\mathrm{d}X}{\mathrm{d}t} = -\frac{X - X_{\mathrm{theo}}(r)}{\tau} f(r) \,, \tag{5.2.2}$$

where τ is the damping timescale, which is set to one tenth of the orbital period at the outer boundary, and $f(r)$ is a quadratic function that goes from 0 to 1 from the start of the damping zone to the outer boundary, see Rometsch et al. (2024), Sect. 3.14.5 for details. I do not damp the surface density so that the mass entering the domain is fully controlled by the inflow conditions set in the outer ghost cells. Note that the initial profile is always defined over the distance to the center of mass, which is not located at the coordinate center when the simulation is centered on one of the stars.

At the inner boundary, we use an outflow boundary condition if the inner radius of the domain contains both stars of the binary. If the grid is centered on one of the stars, we use viscous outflow conditions

$$v_r(R_{\mathrm{min}}) = -b\frac{3\nu}{2R_{\mathrm{min}}} \,,$$

where we choose $b = 5$, following Pierens & Nelson (2008).

5.3 Equilibrium state of a circumbinary disk

In this section, I establish the circumbinary disk around both stars. To achieve this, the inner radius is reduced to 1 a_{bin} and the number of radial cells is increased from 339 to 764 such that the cell sizes are the same as before. The parameters for the outer regions are set to the locally isothermal model described in Table 5.1, Table 5.2, and Table 5.3. An inner radius of 1 a_{bin} was found to be sufficiently small and the chosen grid resolution appropriate for simulating the gap and density ring around the binary in Thun et al. (2017) and Penzlin et al. (2022).

The simulations were then evolved for 60,000 binary orbits to reach an equilibrium state where the time-averaged accretion through the inner boundary is equal to the constant mass injection through the outer boundary. To speed up the convergence process, I stopped the simulations several times and rescaled the gas densities based on the difference between the mass flow through the cells inside the domain and the mass flow of the cells at the outer boundary before restarting them.

Fig. 5.3.1 shows the azimuthally averaged radial surface density profiles after the disk has reached an equilibrium state. The solid blue line represents the density profile when the longitude of periastron of the eccentric gap is aligned with the pericenter of the binary (which is located on the positive x-axis, cf. the second panel in Fig. 5.3.1). The longitude of periastron is determined by the location of the cell outside the gap that has the highest density. The method is described in Thun et al. (2017), Sect. 5.1. For this disk orientation, the mass accretion rate on the binary is highest. The dashed blue line presents the azimuthally averaged radial mass accretion rate averaged over 100 binary orbits leading up to the snapshot time and normalized by the mass injection rate at the outer boundary.

The mass accretion is equal to the mass injection rate at radii greater than 20 $a_{\rm bin}$, indicating that the simulation is in a steady state. On the other hand, the density profile is 20% below the theoretical model. This is mainly caused by the theoretical model neglecting the effects of gravitational smoothing, which are included in the simulation, as explained in Appendix B.4, and the fact that the boundary condition is prescribed using primitive variables while characteristic variables are needed to correctly describe the flow into the domain (Godon 1996). Due to the long viscous timescales in the circumbinary disk, these deviations from the initial theoretical profile are the reason for the initialization times required to reach a steady state.

The orange lines present the same information but at a time when the disk is anti-aligned with the binary, such that the secondary moves closest to the density ring during the apocenter passage of the binary. Despite the secondary moving towards the density ring, the mass accretion rate is lower than in the aligned case.

The structure of the circumbinary disk has been studied many times before (e.g. Miranda et al. 2017; Penzlin et al. 2024; Sytov et al. 2011; Thun et al. 2017). I refer to these studies for an analysis of the structure of the circumbinary disk and cavity. In this study, the circumbinary disk is used only as a boundary condition that feeds the circumstellar disks.

The accretion rate over time is shown in Fig. 5.3.2 as the faded orange region, the accretion rate smoothed over one precession period (1700 $T_{\rm bin}$) as the orange line. When averaged over three precession periods (faded green region), the averaged accretion rate (orange dashed line) is equal to the mass injection at the outer boundary (black line), with a relative deviation of less than one promille, demonstrating that the disk is in equilibrium. The longitude of periastron of the gap is shown as blue dots. It again highlights the relation between mass accretion and the orientation of the disk (remember that $\omega = 0$ means that the disk is aligned with the binary and $\omega = \pm\pi$ anti-aligned) as already described above in relation to Fig. 5.3.1. These results are also in agreement with Muñoz & Lai (2016); Penzlin et al. (2024).

In Penzlin et al. (2022) it was shown that although the accretion to the binary is very different from the accretion to single stars, the accretion from the circumbinary is still driven by viscosity and follows the same scaling laws as in single star disks. This means that the results here can be extrapolated to different disk parameters such as disk mass, temperature, and the α viscosity parameter.

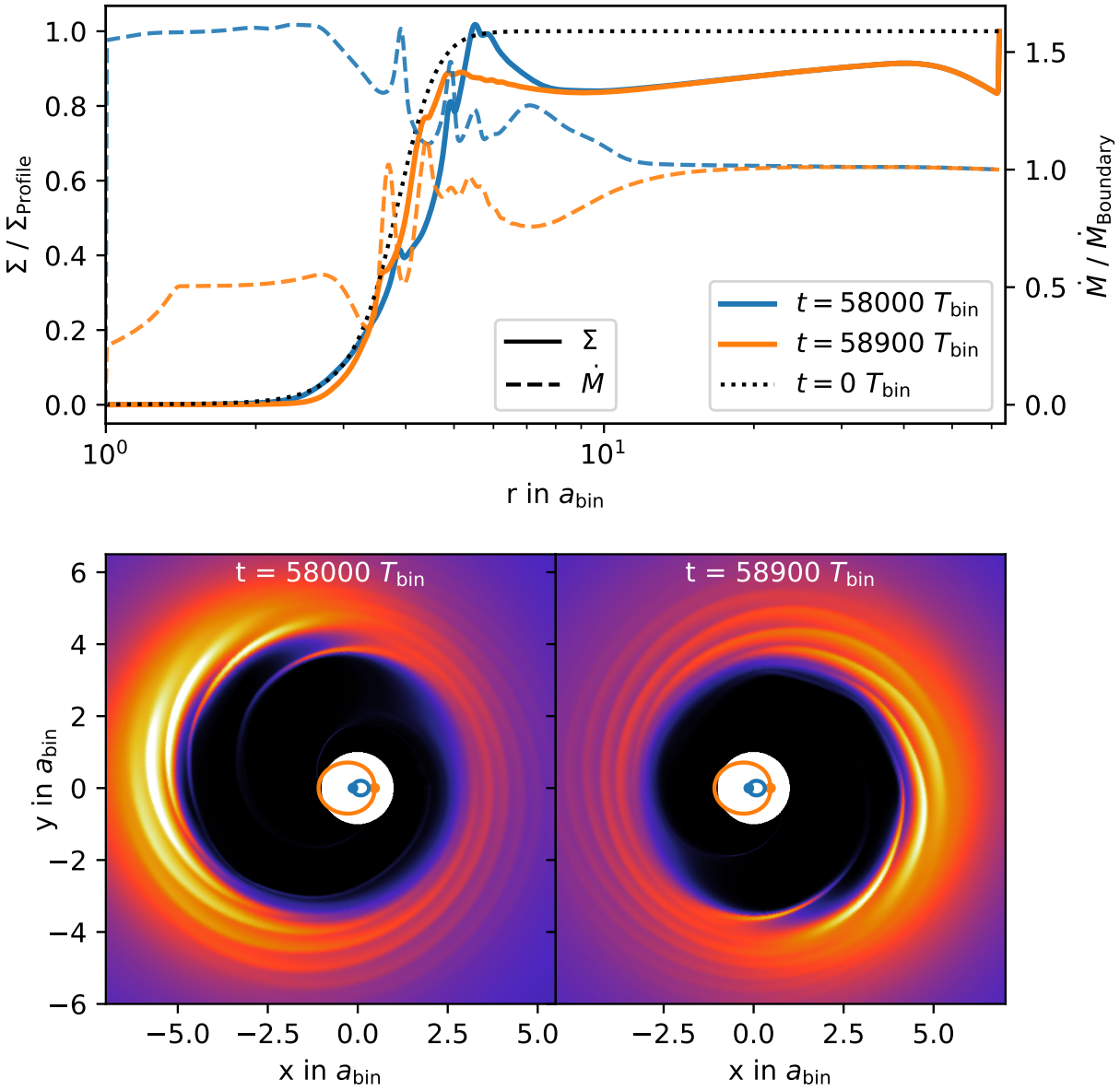

Figure 5.3.1. *Top: Normalized azimuthally averaged radial surface density profiles at different times (solid lines) and the initial surface density profile (black dotted line). The densities are normalized to the initial density profile without cutoff ($\Sigma_0 \cdot r^{-S}$). The dashed lines show the radial profiles of the azimuthally averaged mass accretion rates and are normalized to the inflow rate from the outer boundary.*
Bottom: The two-dimensional surface densities simultaneously with the radial density profiles shown above. The orange line depicts the orbit of the secondary and the blue line the orbit of the primary. The binary is at periastron (closest approach of the stars) at the time of the snapshot.

Table 5.4: *Steady-state disk parameters*

$M_{\mathrm{CBD,init}}(r < 10\ a_{\mathrm{bin}})\ [M_\odot]$	$2 \cdot 10^{-3}$	$1 \cdot 10^{-2}$	$5 \cdot 10^{-2}$
$M_{CBD}(r < 10\ a_{\mathrm{bin}})\ [M_\odot]$	$2.9 \cdot 10^{-3}$	$1.5 \cdot 10^{-2}$	$8 \cdot 10^{-2}$
$M_{CBD}(r < 15\ a_{\mathrm{bin}})\ [M_\odot]$	$5.2 \cdot 10^{-3}$	$2.6 \cdot 10^{-2}$	$13.9 \cdot 10^{-2}$
$M_{CBD}(r < 20\ a_{\mathrm{bin}})\ [M_\odot]$	$7.4 \cdot 10^{-3}$	$3.7 \cdot 10^{-2}$	$19.7 \cdot 10^{-2}$
$\dot{M}\ [M_\odot/yr]$	$1.57 \cdot 10^{-9}$	$7.83 \cdot 10^{-9}$	$3.92 \cdot 10^{-8}$
$P_{\mathrm{prec}}[T_{\mathrm{bin}}]$	1750	1692	1580

The initial model did not consider the density ring around the binary, therefore, the disk mass in the final state will be higher than the initial disk mass. The simulation results are summarized in Table 5.4. Three different disk masses are given, depending on the assumed disk size. The mass accretion rates scale linearly with disk mass, as expected for a passive disk. Note that a finite, torus-shaped disk would produce similar mass accretion rates at significantly lower total disk mass, see Muñoz et al. (2020). Therefore, the mass measured within 10 a_{bin} of an infinite disk could be representative of a finite disk of size 20 a_{bin} or even larger.

The accretion rate in the high-mass case (where the accretion rate is equal to the mass supply rate of the 5% $M_\odot$ circumbinary disk) has an average accretion rate of $\dot{M} = 3.92 \cdot 10^{-8}\ M_\odot/\mathrm{yr}$, which, given the variability of the accretion rate, is consistent with the observed accretion rates of GG Tau A, which range from $\dot{M} = 2 \cdot 10^{-8}\ M_\odot/\mathrm{yr}$ (Hartigan & Kenyon 2003) to $\dot{M} = 6.4 \cdot 10^{-8}\ M_\odot/\mathrm{yr}$ (Phuong et al. 2020). It also matches the average accretion rate of $\dot{M} = 3 \cdot 10^{-8}\ M_\odot/\mathrm{yr}$ found by Keppler et al. (2020) in their modeling of the system.

I analyzed the gravitational stability of the disk using the Toomre parameter Q (Toomre 1964). I found $Q > 10$ for the two lower disk masses and $Q = 2 - 4$ for the highest disk mass. For $Q \lessapprox 5$, self-gravity starts to affect the dynamics inside the disk, while for $Q > 5$ self-gravity is negligible (Lines et al. 2015). Despite self-gravity being relevant in our highest disk mass case, I simulate neither self-gravity nor gravitational feedback from the disk onto the stars in this study. If self-gravity were included, it would mainly affect the outer regions of the disk where Q is lower. For $Q > 1$, self-gravity does not fragment the disk, but rather causes local angular momentum transport, which can be treated with the α viscosity prescription used in this study (Béthune et al. 2021; Lodato & Rice 2004), providing a possible explanation for the large α parameter I used for the circumbinary disk.

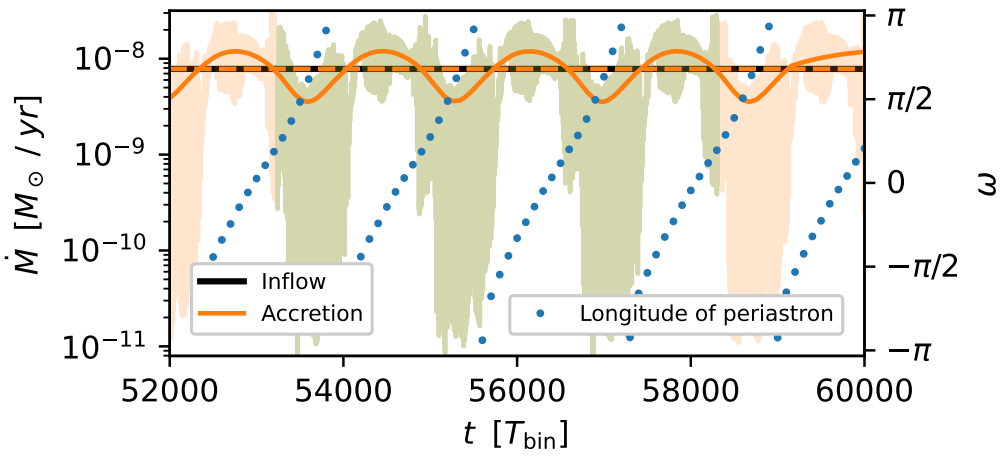

Figure 5.3.2. *Accretion rate through the inner boundary (faded orange region) compared to the mass injection rate at the outer boundary (black line) and the longitude of periastron of the eccentric gap (blue dots) in the $M_d = 1\%M_\odot$ case. Also shown is the accretion rate smoothed over one precession period (orange line), which lasts for 1700 $T_{\rm bin}$ and the average accretion rate (dashed orange line) that was averaged over three precession periods (faded green region). The longitude of periastron is determined from the position of the maximum density in the density ring (cf. the lower panel in Fig. 5.3.1).*

5.4 Stellar accretion rates

In this section, the steady state from the previous section is restarted with a smaller inner radius of $R_{\rm min} = 0.1\ a_{\rm bin}$ (and 1189 radial cells), see plot (c) in Fig. 5.1.1. This way, the inner radius is located within the Roche lobe of the primary, and any mass leaving through the inner boundary can be considered as accretion onto the primary. Additionally, both stars were treated as sinkholes with a size of $R_{\rm Sink} = 0.4\ R_{\rm L}$, where $R_{\rm L}$ is the radius of the Roche lobe, calculated using the formula by Eggleton (1983). During periastron, a sinkhole size of $0.4\ R_{\rm L}$ is equal to $R_{\rm sink} = 3.75\ au$ for the primary and $R_{\rm sink} = 2.25\ au$ for the secondary. These sizes are roughly equal to the disk sizes of the stellar disks I found in previous test runs. Unlike the stellar disks, the sinkhole sizes increase with binary separation, and are a factor of 2.33 larger during apastron.

Cells inside the sinkhole lose a fraction of their mass each time step, with a half emptying time of $10^{-4}\ T_{\rm bin}$, which effectively removes all mass from the cell instantaneously. The accretion mechanism is explained in Rometsch et al. (2024), Sect. 3.13. The mass accretion was only measured, the masses of the stars themselves are kept fixed at the initial value.

The top panel in Fig. 5.4.1 shows the sum of the mass accretion rate onto both stars measured in the simulation with the small inner radius and stellar sinkholes, and compares it to the mass accretion rate onto the binary system through from the previous simulation with the large inner hole. After changing the accretion from a large inner radius (blue lines) that contains both stars to sinkholes around the individual star (orange lines), the mass accretion rate was reduced by 18%. This means that not all mass that the stars pull from the outer gap

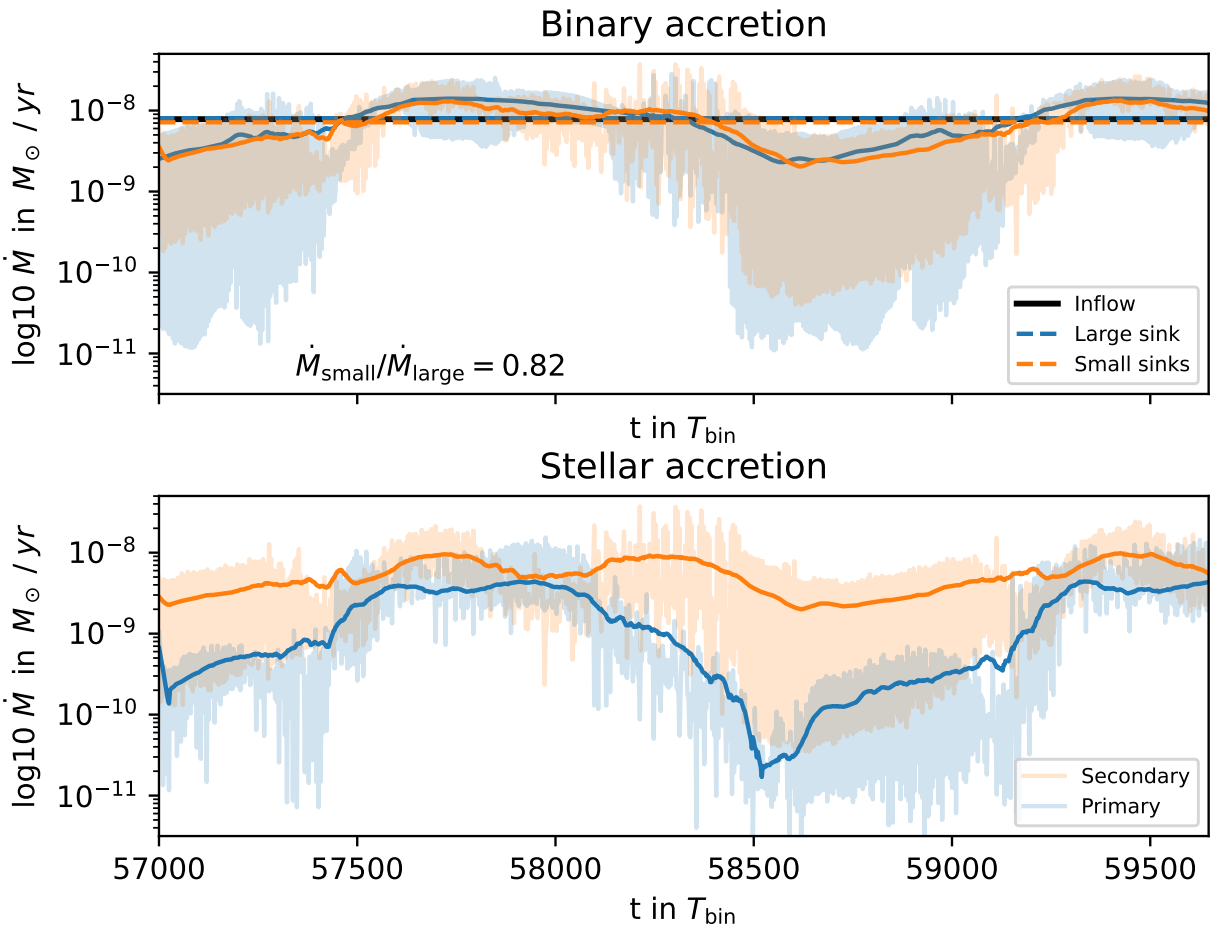

Figure 5.4.1. *Top: Binary accretion over time for the $M_d = 1\%M_\odot$ case, similar to Fig. 5.3.2. Shaded regions present the current accretion rate, the dashed line the accretion rate smoothed over 200 binary orbits, and the dashed line the average accretion rate over a time frame equal to the length of the simulation with the small inner domain radius. The dashed black line is the mass injection rate at the outer boundary.*
Bottom: Sinkhole mass accretion rates on the primary (blue) and secondary (orange) stars measured from the simulation with the small inner radius.

edge is accreted. The mass that is now additionally left over is flung out again and interacts with the circumbinary disk (CBD) at the outer edge of the gap or lingers inside the gap.

Generally, I find more mass inside the gap for smaller inner radii (compare plot (b) in Fig. 5.1.1 with any of (c, d, e, f)), leading to higher minimum accretion rates (compare the shaded regions in Fig. 5.4.1). Based on the study on the impact of inner disk radii on the density ring profile in Thun et al. (2017), Fig. 5 and Penzlin et al. (2022), Fig. 8, I do not expect the additional mass in the outgoing streamers to have a significant impact on the density ring profile. Apart from the lower accretion rate and higher lows in the accretion rate, the simulation with the small inner radius displays the same behavior as the previous simulation.

Due to the smaller inner radius, the accretion rate on the individual stars can be measured, as demonstrated in the lower panel in Fig. 5.4.1. In the low accretion phases, both stars have an accretion minimum. While in the high accretion phase, first the accretion rate of the secondary peaks and then retracts while the primary accretion rate peaks (see lower panel in

Fig. 5.4.1 at $\approx T = 58000\ T_{\rm bin}$). The secondary accretion rate then has another high accretion phase before a low accretion rate begins for both stars.

Overall, the accretion rate on the secondary is visible higher than on the primary. Averaged over the whole simulation duration of 2640 binary orbits, the secondary receives 76% of the total mass accreted by the binary system. Considering that the binary mass ratio in this study is $q = 0.29$, this is in good agreement with several other studies that measured the mass accretion ratio, see Lai & Muñoz (2023), Fig. 11 for a collection of these studies.

5.4.1 Accretion rates in the secondary center

In this section, the same simulation setup as in the previous section is used and started from the same initial conditions, but the grid is now centered on the secondary star. To make the simulation stable in the secondary center, modifications to the code were necessary which are described in detail in Appendix A.

In the previous sections, the grid was always expanded by adding new cells. Here, the positions of the cells change. Therefore, the data from the steady-state simulation from Section 5.3 had to be first interpolated to the new grid.

This was done by converting the positions of the cells and their velocities from polar to Cartesian coordinates. In Cartesian coordinates, to shift the gas cells from the center of mass to the secondary center, one has to simply subtract the position and velocity of the secondary. Afterward, the data was interpolated to the new cell positions using the linear interpolation function *griddata* from *Numpy* and then transformed back to polar coordinates. Higher order interpolation functions tend to overshoot the values and were found to produce negative densities at the gap edges due to the strong gradients in density there.

The resulting mass accretion rates (labeled: Sec.) are compared to the mass accretion rates measured in the center of mass frame (CMS) in Fig. 5.4.2. Note that the time is now measured from the point at which the simulations were restarted from. Together, both stars accrete 16% less mass in the secondary frame. Since the mass accretion is lower over the whole simulation and there is no noticeable jump at the start of the simulation, I conclude that the indirect term in the secondary center is causing the difference and not inaccuracies in the interpolation. Also, the precession behavior changed slightly after the switch to the secondary center, as seen by the earlier transition to a low accretion phase around $t = 1500\ T_{\rm bin}$. Overall, the evolution of the accretion rates is still similar to the CMS simulation.

The reductions in mass accretion rates by reducing the inner radius and again by switching to the secondary center amounts to 34% in total. As mentioned in Section 5.3, the mass accretion rate scales linearly with surface density and disk mass. Coincidentally, while initializing the first simulation, the density ring was neglected, leading to a 50% higher mass inside $10\ a_{\rm bin}$ than intended which would roughly cancel out the reduced mass accretion rates. The current mass accretion rates can therefore also be interpreted as the mass accretion rates caused by a circumbinary disk with the initially intended disk masses. The resulting mass accretion rates are summarized in Table 5.5.

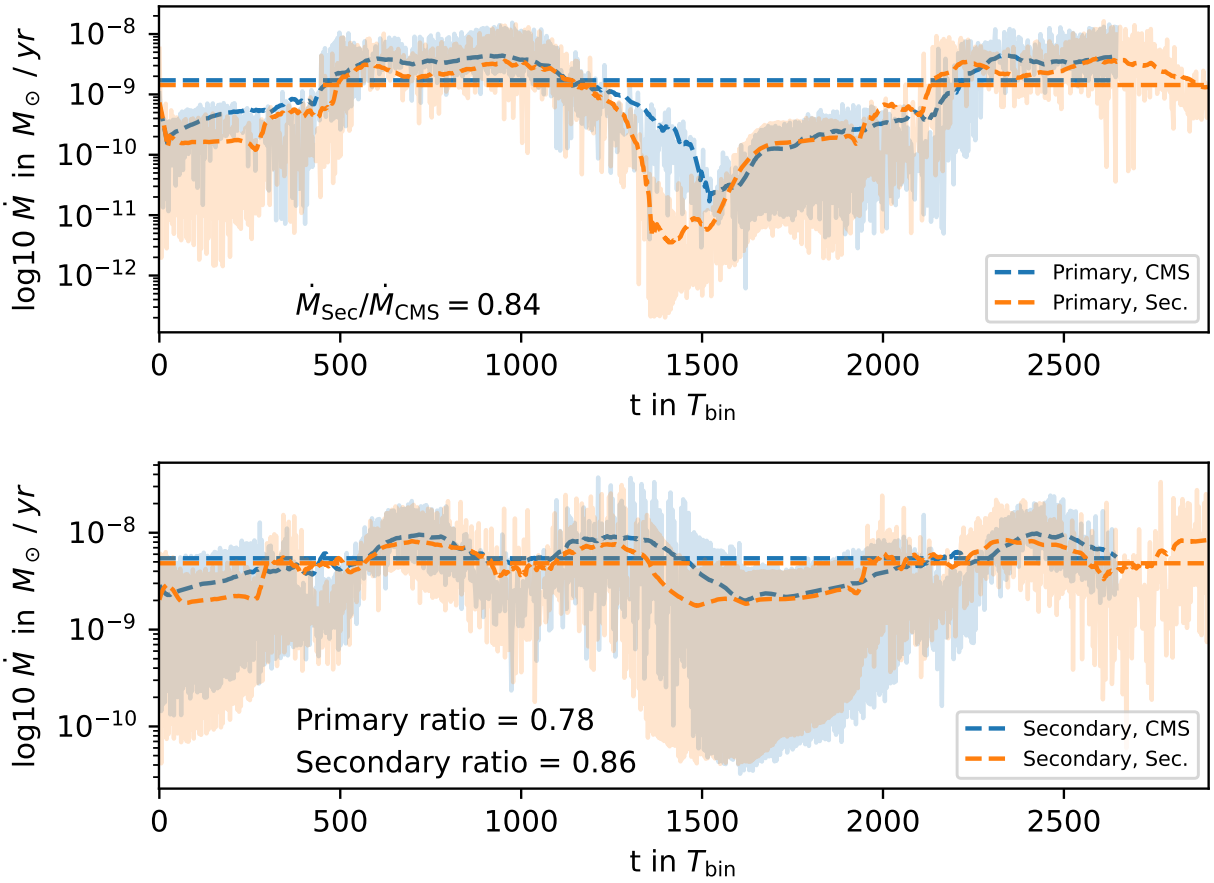

Figure 5.4.2. *Stellar accretion rates over time for the $M_d = 1\% M_\odot$ case for the center of mass frame (*CMS*, blue color) and secondary frame (*Sec.*, orange color). Dash lines represent the mass accretion rates smoothed over 200 binary orbits.*
Top: Primary accretion rates. Bottom: Secondary accretion rates.

Table 5.5: *Mass accretion rates measured in the secondary center.*

$M_{d,\text{init}}(r < 10\, a_{\text{bin}})\ [M_\odot]$	$2 \cdot 10^{-3}$	$1 \cdot 10^{-2}$	$5 \cdot 10^{-2}$
$\dot{M}_{\text{Primary}}\ [M_\odot/yr]$	$2.40 \cdot 10^{-10}$	$1.33 \cdot 10^{-9}$	$7.39 \cdot 10^{-9}$
$\dot{M}_{\text{Secondary}}\ [M_\odot/yr]$	$9.18 \cdot 10^{-10}$	$4.70 \cdot 10^{-9}$	$2.53 \cdot 10^{-8}$

5.5 Secondary disk initialization

Having determined the mass accretion on the secondary, I can now search for a secondary disk mass that will lose the same amount of mass as supplied to the secondary from the circumbinary disk. This is done to speed up the initialization process when combining the simulations with the stellar disks and the circumbinary disk. A snapshot of a disk around the secondary is presented in Fig. 5.5.1. The disk was initialized with a mass of $5.6 \cdot 10^{-4}\ M_\odot$ and evolved for 200 binary orbits. The disk mass was kept constant by scaling up the surface density in every cell after each time step with the ratio of initial disk mass over the current disk mass. The binary parameters were the same as in the previous simulations, see Table 5.1. For the simulations of the stellar disks, the grid resolution was lowered, the domain size was

Table 5.6: *Physical and numerical parameters for initializing the secondary disks.*

Secondary disk mass ($M_{\mathrm{CBD}} = 1\%, 5\%\ M_{\odot}$)	$5.6 \cdot 10^{-4}\ \mathrm{M}_{\odot}$
Secondary disk mass ($M_{\mathrm{CBD}} = 0.2\%\ M_{\odot}$)	$2.4 \cdot 10^{-4}\ \mathrm{M}_{\odot}$
Stellar disk α	10^{-3}
Adiabatic index	$7/5$
Mean molecular weight m_{μ}	2.35
Initial density profile	$\propto r^{-1}$
Initial aspect ratio	0.04
Initial Flaring index	0
$\mathrm{R_{min}} - \mathrm{R_{max}}$	$0.01\ -\ 0.6\ \mathrm{a_{bin}}$
Grid ($\mathrm{N_r} \times \mathrm{N_{\varphi}}$)	580×872

adjusted, and the α parameter was reduced to 10^{-3}, the full parameters are listed in Table 5.6. Additionally, the disk has been truncated outwards according to:

$$\Sigma(r) = \Sigma_0 \cdot (r/[a_{\mathrm{bin}}])^{-S} \cdot \frac{1}{1 + \exp(r - 0.15\ a_{\mathrm{bin}})/(0.015\ a_{\mathrm{bin}})}\ . \tag{5.5.1}$$

The resulting disk eccentricity, longitude of periastron, and mass loss rates are shown in Fig. 5.5.2. The disk behavior changes dramatically during the simulation. This is caused by the initial density profile being too spread out. During the simulation, the disk becomes smaller and denser as seen in the density profiles in Fig. 5.5.1. This restructuring leads to slightly higher aspect ratios h in the inner part of the disk ($0.025 - 0.06\ a_{\mathrm{bin}}$) and lower values in the outer part of the disk ($0.06 - 0.12\ a_{\mathrm{bin}}$). The aspect ratio is a measure for the pressure forces in the disk, and higher pressure forces are expected to drive retrograde precession (Goodchild & Ogilvie 2006).

This initially prograde precession with low eccentricity slows down and the amplitude of the eccentricity oscillation increases. At $t = 100\ T_{\mathrm{bin}}$, the precession rate becomes zero, leading to continuous eccentricity growth and the disk enters a high eccentricity state with a fast retrograde precession, see bottom panel in Fig. 5.5.2. The mass loss rates also depend on the eccentricity of the disk. In the low eccentricity state, the mass ejected from the disk (measured at the outer boundary) is negligible and the accretion onto the star (measured at the inner boundary) is low. In the high eccentricity state, the disk is even more compact, see purple lines ($t = 147$) and the bottom panels in Fig. 5.5.1, leading to a high accretion rate on the star. Additionally, every time the eccentric bulge of the disk is aligned with the pericenter of the binary, the disk overflows the Roche lobe of the secondary (see lower right panel in Fig. 5.5.1). Whether the mass leaving through the outer boundary is accreted onto the primary or ejected towards the circumbinary disk is estimated in Section 5.5. In the high eccentricity state, 11.5% of the mass is lost at the outer boundary compared to $7 \cdot 10^{-4}$ % in the low eccentricity state.

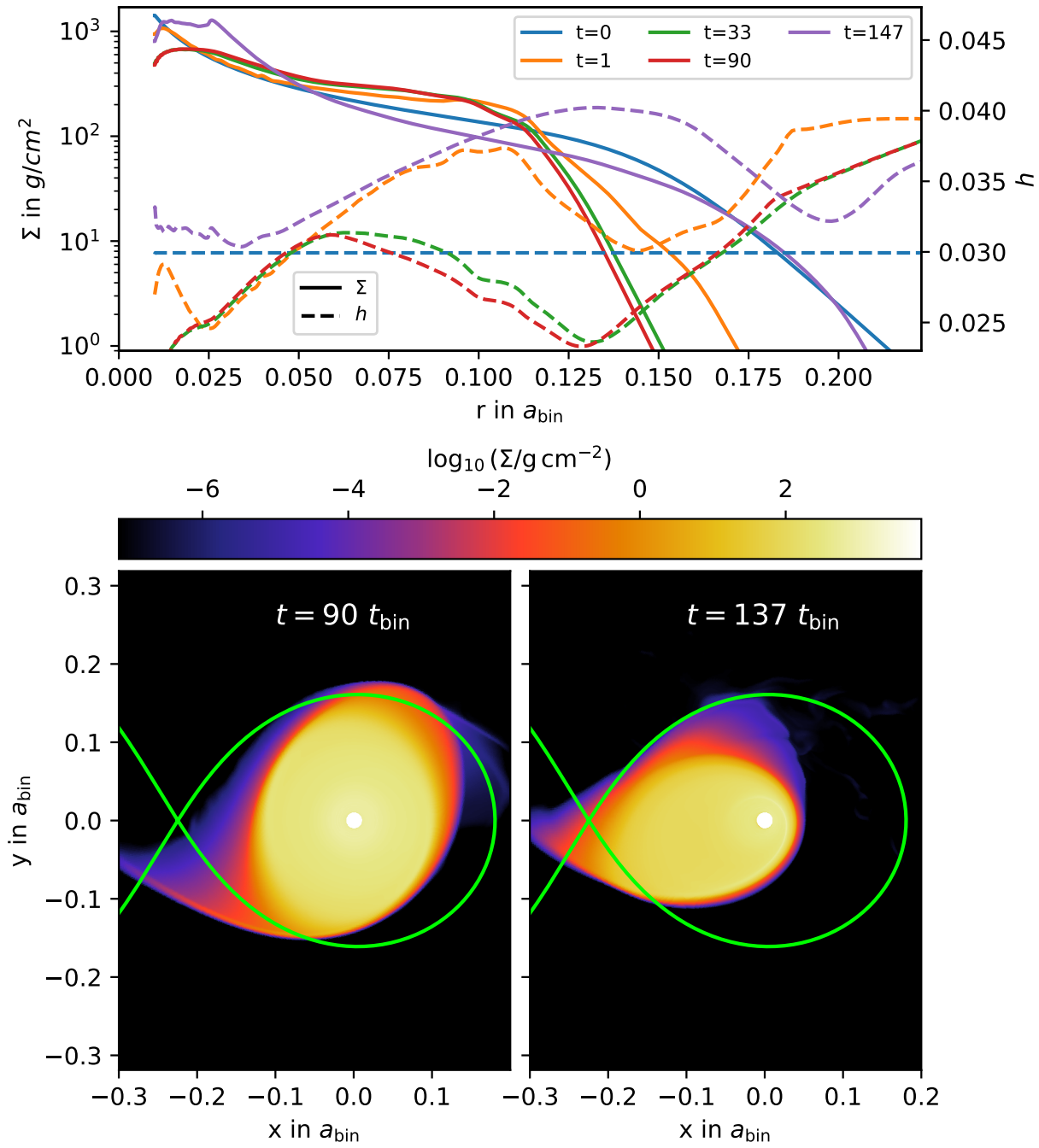

Figure 5.5.1. *Top: Radial azimuthally averaged surface density profiles (solid lines) and mass-weighted radial aspect ratio profiles (dashed lines) at different simulation times given in $T_{\rm bin}$. Bottom: Two-dimensional surface density profiles at the time marked by the black dashed line in Fig. 5.5.2.*

The mass loss rates at $t = 50, 200\, T_{\rm bin}$ are comparable to the mass accretion rates measured in Table 5.5. Therefore, snapshots at these times were used to combine the secondary disk simulations with the circumbinary disk simulation models of $M_d = 1\%, 5\%\ M_\odot$. For the $M_d = 0.2\%\ M_\odot$ case, a lower mass secondary disk simulation was used that did not enter a high eccentricity state and is not shown here. The combined simulations are presented in the next section.

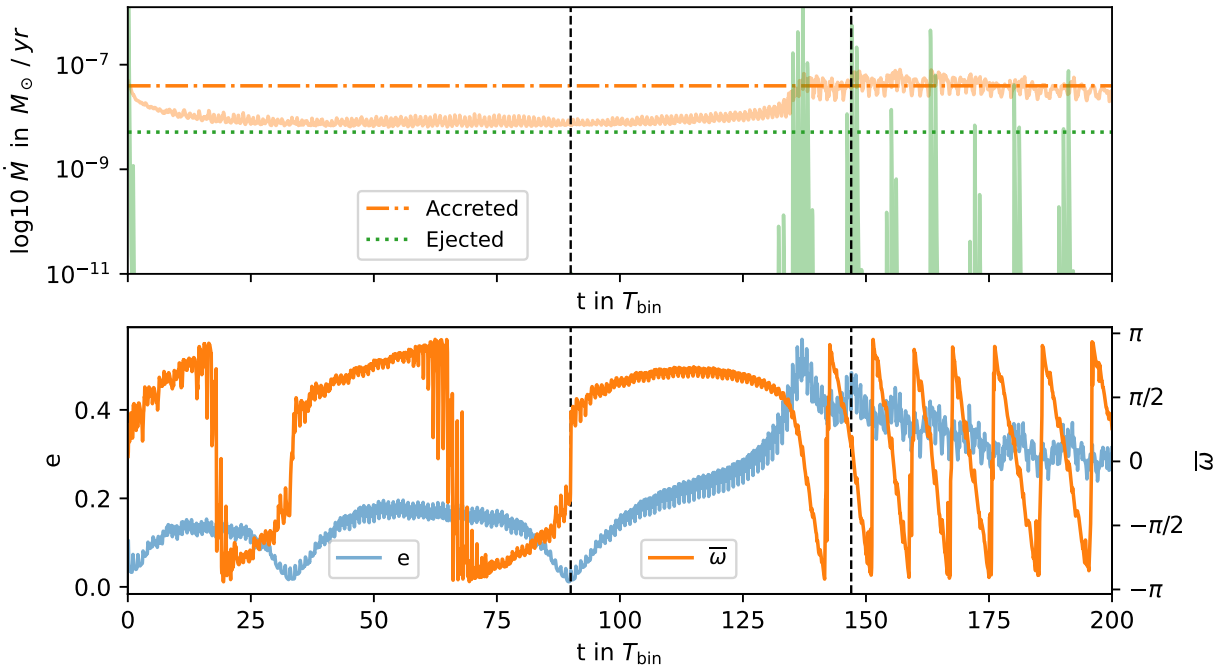

Figure 5.5.2. *Top: Mass loss rates of the secondary disk. The green line represents the mass loss rate measured at the outer boundary and the orange line the mass loss rate at the inner boundary. The vertical dashed lines present the average values over the last 70 binary orbits, starting at* $T_{\text{bin}} = 130$ *where the disk enters the high eccentricity state.*
Bottom: Eccentricity (blue line) and longitude of periastron (orange line) of the secondary disk. The black dashed lines mark the snapshots for the 2D surface density profiles in the bottom panels of Fig. 5.5.1.

5.6 Secondary and circumbinary disk combined

In this section, the simulation from Section 5.4 was extended inwards to 0.01 a_{bin} (and N_r increased to $N_r \times N_\varphi = 1609 \times 1160$) and the inner regions were initialized with the secondary disk from Section 5.5.

The α parameter was linearly interpolated inside the gap region from the value in the circumbinary disk (CBD) to the value in the stellar disks by using the distance (d) to the nearest star:

$$x_i = \frac{d_i - 0.35\ a_{\text{bin}}}{0.55\ a_{\text{bin}} - 0.35\ a_{\text{bin}}}\ , \tag{5.6.1}$$

$$y_i = \max(0, \min(1, x_i))\ , \tag{5.6.2}$$

$$\alpha_i = \alpha_{\text{Star}} + (\alpha_{\text{CBD}} - \alpha_{\text{Star}}) \cdot y_i\ , \tag{5.6.3}$$

$$\alpha = \min(\alpha_1, \alpha_2)\ , \tag{5.6.4}$$

where $\alpha_{\text{CBD}} = 10^{-2}$ and $\alpha_{\text{Star}} = 10^{-3}$. The distance at which the transition is completed, 0.35 a_{bin}, is equal to the maximal extent of the stellar disks found in previous simulations. The distance at which the transition starts, 0.55 a_{bin}, is well within the gap size found in Section 5.3. Therefore, all disks are simulated with a constant α parameter. The simulation parameters are summarized in Table 5.7.

Table 5.7: *Physical and numerical parameters for the global simulations with stellar disks and circumbinary disk.*

Circumbinary disk α	10^{-2}
Stellar disk α	10^{-3}
Adiabatic index	$7/5$
Mean molecular weight m_μ	2.35
$R_{min} - R_{max}$	$0.01 - 60\, a_{bin}$
Grid ($N_r \times N_\varphi$)	1609×1160

Note: The α parameter was interpolated from the circumbinary disk to the stellar disks according to Equations (5.6.1) to (5.6.4). The outer domain (36 to 60 a_{bin}) was damped to the locally isothermal profiles described in Table 5.3.

The resulting mass accretion rates are presented for the high-mass case ($m_{CBD} = 5\%\ M_\odot$) in Fig. 5.6.1 and compared to the accretion rates from the simulation with sinkholes around both stars (Section 5.4). The second panel highlights that the disk acts as a reservoir for mass accretion. With a disk, the accretion is more steady on the orbital timescale. Averaged over the whole simulation, 25% less mass is accreted onto the secondary (1.98 vs $2.65 \cdot 10^{-8}\ M_\odot/yr$) when the secondary disk is included. The accretion by the sinkhole around the primary is increased by $1 \cdot 10^{-9}\ M_\odot/yr$ (or 14%) when the secondary disk is included. The top panel in Fig. 5.6.1 shows the disk mass, the accumulated mass accreted by the sinkhole in the previous simulation (labeled as *supplied mass*, green dash-dotted line), the accumulated accreted mass of the current simulation where the disk is included (labeled as *accreted mass*, orange dashed line), and the difference in accumulated mass accreted by the primary when the secondary is included and when it is not (labeled as Δ *mass accreted by primary*, red dotted line). The accumulated mass is computed as

$$m_{acc}(t) = \int_0^t \dot{m}(t) \mathrm{d}t\ . \tag{5.6.5}$$

The entire mass of the disk is accreted by the star and resupplied by the circumbinary disk within 1800 T_{bin} (120 thousand years). The difference between the accreted and supplied mass is greater than the increase in the accretion rate on the primary, meaning that most of the lost mass is ejected into the gap and potentially accreted by the circumbinary disk instead of being accreted by the stars. The mass should eventually accreted by the stars at later times, but the simulation is computationally too expensive to wait for a new equilibrium to establish in the density ring.

5.6.1 Secondary disk behavior

Fig. 5.6.2 depicts a set of disk quantities focusing on the secondary disk. The quantities were computed as the mass-weighted disk averages, see Jordan et al. (2021), where any cell within 6 au from the secondary, which is equal to 0.3 times the binary semi-major axis, was considered part of the disk.

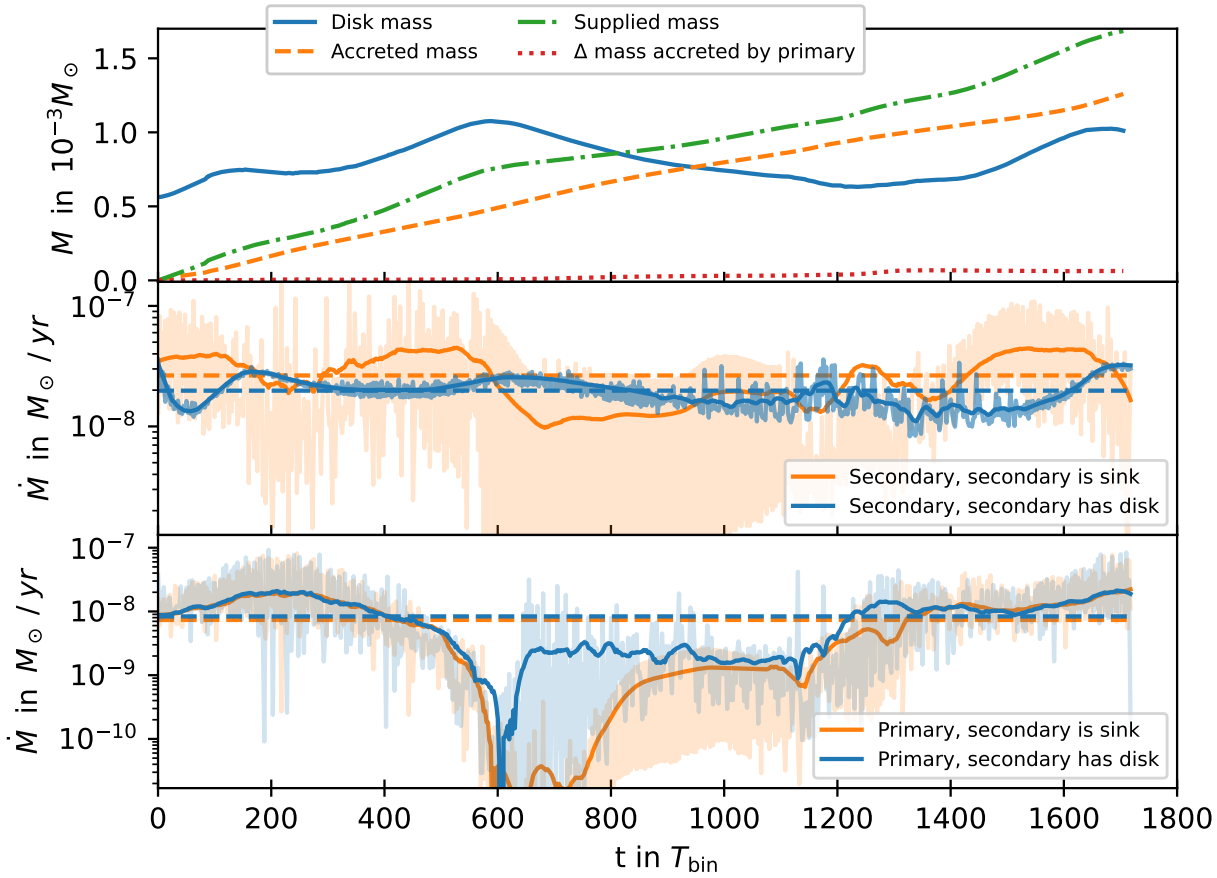

Figure 5.6.1. *Quantities measured for the high-mass case ($m_{\mathrm{CBD}} = 5\%\ M_\odot$). Top panel: Disk mass over time, the accumulated accreted mass, the accumulated supplied mass by the circumbinary disk, and the accumulated difference between primary sinkhole accretion with and without the secondary disk.*
Middle panel: secondary mass accretion rate over time with and without the secondary disk.
Bottom panel: primary sinkhole mass accretion rate over time with and without the secondary disk.

In the global simulation with all three disks, there are different mass accretion rates. The one from the circumbinary disk to the stellar disks, and the one from the stellar disks to the stars. As I discuss the mass exchange from the point of view of the stellar disks, I will refer to the accretion from the CBD to the stars as *supply*, and the accretion onto the stars (which can come from the stellar disk, or from mass streams entering directly into the sinkhole area around the star) as *accretion*.

The top panel in Fig. 5.6.2 shows the disk mass together with the longitude of periastron of the gap. As already shown in Fig. 5.6.1, the stellar accretion rate is relatively constant, and changes in the disk mass are caused by increases or decreases in the mass supply rate from the CBD. Jumps in the longitude of periastron of the cavity are caused by the detection method. The location of the longitude of apastron of the cavity is determined by tracking the highest density in the circumbinary disk, which is located inside a spiral arm, cf. Fig. 5.3.1. If two spiral arms have similar peak densities, the method can switch between the two spiral arms between timesteps, creating jumps in the longitude of apastron of the cavity.

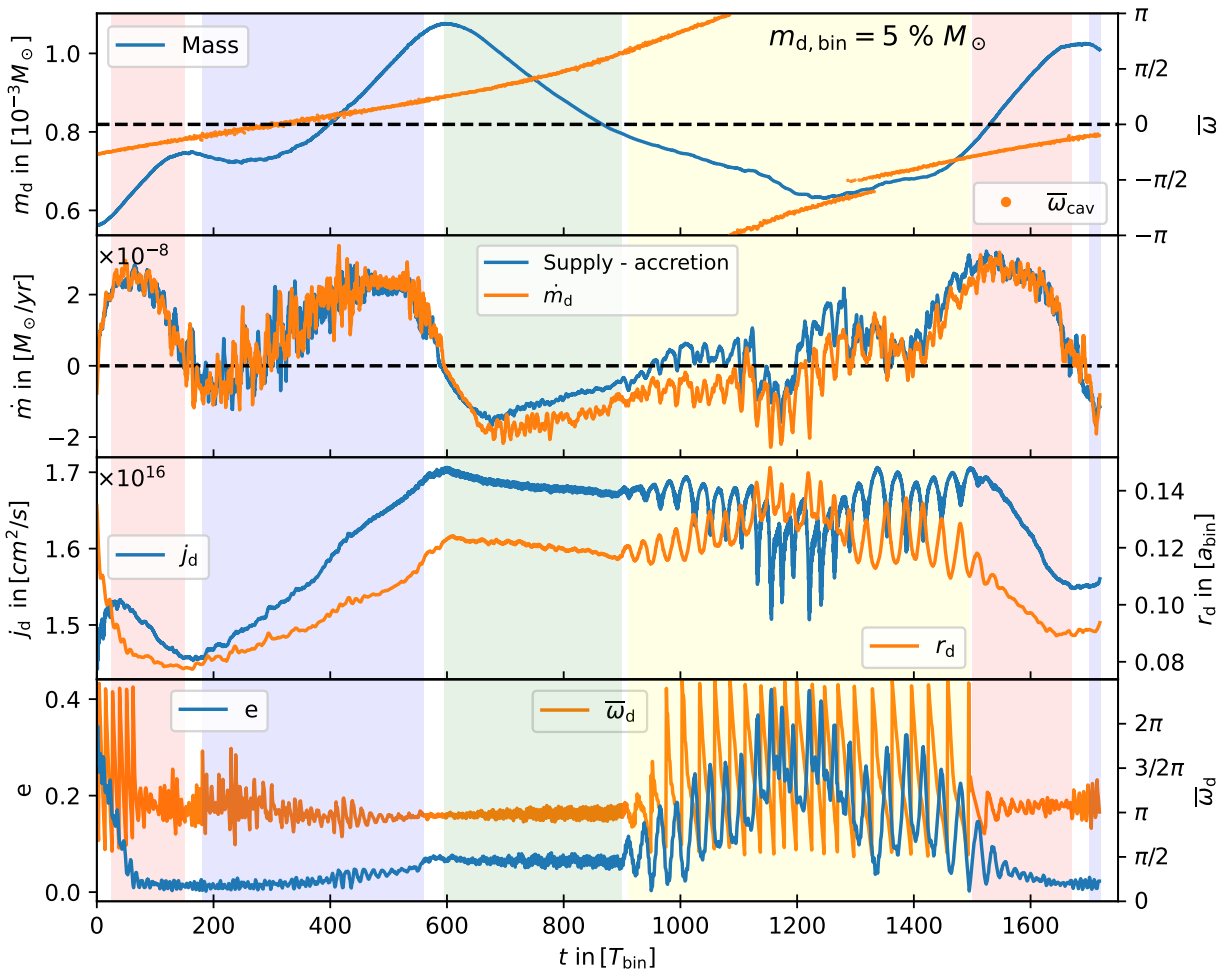

Figure 5.6.2. *Various secondary disk quantities over time for the high disk mass case. The accretion rate and $\dot{m}_d$ are smoothed over 50 binary orbits. See text for info.*

The second panel in Fig. 5.6.2 shows the difference between the accretion rate on the secondary and the supply rate by the CBD (blue line) and the change in disk mass over time (orange line). Differences between these two lines imply that the disk is losing mass by ejection; if the disk is losing mass faster than implied by the accretion rate and supply rate, then additional mass was lost by ejection which was not tracked in the simulation. The third panel shows the specific angular momentum of the disk and the radius of the disk; and the bottom panel shows the longitude of periastron of the disk and the eccentricity of the disk.

From Fig. 5.6.2 I identified 4 different phases, which are marked by the colored background, during one binary disk precession period that I want to discuss in detail. Logarithmic surface density snapshots during each phase are depicted in Fig. 5.6.4. The first phase (red background) is a phase of high mass accretion of low angular momentum gas onto the secondary disk. This phase occurs at the beginning ($t \approx 30\ T_{\rm bin}$) and the end ($t \approx 1500\ T_{\rm bin}$) of the simulation, when the longitude of periastron of the gap is slightly below 0. During this time, the specific angular momentum of the disk, the disk radius, and the eccentricity decrease rapidly.

Viscous effects and tidal torques would not reduce the eccentricity as they typically excite eccentricity (Oyang et al. 2021). Mass accretion removes low angular momentum gas from the inner disk and therefore cannot reduce the specific angular momentum of the disk. Mass ejection does remove high angular momentum gas from the outer edge of the disk, but it can only be active while the disk is filling its Roche lobe, and therefore does not reduce the disk radius, but keeps it static. These results indicate that the loss of specific angular momentum is caused by the mass stream.

A snapshot of the low angular momentum accretion phase is presented in the top row of Fig. 5.6.4. The outer spiral arm travels through the entire gap region and spreads out before falling towards the secondary, while the inner spiral arm slingshots around the primary and impacts the outer spiral arm before being accreted onto the secondary disk.

From the analysis done in this work, it is not clear what determines whether the mass stream deposits negative specific angular momentum to the secondary disk. I would like to note though, that in the frame of the secondary, the angular momentum of the CBD varies with the angle relative to the position of the primary. During binary periastron, the angular momentum of the CBD is maximal near the negative x-axis and minimal with negative values near the x-axis, as demonstrated in Fig. 5.6.3. To better understand of the angular momentum accretion on the disk, one would have to analyze the accretion over singular binary orbits, which was not done here (I only looked at snapshots taken during the binary periastron).

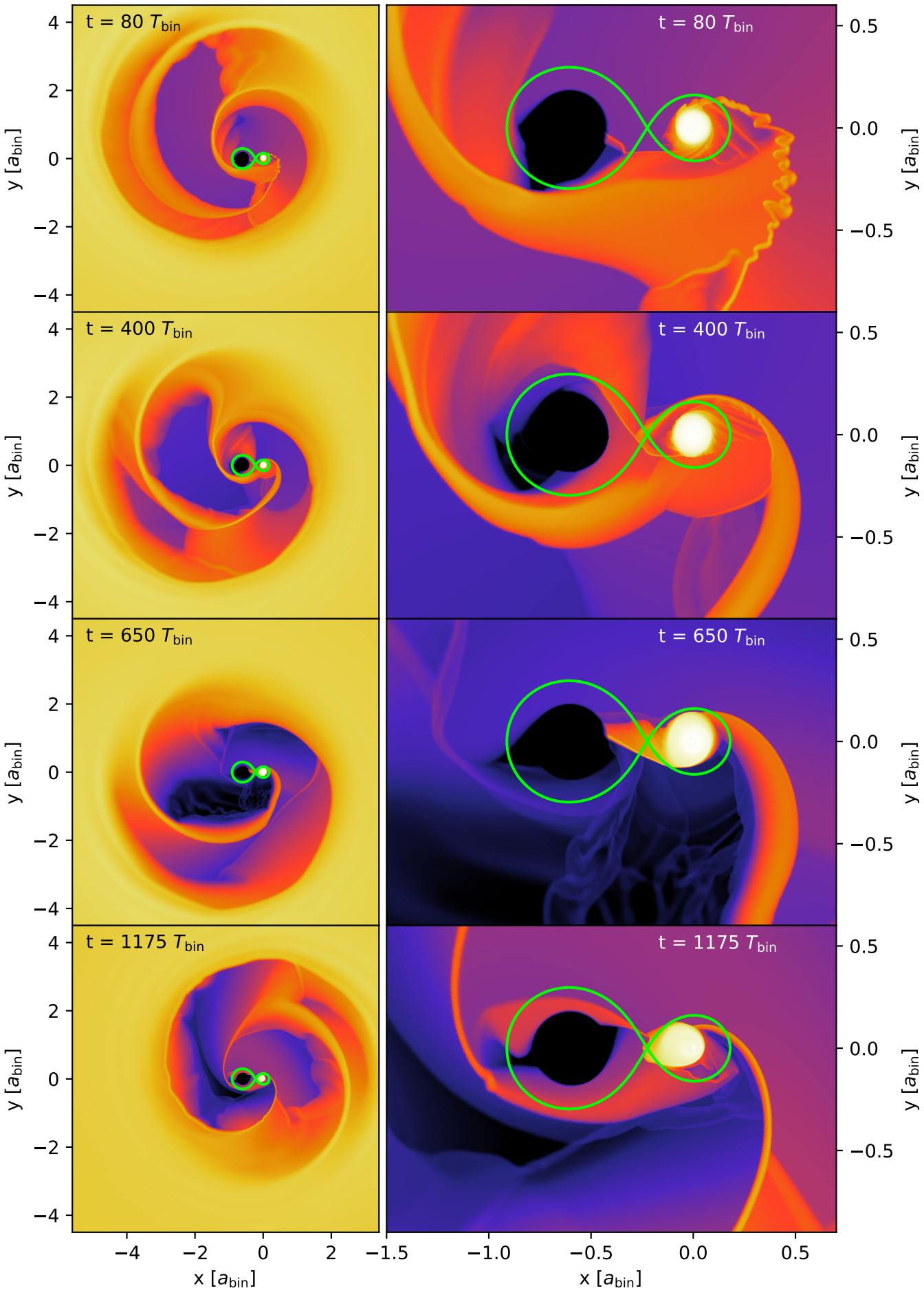

Figure 5.6.4. *Logarithmic surface density snapshots to accompany the lines from Fig. 5.6.2.*

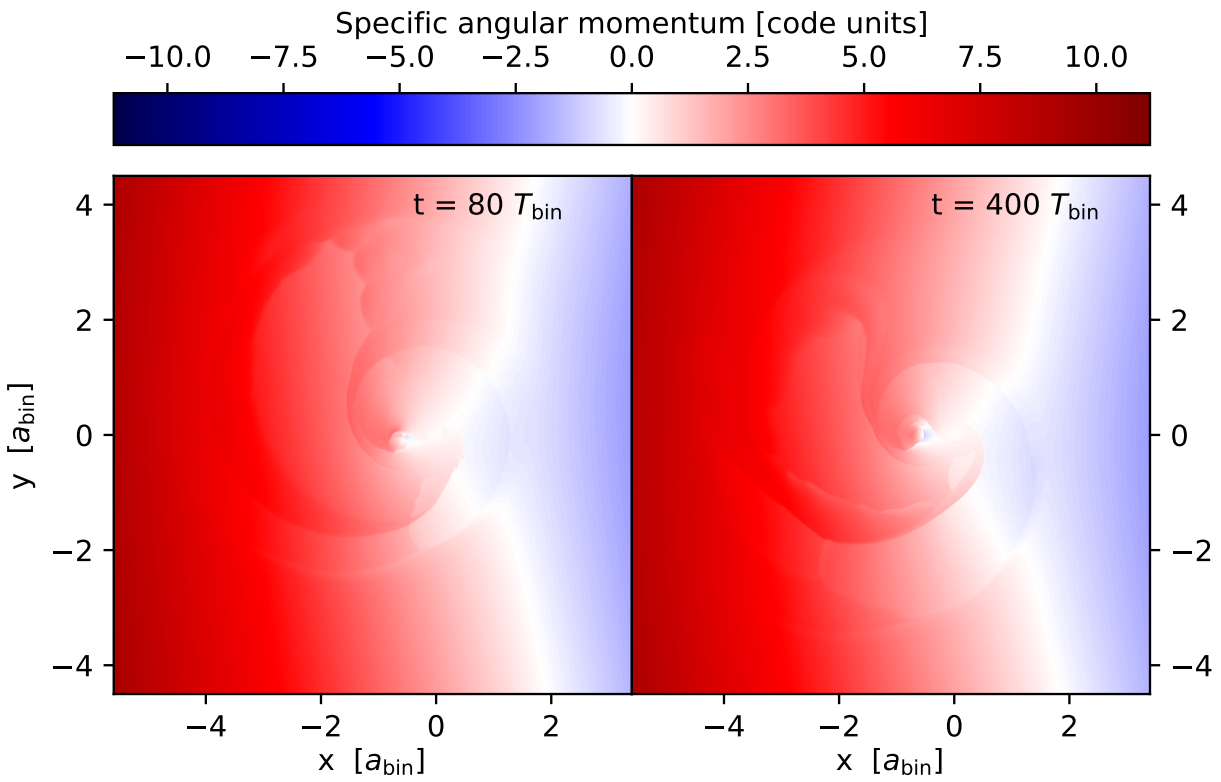

Figure 5.6.3. *Snapshots of the specific angular momentum in the frame of the secondary. The time of the snapshots and the extent of the panels are identical to the two upper left panels in Fig. 5.6.4.*

After the low angular momentum accretion phase, the supply rate drops briefly before rising again, this time supplying the disk with high angular momentum gas as seen by the steep rise in disk radius and specific angular momentum (blue background $t = 200 - 550\ T_{\rm bin}$ in Fig. 5.6.2). During this phase, both spiral arms directly impact the secondary disk, see second panel in Fig. 5.6.4. Towards the end of this growth phase, the disk fills out the Roche lobe of the secondary and its eccentricity grows to 0.05 (at $t = 560\ T_{\rm bin}$) and transitions to the next phase (green background). During this phase, the longitude of periastron of the disk is fixed toward the primary during binary periastron and the eccentricity is constant at an elevated level, see the fourth panel of Fig. 5.6.2). This behavior is indicative of tidal truncation at a resonance radius, similar to that observed during the precursor of a superoutburst in SU UMa dwarf novae (Jordan et al. 2024). Note that for the mass ratio of the binary, the 3:1 orbital resonance radius is roughly equal to the Roche lobe radius of the secondary star. The 3:1 resonance is known to exert strong gravitational torques on the disk, which are thought to drive eccentricity growth (Lubow 1991; Oyang et al. 2021).

The high accretion phase during the blue background phase ends because the outer spiral arm is no longer being pulled towards the binary, but remains inside the CBD. But the quasi-steady, Roche-lobe-filling state of the secondary persists throughout the green phase ($t = 600 - 900\ T_{\rm bin}$), during which the mass supply rate from the CBD remains low. The disk slowly loses mass and angular momentum towards the primary, see the third panel in Fig. 5.6.1, the difference between change in disk mass and the value expected from accretion and

supply in the second panel in Fig. 5.6.2, and the additional accretion by the primary measured in Fig. 5.6.1. This mass loss and the low supply rate from the CBD allow the disk to shrink, which stabilizes the disk against eccentricity growth. The mass supply rate increases steadily as the CBD cavity precesses away from the minimum supply rate near $\omega_{\rm cav} = \pi/2$.

The quasi-steady phase ends when the secondary disk becomes eccentric around $t \approx 900\ T_{\rm bin}$ (yellow background). The mass ejection rate is higher in the high eccentricity state, as seen in the second panel of Fig. 5.6.2. But this increase in mass ejection does not lead to an increase in the primary accretion rate, see the bottom panel in Fig. 5.6.1 at $t = 1000\ T_{\rm bin}$. The disk is precessing in prograde direction and the eccentricity has sharp peaks every time the longitude of apoastron is aligned with the pericenter of the binary (anti-aligned), see the bottom panels in Fig. 5.6.4. The mass supply rate keeps increasing, causing the disk mass to grow despite the high mass ejection.

The high eccentricity phase ends only when the mass stream from the binary supplies low angular momentum mass (red background), shrinking the disk to sizes smaller than the resonance radii where gravitational torques are weak, allowing the disk to circularize.

For the 5% $M_\odot$ case, the secondary disk was initialized with a too low disk mass, so the average disk mass therefore should be slightly higher than shown in Fig. 5.6.2. In the two lower mass cases, the disk was instead initialized with too much mass.

The disk quantities for the 0.2% $M_\odot$ case are shown in Fig. 5.6.5. The behavior of the stellar disk over one precession period of the CBD is similar to the 5% $M_\odot$ case. There are low and high mass supply phases and the high mass supply phases are split into a low and high angular momentum accretion. Consequently, the secondary disk expands, becomes eccentric and then shrinks and becomes circular when low angular momentum gas is accreted. A notable difference is that the low-mass secondary disk does not precess in the high eccentricity state but librates around $\omega_{\rm d} = \pi$, meaning that the eccentric bulge extends toward the primary during periastron (anti-aligned).

Unlike the CBD disk, the secondary disk is not passive and the viscous heating is a significant source of energy. For the high mass case, the disk mass is roughly ten times higher than in the low mass case, although the mass supply rate is a factor of 25 higher, implying $\dot{m} \propto m^{1.4}$ for these two particular simulations.

In a passive disk, the accretion rate scales linearly with disk mass ($\dot{m} \propto m\nu$, $\nu = const$). In a fully active disk, the accretion rate scales with the square of the disk mass because the disk temperature (and with it the viscosity ν) increases linearly with disk mass due to viscous heating (Jordan et al. 2021), therefore $\nu \propto m$ and $\dot{m} \propto m^2$.

The resulting average stellar mass accretion rates and the average secondary disk mass for each simulation are summarized in Table 5.8. Compared to the results with two sinkholes instead of a disk around the disk from Table 5.5, the mass accretion rate of the secondary was reduced by 22% in the high mass case. In the other two simulations, the accretion rate increased, likely because the secondary disk was initialized with too much mass. The increase

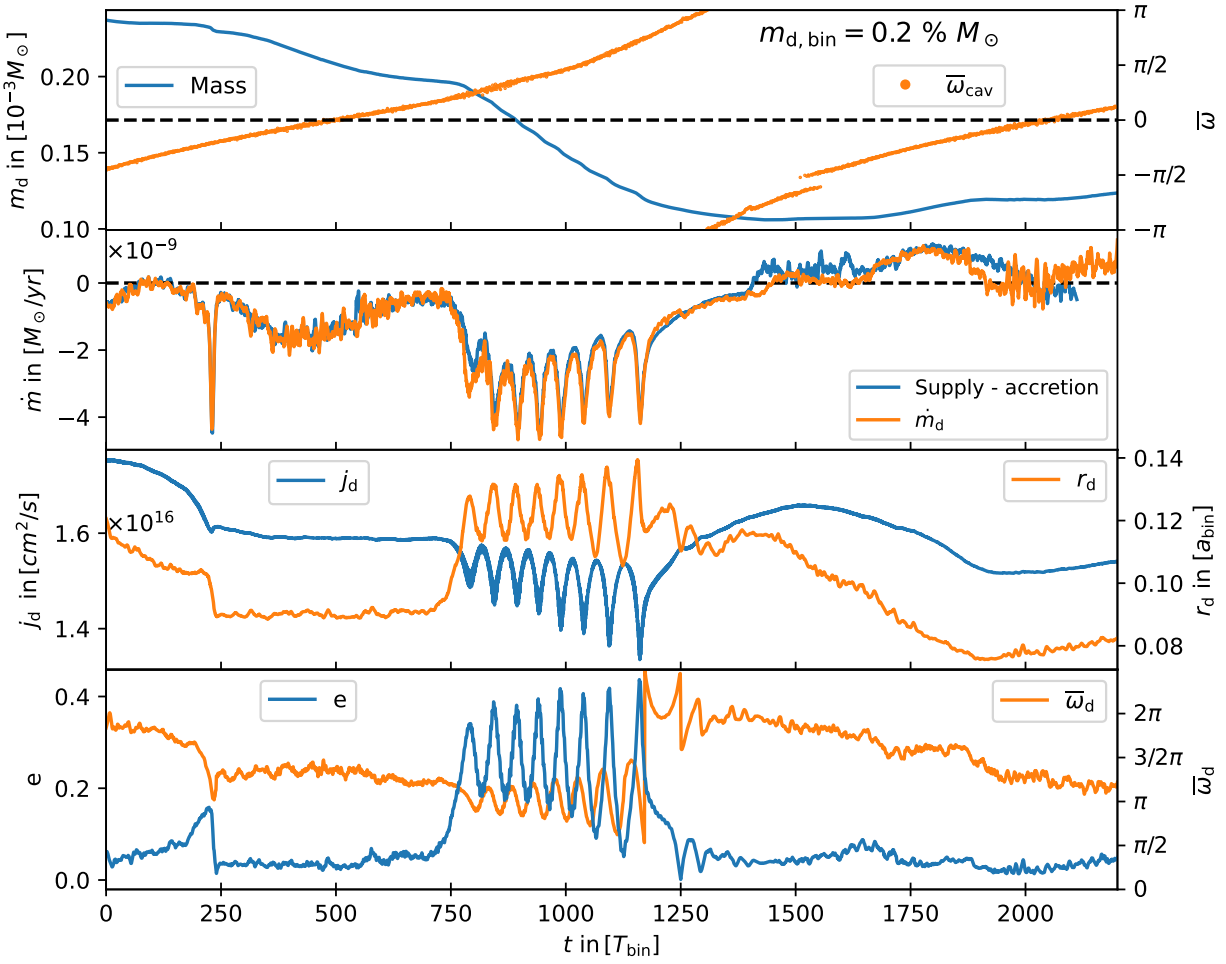

Figure 5.6.5. *Various secondary disk quantities over time for the low disk mass case ($m_{\mathrm{CBD}} = 0.2\%\ M_\odot$). Same as Fig. 5.6.2.*

in mass accretion might therefore also be overestimated. For the high mass case, the accretion rate on the primary was increased by 13% due to being fed mass from the secondary disk.

Table 5.8: *Mass accretion rates measured in the secondary center with a secondary disk.*

$M_{\mathrm{CBD}}\ [M_\odot]$	$2 \cdot 10^{-3}$	$1 \cdot 10^{-2}$	$5 \cdot 10^{-2}$
$\dot{M}_{\mathrm{Prim}}\ [M_\odot/yr]$	$3.00 \cdot 10^{-10}$	$1.53 \cdot 10^{-9}$	$8.37 \cdot 10^{-9}$
$\dot{M}_{\mathrm{Sec}}\ [M_\odot/yr]$	$1.51 \cdot 10^{-9}$	$5.60 \cdot 10^{-9}$	$1.98 \cdot 10^{-8}$
$M_{\mathrm{d,Sec}}\ [M_\odot]$	$1.3 \cdot 10^{-4}$	$2.5 \cdot 10^{-4}$	$8.1 \cdot 10^{-4}$

Note: The $M_{d,\mathrm{CBD}}\ [M_\odot] = 0.2\%$ and 1% values were averaged from 750 T_{bin} to the end of the simulation because in those simulations the secondary disk was initialized too heavy.

5.7 Primary and circumbinary disk combined

In this section, the results from previous simulations are used to initialize a simulation in the primary frame with all three disks: the circumbinary disk (CBD) and the two stellar disks. The simulation parameters are identical to the ones used for the secondary disk simulation,

see Section 5.6 for the global setup and Section 5.5 for the local setup. The primary disk and secondary disk still need to be initialized first, which I described in the next two subsections.

5.7.1 Primary disk initialization

As with the secondary disk, I first initialize the stellar disks in an isolated setup and adjust the initial disk masses until the accretion rates are similar to the primary accretion rates measured in the previous sections. The domain size and grid resolution are the same as for the secondary disk initialization, see Table 5.6. As the primary is more massive, it has a larger Roche lobe and the disk is more extended. The disk is therefore truncated as:

$$\Sigma(r) = \Sigma_0 \cdot (r/[a_{\rm bin}])^{-S} \cdot \frac{1}{1 + \exp(r - 0.25\, a_{\rm bin})/(0.025\, a_{\rm bin})} \,. \tag{5.7.1}$$

The disk quantities for the high mass case are shown in Fig. 5.7.1. The primary disks quickly become eccentric and precesses in a retrograde direction. The same behavior was also observed in the two lower mass simulations, though lower primary disk masses lead to lower eccentricities. The mass loss through the outer boundary is lower than for the secondary disk in the high eccentricity state. For the primary disk, 1.7% of the mass is lost at the outer boundary where it was 11.5% for the secondary disk in the high mass case.

The parameters for the final primary disks are summarized in Table 5.9. The mass loss rates were chosen to be similar to the accretion rates in the center of mass frame during a high accretion rate phase, e.g. around $t = 500\ T_{\rm bin}$ in Fig. 5.4.2. This was done to start at the upper limit of the primary disk mass before starting the global simulation.

Table 5.9: *Primary disk masses and accretion rates for the isolated primary disk simulation.*

$M_{d,\rm CBD}\ [M_\odot]$	$2 \cdot 10^{-3}$	$1 \cdot 10^{-2}$	$5 \cdot 10^{-2}$
$M_{\rm d,Primary}\ [M_\odot]$	$4.68 \cdot 10^{-5}$	$2.05 \cdot 10^{-4}$	$1.92 \cdot 10^{-3}$
Accretion rate $[M_\odot/yr]$	$7.40 \cdot 10^{-10}$	$2.77 \cdot 10^{-9}$	$2.21 \cdot 10^{-8}$
Ejection rate $[M_\odot/yr]$	$1.45 \cdot 10^{-13}$	$3.77 \cdot 10^{-12}$	$2.87 \cdot 10^{-10}$
Disk eccentricity	0.11	0.14	0.24

Note: Except for the disk mass, all simulation parameters are identical to the ones used for the secondary disk simulation, see Table 5.6.

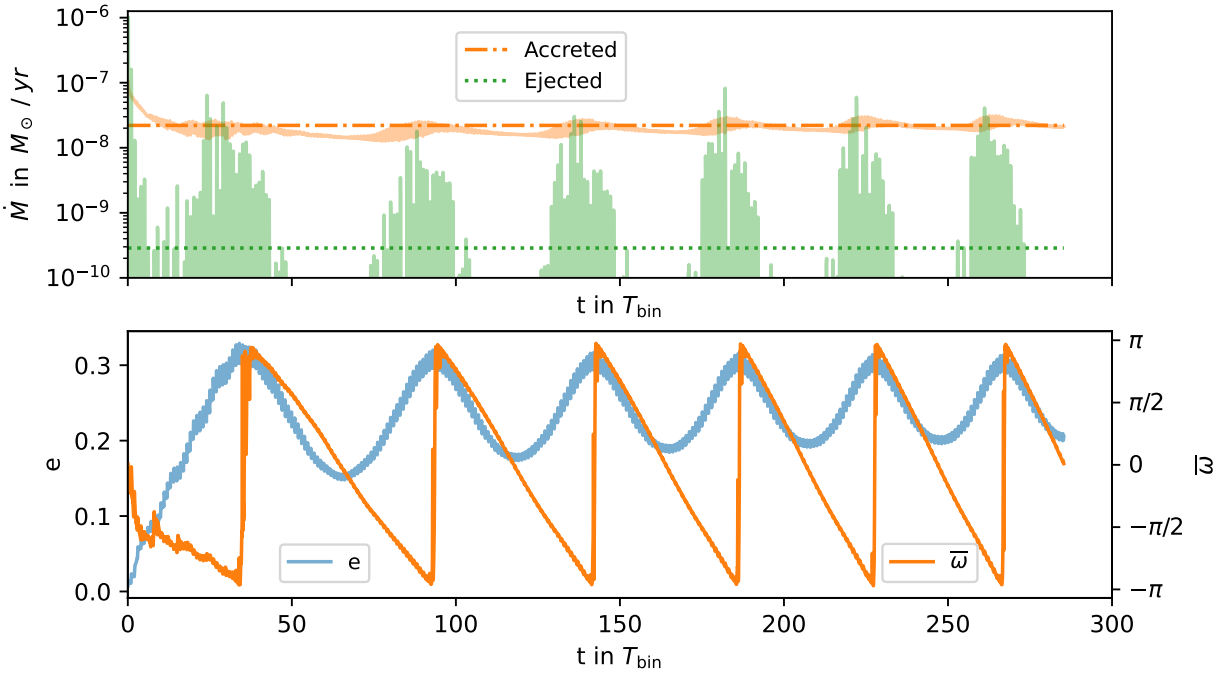

Figure 5.7.1. *Top: Mass loss rates of the primary disk in the high mass case ($m_{CBD} = 5\%\ M\odot$). The green line represents the mass loss rate measured at the outer boundary and the orange line the mass loss rate at the inner boundary. The dashed line presents the average values over the last 170 binary orbits, starting at $T_{bin} = 130$.*
Bottom: Eccentricity (blue line) and longitude of periastron (orange line) of the primary disk.

5.7.2 Secondary disk in the primary center

Due to the logarithmic grid, the secondary disk is poorly resolved in the primary center. Nevertheless, I tried to include it in the simulations. Without modifications, the secondary disk ejected too much mass and reduced the time step of the simulation. Both these were addressed by smoothing the gravitational potential of the secondary star using the smoothing function by Klahr & Kley (2006). The implementation is described in Rometsch et al. (2024), Sect. 3.6. I used a smoothing length of 0.3 times the size of the Roche lobe. The secondary accreted mass from its disk by removing mass according to the mass loss expected from a 1D viscous model, the details are described in Rometsch et al. (2024), Sect. 3.13. The simulation used the same resolution as the global simulation, but a smaller domain: $R_{min} - R_{max} = 0.4 - 1.5\ a_{bin}$ and $N_r \times N_\varphi = 312 \times 1160$.

The resulting density profile during periastron and mass loss rates are shown in Fig. 5.7.2 and compared against the secondary disk in the secondary frame from Section 5.5. The secondary disk in the primary frame does not become eccentric, and during periastron, is smaller and denser than the disk in the secondary frame. The disk size, same as the smoothing that depends on the size of the Roche lobe, increases in size as the binary moves towards apastron which does not occur in the secondary frame. The smoothing length increases so that the ratio of grid cell size to smoothing length is constant, though in retrospect, the smoothing length should have been constant to avoid the artificial oscillation in the disk size. Additionally,

within the first binary orbit, the disk flipped its angular velocity from prograde to retrograde, which is not observed when the simulation is run in the secondary frame.

The mass of the disk was therefore chosen such that its mass ejection rate is between the mass ejection rate of the reference disk in the non-eccentric and the eccentric states. This leads to an overall mass accretion rate that is too low. This could have been corrected by scaling up the accretion rate by a constant factor. But this was not done, because less accretion onto the secondary should lead to more mass being ejected towards the primary and I tried to make a best-case scenario for the primary disk mass.

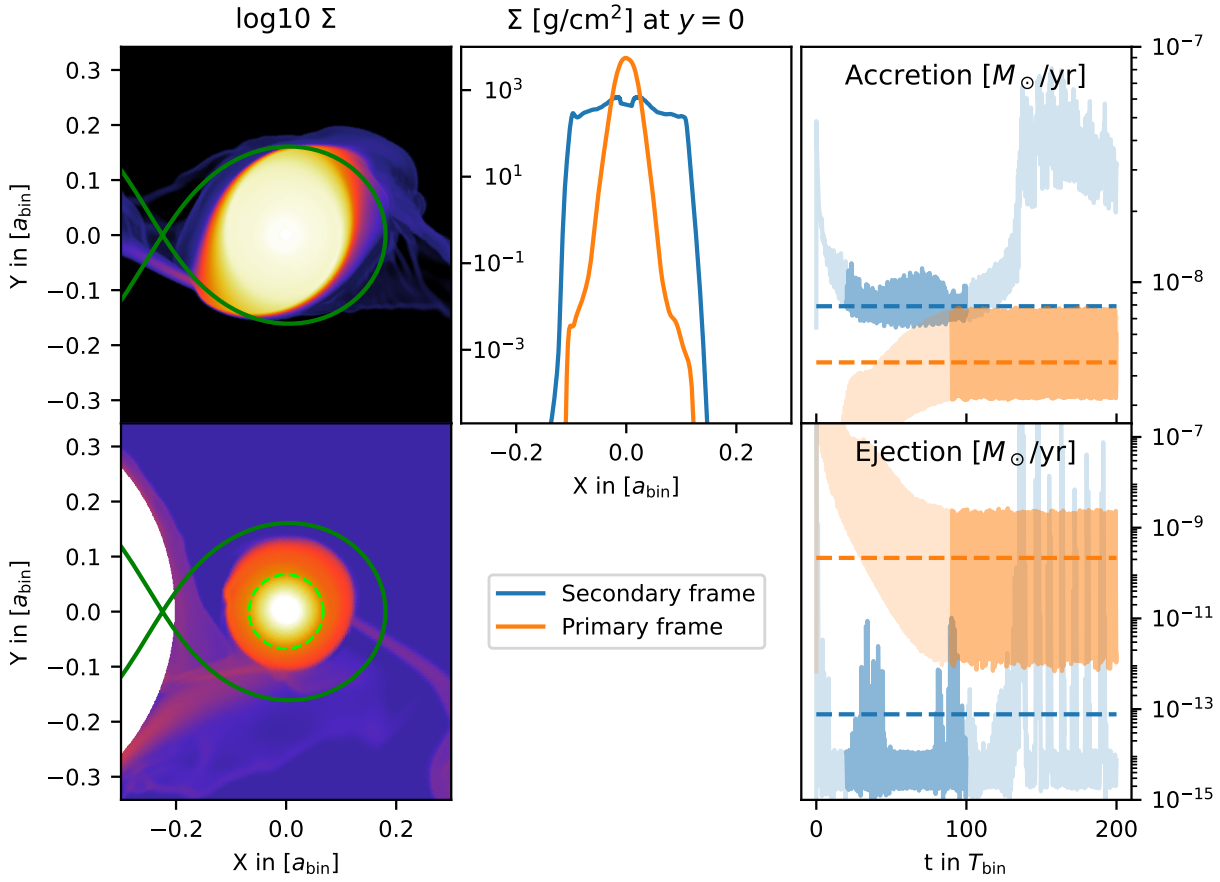

Figure 5.7.2. *Comparison of the surface density profiles during periastron and mass loss rates between the secondary disk simulated in the secondary frame and in the primary frame. Dark green lines indicates the Roche lobe and the green dashed line indicates the smoothing length.*

5.7.3 Primary disk behavior

Finally, the stellar disks from the previous two subsections are combined with the equilibrium circumbinary disk from Section 5.3 just as a high accretion phase starts. The primary disk in Section 5.7 was initialized on a lower resolution grid and was interpolated to the higher resolution grid of the global simulation. I used the same grid resolutions as in Jordan et al. (2021), where I performed a convergence study using a similar setup and found the resolutions to be sufficient to resolve the primary disk.

Then, the simulations for each of the three mass supply rates were evolved for 3300 $T_{\rm bin}$ while the quantities of the primary disk were monitored. Same as for the secondary disk in Section 5.6, the quantities were computed as the mass-weighted disk averages, see Jordan et al. (2021), where any cell within 7 au from the primary, which is equal to 0.35 times the binary semi-major axis, was considered part of the disk.

The disk quantities for the high mass case are shown in Fig. 5.7.3. The first panel shows the disk mass together with the longitude of periastron of the gap. As for the secondary disk, the behavior of the primary disk seems to depend on the precession angle of the CBD. For the simulations in the primary frame, there are no direct comparison simulations with sinkholes. Therefore, the precise mass supply is not known and the second panel instead shows the mass accretion rate of the primary and the time derivative of the disk mass. Based on the low mass ejection rates found in Table 5.9, I assume that the mass supply rate can be estimated as the sum of the accretion rate and the change in the disk mass. The third panel shows the specific angular momentum of the disk and the radius of the disk; and the bottom panel shows the longitude of periastron of the disk and the eccentricity of the disk.

The high supply rate phases are clearly visible from $\dot{m}_{\rm d}$ in Fig. 5.7.3 and there are changes in the specific angular momentum and radius of the disk associated with it. The specific angular momentum increases as the mass supply rate is increasing and decreases when the mass supply rate is decreasing. The disk radius increases sharply when the mass supply rate initially increases, but then reaches a limit and remains constant as the supply rate continues to increase. Once $\dot{m}_{\rm d}$ becomes negative, the disk radius begins to shrink until the next high supply phase starts.

This behavior is opposite to that observed for the secondary disk in Fig. 5.6.2, i.e., at the time when the specific angular momentum increases for the secondary disk, it decreases for the primary disk, and vice versa. The secondary disk has two phases of high mass supply rate separated by a short phase of low supply rate. The secondary disk radius shrinks only during the first high supply rate phase, and it grows during the second high supply rate phase, and remains elevated during the low supply rate phase.

The opposite behavior is likely connected to the opposite sign of the velocities of the binary components. While the secondary is moving left, the primary is moving right. The opposite sign also flips the side of the maximum and minimum angular momentum when simulating the CBD in the frame of the primary, though the effect is weaker than in Fig. 5.6.3 due to the slower velocities of the primary.

In all global simulations, the eccentricity of the primary disk drops rapidly at the beginning of the simulations, which is caused by the mass stream from the CBD, as demonstrated in Fig. 5.8.2. At the same time, the disk stops precessing and instead librates around $\omega_{\rm d} = \pi$, meaning that the disk is anti-aligned and its eccentric bulge is pointing toward the pericenter of the binary. In the $m_{\rm CBD} = 5\%$ case, the disk stays in this low eccentricity state throughout the simulation, with the eccentricity oscillating between 0.02 and 0.11 with a mean value of 0.06. In the lower mass cases the eccentricity does not remain suppressed, as will be shown later.

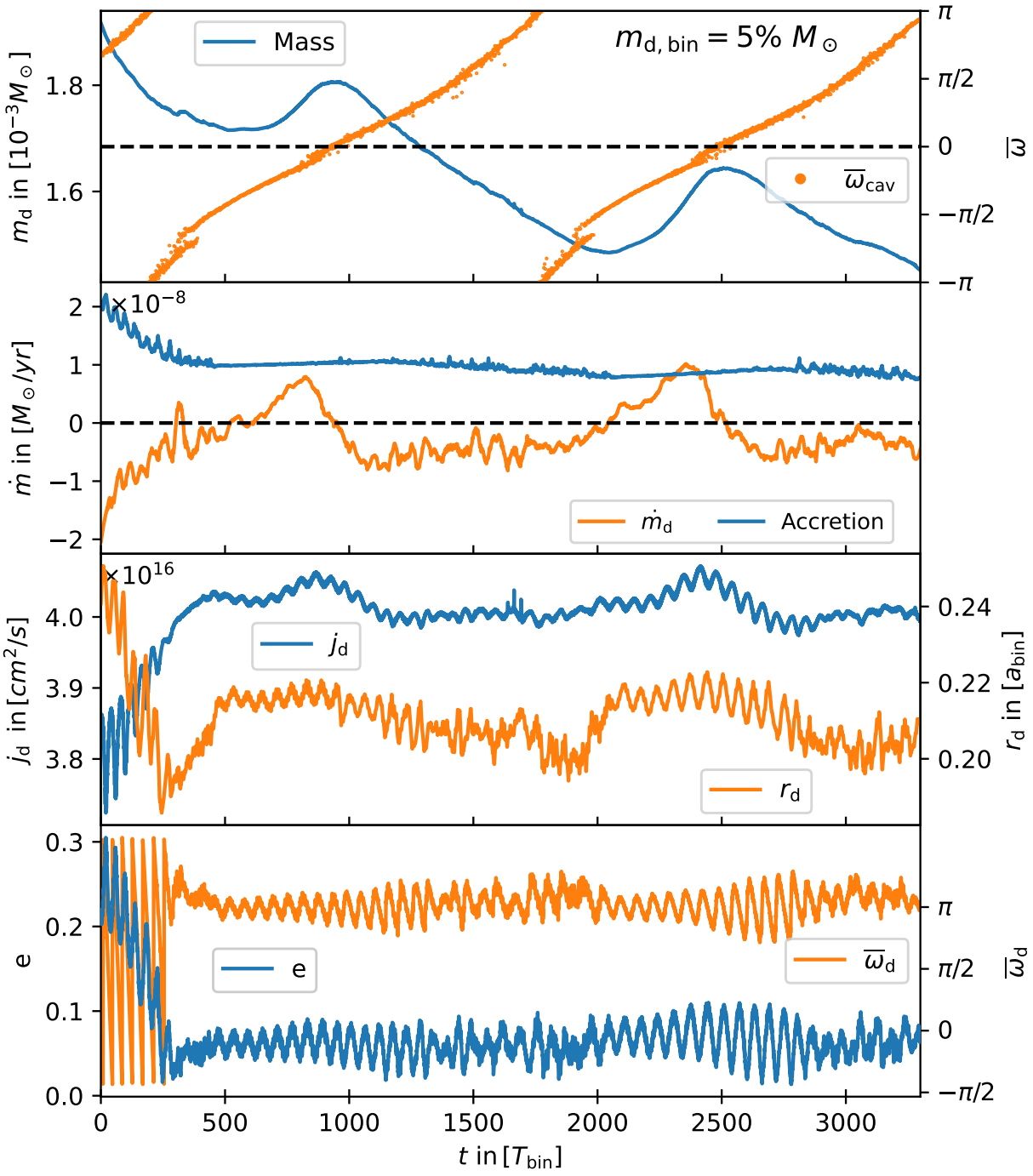

Figure 5.7.3. *Various primary disk quantities over time for the high disk mass case. The accretion rate and $\dot{m}_{\mathrm{d}}$ are smoothed over 50 binary orbits.*

Simulated in isolation, the secondary disk in the frame of the primary was smaller than in the frame of the secondary, see Fig. 5.7.2. In the global simulation, it is significantly larger and overflows its Roche lobe. Interactions with the mass stream, which are the only explanation for the different behavior, are probably exacerbated by the retrograde azimuthal velocity of the secondary disk, which occurs in the frame of the primary.

The too large secondary disk absorbs mass streams that would otherwise have impacted the primary, while ejecting more mass than it should have. This is visualized in Fig. 5.7.4. The supply rate, estimated as the accretion rate plus the time derivative of the disk mass, is

shown as the blue line. It has lower peaks and higher lows than the other simulations. The interaction between the mass streams from the circumbinary disk and the primary disk is therefore underestimated.

For the high mass case, I ran another simulation in which the secondary disk was replaced by a sinkhole with a radius of 0.08 a_{bin}, which is equal to the minimum secondary disk radius found in Fig. 5.6.2. The disk radius, which is determined as the radius containing 99% of the disk mass, is smaller than the physical extent of the disk as it neglects low density regions around the disk that can still interact with the mass streams.

The sinkhole is therefore significantly too small which leads to an overestimation of the interaction between the mass streams and the primary disk. The estimated mass supply rate is shown as the orange line in Fig. 5.7.4 and it shows longer high supply phases. The low supply phase has a lower value because the missing secondary disk cannot feed the primary disk. This can be seen by comparing the supply rate with the supply rate measured in the secondary center with a disk around the secondary (from the simulation in Section 5.6), which is shown as the green line. Also shown is the primary mass accretion rate measured when both stars had a sinkhole instead of a disk, see Section 5.4, as a red dashed line.

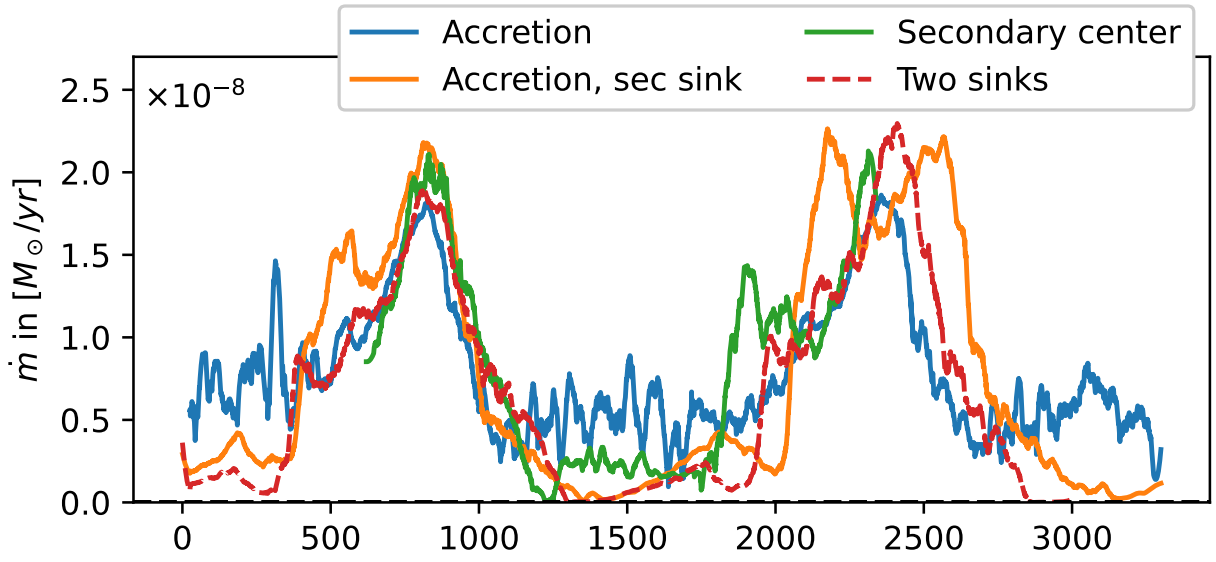

Figure 5.7.4. *Comparison of the mass supply rates to the primary from different simulations, see text for clarification.*

The disk quantities for the simulation with a secondary sinkhole are shown in Fig. 5.7.5. They are similar to the previous one, but the overall mass supply rate is higher and the interaction with the mass streams more pronounced. The changes in the specific angular momentum become larger during the different phases, leading to higher amplitudes in the eccentricity oscillations in the excited state and non-oscillating low eccentricity in the low mass supply phase. The excited and quiescent phases alternate and each lasts about 800 T_{bin}, which is half the duration of one precession period of the circumbinary disk.

The results in this section indicate that the interaction with the circumbinary disk and the secondary disk significantly alter the dynamic of the primary disk and cannot be neglected.

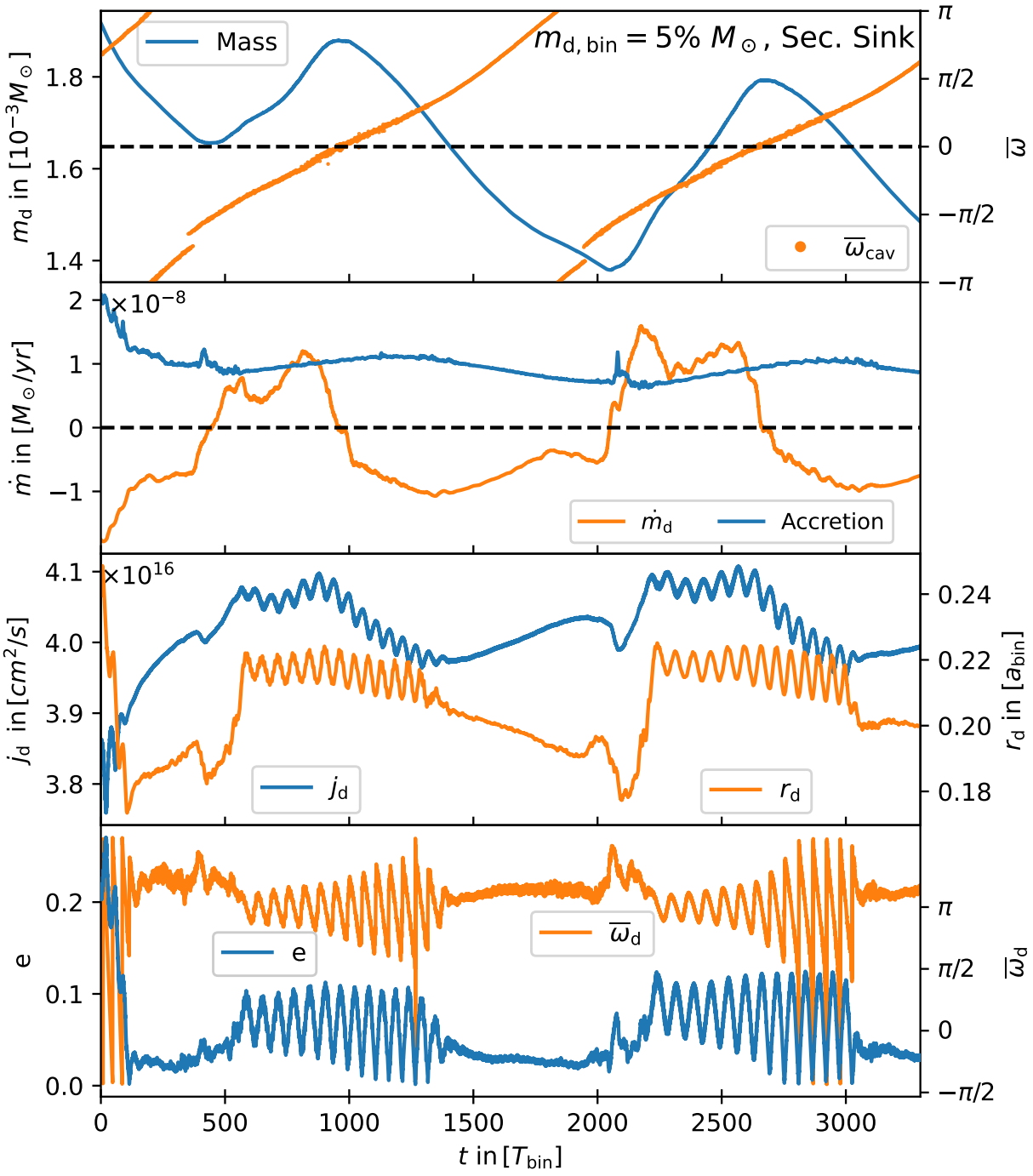

Figure 5.7.5. *Same as Fig. 5.7.3. But for this simulation, the secondary did not have a disk but instead had a sinkhole with a radius of* 0.08 a_{bin}*, which is equal to the minimum secondary disk radius found in Fig. 5.6.2.*

The results for the $m_{\mathrm{CBD}} = 1\%$ and 0.2% cases are shown in Fig. 5.7.6 and Fig. 5.7.7 respectively. Obviously, the primary disk mass is lower. For the 5% case the primary disk mass is $1.5 \cdot 10^{-3}\ M_\odot$ and dropping at the end of the simulation while for the 1% and 0.2% case it rising during the Simulation to $0.3 \cdot 10^{-3}$ and $0.08 \cdot 10^{-3}\ M_\odot$ respectively. Comparing the viscous heating to the heating by stellar irradiation, while neglecting shock and pressure heating, I find that 13% of the heating is due to stellar irradiation in the 5% case, while it is 86% and 99% for the lower mass simulations. The effects of this are visible in Fig. 5.9.1. This

means that the disk is active in the high mass case and passive in the two lower mass cases. The dynamics of the passive low-mass disks therefore depend on the central star. These disks could potentially be in a prograde precession state with lower eccentricities if the central star is cooler, the difference between the two states can be seen in Fig. 5.5.2.

The accretion cycles are still visible, but weaker compared to the high mass case. And unlike the high mass case, both lower mass cases enter a high eccentricity state ($e > 0.2$). For the $m_{\mathrm{CBD}} = 1\%$ simulation, the high eccentricity state is suppressed during the low mass supply phase (e.g. $t = 1400 - 2000\ T_{\mathrm{bin}}$), but still at a higher level ($e \approx 0.1$) than it was in the high mass case. In the $m_{\mathrm{CBD}} = 0.2\%$ simulation, the eccentricity is not fully suppressed during the low mass supply phase and is overall higher than in the other two cases. However, even in the high eccentricity state, the disks librate around $\omega_{\mathrm{d}} = \pi$ instead of precessing as they do when simulated in isolation.

Fig. 5.8.1 shows snapshots of the logarithmic surface density of the $m_{\mathrm{CBD}} = 1\%$ case at different stages of the CBD precession cycle. The first panel shows the CBD and the primary disk at the time when the first high eccentricity phase of the primary disk is about to end. The second panel shows the primary disk in the low mass supply phase where the disk is calming down, i.e. that the amplitude of the eccentricity oscillations is shrinking. During both of these phases, there is no spiral arm directly impacting the primary disk. Rather, the disk is pulling leftover mass from inside the gap.

The third panel shows the primary disk at the beginning of the high mass supply phase, during which the disk expands. The fourth panel shows the primary disk at the time of maximum eccentricity. During both of these phases, one of the spiral arms is directly impacting or at least grazing the primary disk.

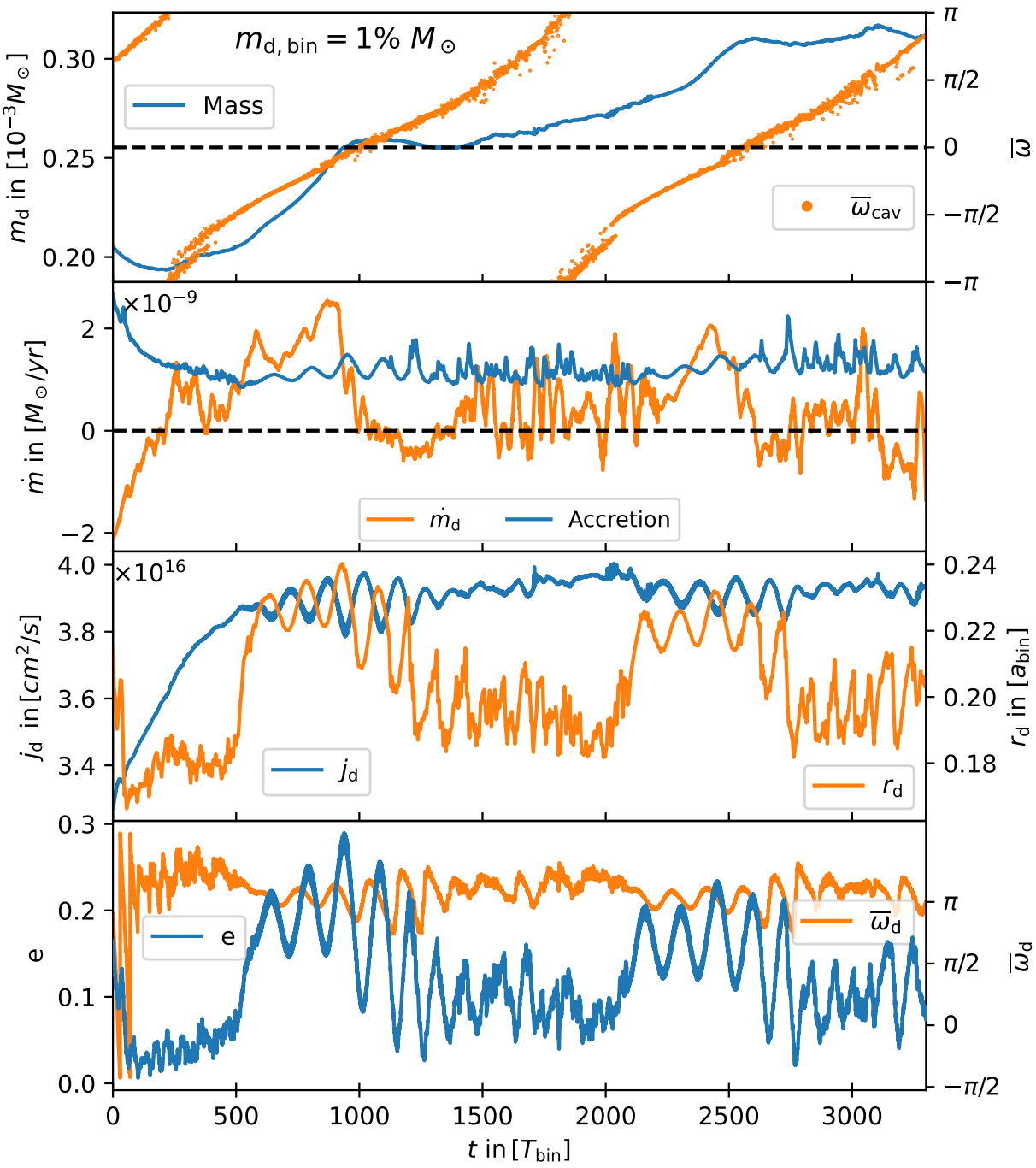

Figure 5.7.6. *Same as Fig. 5.7.3 but the* $m_{\mathrm{CBD}} = 1\%\ M_\odot$ *case.*

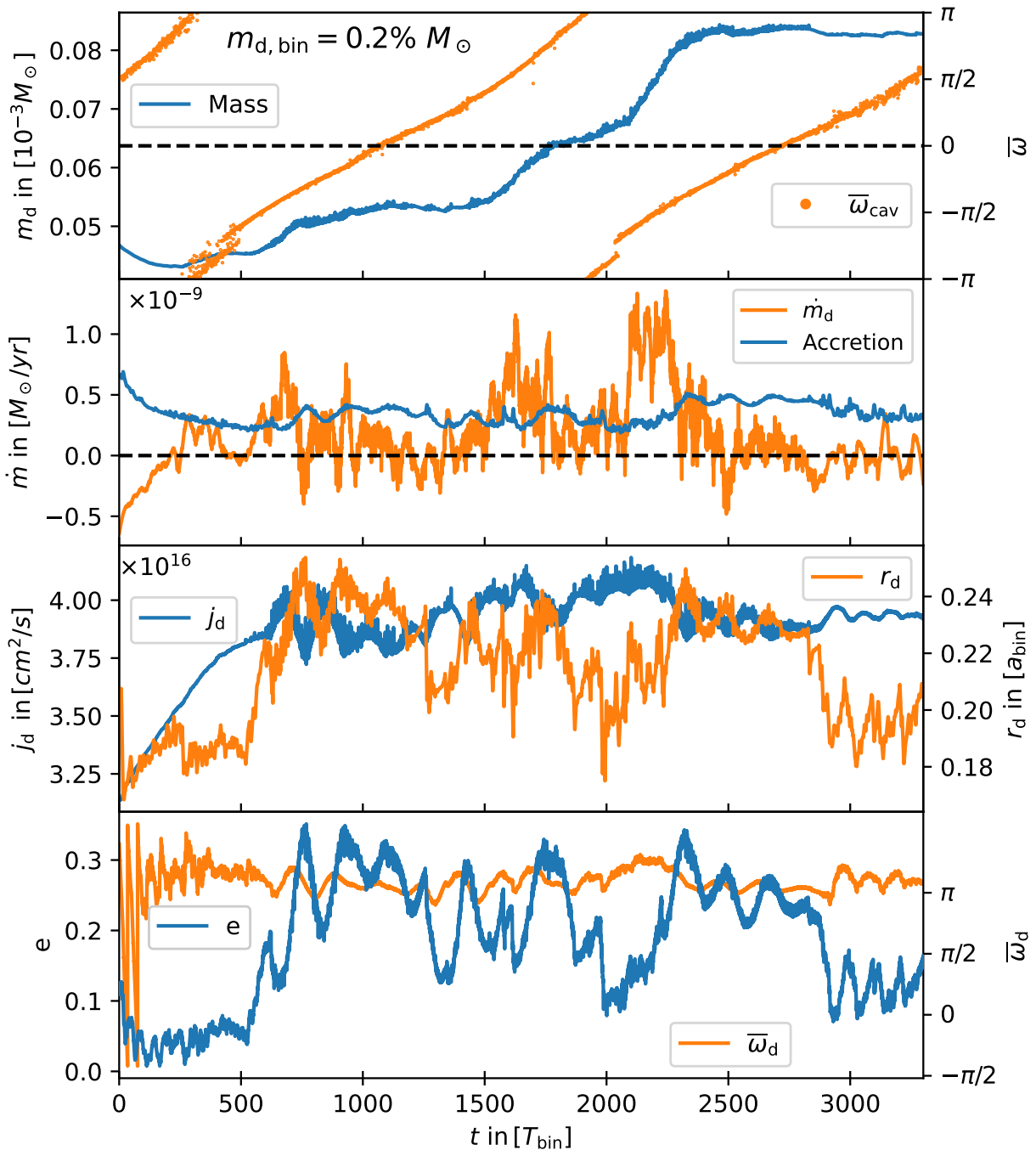

Figure 5.7.7. *Same as Fig. 5.7.3 but the* $m_{CBD} = 0.2\%\ M_\odot$ *case.*

5.8 Summary & discussion

Currently, more than 20 binary stars with separation < 30 au host detected S-type planets (orbiting one of the stars), like e.g. γ-Cephei. The formation of these planets is particularly challenging (Paardekooper et al. 2008; Picogna & Marzari 2013; Thebault & Haghighipour 2015; Thébault et al. 2006). On the other hand, disks like GG Tau or HD 142527 give us an observational glimpse into the condition around the binary stars, which is often not considered for the simulation of the circumprimary/secondary disc. To get a better understanding of the environment in such systems, I created models that combine the circumbinary, primary, and secondary components into one consistent model.

Based on the observations of massive circumbinary disks that feed mass to the central binary (e.g. Kraus et al. 2012; Phuong et al. 2020), I have set up a string of simulations using the FARGOCPT code (Rometsch et al. 2024) to simulate the interaction between the stellar disks and the circumbinary disk (CBD).

The simulations are centered on one of the stars. In this setup, the disk around the central object is optimally resolved, the CBD is well resolved with small inaccuracies due to the strong indirect terms active in the simulation, and the disk around the companion star is poorly resolved.

I then studied the dynamics of the disk around the central object which are relevant for the formation of planets around the individual stars. I found in all my simulations that the mass streams from the CBD affect the dynamics of the stellar disks, completely changing their behavior compared to when they are simulated in isolation.

In Section 5.5, I studied the dynamics of the secondary disk during one precession period of the CBD. Depending on the precession angle of the CBD, the mass streams from the CBD can reduce the specific angular momentum of the secondary disk, causing it to shrink and allowing it to become circular. Then at different stages, the mass stream increases the specific angular momentum of the secondary disk, causing the disk to expand until gravitational torques from the binary drive eccentricity growth and precession. In this expanded state the secondary disk fills its Roche lobe and loses mass to the primary and ejects mass into the cavity. Due to the low luminosity of the secondary and the high densities in the disk, the secondary disk was always active in my simulations, meaning that most of its heat comes from viscous heating rather than stellar irradiation.

In Section 5.7 I studied the dynamics of the primary disk with both the secondary and the CBD included. The dynamics of the primary also depend on the precession angle of the CBD. With mass accretion from the CBD, the primary disk is librating in an anti-aligned orientation with respect to the binary. For the simulation with the highest CBD mass, the primary disk was in a low eccentricity state for the whole simulation. For the two lower disk mass cases, the eccentricity alternated between high and low eccentric states depending on the precession angle of the CBD.

The primary disk in the high mass case is active (heating dominated by viscous heating), while the disks in the two lower mass cases are passive (heating dominated by stellar irradia-

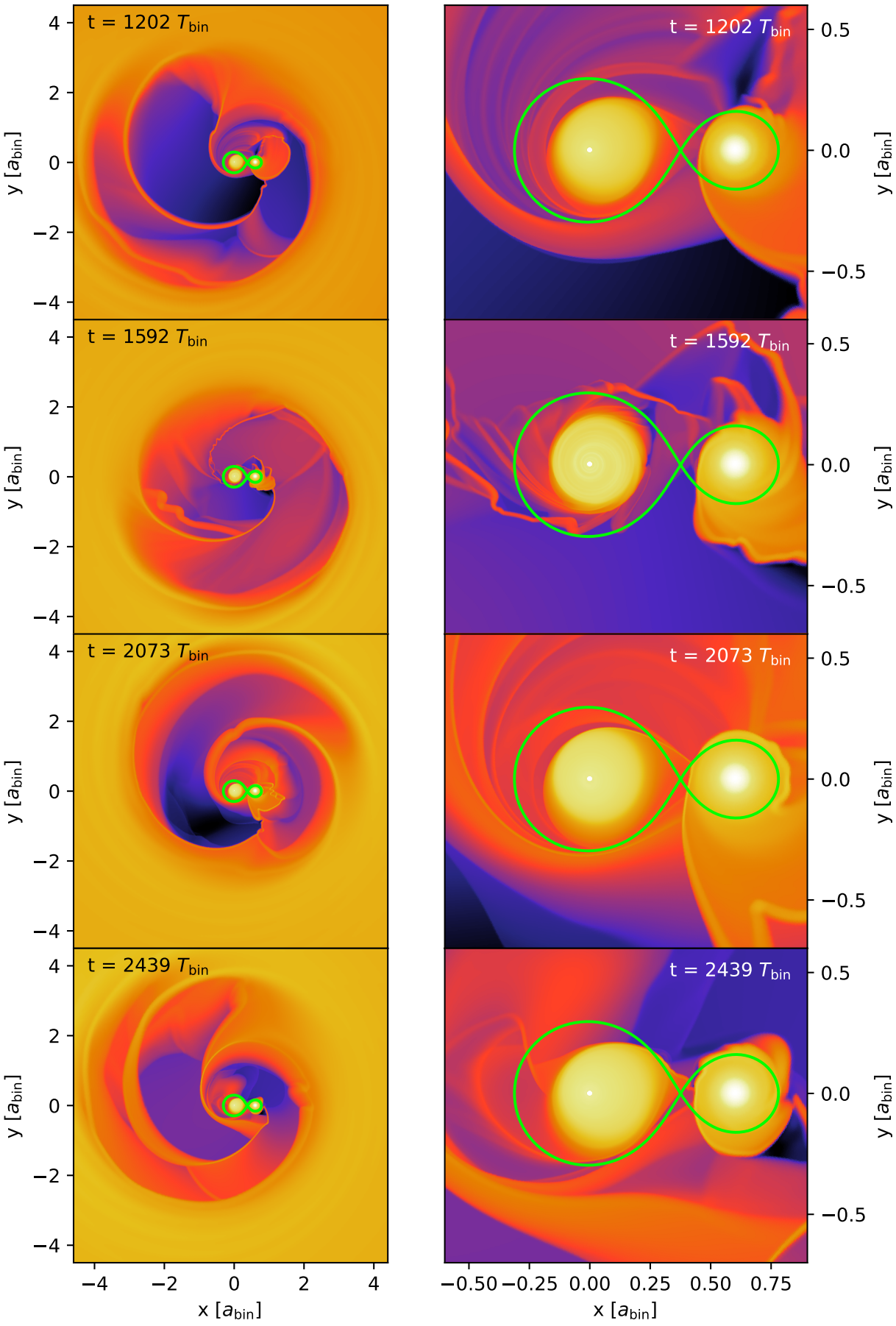

Figure 5.8.1. *Logarithmic surface density snapshots of the* $m_{CBD} = 1\%$ *case to accompany the lines from Fig. 5.7.6.*

tion), see Fig. 5.9.1. If the stellar irradiation is reduced, these disks could potentially be in a prograde precessing state which typically has lower eccentricities, c.f. Fig. 5.5.2.

The secondary disk can also feed mass to the primary disk, potentially affecting its behavior as well. These effects have not been properly captured in the simulations in this work due to the significant challenges of simulating the secondary disk in the frame of the primary.

Comparison to previous work

Stellar disks in close binaries have been simulated in the past in the context of planet formation. These studies found low disk eccentricities in isothermal disks with wave damping by Paardekooper et al. 2008, in non-isothermal simulations by Marzari et al. (2012); Müller & Kley (2012), and isothermal simulations with self-gravity by Marzari et al. (2009). From these simulations, it seemed that planet formation might succeed inside close binaries. In my first paper (Jordan et al. 2021) I conducted a comprehensive parameter study of the primary disk in close binaries. In all cases, I found rather large disk eccentricities that would prevent planetesimals from growing, and I was able to show that the low eccentricity found in previous studies can be explained by a too small domain size and too low grid resolution.

In the simulation in this study, higher mass accretion from the CBD leads to higher primary disk masses and lower eccentricities. With the highest mass case being in a low eccentricity state for the whole simulation. This is opposite to what I found in (Jordan et al. 2021) for the isolated primary disk, where higher disk masses lead to higher eccentricities. Further, the behavior of the stellar disks cycled through different states depending on the precession angle of the CBD. This indicates that it could be the mass stream that is suppressing the eccentricity of the primary disk and causing it to librate.

To further test whether the reduction in eccentricity after the restart in the global simulation is caused by mass accretion or due to direct interaction with the secondary disk, I ran a global simulation with all densities outside the Roche lobe of the primary ($R > 0.6\ a_{\rm bin}$) set to zero, removing any interaction with the circumbinary disk. The initial simulation densities are shown in the upper panel of Fig. 5.8.2. The secondary disk will be accreted by the sinkhole around the secondary and does not interact with the primary disk. With a circumbinary disk, the mass-weighted eccentricity of the primary disk is damped and reaches 0 for a brief moment. Without the circumbinary disk, the eccentricity continues to evolve it did in the local initialization simulation in Fig. 5.7.1.

This test highlights that it is indeed the accretion of mass from the CBD that affects the dynamics of the stellar disks, and that the primary disk, when simulated in isolation, can develop high eccentricities as described in Jordan et al. (2021).

Potential influence of disk-winds

The evolution of protoplanetary disks is thought to be driven not only by viscous angular momentum transport, but also by magnetic wind driven angular momentum removal (Blandford & Payne 1982). Since the angular momentum is removed from the disk, magnetic winds lead to accretion of the disk without spreading the disk outward. In close binaries, the viscous

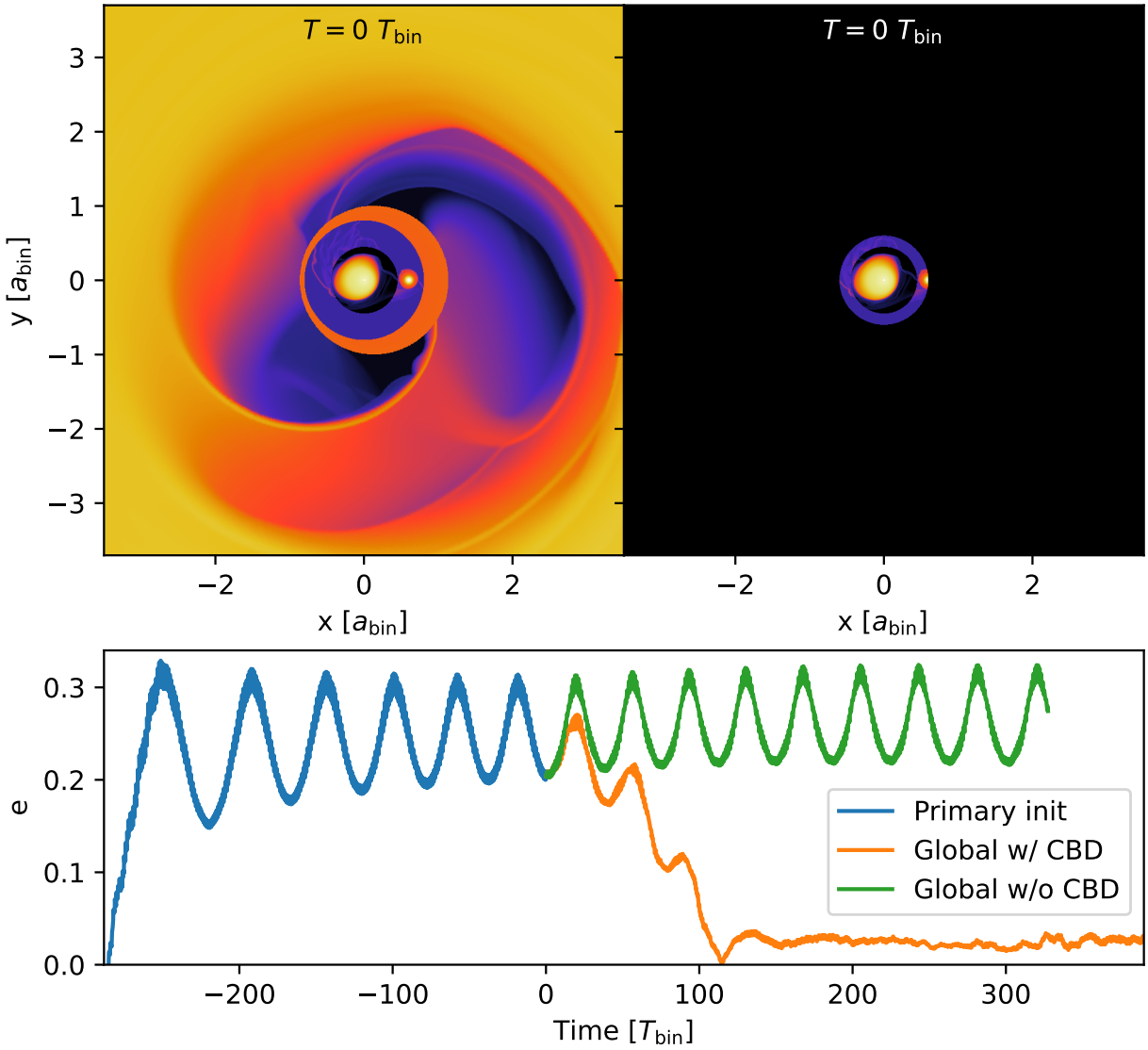

Figure 5.8.2. *Top: Initial logarithmic surface densities of the combined simulations with a sinkhole around the secondary. The left plot presents the original setup used in Section 5.7.3. The right plot presents the same setup, but with the densities outside the Roche lobe of the primary set to zero.*
Bottom: Time evolution of the mass-weighted eccentricity of the primary disk for the local simulation with reduced resolution (blue line), the global simulation with the circumbinary disk (orange line), and the global simulation without the circumbinary disk (green line). Time is set to zero at the start of the global simulations.

spreading of the disk is important to expose the disk to the gravitational torques of the binary and drive eccentricity growth. Therefore, a low-viscous, wind-driven circumstellar disk would be smaller and have a lower eccentricity (Turpin & Nelson 2024). For circumbinary disks, magnetic winds change the gravitational interaction between the disks and the binary, but have no significant effect on the precession and eccentricity of the circumbinary disk (Turpin & Nelson (2024)).

Magnetic winds provide an alternative model to the α-viscosity model and have even been proposed to replace the α-viscosity model entirely due to the lack of known turbulent

processes that could produce the observed mass accretion rates, and the lack of direct observational evidence for turbulence in accretion disks (Rosotti 2023). Nevertheless, modeling magnetic winds has proven to be challenging and the strength of magnetic winds is still poorly constrained (Weder et al. 2023), which is why I did not consider them in this work.

There are also photoevaporative winds, which remove mass without driving accretion. Photoevaporation is caused by the high-energy radiation from nearby stars, the stellar radiation itself is easily detected in observations. Therefore, photoevaporation is expected to be active alongside magnetic winds and viscous evolution, and it is expected to play an important role in the dispersal of protoplanetary disks (Alexander et al. 2014, January). Fig. 5.8.3 shows the surface density profile in the primary frame and, in the lower plot, the mass accretion rate from the simulations together with the photoevaporation rate from Sellek et al. (2024). The photoevaporation rate found in Sellek et al. (2024) for a 1 $M_\odot$ star was, following Picogna et al. (2021), scaled linearly with the stellar masses (0.4, 1.4 $M_\odot$) used in this work. I calculated the photoevaporation rate for each star individually and then added them together.

Considering Fig. 5.8.3 from larger to smaller radii, if the photoevaporation rate is greater than the mass accretion rate, it can be assumed that photoevaporation would blow away any gas viscously moving through that radius, stopping accretion and cutting off the mass supply to the inner regions. In the gap region, mass accretion is pulsed by the binary pulling mass from the inner edge of the circumbinary disk into the gap. The mass pulled by the binary traverses the gap within one binary orbit, which is short compared to the photoevaporation timescale, so I ignore the gap regions in this analysis. The plot shows that the stellar disks are too dense to be affected by photoevaporation and the only critical region is in the circumbinary disk at $r \approx 200$ au. The 0.2 and 1% $M_\odot$ mass cases would be significantly affected by photoevaporation and have their mass supply to the stellar disks reduced. Even in the high-mass case (5%$M_\odot$, green line), the photoevaporation rate in the circumbinary disk reaches 14% of the viscous mass accretion rate, which is not negligible and could affect the results if implemented.

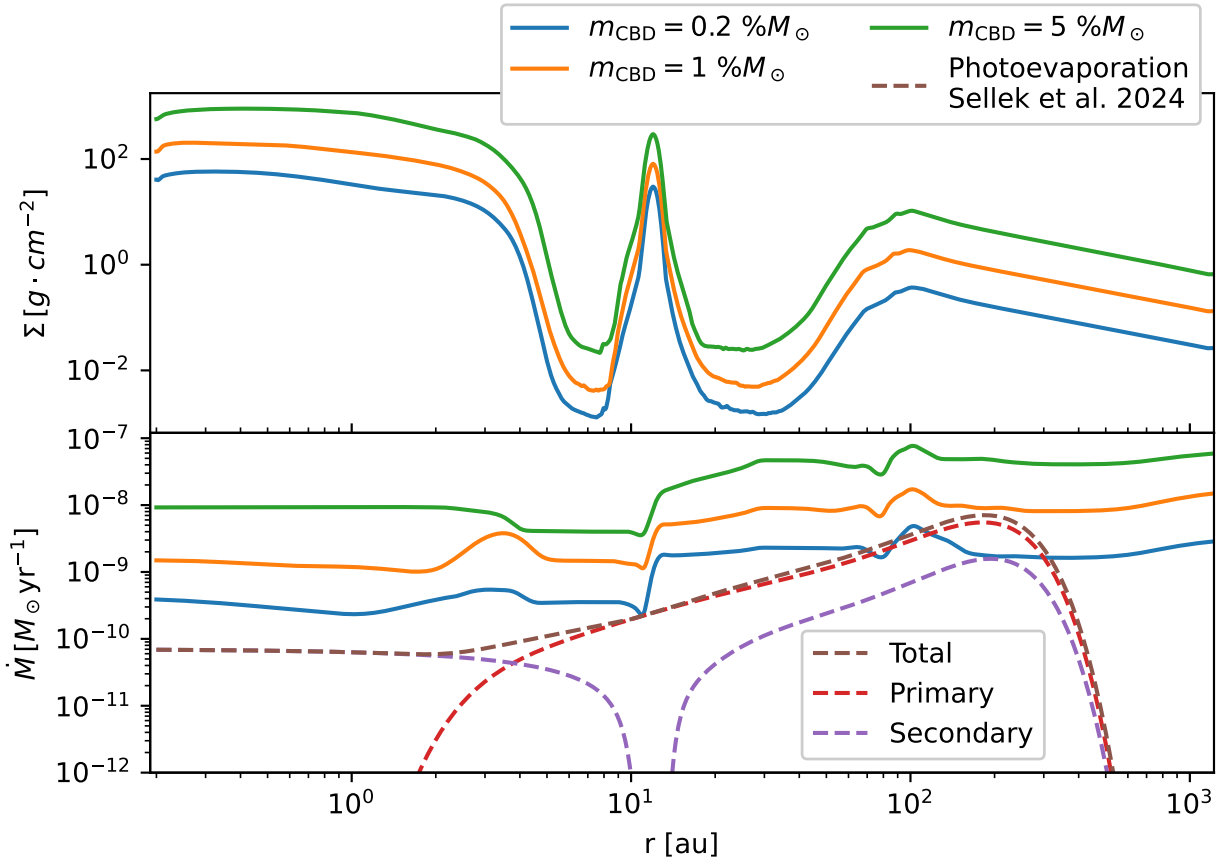

Figure 5.8.3. *Top: Surface density profile in the primary frame.*
Bottom: The viscous mass accretion rate measured during the simulation and the photoevaporation rate according to Sellek et al. (2024). Both, the surface density and the mass accretion rate were averaged over 100 binary periods.

5.9 Implications for planet formation

The detection of massive stellar disks in a close binary system by Rodríguez et al. (1998) and later the detection of planets in close binary systems (Hatzes et al. 2003) raised the question of whether planet formation can succeed in such environments (Marzari & Scholl 2000). In a series of studies, see Thebault & Haghighipour (2015) for a review, it was found that in the planet formation process, the planetesimal growth phase is the most affected by the presence of a perturbing companion star. It was also shown that the eccentricity of the disk and its precession are crucial for whether planetesimals can grow into planets or not (Silsbee & Rafikov 2021).

Disk temperature

The γ Cephei system (Hatzes et al. 2003) contains a massive planet with a mass of 1.9 M_{Jup} (Endl et al. 2011, March), with recent observations suggesting an even higher mass of 9.4 M_{Jup} (Benedict et al. 2018). To have enough material to make the formation of such massive planets feasible, disks with initial masses of around $m_{\mathrm{d}} = 0.01\ M_\odot$ have been used for simulating the primary disk (Marzari et al. 2012; Müller & Kley 2012). Such high disk masses lead to

extremely high gas densities in the small, truncated disk around the primary star. The high densities lead to high temperatures, such that the dust sublimation temperature is exceeded within 1 au from the primary star, and even the outer parts of the disk are still hotter than the ice sublimation temperature (Jordan et al. 2021; Müller & Kley 2012).

The continuously fed disks in the model presented here, in addition to extending the lifetime of the disks, also allow for cooler disks that still have enough mass to form massive planets. Profiles of the surface density and temperature of the primary disk are shown in Fig. 5.9.1. For the high mass case (green lines), the ice sublimation temperature (160 K) is visible as a kink in the temperature profile at $\approx 0.1\ a_{\mathrm{bin}}$ (2 au). At a temperature of 220 K, all ices are sublimated, causing another kink in temperature at $0.05\ a_{\mathrm{bin}}$ (1 au).

For the low mass case (blue lines), due to the disk being passive, the temperature depends only on the distance to the primary star. The ice sublimation temperature is exceeded within $0.05\ a_{\mathrm{bin}}$ (1 au) from the primary.

How temperatures above 1000 K affect dust growth is still unclear other than it does change the collision behavior of dust (Demirci et al. 2017; 2019). The ice line ($t \approx 160$ K) is found to be a crucial location for the early phases of planet formation ([)]drazkowska2017iceline. Therefore, having a cooler disk that contains the ice line inside the disk is beneficial for planet formation. However, unlike around a single star, the companion in a close binary system launches spiral arms through the disk during each binary orbit. The coagulation of pebbles into planetesimals under the effect of repeated shock waves is the least understood phase of planet formation in close binaries (Thebault & Haghighipour 2015).

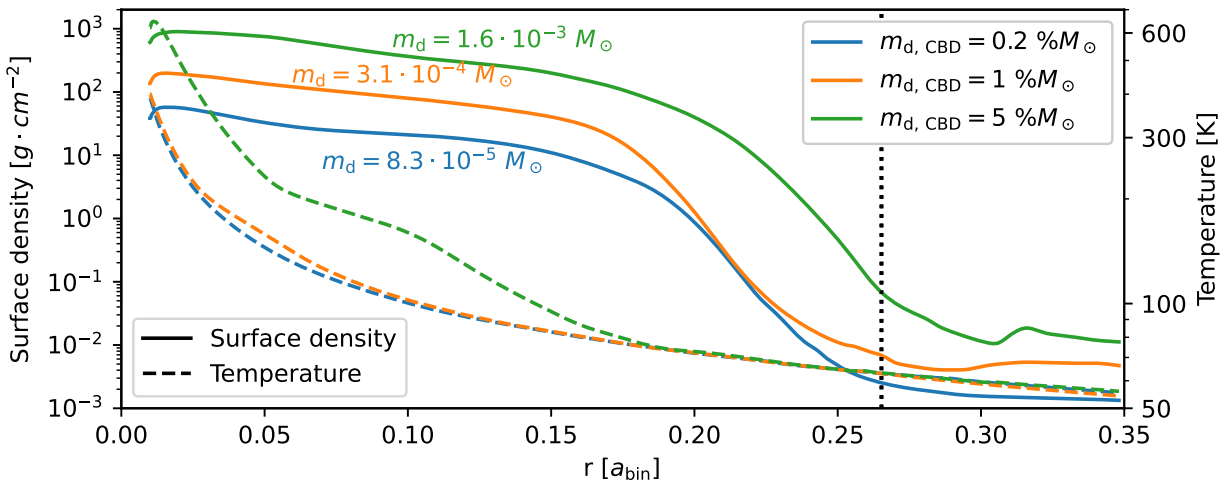

Figure 5.9.1. *Radial profiles of the surface density and temperature of the primary disk for all three mass cases. The profiles are taken at times of low eccentricity.*

Disk dynamics

For the planetesimal growth phase the dynamic of the disk is relevant. While gravitational perturbations affect all planetesimals in the same way, the gas drag depends on the size of the planetesimals. In the case of a circular disk, the companion will excite the eccentricities of the planetesimals which are then damped by the gas. The size dependence of the damping

process, leads to orbital crossings that results in catastrophic collisions between planetesimals of different sizes (Thébault et al. 2006), hindering their growth.

In the case of an eccentric disk, the planetesimals are dragged along the gas and end up with eccentricities that match the eccentricity of the gas disk. This process is again depending on the size of the planetesimals, which is why the eccentricity of the disk and its precession can further increase the collision velocities of planetesimals (Paardekooper et al. 2008).

It has been suggested by Rafikov (2013) that the gravity of the gas disk also plays an important role in the planetesimal growth process. Because the disk gravity is independent of the size of the planetesimals, it can reduce their collision velocities. The effects of the disk gravity have been studied in detail by Rafikov & Silsbee (2015) and used to develop a framework to follow planetesimal growth in a global simulation in Silsbee & Rafikov (2021). It is based on small planetesimals being strongly coupled to the gas disk, causing their eccentricities to match the eccentricity of the gas disk. And large planetesimals being weakly coupled to the gas disk, causing their eccentricities to match the forced eccentricity which is determined by the gravitational perturbations of the companion and the disk. Given the gravity of a static, non-precessing, low eccentric disk that is apsidally aligned to the binary, there exist locations in which the eccentricity of the strongly coupled planetesimals is equal to the eccentricity of the weakly coupled planetesimals. At these locations, planetesimals can grow and planet formation can succeed.

The worst case disk profile for which planet formation can still succeed, given by $\Sigma(r/1\,\mathrm{au}) = 500(r/1\,\mathrm{au})^{-1}$ and $e(r/1\,\mathrm{au}) = 0.02 \cdot r/1\,\mathrm{au}$, is shown in Fig. 5.9.2 by the black lines. Also shown are snapshots from the high mass case during the middle of an eccentricity oscillation (blue lines), see $t = 2708\ t_{\mathrm{bin}}$ in Fig. 5.7.3 and during the following eccentricity minimum (faded blue dashed line). And the high mass case with a sinkhole around the secondary during its quiescent phase (orange lines), see $t = 1750\ t_{\mathrm{bin}}$ in Fig. 5.7.5.

Both disks have higher surface densities but a smaller radius than the lightest density profile that was considered in Silsbee & Rafikov (2021). The eccentricity of the simulation with a secondary disk is oscillating around a value that is 1.5 times higher than the maximum eccentricity which can still allow for planet formation. The quiescent phase of the simulation with a sinkhole around the secondary on the other hand has an eccentricity profile that is well below the eccentricity limit given by Silsbee & Rafikov (2021). Mind however, that the primary disk is in the quiescent phase for slightly less than half of the time and during the rest of the CBD precession period it has a higher mean eccentricity and oscillation amplitude than the simulation with a secondary disk.

The eccentricity of the primary disk oscillates with a period of $60\ t_{\mathrm{bin}} \approx 4000$ yrs, which is comparable to the damping timescale of the eccentricity of the planetesimals (Paardekooper et al. 2008), meaning that the collision velocities of the planetesimals would also oscillate with this period.

The accreting primary disks found in this study are always anti-aligned to the binary orbit. That is, the eccentric bulge (longitude of apastron) points towards the binary pericenter. This

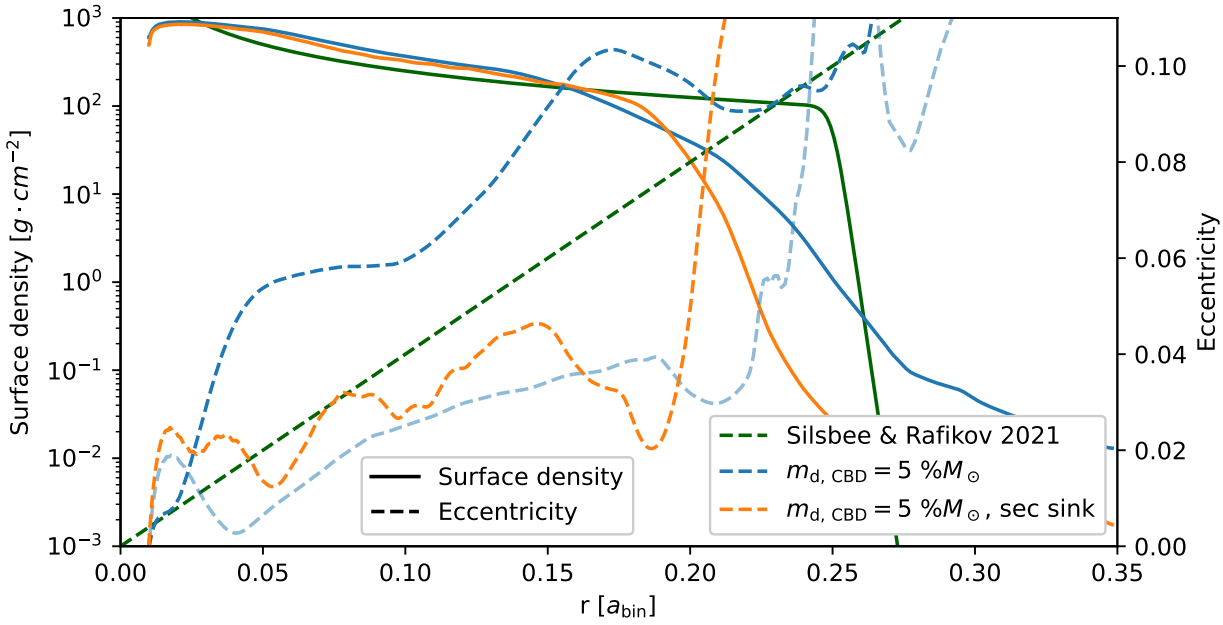

Figure 5.9.2. *Radial profiles of the surface density and eccentricity of the primary disk. Black lines: highest eccentric profiles for which planet formation succeeds from Silsbee & Rafikov (2021).*
Blue line: primary disk profiles from the high mass case. Opaque lines are during the middle of the eccentricity oscillation and the faded line is during the following eccentricity minimum. Orange line: primary disk profiles during the quiescent phase from the simulation with a sinkhole around the secondary.

configuration is found to be unfavorable for planet formation by Silsbee & Rafikov (2021). However, as already noted in their discussion, different studies of disks in close binaries have found different alignments of the disks. The studies cited in Silsbee & Rafikov (2021) consist of Martin et al. (2020), who used the 3D SPH PHANTOM code (Price et al. 2018) and found low eccentric disks that are aligned with the binary orbit and does not precess, and Marzari et al. (2009); Marzari et al. (2012); Müller & Kley (2012); Paardekooper et al. (2008) which all used Zeus-like codes (Stone & Norman 1992). I consider the results of the latter to be unreliable with respect to the disk dynamics due to their low resolutions and small domain sizes, based on the results in Jordan et al. (2021).

5.10 Conclusions & outlook

I conducted 2D non-isothermal simulations to study the interaction between the stellar disks and the circumbinary disk in a close binary system. I found that a massive circumbinary disk with high viscosity ($m_{\mathrm{CBD}} = 5\%\ M_\odot$, $\alpha = 10^{-2}$) can sustain a disk around the primary star with masses of $1.5 \cdot 10^{-3}\ M_\odot$, which is high enough that its gravity can reduce the relative velocities between planetesimals (Silsbee & Rafikov 2021). This also relaxes the time constraint on planet formation in close binaries, because without the mass stream, the primary disk would dissipate in a few 10^5 yrs. It allows for cooler disks that contain the ice line inside the disk while still having enough mass to form massive planets.

Depending on the phase of the circumbinary disk, the mass streams impacting the stellar disks can increase the specific angular momentum of the disk and drive eccentricity growth, or reduce the specific angular momentum and allow the disk to circularize. For the primary disk, the high rate of mass accretion damps the eccentricity and causes the disk to librate around an anti-aligned configuration with the binary.

The size of the secondary disk determines how much of the mass streams of the circumbinary is accreted by the secondary disk, or let through to impact the primary disk. A large secondary disk absorbs most of the mass streams, causing the primary disk to continuously be in a low eccentricity, oscillating state. For a small secondary disk, the influence of the mass streams causes the primary disk to alternate between an oscillating state and a quiescent state with low eccentricity and fixed longitude of periastron.

While the disk mass and low eccentricity are suitable for planetesimal growth, the misaligned configuration of the disk is unfavorable for planet formation. This results in larger initial planetesimal sizes of $d_{p,\,\mathrm{init}} \geq 10$ km required for planetesimal growth to occur (Silsbee & Rafikov 2021).

As the dynamic of the disks cannot be described analytically, the next step could be to place dust particles and planetesimals in the circumbinary disk and measure their relative velocities and movement. Due to the low gas densities at the outer edge of the disk, the inward drift of particles will be slow in that region, potentially leading to an accumulation of particles there.

It should be kept in mind that planet formation also occurs in the circumbinary disk (Coleman et al. 2023, e.g.), which means that the stellar disks could accrete material from all stages of planet formation from the circumbinary disk and thereby jump-start the formation of planets around the individual stars.

There are also many physical processes that are missing from the simulations in this work that could affect the dynamics of the disks and thus the likelihood of planet formation. In Marzari et al. (2009), it was shown that including disk self-gravity can affect the disk eccentricity and precession. In the context of planet-disk interactions (Ziampras et al. 2023), it was shown that in-plane radiative diffusion can change how spiral waves are cooled and deposit their angular momentum in the disk. This means that it also affects the eccentricity and precession of the disk. Including in-plane radiative diffusion causes the disk to behave more similarly to a locally isothermal equation of state. For disks in close binaries, locally isothermal disks are found to have higher eccentricities than disks simulated with the non-isothermal setup used in this work (Marzari et al. 2012; Müller & Kley 2012).

Most important are the effects of simulating in 3D. In the context of cataclysmic variables, it was found that in 3D vertical pressure forces can dampen the eccentricity of the disk (Oyang 2022, Sect. 4). In 3D, disks are also found to precess faster in prograde direction (Smith et al. 2007). And Duffell et al. (2024), Sect. 6.1 also found faster precession rates for the circumbinary disk in 3D compared to 2D.

With the high numerical cost of all three of the mentioned physical processes, a full understanding of the dynamics and interaction of the binary and stellar disks can keep scientists busy for years to come. Nevertheless, from the growing number of detections of flat, coplanar multi-planet systems around the primary star in close binaries[2], it seems evident that planet formation can succeed in such environments. The simulation in this study paints a complex picture of the environment in which these planets form. They demonstrate that understanding the environment beyond the single star is relevant to the disc and thus to planet formation in close binaries, even beyond the system studied here.

[2] See https://exoplanet.eu/planets_binary/ for an up-to-date list of detected S-type planets

6 Parameter study of dwarf nova outburst cycles

In this chapter, I present our paper Jordan et al. (2024), in which we modified our code to simulate dwarf novae. In our simulations, we focused on SU UMa systems and their superoutbursts with their superhumps. Superhumps are interesting features because they are also observed in other close binary systems, such as AM CVn (Boneva et al. 2022) and low-mass X-ray binaries (Chou & Jhang 2023), the former being cataclysmic variables in which the companion star is a helium white dwarf instead of a main sequence star, and the latter being binaries in which mass is transferred to a primary neutron star or black hole. Superhumps are often explained by tidal dissipation in an eccentric precessing disk, called the thermal-tidal instability (TTI) model (Osaki 1989).

But the TTI model has recently fallen out of favor because of superhumps observed in an SU UMa system during a normal outburst in the middle of the outburst cycle (Imada et al. 2012), raising the question of why the outburst did not turn into a superoutburst. Because of observations of superhumps in U Gem (Smak & Waagen 2004), a system above the period gap where the disk is not expected to reach the 3:1 resonance nor become eccentric. And because of discrepancies between theoretical and observed superhump amplitudes (Smak 2020). Instead, a variable mass transfer model is used to explain the superhumps, although the mechanism that could cause such variable mass transfer is unknown (Smak 2009a).

Previous simulations of the superhump phenomena in SU UMa systems used an isothermal equation of state, meaning that the temperature was prescribed, Kley et al. (2008); Smith et al. (2007); Whitehurst (1988). Therefore, these simulations could only probe either the quiescent state or the outburst state. Our paper aimed to improve upon the previous simulations. Advances in the modeling of accretion disks and the increase in computational resources allowed us to simulate dwarf nova systems with higher grid resolutions and more realistic thermodynamics for the gas. We implemented the disk instability model of Mineshige & Osaki (1983) into our code, and since our code was already capable of simulating binary-disk interactions, it could automatically also model the TTI. We used our model to self-consistently simulate full outburst cycles, which to my knowledge has not been achieved before, and compared our results with observations.

All in all, we found better agreement between the TTI model and the observations than the critics assumed. We found stronger gravitational torques (compare Hameury 2020) and larger superhump amplitudes than previous studies, compare Smak (2009). Our simulated shapes of superhumps and their evolution resembled those found in the observations. The simulations also produced several different outburst behaviors found in the observations, simply by varying the companion mass, such as delayed outbursts and long outbursts. While the similarity of our simulated light curves to the observed ones looks convincing, we also found a list of known discrepancies of the current TTI models, which we discuss in detail along with how our model could be improved.

A&A, 689, A354 (2024)
https://doi.org/10.1051/0004-6361/202348726
© The Authors 2024

Astronomy & Astrophysics

Two-dimensional simulations of disks in close binaries

Simulating outburst cycles in cataclysmic variables

L. M. Jordan[1,⋆], D. Wehner[1,2], and R. Kuiper[2]

[1] Institute of Astronomy and Astrophysics, University of Tübingen, Auf der Morgenstelle 10, 72076 Tübingen, Germany
[2] Faculty of Physics, University of Duisburg-Essen, Lotharstraße 1, 47057 Duisburg, Germany

Received 24 November 2023 / Accepted 11 July 2024

ABSTRACT

Context. Previous simulations of cataclysmic variables studied either the quiescence, or the outburst state in multiple dimensions or they simulated complete outburst cycles in one dimension using simplified models for the gravitational torques.
Aims. We self-consistently simulate complete outburst cycles of normal and superoutbursts in cataclysmic variable systems in two dimensions. We study the effect of different α viscosity parameters, mass transfer rates, and binary mass ratios on the disk luminosities, outburst occurrence rates, and superhumps.
Methods. We simulate non-isothermal, viscous accretion disks in cataclysmic variable systems using a modified version of the FARGO code with an updated equation of state and a cooling function designed to reproduce s-curve behavior.
Results. Our simulations can model complete outburst cycles using the thermal tidal instability model. We find higher superhump amplitudes and stronger gravitational torques than previous studies, resulting in better agreement with observations.

Key words. accretion, accretion disks – hydrodynamics – instabilities – binaries: close – stars: dwarf novae – novae, cataclysmic variables

1. Introduction

Dwarf nova outbursts are regularly occurring brightness variations of the gas disk around a white dwarf in cataclysmic variable systems (CVs). CVs are compact systems consisting of a white dwarf whose accretion disk is fed by a Roche-lobe-overfilling companion. They are divided into subclasses based on their outburst characteristics, we refer to Warner (2003) for a comprehensive overview and to Inight et al. (2023) for a more recent and compact overview and observational catalog of these systems.

CVs undergoing dwarf nova outbursts can be separated into two distinct populations by an orbital period gap at around 2.8 h (Schreiber et al. 2024). Assuming typical white dwarf masses of 0.8 $M_\odot$ in CVs (Pala et al. 2022), one can convert the period gap into a mass ratio gap of donor star mass divided by white dwarf mass of $q = M_{\rm don}/M_{\rm wd} \approx 0.3$ (Inight et al. 2023). Below the period gap (at low mass ratios) resides the SU Ursae Majoris (SU UMa) category, which is characterized by two different types of recurring outbursts: Normal outbursts, lasting only for 2–20 days, have amplitudes between 2 and 5 mag, recurrence rates from 10 days to tens of years, and superoutbursts, which are 5–10 times longer and are 0.7, mag brighter, and occur every few normal outbursts. During a superoutburst, smaller brightness variations occur, called superhumps which have periods that are typically slightly larger than the binary period. For systems above the period gap, both superoutbursts and superhumps are rarely observed (Patterson et al. 2005).

To explain the normal outbursts, a thermal disk instability model has been developed based on opacity changes around the ionization temperature of hydrogen and the subsequent transition from a radiative to a convective disk (Meyer & Meyer-Hofmeister 1981). Mineshige & Osaki (1983) noted that a varying α viscosity parameter (Shakura & Sunyaev 1973) from 0.01 during the quiescent phase to 0.1 during the outburst phase is needed to explain the observed cycles. This increase in α is attributed to the magnetorotational instability (MRI) (e.g. Lasota 2001, Sect. 2.4). First discovered by Velikhov (1959), Chandrasekhar (1960) for rotating cylinders and later rediscovered in the context of accretion disks by Balbus & Hawley (1991). However, it was only later confirmed in 3D magnetohydrodynamic (MHD) simulations that effective α values as high as 0.1 can be reached by convection-enhanced MRI (Oyang et al. 2021; Pjanka & Stone 2020). It should be noted that these high α values were obtained in local shearing box simulations and global MHD simulations often find lower values (Oyang et al. 2021; Pjanka & Stone 2020).

Coleman et al. (2016) used the viscosity-temperature relation found in Hirose et al. (2014) in 1D CVs simulations and were able to successfully simulate outburst cycles, but they also found sawtooth-like reflares during their outbursts that are not observed.

In the thermal-tidal disk instability (TTI) (Osaki 1989), superoutbursts are thought to be caused by an increase in the tidal torques when the disk grows to the 3:1 resonance radius during a normal outburst. For SU Uma systems ($q \lesssim 0.3$), the 3:1 resonance is located at ≈0.45 times the binary separation. If the disk grows to this size, it becomes tidally unstable and eccentric (Lubow 1991; Kley et al. 2008). The tidal torques cause the disk to shrink and release additional gravitational energy, which can explain the increased outburst duration and luminosity (Osaki 1989). In this model, the superhump phenomenon is caused by the precession of the eccentric disk (Whitehurst 1988).

⋆ Corresponding author; lucas.jordan@uni-tuebingen.de

Open Access article, published by EDP Sciences, under the terms of the Creative Commons Attribution License (https://creativecommons.org/licenses/by/4.0), which permits unrestricted use, distribution, and reproduction in any medium, provided the original work is properly cited.
This article is published in open access under the Subscribe to Open model. Subscribe to A&A to support open access publication.

Observations of superoutbursts and superhumps in systems well above the period gap such as U Gem are seen as a challenge to the TTI (Smak & Waagen 2004) as the disks are expected to be smaller than the resonances that cause tidal torques. Although more recent observations of U Gem do find features that are consistent with tidal dissipation (Echevarría et al. 2023). In addition, Smak (2009b,a) argued that the TTI fails to explain the magnitude of the superhumps and proposed a superoutburst model based on a varying mass transfer rate from the donor star. However, there are no known mechanisms that can increase the mass transfer rate by several orders of magnitude, which would be required to explain the outbursts without the TTI.

A more recent issue with the TTI is brought up by global inviscid 3D MHD simulations (Ju et al. 2017). They find that angular momentum transport through spiral shocks and MRI produces less eccentric disks than simulations using the α viscosity model with the same effective $\alpha_{\rm eff}$ parameter. This is also confirmed by Oyang et al. (2021). They also explicitly show that the magnetic forces reduce the eccentricity of the disk, opposite to the viscous forces used in the α prescription, which are supposed to approximate the MRI.

However, there are concerns that the MRI is currently not properly resolved in global MHD simulations, resulting in numerical diffusivity that suppresses the MRI and potentially changing its behavior altogether (Nixon et al. 2024).

This work is a continuation of Kley et al. (2008) who were the first to use a grid code to study eccentric disks in close binaries. Using a locally isothermal model with constant kinematic shear viscosity, they studied the eccentricity growth rates of the disk. They found that the viscosity is positively correlated with the eccentricity growth rate and the final equilibrium eccentricity, that the inner boundary condition has a strong effect on the disk eccentricity, and that the mass stream can stabilize the disk and prevent eccentricity growth for low viscosity parameters. The aspect ratio $h = H/r$ (ratio between the scale height of the disk and the distance to the central white dwarf), as an indicator of the pressure forces in the gas, and the tidal interaction with the binary determine the precession rate of the disk, as expected from theoretical models (Goodchild & Ogilvie 2006). Kley et al. (2008) also found that the eccentricity growth rate and equilibrium value are maximized for a specific aspect ratio and decrease for lower or higher aspect ratios. This result is reproduced in similar studies of protoplanetary disks in close binaries (Marzari et al. 2012; Jordan et al. 2021). Following the analysis presented in Lubow (1991), Kley et al. (2008) studied the mode coupling of the binary potential with the disk. By removing the $m = 3$ Fourier mode from the gravitational potential, they showed that it is the dominant but not the only mode driving eccentricity growth. This analysis of the contributions of the individual modes to the eccentricity growth was confirmed and expanded upon in Oyang et al. (2021).

In this study, we conduct two-dimensional vertically non-isothermal hydrodynamical simulations using the α viscosity prescription and a sophisticated equation of state that accounts for the dissociation and ionization of hydrogen, adopted from Vaidya et al. (2015). In addition, we have implemented the cooling function that reproduces the S-shaped equilibrium curve during CVs outbursts by Ichikawa & Osaki (1992) and the α scaling by Ichikawa et al. (1993). We use this code to perform a parameter study on the unknown parameters of the disk instability model and describe their effect on the outburst cycle of CVs.

Our paper is organized as follows: In Sect. 2 we reiterate the thermal tidal instability model, in Sect. 3 we describe our physical model, in Sect. 4 we describe our fiducial model and its outburst cycle, in Sect. 5 we change different parameters, one at a time, and study their effect on the outburst cycle and superhumps, and summarize our results in Sect. 6.

2. Disk instability model

In a cataclysmic variable system, the donor star overflows its Roche lobe, causing mass to be pushed from its surface towards the white dwarf through the inner L_1 point between the two stars (Lubow & Shu 1975). Due to the conservation of angular momentum, the gas starts to form a disk at the circularization radius, and an over-dense ring forms at the outer edge of the disk.

The disk is initially in a cold, radiative state. Due to the viscous heating, the temperature inside the disk increases along with the gas density and eventually exceeds the ionization temperature of hydrogen, causing the opacity to increase. The high opacity prevents the disk from cooling efficiently and causes the disk to become convective and angular momentum transport is increased.

This transition from a cold to a hot state is called thermal instability, which can start either inside the outer density ring or near the white dwarf and expand until the entire disk is in an outburst state. In the outburst state, the angular momentum transport is increased due to the higher temperature. Additionally, the α parameter is also increased, which is necessary to match observations (Mineshige & Osaki 1983; Smak 1984). The beginning of such an outburst can be seen in the first panel in Fig. 1. Due to the increased angular momentum transport during the outburst state, the disk expands and loses mass until the density and temperature in the outer ring drop low enough to revert to the cold state, launching a cooling wave, which sweeps over the disk and resets it to the quiescent state.

In the tidal-thermal instability (TTI) model, the disk expands beyond a critical radius during an outburst (cf. second panel in Fig. 1), which increases the tidal torques acting on the disk. The tidal torques cause eccentricity growth (see third panel) and tidal dissipation which raises the temperature of the disk and prolongs the outburst (Whitehurst 1988; Kley et al. 2008; Oyang et al. 2021). The brightness variations known as superhumps can then be explained by the donor star moving past the bulge of the eccentric, precessing disk.

3. Numerical model

We perform two-dimensional non-isothermal hydrodynamic simulations of a cataclysmic variable system using the α viscosity prescription (Shakura & Sunyaev 1973). The simulations include the circumstellar accretion disk around the white dwarf and the gas transfer stream from the donor star. The system is assumed to be coplanar and the donor star is in a circular orbit around the white dwarf, while both stars are treated as point masses. For the disk, we solve the equations under the assumption of the restricted 3-body problem in the rotating frame of reference of the system, with the origin fixed at the position of the white dwarf. Consequently, gas feels the gravitational potential of the binary system and the indirect force due to the gravitational pull of the donor star on the white dwarf. We neglect the self-gravity of the gas and the gravitational feedback of the gas on the binary system. We use an updated version of the FARGO code (Masset 2000; Baruteau 2008) for our simulations.

The FARGO code is based on the ZEUS2D code (Stone & Norman 1992), which uses an explicit second-order upwind

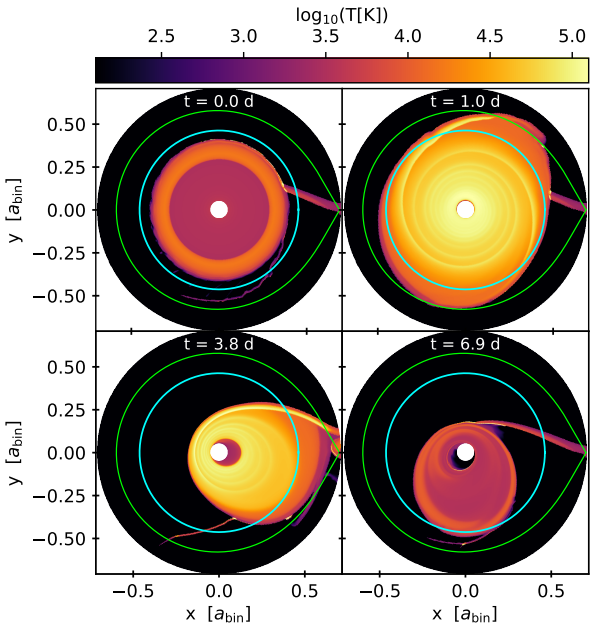

Fig. 1. Two-dimensional snapshots of the mid-plane temperature before and during a superoutburst for our fiducial setup, whose parameters are listed in Table 1. The cyan circle indicates the 3:1 resonance and the green line indicates the Roche lobe. The time in days is measured from the beginning of the outburst and one day is equal to 14.1 binary orbits (1.7 h). The simulation ran in a corotating reference frame, with the donor star fixed on the right side.

scheme on a staggered grid for advection and an operator splitting technique to solve the source terms of the Navier-Stokes equations. All derivatives are first order in space and time. To improve the treatment of shocks in the used upwind scheme, we apply the artificial viscosity by Tscharnuter & Winkler (1979) to ensure the correct jump conditions through the shock front and the correct shock velocity. The scale height of the gas is computed from the gravity of both stars (compare Günther et al. 2004) and we reduce the viscosity of specific cells at the outer edge of the disk for numerical stability. Test cases and the implementation of all the modules we use are described in detail in Rometsch et al. (2024). The code and our fiducial setup are publicly available under AGPLv3 on github[1].

3.1. Physical basics

The code solves the vertically integrated hydrodynamic equations in polar coordinates (r, ϕ) in the mid-plane ($z = 0$). The coordinate system is centered on the white dwarf and in the corotating frame of reference of the binary. The gas velocity is given as $\boldsymbol{v} = (v_r, r\Omega)$, where omega is the angular velocity in the corotating frame. We used the standard momentum equations and refer to Rometsch et al. (2024) for details on the implementation. The energy equation is given by

$$\frac{\partial e}{\partial t} + \nabla \cdot (e\boldsymbol{v}) = -P\nabla \cdot \boldsymbol{v} + Q_+ - Q_-, \tag{1}$$

where e is the vertically integrated internal energy density, P the vertically integrated pressure, $\boldsymbol{v}$ the gas velocity and Q_+ and Q_- are the heating and cooling source terms.

[1] https://github.com/rometsch/fargocpt

We used a non-perfect ideal equation of state (EoS) that accounts for hydrogen ionization and dissociation. The implementation of this EoS follows Vaidya et al. (2015). It uses multiple adiabatic indices to relate thermodynamic quantities. The effective adiabatic index $\gamma_{\rm eff}$ relates the vertically integrated pressure P to the internal energy density e:

$$P = \frac{R\Sigma T_{\rm mid}}{\mu} = (\gamma_{\rm eff} - 1)e, \tag{2}$$

where $R = k_{\rm B}/m_{\rm H}$ is the specific gas constant, Σ is surface density, $T_{\rm mid}$ is the mid-plane temperature, and μ is the mean molecular weight. The temperature inside the cell is assumed to be vertically isothermal and is labeled as $T_{\rm mid}$ to distinguish it from the brightness temperature $T_{\rm eff}$ at the surface of the disk. The relation for the speed of sound, using the first adiabatic index Γ_1, is given by

$$c_s = \sqrt{\frac{\Gamma_1 P}{\Sigma}}, \tag{3}$$

where Σ is the surface density. The gas is heated by viscous heating due to shear viscosity and shock dissipation due to artificial viscosity:

$$Q_+ = \frac{1}{2\nu\Sigma}\left[\sigma_{rr}^2 + 2\sigma_{r\phi}^2 + \sigma_{\phi\phi}^2\right] + \frac{2\nu\Sigma}{9}(\nabla\boldsymbol{v})^2 + Q_{\rm art}, \tag{4}$$

where σ_{ij} are the coefficients of the viscous stress tensor in polar coordinates, $\nu = \alpha H c_s$ is the kinematic shear viscosity according to Shakura & Sunyaev (1973), $Q_{\rm art}$ is the shock heating due to our artificial viscosity, which is implemented as an artificial pressure (see Appendix B Stone & Norman 1992) and behaves the same as bulk viscosity. We use an artificial viscosity constant of $\sqrt{2}$ in all our simulations and the only sources of shocks, where shock heating will be active, are the spiral waves due to the interaction with the binary potential and the impact of the gas stream on the disk.

In our early tests, we found that a constant $\alpha_{\rm cold}$ parameter tended to produce outbursts that start inside and move outward, with outside-in outbursts only occurring in simulations with high mass transfer rates. However, observations show that many outbursts are outside-in (Vogt 1983). We have therefore copied the solution of Ichikawa et al. (1993) for this problem and used a varying $\alpha_{\rm cold}$ for all simulations in this work:

$$\alpha_{\rm cold} = \alpha_{\rm cold,0}\left(\frac{r}{r_0}\right)^{0.3} \tag{5}$$

with $\alpha_{\rm cold,0} = 0.01$–$0.04$, which is in the range deduced from the recurrence times from observations $\alpha \lessapprox 0.01$ (Cannizzo et al. 2012) and more recent MRI simulations $\alpha \approx 0.03$ (Hirose et al. 2014; Scepi et al. 2018). An outwardly increasing α parameter is supported by the observations of Mineshige & Wood (1989).

By fitting a viscous model to observational data, Kotko & Lasota (2012) found that the alpha viscosity parameter should be of the order of $\alpha_{\rm hot} \approx 0.1$–$0.2$.

The increase in angular momentum transport as the disk transitions from the quiescent to the outburst state was modeled by a temperature-dependent α parameter, which changes smoothly from $\alpha_{\rm cold}$ to $\alpha_{\rm hot}$ for increasing temperatures and vice versa for decreasing temperatures. We followed the approach of Ichikawa & Osaki (1992), where α is given by

$$\log\alpha = \log\alpha_{\rm cold} + \frac{1}{2}(\log\alpha_{\rm hot} - \log\alpha_{\rm cold})\left[1 - \tanh\frac{4 - \log T_{\rm mid}/{\rm K}}{0.4}\right], \quad (6)$$

where $T_{\rm mid}$ is the mid-plane temperature in Kelvin, the transition between $\alpha_{\rm cold}$ and $\alpha_{\rm hot}$ occurs around $T_{\rm mid} = 10^4$ K. For cooling, we used the prescription from Ichikawa & Osaki (1992). The model divides the cooling function into a cold radiative branch, a hot convective branch, and an intermediate branch. For the cold branch, they used opacities based on Cox & Stewart (1969) and a flux of

$$F = \tau\sigma_{\rm SB}T_{\rm mid}^4$$

for the optically thin regime to derive the radiative flux through the surface of the disk:

$$\log F_{\rm cool} = 9.49\log T_{\rm mid} + 0.62\log\Omega + 1.62\log\Sigma + 0.31\log\mu - 25.48, \quad (7)$$

where τ is the optical depth, $\sigma_{\rm SB}$ is the Stefan-Boltzmann constant. For this formula, all quantities are given in cgs units. The cold branch applies to temperatures $T_{\rm mid} < T_A$, where T_A is the temperature at which

$$\tau\sigma T_A^4 = F_{\rm cool}(T_A) = F_A. \quad (8)$$

The radiative losses of the hot branch were derived using a one-zone model for an optically thick disk:

$$F = \frac{16\sigma T_{\rm mid}^4}{3\kappa\rho H}. \quad (9)$$

Using Kramer's law for the opacity of ionized gas, the radiative flux through the surface of the disk can be approximated as

$$\log F_{\rm hot} = 8\log T_{\rm mid} + \log\Omega + 2\log\Sigma + 0.5\log\mu - 25.49, \quad (10)$$

where again this expression is in cgs units. The hot branch is valid for temperatures $T_{\rm mid} > T_B$, where T_B is the temperature at which

$$F_{\rm hot,c}(T_B) = F_B \quad (11)$$

where $\log F_B/[{\rm erg\,s^{-1}\,cm^{-2}}] = K(r)$ is an approximation for the flux at the start of the hot branch based on Fig. 3 in Mineshige & Osaki (1983):

$$K(r) = 11 + 0.4\log\left[\frac{2\cdot 10^{10}\,{\rm cm}}{r}\right]. \quad (12)$$

The radiative losses in the intermediate branch are given by an interpolation between the hot and cold branches:

$$\log F_{\rm int} = (\log F_A/[{\rm erg\,s^{-1}cm^{-2}}] - K(r))\log\frac{T_c}{T_B}/\log\frac{T_A}{T_B} + K(r). \quad (13)$$

This interpolation formula is only valid for $F_B > F_A$, cases where $F_B < F_A$ are handled by setting $F_B = F_A$ and $F_{\rm int} = F_A$. The radiative losses due to surface cooling are then given by $Q_{\rm cool}^{\rm TI} = 2F$ where F is the radiative flux pieced together from the cool, intermediate, and hot branches as described above.

The surface cooling inside the intermediate branch has a weaker dependence on the disk temperature than the viscous heating of Eq. (4). If the disk enters the intermediate branch from the cold branch, it will heat up faster the hotter it is, leading to runaway heating. If the disk enters the intermediate branch from the hot branch, it will cool faster the colder it is, resulting in runaway cooling. This is the intended effect of the cooling prescription used in disk instability models, as it leads to outbursts and subsequent return to quiescence. It also allows us to predict the conditions necessary to start an outburst by looking at Eq. (7). The mean molecular weight and the gas temperature are self-consistently solved in the code, leaving only the surface density and the angular velocity as parameters that can trigger an outburst. For this reason, studies of the disk instability model often define a critical surface density at which an outburst is triggered. The critical surface density can also be converted into a critical temperature by a heating model and into a critical mass accretion rate by an angular momentum transport model (Lasota et al. 2008).

Since the white dwarf mass is fixed in our study, the critical surface density of our model is only a function of the distance to the white dwarf through $\Omega \propto r^{-3/2}$, meaning that at larger radii higher surface densities and higher temperatures are needed to trigger an outburst. Physically, this dependence of the model is explained by the fact that the outburst starts with the onset of convection in the disk (Meyer & Meyer-Hofmeister 1981), which depends not only on the opacity of the gas, but also on the vertical gravity, for which the white dwarf is the dominant source.

The cooling prescription from Ichikawa & Osaki (1992) was developed for conditions inside the accretion disk, and we found that it is not suitable to handle the low-density regions outside the truncation radius. Therefore, we used a different cooling technique at low densities:

$$Q_- = \begin{cases} Q_{-,\rm TI}, & \Sigma > 2.0\frac{\rm g}{\rm cm^2} \\ Q_{-,\rm rad}, & \text{else} \end{cases}. \quad (14)$$

where $Q_{-,\rm rad}$ is the surface cooling according to Hubeny (1990) with the opacity table from Lin & Papaloizou (1985). The change of the cooling prescription is done only for numerical stability reasons and has a negligible effect on the overall simulation.

Fig. 2 shows a comparison of the model from Ichikawa & Osaki (1992) for our fiducial parameters with the more recent values from MRI simulations (Scepi et al. 2018). The top panel shows the thermal equilibrium curve for which the models agree near the instability (at $\Sigma \approx 200\,{\rm g/cm^2}$) and in qualitative agreement further away from the instability. The bottom panel shows the α parameter as a function of the mid-plane temperature. Here, the models are in good agreement in the cold state and during the transition to the hot state. After the transition to the hot state, shearing box MRI simulations find that the turbulence becomes weaker again. This is thought to happen because the opacity in the ionized state is given by Kramers law $\kappa \propto T^{-7/2}$, which decreases with increasing temperature, quenching the convection (Hirose et al. 2014; Scepi et al. 2018). We also ran simulations with the MRI-based α prescription from Coleman et al. (2016), but found reflares after the outbursts. We chose the bimodal α prescription over the MRI-based one because it more accurately reproduces observations where reflares are uncommon. For a discussion of these different α prescriptions, we refer to Coleman et al. (2016).

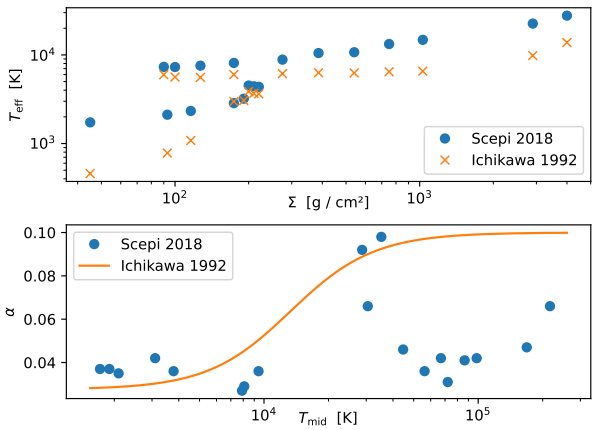

Fig. 2. Top panel: thermal equilibria [$T_{\rm eff}$] vs. [Σ] from the shearing box simulations in Scepi et al. (2018) (data taken from their Table 1) and the model from Ichikawa & Osaki (1992) for the same input parameters. Bottom panel: the measured α parameters in Scepi et al. (2018) and the interpolation function Eq. (6) as a function of the mid-plane temperature.

3.2. Numerical considerations

We used a fixed white dwarf mass of $M_{\rm wd} = 0.765\,M_\odot$ and a fiducial mass of $M_{\rm don} = 0.092\,M_\odot$ for the donor star. This gives us a fiducial mass ratio of $q = M_{\rm wd}/M_{\rm don} = 0.12$ and an inner Lagrange L_1 point at $L_1 = R_{\rm max} = 0.7a_{\rm bin}$, which we used as the outer radius of our simulation domain. We then changed the mass ratio by changing the mass of the donor star while adjusting the outer radius of the domain accordingly. The minimum radius of our domain is always $R_{\rm min} = 0.05\,a_{\rm bin} \approx 2.2 \cdot 10^9$ cm and was chosen for legacy reasons and the high computational cost of reducing it. The inner radius is three times the radius of the white dwarf, assuming a radius of $R_{\rm wd} = 0.73 \cdot 10^9$ cm (Mathew & Nandy 2017). Our inner radius could be interpreted as the radius within which the disk is rapidly emptied by magnetic winds. Magnetic winds produce a roughly constant inner radius, while optical winds are not expected to truncate the disk during the outburst state (Tetarenko et al. 2018). According to Scepi et al. (2019), the radius of the magnetic wind-dominated region is

$$r_\mu = 1.9 \cdot 10^9 \mu_{30}^{4/7} \dot{M}_{16}^{-2/7} M_1^{-1/7}, \tag{15}$$

where $\mu_{30} = \mu/(10^{30}\,{\rm G\,cm^3})$, $\dot{M}_{16} = \dot{M}_{\rm tr}/10^{16}\,{\rm g\,s^{-1}}$ $M_1 = M_{\rm wd}/M_\odot$. Assuming an average mass accretion rate equal to our fiducial mass transfer rate of $\dot{M}_{\rm tr} = 1.5 \cdot 10^{-10}\,{\rm M_\odot/yr} \approx 10^{16}\,{\rm g\,s^{-1}}$, we find a magnetic dipole moment of $1.2\mu_{30}$ for our inner domain radius. The dipole moment can be translated into a magnetic field strength of $B = \mu R_{\rm wd}^3 \approx 3$ kG, which is a weak magnetic field for a white dwarf (Landstreet et al. 2016).

We initialized all of our models with a constant surface density of $\Sigma_0 = 8.7\,{\rm g\,cm^{-2}}$ throughout the domain. This results in an initial disk mass of $M_{\rm d} = 2 \cdot 10^{-11} M_{\rm wd} \approx 3 \cdot 10^{22}$ g, which is roughly the disk mass after a superoutburst for our fiducial model. For numerical stability, we used a density floor of $\Sigma_{\rm floor} = 10^{-8} \cdot \Sigma_0$ as the minimum surface density for the simulation. If a cell fell below this surface density, it was reset to the floor value. Similarly, we used a temperature floor of 10 K and a temperature ceiling of $3 \cdot 10^5$ K. All cells outside the tidal truncation radius are typically at the density floor at all times, but we did not notice any cells reaching either the temperature floor or the temperature ceiling.

3.3. Analysis

All disk quantities were measured as snapshots during the simulation at a rate of 100 times per binary orbit. In this section we define the disk quantities used in the evaluation which consist of eccentricity, longitude of pericenter, luminosity, mass, radius, aspect ratio, and the torque exerted by the gas on the donor star. In addition to these quantities, we have also tracked the mass leaving through the inner and outer boundaries during our simulations.

For specific time frames of the fiducial model, we measured the gravitational torque density using the formula by Miranda et al. (2017):

$$\frac{{\rm d}T_{\rm grav}}{{\rm d}r} = -\int r\Sigma \frac{\partial \Phi}{\partial \varphi} {\rm d}\varphi \tag{16}$$

where Φ is the smoothed gravitational potential of the binary system in the frame of the white dwarf:

$$\Phi = -\frac{GM_{\rm wd}}{|\mathbf{r} - \mathbf{r}_{\rm wd}| + \epsilon} - \frac{GM_{\rm don}}{|\mathbf{r} - \mathbf{r}_{\rm don}| + \epsilon} - GM_{\rm don} \frac{\mathbf{r}_{\rm wd} - \mathbf{r}_{\rm don}}{|\mathbf{r}_{\rm wd} - \mathbf{r}_{\rm don}|^3} \cdot \mathbf{r}, \tag{17}$$

where G is the gravitational constant, $\epsilon = 0.6\,H$ is the gravitational smoothing length (Müller et al. 2012), and H is the disk scale height. The last term in the potential is the indirect term caused by the donor star accelerating the white dwarf.

The torque Γ_z exerted by the disk on the donor star, which was monitored during all simulations, is calculated in Cartesian coordinates as follows

$$\Gamma_z = M_{\rm don} \left[\mathbf{r}_{\rm don} \times \int G\Sigma \frac{\mathbf{r} - \mathbf{r}_{\rm don}}{\sqrt{|\mathbf{r} - \mathbf{r}_{\rm don}|^2 + \epsilon^2}^3} {\rm d}x\,{\rm d}y \right] \cdot \hat{e}_z. \tag{18}$$

Note that this torque is only measured, not applied to the stars. Compared to the torque exerted on the disk by the binary, this torque has the opposite sign and does not take into account the effects of the indirect term on the gas. For this reason, we made only a qualitative evaluation of the donor star torque.

The disk luminosity is computed by integrating the radiative losses Q_- from Eq. (14) over the surface of the disk:

$$L_{\rm d} = \int\int Q_- r\,{\rm d}\varphi {\rm d}r. \tag{19}$$

We have noticed several luminosity peaks in our data. We believe that these are caused by numerical instabilities at the outer edge of the disk, where strong density gradients occur. Therefore, we have replaced individual exceptionally bright data points with the average of the two neighboring points.

If the luminosity gradient at the top of a luminosity peak was exceptionally high, we removed the data points from our dataset, up to a maximum of five data points per luminosity peak. This only affected a few superhumps at the beginning of a superoutburst.

We calculated the effective temperature, or brightness temperature, of a gas cell as

$$T_{\rm eff} = \left[\frac{Q_-}{2\sigma_{\rm SB}} \right]^{1/4}, \tag{20}$$

and used this temperature to compare against the brightness temperatures measured from observations.

The eccentricity of the disk and the longitude of pericenter ω_d are calculated as a mass-weighted average. We used the same formulation as in previous studies (e.g. Kley et al. 2008):

$$e_d = \frac{1}{M_d} \int \int e \Sigma r \, d\varphi dr, \tag{21}$$

where M_d is the total disk mass:

$$M_d = \int \int \Sigma r \, d\varphi dr. \tag{22}$$

Our disk radius is defined as the radius of the ring containing 99% of the total disk mass when the mass is integrated from the innermost to the outermost ring.

For the evaluation, we used only data starting after the first outburst to remove the effects of our initial conditions. We used smoothing to reduce the noise in spontaneously measured quantities such as disk eccentricity, longitude of periastron, the aspect ratio, or the disk radius, which oscillate on timescales of the binary period. The quantities were smoothed in two passes. The first pass smoothed the quantities with a Hamming window two binary periods wide, and the second pass with a window one binary period wide.

3.4. Boundary conditions

We used strict outflow boundaries at the inner boundary and strict outflow boundaries at the outer boundary, except for the small region around the Lagrange $L1$ point where the mass inflow stream originates. At each boundary, the azimuthal velocity was always set to the pressure-supported Keplerian velocity:

$$v_\varphi = \sqrt{\frac{GM_{wd}}{r}(1 - h^2)}, \tag{23}$$

where $h = 0.002$ was assumed to be constant, which is the aspect ratio we typically find in our simulations during the quiescence state. The energy and surface density were set to zero gradient conditions and the radial velocity was zero gradient for outflow from the domain and zero for inflow.

We computed the width of the mass stream using the approximation function in Warner (2003, Sect. 2.4.1), assuming a stream temperature of $T_{stream} = 1500K$. We then smoothed the mass stream with a Gaussian profile over three times its width. We have found that the initial stream width and temperature are unimportant, since both quickly reach a new equilibrium upon entering the simulation domain. Identical to Kley et al. (2008), we set the initial radial velocity of the mass stream to be $2 \cdot 10^{-3} \, v_K(a_{bin})$, where $v_K(a_{bin})$ is the Keplerian velocity of the donor star. Then we set the surface density to a value that produces the desired mass inflow rate $\dot{M}_{tr}$.

We ran one simulation with a variable mass flow rate from the donor star, using the prescription by Hameury et al. (2000). It is supposed to model the increase in mass transfer due to the illumination of the donor star by the disk and the accretion luminosity of the white dwarf during the outburst. While there is observational support for an increase in mass transfer by a factor of two during outbursts (Smak 1995), models on irradiation of the donor star do not agree on the increase in mass transfer, see Osaki & Meyer (2004) or Viallet & Hameury (2008) and Cambier (2015). Following Hameury et al. (2000), we based the mass transfer rate on the accretion rate of the white dwarf:

$$\dot{M}_{tr} = \max(\dot{M}_0, \; b\dot{M}_{acc}), \tag{24}$$

where b is a free parameter for which we used 0.5 (Hameury et al. 2000). To reduce the noise in the white dwarf mass accretion $\dot{M}_{acc}$, we computed the current mass accretion as an exponentially weighted moving average:

$$\dot{M}_{acc} = \frac{\Delta M_{acc}}{dt} \cdot c + (1 - c)\dot{M}_{acc}^{old} \tag{25}$$

where dt is the timestep length, ΔM_{acc} is the mass that has left the domain through the inner boundary during the timestep, and $c = dt/t_{avg}$ where $t_{avg} = 10T_{bin}$ and $\dot{M}_{acc}^{old}$ is the mass accretion rate from the previous step.

3.5. Boundary test

In this section, we present a locally isothermal model to evaluate our choice of boundary conditions. The disk is initialized with a mass of $M_d = 2 \cdot 10^{-11} M_{wd}$ and mass transfer is disabled. The model used a constant aspect ratio of $h = 0.03$ and a constant viscosity parameter of $\alpha = 0.1$ to model a disk in the outburst state. The setup is similar to the one used in Kley et al. (2008) and therefore the disk eccentricity is expected to grow exponentially until the growth is balanced by mass ejection from the outer disk. The equilibrium eccentricity is determined by the aspect ratio and the viscosity parameter (Kley et al. 2008). We used strict outflow conditions at the inner and outer boundaries for the fiducial model.

In addition to the outflow conditions at the inner boundary, we tested the effect of reflecting inner boundary conditions and wave damping at the inner boundary by damping the azimuthal velocity and surface density to the azimuthally averaged values using the damping prescription by de Val-Borro et al. (2006) on damping time scales of 10^{-1}, $3 \cdot 10^{-2}$, and 10^{-2} orbital periods at the radius of the inner boundary. We also tested a viscous outflow condition where the surface density was set to zero gradient and the radial velocity to a constant times the viscous speed:

$$v_r = -\frac{3}{2} s \frac{\nu_{kin}}{R_{min}}, \tag{26}$$

where ν_{kin} is the kinematic shear viscosity and $s = 0.2, 15$.

We also ran another test with mass transfer and another test where we moved the outer outflow boundary to $6\,a_{bin}$ and applied wave damping inside the 3–$6\,a_{bin}$ by damping the azimuthal velocity to the azimuthally averaged value, and the surface density and radial velocity to zero on a damping timescale of 10^{-1} orbital periods at the distance of the outer domain radius.

The time evolution of the mass-averaged disk eccentricity for all the different boundary conditions are shown in Fig. 3. The outer boundary conditions affect the growth rate and the time at which the eccentricity growth starts, but do not affect the equilibrium eccentricity. The simulation with the mass transfer stream starts its eccentricity growth at the beginning of the simulation. Its eccentricity grows faster than in the reference case without mass transfer. Similar results were found in Kley et al. (2008), but in our case the eccentricity growth is increased even more.

To compare the results, we define the start of eccentricity growth as the first time the eccentricity reaches 0.05 and the duration of eccentricity growth as the time it takes for the eccentricity to grow from 0.05 to 95% of its equilibrium value. Using these definitions, we find that eccentricity growth starts at $10\,T_{bin}$ for the simulation with mass stream, and its growth time is $42\,T_{bin}$. The simulation with the outer boundary at $6\,a_{bin}$ has a similar eccentricity growth time, $43\,T_{bin}$, but starts its growth at $26\,T_{bin}$. Both simulations eventually reach the same equilibrium eccentricity as the reference simulation. Simulations with

the outer boundary at the inner L_1 point all start their eccentricity growth around 32 $T_{\rm bin}$ with growth times ranging from 46 to 73 $T_{\rm bin}$ depending on the equilibrium eccentricity.

For the value of the equilibrium eccentricity, we find three distinct groups, depending on the inner boundary condition, with a representative of each group shown in Fig. 4. For evaluation, we used the radial profile of the azimuthally mass-averaged eccentricity (solid lines) and the azimuthally averaged surface density (dashed lines). All profiles were averaged over 20 snapshots taken between 140 and 160 binary periods.

The reflecting inner boundary simulation leads to a high density at the inner boundary, which then decays outward with a power-law profile until it is tidally truncated by the companion. We also find that the disk has a retrograde precession, which we attribute to the increased pressure forces due to the strong density gradient. The eccentricity is zero at the inner boundary and grows slowly with increasing radius, and the total disk eccentricity is the lowest of all our simulations. The same behavior was already found in Kley et al. (2008), except that in their study the simulation with the outflow boundary had the lowest eccentricity. We found similar results for the simulation with viscous outflow $s = 0.2$ and damping conditions with a damping time scale of $\tau = 10^{-2}$ orbital periods.

The simulation with a damping timescale of $\tau = 10^{-1}$ orbital periods, as well as the simulation with the viscous outflow with $s = 15$ has a constant radial surface density profile towards the inner region and a prograde precession. The eccentricity is still forced to zero at the inner boundary, but quickly rises to a high value that remains almost constant throughout the disk. The average disk eccentricity is the highest for our locally isothermal test runs.

The simulations with outflow at the inner boundary develop an inner eccentric hole as seen in Fig. 1 or by the density drop in Fig. 4. The disk also has a prograde precession. This is the only boundary condition that does not force the eccentricity to zero. The eccentricity at the inner boundary is high, but then drops to a lower level for the rest of the disk. The average disk eccentricity is lower than for the damped inner boundary, but still higher than for the reflecting boundary condition. The simulations with mass transfer stream or damping at the outer boundary have the same precession rate and produce the same radial profiles as the simulation with only outflow at the outer boundary.

Finally, we repeated the simulation with the outflow at the inner and outer boundaries, but with a reduced inner radius of $0.0167\,a_{\rm bin}$, one third of the fiducial inner radius and equal to a typical white dwarf radius of $R_{\rm wd} = 7.3 \cdot 10^9$ cm. For the smaller inner radius we find an equilibrium eccentricity of 0.5, 6% higher than for the fiducial inner radius ($e = 0.47$), and a prograde precession rate of $0.068 P_{\rm bin}^{-1}$, 33% slower than for the fiducial model ($\dot{\omega} = 0.101 T_{\rm bin}^{-1}$). Higher eccentricity and faster retrograde precession are also found by Jordan et al. (2021) for smaller inner radii with a reflective inner boundary condition. We conclude that the outer boundary affects the eccentricity growth, but not the equilibrium eccentricity. From the boundaries tested, the mass transfer stream seems to have a stronger effect than moving the boundary outward and adding wave-damping regions at the outer boundary. Because the mass transfer is implemented as a boundary condition, the outer domain radius must be located at the inner L_1 point for the mass transfer stream to work. Therefore, we cannot test the effect of both mass transfer and a larger outer domain radius at the same time. We therefore assume that both effects are independent and the effect of a larger outer domain radius is less relevant while the mass transfer stream is active.

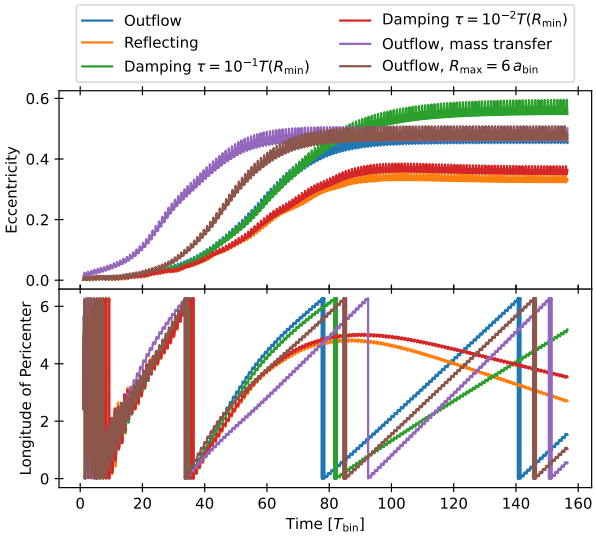

Fig. 3. Top panel: Disk eccentricity evolution for locally isothermal models with different boundary conditions. Bottom panel: Time evolution of the longitude of pericenter of the disk in radians.

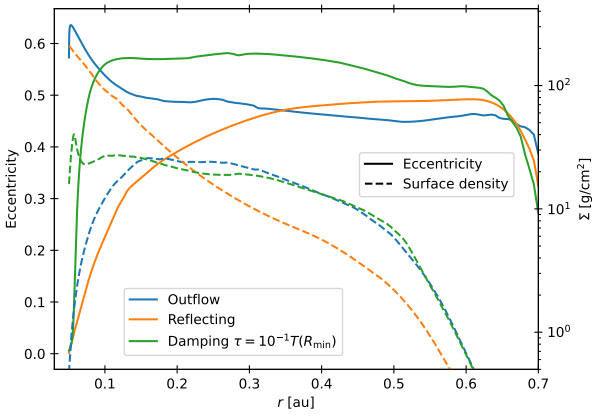

Fig. 4. Radial profiles of mass-weighted azimuthally averaged disk eccentricity and azimuthally averaged surface density. All profiles were also averaged over 20 simulation snapshots from simulation times 140 to 160 binary periods.

It has been previously shown that the inner boundary has a significant influence on the outburst behavior of dwarf novae (Kley et al. 2008; Hameury & Lasota 2017; Scepi et al. 2019). Here we have shown that by using a damping zone near the inner boundary or by imposing a radial outflow velocity, one can smoothly transition from an outflow boundary that produces a prograde precessing disk to a reflective boundary that produces a retrograde precessing disk with lower eccentricity by adjusting either the damping timescale or the outflow velocity. Since we used different boundary conditions and obtained the same results, we conclude that the effects of the boundaries are due to the physical conditions they impose on the disk, and that the effects of numerical oscillations that occur when the boundaries are implemented using the primitive variables instead of the characteristic variables, as discussed in Godon (1996), are negligible.

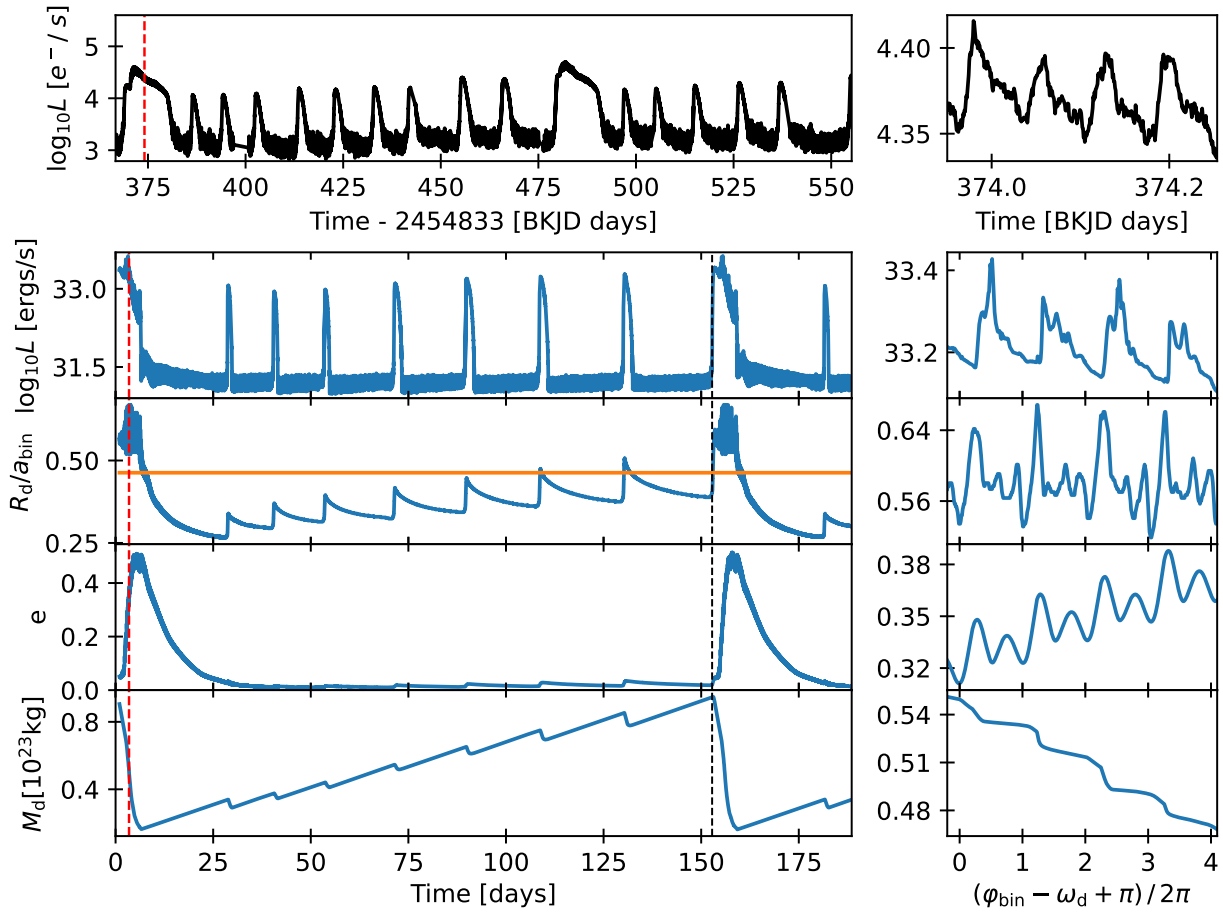

Fig. 5. The upper panels show Kepler data of V1504 Cygni over an equal length time frame as the simulated data below. The binary period is 1.7 hours, and one day is equal to 14.1 binary periods. The extent of the y-axis in the left panel is the same as in the plot below, but in the right panel, the extent of the y-axis is reduced by a factor of 3.8 compared to the plot below. Bottom left panel: Luminosity, disk radius, eccentricity, and total mass as a function of time for the fiducial model. The orange line indicates the 3:1 orbital resonance radius. The red dashed line indicates the time at which the right panel is zoomed in and the black dashed line indicates the start of the second superoutburst. Bottom right panel: Zoom in on the same quantities during a superoutburst as a function of the longitude of pericenter of the disk relative to the position of the binary. The angles are shifted by π and normalized so that integer values indicate that the binary passes the bulge of the eccentric disk.

4. Fiducial model

We adopted the physical parameters of the SU UMa dwarf nova system V1504 Cygni (Coyne et al. 2012) for our fiducial model. This system has been observed for a long period of time by the Kepler telescope and its light curves are well studied (Cannizzo et al. 2012; Osaki & Kato 2014). We acquired the Kepler data via the Python package *Lightkurve* (Lightkurve Collaboration 2018; Astropy Collaboration 2022). For the mass transfer rate, we choose a fiducial value of $1.5 \times 10^{-10}\,M_\odot/\mathrm{yr} \approx 10^{16}\,\mathrm{g/s}$ which is within the range of transfer rates estimated from observations of dwarf novae systems below the period gap (Dubus et al. 2018). In these systems, mass transfer is thought to be caused by the loss of angular momentum of the binary due to gravitational radiation. For our fiducial mass ratio, we chose a value of $q = 0.12$, which is at the lower end of the estimates for V1504 Cygni by Coyne et al. (2012). The combination of mass transfer rate and mass ratio used in the fiducial model was chosen to produce an outburst supercycle comparable to observations of V1504 Cyg. The parameters for the fiducial model are summarized in Table 1. In Figure 5, we present several disk quantities over time for the fiducial model for the duration of a supercycle and the light curve of V1504 Cygni during a time frame with the same duration. The light curve shows a sequence of normal outbursts between two superoutbursts. Our simulated outburst amplitudes are generally larger than those observed. We have confirmed that this is due to our choice of cooling model, which we discuss at the end of this paper. We believe that this is caused by the low cooling on the hot branch of our model (Eq. (10)) leading to too high mid-plane temperatures. We see the effects of this several times throughout this paper.

Except for the first normal outburst after a superoutburst, successive normal outbursts increase in amplitudes, outburst duration, and duration of the quiescent phase. The density distribution of the disk after a superoutburst is affected by the ringing down from the highly eccentric state that developed during the superoutburst to the circular state during the quiescent phase. This effect is highlighted in Fig. 7 and leads to higher densities inside the disk. The additional mass inside the disk increases the outburst luminosity. This causes the first normal outburst after a

Table 1. Parameters of the fiducial model.

System parameters:	
$M_{\rm wd}$	$0.765\,{\rm M}_\odot$
$M_{\rm don}$	$0.092\,{\rm M}_\odot$
q	0.12
$a_{\rm bin}$	$0.684\,{\rm R}_\odot$
$P_{\rm bin}$	1.7 h
$\dot{M}_{\rm tr}$	$1.5 \times 10^{-10}\ \frac{\rm M_\odot}{\rm y}$
Viscosity:	
$\alpha_{\rm cold}$	$0.02 \cdot (\frac{r}{0.28\,{\rm R}_\odot})^{0.3}$
$\alpha_{\rm hot}$	0.1
Grid:	
$R_{\rm min} - R_{\rm max}$	0.05–$0.703\,{\rm R}_\odot$
$N_r \times N_\varphi$	450×1070

Notes. The parameters are chosen to resemble the ones found for the System V1504 Cygni (Coyne et al. 2012).

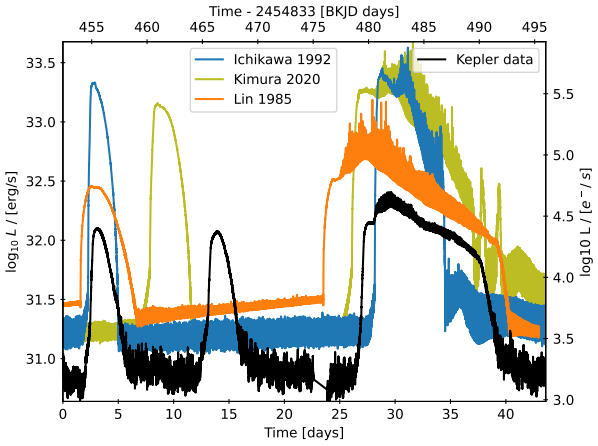

Fig. 6. Comparison of the luminosity curves for the fiducial model using the cooling prescription from Ichikawa & Osaki (1992) (blue line), the revised version of that cooling prescription from Kimura et al. (2020) (yellow line) and a model using surface cooling with opacities from (Lin & Papaloizou 1985) (orange line) as well as Kepler data of V1504 Cygni (black line).

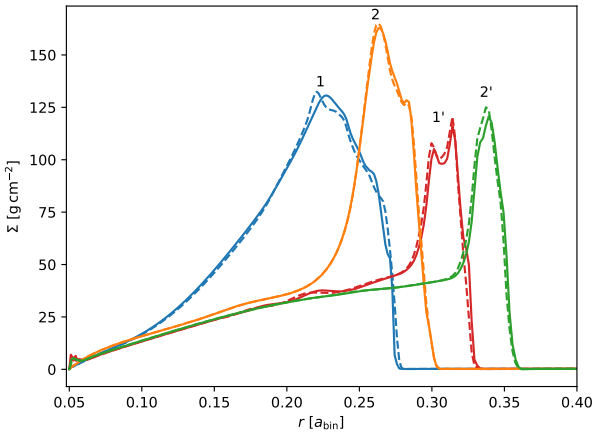

Fig. 7. Azimuthally averaged density distributions as a function of radius before (1, 2) and after (1′ and 2′) the first and second normal outbursts following a superoutburst. The solid lines are taken from the first and the dashed lines from the second supercycle of the fiducial model.

superoutburst to be brighter than the next normal outburst. However, we observed this effect only in simulations with mass ratios of $q = 0.25$ or lower, and did not observe it for V1504 Cygni, with a few exceptions. This could be explained by the different quiescent periods after a superoutburst, which will affect the mass of the disk during the first normal outburst. We often find a long quiescent period after a superoutburst in our simulations, while observations of V1504 Cygni find short quiescent periods after superoutbursts.

Looking more closely at the luminosity during the quiescent phases, it can be seen that the quiescent luminosity increases with the disk mass. This effect follows directly from our viscous heating model since the viscous heating (Eq. (4)) is proportional to the surface density and, via the α viscosity prescription, also to the mid-plane temperature. This effect is also observed in other studies (e.g. Hameury et al. 1998) and is generally considered to be a weakness of these models (Hameury 2020). Since it is not found in observations.

The noise in the luminosity during the quiescence is caused by the hot spot where the mass stream impacts the disk. We restarted the simulation during the quiescence without the mass stream and found the luminosity to be nearly constant and 60% lower (corresponding to a drop of 0.4 on the log scale in the second panel of Fig. 5) than with the mass stream active. The average effective temperature of the hot spot is $T_{\rm eff} \approx 40 \cdot 10^3$ K with peak temperatures of $100 \cdot 10^3\,K$, these values are significantly higher than the brightness temperatures measured from observations of up to $15 \cdot 10^3$ K for the OY carinae system (Wood et al. 1989).

The too high hot spot temperatures could be explained by the lack of in-plane radiative diffusion in our simulation and the 2D approach underestimates the spread of the stream. In addition, our viscosity and cooling model may not be applicable to the hot spot because they were developed for conditions inside the disk.

For the quiescent disk, Wood et al. (1989) measured brightness temperatures $T_{\rm eff}$ of 4400 K at the center of the disk and 3300 K at the outer rim, while we measure 3000 K near the inner boundary and 2400 K near the outer rim and 4000 K inside the outer density ring in our simulations. During the initial rise of a superoutburst, we measure effective gas temperatures from $20 \cdot 10^3$ K near the inner boundary to $6 \cdot 10^3$ K at the outer boundary of the disk. Given our large inner boundary, which limits the disk extension towards the white dwarf, these temperatures are in good agreement with the brightness temperatures of $25 \cdot 10^3$ K to $6 \cdot 10^3$ K measured from OY Carinae during superoutbursts by Bruch et al. (1996) and Pratt et al. (1999).

We simulated our fiducial model for three supercycles and found no significant differences between the cycles. The precise periodicity of our supercycles is highlighted by the dashed lines in Fig. 7. It shows the density distribution during the normal outbursts after the second superoutburst and it exactly matches the density distributions measured after the first superoutburst.

Both the spiral waves during a superoutburst and the outer density ring in Fig. 7 could overflow the disk, similar to the hydraulic jumps at spiral waves observed in protoplanetary disks (Boley & Durisen 2006; Picogna & Marzari 2013). Both of these 3D effects could influence the mass transport in the disk and thus the outburst conditions, but are not included in our simulations.

4.1. Normal outbust

Fig. 8 shows the light curve and disk radius evolution of an outside-in and an inside-out outburst from our $\alpha_{\rm cold}$ = 0.04 model. The outburst starts when the disk reaches the intermediate branch in the Ichikawa & Osaki (1992) model at about $T_{\rm mid} \approx 3000\,{\rm K}$ in the outer rim of the disk. In this regime, the cooling rates increase less with increasing temperature than the viscous heating, causing the temperature to rise faster.

The temperature rise is initially slow and confined to the density ring around the disk which causes the slow rise at the beginning of the blue curve in Fig. 8. Once the temperature in the ring reaches $T_{\rm mid} \approx 13 \cdot 10^3$ K, the α parameter of Eq. (6) grows rapidly and the temperature and α jump to $T_{\rm mid} \approx 50 \cdot 10^3$ K and $\alpha_{\rm hot}$ and launch a heating wave inward, seen as the steep rise in luminosity and disk radius. Due to the disk spreading by angular momentum transport, the gas density and temperature at the outer edge drop below their critical values, and a cooling wave is launched that moves inward and causes the luminosity to drop and the disk to start shrinking.

Note that the outburst starts near the outer edge of the disk and two heating waves are launched, one traveling inward and one outward. But the outward wave quickly reaches the edge, while the inward wave traverses the majority of the disk. Therefore, we mention the inward wave only when the outburst starts in the outer rim and call it an outward-in outburst and similarly, we mention the outward wave only when the outburst starts in the inner disk and call it an inside-out outburst.

In the case of the inside-out outburst (Fig. 8, orange curve), the slow initial rise is much shorter and the heating wave travels at about half the speed of the outside-in wave. This gives the outburst a more symmetrical shape, which was already studied in Smak (1984). The growth of the disk radius is delayed until the heating wave has reached the outer edge of the disk. From this point on, the evolution is identical to the outside-in outburst. Whether an outburst starts inside-out or outside-in depends on whether the inward transport of gas by viscosity is more effective than the mass pileup at the outer rim (Lasota 2001, Sect. 4.4).

For comparison, the light curve of V344 Lyr during two consecutive outbursts is shown in Fig. 9. The presumed inside-out outburst of V344 Lyr (orange line) occurs after an unusually long quiescent period. The light curve also displays negative superhumps that could be caused by a tilted disk, which in turn would explain the long quiescent period. This would lead to a higher mass build-up and a higher outburst amplitude Cannizzo et al. (2012).

After the growth phase during the ourburst ends, the disk radius shrinks due to the accretion of low angular momentum gas from the mass stream. Overall we find a slow upward trend in the disk radius over time. Similarly, the eccentricity also increases slightly during each normal outburst and decreases during the quiescent state, also with a slow upward trend.

4.2. Superoutbust

With the steady increase in disk radius and eccentricity, the radius will exceed the 3:1 resonance at some point during an outburst, leading to significantly increased tidal forces. The gravitational torque density during the quiescent phase and the superoutburst is presented in Fig. 10. During the quiescent phase (blue line), the tidal torque is limited to the outer rim of the disk and has similar positive and negative contributions, such that the total

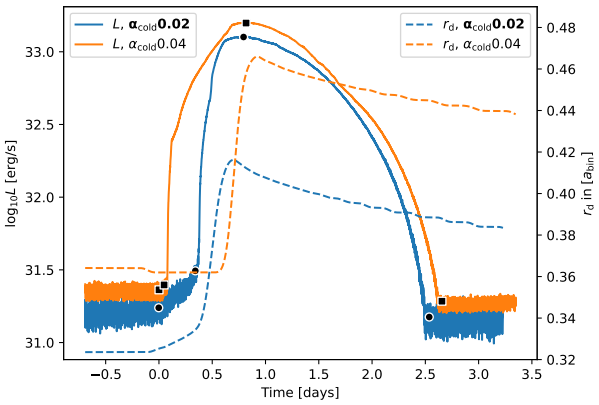

Fig. 8. Luminosity and disk radius evolution during a normal, outside-in outburst of our fiducial model ($\alpha_{\rm cold}$ = 0.02) and an inside-out outburst of our $\alpha_{\rm cold}$ = 0.04 model. Squares and dots indicate what we define as the start of the outburst, the start of the heating wave, the peak, and the end of the outburst.

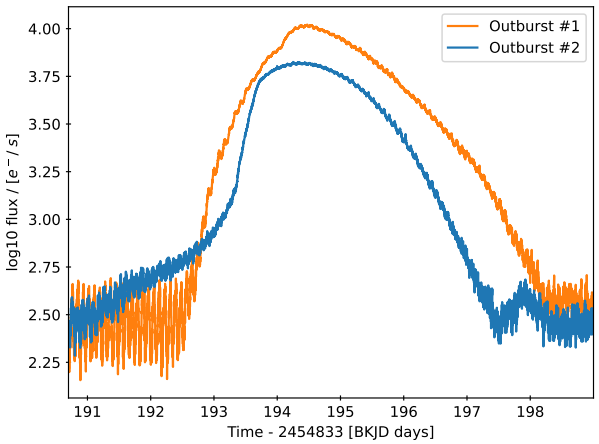

Fig. 9. Kepler luminosity data during two consecutive outbursts of V344 Lyr for comparison with Fig. 8.

tidal torque acting on the disk is weak and negative. During a superoutburst, the torques are amplified and reach further into the disk.

We measure strong negative torques at the outer rim that prevent the disk from expanding further and keep the outer parts optically dense and hot. In addition, the total torques are always negative and release additional tidal energies that heat the disk. Both effects prevent the cooling wave from being launched and thus prolong the outburst. The highest torque density amplitudes occur during the early stages of the superoutburst when the eccentricity is still low (orange line). The strongest total torques occur during the eccentricity growth phase (red line) and are almost two orders of magnitude stronger than during the quiescent phase. The disk is restructured and the eccentricity grows until the torques are again confined to the outer regions of disk (green line).

The 3:1 resonance seems to be a good reference radius at which the strength of the tidal interaction begins to increase and eccentricity begins to grow (see the second plot in Fig. 5), but recent studies have shown that the 3:1 resonance is not the

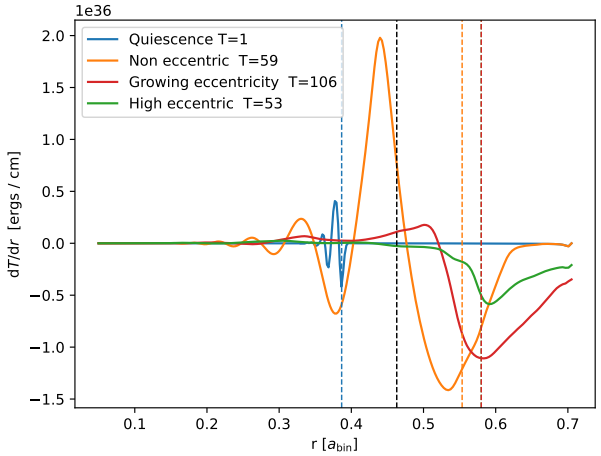

Fig. 10. Azimuthal and time-averaged (over $10\,P_{bin}$) gravitational torque density Eq. (16) during different stages of a superoutburst. The vertical dashed lines are the time-averaged disk radii during the same time frame. The black vertical line indicates the position of the 3:1 resonance. The legend also notes the total integrated torques exerted on the disk, normalized to the torque during quiescence.

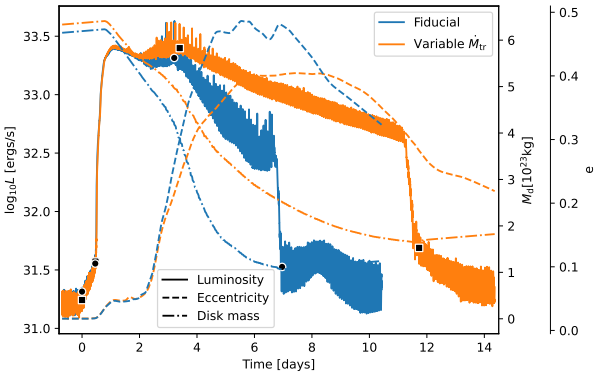

Fig. 11. Evolution of several quantities during a superoutburst for our fiducial model (blue) and variable mass transfer model using Eq. (24) (orange). The solid lines represent the disk luminosity while the dots and squares indicate the timestamps of the start, the peak, and the end of the outburst. Also shown are the mass-weighted disk eccentricity (dashed line) and the disk mass (dash-dotted line).

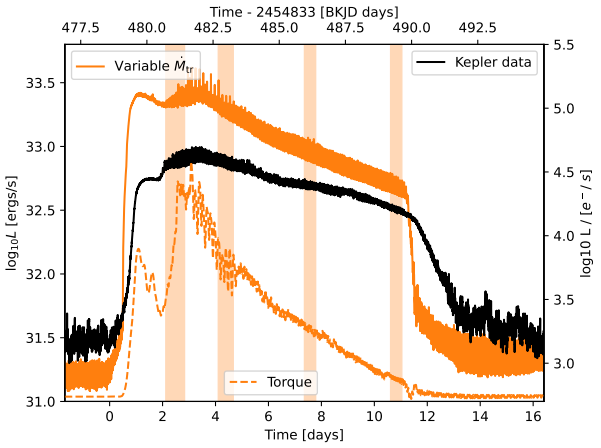

Fig. 12. Luminosity evolution during a superoutburst for our variable mass transfer model (orange line, same as in Fig. 11) and Kepler data of V1504 Cygni (black line). The shaded regions indicate the time frames presented in Fig. 14. The orange dashed line is the torque exerted by the disk on the donor star. No units are given for the torque because we are only making a qualitative assessment.

only relevant mode for eccentricity growth (Kley et al. 2008; Oyang et al. 2021).

We compared the absolute values of the torques measured in Fig. 10 to the torque estimated due to our fiducial mass transfer rate via the approximation by King(1988, Eq. 8):

$$T_{tr} = J\frac{\dot{M}_{tr}}{M_{don}} \cdot (4/3 - q), \tag{27}$$

where

$$J = M_{wd}M_{don}\sqrt{Ga_{bin}/(M_{wd} + M_{don})} \tag{28}$$

is the angular momentum of the binary. This equation assumes that the gas is transferred from the donor star to the white dwarf and the torque, when averaged over time, should be equal to the tidal torques measured in Fig. 10 plus the direct torque due to the mass stream.

We find a mass transfer torque $T_{tr} = 2.4 \cdot 10^{34}$ ergs, which is 21 times larger than the gas torque during quiesence and five times smaller than the peak gas torque during the superoutburst. Note that our binary system is on a fixed orbit, and the stars do not feel the effect of this angular momentum transport or gas accretion in our simulations.

Fig. 11 depicts a zoom in on several quantities during a superoutburst for our fiducial model and our variable mass transfer model, where the mass transfer rate was increased by a factor of about eight during the superoutburst. It demonstrates how the increased mass transfer rate dampens the eccentricity which reduces the mass loss and also provides mass during the outburst, resulting in a longer outburst. Without the increased mass transfer, the rapid luminosity decline causes the superhumps to appear to increase in amplitude.

The outbursts start as an outside-in outburst and then remain in the outburst state while the disk fills the entire Roche lobe of the white dwarf (see the second panel in Fig. 1). This phase lasts ≈1 day. During this phase the luminosity decreases due to mass loss and a decrease in gravitational interaction with the donor star (see also Fig. 12). Then the gravitational interaction suddenly increases, leading to higher luminosities, eccentricity growth, and the appearance of superhumps. After another ≈1 day has passed, the eccentricity reaches a value of $e \gtrapprox 0.2$ and the torque on the disk, the luminosity, and the superhump amplitudes reach their peaks.

The right panel in Fig. 5 shows a zoom-in around the red dashed vertical line in the left panel. The x-axis is the difference between the binary angle and the longitude of pericenter of the disk. It is shifted by π and normalized so that integers indicate the time at which the binary is flying past the bulge (apocenter) of the eccentric disk. Most of the mass loss occurs shortly after the apocenter passage, when the eccentricity and radius peak. In our fiducial model, 84% of the mass leaves the domain through the inner boundary and 16% is ejected through the outer boundary. During a normal outburst, only $\approx 3 \cdot 10^{-3}$% of the mass is ejected. The mass that leaves the simulation domain through the outer boundary is either ejected from the system, reaccreted on the

disk, or accreted on the donor star. Since the disk overflows the Roche lobe of the white dwarf during the superoutburst and the spiral arm of the disk extends towards the donor star in the third panel of Fig. 1, it seems likely that most of the ejected mass would be accreted by the donor star and interacts with its surface. For our simulation with a variable mass stream, we measure less eccentricity during the superoutburst and the amount of mass ejected through the outer boundary was reduced to 4% of the total mass loss.

After the disk has reached a highly eccentric state $e \geq 0.2$, the surface area of the disk starts to exponentially decay (not shown) and the gravitational interaction with the donor star weakens. At this stage, any further eccentricity growth leads to an increase in the mass loss of the disk in addition to the viscous accretion (see the blue dashed-dotted line at $t = 4$ days in Fig. 11). Although the disk surface area shrinks, the disk radius remains relatively constant throughout the superoutburst, but one should keep in mind that our disk radius (defined as the smallest grid radius that contains 99% of the disk mass) is tracking the extent of the tip of the eccentric disk and not the semi-major axis of an ellipse.

The disk cools down until a cooling wave is launched at the outer rim and the disk quickly shrinks back to the 3:1 resonance radius. The disk still has a significant eccentricity $e \approx 0.3$ after returning to the quiescent state, which then slowly dissipates and in some cases lasts until the next normal outburst. The dissipation of eccentricity also affects the density structure of the disk as shown in Fig. 7. In many of our simulations, we also find a small luminosity bump after the superoutburst (e.g. at $t = 8\,d$ in Fig. 11), coinciding with the phase of the fastest eccentricity decay.

The rapid luminosity decline of the fiducial superoutburst, the growth of superhump amplitudes during the decline, the flattening of the light curve before the end of the outburst, and the small luminosity bump afterward are all features that are not found in observations. The variable mass transfer solves these problems and better reproduces the observations. However, it is not clear from our simulations to what extent a variable mass transfer rate is necessary to reproduce the observations, because the effects described in our fiducial model can also be explained by the choice of the cooling prescription (see Fig. 6), the overestimation of the eccentricity due to simulating in 2D (compare Latter & Ogilvie (2006) or Oyang (2022, Ch. 4), and the overestimation in mass loss due to our too large inner boundary.

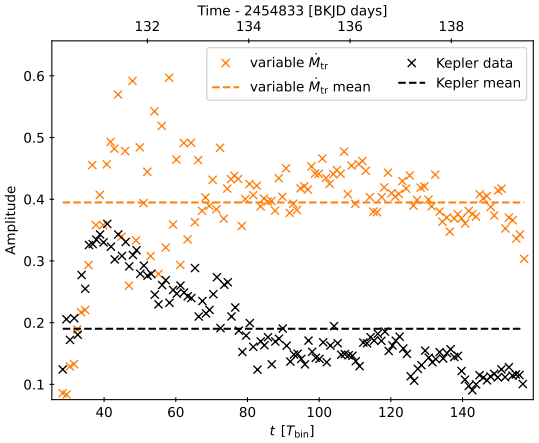

Fig. 13. Superhump amplitudes for the variable mass transfer model and V1504 Cygni measured from the data presented in Fig. 12.

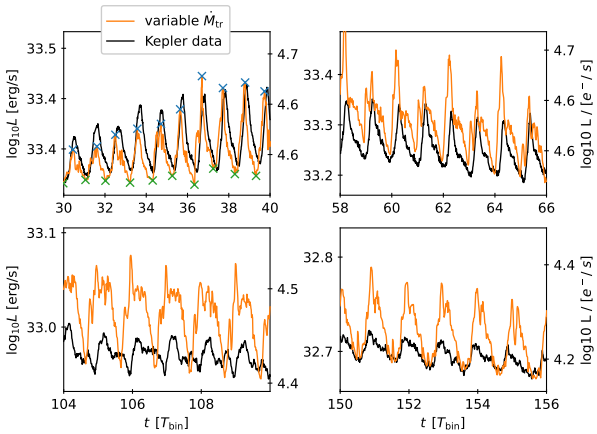

Fig. 14. Luminosity of the variable mass transfer model and Kepler data of V1504 Cygni during different phases of the superoutburst as indicated in Fig. 12. The time is measured from the start of the superoutburst. The crosses indicate the minima and maxima of the superhumps used in further evaluation.

4.3. Superhumps

The top right plot in the bottom panel in Fig. 5 shows the disk luminosity as a function of the angle between the disk apocenter and the donor star. The x-axis is normalized so that integer numbers indicate the time at which the binary passes the bulge (apocenter) of the eccentric disk. The disk is slowly precessing prograde ($T_{prec} \approx 55 T_{bin}$) such that one unit of the normalized angle covers close to one binary period. As the donor star passes the apocenter of the disk, two spiral arms are launched that travel inward into the disk (visible in the second panel of Fig. 1) and dissipate energy. The energy dissipation starts after a delay of about $1/6\,T_{bin}$ and is completed after another $1/3\,T_{bin}$.

We interpret and label these brightness variations as superhumps. In our fiducial model (blue line), we find an increase of factor two in superhump amplitudes in later stages of the superoutburst (see Fig. 11). This behavior is opposite to observed superhumps, which become weaker as the outburst progresses, as can be seen in Fig. 12 and Fig. 13. The increase in amplitude is caused by narrow luminosity peaks during the superhump. The peaks are caused by the high eccentricities and amplified by the rapid luminosity decline in our simulations. High superhump amplitudes caused by spikes in luminosity are usually discarded when analyzing superhump amplitudes (Kato et al. 2012, Sect. 4.7.1). Since all of our simulations with constant mass transfer rates develop superhump brightnesses with narrow peaks, we used the variable mass transfer model for our superhump analysis in this section and compared it to an observed superoutburst of V1504 Cygni.

The light curve data used for the evaluation is presented in Fig. 12. The shaded regions indicate an arbitrary selection of time frames at different outburst stages. A zoom in on these time frames is given in Fig. 14, note that the plots cover different time scales while the y-axis is always fixed to cover a range of 0.26 $\log_{10}L$. The maxima and minima of these superhumps are marked by blue and green crosses, respectively. The superhump excess and amplitudes are later calculated from these extrema.

The first panel in Fig. 14 shows the onset of superhumps during the rapid eccentricity growth phase. Once the average disk eccentricity exceeds $e > 0.1$, the superhumps reach their full strength with a single, symmetrical peak. The second panel depicts the superhumps during the weaker eccentricity growth phase (at $t = 58\,T\mathrm{bin} \approx 4$ days in Fig. 11). In our simulations, the central peak is weakened for every second superhump which does not happen in the observed superhumps. In both cases, the superhumps become more asymmetric, with a fast rise and a slower decline in luminosity.

During the phase when the eccentricity has reached its maximum, the superhumps have a short, small peak with an almost flat plateau (third panel). We also find this behavior in the observed superhumps, but our simulations significantly overestimate the superhump amplitudes. At the end of the outburst (fourth panel), the minima between the superhumps become wider, in agreement with the observations. The observed superhump amplitudes become smaller while our simulated superhumps remain at a constant level and develop a double-peak structure.

4.3.1. Superhump excess

We calculated the superhump excess from the maxima and minima, shown in Fig. 16. The raw data is quite noisy and has a grid-like shape due to our quantity sampling rate of 100 times per binary orbit. The data is smoothed by convolving with a normalized Hamming window of size 20 (black dots), and the resulting curve tracks the disk precession rate (orange line), which is computed from the mass-weighted longitude of pericenter of the disk. The disk precession rate is plotted in Fig. 15.

Because our evaluation function averages the angle of the longitude of pericenter of all cells, we get incorrect results whenever the longitude of pericenter of the disk is close to 2π. We have filtered out the incorrect results, causing gaps in the precession rate curve. Our precession curve can be explained by the theoretical model by Goodchild & Ogilvie (2006), which predicts that gravitational forces cause prograde precession and pressure forces cause retrograde precession. After a short initialization phase, the precession timescale settles to about $t_{\mathrm{prec}} = 50P_{\mathrm{bin}}$. From there, it slows down to $t_{\mathrm{prec}} = 60P_{\mathrm{bin}}$ due to a reduction in the gravitational interaction with the binary. As the disk cools down (seen as an increase in $-h^2$), the pressure forces weaken and the prograde precession rate increases again.

The smoothed superhump excess computed from the Kepler data of V1504 Cygni (black dots) is similar in shape to our simulated superhump excess, but due to the noise in the data, we cannot confirm the trend described above. The superhump excess is, on average, larger than in our simulations, indicating again that our disks are too hot during the outburst state.

4.3.2. Superhump amplitudes

Fig. 13 shows the amplitudes from our variable mass transfer model that are calculated as (Smak 2009b):

$$A = \frac{L_{\mathrm{max}}}{L_{\mathrm{min}}} - 1. \tag{29}$$

We find alternating 0.3 and 0.6 amplitudes during the first half of the outburst $t \lessapprox 70\,P_{\mathrm{bin}}$, which then transition to more stable amplitudes with a mean of $A = 0.4$. These amplitudes are a factor of four larger than the 2D simulations presented in Smak (2009b) and on average a factor of two larger than the observed

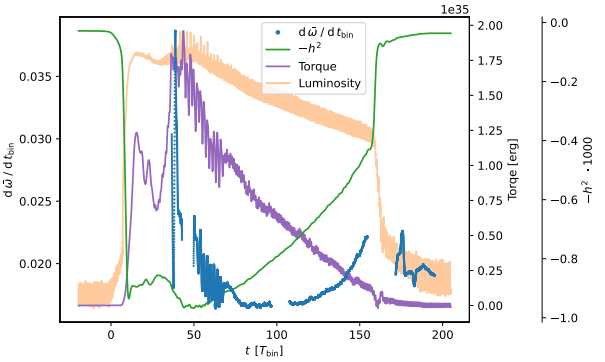

Fig. 15. The disk precession rate during a superoutburst, together with the torque exerted by the disk on the donor star and the negative of the gas aspect ratio squared. The luminosity curve in the background is for orientation only.

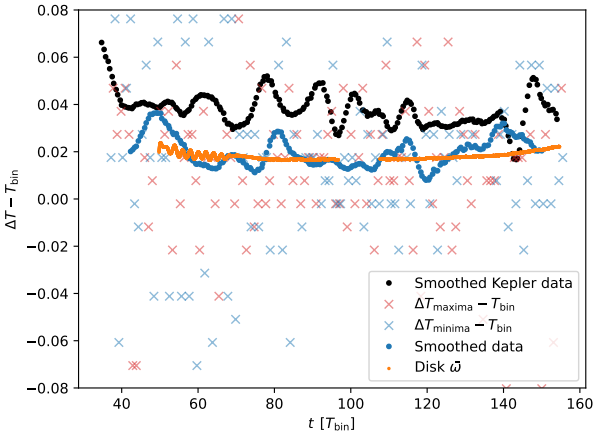

Fig. 16. Superhump excess calculated from adjacent peaks or minima for our variable mass transfer model (red or blue crosses, see the first panel in Fig. 14). The blue dots are an average of nearby data points and the orange dots are the precession rate of the disk. The black dots are the superhump excess computed from Kepler data of V1504 Cygni using an orbital period of 1.668 h (Coyne et al. 2012).

superhumps. In this respect, our superhump amplitudes seem to be in agreement with the observed ones, since 3D simulations tend to find amplitudes that are lower by a factor of 2–4 than 2D simulations (Smak 2009b).

It should also be noted that the superhump amplitudes in our models arise purely from tidal dissipation within the disk and we could not find a relation between the mass transfer rate and the superhump amplitude. In Fig. 17, we compare the fiducial model during the high eccentricity phase of a superoutburst with a copy of the fiducial model that was restarted without any mass transfer from the donor star. By turning off the mass transfer, the superhump amplitudes even increase due to lower luminosity minima and higher second luminosity peaks.

4.3.3. Late superhumps

While the disk is still eccentric, the quiescent phase and normal outbursts following a superoutburst can also produce superhump-like brightness variations, called late superhumps.

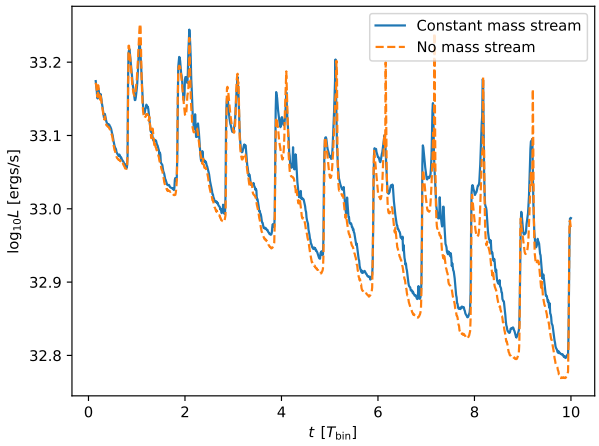

Fig. 17. Luminosity curves for the fiducial model during the high eccentricity phase of a superoutburst compared to a restart with the mass transfer turned off.

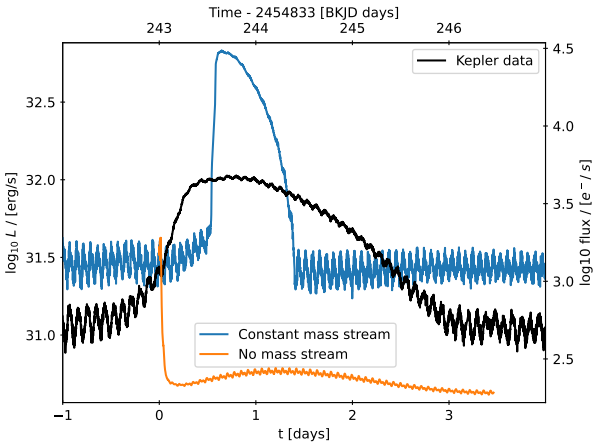

Fig. 18. Luminosities during the first normal outburst following a superoutburst. The black line presents Kepler data of V344 Lyr, the blue line is for our $\dot{M}_{\rm tr} = 2.5 \cdot 10^{-10} {\rm M}_\odot/{\rm yr}$ model and the orange is a simulation of the same model but restarted with the mass transfer turned off.

We find late superhumps in all our simulations, which are caused by the varying impact velocity of the mass stream on the eccentric disk. This is in agreement with Rolfe et al. (2001), who measured the shape of the accretion disk in the eclipsing dwarf nova system IY UMa and found an eccentric disk, and that the brightness variations of the system can be explained by a varying impact velocity of the mass stream.

We present the light curve of a normal outburst following a superoutburst for one of our simulations together with Kepler data of V344 Lyr in Fig. 18. We do not observe these variations for non-eccentric disks, as seen in the quiescent luminosities in Fig. 8. We also found that the brightness variations disappear when the mass stream is turned off while the disk is eccentric, as shown by the blue and orange lines in Fig. 18. This confirms that they are caused by the mass stream impacting an eccentric disk.

4.3.4. Hot spot luminosity

We extracted the luminosity of the hot spot by comparing the luminosities of the simulations with and without mass transfer in Fig. 18. For the quiescent luminosity with mass transfer, we measure $L_{\rm d} = 2.94 \cdot 10^{31}$ ergs/s averaged from the start of the plot until time $t = 0$ d. The average luminosity without mass transfer is $L_{\rm d} = 0.89 \cdot 10^{31}$ ergs/s measured from $t = 0.5$ d to $t = 3.5$ d. For the high mass transfer model depicted in Fig. 18, we find that the hot spot contributes $L_{\rm hs} = 2.05 \cdot 10^{31}$ ergs/s to the total luminosity and is more than two times brighter than the disk itself.

The luminosity of the hotspot can also be estimated using the formula in Smak (2002):

$$L_{\rm impact} = \frac{1}{2} G \frac{M_{\rm bin}}{a_{\rm bin}} \dot{M}_{\rm tr} \Delta u^2, \tag{30}$$

where $M_{\rm bin}$ is the binary mass, $a_{\rm bin}$ is the binary separation, and Δu is a dimensionless equivalent of the impact velocity. Using the estimate for the Roche radius from Eggleton (1983) and $q = 0.12$, we find $\Delta u^2 \approx 2$ using the interpolation formula from Smak (2002). This results in an estimated hot spot luminosity of $L_{\rm impact} = 3.74 \cdot 10^{31}$ ergs/s. The approximate hot spot luminosity is about twice as large as our measured hot spot luminosity, which could indicate that not all of the kinetic energy of the mass stream is converted into luminosity in our simulations. However, it should be noted that the shock heating is added to the heating source term and therefore does not conserve the total energy, but numerical errors of this magnitude seem unlikely.

Studies that decompose the light curves of eclipsing CVs also find hot spot luminosities that are comparable to the disk luminosity (Bąkowska & Olech 2015) or brighter than the disk luminosity (McAllister et al. 2019, Fig. 1). Our simulations do not include contributions to the light curve from the white dwarf, its boundary layer, and the donor star, which means that the total quiescent luminosity is underestimated and the importance of the disk and hot spot luminosities are overestimated.

4.3.5. Flickering

The noise in the quiescent luminosity in our simulations could be associated with the flickering found in observations. In our simulations, it is caused by random fluctuations in the hot spot that stop when the mass stream is turned off (see the orange line in Fig. 18). The residual oscillations for the simulation without mass transfer are caused by tidal dissipation due to the eccentric disk, and we confirmed that they do not occur for circular disks (not shown).

The amplitudes of these fluctuations caused by the mass stream depend, in addition to physical parameters, on the time step size of our integration scheme. We believe this is due to the compression and shock heating being added in a separate integration step from the surface cooling. This causes the temperature in the hot spot to overshoot the equilibrium temperature, which causes the surface cooling to be too effective in the next integration step, causing oscillations around the equilibrium temperature.

Therefore, it is likely that the agreement of the flickering amplitudes in our simulations with the observed amplitudes is coincidental. Note that this statement applies only to the flickering (random noise) in the quiescent luminosity, and not to the late superhumps depicted in Fig. 18, which we believe to be physical.

Observations of dwarf novae find that most of the flickering originates from a region close to the white dwarf, which is not included in our simulations, with additional contributions

Table 2. Overview of all simulation parameters and the evaluation of superoutbursts.

Name	$q_{\rm bin}$	$\alpha_{\rm hot}$	$\alpha_{\rm cold}$	$\dot{M}_{\rm tr}$ [$\frac{M_\odot}{\rm yr}$]	Inflow	duration [d]	delay [d]	e	h [%]	V mag	SH mag	SH excess [%]
Fid	0.12	0.10	0.02	$1.5 \cdot 10^{-10}$	const	6.9	1.7	0.48	3.0	5.1	0.52	2.3
q08	**0.08**	0.10	0.02	$1.5 \cdot 10^{-10}$	const	7.1	1.8	0.54	3.1	5.5	0.43	1.8
q16	**0.16**	0.10	0.02	$1.5 \cdot 10^{-10}$	const	7.2	2.0	0.55	2.8	4.9	0.66	3.0
q25	**0.25**	0.10	0.02	$1.5 \cdot 10^{-10}$	const	6.5	2.3	0.55	2.7	4.5	0.83	4.4
q30	**0.30**	0.10	0.02	$1.5 \cdot 10^{-10}$	const	6.1	2.1	0.57	2.7	4.5	0.87	5.2
q35	**0.35**	0.10	0.02	$1.5 \cdot 10^{-10}$	const	5.9	2.4	0.52	2.6	4.3	1.03	5.8
q40	**0.40**	0.10	0.02	$1.5 \cdot 10^{-10}$	const	5.6	2.6	0.53	2.6	4.4	1.18	6.4
ah7	0.12	**0.07**	0.02	$1.5 \cdot 10^{-10}$	const	8.5	1.9	0.47	3.0	4.9	0.61	2.2
ah13	0.12	**0.13**	0.02	$1.5 \cdot 10^{-10}$	const	5.7	1.1	0.49	2.9	5.3	0.47	2.6
ah16	0.12	**0.16**	0.02	$1.5 \cdot 10^{-10}$	const	5.6	1.4	0.48	2.7	5.1	0.47	3.0
ah20	0.12	**0.20**	0.02	$1.5 \cdot 10^{-10}$	const	5.4	1.7	0.49	2.7	5.2	0.46	3.2
ac1	0.12	0.10	**0.01**	$1.5 \cdot 10^{-10}$	const	7.0	1.8	0.48	2.9	5.2	0.51	2.4
ac4	0.12	0.10	**0.04**	$1.5 \cdot 10^{-10}$	const	7.2	2.1	0.48	2.8	4.6	0.54	2.3
Mtr05	0.12	0.10	0.02	$\mathbf{5 \cdot 10^{-11}}$	const	7.1	1.8	0.51	3.0	5.8	0.50	2.5
Mtr10	0.12	0.10	0.02	$\mathbf{1 \cdot 10^{-10}}$	const	7.2	1.9	0.49	3.0	5.5	0.50	2.7
Mtr25	0.12	0.10	0.02	$\mathbf{2.5 \cdot 10^{-10}}$	const	7.1	1.2	0.47	2.9	4.4	0.52	2.4
Mtr var	0.12	0.10	0.02	$1.5 \cdot 1.5^{-10}$	**Eq.** (24)	11.7	1.9	0.40	3.1	5.4	0.41	2.0

Notes. The parameter that was changed from the fiducial model is highlighted in bold. For each superoutburst, we measured the outburst duration in days, the delay from the start of the outburst until the appearance of superhumps in days, the maximal disk eccentricity, aspect ratio, visual magnitude, superhump magnitude, and superhump excess. We list the mean of the measurements if multiple superoutbursts occurred in a simulation. The superhump delay is measured from the first torque maxima during the precursor to the second torque maxima during the eccentricity growth phase, compare Fig. 15.

from the hot spot (Bruch 1996; McAllister et al. 2015). There are other proposed sources of flickering, but it is not yet clear which are the relevant ones. We refer to Bruch (2021) for a discussion of this topic.

5. Physical parameter study

In addition to the fiducial model, we ran 17 other simulations, where we changed one parameter from the fiducial model in each setup. The parameters that we changed are the viscosity parameters $\alpha_{\rm hot}$ and $\alpha_{\rm cold}$, the mass transfer rate $\dot{M}_{\rm tr}$ and the mass ratio q. All simulation parameters and characteristics of the superoutbursts are listed in Table 2.

5.1. Viscosity

The effect of different $\alpha_{\rm hot}$ parameters is shown in Fig. 19, where normal outbursts are marked with dots and superoutbursts with squares. The plot starts at the time of the second outburst because the first normal outburst was used as the initialization time. We performed the same analysis for two different outburst cycles from the Kepler data of V1504 Cyg, which is given in Fig. 20.

Higher $\alpha_{\rm hot}$ causes the outbursts to evolve faster, the initial heating wave moving slightly faster across the disk and the cooling wave becoming significantly faster, reducing the duration of normal outbursts (second panel in Fig. 19). The larger increase in the cooling wave speed compared to the heating wave increases the symmetry of the normal outbursts, where the symmetry is defined as the time from launching the heat wave to the peak luminosity of the outburst divided by the total duration of the outburst (compare the markings in Fig. 8). The higher viscosity during the outburst state increases the radius growth so that there are fewer normal outbursts between superoutbursts as can be seen in the first panel where the first superoutburst occurs after four normal outbursts (including the first outburst not shown in the plot) for the high $\alpha_{\rm hot}$ = 0.16 and 0.2 simulations and six outbursts for the lowest $\alpha_{\rm hot}$ = 0.07 simulations.

In our model (see Equations (7), (8)), the temperature required for starting an outburst increases with radius while the temperature itself is proportional to the surface density due to viscous heating. Larger disk radii therefore lead to longer quiescent periods between outbursts.

The higher dissipation also increases the outburst luminosity, as shown by the increase in visual magnitude in the first panel of Fig. 19. Although for the superoutbursts, the peak luminosity is measured at the hump caused by the increased tidal interaction. At this time, the increase in mass loss due to higher viscosity counteracts the increase in viscous dissipation, and we find no trend in the amplitudes of superoutbursts. The faster mass loss also causes the disk to be cooler at the time when superhumps appear, leading to an overall faster disk precession or equally superhump excess (see Table 2). The superhump amplitudes are too noisy with too few data points to determine a trend and have magnitudes around 0.5 regardless of $\alpha_{\rm hot}$. We have not used the second half of the superhump amplitudes, because the increase in superhump magnitude in later stages is not compatible with observations.

Comparing these results with the observed trends (Fig. 20), it is clear that dwarf novae systems have more variability in their outburst properties than our 2D simulations with a constant mass transfer rate. We can still see the increasing trend in brightness and duration for successive outbursts. The durations of the normal outbursts are best matched by the $\alpha_{\rm hot}$ = 0.07 and 0.1 models and the symmetry by the $\alpha_{\rm hot}$ = 0.1 and 0.13 models. However, it is important to note that this similarity is specific to this setup and that other parameters, namely the binary mass ratio, the mass transfer rate, and also the cooling prescription will affect the same outburst properties.

The $\alpha_{\rm cold}$ parameter only affects the disk during quiesence. It has little effect on the quiescent duration because the change in viscous dissipation is balanced by the change in mass transport. The effective temperature during the quiescent phase before a

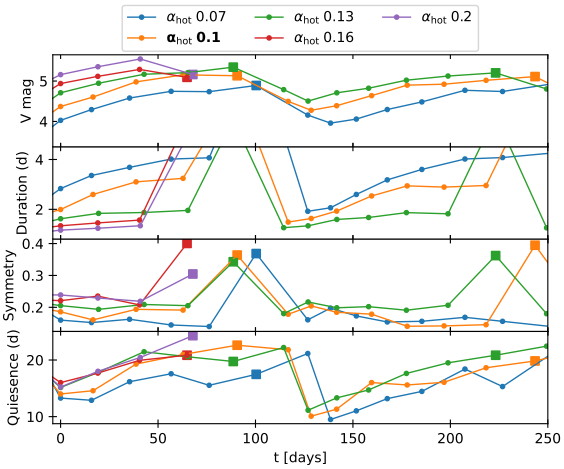

Fig. 19. The visual magnitude, duration, and symmetry of the outbursts, and the quiescent duration between outbursts for different α_{hot} parameters.

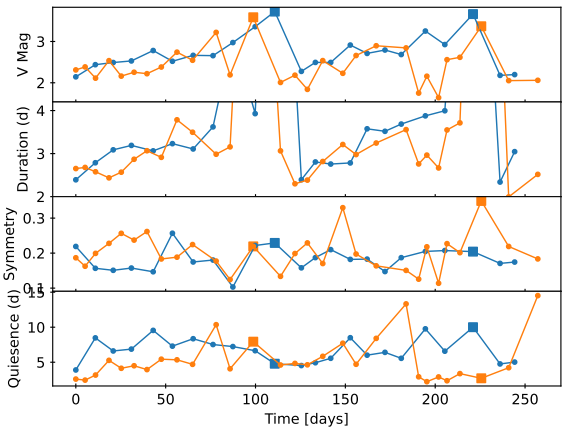

Fig. 20. Same as Fig. 19 but for Kepler data of V1504 Cyg. The two lines represent two different outburst cycles.

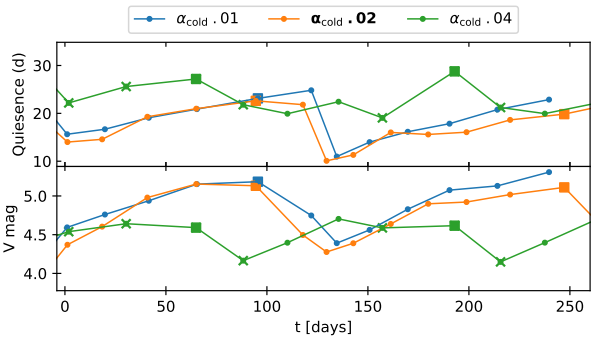

Fig. 21. Quiescent duration between outbursts for different α_{cold} parameters. Dots indicate normal outbursts, crosses indicate inside-out normal outbursts, and squares indicate superoutbursts.

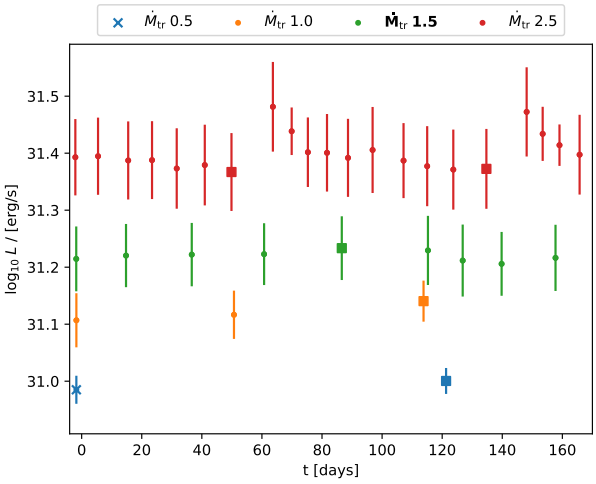

Fig. 22. Mean and standard deviation of the quiescent luminosity over the 10 binary orbits leading up to an outburst for different mass transfer rates. Mass transfer rates are given in units of $10^{-10}\,M_\odot$/yr.

superoutburst changes from $T_{eff} \approx 1900–2300$ K ($\alpha_{cold} = 0.01$, inner disk to outer disk) to 2400–3000 K ($\alpha_{cold} = 0.02$) and 3200–3800 K ($\alpha_{cold} = 0.04$). The peak temperature in the density ring during the same time was $T_{eff} = 4200$ K, independent of α_{cold}. The increase in the quiescent luminosity reduces the visual magnitude compared to the following outburst, even though the absolute luminosity during the outbursts is the same. For $\alpha_{cold} = 0.04$, the mass transport through the disk is strong enough such that the outburst conditions are reached in the inner disk first, triggering an inside-out outburst, which is indicated by a cross in Fig. 21. The inside-out outbursts do not have the radius-quiescence relation of the outside-in outbursts, so the quiescence durations are random with a small spread instead of increasing monotonically.

5.2. Mass transfer rate

The mass transfer rate directly affects the strength of the hot spot, which accounts for much of the brightness of the disk during quiescence. In Fig. 22 we plot the averaged luminosity and its standard deviation computed over 10 binary orbits before the start of an outburst for different mass transfer rates. We find an increasing trend in both these quantities with mass transfer rate. Increasing the mass transfer rate accelerates the rate at which the critical conditions are reached in the outer density ring. The shorter quiescence periods for higher mass transfer rates then result in the disk having less total mass at the start of the outburst, leading to weaker outbursts with lower brightness and less radial growth. The increased quiescent luminosity and the reduced outburst luminosity both reduce the visual magnitude of the outbursts for higher mass transfer rates as seen in the third panel of Fig. 23.

The averaged quiescence duration for each simulation follows the $t_{accum} \propto \dot{M}_{tr}^{-2}$ relation from Osaki (1995). For the lowest mass transfer rate of $0.5 \cdot 10^{-10}\,M_\odot$/yr, the quiescent duration becomes long for the outbursts to switch to inside-out (indicated by crosses instead of dots in Fig. 23). Overall, the transfer rate has no effect on the duration of the normal- or superoutbursts with the one exception being the inside-out outburst of the low transfer model.

Due to the weaker outbursts, the higher mass transfer simulations require more outbursts to reach the 3:1 radius, but do so in

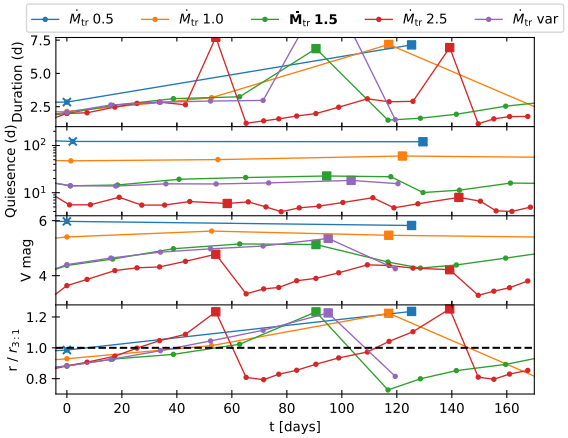

Fig. 23. Outburst duration, quiescent duration and visual magnitude, and the disk radius at the time of the maximum luminosity for different mass transfer rates. The mass transfer rates are given in units of 10^{-10} $M_\odot$/yr.

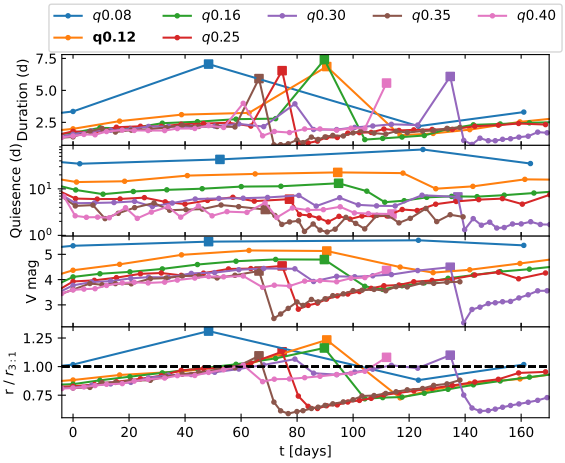

Fig. 24. Same as Fig. 23 but for different binary mass ratios q.

less time due to the significantly shorter accumulation timescale. We find no change in disk precession rate during a superoutburst with mass transfer rate and no change in the average superhump amplitude. However, the variability of the superhump amplitudes does increase with increasing mass transfer rate.

5.3. Mass ratio

Fig. 24 shows the outburst characteristics for different binary mass ratios q. Changing the mass ratio has similar characteristics in many cases to changing the mass transfer rates discussed in the previous section. Higher mass ratios result in smaller and more compact disks. The energy dissipation in the hot spot depends on the mass transfer rate and the relative velocity between the edge of the disk and the mass stream, which in turn depends on the disk size (Smak 2002). Consequently, we find brighter hot spots for smaller disk radii. During quiescence, the hot spot is the dominant luminosity source of the disk, so smaller disks will have higher quiescence luminosities. For the fiducial model, we find that the hot spot is 2.7 times brighter than the rest of the disk. We estimated this by comparing the quiescent luminosity with the luminosity of the disk after the mass transfer is turned off (see Fig. 18).

In addition, the conditions for an outburst are more easily met and the outburst frequency is increased. The more frequent outbursts lead to lower total disk masses, resulting in overall weaker outbursts. The increasing quiescent luminosity and decreasing outburst luminosity for higher mass ratios lead to the reduced visual magnitudes shown in the third panel of Fig. 24. The normal outburst durations have lower minima for higher mass ratios (compare the second cycle in the first panel of Fig. 24). However, we do not find a clear trend in the superoutburst durations, and our simulations did not run long enough to observe a trend in the supercycle duration.

For the higher mass ratios (and also for the higher mass transfer rate), the outer density ring is constantly at the critical temperature for an outburst (mid-plane temperatures of $T_{\rm mid} \approx 9000$ K). The simulations often launch weak heating waves that dissipate without leaving the density ring and without making the jump to $\approx 50 \cdot 10^3$ K observed in successful outbursts. These

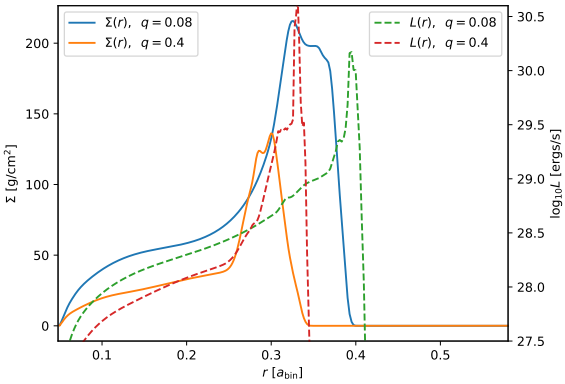

Fig. 25. Snapshots of the radial profiles of the surface density Σ and the disk luminosity L at radius r just before a superoutburst.

conditions are highlighted in Fig. 25, which shows the radial density profile and luminosity for each ring for the lowest and highest mass ratio simulations.

The constant critical temperature in the outer density ring can be seen in the $q = 0.4$ simulation by the rise in luminosity inside the density ring, which does not occur in the $q = 0.08$ simulation. The plot also shows that the inner disk is colder for higher mass ratios and that the majority of the luminosity originates at the outer edge of the disk, outside of the density ring.

Simulations with mass ratios of $q = 0.3$ and higher produce reflares at the end of or just after superoutbursts. An example of these is shown in the first panel of Fig. 26. The first panel in Fig. 27 shows the reflares observed for V3101 Cyg for comparison. We explain these reflares with the increase in density in the inner parts of the disk due to the eccentricity dissipation observed in Fig. 7. As mentioned above, at these mass ratios, the outer density ring is constantly at the critical temperature and launches heating waves that can now propagate into the disk due to the increased density. Alternatively, these reflares have been explained by a mass transfer instability where the mass transfer is increased by several orders of magnitude (Hameury & Lasota 2021).

In our simulations, the superhump amplitudes increase with mass ratio (see Table 2). Since our superhump amplitudes for

simulations with constant mass transfer rates are enhanced by narrow peaks not found in the observations, we see no value in evaluating the magnitudes further than the noted trend.

As can be seen in Table 2, the delay from precursor to superhumps and the superhump excess (or equivalently, the disk precession rate) increase with the binary mass ratio. Our superhump excess scales with the mass ratio as $e(q) = 0.43 \cdot q - 0.28 \cdot q^2$, these values are about only half of the observed excess, which also has a different scaling: $e_{\rm obs}(q) = 0.18 \cdot q + 0.29 \cdot q^2$ (Patterson et al. 2005). Our results are similar to the 2D SPH simulations of Smith et al. (2007). In this study they also performed 3D simulations that are in better agreement with observations. We also ran simulations with other cooling functions that resulted in cooler disks (cf. Fig. 6), but still found precession rates that were too low. Thus, the fact that our disks precess too slowly is probably due to the dimensionality of the simulations.

5.4. Mass ratio period gap

Observations find a period gap at $P_{\rm bin} = 2.8\,h$, which can be translated to a critical mass ratio of $q_{\rm crit} \approx 0.3$ (Inight et al. 2023) Systems with higher mass ratios typically do not produce superhumps. Although there are a few known exceptions (Hameury 2020, Sect. 4.7).

In our simulations, we found superoutbursts and superhumps for all mass ratios from $q = 0.08$ to 0.4, and each outburst evolved the same way, by first exceeding the 3:1 resonance radius, then filling out the Roche lobe and becoming eccentric, as shown in Fig. 1. These results are consistent with the 2D simulations in Smith et al. (2007), which found superhumps over an even wider range of mass ratios, but they also found a critical mass ratio of $q_{\rm crit} \approx 0.24$ for their 3D simulations above which no superhumps appeared. However, we do find that the time from the precursor outburst to the development of superhumps increases with the mass ratio (Table 2).

At high mass ratios, failed superoutbursts start to appear, which look like a precursor outburst to a superoutburst, but then launch a cooling wave instead of starting eccentricity growth. The light curve of a failed superoutburst is shown in the second panel of Fig. 26, the outburst has the same shape as the precursor of the superoutburst in the top panel. These outbursts could be interpreted as wide outbursts in systems above the period gap such as SS Cygni (see the second panel in Fig. 27). Buat-Ménard et al. (2001) explains these outbursts by an increase in tidal dissipation delaying the cooling wave. We argue that the tidal torques that stop the disk expansion and thus prevent further cooling by disk thinning are the more important effects in delaying the launching of the cooling wave. The delayed cooling wave gives these outbursts a flat top in the aspect ratio, which is different from the peak in the aspect ratio is seen in the normal outburst in the panel below, where the cooling wave is launched while the luminosity is still increasing.

The superoutburst in our $q = 0.08$ simulation behaves the opposite, it starts as a normal outburst as indicated by the shape of the aspect ratio curve in the fourth panel of Fig. 26, but as the cooling wave is moves inward, the eccentricity starts to grow and the tidal instability becomes active. This sequence of events is the same as described in Osaki & Kato (2014) for the observations of delayed superoutbursts in the CVs V1504 Cygni and V344 Lyrae. The third panel in Fig. 27 presents such a delayed superoutburst observed in V1504 Cygni. In our case, however, the cooling wave is only halfway through the disk when the tidal instability is launched, so that precursor and superoutburst are not separated in luminosity.

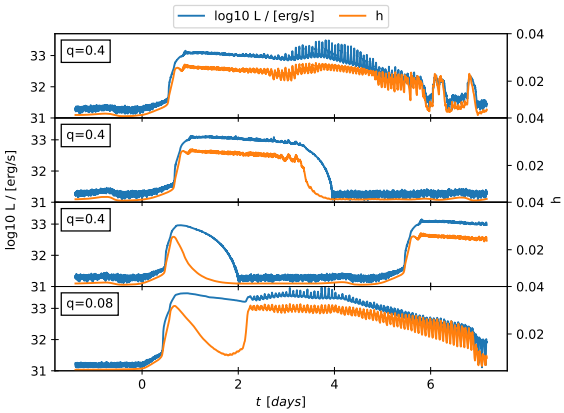

Fig. 26. Time evolution of the disk luminosities and the mass-weighted average of the aspect ratio for specific outbursts.

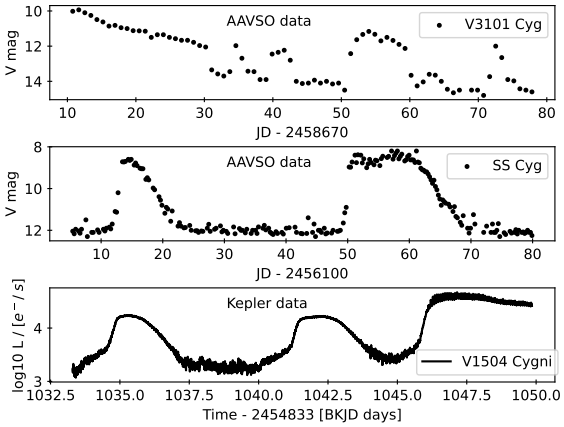

Fig. 27. Observed time evolution of luminosities for comparison with Fig. 26. The AAVSO data has been binned with a bin size of three times the cadence time to reduce noise.

The low mass ratio simulations develop a superoutburst after the launch of the cooling wave, and the high mass ratio simulations do not develop a superoutburst even after staying in the outburst state for 2 days, indicating that it becomes more difficult to launch a superoutburst with an increasing mass ratio even in 2D.

6. Discussion and summary

In this study, we have performed 2D non-isothermal hydrodynamic simulations of outburst cycles in cataclysmic variable (CV) systems. Previous 2D simulations of CVs have used a locally isothermal equation of state (Smith et al. 2007; Wood & Burke 2007; Kley et al. 2008; Montgomery 2009) and could only study either the quiescent state or the outburst state. On the other hand, more realistic 3D simulations of full outburst cycles are not yet computationally feasible (Oyang 2022). While sophisticated 1D simulations of outburst cycles exist, see Hameury (2020) for a review, they cannot model the effects of disk eccentricity and have to approximate the gravitational torques acting on the disk.

We used a modified version of the FARGO code (Masset 2000) and added a non-perfect ideal equation of state (EoS)

from Vaidya et al. (2015) that takes into account hydrogen ionization and dissociation. The gas was heated by viscous heating using the α parameter scaling from Ichikawa et al. (1993) and shock heating from Stone & Norman (1992, Appendix B). We used the cooling function from Ichikawa & Osaki (1992) which was developed to reproduce the S-shaped equilibrium curve during CVs outbursts. The momentum advection and compressive heating were not changed and are described in Rometsch et al. (2024)[2].

Using this model and feeding the disk with a mass stream, we were able to self-consistently produce outburst cycles with normal outbursts and superoutbursts. We chose the parameters for our fiducial model so that the cycle duration and the number of normal outbursts in a cycle were consistent with observations of the V1504 Cygni system. From there, we performed a parameter study by changing a single parameter at a time. Our results are in agreement with the predictions of the thermal tidal instability model of Osaki (1989).

The $\alpha_{\rm cold}$ affects the luminosity and the diffusion timescale in the quiescent state while the mass transfer rate affects the accumulation timescale and the tidal energy dissipation in the hotspot. As described in Lasota (2001, Sect. 4.4), if the diffusion timescale is shorter than the accumulation timescale, outbursts are launched inside-out, otherwise they are launched outside-in. The variable mass transfer function, which scales the mass transfer rate with the accreted mass by Hameury et al. (2000), prolongs the superoutburst and improves the overall similarity to observed superoutbursts. The $\alpha_{\rm hot}$ parameter affects the energy dissipation during outbursts and their timescales. For the cooling function from Ichikawa & Osaki (1992), the value of the $\alpha_{\rm hot}$ parameter should be close to 0.1, higher values produce normal outburst durations that are shorter than observed.

The mass ratio of the binary determines the gravitational forces acting on the disk and thus affects the disk radius. For larger disk radii, caused by lower mass ratios, the model requires higher densities to trigger an outburst (Ichikawa & Osaki 1992). If the mass transfer rate is unchanged, this leads to longer quiescent phases, which is in agreement with observations of SU UMa systems (Menou 2000). The balance between gravitational and pressure forces also determines the precession rate of the disk (Goodchild & Ogilvie 2006), which we interpret as the superhump excess. We find faster precession and higher superhump excess for higher mass ratios, although our mass ratio to superhump excess scaling is too weak compared to the observations (Patterson et al. 2005) and it seems that 3D simulations are needed to get better agreement (Smith et al. 2007).

We also find higher superhump amplitudes for higher mass ratios. This trend seems to be opposite to observations that find higher amplitudes for longer binary orbital periods (lower mass ratios) (Kato et al. 2012, Sect. 4.7.1). In addition, there are several other caveats to our model.

In our model, the disk expands due to the enhanced angular momentum transfer during an outburst and contracts during the quiescent phase due to accreting low angular momentum gas from the donor star. Overall, the disk radius and mass increase with time. The conditions required to start an outburst in the model of Ichikawa & Osaki (1992) require higher densities at larger radii. For our constant mass transfer, it will therefore take more time to reach the critical densities at larger radii, and these higher densities will cause more viscous heating, leading to higher luminosities. While the monotonically increasing outburst luminosity is found in observations of V1504 Cygni (Cannizzo et al. 2012), the observed quiescent durations do not show clear trends. This could be introduced in simulations with non-constant mass transfer rates, but the exact physics behind the mass transfer rate is currently poorly understood. The luminosity increase for the first normal outburst after a superoutburst was not looked at in Cannizzo et al. (2012), but it also cannot be confirmed from their light curves.

Our simulations also produce outburst magnitudes that are too large, caused by the cooling model we took from Ichikawa & Osaki (1992) and used outside its intended purpose. We used this cooling function because the surface cooling with the Lin & Papaloizou (1985) opacity we used before required a too low temperature threshold ≈3000 K for the viscosity switch to produce outburst cycles, and it tended not to return to quiescence after a superoutburst if the mass transfer rate was too high. The effects of the different cooling functions are shown in Fig. 6, the model using the Lin & Papaloizou (1985) opacity has only half the mass transfer rate of the other models.

We also tested the cooling prescription by Kimura et al. (2020) (yellow line in Fig. 6), which is a revised version of the Ichikawa & Osaki (1992) cooling function with more efficient cooling on the hot branch. It produces a colder but still too hot outburst state and causes reflares where there were none for the fiducial model.

Opacity-based cooling leads to lower mid-plane temperatures during outbursts, which increases their duration due to the lower viscosity (compare the orange line in Fig. 6). The lower outburst temperatures increase the superhump excess from 1.8% to 2.1% for the variable mass transfer model, which is still well below the observed excess of 3.7%. Lower mid-plane temperatures would also make tidal dissipation heating more relevant, so that the superoutburst would be brighter compared to the precursor outburst, as is the case in observations. The same effect would also increase the superhump magnitudes, which is necessary since they are expected to be reduced by a factor of 2–4 when 3D effects are included (Smak 2009b).

The heating and cooling prescriptions in our model do not seem to be appropriate for the hot spot, and we found average hot spot temperatures that are a factor of three higher, with spontaneous peaks up to a factor of seven higher, than temperatures estimated from observations by Wood et al. (1989). Despite the excessively high temperatures, the total energy emitted by the hot spot is half of the value of theoretical estimates, see Sect. 4.3.4.

The amplitude of the flickering in the light curve caused by the hot spot is compatible with the amplitude found in observations, see Fig. 5. However, it should be noted that the flickering amplitude in our simulations depends on the mass transfer rate (Fig. 22), the cooling prescription (Fig. 6), and we find that it also scales with the numerical timestep size. There are several potential sources of flickering (Bruch 2021) of which only the hot spot is included in our model. Therefore, the flickering caused by the hotspot is overestimated in our simulations and the agreement with the observations seems to be a coincidence.

The model also predicts a monotonically increasing quiescent luminosity where observations find constant to decreasing luminosities. In our model, the quiescent luminosity increases due to the increasing viscous dissipation with increasing disk mass as well as the increasing tidal dissipation in the hot spot due to the shrinking disk radius. Our model therefore fails to explain the observed quiescence luminosities.

There are several 3D effects that we cannot model in 2D, but that are important for outburst behavior, such as eccentricity damping by vertical pressure forces (Oyang 2022, Chapter 4)

[2] github https://github.com/rometsch/fargocpt

or tilted disks that can explain negative superhump excess (Wood & Burke 2007; Montgomery 2009, 2012a,b). A three-dimensional mass stream could also overflow and underflow the disk, depositing its mass at different radii, see Godon (2019) for a recent study on this topic. This effect would change the evolution during quiescence (Kunze et al. 2001), the outbursts themselves (Schreiber & Hessman 1998), and the outburst recurrence rate (Kimura et al. 2020).

Nevertheless, our 2D simulations model the gravitational torques and allow us to study the effects of disk eccentricity on the outbursts. The main results of our study are the high superhump amplitudes we find in our simulation, the lack thereof in previous simulations is used as a criticism of the TTI model in Smak (2009b). We find gravitational torques during superoutbursts that are enhanced by almost two orders of magnitude (see Fig. 10) compared to the quiescent torques, which is higher than other studies assumed (cf. Sect. 5.3 Hameury 2020). Our model can reproduce complex outburst mechanisms such as delayed outbursts, long normal outbursts, and reflares at the end of superoutbursts, see Fig. 26, which we think should give credence to the TTI model of Osaki (1989).

Acknowledgements. This paper is dedicated to our friend and mentor Wilhelm Kley who introduced us to this topic. The authors acknowledge support from the High Performance and Cloud Computing Group at the Zentrum für Datenverarbeitung of the University of Tübingen, the state of Baden-Württemberg through bwHPC and the German Research Foundation (DFG) through grant no INST 37/935-1 FUGG. RK acknowledges financial support via the Heisenberg Research Grant funded by the German Research Foundation (DFG) under grant no. KU 2849/9. We acknowledge with thanks the variable star observations from the AAVSO International Database contributed by observers worldwide and used in this research.

References

Astropy Collaboration (Price-Whelan, A. M., et al.) 2022, ApJ, 935, 167
Bąkowska, K., & Olech, A. 2015, Acta Astron., 65, 351
Balbus, S. A., & Hawley, J. F. 1991, ApJ, 376, 214
Baruteau, C. 2008, Ph.D. Thesis, Observatoire de Paris
Boley, A. C., & Durisen, R. H. 2006, ApJ, 641, 534
Bruch, A. 1996, A&A, 312, 97
Bruch, A. 2021, MNRAS, 503, 953
Bruch, A., Beele, D., & Baptista, R. 1996, A&A, 306, 151
Buat-Ménard, V., Hameury, J. M., & Lasota, J. P. 2001, A&A, 366, 612
Cambier, H. 2015, MNRAS, 452, 3620
Cannizzo, J. K., Smale, A. P., Wood, M. A., Still, M. D., & Howell, S. B. 2012, ApJ, 747, 117
Chandrasekhar, S. 1960, Proc. Nat. Acad. Sci., 46, 253
Coleman, M. S. B., Kotko, I., Blaes, O., Lasota, J. P., & Hirose, S. 2016, MNRAS, 462, 3710
Cox, A. N., & Stewart, J. N. 1969, Nauchnye Informatsii, 15, 1
Coyne, R., Shenoy, A., MacLachlan, G., et al. 2012, ArXiv e-prints [arXiv:1206.6762]
de Val-Borro, M., Edgar, R. G., Artymowicz, P., et al. 2006, MNRAS, 370, 529
Dubus, G., Otulakowska-Hypka, M., & Lasota, J.-P. 2018, A&A, 617, A26
Echevarría, J., Ramírez, S. H., Fuentes, M., et al. 2023, Rev. Mex. Astron. Astrofis., 59, 191
Eggleton, P. P. 1983, ApJ, 268, 368
Godon, P. 1996, MNRAS, 282, 1107
Godon, P. 2019, ApJ, 870, 112
Goodchild, S., & Ogilvie, G. 2006, MNRAS, 368, 1123
Günther, R., Schäfer, C., & Kley, W. 2004, A&A, 423, 559
Hameury, J. M. 2020, Adv. Space Res., 66, 1004
Hameury, J. M., & Lasota, J. P. 2017, A&A, 602, A102
Hameury, J. M., & Lasota, J. P. 2021, A&A, 650, A114
Hameury, J.-M., Menou, K., Dubus, G., Lasota, J.-P., & Hure, J.-M. 1998, MNRAS, 298, 1048
Hameury, J.-M., Lasota, J.-P., & Warner, B. 2000, A&A, 353, 244
Hirose, S., Blaes, O., Krolik, J. H., Coleman, M. S. B., & Sano, T. 2014, ApJ, 787, 1
Hubeny, I. 1990, ApJ, 351, 632
Ichikawa, S., & Osaki, Y. 1992, PASJ, 44, 15
Ichikawa, S., Hirose, M., & Osaki, Y. 1993, PASJ, 45, 243
Inight, K., Gänsicke, B. T., Breedt, E., et al. 2023, MNRAS, 524, 4867
Jordan, L. M., Kley, W., Picogna, G., & Marzari, F. 2021, A&A, 654, A54
Ju, W., Stone, J. M., & Zhu, Z. 2017, ApJ, 841, 29
Kato, T., Maehara, H., Miller, I., et al. 2012, PASJ, 64, 21
Kimura, M., Osaki, Y., Kato, T., & Mineshige, S. 2020, PASJ, 72, 22
King, A. R. 1988, QJRAS, 29, 1
Kley, W., Papaloizou, J. C. B., & Ogilvie, G. I. 2008, A&A, 487, 671
Kotko, I., & Lasota, J. P. 2012, A&A, 545, A115
Kunze, S., Speith, R., & Hessman, F. V. 2001, MNRAS, 322, 499
Landstreet, J. D., Bagnulo, S., Martin, A., & Valyavin, G. 2016, A&A, 591, A80
Lasota, J.-P. 2001, New Astron Rev., 45, 449
Lasota, J. P., Dubus, G., & Kruk, K. 2008, A&A, 486, 523
Latter, H. N., & Ogilvie, G. I. 2006, MNRAS, 372, 1829
Lightkurve Collaboration (Cardoso, J. V. d. M., et al.) 2018, Astrophysics Source Code Library [record ascl:1812.013]
Lin, D. N. C., & Papaloizou, J. 1985, in Protostars and Planets II, eds. D. C. Black, & M. S. Matthews, 981
Lubow, S. H. 1991, ApJ, 381, 259
Lubow, S. H., & Shu, F. H. 1975, ApJ, 198, 383
Marzari, F., Baruteau, C., Scholl, H., & Thebault, P. 2012, A&A, 539, A98
Masset, F. 2000, A&AS, 141, 165
Mathew, A., & Nandy, M. K. 2017, RAA, 17, 061
McAllister, M. J., Littlefair, S. P., Baraffe, I., et al. 2015, MNRAS, 451, 114
McAllister, M., Littlefair, S. P., Parsons, S. G., et al. 2019, MNRAS, 486, 5535
Menou, K. 2000, Science, 288, 2022
Meyer, F., & Meyer-Hofmeister, E. 1981, A&A, 104, L10
Mineshige, S., & Osaki, Y. 1983, PASJ, 35, 377
Mineshige, S., & Wood, J. H. 1989, MNRAS, 241, 259
Miranda, R., Muñoz, D. J., & Lai, D. 2017, MNRAS, 466, 1170
Montgomery, M. M. 2009, MNRAS, 394, 1897
Montgomery, M. M. 2012a, ApJ, 745, L25
Montgomery, M. M. 2012b, ApJ, 753, L27
Müller, T. W. A., Kley, W., & Meru, F. 2012, A&A, 541, A123
Nixon, C. J., Pringle, C. C. T., & Pringle, J. E. 2024, J. Plasma Phys., 90, 905900101
Osaki, Y. 1989, PASJ, 41, 1005
Osaki, Y. 1995, PASJ, 47, 47
Osaki, Y., & Kato, T. 2014, PASJ, 66, 15
Osaki, Y., & Meyer, F. 2004, A&A, 428, L17
Oyang, B. 2022, Ph.D. Thesis, University of California, Santa Barbara, USA
Oyang, B., Jiang, Y.-F., & Blaes, O. 2021, MNRAS, 505, 1
Pala, A., Gänsicke, B., Belloni, D., et al. 2022, MNRAS, 510, 6110
Patterson, J., Kemp, J., Harvey, D. A., et al. 2005, PASP, 117, 1204
Picogna, G., & Marzari, F. 2013, A&A, 556, A148
Pjanka, P., & Stone, J. M. 2020, ApJ, 904, 90
Pratt, G. W., Hassall, B. J. M., Naylor, T., Wood, J. H., & Patterson, J. 1999, MNRAS, 309, 847
Rolfe, D. J., Haswell, C. A., & Patterson, J. 2001, MNRAS, 324, 529
Rometsch, T., Jordan, L. M., Moldenhauer, T. W., et al. 2024, A&A, 684, A192
Scepi, N., Lesur, G., Dubus, G., & Flock, M. 2018, A&A, 609, A77
Scepi, N., Dubus, G., & Lesur, G. 2019, A&A, 626, A116
Schreiber, M. R., & Hessman, F. V. 1998, MNRAS, 301, 626
Schreiber, M. R., Belloni, D., & Schwope, A. D. 2024, A&A, 682, L7
Shakura, N. I., & Sunyaev, R. A. 1973, A&A, 24, 337
Smak, J. 1984, Acta Astron., 34, 161
Smak, J. 1995, Acta Astron., 45, 355
Smak, J. 2002, Acta Astron., 52, 263
Smak, J. 2009a, Acta Astron., 59, 121
Smak, J. 2009b, Acta Astron., 59, 103
Smak, J., & Waagen, E. O. 2004, Acta Astron., 54, 433
Smith, A. J., Haswell, C. A., Murray, J. R., Truss, M. R., & Foulkes, S. B. 2007, MNRAS, 378, 785
Stone, J. M., & Norman, M. L. 1992, ApJS, 80, 753
Tetarenko, B. E., Lasota, J. P., Heinke, C. O., Dubus, G., & Sivakoff, G. R. 2018, Nature, 554, 69
Tscharnuter, W. M., & Winkler, K. H. A. 1979, Comput. Phys. Commun., 18, 171
Vaidya, B., Mignone, A., Bodo, G., & Massaglia, S. 2015, A&A, 580, A110
Velikhov, E. P. 1959, Sov. J. Exp. Theor. Phys., 9, 995
Viallet, M., & Hameury, J. M. 2008, A&A, 489, 699
Vogt, N. 1983, A&A, 128, 29
Warner, B. 2003, Cataclysmic Variable Stars (Cambridge, UK: Cambridge University Press)
Whitehurst, R. 1988, MNRAS, 232, 35
Wood, M. A., & Burke, C. J. 2007, ApJ, 661, 1042
Wood, J. H., Horne, K., Berriman, G., & Wade, R. A. 1989, ApJ, 341, 974

7 Summary and outlook

In my thesis, I developed the two-dimensional FargoCPT code to be able to handle simulations of disks in close binaries, and then used the code to gain new insights into planet formation in close binaries and cataclysmic variables.

Planet formation in close binaries

In Chapter 4 (Jordan et al. 2021) we identified numerical issues in the simulations of Gyergyovits et al. (2014); Marzari et al. (2012); Müller & Kley (2012). For larger domain sizes and higher grid resolutions, non-isothermal simulations of the primary disk produce similar results to the simpler isothermal simulations in Kley et al. (2008); Marzari et al. (2009); Marzari et al. (2012); Müller & Kley (2012); Paardekooper et al. (2008) which found disk eccentricities that are too high for planet formation to succeed.

I then extended the simulations in Chapter 5 to also include the circumbinary disk and circumstellar disks. Running these simulations required improvements to the indirect term prescription and a different artificial viscosity method, which is explained in detail in A. For these global simulations, I found that the dynamics of the stellar disks are determined by the mass transfer from the circumbinary disks. Depending on the precession phase of the circumbinary disk, the stellar disks have quiescent phases that satisfy the low eccentricity requirement of Silsbee & Rafikov (2021) for successful planetesimal growth, but also excited phases that would lead to destructive collisions.

While the dynamics of the stellar disks are more complex due to the cycling through different phases, the interactions between the disks open up new promising pathways for planet formation in close binaries. A possible next step would be to repeat the simulations with the addition of dust and planetesimals, which are already fully implemented in the FargoCPT code. From these simulations one could study their migration from the circumbinary disk to and through the circumstellar disks, as well as their relative velocities, which would reveal more about the possibility of planet formation in such systems.

Cataclysmic variables

In Chapter 6 (Jordan et al. 2024) we updated the FargoCPT code with several functions to simulate the outburst cycles of cataclysmic variables. Among other things, we added a Roche lobe overflow function, a stable viscosity update step, and a sophisticated equation of state that can model hydrogen ionization. We then used our code to put the thermal-tidal instability (TTI) model by Osaki (1989) to the test and conducted a parameter study of how the binary mass ratio, the mass transfer rate, and the viscosity parameters affect the outburst behavior of the disk.

By self-consistently evolving the disk mass, disk temperature, and interaction with the binary potential, our model was able to reproduce full outburst cycles and the shapes of the superhumps, which has not been achieved before in this combination. It also reproduced complex outburst behaviors of different cataclysmic variable systems by changing only the binary parameters. Our model suggests that the TTI model is a viable explanation for the outburst behavior of cataclysmic variables. This is an important result because it suggests that the variable mass transfer model may not be necessary. This model has become more popular in recent years due to doubts about the TTI model, but has no physical explanation for the large variations in mass transfer needed to explain the observations (Hameury 2020).

I conclude that the TTI model with modest mass transfer variations has the potential to explain the observed outburst behavior of cataclysmic variables. However, the model does need further refinement, such as more accurate treatment of the gas opacity and three-dimensional effects.

Code development

Throughout my thesis I have done a lot of code development and verification of the correctness of the code in the form of unit tests. This includes the study of the indirect term prescription in Appendix A, where we showed that a circumbinary disk in the frame of one of the stars can be simulated with small changes in the code, and for which companion masses the code changes become relevant. In Appendix C (Joseph et al. 2023) we clarified which parts of the spiral instability described in Speith & Kley (2003) are physical and which are not, and used the viscously spreading ring setup to test the accuracy of the viscosity prescription as well as the magnitude of the numerical diffusion in Cartesian hydrodynamic codes. In Appendix B, I described how gravitational smoothing is applied in hydrodynamical codes and what effect it has on a steady-state accretion disk. Then I tested how it could be improved and how it affects planet-disk interactions.

Similarly, my colleague Thomas Rometsch has done the same thing in the context of planet-disk interactions. Our entire FargoCPT code is documented in Chapter 3 (Rometsch et al. 2024) and is freely available at https://github.com/rometsch/fargocpt. Due to our combined contributions to the code, it currently offers unique simulation capabilities compared to other publicly available planet-disk and binary-disk simulation tools. We have put a lot of effort into making the code more foolproof and easier to use, and hope that it will be useful to students and researchers in the future.

8 Acknowledgements

I would like to thank my supervisor Wilhelm Kley for his guidance and support, and for being part of the very friendly and productive Computational Physics Group at the University of Tübingen, that he founded and led. I would also like to thank the other staff of his group, Heike Fricke and Christoph Schäfer for their help and support, and Rolf Kuiper and Klaus Werner for stepping in when necessary. I would like to thank my colleagues Tobias Moldenhauer, Thomas Rometsch, Anna Penzlin, Dennis Wehner, Alexandros Ziampras, Andree Oliva, Gabriel Marleau and many other group members for useful discussions and for making the time during my Ph.D. very enjoyable and fun. Additional special thanks to Anna, Thomas, Dennis and my mother for proofreading.

I would also like to thank Manuel Nonnenmacher, Sebastian Völkel, Kevin Marolt, Daniel Mieg, Martin Bohnert, Jonas Leister, and other students for making studying physics in Tübingen a great time. And I would like to thank my parents and my siblings for their support and encouragement.

I acknowledge support by the High Performance and Cloud Computing Group at the Zentrum für Datenverarbeitung of the University of Tübingen, the state of Baden-Württemberg through bwHPC and the German Research Foundation (DFG) through grant no INST 37/935-1 FUGG.

Bibliography

Alexander, R., Pascucci, I., Andrews, S., Armitage, P., & Cieza, L. (2014, January). The Dispersal of Protoplanetary Disks. In H. Beuther, R. S. Klessen, C. P. Dullemond, & T. Henning (Eds.), *Protostars and planets vi* (pp. 475–496). https://doi.org/10.2458/azu_uapress_9780816531240-ch021

Andrews, S. M., & Williams, J. P. (2005). Circumstellar Dust Disks in Taurus-Auriga: The Submillimeter Perspective. ApJ, *631*(2), 1134–1160. https://doi.org/10.1086/432712

Ansdell, M., Williams, J. P., Trapman, L., van Terwisga, S. E., Facchini, S., Manara, C. F., van der Marel, N., Miotello, A., Tazzari, M., Hogerheijde, M., Guidi, G., Testi, L., & van Dishoeck, E. F. (2018). ALMA Survey of Lupus Protoplanetary Disks. II. Gas Disk Radii. ApJ, *859*(1), Article 21, 21. https://doi.org/10.3847/1538-4357/aab890

Armitage, P. J. (2015). Physical processes in protoplanetary disks. *arXiv e-prints*, Article arXiv:1509.06382, arXiv:1509.06382. https://doi.org/10.48550/arXiv.1509.06382

Armitage, P. J., & Kley, W. (2019). From Protoplanetary Disks to Planet Formation. *From Protoplanetary Disks to Planet Formation: Saas-Fee Advanced Course 45. Swiss Society for Astrophysics and Astronomy*. https://doi.org/10.1007/978-3-662-58687-7

Artymowicz, P., & Lubow, S. H. (1994). Dynamics of Binary-Disk Interaction. I. Resonances and Disk Gap Sizes. ApJ, *421*, 651. https://doi.org/10.1086/173679

Astropy Collaboration, Price-Whelan, A. M., Lim, P. L., Earl, N., Starkman, N., Bradley, L., Shupe, D. L., Patil, A. A., Corrales, L., Brasseur, C. E., Nöthe, M., Donath, A., Tollerud, E., Morris, B. M., Ginsburg, A., Vaher, E., Weaver, B. A., Tocknell, J., Jamieson, W., … Astropy Project Contributors. (2022). The Astropy Project: Sustaining and Growing a Community-oriented Open-source Project and the Latest Major Release (v5.0) of the Core Package. ApJ, *935*(2), Article 167, 167. https://doi.org/10.3847/1538-4357/ac7c74

Bae, J., Nelson, R. P., & Hartmann, L. (2016). The Spiral Wave Instability Induced by a Giant Planet. I. Particle Stirring in the Inner Regions of Protoplanetary Disks. ApJ, *833*(2), Article 126, 126. https://doi.org/10.3847/1538-4357/833/2/126

Baptista, R., & Schlindwein, W. (2022). Challenging the Disk Instability Model. I. The Case of YZ LMi. AJ, *163*(3), Article 108, 108. https://doi.org/10.3847/1538-3881/ac3fb8

Baruteau, C. (2008). *Toward predictive scenarios of planetary migration* [Doctoral dissertation, CEA Saclay, Service d'Astrophysique, 91191 Gif/Yvette Cedex, France].

Bate, M. R. (2011). Collapse of a molecular cloud core to stellar densities: the formation and evolution of pre-stellar discs. MNRAS, *417*(3), 2036–2056. https://doi.org/10.1111/j.1365-2966.2011.19386.x

Bate, M. R. (2019). The statistical properties of stars and their dependence on metallicity. MNRAS, *484*(2), 2341–2361. https://doi.org/10.1093/mnras/stz103

Bate, M. R. (2022). Dust coagulation during the early stages of star formation: molecular cloud collapse and first hydrostatic core evolution. MNRAS, *514*(2), 2145–2161. https://doi.org/10.1093/mnras/stac1391

Bath, G. T., & Pringle, J. E. (1981). The evolution of viscous discs. I - Mass transfer variations. MNRAS, *194*, 967–986. https://doi.org/10.1093/mnras/194.4.967

Behmard, A., Dai, F., & Howard, A. W. (2022). Stellar Companions to TESS Objects of Interest: A Test of Planet-Companion Alignment. AJ, *163*(4), Article 160, 160. https://doi.org/10.3847/1538-3881/ac53a7

Belloni, D., & Schreiber, M. R. (2023). Formation and Evolution of Accreting Compact Objects. In *Handbook of x-ray and gamma-ray astrophysics* (p. 129). https://doi.org/10.1007/978-981-16-4544-0_98-1

Benedict, G. F., Harrison, T. E., Endl, M., & Torres, G. (2018). A Mass for γ Cep Ab. *Research Notes of the American Astronomical Society*, *2*(2), Article 7, 7. https://doi.org/10.3847/2515-5172/aabe7e

Benítez-Llambay, P., & Masset, F. S. (2016). Fargo3d: A new gpu-oriented mhd code. *The Astrophysical Journal Supplement Series*, *223*(1), 11. http://stacks.iop.org/0067-0049/223/i=1/a=11

Béthune, W., Latter, H., & Kley, W. (2021). Spiral structures in gravito-turbulent gaseous disks. A&A, *650*, Article A49, A49. https://doi.org/10.1051/0004-6361/202040094

Bitsch, B., Morbidelli, A., Johansen, A., Lega, E., Lambrechts, M., & Crida, A. (2018). Pebble-isolation mass: Scaling law and implications for the formation of super-Earths and gas giants. A&A, *612*, Article A30, A30. https://doi.org/10.1051/0004-6361/201731931

Blandford, R. D., & Payne, D. G. (1982). Hydromagnetic flows from accretion disks and the production of radio jets. MNRAS, *199*, 883–903. https://doi.org/10.1093/mnras/199.4.883

Blum, J., & Wurm, G. (2008). The growth mechanisms of macroscopic bodies in protoplanetary disks. ARA&A, *46*, 21–56. https://doi.org/10.1146/annurev.astro.46.060407.145152

Blum, J., Gundlach, B., Krause, M., Fulle, M., Johansen, A., Agarwal, J., von Borstel, I., Shi, X., Hu, X., Bentley, M. S., Capaccioni, F., Colangeli, L., Della Corte, V., Fougere, N., Green, S. F., Ivanovski, S., Mannel, T., Merouane, S., Migliorini, A., … Snodgrass, C. (2017). Evidence for the formation of comet 67P/Churyumov-Gerasimenko through gravitational collapse of a bound clump of pebbles. MNRAS, *469*, S755–S773. https://doi.org/10.1093/mnras/stx2741

Bodenheimer, P., & Pollack, J. B. (1986). Calculations of the accretion and evolution of giant planets: The effects of solid cores. Icarus, *67*(3), 391–408. https://doi.org/10.1016/0019-1035(86)90122-3

Boneva, D., Zamanov, R., Boeva, S., Latev, G., Nikolov, Y., Cvetković, Z., & Dimitrov, W. (2022). Recent observations of humps and superhumps and an estimation of outburst parameters of the AM CVn star CR Boo. Ap&SS, *367*(11), Article 110, 110. https://doi.org/10.1007/s10509-022-04149-z

Boss, A. P. (1997). Giant planet formation by gravitational instability. *Science*, *276*, 1836–1839. https://doi.org/10.1126/science.276.5320.1836

Boss, A. P. (2010). Formation of Giant Planets by Disk Instability on Wide Orbits Around Protostars with Varied Masses. *AAS/Division for Planetary Sciences Meeting Abstracts #42*, *42*, Article 52.01, 52.01.

Branch, D., & Tammann, G. A. (1992). Type IA supernovae as standard candles. ARA&A, *30*, 359–389. https://doi.org/10.1146/annurev.aa.30.090192.002043

Brisset, J., Heißelmann, D., Kothe, S., Weidling, R., & Blum, J. (2016). Submillimetre-sized dust aggregate collision and growth properties. Experimental study of a multi-particle system on a suborbital rocket. A&A, *593*, Article A3, A3. https://doi.org/10.1051/0004-6361/201527288

Bromley, B. C., & Kenyon, S. J. (2015). Planet Formation around Binary Stars: Tatooine Made Easy. ApJ, *806*(1), Article 98, 98. https://doi.org/10.1088/0004-637X/806/1/98

Buat-Ménard, V., Hameury, J. .-., & Lasota, J. .-. (2001). The nature of dwarf nova outbursts. A&A, *366*, 612–622. https://doi.org/10.1051/0004-6361:20000107

Cazzoletti, P., Ricci, L., Birnstiel, T., & Lodato, G. (2017). Testing dust trapping in the circumbinary disk around GG Tauri A. A&A, *599*, Article A102, A102. https://doi.org/10.1051/0004-6361/201629721

Ceppi, S., Cuello, N., Lodato, G., Longarini, C., Price, D. J., Elsender, D., & Bate, M. R. (2024). Probing initial distributions of orbital eccentricity and disc misalignment via polar discs. A&A, *682*, Article A104, A104. https://doi.org/10.1051/0004-6361/202348375

Chambers, J. E. (2001). Making More Terrestrial Planets. Icarus, *152*(2), 205–224. https://doi.org/10.1006/icar.2001.6639

Chiang, E. I., & Goldreich, P. (1997). Spectral Energy Distributions of T Tauri Stars with Passive Circumstellar Disks. ApJ, *490*(1), 368–376. https://doi.org/10.1086/304869

Chomiuk, L., Metzger, B. D., & Shen, K. J. (2021). New Insights into Classical Novae. ARA&A, *59*, 391–444. https://doi.org/10.1146/annurev-astro-112420-114502

Chou, Y., & Jhang, Y.-W. (2023). Updated Orbital Ephemeris and Detection of Superhump Modulation in X-Ray Band for the Ultra-compact Low Mass X-Ray Binary 4U 1820-30. ApJ, *951*(1), Article 42, 42. https://doi.org/10.3847/1538-4357/acd376

Christian, S., Vanderburg, A., Becker, J., Yahalomi, D. A., Pearce, L., Zhou, G., Collins, K. A., Kraus, A. L., Stassun, K. G., de Beurs, Z., Ricker, G. R., Vanderspek, R. K., Latham, D. W., Winn, J. N., Seager, S., Jenkins, J. M., Abe, L., Agabi, K., Amado, P. J., … Ziegler, C. (2022). A Possible Alignment Between the Orbits of Planetary Systems and their Visual Binary Companions. AJ, *163*(5), Article 207, 207. https://doi.org/10.3847/1538-3881/ac517f

Cieza, L. A., Padgett, D. L., Allen, L. E., McCabe, C. E., Brooke, T. Y., Carey, S. J., Chapman, N. L., Fukagawa, M., Huard, T. L., Noriga-Crespo, A., Peterson, D. E., & Rebull, L. M. (2009). Primordial Circumstellar Disks in Binary Systems: Evidence for Reduced Lifetimes. ApJ, *696*(1), L84–L88. https://doi.org/10.1088/0004-637X/696/1/L84

Coleman, G. A. L., Nelson, R. P., & Triaud, A. H. M. J. (2023). Global N-body simulations of circumbinary planet formation around Kepler-16 and -34 analogues I: Exploring the pebble accretion scenario. MNRAS, *522*(3), 4352–4373. https://doi.org/10.1093/mnras/stad833

Coppejans, D. L., Körding, E. G., Knigge, C., Pretorius, M. L., Woudt, P. A., Groot, P. J., Van Eck, C. L., & Drake, A. J. (2016). Statistical properties of dwarf novae-type cataclysmic variables: the outburst catalogue. MNRAS, *456*(4), 4441–4454. https://doi.org/10.1093/mnras/stv2921

Cox, E. G., Harris, R. J., Looney, L. W., Chiang, H.-F., Chandler, C., Kratter, K., Li, Z.-Y., Perez, L., & Tobin, J. J. (2017). Protoplanetary Disks in ρ Ophiuchus as Seen from ALMA. ApJ, *851*(2), Article 83, 83. https://doi.org/10.3847/1538-4357/aa97e2

Crida, A., Baruteau, C., Kley, W., & Masset, F. (2009). The dynamical role of the circumplanetary disc in planetary migration. A&A, *502*(2), 679–693. https://doi.org/10.1051/0004-6361/200811608

Czekala, I., Chiang, E., Andrews, S. M., Jensen, E. L. N., Torres, G., Wilner, D. J., Stassun, K. G., & Macintosh, B. (2019). The Degree of Alignment between Circumbinary Disks and Their Binary Hosts. ApJ, *883*(1), Article 22, 22. https://doi.org/10.3847/1538-4357/ab287b

D'Angelo, G., Henning, T., & Kley, W. (2003). Thermohydrodynamics of Circumstellar Disks with High-Mass Planets. ApJ, *599*(1), 548–576. https://doi.org/10.1086/379224

de Val-Borro, M., Edgar, R. G., Artymowicz, P., Ciecielag, P., Cresswell, P., D'Angelo, G., Delgado-Donate, E. J., Dirksen, G., Fromang, S., Gawryszczak, A., Klahr, H., Kley, W., Lyra, W., Masset, F., Mellema, G., Nelson, R. P., Paardekooper, S. .-., Peplinski, A., Pierens, A., … Speith, R. (2006). A comparative study of disc-planet interaction. MNRAS, *370*(2), 529–558. https://doi.org/10.1111/j.1365-2966.2006.10488.x

Demirci, T., Krause, C., Teiser, J., & Wurm, G. (2019). Onset of planet formation in the warm inner disk. Colliding dust aggregates at high temperatures. A&A, *629*, Article A66, A66. https://doi.org/10.1051/0004-6361/201935767

Demirci, T., Teiser, J., Steinpilz, T., Landers, J., Salamon, S., Wende, H., & Wurm, G. (2017). Is There a Temperature Limit in Planet Formation at 1000 K? ApJ, *846*(1), Article 48, 48. https://doi.org/10.3847/1538-4357/aa816c

Di Folco, E., Dutrey, A., Le Bouquin, J. .-., Lacour, S., Berger, J. .-., Köhler, R., Guilloteau, S., Piétu, V., Bary, J., Beck, T., Beust, H., & Pantin, E. (2014). GG Tauri: the fifth element. A&A, *565*, Article L2, L2. https://doi.org/10.1051/0004-6361/201423675

Dipierro, G., Price, D., Laibe, G., Hirsh, K., Cerioli, A., & Lodato, G. (2015). On planet formation in hl tau. *Monthly Notices of the Royal Astronomical Society: Letters*, *453*(1), L73–L77. https://doi.org/https://doi.org/10.1093/mnrasl/slv105

Dominik, C., & Tielens, A. G. G. M. (1997). The Physics of Dust Coagulation and the Structure of Dust Aggregates in Space. ApJ, *480*(2), 647–673. https://doi.org/10.1086/303996

Draine, B. T. (1995). Grain Destruction in Interstellar Shock Waves. Ap&SS, *233*(1-2), 111–123. https://doi.org/10.1007/BF00627339

Drążkowska, J., & Alibert, Y. (2017). Planetesimal formation starts at the snow line. A&A, *608*, Article A92, A92. https://doi.org/10.1051/0004-6361/201731491

Drążkowska, J., Bitsch, B., Lambrechts, M., Mulders, G. D., Harsono, D., Vazan, A., Liu, B., Ormel, C. W., Kretke, K., & Morbidelli, A. (2023, July). Planet Formation Theory in the Era of ALMA and Kepler: from Pebbles to Exoplanets. In S. Inutsuka, Y. Aikawa, T. Muto, K. Tomida, & M. Tamura (Eds.), *Protostars and planets vii* (p. 717, Vol. 534). https://doi.org/10.48550/arXiv.2203.09759

Dubrulle, B., Morfill, G., & Sterzik, M. (1995). The dust subdisk in the protoplanetary nebula. Icarus, *114*(2), 237–246. https://doi.org/10.1006/icar.1995.1058

Dubus, G., Otulakowska-Hypka, M., & Lasota, J.-P. (2018). Testing the disk instability model of cataclysmic variables. A&A, *617*, Article A26, A26. https://doi.org/10.1051/0004-6361/201833372

Duchêne, G., & Kraus, A. (2013). Stellar Multiplicity. ARA&A, *51*(1), 269–310. https://doi.org/10.1146/annurev-astro-081710-102602

Duffell, P. C., Dittmann, A. J., D'Orazio, D. J., Franchini, A., Kratter, K. M., Penzlin, A. B. T., Ragusa, E., Siwek, M., Tiede, C., Wang, H., Zrake, J., Dempsey, A. M., Haiman, Z., Lupi, A., Pirog, M., & Ryan, G. (2024). The Santa Barbara Binary-disk Code Comparison. ApJ, *970*(2), Article 156, 156. https://doi.org/10.3847/1538-4357/ad5a7e

Dullemond, C. P., Birnstiel, T., Huang, J., Kurtovic, N. T., Andrews, S. M., Guzmán, V. V., Pérez, L. M., Isella, A., Zhu, Z., Benisty, M., Wilner, D. J., Bai, X.-N., Carpenter, J. M., Zhang, S., & Ricci, L. (2018). The Disk Substructures at High Angular Resolution Project (DSHARP). VI. Dust Trapping in Thin-ringed Protoplanetary Disks. ApJ, *869*(2), Article L46, L46. https://doi.org/10.3847/2041-8213/aaf742

Dupuy, T. J., Kratter, K. M., Kraus, A. L., Isaacson, H., Mann, A. W., Ireland, M. J., Howard, A. W., & Huber, D. (2016). Orbital Architectures of Planet-hosting Binaries. I. Forming Five Small Planets in the Truncated Disk of Kepler-444A. ApJ, *817*(1), Article 80, 80. https://doi.org/10.3847/0004-637X/817/1/80

Dupuy, T. J., Kraus, A. L., Kratter, K. M., Rizzuto, A. C., Mann, A. W., Huber, D., & Ireland, M. J. (2022). Orbital architectures of planet-hosting binaries - II. Low mutual inclinations between planetary and stellar orbits. MNRAS, *512*(1), 648–660. https://doi.org/10.1093/mnras/stac306

Dvorak, R. (1982). Planetenbahnen in Doppelsternsystemen. *Oesterreichische Akademie Wissenschaften Mathematisch naturwissenschaftliche Klasse Sitzungsberichte Abteilung*, *191*(10), 423–437.

Eggleton, P. P. (1983). Aproximations to the radii of Roche lobes. ApJ, *268*, 368–369. https://doi.org/10.1086/160960

Elsender, D., Bate, M. R., Lakeland, B. S., Jensen, E. L. N., & Lubow, S. H. (2023). On the frequencies of circumbinary discs in protostellar systems. MNRAS, *523*(3), 4353–4364. https://doi.org/10.1093/mnras/stad1695

Endl, M., Cochran, W. D., Hatzes, A. P., & Wittenmyer, R. A. (2011, March). News from the γ Cephei Planetary System. In S. Schuh, H. Drechsel, & U. Heber (Eds.), *Planetary systems beyond the main sequence* (pp. 88–94, Vol. 1331). https://doi.org/10.1063/1.3556187

Ferrone, S., Delbo, M., Avdellidou, C., Melikyan, R., Morbidelli, A., Walsh, K., & Deienno, R. (2023). Identification of a 4.3 billion year old asteroid family and planetesimal population in the Inner Main Belt. A&A, *676*, Article A5, A5. https://doi.org/10.1051/0004-6361/202245594

Fitzmaurice, E., Martin, D. V., & Fabrycky, D. C. (2022). Sculpting the circumbinary planet size distribution through resonant interactions with companion planets. MNRAS, *512*(4), 5023–5036. https://doi.org/10.1093/mnras/stac741

Foucart, F., & Lai, D. (2013). Assembly of Protoplanetary Disks and Inclinations of Circumbinary Planets. ApJ, *764*(1), Article 106, 106. https://doi.org/10.1088/0004-637X/764/1/106

Fragner, M. M., & Nelson, R. P. (2010). Evolution of warped and twisted accretion discs in close binary systems. A&A, *511*, Article A77, A77. https://doi.org/10.1051/0004-6361/200913088

Fromang, S., & Nelson, R. P. (2009). Global MHD simulations of stratified and turbulent protoplanetary discs. II. Dust settling. A&A, *496*(3), 597–608. https://doi.org/10.1051/0004-6361/200811220

Garraffo, C., Drake, J. J., Alvarado-Gomez, J. D., Moschou, S. P., & Cohen, O. (2018). The Magnetic Nature of the Cataclysmic Variable Period Gap. ApJ, *868*(1), Article 60, 60. https://doi.org/10.3847/1538-4357/aae589

Godon, P. (1996). Non-reflective boundary conditions and the viscous instability in accretion discs. MNRAS, *282*(4), 1107–1113. https://doi.org/10.1093/mnras/282.4.1107

Goodchild, S., & Ogilvie, G. (2006). The dynamics of eccentric accretion discs in superhump systems. MNRAS, *368*(3), 1123–1131. https://doi.org/10.1111/j.1365-2966.2006.10197.x

Günther, R., & Kley, W. (2002). Circumbinary disk evolution. A&A, *387*, 550–559. https://doi.org/10.1051/0004-6361:20020407

Gyergyovits, M., Eggl, S., Pilat-Lohinger, E., & Theis, C. (2014). Disc-protoplanet interaction. Influence of circumprimary radiative discs on self-gravitating protoplanetary bodies in binary star systems. A&A, *566*, Article A114, A114. https://doi.org/10.1051/0004-6361/201321854

Haffert, S., Bohn, A., De Boer, J., Snellen, I., Brinchmann, J., Girard, J., Keller, C., & Bacon, R. (2019). Two accreting protoplanets around the young star pds 70. *Nature Astronomy*, *3*(8), 749–754. https://doi.org/https://doi.org/10.1038/s41550-019-0780-5

Hameury, J. M. (2020). A review of the disc instability model for dwarf novae, soft X-ray transients and related objects. *Advances in Space Research*, *66*(5), 1004–1024. https://doi.org/10.1016/j.asr.2019.10.022

Hamuy, M., Phillips, M. M., Suntzeff, N. B., Schommer, R. A., Maza, J., & Aviles, R. (1996). The Absolute Luminosities of the Calan/Tololo Type IA Supernovae. AJ, *112*, 2391. https://doi.org/10.1086/118190

Harris, R. J., Andrews, S. M., Wilner, D. J., & Kraus, A. L. (2012). A Resolved Census of Millimeter Emission from Taurus Multiple Star Systems. ApJ, *751*(2), Article 115, 115. https://doi.org/10.1088/0004-637X/751/2/115

Hartigan, P., & Kenyon, S. J. (2003). A Spectroscopic Survey of Subarcsecond Binaries in the Taurus-Auriga Dark Cloud with the Hubble Space Telescope. ApJ, *583*(1), 334–357. https://doi.org/10.1086/345293

Hatzes, A. P., Cochran, W. D., Endl, M., McArthur, B., Paulson, D. B., Walker, G. A. H., Campbell, B., & Yang, S. (2003). A Planetary Companion to γ Cephei A. ApJ, *599*(2), 1383–1394. https://doi.org/10.1086/379281

Heath, R. M., & Nixon, C. J. (2020). On the orbital evolution of binaries with circumbinary discs. A&A, *641*, Article A64, A64. https://doi.org/10.1051/0004-6361/202038548

Holman, M. J., & Wiegert, P. A. (1999). Long-Term Stability of Planets in Binary Systems. AJ, *117*(1), 621–628. https://doi.org/10.1086/300695

Hōshi, R. (1979). Accretion Model for Outbursts of Dwarf Nova. *Progress of Theoretical Physics*, *61*(5), 1307–1319. https://doi.org/10.1143/PTP.61.1307

Hoyle, F., & Fowler, W. A. (1960). Nucleosynthesis in Supernovae. ApJ, *132*, 565. https://doi.org/10.1086/146963

Ida, S., & Makino, J. (1993). Scattering of Planetesimals by a Protoplanet: Slowing Down of Runaway Growth. Icarus, *106*(1), 210–227. https://doi.org/10.1006/icar.1993.1167

Imada, A., Izumiura, H., Kuroda, D., Yanagisawa, K., Kawai, N., Omodaka, T., & Miyanoshita, R. (2012). Discovery of Superhumps during a Normal Outburst of SU Ursae Majoris. PASJ, *64*, L5. https://doi.org/10.1093/pasj/64.5.L5

Ivanova, N., & Nandez, J. L. A. (2016). Common envelope events with low-mass giants: understanding the transition to the slow spiral-in. MNRAS, *462*(1), 362–381. https://doi.org/10.1093/mnras/stw1676

Jones, A. P., Tielens, A. G. G. M., Hollenbach, D. J., & McKee, C. F. (1994). Grain Destruction in Shocks in the Interstellar Medium. ApJ, *433*, 797. https://doi.org/10.1086/174689

Jordan, L. M., Wehner, D., & Kuiper, R. (2024). Two-dimensional simulations of disks in close binaries: Simulating outburst cycles in cataclysmic variables. A&A, *689*, Article A354, A354. https://doi.org/10.1051/0004-6361/202348726

Jordan, L. M., Kley, W., Picogna, G., & Marzari, F. (2021). Disks in close binary stars. γ-Cephei revisited. A&A, *654*, Article A54, A54. https://doi.org/10.1051/0004-6361/202141248

Jordan, L. M., & Rometsch, T. (2025). Hydrodynamical simulations with strong indirect terms in FARGO-like codes: Numerical aspects of the non-inertial frame and artificial viscosity. A&A, *693*, Article A177, A177. https://doi.org/10.1051/0004-6361/202450383

Joseph, J., Ziampras, A., Jordan, L., Turpin, G. A., & Nelson, R. P. (2023). Measuring the numerical viscosity in simulations of protoplanetary disks in Cartesian grids. The viscously spreading ring revisited. A&A, *678*, Article A134, A134. https://doi.org/10.1051/0004-6361/202245601

Kanagawa, K. D., Muto, T., & Tanaka, H. (2021). Dust rings as a footprint of planet formation in a protoplanetary disk. *The Astrophysical Journal*, *921*(2), 169. https://doi.org/10.3847/1538-4357/ac282b

Keppler, M., Penzlin, A., Benisty, M., van Boekel, R., Henning, T., van Holstein, R. G., Kley, W., Garufi, A., Ginski, C., Brandner, W., Bertrang, G. H. .-., Boccaletti, A., de Boer, J., Bonavita, M., Brown Sevilla, S., Chauvin, G., Dominik, C., Janson, M., Langlois, M., … Wildi, F. (2020). Gap, shadows, spirals, and streamers: SPHERE observations of binary-disk interactions in GG Tauri A. A&A, *639*, Article A62, A62. https://doi.org/10.1051/0004-6361/202038032

Klahr, H., & Kley, W. (2006a). 3D-radiation hydro simulations of disk-planet interactions. I. Numerical algorithm and test cases. A&A, *445*(2), 747–758. https://doi.org/10.1051/0004-6361:20053238

Klahr, H., & Kley, W. (2006b). 3D-radiation hydro simulations of disk-planet interactions. I. Numerical algorithm and test cases. A&A, *445*(2), 747–758. https://doi.org/10.1051/0004-6361:20053238

Kley, W., & Nelson, R. P. (2008). Planet formation in binary stars: the case of γ Cephei. A&A, *486*(2), 617–628. https://doi.org/10.1051/0004-6361:20079324

Kley, W., Papaloizou, J. C. B., & Ogilvie, G. I. (2008). Simulations of eccentric disks in close binary systems. A&A, *487*(2), 671–687. https://doi.org/10.1051/0004-6361:200809953

Kokubo, E., & Ida, S. (1998). Oligarchic Growth of Protoplanets. Icarus, *131*(1), 171–178. https://doi.org/10.1006/icar.1997.5840

Kothe, S., Blum, J., Weidling, R., & Güttler, C. (2013). Free collisions in a microgravity many-particle experiment. III. The collision behavior of sub-millimeter-sized dust aggregates. Icarus, *225*(1), 75–85. https://doi.org/10.1016/j.icarus.2013.02.034

Kratter, K. M., Matzner, C. D., Krumholz, M. R., & Klein, R. I. (2010). On the Role of Disks in the Formation of Stellar Systems: A Numerical Parameter Study of Rapid Accretion. ApJ, *708*(2), 1585–1597. https://doi.org/10.1088/0004-637X/708/2/1585

Kraus, A. L., Ireland, M. J., Hillenbrand, L. A., & Martinache, F. (2012). The Role of Multiplicity in Disk Evolution and Planet Formation. ApJ, *745*(1), Article 19, 19. https://doi.org/10.1088/0004-637X/745/1/19

Kraus, A. L., Ireland, M. J., Huber, D., Mann, A. W., & Dupuy, T. J. (2016). The Impact of Stellar Multiplicity on Planetary Systems. I. The Ruinous Influence of Close Binary Companions. AJ, *152*(1), Article 8, 8. https://doi.org/10.3847/0004-6256/152/1/8

Krot, A. N., Amelin, Y., Bland, P., Ciesla, F. J., Connelly, J., Davis, A. M., Huss, G. R., Hutcheon, I. D., Makide, K., Nagashima, K., Nyquist, L. E., Russell, S. S., Scott, E. R. D., Thrane, K., Yurimoto, H., & Yin, Q. .-. (2009). Origin and chronology of chondritic components: A review. Geochim. Cosmochim. Acta, *73*(17), 4963–4997. https://doi.org/10.1016/j.gca.2008.09.039

Lada, C. J., & Lada, E. A. (2003). Embedded Clusters in Molecular Clouds. ARA&A, *41*, 57–115. https://doi.org/10.1146/annurev.astro.41.011802.094844

Lai, D., & Muñoz, D. J. (2023). Circumbinary Accretion: From Binary Stars to Massive Binary Black Holes. ARA&A, *61*, 517–560. https://doi.org/10.1146/annurev-astro-052622-022933

Lambrechts, M., & Johansen, A. (2012). Rapid growth of gas-giant cores by pebble accretion. A&A, *544*, Article A32, A32. https://doi.org/10.1051/0004-6361/201219127

Lambrechts, M., & Johansen, A. (2014). Forming the cores of giant planets from the radial pebble flux in protoplanetary discs. A&A, *572*, Article A107, A107. https://doi.org/10.1051/0004-6361/201424343

Lambrechts, M., Johansen, A., & Morbidelli, A. (2014). Separating gas-giant and ice-giant planets by halting pebble accretion. A&A, *572*, Article A35, A35. https://doi.org/10.1051/0004-6361/201423814

Lambrechts, M., Morbidelli, A., Jacobson, S. A., Johansen, A., Bitsch, B., Izidoro, A., & Raymond, S. N. (2019). Formation of planetary systems by pebble accretion and migration. How the radial pebble flux determines a terrestrial-planet or super-Earth growth mode. A&A, *627*, Article A83, A83. https://doi.org/10.1051/0004-6361/201834229

Lasota, J.-P. (2001). The disc instability model of dwarf novae and low-mass X-ray binary transients. New A Rev., *45*(7), 449–508. https://doi.org/10.1016/S1387-6473(01)00112-9

Li, A., & Draine, B. T. (2001). Infrared Emission from Interstellar Dust. II. The Diffuse Interstellar Medium. ApJ, *554*(2), 778–802. https://doi.org/10.1086/323147

Li, R., & Youdin, A. N. (2021). Thresholds for Particle Clumping by the Streaming Instability. ApJ, *919*(2), Article 107, 107. https://doi.org/10.3847/1538-4357/ac0e9f

Lichtenberg, T., Schaefer, L. K., Nakajima, M., & Fischer, R. A. (2023, July). Geophysical Evolution During Rocky Planet Formation. In S. Inutsuka, Y. Aikawa, T. Muto, K. Tomida, & M. Tamura (Eds.), *Protostars and planets vii* (p. 907, Vol. 534). https://doi.org/10.48550/arXiv.2203.10023

Lightkurve Collaboration, Cardoso, J. V. d. M., Hedges, C., Gully-Santiago, M., Saunders, N., Cody, A. M., Barclay, T., Hall, O., Sagear, S., Turtelboom, E., Zhang, J., Tzanidakis, A., Mighell, K., Coughlin, J., Bell, K., Berta-Thompson, Z., Williams, P., Dotson, J., & Barentsen, G. (2018, December). Lightkurve: Kepler and TESS time series analysis in Python.

Lim, J., Simon, J. B., Li, R., Armitage, P. J., Carrera, D., Lyra, W., Rea, D. G., Yang, C.-C., & Youdin, A. N. (2024). Streaming Instability and Turbulence: Conditions for Planetesimal Formation. ApJ, *969*(2), Article 130, 130. https://doi.org/10.3847/1538-4357/ad47a2

Lin, D. N. C., & Papaloizou, J. (1985, January). On the dynamical origin of the solar system. In D. C. Black & M. S. Matthews (Eds.), *Protostars and planets ii* (pp. 981–1072).

Lines, S., Leinhardt, Z. M., Baruteau, C., Paardekooper, S. .-., & Carter, P. J. (2015). Modelling circumbinary protoplanetary disks. I. Fluid simulations of the Kepler-16 and 34 systems. A&A, *582*, Article A5, A5. https://doi.org/10.1051/0004-6361/201526295

Lodato, G., & Rice, W. K. M. (2004). Testing the locality of transport in self-gravitating accretion discs. MNRAS, *351*(2), 630–642. https://doi.org/10.1111/j.1365-2966.2004.07811.x

Lodato, G. (2008). Classical disc physics. New A Rev., *52*(2-5), 21–41. https://doi.org/10.1016/j.newar.2008.04.002

Long, F., Andrews, S. M., Rosotti, G., Harsono, D., Pinilla, P., Wilner, D. J., Öberg, K. I., Teague, R., Trapman, L., & Tabone, B. (2022). Gas Disk Sizes from CO Line Observations: A Test of Angular Momentum Evolution. ApJ, *931*(1), Article 6, 6. https://doi.org/10.3847/1538-4357/ac634e

Lubow, S. H., & Shu, F. H. (1975). Gas dynamics of semidetached binaries. ApJ, *198*, 383–405. https://doi.org/10.1086/153614

Lubow, S. H. (1991). A Model for Tidally Driven Eccentric Instabilities in Fluid Disks. ApJ, *381*, 259. https://doi.org/10.1086/170647

Macías, E., Guerra-Alvarado, O., Carrasco-González, C., Ribas, Á., Espaillat, C. C., Huang, J., & Andrews, S. M. (2021). Characterizing the dust content of disk substructures in TW Hydrae. A&A, *648*, Article A33, A33. https://doi.org/10.1051/0004-6361/202039812

Manara, C. F., Tazzari, M., Long, F., Herczeg, G. J., Lodato, G., Rota, A. A., Cazzoletti, P., van der Plas, G., Pinilla, P., Dipierro, G., Edwards, S., Harsono, D., Johnstone, D., Liu, Y., Menard, F., Nisini, B., Ragusa, E., Boehler, Y., & Cabrit, S. (2019). Observational constraints on dust disk sizes in tidally truncated protoplanetary disks in multiple systems in the Taurus region. A&A, *628*, Article A95, A95. https://doi.org/10.1051/0004-6361/201935964

Marois, C., Macintosh, B., Barman, T., Zuckerman, B., Song, I., Patience, J., Lafrenière, D., & Doyon, R. (2008). Direct Imaging of Multiple Planets Orbiting the Star HR 8799. *Science*, *322*(5906), 1348. https://doi.org/10.1126/science.1166585

Martin, D. V., & Fitzmaurice, E. (2022). Running the gauntlet - survival of small circumbinary planets migrating through destabilizing resonances. MNRAS, *512*(1), 602–616. https://doi.org/10.1093/mnras/stac090

Martin, D. V., Triaud, A. H. M. J., Udry, S., Marmier, M., Maxted, P. F. L., Collier Cameron, A., Hellier, C., Pepe, F., Pollacco, D., Ségransan, D., & West, R. (2019). The BEBOP radial-velocity survey for circumbinary planets. I. Eight years of CORALIE observations of 47 single-line eclipsing binaries and abundance constraints on the masses of circumbinary planets. A&A, *624*, Article A68, A68. https://doi.org/10.1051/0004-6361/201833669

Martin, R. G., Lissauer, J. J., & Quarles, B. (2020). Evolution of α Centauri b's protoplanetary disc. MNRAS, *496*(2), 2436–2447. https://doi.org/10.1093/mnras/staa1674

Martin, R. G., & Lubow, S. H. (2017). Polar Alignment of a Protoplanetary Disk around an Eccentric Binary. ApJ, *835*(2), Article L28, L28. https://doi.org/10.3847/2041-8213/835/2/L28

Martin, R. G., & Lubow, S. H. (2018). Polar alignment of a protoplanetary disc around an eccentric binary - II. Effect of binary and disc parameters. MNRAS, *479*(1), 1297–1308. https://doi.org/10.1093/mnras/sty1648

Marzari, F., Baruteau, C., Scholl, H., & Thebault, P. (2012). Eccentricity of radiative disks in close binary-star systems. A&A, *539*, Article A98, A98. https://doi.org/10.1051/0004-6361/201118075

Marzari, F., & Scholl, H. (2000). Planetesimal Accretion in Binary Star Systems. ApJ, *543*(1), 328–339. https://doi.org/10.1086/317091

Marzari, F., Scholl, H., Thébault, P., & Baruteau, C. (2009). On the eccentricity of self-gravitating circumstellar disks in eccentric binary systems. A&A, *508*(3), 1493–1502. https://doi.org/10.1051/0004-6361/200912251

Masset, F. (2000). FARGO: A fast eulerian transport algorithm for differentially rotating disks. A&AS, *141*, 165–173. https://doi.org/10.1051/aas:2000116

Masset, F. S. (2002). The co-orbital corotation torque in a viscous disk: Numerical simulations. A&A, *387*, 605–623. https://doi.org/10.1051/0004-6361:20020240

Mathis, J. S., Rumpl, W., & Nordsieck, K. H. (1977). The size distribution of interstellar grains. ApJ, *217*, 425–433. https://doi.org/10.1086/155591

Menou, K., & Goodman, J. (2004). Low-Mass Protoplanet Migration in T Tauri α-Disks. ApJ, *606*(1), 520–531. https://doi.org/10.1086/382947

Meyer, F., & Meyer-Hofmeister, E. (1981). On the elusive cause of cataclysmic variable outbursts. A&A, *104*, L10–L12.

Mineshige, S., & Osaki, Y. (1983). Disk-instability model for outbursts of dwarf novae Time-dependent formulation and one-zone model. PASJ, *35*(3), 377–396.

Miotello, A., Testi, L., Lodato, G., Ricci, L., Rosotti, G., Brooks, K., Maury, A., & Natta, A. (2014). Grain growth in the envelopes and disks of Class I protostars. A&A, *567*, Article A32, A32. https://doi.org/10.1051/0004-6361/201322945

Miranda, R., Muñoz, D. J., & Lai, D. (2017). Viscous hydrodynamics simulations of circumbinary accretion discs: variability, quasi-steady state and angular momentum transfer. MNRAS, *466*(1), 1170–1191. https://doi.org/10.1093/mnras/stw3189

Mizuno, H. (1980). Formation of the Giant Planets. *Progress of Theoretical Physics*, *64*(2), 544–557. https://doi.org/10.1143/PTP.64.544

Montesinos, M., Cuello, N., Olofsson, J., Cuadra, J., Bayo, A., Bertrang, G. H. .-., & Perrot, C. (2021). Radiative Scale Height and Shadows in Protoplanetary Disks. ApJ, *910*(1), Article 31, 31. https://doi.org/10.3847/1538-4357/abe3fc

Morbidelli, A., Lambrechts, M., Jacobson, S., & Bitsch, B. (2015). The great dichotomy of the Solar System: Small terrestrial embryos and massive giant planet cores. Icarus, *258*, 418–429. https://doi.org/10.1016/j.icarus.2015.06.003

Morbidelli, A., & Nesvorny, D. (2012). Dynamics of pebbles in the vicinity of a growing planetary embryo: hydro-dynamical simulations. A&A, *546*, Article A18, A18. https://doi.org/10.1051/0004-6361/201219824

Müller, T. W. A., & Kley, W. (2012). Circumstellar disks in binary star systems. Models for γ Cephei and α Centauri. A&A, *539*, Article A18, A18. https://doi.org/10.1051/0004-6361/201118202

Müller, T. W. A., Kley, W., & Meru, F. (2012). Treating gravity in thin-disk simulations. A&A, *541*, Article A123, A123. https://doi.org/10.1051/0004-6361/201118737

Muñoz, D. J., & Lai, D. (2016). Pulsed Accretion onto Eccentric and Circular Binaries. ApJ, *827*(1), Article 43, 43. https://doi.org/10.3847/0004-637X/827/1/43

Muñoz, D. J., Lai, D., Kratter, K., & Miranda, R. (2020). Circumbinary Accretion from Finite and Infinite Disks. ApJ, *889*(2), Article 114, 114. https://doi.org/10.3847/1538-4357/ab5d33

Muñoz, D. J., Miranda, R., & Lai, D. (2019). Hydrodynamics of Circumbinary Accretion: Angular Momentum Transfer and Binary Orbital Evolution. ApJ, *871*(1), Article 84, 84. https://doi.org/10.3847/1538-4357/aaf867

Musiolik, G., & Wurm, G. (2019). Contacts of Water Ice in Protoplanetary Disks—Laboratory Experiments. ApJ, *873*(1), Article 58, 58. https://doi.org/10.3847/1538-4357/ab0428

Nero, D., & Bjorkman, J. E. (2009). Did Fomalhaut, HR 8799, and HL Tauri Form Planets Via the Gravitational Instability? Placing Limits on the Required Disk Masses. ApJ, *702*(2), L163–L167. https://doi.org/10.1088/0004-637X/702/2/L163

Nesvorný, D., Li, R., Youdin, A. N., Simon, J. B., & Grundy, W. M. (2019). Trans-Neptunian binaries as evidence for planetesimal formation by the streaming instability. *Nature Astronomy*, *3*, 808–812. https://doi.org/10.1038/s41550-019-0806-z

Offner, S. S. R., Moe, M., Kratter, K. M., Sadavoy, S. I., Jensen, E. L. N., & Tobin, J. J. (2023, July). The Origin and Evolution of Multiple Star Systems. In S. Inutsuka, Y. Aikawa, T. Muto, K. Tomida, & M. Tamura (Eds.), *Protostars and planets vii* (p. 275, Vol. 534). https://doi.org/10.48550/arXiv.2203.10066

Ormel, C. W., & Klahr, H. H. (2010). The effect of gas drag on the growth of protoplanets. Analytical expressions for the accretion of small bodies in laminar disks. A&A, *520*, Article A43, A43. https://doi.org/10.1051/0004-6361/201014903

Ormel, C. W., Vazan, A., & Brouwers, M. G. (2021). How planets grow by pebble accretion. III. Emergence of an interior composition gradient. A&A, *647*, Article A175, A175. https://doi.org/10.1051/0004-6361/202039706

Osaki, Y. (1985). Irradiation-induced mass-overflow instability as a possible cause of superoutbursts in SU UMa stars. A&A, *144*, 369–380.

Osaki, Y. (1989). A model for the superoutburst phenomenon of SU Ursae MAjoris stars. PASJ, *41*, 1005–1033.

Oyang, B. (2022). *Magnetohydrodynamic simulations of am cv accretion disks* [Doctoral dissertation, University of California, Santa Barbara]. https://www.proquest.com/dissertations-theses/magnetohydrodynamic-simulations-am-cv-accretion/docview/2661871551/se-2

Oyang, B., Jiang, Y.-F., & Blaes, O. (2021). Investigating lack of accretion disc eccentricity growth in a global 3D MHD simulation of a superhump system. MNRAS, *505*(1), 1–17. https://doi.org/10.1093/mnras/stab1212

Özdönmez, A., Ege, E., Güver, T., & Ak, T. (2018). A new catalogue of Galactic novae: investigation of the MMRD relation and spatial distribution. MNRAS, *476*(3), 4162–4186. https://doi.org/10.1093/mnras/sty432

Paardekooper, S. .-., Thébault, P., & Mellema, G. (2008). Planetesimal and gas dynamics in binaries. MNRAS, *386*(2), 973–988. https://doi.org/10.1111/j.1365-2966.2008.13080.x

Paardekooper, S.-J., & Mellema, G. (2004). Planets opening dust gaps in gas disks. *Astronomy & Astrophysics*, *425*(1), L9–L12. https://doi.org/https://doi.org/10.1051/0004-6361:200400053

Paczynski, B., & Sienkiewicz, R. (1981). Gravitational radiation and the evolution of cataclysmic binaries. ApJ, *248*, L27–L30. https://doi.org/10.1086/183616

Paszun, D., & Dominik, C. (2009). Collisional evolution of dust aggregates. From compaction to catastrophic destruction. A&A, *507*(2), 1023–1040. https://doi.org/10.1051/0004-6361/200810682

Patterson, J. (2011). Distances and absolute magnitudes of dwarf novae: murmurs of period bounce. MNRAS, *411*(4), 2695–2716. https://doi.org/10.1111/j.1365-2966.2010.17881.x

Patterson, J., Kemp, J., Harvey, D. A., Fried, R. E., Rea, R., Monard, B., Cook, L. M., Skillman, D. R., Vanmunster, T., Bolt, G., Armstrong, E., McCormick, J., Krajci, T., Jensen, L., Gunn, J., Butterworth, N., Foote, J., Bos, M., Masi, G., & Warhurst, P. (2005). Superhumps in Cataclysmic Binaries. XXV. q_{crit}, $\epsilon(q)$, and Mass-Radius. PASP, *117*(837), 1204–1222. https://doi.org/10.1086/447771

Pecaut, M. J., & Mamajek, E. E. (2013). Intrinsic Colors, Temperatures, and Bolometric Corrections of Pre-main-sequence Stars. ApJS, *208*(1), Article 9, 9. https://doi.org/10.1088/0067-0049/208/1/9

Penzlin, A. B. T., Booth, R. A., Nelson, R. P., Schäfer, C. M., & Kley, W. (2024). Viscous circumbinary protoplanetary discs - I. Structure of the inner cavity. MNRAS, *532*(3), 3166–3179. https://doi.org/10.1093/mnras/stae1689

Penzlin, A. B. T., Kley, W., Audiffren, H., & Schäfer, C. M. (2022). Binary orbital evolution driven by a circumbinary disc. A&A, *660*, Article A101, A101. https://doi.org/10.1051/0004-6361/202141399

Penzlin, A. B. T., Kley, W., & Nelson, R. P. (2021). Parking planets in circumbinary discs. A&A, *645*, Article A68, A68. https://doi.org/10.1051/0004-6361/202039319

Pérez, L. M., Benisty, M., Andrews, S. M., Isella, A., Dullemond, C. P., Huang, J., Kurtovic, N. T., Guzmán, V. V., Zhu, Z., Birnstiel, T., Zhang, S., Carpenter, J. M., Wilner, D. J., Ricci, L., Bai, X.-N., Weaver, E., & Öberg, K. I. (2018). The Disk Substructures at High Angular Resolution Project (DSHARP). X. Multiple Rings, a Misaligned Inner Disk, and a Bright Arc in the Disk around the T Tauri star HD 143006. ApJ, *869*(2), Article L50, L50. https://doi.org/10.3847/2041-8213/aaf745

Perri, F., & Cameron, A. G. W. (1974). Hydrodynamic Instability of the Solar Nebula in the Presence of a Planetary Core. Icarus, *22*(4), 416–425. https://doi.org/10.1016/0019-1035(74)90074-8

Phuong, N. T., Dutrey, A., Diep, P. N., Guilloteau, S., Chapillon, E., Di Folco, E., Tang, Y. .-., Piétu, V., Bary, J., Beck, T., Hersant, F., Hoai, D. T., Huré, J. M., Nhung, P. T., Pierens, A., & Tuan-Anh, P. (2020). GG Tauri A: gas properties and dynamics from the cavity to the outer disk. A&A, *635*, Article A12, A12. https://doi.org/10.1051/0004-6361/201936173

Picogna, G., & Marzari, F. (2013). Three-dimensional modeling of radiative disks in binaries. A&A, *556*, Article A148, A148. https://doi.org/10.1051/0004-6361/201321860

Picogna, G., Ercolano, B., & Espaillat, C. C. (2021). The dispersal of protoplanetary discs - III. Influence of stellar mass on disc photoevaporation. MNRAS, *508*(3), 3611–3619. https://doi.org/10.1093/mnras/stab2883

Pierens, A., & Nelson, R. P. (2008). Constraints on resonant-trapping for two planets embedded in a protoplanetary disc. A&A, *482*(1), 333–340. https://doi.org/10.1051/0004-6361:20079062

Piso, A.-M. A., & Youdin, A. N. (2014). On the Minimum Core Mass for Giant Planet Formation at Wide Separations. ApJ, *786*(1), Article 21, 21. https://doi.org/10.1088/0004-637X/786/1/21

Plummer, H. C. (1911). On the problem of distribution in globular star clusters. MNRAS, *71*, 460–470. https://doi.org/10.1093/mnras/71.5.460

Polak, B., & Klahr, H. (2023). High-resolution Study of Planetesimal Formation by Gravitational Collapse of Pebble Clouds. ApJ, *943*(2), Article 125, 125. https://doi.org/10.3847/1538-4357/aca58f

Price, D. J., Wurster, J., Tricco, T. S., Nixon, C., Toupin, S., Pettitt, A., Chan, C., Mentiplay, D., Laibe, G., Glover, S., Dobbs, C., Nealon, R., Liptai, D., Worpel, H., Bonnerot, C., Dipierro, G., Ballabio, G., Ragusa, E., Federrath, C., … Lodato, G. (2018). Phantom: A Smoothed Particle Hydrodynamics and Magnetohydrodynamics Code for Astrophysics. PASA, *35*, Article e031, e031. https://doi.org/10.1017/pasa.2018.25

Rafikov, R. R. (2013). Planet Formation in Small Separation Binaries: Not so Secularly Excited by the Companion. ApJ, *765*(1), Article L8, L8. https://doi.org/10.1088/2041-8205/765/1/L8

Rafikov, R. R., & Silsbee, K. (2015). Planet Formation in Stellar Binaries. II. Overcoming the Fragmentation Barrier in α Centauri and γ Cephei-like Systems. ApJ, *798*(2), Article 70, 70. https://doi.org/10.1088/0004-637X/798/2/70

Raghavan, D., McAlister, H. A., Henry, T. J., Latham, D. W., Marcy, G. W., Mason, B. D., Gies, D. R., White, R. J., & ten Brummelaar, T. A. (2010). A survey of stellar families: Multiplicity of solar-type stars. *The Astrophysical Journal Supplement Series*, *190*(1), 1. https://doi.org/10.1088/0067-0049/190/1/1

Ribas, Á., Bouy, H., & Merín, B. (2015). Protoplanetary disk lifetimes vs. stellar mass and possible implications for giant planet populations. A&A, *576*, Article A52, A52. https://doi.org/10.1051/0004-6361/201424846

Ritter, H. (2010). Formation and evolution of cataclysmic variables . Mem. Soc. Astron. Italiana, *81*, 849.

Rodríguez, L. F., D'Alessio, P., Wilner, D. J., Ho, P. T. P., Torrelles, J. M., Curiel, S., Gómez, Y., Lizano, S., Pedlar, A., Cantó, J., & Raga, A. C. (1998). Compact protoplanetary disks around the stars of a young binary system. Nature, *395*(6700), 355–357. https://doi.org/10.1038/26421

Rometsch, T., Jordan, L. M., Moldenhauer, T. W., Wehner, D., Rendon Restrepo, S., Müller, T. W. A., Picogna, G., Kley, W., & Dullemond, C. P. (2024). FARGOCPT: 2D Multiphysics

code for simulating disk interactions with stars, planets, and particles. A&A, *684*, Article A192, A192. https://doi.org/10.1051/0004-6361/202348687

Rosotti, G. P. (2023). Empirical constraints on turbulence in proto-planetary discs. New A Rev., *96*, Article 101674, 101674. https://doi.org/10.1016/j.newar.2023.101674

Rosotti, G. P., Teague, R., Dullemond, C., Booth, R. A., & Clarke, C. J. (2020). The efficiency of dust trapping in ringed protoplanetary discs. MNRAS, *495*(1), 173–181. https://doi.org/10.1093/mnras/staa1170

Rota, A. A., Manara, C. F., Miotello, A., Lodato, G., Facchini, S., Koutoulaki, M., Herczeg, G., Long, F., Tazzari, M., Cabrit, S., Harsono, D., Ménard, F., Pinilla, P., van der Plas, G., Ragusa, E., & Yen, H. .-. (2022). Observational constraints on gas disc sizes in the protoplanetary discs of multiple systems in the Taurus region. A&A, *662*, Article A121, A121. https://doi.org/10.1051/0004-6361/202141035

Rotondo, M., Rueda, J. A., Ruffini, R., & Xue, S.-S. (2011). Relativistic Feynman-Metropolis-Teller theory for white dwarfs in general relativity. Phys. Rev. D, *84*(8), Article 084007, 084007. https://doi.org/10.1103/PhysRevD.84.084007

Schlindwein, W., & Baptista, R. (2024). Mass-transfer Outburts reborn: Modeling the light curve of the dwarf nova EX Draconis. *arXiv e-prints*, Article arXiv:2408.15814, arXiv:2408.15814. https://doi.org/10.48550/arXiv.2408.15814

Schräpler, R., Blum, J., Seizinger, A., & Kley, W. (2012). The Physics of Protoplanetesimal Dust Agglomerates. VII. The Low-velocity Collision Behavior of Large Dust Agglomerates. ApJ, *758*(1), Article 35, 35. https://doi.org/10.1088/0004-637X/758/1/35

Seizinger, A., & Kley, W. (2013). Bouncing behavior of microscopic dust aggregates. A&A, *551*, Article A65, A65. https://doi.org/10.1051/0004-6361/201220946

Sellek, A. D., Grassi, T., Picogna, G., Rab, C., Clarke, C. J., & Ercolano, B. (2024). Photoevaporation of protoplanetary discs with PLUTO+PRIZMO: I. Lower X-ray–driven mass-loss rates due to enhanced cooling. A&A, *690*, Article A296, A296. https://doi.org/10.1051/0004-6361/202450171

Shakura, N. I., & Sunyaev, R. A. (1973). Black holes in binary systems. Observational appearance. A&A, *24*, 337–355.

Shara, M. M., Livio, M., Moffat, A. F. J., & Orio, M. (1986). Do Novae Hibernate during Most of the Millennia between Eruptions? Links between Dwarf and Classical Novae, and Implications for the Space Densities and Evolution of Cataclysmic Binaries. ApJ, *311*, 163. https://doi.org/10.1086/164762

Silsbee, K., & Rafikov, R. R. (2021). Planet formation in stellar binaries: global simulations of planetesimal growth. A&A, *652*, Article A104, A104. https://doi.org/10.1051/0004-6361/202141139

Simon, J. I., Cuzzi, J. N., McCain, K. A., Cato, M. J., Christoffersen, P. A., Fisher, K. R., Srinivasan, P., Tait, A. W., Olson, D. M., & Scargle, J. D. (2018). Particle size distributions in chondritic meteorites: Evidence for pre-planetesimal histories. *Earth and Planetary Science Letters*, *494*, 69–82. https://doi.org/10.1016/j.epsl.2018.04.021

Simonsen, M., Boyd, D., Goff, W., Krajci, T., Menzies, K., Otero, S., Padovan, S., Poyner, G., Roe, J., Sabo, R., Sjoberg, G., Staels, B., Stubbings, R., Toone, J., & Wils, P. (2014). Z Cam Stars in the Twenty-First Century. *JAAVSO*, *42*(1), 177. https://doi.org/10.48550/arXiv.1402.0207

Smak, J. (2009a). New Interpretation of Superhumps. Acta Astron., *59*(1), 121–130.

Smak, J. (2009b). On the Amplitudes of Superhumps. Acta Astron., *59*(1), 103–107.

Smak, J. (2020). On the Periods and Nature of Superhumps. Acta Astron., *70*(4), 317–321. https://doi.org/10.32023/0001-5237/70.4.6

Smak, J., & Waagen, E. O. (2004). The 1985 Superoutburst of U Geminorum. Detection of Superhumps. Acta Astron., *54*, 433–442.

Smallwood, J. L., Martin, R. G., & Lubow, S. H. (2023). Formation of polar circumstellar discs in binary star systems. MNRAS, *520*(2), 2952–2964. https://doi.org/10.1093/mnras/stad338

Smith, A. J., Haswell, C. A., Murray, J. R., Truss, M. R., & Foulkes, S. B. (2007). Comprehensive simulations of superhumps. MNRAS, *378*(3), 785–800. https://doi.org/10.1111/j.1365-2966.2007.11840.x

Speith, R., & Kley, W. (2003). Stability of the viscously spreading ring. A&A, *399*, 395–407. https://doi.org/10.1051/0004-6361:20021783

Spruit, H. C., & Ritter, H. (1983). Stellar activity and the period gap in cataclysmic variables. A&A, *124*(2), 267–272.

Steinpilz, T., Joeris, K., Jungmann, F., Wolf, D., Brendel, L., Teiser, J., Shinbrot, T., & Wurm, G. (2020). Electrical charging overcomes the bouncing barrier in planet formation. *Nature Physics*, *16*(2), 225–229. https://doi.org/10.1038/s41567-019-0728-9

Stone, J. M., & Norman, M. L. (1992). ZEUS-2D: A Radiation Magnetohydrodynamics Code for Astrophysical Flows in Two Space Dimensions. I. The Hydrodynamic Algorithms and Tests. ApJS, *80*, 753. https://doi.org/10.1086/191680

Sytov, A. Y., Kaigorodov, P. V., Fateeva, A. M., & Bisikalo, D. V. (2011). Structure of the circumbinary envelopes of young binary stars with elliptical orbits. *Astronomy Reports*, *55*(9), 793–800. https://doi.org/10.1134/S1063772911090071

Taam, R. E., & Spruit, H. C. (1989). The Disrupted Magnetic Braking Hypothesis and the Period Gap of Cataclysmic Variables. ApJ, *345*, 972. https://doi.org/10.1086/167966

Thebault, P., & Haghighipour, N. (2015). Planet Formation in Binaries. In *Planetary exploration and science: Recent results and advances* (pp. 309–340). https://doi.org/10.1007/978-3-662-45052-9_13

Thébault, P., Marzari, F., & Scholl, H. (2006). Relative velocities among accreting planetesimals in binary systems: The circumprimary case. Icarus, *183*(1), 193–206. https://doi.org/10.1016/j.icarus.2006.01.022

Thébault, P., Marzari, F., & Scholl, H. (2008). Planet formation in α Centauri A revisited: not so accretion friendly after all. MNRAS, *388*(4), 1528–1536. https://doi.org/10.1111/j.1365-2966.2008.13536.x

Thébault, P., Marzari, F., Scholl, H., Turrini, D., & Barbieri, M. (2004). Planetary formation in the γ Cephei system. A&A, *427*, 1097–1104. https://doi.org/10.1051/0004-6361:20040514

Thun, D., Kley, W., & Picogna, G. (2017). Circumbinary discs: Numerical and physical behaviour. A&A, *604*, Article A102, A102. https://doi.org/10.1051/0004-6361/201730666

Tiede, C., Zrake, J., MacFadyen, A., & Haiman, Z. (2020). Gas-driven Inspiral of Binaries in Thin Accretion Disks. ApJ, *900*(1), Article 43, 43. https://doi.org/10.3847/1538-4357/aba432

Tokovinin, A. (2014). From Binaries to Multiples. II. Hierarchical Multiplicity of F and G Dwarfs. AJ, *147*(4), Article 87, 87. https://doi.org/10.1088/0004-6256/147/4/87

Tokovinin, A. (2021). Architecture of Hierarchical Stellar Systems and Their Formation. *Universe*, *7*(9), 352. https://doi.org/10.3390/universe7090352

Toomre, A. (1964). On the gravitational stability of a disk of stars. ApJ, *139*, 1217–1238. https://doi.org/10.1086/147861

Trapman, L., Ansdell, M., Hogerheijde, M. R., Facchini, S., Manara, C. F., Miotello, A., Williams, J. P., & Bruderer, S. (2020). Constraining the radial drift of millimeter-sized grains in the protoplanetary disks in Lupus. A&A, *638*, Article A38, A38. https://doi.org/10.1051/0004-6361/201834537

Tscharnuter, W. M., & Winkler, K. .-. A. (1979). A method for computing selfgravitating gas flows with radiation. *Computer Physics Communications*, *18*, 171–199. https://doi.org/10.1016/0010-4655(79)90111-5

Turpin, G. A., & Nelson, R. P. (2024). Orbital evolution of close binary systems: comparing viscous and wind-driven circumbinary disc models. MNRAS, *528*(4), 7256–7273. https://doi.org/10.1093/mnras/stae109

Vartanyan, D., Garmilla, J. A., & Rafikov, R. R. (2016). Tatooine Nurseries: Structure and Evolution of Circumbinary Protoplanetary Disks. ApJ, *816*(2), Article 94, 94. https://doi.org/10.3847/0004-637X/816/2/94

Vorobyov, E. I., Kulikov, I., Elbakyan, V. G., McKevitt, J., & Güdel, M. (2024). Dust growth and pebble formation in the initial stages of protoplanetary disk evolution. A&A, *683*, Article A202, A202. https://doi.org/10.1051/0004-6361/202348023

Wada, K., Tanaka, H., Suyama, T., Kimura, H., & Yamamoto, T. (2008). Numerical Simulation of Dust Aggregate Collisions. II. Compression and Disruption of Three-Dimensional Aggregates in Head-on Collisions. ApJ, *677*(2), 1296–1308. https://doi.org/10.1086/529511

Wang, B., & Han, Z. (2012). Progenitors of type Ia supernovae. New A Rev., *56*(4), 122–141. https://doi.org/10.1016/j.newar.2012.04.001

Warner, B. (1995). *Cataclysmic variable stars* (Vol. 28).

Weder, J., Mordasini, C., & Emsenhuber, A. (2023). Population study on MHD wind-driven disc evolution. Confronting theory and observation. A&A, *674*, Article A165, A165. https://doi.org/10.1051/0004-6361/202243453

Weidenschilling, S. J. (1977). Aerodynamics of solid bodies in the solar nebula. MNRAS, *180*, 57–70. https://doi.org/10.1093/mnras/180.2.57

Weingartner, J. C., & Draine, B. T. (2001). Dust Grain-Size Distributions and Extinction in the Milky Way, Large Magellanic Cloud, and Small Magellanic Cloud. ApJ, *548*(1), 296–309. https://doi.org/10.1086/318651

Wetherill, G. W., & Stewart, G. R. (1989). Accumulation of a swarm of small planetesimals. Icarus, *77*(2), 330–357. https://doi.org/10.1016/0019-1035(89)90093-6

Whitehurst, R. (1988). Numerical simulations of accretion discs - I. Superhumps : a tidal phenomenon of accretion discs. MNRAS, *232*, 35–51. https://doi.org/10.1093/mnras/232.1.35

Williams, J. P., & Cieza, L. A. (2011). Protoplanetary Disks and Their Evolution. ARA&A, *49*(1), 67–117. https://doi.org/10.1146/annurev-astro-081710-102548

Wurm, G., & Teiser, J. (2021). Understanding planet formation using microgravity experiments. *Nature Reviews Physics*, *3*(6), 405–421. https://doi.org/10.1038/s42254-021-00312-7

Youdin, A. N., & Goodman, J. (2005). Streaming Instabilities in Protoplanetary Disks. ApJ, *620*(1), 459–469. https://doi.org/10.1086/426895

Zagaria, F., Clarke, C. J., Booth, R. A., Facchini, S., & Rosotti, G. P. (2023). Observing Planetesimal Formation under Streaming Instability in the Rings of HD 163296. ApJ, *959*(2), Article L15, L15. https://doi.org/10.3847/2041-8213/ad0c54

Zagaria, F., Rosotti, G. P., & Lodato, G. (2021a). On dust evolution in planet-forming discs in binary systems - I. Theoretical and numerical modelling: radial drift is faster in binary discs. MNRAS, *504*(2), 2235–2252. https://doi.org/10.1093/mnras/stab985

Zagaria, F., Rosotti, G. P., & Lodato, G. (2021b). On dust evolution in planet-forming discs in binary systems - II. Comparison with Taurus and ρ Ophiuchus (sub-)millimetre observations: discs in binaries have small dust sizes. MNRAS, *507*(2), 2531–2549. https://doi.org/10.1093/mnras/stab2024

Zanazzi, J. J., & Lai, D. (2018). Inclination evolution of protoplanetary discs around eccentric binaries. MNRAS, *473*(1), 603–615. https://doi.org/10.1093/mnras/stx2375

Zhang, Z., Bowler, B. P., Dupuy, T. J., Brandt, T. D., Brandt, G. M., Cochran, W. D., Endl, M., MacQueen, P. J., Kratter, K. M., Isaacson, H. T., Franson, K., Kraus, A. L., Morley, C. V., & Zhou, Y. (2023). The McDonald Accelerating Stars Survey: Architecture of the Ancient Five-planet Host System Kepler-444. AJ, *165*(2), Article 73, 73. https://doi.org/10.3847/1538-3881/aca88c

Ziampras, A., Nelson, R. P., & Rafikov, R. R. (2023). Modelling planet-induced gaps and rings in ALMA discs: the role of in-plane radiative diffusion. MNRAS, *524*(3), 3930–3947. https://doi.org/10.1093/mnras/stad1973

Zorotovic, M., Schreiber, M. R., & Gänsicke, B. T. (2011). Post common envelope binaries from SDSS. XI. The white dwarf mass distributions of CVs and pre-CVs. A&A, *536*, Article A42, A42. https://doi.org/10.1051/0004-6361/201116626

Zorotovic, M., & Schreiber, M. R. (2020). Cataclysmic variable evolution and the white dwarf mass problem: A Review. *Advances in Space Research*, *66*(5), 1080–1089. https://doi.org/10.1016/j.asr.2019.08.044

Zsom, A., Ormel, C. W., Güttler, C., Blum, J., & Dullemond, C. P. (2010). The outcome of protoplanetary dust growth: pebbles, boulders, or planetesimals? II. Introducing the bouncing barrier. A&A, *513*, Article A57, A57. https://doi.org/10.1051/0004-6361/200912976

Zurlo, A., Gratton, R., Pérez, S., & Cieza, L. (2023). Observations of planet forming disks in multiple stellar systems. *European Physical Journal Plus*, *138*(5), Article 411, 411. https://doi.org/10.1140/epjp/s13360-023-04041-x

A Treating strong indirect terms in the FARGO code

When I started to simulate the circumbinary disk in the center of one of the stars for the project described in Chapter 5, the simulations initially failed due to numerical problems. I then proceeded to solve these problems, as can be seen from the results in Chapter 5. Later, I decided to study more closely the changes made to the code, their effects, and the companion masses at which these changes become necessary.

The results are published in the paper Jordan & Rometsch (2025), which starts on the next page.

A&A, 693, A177 (2025)
https://doi.org/10.1051/0004-6361/202450794
© The Authors 2025

Astronomy & Astrophysics

Hydrodynamical simulations with strong indirect terms in FARGO-like codes

Numerical aspects of the non-inertial frame and artificial viscosity

Lucas M. Jordan[1,⋆] and Thomas Rometsch[2]

[1] Institut für Astronomie und Astrophysik, Universität Tübingen, Auf der Morgenstelle 10, 72076 Tübingen, Germany
[2] Zentrum für Astronomie (ZAH), Institut für Theoretische Astrophysik (ITA), Universität Heidelberg, Albert-Ueberle-Str. 2, 69120 Heidelberg, Germany

Received 15 April 2024 / Accepted 26 November 2024

ABSTRACT

Context. Binary star systems allow us to study the planet formation process under extreme conditions. In the early stages, these systems contain a circumbinary disk and a disk around each star. To model the interactions between these disks in the frame of one of the stars, strong fictitious forces must be included in the simulations. The original FARGO and the FARGO3D codes fail to correctly simulate such systems if the indirect term becomes too strong.
Aims. We present a different way to compute the indirect term that, together with a tensor artificial viscosity prescription, allows the FARGO code to simulate the circumbinary disks in a non-inertial frame of reference. In this way, the FARGO code can be used to study interactions between circumstellar and circumbinary disks.
Methods. We first evaluated the accuracy of the standard implementation and our proposed indirect term prescription using a simple N-body test case. We then analytically estimated the effect of the default artificial viscosity used in the FARGO code in the limit of large distances to the N-body system. Finally, we evaluated the effects of the different prescriptions by performing hydrodynamical simulations in a non-inertial frame of reference.
Results. By updating the indirect term prescription and the artificial viscosity, we were able to successfully simulate a circumbinary disk in a frame that is centered on the less massive star. We find that updating the indirect term becomes relevant when the indirect term becomes stronger than the direct gravitational forces, which occurs for mass ratios of $q \gtrsim 5\%$. The default artificial viscosity used in the FARGO code inherently produces artificial pressure in a non-inertial frame of reference even in the absence of shocks. This leads to artificial mass ejection from the Hill sphere, starting at brown dwarf masses ($q \gtrsim 1\%$). These problems can be mitigated by using a tensor artificial viscosity formulation. For high mass ratios, $q \gtrsim 1\%$, it is also becomes important to initialize the disk in the center-of-mass frame. We expect our proposed changes to be relevant for other grid-based hydrodynamic codes where strong indirect terms occur, or for codes that use artificial viscosity.

Key words. accretion, accretion disks – hydrodynamics – methods: numerical – protoplanetary disks – planet-disk interactions – binaries: general

1. Introduction

When studying astrophysical hydrodynamics simulations, it is of interest to conduct such studies in a non-inertial frame of reference, that is to center the simulation on one star of a binary system to study its circumstellar disk. The non-inertial frame of reference introduces fictitious forces that must be taken into account in the simulation.

The indirect term is supposed to compensate for the forces acting on the center of the frame of reference so that it does not move. In extreme cases, the force due to the indirect term dominates the total force acting on the gas. Under such conditions, an overly simplistic approach for handling the indirect term can become the limiting factor in the accuracy of the entire simulation.

In this paper, we discuss the artificial viscosity and the indirect term used in the FARGO and FARGO3D codes (Masset 2000; Benítez-Llambay & Masset 2016) and show that they cause problems when simulating extreme setups. We then propose a more accurate method for handling the indirect term and the use of the tensor artificial viscosity by Tscharnuter & Winkler (1979) and show that they are more accurate at simulating systems with strong indirect terms. The methods presented in this paper have already been mentioned in Rometsch et al. (2024). In this paper, we explain the methods in detail and explore when they become necessary.

In Sect. 2 we compare two strategies for calculating the indirect term in a binary star system by testing how well the primary component of the binary remains fixed in a reference frame centered on the primary. We discuss two forms of artificial viscosity that are commonly used in grid codes in Sect. 3, and then use the proposed changes to run hydrodynamical simulations with strong indirect terms in Sect. 4. We then evaluate the relevance of our modifications to planetary disk simulations in Sect. 5 and discuss our results in Sect. 6.

2. N-body example on applying the indirect term

In the FARGO and FARGO3D codes, the indirect term is calculated at the beginning of the time step and then added to

⋆ Corresponding author; lucas.jordan@uni-tuebingen.de

Open Access article, published by EDP Sciences, under the terms of the Creative Commons Attribution License (https://creativecommons.org/licenses/by/4.0), which permits unrestricted use, distribution, and reproduction in any medium, provided the original work is properly cited.
This article is published in open access under the Subscribe to Open model. Subscribe to A&A to support open access publication.

the potential that is then derived numerically to calculate the acceleration on the gas. Next, the source terms due to pressure, viscosity, and artificial viscosity and, finally, the transport step are calculated and applied.

In this section, we construct a pure N-body test case where only gravitational forces are considered, using the REBOUND code (Rein & Liu 2012). This is a model of the full action to study the effects of different protocols for including the indirect term.

We initialized a binary star system in REBOUND and shifted it into the frame of the primary star. We then updated the velocities of the N-body in time with the indirect term using a forward Euler step in time before applying the standard REBOUND integration step. We used the *IAS15* integrator (Rein & Spiegel 2015) that is accurate to machine precision. We therefore assumed that any motion of the central object is due to inaccuracies in the indirect term protocols. This allowed us to measure their quality by how little the central object moves.

For a binary star system with masses m_1, m_2 and positions $\mathbf{x_1}$, $\mathbf{x_2}$, the indirect term is simply given by the negative of the acceleration of the primary by the secondary:

$$a_{\mathrm{Ind},1} = m_2 \frac{\mathbf{x_1} - \mathbf{x_2}}{|\mathbf{x_1} - \mathbf{x_2}|^3}. \tag{1}$$

This formulation is identical to the implementation in the FARGO code. We call it the Euler protocol because the velocity update is similar to a Euler integrator in the sense that it updates the velocity with a single step forward in time using the positions at the beginning of a time step.

As an alternative, we propose to use the acceleration experienced by the primary during its entire update step to compute the indirect term. In our case, we extracted the acceleration on the central object from the REBOUND code by measuring the change in velocity during the entire integration step:

$$a_{\mathrm{Ind},2} = -\frac{\mathbf{v}_1(t + \Delta t) - \mathbf{v}_1(t)}{\Delta t}, \tag{2}$$

where Δt is the size of the time step and $\mathbf{v}_1(t)$ is the velocity of the central object at the time t. To obtain the indirect term at the beginning of the time step, we created a copy of the N-body system and then integrated the copy with all the external forces acting on it to compute the accelerations. Assuming that the velocity of the central object at the start of the time step is zero, which is satisfied in a frame centered on it, Eq. (2) simply represents a velocity shift to the frame of the central object. For this reason, we call this method the shift protocol for the indirect term. We also computed the acceleration using a fifth-order Runge–Kutta scheme and found identical results up to the accuracy of the integration scheme.

For our test, we used a circular binary system with a mass ratio of $m_2/m_1 = 0.1$ and chose the units so that the total mass, binary separation, and gravitational constant are all equal to one. With this setup, one binary period is $P_{\mathrm{bin}} = 2\pi$ that is divided into 250 steps $\Delta t = 2\pi/250$ for integration. The primary star was initially placed in the coordinate center.

The time evolution of the primary star in simulations using the Euler and shift protocols for considering the indirect term are shown in Fig. 1. Neither implementation keeps the primary fixed at $x = 0$. For the shift protocol, the velocity is zero at the end of each time step, and the primary drifts on a circle. For the Euler protocol, the primary reaches zero velocity only after each full binary orbit and moves away from the origin. By design, the shift protocol keeps the primary at zero velocity. Any motion is only due to drift during the integration step as the primary is accelerated from $-\Delta t a_{\mathrm{Ind},2}$ to 0.

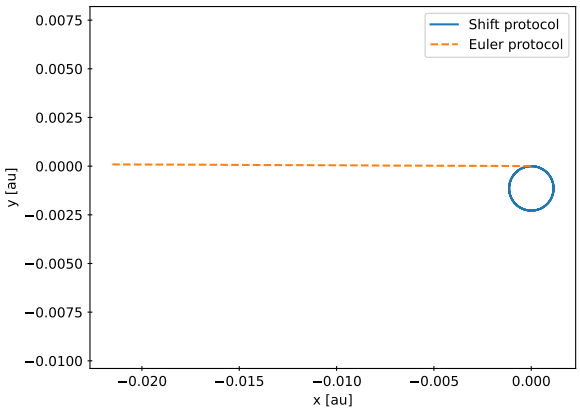

Fig. 1. Time evolution over three binary periods of the primary under the influence of the indirect term protocols of Eqs. (1) and (2).

For the next test, we shifted the binary system into the primary frame at the end of each time step to fix the primary at the coordinate center. This is intended to simulate the implementation of the FARGO codes in which the central object is implicit; in other words, the central object is not integrated, and the other N-body objects feel the indirect term at each substep of a fifth-order scheme, so that they are held in the frame of the central object with high accuracy.

We then added massless test particles that were integrated alongside the binary. Their velocities were updated with the indirect term at the beginning of the time step by adding $\boldsymbol{a}_{\mathrm{Ind}}\,\Delta t$, but were not shifted into the primary frame at the end of each time step. They represent gas cells on a fixed grid and therefore cannot be shifted to the primary frame. We also added a test particle that is shifted to the primary frame along with the binary after each time step as a reference. We modeled the time step criteria of a hydrocode by scaling the time step by the inverse velocity of the innermost particle, normalized by the Kepler velocity for a circular orbit at the same semi-major axis:

$$\Delta t = \frac{2\pi}{250} \cdot \frac{v_{\mathrm{k}}}{v_{\mathrm{test},1}}, \tag{3}$$

which mimics the CFL criteria of the FARGO code.

The resulting evolution of the semi-major axis and eccentricity for test particles starting at $3, 4, 20\,a_{\mathrm{bin}}$ are shown in Fig. 2. The first three rows correspond to a different initial semi-major axis, a_0, and the bottom row shows a zoom in for the case of $a_0 = 20\,a_{\mathrm{bin}}$. The left and right columns of the panels show the semi-major axis, a, of the test particles and their eccentricity, e, as a function of time, respectively. We note that the two columns show the quantities over different time frames.

In total, we identified four different oscillations in the particle orbits. The first has a period equal to the synodic period of the binary. They can be seen in the semi-major axis evolution of the innermost particle starting at $3\,a_{\mathrm{bin}}$ in the upper-left panel in Fig. 2. They are characterized by their double peaks and valleys during a binary period as the particles move through the potential of the binary. This oscillation is always present for the reference particle and is visible in the semi-major axis and eccentricity. In the simulations with an indirect term, this oscillation is dominated by other oscillations and is no longer visible at larger radii.

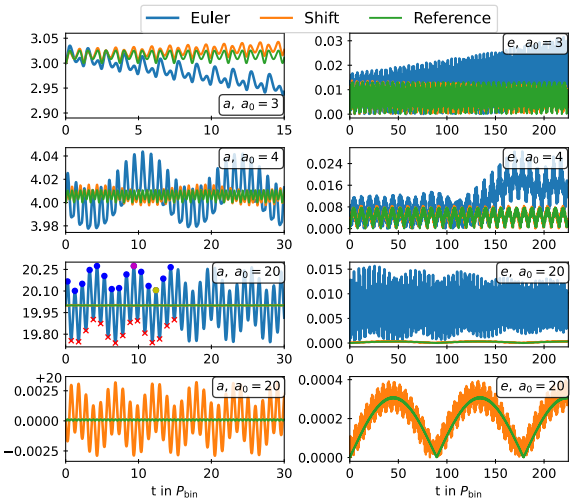

Fig. 2. Time evolution of the semi-major axis and eccentricity of two test particles under the influence of the indirect term in Eq. (1) and Eq. (2) respectively and an exact reference case without an indirect term.

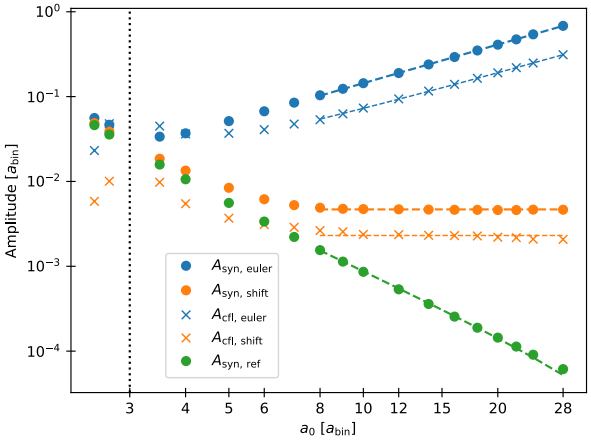

Fig. 3. Amplitudes of the semi-major axis oscillations as a function of the initial semi-major axis. The dotted line at 3 $a_{\rm bin}$ indicates the initial position of the particle that is used for the time step criteria. The dashed lines represent the best least squares fit with a power law model.

The second oscillation has a frequency of the orbital period of the particles. This oscillation occurs only in the eccentricity of the particles, and it is clearly visible in the lower-right panel. For reference, the particles at 20 $a_{\rm bin}$ have a period of ≈90 $P_{\rm bin}$.

In addition to these two physical oscillations, we find two purely numerical oscillations for the particles with an indirect term, which do not occur for the reference particle. The first numerical oscillation also has a period equal to the synodic period of the binary, but produces only a single peak and valley instead of the two for the oscillation due to the binary potential. We associate this oscillation with the residual motion due to the indirect term protocols, similar to those shown in Fig. 1 for the central object. Examples of this oscillation can be seen in the semi-major axis evolution of the particles starting at 20 $a_{\rm bin}$ (third and fourth panels on the left in Fig. 2). They also appear in the eccentricity of the particles, but cannot be seen individually because the eccentricity plots cover a larger time frame.

Finally, in simulations with indirect terms, the outer particles also oscillate due to the feedback from the time-stepping criteria that is calculated from the velocity of the innermost particle (see Eq. (3)). The frequency of this oscillation is the beat frequency between the orbital frequency of the particle itself and the innermost particle. This CFL oscillation causes the height of the peaks and valleys to oscillate during the synodic period, as seen in the semi-major axis and eccentricity for particles starting at 4 $a_{\rm bin}$ and 20 $a_{\rm bin}$.

In addition to the oscillations, we observe other differences between the reference particles and the particles subject to an indirect term. For the Euler protocol, the innermost particle (top row of Fig. 2) drifts inward, and its eccentricity increases. For the shift protocol, the particle drifts outward at one-third the drift of the of the Euler protocol particle, and its eccentricity does not increase. The sign of the drift direction and the sign of the deviations from the reference particle in general, are reversed by applying the indirect term after the integration step instead of before. The drift of the innermost particles is caused by the variable time step and does not occur with a constant time step.

The second row shows the time evolution of the second particle that started at a distance of 4 $a_{\rm bin}$. The particles subject to the indirect terms are no longer drifting. At $t = 150\,P_{\rm bin}$ the time step variations induce an eccentricity growth in the simulation using the Euler protocol. We ran an additional simulation where the time step from the Euler protocol simulation was copied and used for the outer particle with the shift-based protocol starting at 4 $a_{\rm bin}$ (not shown), which also caused it to increase its eccentricity, but at half the rate of the case where both particles used the Euler protocol.

The third row shows the particle at a distance of 20 bin, and the fourth row shows the same data again, but without the particle affected by the Euler protocol. For the Euler protocol, the eccentricity is higher by a factor of 35 and oscillates at twice the rate of its binary period. The eccentricity of the shift protocol particle has the oscillation with its binary period as the dominant oscillation and still resembles the time evolution of the reference particle. We repeated the test and measured the amplitudes of the oscillations in the semi-major axis of the outer test particle for different binary mass ratios, time step sizes, and initial semi-major axes.

An example of how we measured the oscillation amplitudes is shown in the third panel on the left in Fig. 2. We measured the amplitude of the combined physical and shift protocol oscillations during the synodic period, $A_{\rm syn}$, as the differences between the maxima (blue dots) and the subsequent minima (red crosses) of the semi-major axis. We defined the amplitude of the oscillations due to the CFL criteria, $A_{\rm CFL}$, as the difference between the highest and lowest maximum of the semi-major axis, as indicated by the purple and yellow dots. The amplitudes were always measured during the first 30 binary orbits, so that the particles were still close to their initial positions. We ignored the numerical drift and used the initial semi-major axis of the particle for the evaluation. The initial semi-major axis of the particle used for the time step criteria was kept at 3 $a_{\rm bin}$, while the other particle was varied from 2.5 to 28 $a_{\rm bin}$. The resulting amplitudes for the different indirect term protocols as a function of the initial semi-major axis are given in Fig. 3.

We evaluated the trends of the amplitudes by fitting a power law model to the data of the form:

$$A = A_0 + c_1 a_0^{n_1} \cdot c_2 q^{n_2} \cdot c_3 \Delta t^{n_3}\,, \tag{4}$$

Table 1. Scaling of the oscillation amplitudes in semi-major axis found in Fig. 3 for the indirect term protocols for particles beyond 8 $a_{\rm bin}$.

Protocol	$\frac{\mathrm{d}\log A_{\rm syn}}{\mathrm{d}\log a_0}$	$\frac{\mathrm{d}\log A_{\rm syn}}{\mathrm{d}\log \Delta t}$	$\frac{\mathrm{d}\log A_{\rm syn}}{\mathrm{d}\log q}$
Reference	–2.5	0	1
Shift	0	1	1
Euler	1.5	1	1
	$\frac{\mathrm{d}\log A_{\rm cfl}}{\mathrm{d}\log a_0}$	$\frac{\mathrm{d}\log A_{\rm cfl}}{\mathrm{d}\log \Delta t}$	$\frac{\mathrm{d}\log A_{\rm cfl}}{\mathrm{d}\log q}$
Reference	–	–	–
Shift	0	1	2
Euler	1.5	1	2

where a_0 is the initial semi-major axis of the particle, $q = m_2/m_1$ is the mass ratio of the binary, and Δt is the time step size. The power law indices n_i were fixed to the values in Table 1, while the constant A_0 and the coefficients c_i were determined by a least squares fit. For all fitted parameters, we find relative 2σ errors of less than 11% that we interpret as confirmation of the power law indices given in Table 1. The fits for the radial dependencies are plotted in Fig. 3 as dashed lines. The other power law dependencies for time step and binary mass ratio were determined in the same way.

For both indirect term protocols, we find oscillation amplitudes that scale linearly with the time step size, as expected from a first-order method. The amplitudes of the synodic oscillations depend linearly on the mass ratio, identical to the reference model, since they are physical and caused by the perturbations of the companion star that scale linearly with its mass. The amplitudes of the oscillations due to the CFL criteria scale with the square of the companion mass, because they depend on the strength of the perturbation as well as on the velocity variations of the innermost particle according to Eq. (3).

From the reference particles we infer that the amplitude of the synodic oscillations due to the variations in the binary potential scale with the initial semi-major axis as $a_0^{-2.5}$. For the shift protocol, the amplitude of the synodic oscillations reaches a constant floor value at distances above 8 $a_{\rm bin}$. We interpret this as the oscillations being dominated by the potential close to the binary. This causes the particle using the shift protocol to behave similarly to the reference particle at distances below 8 $a_{\rm bin}$ while beyond 8 $a_{\rm bin}$, the numerical oscillations dominate and their behavior diverges. For the Euler protocol, the numerical oscillation amplitudes increase with $a_0^{1.5}$ and are already significantly larger than the reference amplitude at an initial separation of 4 $a_{\rm bin}$.

For both the synodic period oscillation and the time step criteria oscillation, the magnitude of the errors of the Euler protocol at large radii is a factor of $(a_0/a_{\rm bin})^{1.5}$ larger than the errors of the shift protocol. Since $a_0 > a_{\rm bin}$ for circumbinary particles, the errors of the Euler protocol will always be larger than the errors of the shift protocol in this case.

We repeated similar tests for particles on an s-type orbit, that is, orbiting the central object with the companion as an outside perturber. For this configuration, the indirect term will always be weaker than the direct gravitational forces. We used the same binary setup as before and put the inner particle used for the time step criteria at 0.3 $a_{\rm bin}$ and the outer particle at 0.5 $a_{\rm bin}$. We reduced the time step so that the orbit of the inner particle was resolved with 250 steps. For this setup, both indirect term protocols induced an artificial inward drift that scales linearly with the time step size, with the shift protocol leading to a 20% faster drift than the Euler protocol. The deviations of the oscillation amplitudes from the reference particle are on the order of 10^{-3} and can be positive or negative depending on the time step size for both protocols. Thus, we do not find a clear trend of increasing inaccuracies as we did for the p-type orbits before.

We conclude that single-step-forward-in-time methods for the indirect term introduce inaccuracies that scale with the time step size and the strength of the indirect term. When the time step is determined by the velocity of a particle, analogous to a cell in a hydrodynamic simulation, it creates a feedback effect that causes the particle itself to migrate and induce oscillations in the other particles. We have introduced a new method for calculating the indirect term that is more accurate and stable for p-type orbits (orbits around both binary stars) than the standard indirect term protocol typically used in hydrocodes.

3. Artificial viscosity

The FARGO codes use a second-order upwind scheme for the hydrodynamic advection that cannot handle discontinuities and requires artificial viscosity to spread shocks over multiple grid cells. By default, FARGO codes use the artificial viscosity developed by Von Neumann & Richtmyer (1950, hereafter VNR50), which acts as a bulk viscosity and enters the equation of motion as an anisotropic artificial pressure to counteract compression. The implementation of the artificial viscosity is described in Stone & Norman (Section 4.3 1992, hereafter SN92), who define the artificial viscosity in one dimension and apply it to each dimension independently:

$$Q_i = \begin{cases} c^2 \Delta x_i^2 \Sigma \left(\frac{\partial v_i}{\partial x_i}\right)^2 & \text{if } \frac{\partial v_i}{\partial x_i} < 0 \\ 0 & \text{otherwise,} \end{cases} \tag{5}$$

where c is the artificial viscosity constant that measures the number of cells over which the shock spreads, for which values around 2 are typically recommended, and Δx_i is the cell size along direction i. We note the misprint in Eqs. (33) and (34) by SN92, where they forgot to square the artificial viscosity constant c.

Tscharnuter & Winkler (1979, hereafter TW79) raised concerns about the formulation of artificial viscosity by VNR50 being used on curve-linear coordinate systems, since it is formally valid only for Cartesian coordinates. They show that it can create artificial pressure in curve-linear coordinates even when there are no shocks. A specific example is given in Bodenheimer et al. (2006, Section 6.1.4) where they show that the artificial viscosity by VNR50 creates an artificial pressure that accelerates the collapse of a free-falling spherical gas cloud ($|v_r| \propto r$) even though the flow is smooth.

TW79 proposed a tensor artificial viscosity, analogous to the viscous stress tensor, which is independent of the coordinate system and frame of reference. An implementation of this artificial viscosity is also described in SN92, Appendix B, who added two additional constraints to the artificial viscosity prescription by TW79: the artificial viscosity constant must be the same in all directions (isotropy), and the off-diagonal elements of the tensor must be zero to avoid artificial angular momentum transport. The resulting artificial viscosity pressure tensor is given by:

$$\mathbf{Q} = \begin{cases} c^2 \Delta x^2 \Sigma \nabla \mathbf{v} \left[\nabla \otimes \mathbf{v} - \frac{1}{3} \nabla \mathbf{v}\, \mathbf{I}\right] & \text{if } \nabla \mathbf{v} < 0, \\ 0 & \text{otherwise,} \end{cases} \tag{6}$$

where c is again a dimensionless parameter near unity and Δx is the maximum cell extension in any direction.

We can analytically estimate the effect of the more naive approach given in Eq. (5) for a disk in a non-inertial frame. We considered the case of a Keplerian gas disk around a circular two-body system in the center-of-mass frame, where the primary moves at a velocity of $\mathbf{v}_0$. If the radial velocity of the gas is neglected, the gas has the Cartesian velocity components:

$$v_x = -v_\mathrm{k} \sin(\phi) \qquad \text{and} \qquad v_y = v_\mathrm{k} \cos(\phi), \tag{7}$$

where v_k is the Keplerian velocity and ϕ is the angle in the center-of-mass frame. We then shifted the whole system to the primary frame by subtracting its position and velocity from the gas and binary. After shifting to the primary center, the gas has the following velocity components:

$$v_r = v_\mathrm{k} \sin(\varphi - \phi) + v_0 \sin(\varphi - \varphi_0), \tag{8}$$
$$v_\varphi = v_\mathrm{k} \cos(\varphi - \phi) + v_0 \cos(\varphi - \varphi_0), \tag{9}$$

where φ is the angle in the primary frame and φ_0 is the azimuthal angle of the companion in the primary frame. Without loss of generality, we assumed $\varphi_0 = 0$, meaning that the binary is located on the x-axis and the secondary moves in the positive y-direction in the primary frame. In addition, we made the simplifying assumption that the length of the position vector of the cell is much greater than the length of the shift vector from the center of mass to the primary, so that its angular position is the same in the center-of-mass frame and in the primary frame: $\phi \approx \varphi$. Under these assumptions, the velocity of the gas has no radial dependence. This causes the radial component of the artificial pressure in Eq. (5), which depends only on the radial derivatives of the radial velocity, to always be zero. Therefore, we do not consider the radial velocity any further. The azimuthal velocity becomes:

$$v_\varphi = v_\mathrm{k} + v_0 \cos(\varphi). \tag{10}$$

Putting this velocity into Eq. (6) results in zero artificial viscosity, while putting it into Eq. (5) results in an artificial viscosity of:

$$Q_\varphi = \begin{cases} c^2 \Sigma \left[-\Delta\varphi \cdot v_0 \sin(\varphi)\right]^2 & \text{if } 0 < \varphi < \pi \\ 0 & \text{if } \pi < \varphi < 2\pi \end{cases}, \tag{11}$$

where $\Delta\varphi = 2\pi/N_\varphi$ is the angular cell size of the grid and N_φ is the number of azimuthal grid cells. The acceleration due to the artificial viscosity is then:

$$\frac{\partial v_\varphi}{\partial t} = -\frac{1}{\Sigma}\frac{1}{r}\frac{\partial Q_\varphi}{\partial \varphi} = \begin{cases} -\frac{1}{r} c^2 \Delta\varphi^2 v_0^2 \sin(2\varphi) & \text{if } 0 < \varphi < \pi \\ 0 & \text{if } \pi < \varphi < 2\pi, \end{cases} \tag{12}$$

If we use units for which $GM = 1$, and assume that the cell is far enough away from the two-body object that the distance to the primary at the center is approximately equal to the distance to the companion, we find the ratio of the artificial acceleration, $\dot{v}_{\varphi,\,\mathrm{art}}$, to the magnitude of the direct gravitational acceleration caused by the companion, $|\mathbf{a}_2|$, to be:

$$\frac{\dot{v}_{\varphi,\,\mathrm{art}}}{|\mathbf{a}_2|} = c^2 \Delta\varphi^2 \frac{r}{a} \frac{q}{(1+q)} \sin(2\varphi), \tag{13}$$

where q is the mass ratio of the companion to the primary and a is the semi-major axis. For typical values used in planet-disk interaction simulations with a Jupiter-mass planet, such as

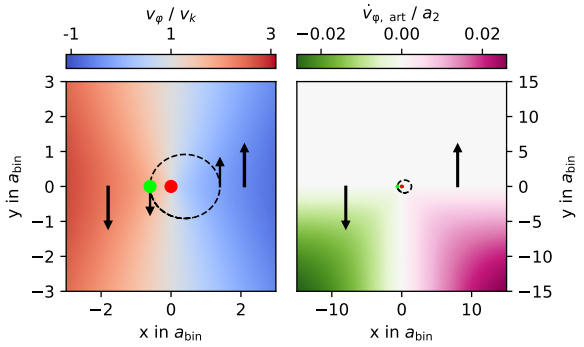

Fig. 4. Snapshot of the azimuthal velocity (left) and artificial acceleration due to Eq. (13) in the frame of the secondary (right). The red dot represents the secondary, the green dot represents the primary, and the black dashed line represents the orbit of the primary. The arrows indicate the direction of motion and are not to scale. The binary and grid parameters are the same as in Sect. 4.

$c = \sqrt{2}$, $q = 10^{-3}$, $r = 10\,a$, and $N_\varphi = 1024$, we find a ratio of the artificial acceleration to the acceleration caused by the planet of up to $7.5 \cdot 10^{-7}$. Assuming a locally isothermal equation of state and a scale height of $h = 0.05$, the maximum artificial pressure due to Eq. (11) is $3 \cdot 10^{-7}$ times the pressure of the gas.

For a circumbinary disk, this ratio becomes much larger and very relevant in the simulations. The artificial accelerations due to Eq. (13) are shown in Fig. 4 for a binary system in the frame of the secondary. The simulation parameters are the same as in Sect. 4, the binary has a mass ratio of $q = 2$ and an eccentricity of $e_\mathrm{bin} = 0.4$, the grid has $N_\varphi = 315$ azimuthal cells, and the artificial viscosity constant is $c = \sqrt{2}$. The binary is currently in the pericenter. For the parameters of this model, our estimate for the artificial pressure using Eq. (13) predicts a force during the binary periastron passage that is 0.6% of the gravitational force of the primary at $r = 5\,a_\mathrm{bin}$, which is two-thirds of the pressure forces of the gas itself.

The left panel is zoomed in on the binary and depicts the azimuthal velocity of the gas according to Eq. (10) normalized by the Keplerian velocity. It is shown to visualize the setup and its extreme case where the velocity of the gas is dominated by the velocity of the frame. The right panel depcits the resulting acceleration field due to the SN artificial viscosity normalized by the gravitational acceleration caused by the primary (Eq. (13)). The right panel of Fig. 4 covers the same area as Fig. 5.

The depicted acceleration field rotates with the binary. Looking at a fixed cell far from the binary (with a slower orbital frequency than that of the binary) as the acceleration field rotates with the binary, the deceleration and subsequent acceleration result in an epicyclic motion with the same frequency as the orbital frequency of the binary. In a non-isothermal simulation, the artificial viscosity in Eq. (11) would be used to calculate the shock heating of the gas and the gas would be artificially heated.

If the binary is eccentric, then the accelerations during a binary orbit would not cancel each other out, instead the acceleration during the binary periastron passage would be higher than during the apastron passage. This leads to a residual acceleration field with the same shape as the one presented in Fig. 4. The deceleration and acceleration during an orbit is a similar pattern to a particle on an eccentric orbit. In this case, the artificial acceleration could excite an eccentricity with a preferred direction based on the location of the binary periastron.

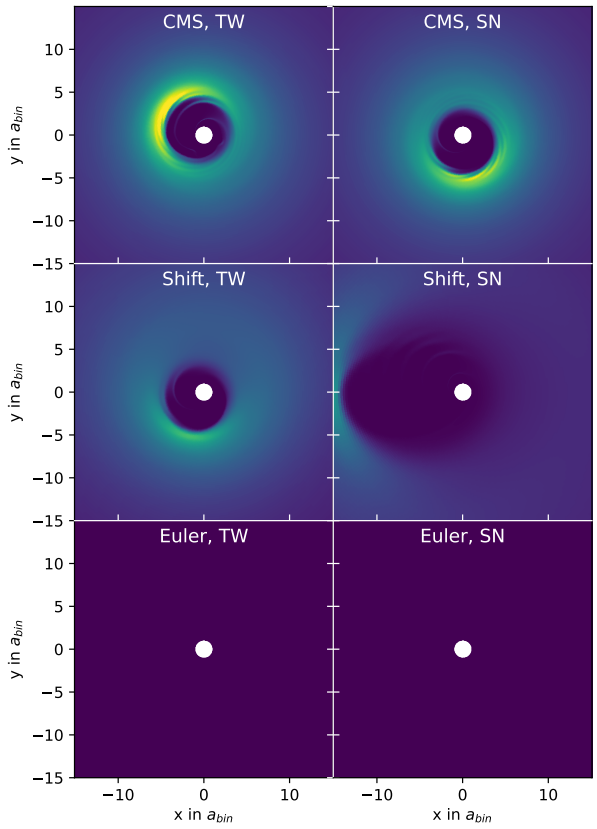

Fig. 5. Snapshot of the surface density after 5000 binary orbits of a massless disk around a binary system with $q_{\rm bin} = 0.5$ and $e_{\rm bin} = 0.4$. The plots show the results for different combinations of coordinate centers, artificial viscosity, and indirect term protocol. All plots use the same linear color scale.

A circumplanetary disk in the frame of the star will have similar problems. The circular motion around the planet will appear as radial and azimuthal velocity components oscillating around the planet in the frame of the central star. The resulting radial and azimuthal velocity gradients are treated as shocks by the artificial viscosity prescription in Eq. (5). In addition, the resolution in the vicinity of a planet on a logarithmic polar grid is typically much lower than the global resolution. We analyze the influence of the different choices of artificial viscosity on a circumplanetary disk further in Appendix A. In our tests presented in Sect. 5, we find that the disks around the companion begin to behave differently for the two artificial viscosity prescriptions at companion masses of 3 $M_{\rm Jup}$ ($q \geq 3 \cdot 10^{-3}$).

4. Circumbinary disk in non-inertial frame

To highlight the importance of our changes to the indirect term and the use of the artificial viscosity by TW79, we constructed a test by simulating a circumbinary disk in the center-of-mass frame and in the center of the secondary star. For all our hydrodynamical simulations, we used the FARGOCPT code that is freely available on GitHub[1] and described in detail in Rometsch et al. (2024).

[1] https://github.com/rometsch/fargocpt

The simulations are locally isothermal and we used the α viscosity prescription from Shakura & Sunyaev (1973) ($\alpha = 0.01$, $h = 0.04 \cdot (d/a_{\rm bin})^{0.3}$, $GM = 1$). The surface density was initialized as $\Sigma(d) = \Sigma_0 \cdot (d/a_{\rm bin})^{-1.1}$. The gas velocities and surface densities were always initialized in the center-of-mass frame, and d is the distance to the center of mass, which is not equal to the r coordinate of the grid in the secondary frame. The setup is intended to model a steady state accretion disk around a binary star system. The artificial viscosity constant was set to $c = \sqrt{2}$.

The domain is logarithmically spaced from 1 to 60 $a_{\rm bin}$ in the radial direction and uniformly spaced from 0 to 2π in the azimuthal direction with a resolution of $N_r \times N_\varphi = 207 \times 315$, or equally, 2 cells per scale height at $r = 1\,a_{\rm bin}$. The resolution was chosen low to make this a stress test for the numerical scheme. The disk was damped to the initial conditions from 36 to 60 $a_{\rm bin}$ on a timescale of 10^{-3} Keplerian orbital periods at 60 $a_{\rm bin}$. We applied strict outflow conditions at the inner boundary, and in case a star enters the simulation domain, we added a sink hole around each star that removes a fraction of the gas within its Roche lobe with a half-emptying time of $10^{-2}\,T_{\rm orb}$. The removed mass was included in the accretion rate, but was not added to the mass of the stars. We used a density floor of $10^{-7} \cdot \Sigma_0$ for numerical stability, meaning that if the density of a cell falls below this value, it will be set to this value. The gravity of the gas was ignored. The mass of the secondary was $m_{\rm Sec} = 0.5$ and $m_{\rm Prim} = 1$ for the primary star. The binary eccentricity of $e_{\rm bin} = 0.4$ caused the primary to enter the simulation domain during its orbit when the simulation was centered on the secondary. To prevent this from causing numerical problems, we smoothed the gravitational potential of the primary within a radius of $0.5\,R_{\rm Hill}$ around it using the third-order polynomial prescription by Klahr & Kley (2006, Eq. (4)). To make the time step size comparable between the simulations, we used a Courant number of 0.4 in simulations using the artificial viscosity by Stone & Norman (1992) and a Courant number of 0.5 in simulations using the artificial viscosity by Tscharnuter & Winkler (1979).

We ran the setup with different combinations of coordinate centers (default is centered on the secondary and 'CMS' indicates the simulation is in the center-of-mass system) and artificial viscosity ("TW" is the artificial viscosity by TW79 and "SN" is the artificial viscosity by VNR50, implemented as described in SN92). The 'CMS' simulations are a reference case for the indirect term experiments, since the indirect term vanishes in the center-of-mass system.

Snapshots of the surface densities after 5000 $T_{\rm bin}$ are shown in Fig. 5. The top row shows the simulation in the center-of-mass frame, where there are no indirect forces. For both artificial viscosities, the disks become eccentric and precess in the prograde direction, which is the expected behavior for a circumbinary disk (Duffell et al. 2024). By evaluating the disk quantities averaged between t = 5000–8000 $T_{\rm bin}$, we find that compared to TW, the disk simulated with the SN artificial viscosity has a 13% faster precession rate, 9% higher eccentricity, 2% larger gap, and 12% lower peak density at longitude at apoastron. While these differences are significant, we expect them to become negligible when using an appropriate grid resolution (higher than 8 cells per scale height).

In the second row, the grid of the hydrodynamics simulation was centered on the secondary star of the binary and the shift-based indirect term protocol was used. Here, the choice of the artificial viscosity is more significant. For the TW artificial viscosity, the inner gap becomes eccentric and precesses, resembling the CMS simulations. However, the precession time

is roughly a factor of 4 longer than in the CMS simulations, the densities in the ring outside the gap are lower and the spiral patterns inside the density ring do not form.

For "SN" artificial viscosity, the simulation evolves similar to the others at the start, but instead of precessing, the longitude of apoastron (eccentric bulge) of the gap remains at $\varphi = \pi/2$ (the negative y-axis). At about $T = 1500\,T_{\rm bin}$, the eccentricity of the gap starts to grow, while the longitude of apoastron moves towards $\varphi = \pi$ (negative x-axis), which is also the position of the periastron of the binary, and stays there. The indirect term is the strongest towards the pericenter of the binary ($\varphi_0 = \pi$). If we substitute $\varphi \rightarrow \varphi - \varphi_0$ in Eq. (12), we find that the gas is decelerated from $\varphi = \pi$ to $\varphi = 3/2\pi$ and accelerated from $\varphi = 3/2\pi$ to $\varphi = 2\pi$. The gas thus has the maximum velocity due to the artificial acceleration at the x-axis ($\varphi = 0$), compare Fig. 4. This is in consistent with the preferred position of the longitude of pericenter of the eccentric disk that we find in the simulation. At the end of the simulation at $8000\,T_{\rm bin}$, the gap edge extended to $13\,a_{\rm bin}$ compared to the $4.5\,a_{\rm bin}$ for the TW artificial viscosity and also both the CMS simulations.

The eccentricity of the disk increases and decreases depending on the phase of the disk due to interaction with the binary potential. Therefore, the eccentricity instability is caused by the SN artificial viscosity preventing the disk from precessing and holding it in a position where the eccentricity is increasing. If the artificial forces are too weak to stop the precession, the artificial accelerations in Fig. 4 cancel out over a precession period, and the artificial viscosities can converge at increasing resolutions. In simulations using the Euler protocol, the disk completely dispersed within the first 200 binary orbits.

We repeated the test for different resolutions. When the resolution was reduced to $N_r \times N_\varphi = 104 \times 156$, the shift-based, TW artificial viscosity simulation also became unstable. When the resolution was doubled to $N_r \times N_\varphi = 411 \times 628$, the simulation using the shift-based indirect term with the SN artificial remained stable for the entire simulation time of $7000\,T_{\rm bin}$. In both cases, the center-of-mass frame and the secondary frame, the SN artificial viscosity produced different precession rates and mass accretion rates through the inner boundary compared to the equivalent simulation using the TW artificial viscosity.

The surface densities of our high resolution (12 cells per scale height) runs are shown in Fig. 6. An inner domain radius of $1\,a_{\rm bin}$ is barely sufficient for a simulation in the center-of-mass frame (Thun et al. 2017), and in a star-centered simulation the inner boundary will be even closer to the circumbinary disk. Therefore, we have reduced the inner domain radius to $0.5\,a_{\rm bin}$ for the simulations that are centered on the secondary, leading to a grid resolution of 1439×1885. Even at this resolution, the disk becomes unstable right at the beginning of the simulation if the Euler protocol is used, as shown in the top-right plot in Fig. 6. The highly eccentric disk does not precess and remains in the depicted orientation. In a previous run with a larger inner domain radius, the disk aligned with the positive y-axis, so we do not find a preferred orientation for this instability. We note that the instability here is caused by the indirect term protocol, as opposed to the instability caused by the artificial viscosity we found at lower resolutions that leads to an alignment with the negative x-axis.

With the shift protocol, the disks in the secondary frame produce the same gap profile as the CMS reference case and also precess. The similarity of the dynamic of the disks can also be seen by the similarity of the mass accretion rates shown in Fig. 7. At the start of the simulations, the mass accretion rates are nearly identical and then slowly drift apart due to differences in indirect

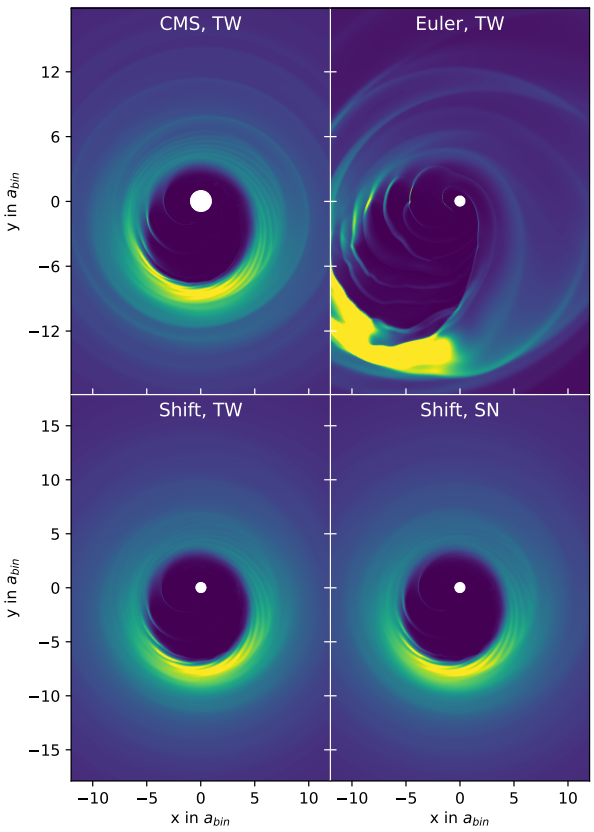

Fig. 6. Snapshot of the surface densities of the high resolution simulations with a binary eccentricity of 0.4. We plot the simulation using the Euler indirect at a simulation time of $t = 800\,T_{\rm bin}$, and the other simulations at $t = 4000\,T_{\rm bin}$. All plots use the same linear color scale.

term and artificial viscosity. Compared to the CMS simulation, the SN artificial viscosity underestimates the mass accretion rate by 11.4% and the TW artificial viscosity by 12.5%. The lower mass accretion rate can be partly attributed to the smaller inner domain radius, but also to different reference frame. We have also conducted simulations with even smaller inner radii, which are not shown here, where the inner radius was contained within the Roche lobe of the stars for both setups, and still found lower mass accretion rates in the star-centered simulation.

From Eq. (13) we estimate that the artificial pressure forces caused by the SN artificial viscosity are 2% of the pressure forces of the gas, which is consistent with the small deviations we observe in Fig. 7. The accuracy of the indirect term could be further improved by using smaller time steps, which automatically occurs when the radius of the inner domain is reduced to include the circumstellar disks.

5. Protoplanetary disk with hot Jupiter

In this section, we test whether our proposed changes are relevant to more common scenarios of planet-disk interactions. We used a setup of a central star of mass $m_{\rm star} = 1\,M_\odot$ and a companion object with masses of $m = [1, 3, 10, 50]\,M_{\rm Jup}$ (corresponding to mass ratios of $q \approx 0.1\%, 0.3\%, 1\%, 5\%$) on a circular orbit ($e = 0$) with an initial semi-major axis of 1 au. At the beginning of the simulation, the companion was on a fixed orbit and was

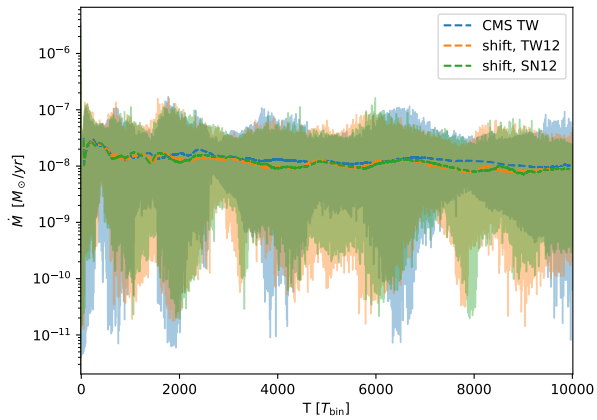

Fig. 7. Mass accretion rate of the circumbinary disk through the inner boundary over time. The dashed lines show the moving average over 100 binary orbits.

treated as massless when interacting with the disk. The mass of the companion felt by the gas was then ramped up over the first 50 orbital periods according to

$$m(t) = \begin{cases} m \cdot \left[1.0 - \cos^2(t \cdot 2\pi/50T_{\rm orb})\right], & t < 50T_{\rm orb} \\ m, & t \geq 50T_{\rm orb}. \end{cases} \tag{14}$$

Despite the mass ramping, the gas velocities were always initialized in the center-of-mass frame of the N-body system with their fully ramped-up masses.

The gravitational potential of the N-body system at the position of a cell was computed as a Plummer potential with a smoothing length of $\epsilon = 0.6H$ (Müller et al. 2012), where $H = h \cdot r$ is the gas scale height. The potential reads:

$$\Phi_i = -G \sum_k^{N_{\rm nb}} \frac{M_k}{s_{ik}}, \tag{15}$$

where G is the gravitational constant, $s_{ik} = \sqrt{d_{ik}^2 + \epsilon^2}$, is the smoothed distance between the gas cell i and the N-body object k with mass M_k. Similarly, the force exerted by the gas on the N-body objects was calculated as

$$\mathbf{a}_k = -G \sum_i^{N_{\rm cell}} f_{\rm sm}(s_{ik}) \frac{m_i}{s_{ik}^3} \mathbf{d}_{ik}, \tag{16}$$

where m_i is the mass of the gas cell and $f_{\rm sm}$ is the smoothing function by Crida et al. (2009):

$$f_{\rm sm}(s) = \left[\exp\left(-10\left(\frac{s}{0.8\, r_H} - 1\right)\right) + 1\right]^{-1}, \tag{17}$$

where r_H is the Hill radius according to Eggleton (1983). The smoothing was applied only to the companion object, not to the star. It acts as a filter to remove the effects of a disk around the companion, since the disk is poorly resolved and not realistically modeled in our setup.

The disk was locally isothermal ($\alpha = 10^{-3}$, $h = 0.05$). The simulation domain ranges from 0.25 au to 25 au and the cells are spaced logarithmically in the radial direction and uniformly in the azimuthal direction with a resolution of $N_r \times N_\varphi = 739 \times 1005$, which corresponds to eight cells per scale height. The surface density was initialized as

$$\Sigma(d) = 200\,\mathrm{g\,cm^{-2}} \cdot (d/1\mathrm{au})^{-0.5} \cdot \frac{1}{1 + \exp[(d - 12\,\mathrm{au})/0.25\,\mathrm{au}]}, \tag{18}$$

where d is the distance to the center-of-mass of the N-body system. We applied strict outflow boundary conditions at the inner and outer boundaries. Since the location of the boundaries depends on the frame of reference, we added an exponential cut-off at 12 au to prevent the disk from interacting with the outer boundary instead of applying damping conditions in the outer regions. We measured the accretion on the companion using the accretion model of Kley (1999), that is, we removed a fraction of the gas from the Hill sphere of the companion at each time step with a half-emptying time of $1000\,T_{\rm orb}$. The mass of the gas and its momentum were added to the companion.

The first 200 orbital periods were used for initialization, during which time the disk exerted no force on the star or companion, and gas accretion by the companion was not active. Then disk feedback and companion accretion were activated, and the simulations were run for another 1800 orbital periods. The companion then migrated under the gravitational influence of the disk and due to momentum accretion. The gravitational force of the gas on the star was added to the indirect term of the simulation. The N-body system was always shifted to the frame of the star at the end of each time step.

The way the disk is initialized can affect the long-term evolution of the disk. In our previous runs, the simulations centered on the star were also initialized around the star so that the surface density was a function of the distance of the cell from the star, and the initial gas velocity was computed with the mass of the star. This caused the disk to become eccentric for high companion masses ($m \gtrapprox 10\ M_{\rm Jup}$) as the companion ramped up in mass. An example of this is shown in the third row of Fig. 8. For $m = 10\ M_{\rm Jup}$ (left side) these effects start to become noticeable, while for $m = 50\ M_{\rm Jup}$ (right side) the entire disk and the gap around the companion become eccentric. This does not happen if the disk is initialized using the distance to the center of mass and the total mass of the N-body system to compute the velocities, as demonstrated for simulations centered on the star (second row) and centered on the center of mass (first row).

For even more massive stellar-mass companions, it is no longer possible to ramp up the mass of the companion, because the missing gravity from the not yet fully ramped up companion would cause the disk to deform before the companion reaches its final mass. Without ramping, longer initialization times are required because strong shocks occur during the clearing of the gap that depend on the artificial viscosity. These initialization artifacts then resolve on viscous time scales.

The advantage of centering the disk on the primary instead of the center of mass is also demonstrated in Fig. 8. At high masses (top-right panel), the primary orbits inside the inner radius, causing its stellar disk to quickly accrete through the inner boundary. This does not happen when the simulation is centered on the primary (middle-right panel), in which case the disk is optimally resolved by the grid, which is the main motivation for this study.

After an initialization phase of 200 companion orbits, we enabled the interaction between the disk and the companion and continued the simulations, meaning that the companion migrates under the gravitational influence of the disk, while the gravity of the gas on the star was added to the indirect term of the

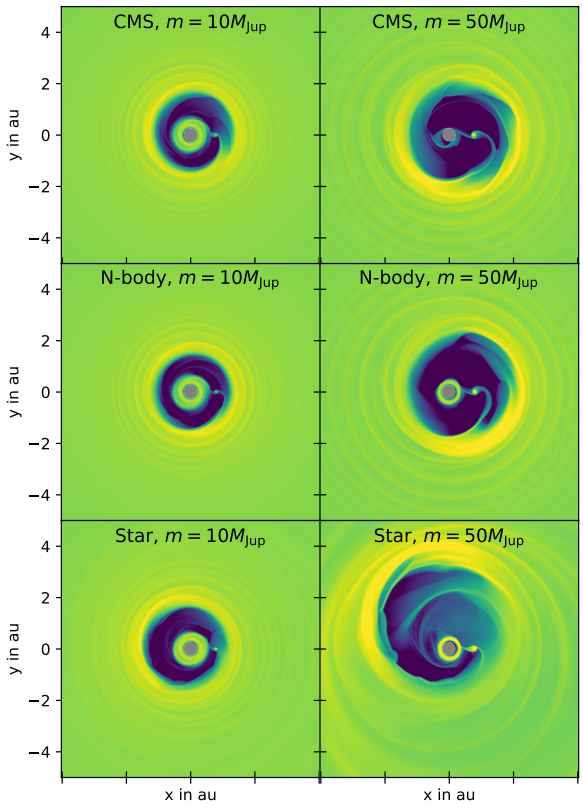

Fig. 8. Snapshot of the logarithm of the surface density of a massless disk at the end of the initialization period ($t = 200\ P_{\rm orb}$). "CMS" indicates that the simulation is in the center-of-mass system, and "star" indicates that the simulation is centered on the star and the disk has been initialized around the star. "N-body" indicates that the simulation is centered on the star, but the disk has been initialized around the center of mass of the N-body system. All plots use the same color scale.

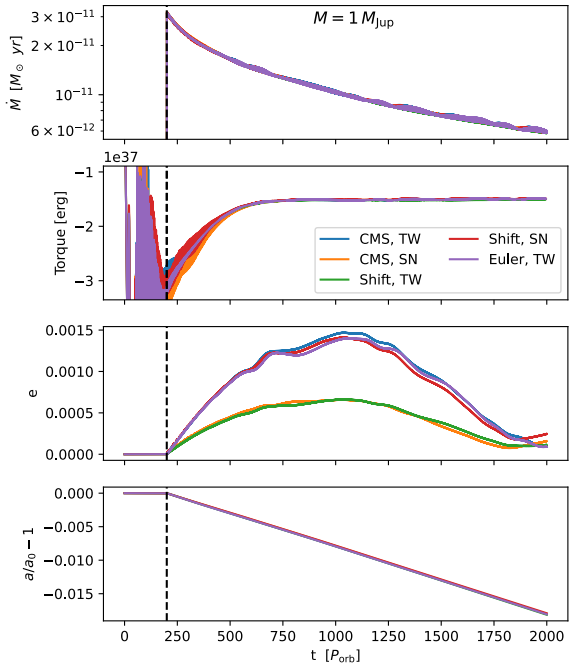

Fig. 9. Various quantities measured for a $m = 1\ M_{\rm Jup}$ companion. Plotted are the mass accretion rate by the companion, the gas torques exerted by the disk on the companion, the eccentricity, and the normalized semi-major axis of the companion.

simulation. With feedback enabled, the forces exerted on the binary system can move its center of mass, so we shifted the N-body system to the new center of mass of the binary after each time step. This was not necessary during the initialization phase because the forces were turned off and the center of mass of the binary stayed put.

We then monitored the mass accretion rate on the companion, the torque exerted by the gas on the companion, the eccentricity and the semi-major axis of the companion. The results for a $m = 1\ M_{\rm Jup}$ companion are shown in Fig. 9. We find no significant differences between the different artificial viscosities, indirect term protocols, or coordinate centers. The gas torques oscillate for a longer time in the SN artificial viscosity simulations, but they settle to the same value as in the TW artificial viscosity simulations and from then on evolve the same. Although the eccentricity variations display factor of 2 difference between the runs, the overall level of planetary eccentricity is too small ($\sim 10^{-3}$) to be considered a significant effect, and the differences do not appear to be related to the artificial viscosity or the indirect term protocol.

For higher masses of $m = 3\ M_{\rm Jup}$ and $m = 10\ M_{\rm Jup}$, we find small differences within the Hill sphere of the companion that we can directly attribute to the different artificial viscosity prescriptions (cf. Fig. A.2). Globally, we find that the time at which the gap becomes eccentric is different for each setup. When the gap becomes eccentric, the density inside the gap is higher, leading to higher accretion (see first panel in Fig. 10) and the gas torque changes (see second panel). The differences in gas torque then lead to different eccentricities and migration rates of the companion. Most of the differences between the setups can be explained by the different time at which the gap becomes eccentric. We find found no trend in how the artificial viscosity or the indirect term protocol affects the timing of this transition. While the simulations are in the same state, they evolve similarly.

For our high-mass companions ($m = 30\ M_{\rm Jup}$ and $m = 50\ M_{\rm Jup}$), we find significant differences in mass accretion between the artificial viscosities, as shown in Fig. 11. The artificial viscosities eject mass from the Hill sphere of the companion (cf. Fig. A.3) resulting in lower mass accretion rates. As depicted in the first panel of Fig. 11, we find ≈50% higher accretion rates and ≈50% more mass inside the Hill sphere for the TW artificial viscosity. This difference increases to almost 100% for the $m = 50\ M_{\rm Jup}$ companion.

Because we have ignored the gravitational effect of the gas inside its Hill sphere on the companion by Eq. (17), the differences in gas torque are an indication of the effects of the different setups far away from the companion. Again, we find that there are differences in gas torque and companion eccentricity between the setups, but without a clear trend. This means that there is no strict increase or decrease in gas torque or eccentricity when changing the artificial viscosity or the indirect term prescription.

However, in most of our simulations, we find that the companion migrates inwards faster for the TW artificial viscosity. For example, in the last panel of Fig. 11, we find 7% faster inward migration for the TW artificial viscosity than the SN artificial

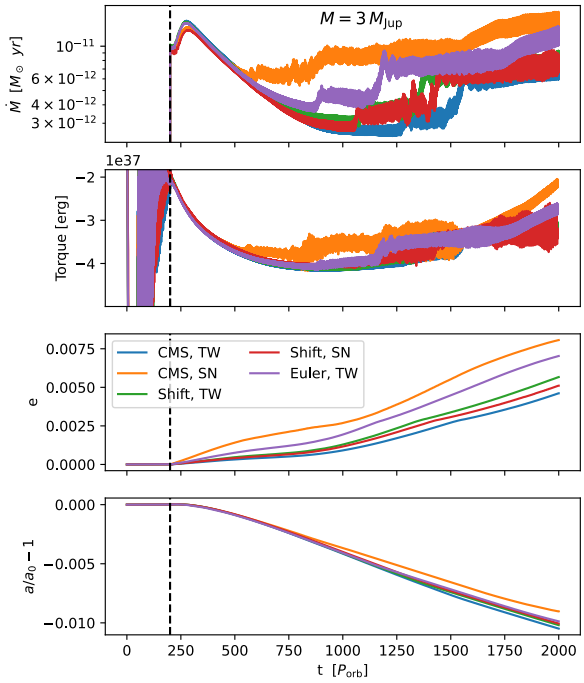

Fig. 10. Same as Fig. 9 but for a $m = 3\ M_{\rm Jup}$ companion.

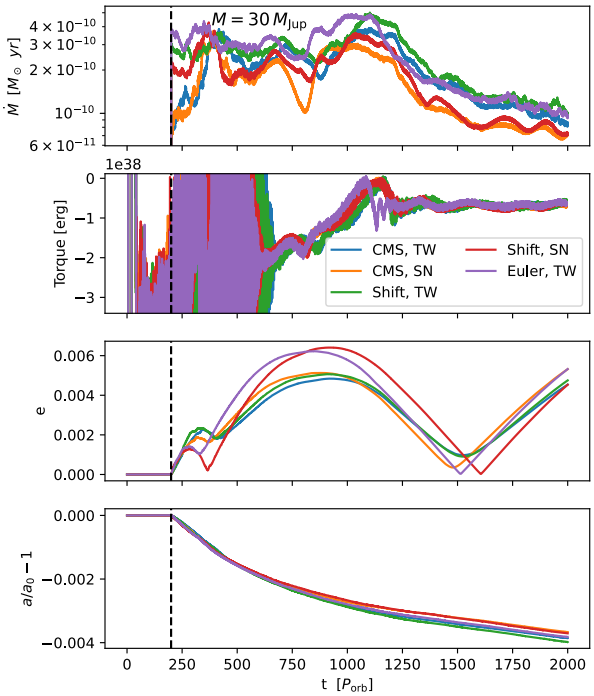

Fig. 11. Same as Fig. 9 but for a $m = 30\ M_{\rm Jup}$ companion.

viscosity in the primary frame and 5% faster in the center-of-mass frame. We analyzed what causes this difference and found that in the center-of-mass frame, the gas torque on the planet is stronger for the TW artificial viscosity; and in the primary frame, the indirect term due to the gas feedback on the central star, which results in a positive torque on the companion, is weaker for the TW artificial viscosity. At the end of the simulations (t = 1800 $T_{\rm orb}$ to 2000 $T_{\rm orb}$), the migration rates are similar for all setups. It remains to be determined whether the faster inward migration observed with the TW artificial viscosity represents a consistent trend or a coincidental effect.

6. Summary and conclusions

We have presented two modifications to the FARGO code (Masset 2000) that allow us to simulate a circumbinary disk in the frame of one of the stars, which to our knowledge was not possible before. One of the proposed modifications is the use of the tensor artificial viscosity by Tscharnuter & Winkler (1979) and the other is a new method for calculating the indirect term. We have also tested their relevance to simulations of planet-disk interactions.

First, we studied the indirect term prescription, that is, the consideration of fictitious forces due to a non-inertial frame of reference. In Sect. 2, we noted that the standard method of applying the indirect term is comparable to a forward Euler step and produces results comparable to that of a Euler integrator. It fails to keep the central object at the coordinate center and similarly fails to keep other objects in the frame of the central object. We proposed to precompute the effective acceleration experienced by the central object over the entire time step and use it as the indirect term. This method is comparable to advancing the whole system in time and then subtracting the velocity of the central object at the end of the time step. This shift-based indirect term will by design keep the velocity of the central object at the end of the time step at 0. We then showed that at large radii, $r > 2\ a_{\rm bin}$, it is significantly better at modeling the effects on a non-inertial frame of reference than the default method.

The proposed shift-based indirect term protocol should also be applicable to other grid codes used to simulate the interaction of disks with stars and planets. For example, the PLUTO code has a hydrodynamics solver that uses a higher-order time-stepping scheme, but in the versions known to the authors, the synchronization between the hydrodynamics and N-body solvers is performed once per integration time step and the indirect term is applied as a single Euler step. We expect that synchronization at each substep would improve the accuracy of the evolution of the combined N-body and hydrodynamics system. How this plays out in practice remains to be seen.

In Sect. 3 we listed literature (Tscharnuter & Winkler 1979; Stone & Norman 1992; Bodenheimer et al. 2006), which already noted that the artificial viscosity by Von Neumann & Richtmyer (1950), which is the default artificial viscosity in the FARGO (Masset 2000) and FARGO3D codes (Benítez-Llambay & Masset 2016), is not suitable for curvilinear coordinates and can cause artificial pressure for smooth gas flows even in the absence of shocks. They also stated that the tensor artificial viscosity by TW79 should be preferred because it takes into account the geometry of the grid and is independent of the frame of reference. We confirmed these claims and showed that the artificial viscosity by VNR50 inherently produces an artificial pressure in a smooth Keplerian disk that arises from the velocity gradients in the non-inertial frame of reference and scales with the number of azimuthal cells as $1/N_\varphi^2$.

In Sect. 4, we simulated a circumbinary disk in the center of the lower-mass companion of a binary system. In this setup, the indirect forces reach magnitudes several times stronger than the

direct gravitational forces of the N-body system, and the standard indirect term prescription causes the disk to disperse. Our shift-based indirect term prescription keeps the disk stable, even at low resolutions, and allows the simulations to converge to a reference simulation in the center-of-mass frame with increasing spatial and temporal resolution.

At low resolutions, the artificial pressure generated by the VNR50 artificial viscosity caused by the velocity gradients in the non-inertial frame of reference, was strong enough to prevent the disk from precessing, leading to significant eccentricity growth in the disk. At high resolutions (>8 cells per scale height) the simulation starts to converge for the different artificial viscosities.

We then tested the relevance of our changes to planet-disk interaction simulations in Sect. 5. At low companion masses of $m \leq 1\,M_{\rm Jup}$, we find no differences between the artificial viscosities or the indirect term protocols. The default methods in the original FARGO code (Masset 2000) are sufficient for these simulations.

For companion masses $m \geq 3\,M_{\rm Jup}$ it becomes relevant to initialize the disk in the center-of-mass frame instead of the center of the star. Otherwise, the shift of the center of mass caused by the ramping of the companion mass can cause the disk to become eccentric. In addition, the artificial viscosity by VNR50 produces artificial pressure inside the Hill sphere of the companion (see also Appendix A).

For even higher masses, $m \geq 30\,M_{\rm Jup}$, it does become necessary to initialize the disk in the center-of-mass frame or the disk will become unstable as the companion mass ramps up. In addition, the artificial viscosity VNR50 ejects significant amounts of mass from the Hill sphere of the companion, resulting in lower mass accretion rates. We also found differences in the gas feedback from the companion depending on the choice of artificial viscosity and indirect term protocol, but these differences are small.

In summary, we find that the methods used in the FARGO code (Masset 2000) are sufficient for simulating planet-disk interactions in the frame of a central star, but issues arise for more massive companion objects. When the companion mass approaches the brown dwarf mass, the frame in which the disk is initialized has to be adjusted, and the artificial viscosity by Von Neumann & Richtmyer (1950) will cause artificial mass ejection from the Hill sphere of the companion. Initializing the disk in the center-of-mass frame would also be relevant for any other grid code centered on the star.

For stellar mass companions, the artificial acceleration caused by the Von Neumann & Richtmyer (1950) artificial viscosity due to the indirect term can cause eccentricity growth throughout the disk. Problems related to artificial viscosity can be mitigated by using the tensor artificial viscosity by Tscharnuter & Winkler (1979). In addition, for stellar mass companions, the indirect term becomes several times stronger than the direct gravitational forces of the N-body system inside the circumbinary disk. In such cases, more accurate indirect-term prescriptions should be used. We believe that the shift-based indirect term protocol presented in this work is a good choice when the indirect term is applied in a single step per time step.

Acknowledgements. TR acknowledges funding from the Deutsche Forschungsgemeinschaft (DFG) research group FOR 2634 "Planet Formation Witnesses and Probes: Transition Disks" under grants KL 650/29-2. The authors acknowledge support by the High Performance and Cloud Computing Group at the Zentrum für Datenverarbeitung of the University of Tübingen, the state of Baden-Württemberg through bwHPC and the German Research Foundation (DFG) through grant INST 37/935-z1 FUGG.

References

Benítez-Llambay, P., & Masset, F. S. 2016, ApJS, 223, 11
Bodenheimer, P., Laughlin, G. P., Rozyczka, M., et al. 2006, Numerical Methods in Astrophysics: An Introduction. Series in Astronomy and Astrophysics (Taylor & Francis)
Crida, A., Baruteau, C., Kley, W., & Masset, F. 2009, A&A, 502, 679
Duffell, P. C., Dittmann, A. J., D'Orazio, D. J., et al. 2024, ApJ, 970, 156
Eggleton, P. P. 1983, ApJ, 268, 368
Klahr, H., & Kley, W. 2006, A&A, 445, 747
Kley, K. 1999, MNRAS, 303, 696
Masset, F. 2000, A&AS, 141, 165
Müller, T. W. A., Kley, W., & Meru, F. 2012, A&A, 541, A123
Rein, H., & Liu, S. F. 2012, A&A, 537, A128
Rein, H., & Spiegel, D. S. 2015, MNRAS, 446, 1424
Rometsch, T., Jordan, L. M., Moldenhauer, T. W., et al. 2024, A&A, 684, A192
Shakura, N. I., & Sunyaev, R. A. 1973, A&A, 500, 33
Stone, J. M., & Norman, M. L. 1992, ApJS, 80, 753
Thun, D., Kley, W., & Picogna, G. 2017, A&A, 604, A102
Tscharnuter, W. M., & Winkler, K. H. A. 1979, Comput. Phys. Commun., 18, 171
Von Neumann, J., & Richtmyer, R. D. 1950, J. Appl. Phys., 21, 232

Jordan, L. M., and Rometsch, T.: A&A, 693, A177 (2025)

Appendix A: Companion disk

In Sect. 5 we measured the effects of the artificial viscosities far from the companion by excluding the torques inside the Hill sphere. While the accretion rate depends on the amount of mass inside the Hill sphere, it is unclear how much it is affected by the different migration rates.

In this section, we isolate the effects of the artificial viscosities inside the Hill sphere of the companion. To achieve this, we ran simulations with the same parameters as in Sect. 5, but kept the central star and companion on fixed orbits by disabling disk feedback. Additionally, we tried to remove the circumstellar disk by reducing the domain size to 0.6 au to 1.5 au with a resolution of $N_r \times N_\varphi = 147 \times 1005$ (cell sizes remained the same). Removing the circumstellar disk from the simulation isolates the gap region, and thus, we are able to avoid contributions to the mass of the Hill sphere that would otherwise stem from gas traversing the gap. As before, we used strict outflow conditions at both boundaries. To reach a steady state, we kept the mass inside the simulation domain constant by rescaling the surface density of each cell after each time step by a factor equal to the initial gas mass divided by the current gas mass. This density rescaling function adds the outflowing mass preferentially to cells with high density. Since gas feedback is not considered here, the surface density cancels out in the momentum equations and the actual disk mass is not relevant.

The surface density profiles after 200 orbital periods are shown in Fig. A.1 for different companion masses, m. In principle, the $3M_{\rm Jup}$ planet in the upper plot clears its orbit, but because the mass is replenished by the density rescaling function, the gap region appears to be filled with gas. What the plot actually shows is the density ratio between the gap region and the circumplanetary disk. While this setup is not physical, it allows us to compare the effects of the different numerical methods by measuring the amount of mass held inside the Hill sphere of the companion.

The normalized amount of mass inside the Hill sphere over time is shown in Fig. A.2 for the $m = 3M_{\rm Jup}$ companion. Neither the frame of reference nor the indirect term prescription affects the amount of mass around the companion, but for the artificial viscosities, differences become visible after 100 $P_{\rm orb}$. At the end of the simulation, the Hill sphere contains 8% more mass for the SN artificial viscosity. We repeated this test for a $m = 1M_{\rm Jup}$ companion, and found a difference of only 0.3% in mass inside the Hill sphere. Similar to the long range effects probed in Sect. 5, we again find that the choice of artificial viscosity will affect the simulations at these companion masses.

For companion masses $m = 10M_{\rm Jup}$ and above, the companion clears its orbit and almost all of the gas mass accumulates inside the Hill sphere (see the lower plot in Fig. A.1). Since the mass inside the Hill sphere is the same for all setups, we measure the effect of the artificial viscosities by how much mass is ejected from the companion disk through the inner and outer boundaries of the domain.

The two lower panels in Fig. A.3 show the mass loss rates for the different setups with a $m = 50M_{\rm Jup}$ companion. The effects of the indirect term protocol are still negligible. The artificial viscosity again has the largest effect with the SN artificial viscosity leading to 10 times more mass ejection than the TW artificial viscosity in the CMS and 5 times more in the primary frame simulations. At this mass, the frame of reference also makes a difference with the primary frame simulations ejecting 3 and 1.5 times more mass than the CMS simulations for the TW and SN artificial viscosities, respectively. Without the mass

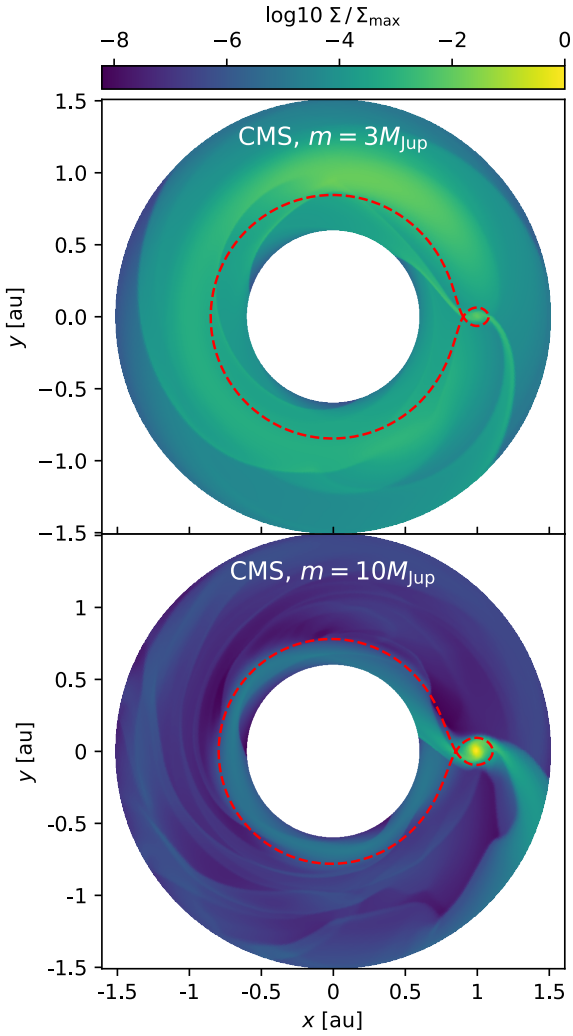

Fig. A.1. Surface densities after 200 orbital periods for different companion masses. The dashed cyan line represents the Roche lobe of the system. Both simulations were run in the center-of-mass frame and used the TW artificial viscosity. Both plots use the same color scale.

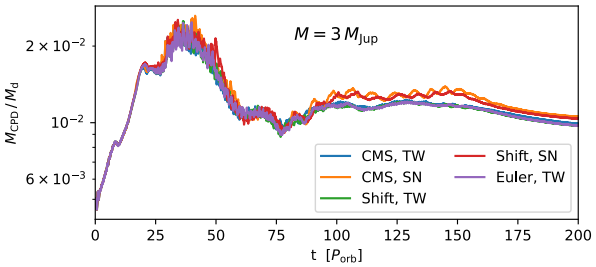

Fig. A.2. Disk inside the Hill sphere of a $m = 3\ M_{\rm Jup}$ companion divided by the total gas mass inside the simulation domain for different simulation setups.

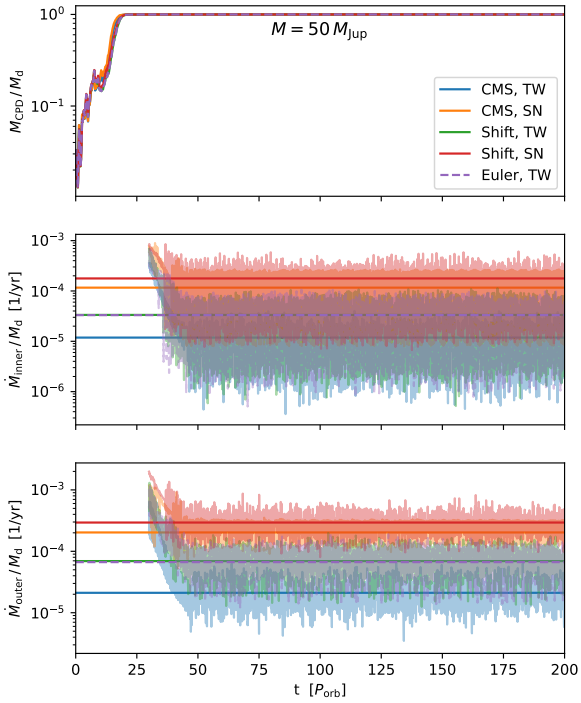

Fig. A.3. Disk mass and mass loss rates over time for a $m = 50\ M_{\rm Jup}$ companion for different setups. Top panel: Mass inside the Hill sphere of the companion. Second panel: Mass loss rate through the inner boundary. Bottom panel: Mass loss rate through the outer boundary. All quantities are normalized to the total gas mass inside the domain.

replenishment function, the companion disks would lose mass, leaving less mass for accretion and explaining the different mass accretion rates found in Fig. 11.

For the $m = 10 M_{\rm Jup}$ the mass loss is higher for the TW artificial viscosity by a factor of 12% and 100% for the inner and outer boundary respectively, which is similar to the higher disk masses measured for the $m = 3 M_{\rm Jup}$ companion in Fig. A.2. This implies that between 10 and 30 Jupiter masses, the SN artificial viscosity becomes more active and changes from lower to higher mass ejection than the TW artificial viscosity.

B Gravitational smoothing in two-dimensional simulations

In this chapter, I want to discuss how two-dimensional hydrodynamic codes, used to simulate accretion disks around stars, treat the gravity from stellar and planetary objects inside the disk. I test how the planet-disk interaction changes when the planet is allowed to affect the disk scale height, what problems this change brings, and how these problems can be handled.

Some of the findings in this chapter were already mentioned in Rometsch et al. (2024), but will be explained in more detail here. A discussion about the effects of vertical stratification of an isothermal gas in three dimensions can be found in Armitage (2015), Sec. 1.1. Here, the effects of different two-dimensional approximations for the vertical stratification found in the literature are discussed.

The results in this chapter are produced using a simple local isothermal model in various Python scripts and 2D hydro simulations. To fully corroborate the results in this chapter, a comparison between full 3D and 2D simulations would be necessary, which was not performed here. This chapter is structured as follows: Appendix B.1 introduces the basic equations of the scale height of the disk and the gravitational force in two dimensions. Appendix B.2 lists three methods commonly found in simulation codes for calculating the gravitational force from an N-body object onto a gas cell and their effect on the equilibrium angular frequency. Appendix B.3 discusses the usage of the smoothing by Klahr & Kley (2006) in 2D simulations. Appendix B.4 evaluates the effects of smoothing on the viscous steady state. Appendix B.5 uses a locally isothermal model to compare different 2D approaches to calculate the gravitational force against the results from a 3D model. Empirical formulas for the ϵ smoothing parameter are fitted that best reproduce the 3D force. Appendix B.6 compares the torque acting on a planet inside a 2D disk for different scale height models, force calculations, and smoothing methods.

B.1 Basic equations of a thin disk

The reduction of the equations for a 3D gas disk to a 2D polar disk is achieved by vertically integrating all the equations. The integration will turn a density $\rho[\mathrm{g/cm^3}]$ to a surface density $\Sigma[\mathrm{g/cm^2}]$ through

$$\Sigma = \int_{-\infty}^{\infty} \rho \, \mathrm{d}z \,, \tag{B.1.1}$$

where z is the distance from the midplane. This step approximates the disk as infinitesimally thin. The approximation is justified by observations of protoplanetary disks, which show that disks are indeed very thin with $z/r \leq 0.04$, where r is the distance from the star (Rosotti 2023, Section 4.1). Simulating disks in two dimensions is also necessary for a wide range of studies due to the immense reduction in computational cost. While protoplanetary disks are thin,

completely ignoring their vertical extent will overestimate the gravitational force and produce wrong results when interacting with stars and planets as illustrated in Fig. B.1.1. A Plummer potential (Plummer 1911) with a smoothing parameter s is often used to approximate the effect of vertical stratification in two dimensions and to improve numerical stability at small distances:

$$\Phi(r) = -\frac{GM}{\sqrt{r^2 + s^2}} \,. \tag{B.1.2}$$

It was shown (Masset 2002; Müller et al. 2012) that a smoothing length of $s = \epsilon H$, where H is the thickness of the disk and $\epsilon \approx 0.6$ is a fitting constant, is a good approximation to realistically model the interaction of the gas with small, Earth-like planets.

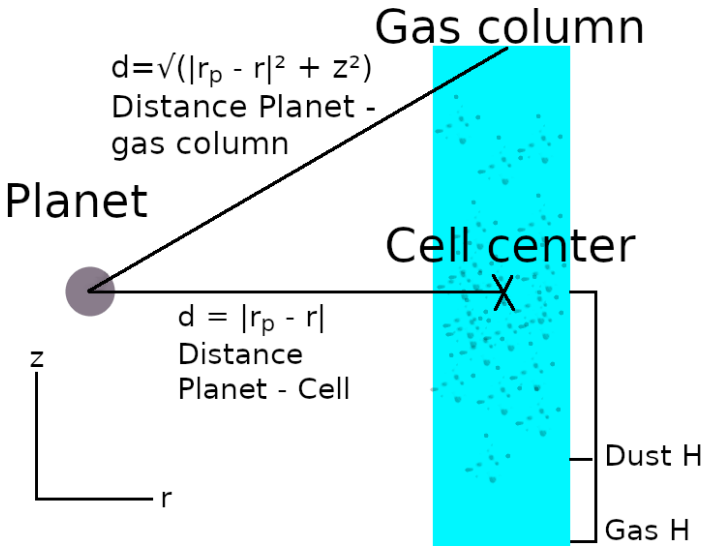

Figure B.1.1. *A schematic drawing of a gas cell near a planet, illustrating the need for smoothing when calculating the gravitational force in two dimensions. When calculating the gravitational force in 2D, all mass in the cell is assumed to be located at the cell center. In reality, the gas is spread out vertically and is therefore farther away from the planet than the cell center; this vertical spreading can be approximated by smoothing the potential or by smoothing the gravitational force. But when applying the smoothing to gas and dust with different smoothing lengths, the velocity difference will be artificially enhanced.*

The thickness of the disk is given by the balance between pressure and gravity from the central star with mass M. In a hydrostatic equilibrium, both forces are equal:

$$\frac{1}{\rho}\frac{\mathrm{d}P}{\mathrm{d}z} = -\frac{\mathrm{d}\Phi}{\mathrm{d}z} = -\frac{GM}{r^2 + z^2}\frac{z}{\sqrt{r^2 + z^2}} \,, \tag{B.1.3}$$

where G is the gravitational constant. When the disk is assumed to be locally isothermal (constant temperature in the whole gas column) where the sound speed $c_{s,\,\mathrm{iso}}$is given by a fraction of the Keplerian velocity ($v_\mathrm{K} = \sqrt{GM/r}$) and pressure by $P = \rho c_{s,\,\mathrm{iso}}^2$, the equation can be solved using the thin disk approximation ($\sqrt{r^2 + z^2} \approx r$) leading to the well-known vertical density distribution in hydrostatic equilibrium (e.g. Lodato 2008):

$$\rho(z) = \rho_0 \exp\left(-\frac{z^2}{2H^2}\right) , \tag{B.1.4}$$

where $\rho_0 = \Sigma/\sqrt{2\pi}$ is the midplane density and the scale height H is given by

$$H = \frac{c_{s,\,\mathrm{iso}}}{\Omega_k}\,, \tag{B.1.5}$$

with $\Omega_k = \sqrt{GM/r^3}$ being the Keplerian orbital frequency. In other words, the thickness of the disk is the height at which the gas density has dropped to 61% of the midplane density and the height under which 68% of the total disk mass is contained. The scale height is often written as $H = r \cdot h$, where h is the aspect ratio of the disk with typical values being around $h = 0.05$. When a disk is illuminated by the star, it becomes flared and the aspect ratio $h = h_0 r^F$ increases outward with the Flaringindex F. For passive disks, where the heating is dominated by the irradiation of the star, a Flaringindex of $F = 2/7$ is typically assumed Chiang & Goldreich 1997.

In the original FARGO code, only the gravity of the central object is considered when the scale height is calculated and the smoothing is only applied to the planets in the system. As illustrated in Fig. B.1.1, the smoothing approximates the physical fact that the gas is vertically stratified and therefore should be applied on every point mass object inside the disk equally. Further, the original FARGO code uses the position of the planet to calculate the scale height used for smoothing. While this is computationally simpler because the smoothing length is then identical for all gas cells, it does not represent the vertical stratification of the disk; instead, the position of the gas cell itself should be used to calculate its scale height.

The gravitational force from multiple objects is simply the sum of the gravitational force from each individual object. Therefore, it is physically more accurate to include the effects of all N-body objects inside the disk when computing the hydrostatic equilibrium Eq. (B.1.3), and the height of the disk and there is no reason not to do so. The disk thickness under the influence of multiple objects can be calculated as (Günther & Kley 2002):

$$H(r) = \left[\sum_i \frac{1}{H_i^2}\right]^{-1/2} = \left[\sum_i \frac{1}{c_{s,\,\mathrm{iso}}^2}\frac{GM_i}{|\mathbf{r}-\mathbf{r}_i|^3}\right]^{-1/2}. \tag{B.1.6}$$

This formulation is identical to the one presented in D'Angelo et al. (2003) while Müller et al. (2012) presented another formulation for small planets.

For simplicity, it is assumed that only the central star heats up and contributes to the disk temperature; therefore, the standard definition of sound speed, which is another measure for the gas temperature, is used:

$$c_{s,\,\mathrm{iso}}(r) = h_0 r^F \sqrt{\frac{GM}{r}}\,. \tag{B.1.7}$$

It was also tested and confirmed that setting up the same aspect ratio around every object and interpolating by distance does not alter the results presented here:

$$h(r) = \left[\sum_i \frac{1}{h_i^2}\right]^{-1/2} = \left[\sum_i \frac{1}{c_{s,\,\mathrm{iso},\,i}^2}\frac{GM_i}{|\mathbf{r}-\mathbf{r}_i|}\right]^{-1/2}. \tag{B.1.8}$$

$$c_{s,\,\mathrm{iso}}(r) = \sqrt{\sum_i h_0^2 |\mathbf{r} - \mathbf{r}_i|^{2F} \frac{GM_i}{|\mathbf{r} - \mathbf{r}_i|}}\,, \tag{B.1.9}$$

putting Eq. (B.1.9) in Eq. (B.1.8) would reproduce $h(r) = h_0$ (if $F = 0$) throught the whole domain.

The forces acting on the gas cell due to the gravitational potential of the N-body system are computed as the divergence of the potential:

$$\mathbf{F} = -\nabla\Phi. \tag{B.1.10}$$

Sometimes, the force of an unsmoothed potential is computed and then smoothed:

$$\mathbf{F}(\mathbf{r}) = -\sum_i \frac{GM_i m}{|\mathbf{r} - \mathbf{r}_i|^2 + H^2\epsilon^2}\hat{r}_i\,, \tag{B.1.11}$$

where m is the mass of the gas cell at position $\mathbf{r}$.

B.2 Smoothed force vs. smoothed potential

To illustrate the differences between force smoothing and potential smoothing, the setup is simplified by considering only a disk around a single star with mass M located at the coordinate center ($\mathbf{r}_s = 0$). One can then compute the acceleration in the radial direction:

$$\Phi = -\frac{GMm}{\sqrt{r^2 + \epsilon^2 H^2}} \tag{B.2.1}$$

$$F_{r,\,\mathrm{pot}}(r) = -\frac{\partial\Phi}{\partial r} \tag{B.2.2}$$

$$-\frac{\partial\Phi}{\partial r} = -\frac{GMm}{r^2}\frac{1 + (F+1)\epsilon^2 h^2}{\sqrt{1 + \epsilon^2 h^2}^3}\,. \tag{B.2.3}$$

For this simplified setup, the smoothed force from Eq. (B.1.11) becomes

$$F_{r,\,\mathrm{force}}(r) = -\frac{GMm}{r^2}\frac{1}{1 + \epsilon^2 h^2}\,. \tag{B.2.4}$$

It is now easy to see, that Eq. (B.2.3) is the smoothed force from Eq. (B.2.4) times an extra factor that is greater than 1, i.e. smoothing the force will lead to weaker gravitational interaction than smoothing the potential. Sometimes the force is also smoothed as

$$F_{r,\,\mathrm{force},3}(r) = -\frac{GMm}{r^2}\frac{1}{\sqrt{1 + \epsilon^2 h^2}^3}\,. \tag{B.2.5}$$

In this version, the force is even more weakened than in the other smoothed force case Eq. (B.2.4).

The effects of the difference between the smoothing methods can be quantified by their effect on the azimuthal velocity of gas on a circular orbit. For a Keplerian orbit, the gravitational pull from the central object is balanced by the centrifugal force; a gas disk will feel an

additional force due to the pressure gradient in the disk. The pressure force will push the gas outwards where a slower velocity is needed to balance the gravitational force, the gas thus orbits the star with sub-Keplerian speed. The orbital frequency of the gas is given by e.g. Lodato (2008):

$$r\omega^2 = \frac{1}{\Sigma}\frac{\partial P}{\partial r} + \frac{\partial \Phi}{\partial r} \,. \tag{B.2.6}$$

Using the standard definitions (Lodato 2008) of $P = \Sigma c_{s,\,\mathrm{iso}}^2$ with $c_{s,\,\mathrm{iso}} = v_k h$, $h = h_0 r^F$ and $\Sigma = \Sigma_0 r^{-S}$, this equation can be solved to

$$\omega_{\mathrm{pot}} = \omega_k \sqrt{(2F - S - 1)h^2 + \frac{1 + (F+1)h^2\epsilon^2}{\sqrt{1 + h^2\epsilon^2}^3}} \tag{B.2.7}$$

for the potential smoothing in Eq. (B.2.3), where $\omega_k = \sqrt{GM/r^3}$ is the Keplerian orbital frequency. The first term under the square root arises due to the pressure support and the second term from the gravitation smoothing. For the force smoothing from Eqs Eqs. (B.2.4) and (B.2.5), the equation solves to:

$$\omega_{\mathrm{force}} = \omega_k \sqrt{(2F - S - 1)h^2 + \frac{1}{1 + h^2\epsilon^2}} \,, \tag{B.2.8}$$

$$\omega_{\mathrm{force,3}} = \omega_k \sqrt{(2F - S - 1)h^2 + \frac{1}{\sqrt{1 + h^2\epsilon^2}^3}} \,. \tag{B.2.9}$$

Most studies do not smooth the gravitational potential of the central object, leading to the orbital frequency that is expected at the midplane:

$$\omega = \omega_k \sqrt{(2F - S - 1)h^2 + 1} \,. \tag{B.2.10}$$

For the standard disk parameters $GM = 1$, $h_0 = 0.05$, $F = 0$, $\epsilon = 0.6$ and $S = 0.5$, the gas will rotate 0.18% slower than the pure Keplerian velocity due to the pressure support in Eq. (B.2.10), 0.2% slower if the potential from Eq. (B.2.7) is used, and 0.22% slower if the force is smoothed according to Eq. (B.2.8). Compared to the velocity reduction when only the pressure support is considered, smoothing the potential reduces the velocity by an additional 12% of the pressure support, smoothing the force reduces it by 24%, and smoothing the force and direction vector Eq. (B.2.5) reduces it by 36%. Using a disk profile for a steady accretion disk: $h_0 = 0.05$, $F = 2/7$, and $S = 1.1$, and increasing $\epsilon = 1$ increases the sub-Keplarian deficit by 14% and 65% over pressure support only for potential and force smoothing, respectively.

The conclusions from comparing these velocities are:

- Smoothing the potential or the force leads to lower equilibrium velocities than expected from pressure support alone. Depending on the applied smoothing, Eqs. (B.2.7) to (B.2.9) could be used instead for initializing the azimuthal gas velocities.

- When calculating the feedback from the disk to the planets, the force is usually smoothed; but if the code uses potential smoothing for the gas (as is the case for the official FARGO codes (Benítez-Llambay & Masset 2016; Masset 2000)), the forces from the gas on the planet will be different than from the planet on the gas, when they should be the same.
- When dust particles are inside the disk, they will be at a specific height from the midplane. If we assume that the dust is in the midplane ($z = 0$), then it will interact with gas that is also at the midplane and would have the unsmoothed orbital frequency from Eq. (B.2.10). However, if the code only provides the vertically averaged velocities with gravitational smoothing from Eqs. (B.2.7) to (B.2.8), gas drag experienced by the dust will be overestimated if these effects are not considered. Typically, the force on the dust is smoothed with a dust scale height H_d that is lower than the gas scale height (e.g. Dubrulle et al. 1995). Then the gas drag will still be overestimated, but to a lesser degree.

B.3 Different forms of smoothing

As discussed above, there are different ways to smooth the gravitational force and different ways to calculate the scale height. If an object inside the disk affects (reduces) the scale height of the disk, using a fraction of the scale height as the smoothing length will not be enough to guarantee numerical stability. In this case, the potential smoothing proposed by Klahr & Kley (2006) can be added on top of the epsilon smoothing. If $r_{sm} = \sqrt{r^2 + H^2\epsilon^2}$ and s is a smoothing length that is given as a fraction of the hill radius of the object, then the numerically stable potential can then be defined as:

$$\Phi = \begin{cases} -\frac{GMm}{r_{sm}}\left[\left(\frac{r_{sm}}{s}\right)^4 - 2\left(\frac{r_{sm}}{s}\right)^3 + 2\frac{r_{sm}}{s}\right] & \text{if } r_{sm} < s \\ -\frac{GMm}{r_{sm}} & \text{else} \end{cases} \tag{B.3.1}$$

when derived in the radial direction to produce the force, the equation becomes:

$$F = \begin{cases} -\frac{GMm}{r_{sm}^2}\left[4\left(\frac{r_{sm}}{s}\right)^3 - 3\left(\frac{r_{sm}}{s}\right)^4\right] & \text{if } r_{sm} < s \\ -\frac{GMm}{r_{sm}^2} & \text{else.} \end{cases} \tag{B.3.2}$$

The effects of the different smoothing methods are shown in B.3.1. The effects of smoothing the potential and smoothing the force together with the direction vector Eq. (B.2.5) are visibly identical, therefore only the potential version is shown and discussed. Smoothing the potential while only considering the gravity of the primary for the scale height (red line) overestimates the disk thickness, especially close to the secondary; this will lead to too low gravitational forces even at larger distances from the planet where it is not needed for stability. When the force is smoothed and only the gravity of the primary is considered in the calculation of the scale height (blue line), the force at the position of the companion does not diverge, but is non-zero and has a sign flip, such that gas close to the companion would oscillate

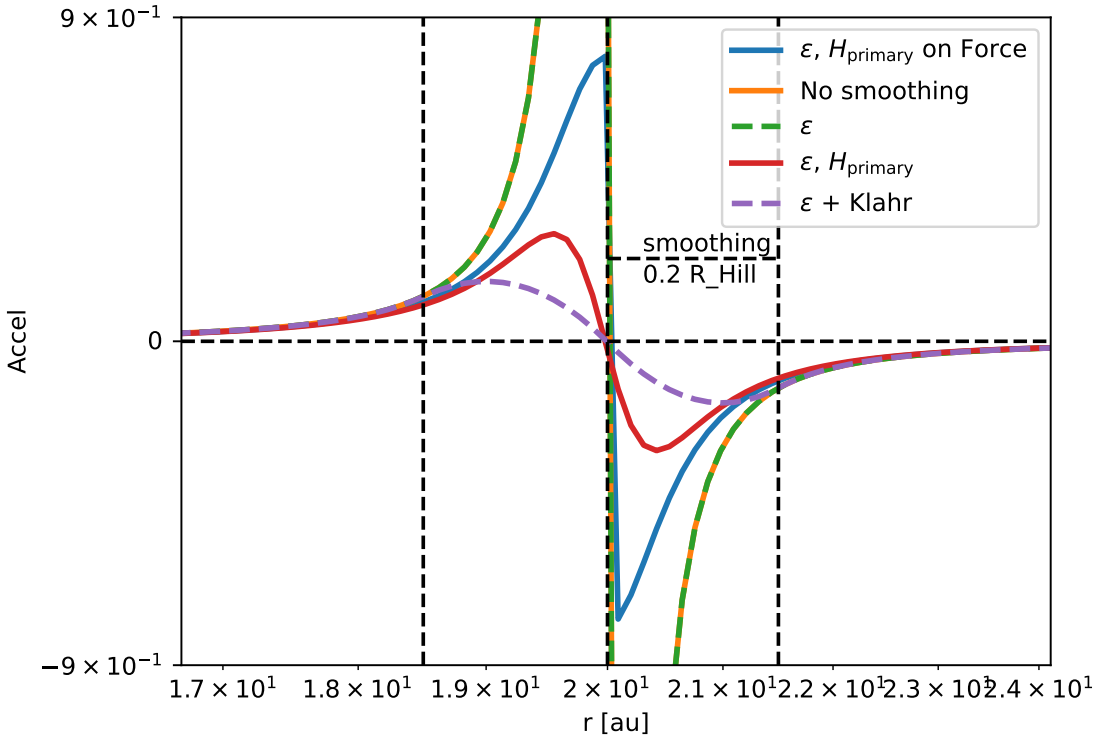

Figure B.3.1. *The radial acceleration the gas experiences around the secondary star in a binary with a mass ratio of $q = 0.286$, a smoothing parameter of $\epsilon_0 = 0.6$, an aspect ratio of $h_0 = 0.05$, and without flaring ($F = 0$) for different methods of computing the scale height and for applying the smoothing. Unless otherwise specified, the scale height is calculated with Eq. (B.1.6). The blue line is the result of the direct force smoothing from Eq. (B.2.4); the orange line without any smoothing, the green dashed line with ϵ smoothing from Eq. (B.2.1); the red line uses ϵ smoothing, but only the primary star has effect on the scale height, the red line also represents the smoothing from Eq. (B.2.5), and finally the purple dashed line is the same as the green line, but with additional smoothing from Klahr & Kley (2006) Eq. (B.3.1).*

through the companion. When smoothing the potential and considering all objects for the scale height (green dashed line) the smoothing length is negligible close to the companion and the force diverges like in the case without smoothing (orange line). This is not numerically stable and causes simulations with Jupiter mass planets to crash. Adding the smoothing from Klahr & Kley 2006b to the potential smoothing with N-body scale height does reduce the forces close to the secondary for numerical stability and the gravitational force transitions smoothly through zero at the position of the companion. Outside the smoothing range, the force is unchanged. This type of smoothing is purely for numerical stability, but without mesh refinement strategies, the grid resolution within the numerically smoothed area is too low to resolve the gas disk, and the results would not be physical anyway.

The conclusion from this section is that if one chooses to use the gravity from all N-body objects to compute the disk thickness, then additional smoothing, such as the smoothing from Klahr & Kley (2006), is required to guarantee numerical stability.

B.4 Steady state with smoothed potential

As highlighted in Eqs. (B.2.7), (B.2.8) and (B.2.10), a smoothed gravitational force will alter the equilibrium azimuthal velocity:

$$\omega_{\mathrm{pot}} = \omega_k \sqrt{(2F - S - 1)h^2 + \frac{1 + (F+1)h^2\epsilon^2}{\sqrt{1 + h^2\epsilon^2}^3}} \,. \tag{B.4.1}$$

This will change the radial velocity that is determined for a viscous disk from the conservation of angular momentum and the conservation of mass (e.g. Lodato 2008):

$$\Sigma v_r \frac{\partial(r^2\Omega)}{\partial r} = \frac{1}{r}\frac{\partial}{\partial r}(\nu\Sigma r^3 \frac{d\Omega}{dr}) \,, \tag{B.4.2}$$

where $\nu = \alpha c_s H$ is the kinematic viscosity by the α prescription (Shakura & Sunyaev 1973). Assuming Keplerian rotation profiles, this equation can be solved analytically to:

$$v_r = -3\frac{\nu}{r}(2F - S + 1) \tag{B.4.3}$$

but the code will develop velocities according to Eq. (B.4.1) and use it to numerically solve Eq. (B.4.2). Under these conditions, the equation for the radial velocity becomes unpractical to solve analytically. Therefore, if one wants to initialize the simulation in a viscous steady state, they have to solve Eq. (B.4.2) numerically.

Fig. B.4.1 shows the azimuthally averaged simulation results for a steady-state accretion disk using the FARGOCPT code that uses the potential smoothing approach Eq. (B.2.7). The setup is locally isothermal with $G = M = 1$, $h_0 = 0.1$, $S = 1.13$, $F = 0.3$ and $\alpha = 0.1$. The grid is radially logarithmic $r \in [1, 100]$ and linear in azimuth $\varphi \in [0, 2\pi]$ with $N_r \times N_\varphi = 196 \times 270$. The physical parameters were chosen by a fitting script to generate a steady-state accretion disk: $\dot{M} = -2\pi r v_r \Sigma = const$ where a five-point stencil method for the numerical derivative was used to solve Eq. (B.4.2) for v_r. Two simulations were run, one using pressure support only to compute the azimuthal velocity Eq. (B.2.10) and radial velocity Eq. (B.4.3) to generate the initial profile, and the other using azimuthal velocity for a smoothed potential Eq. (B.2.7) and numerical solver for the radial velocity Eq. (B.4.2). The outermost ring is set to the initial profile during the entire simulation. From the second plot in Fig. B.4.1 it can be seen that both simulations (solid blue and dashed orange lines) are in a steady state, as the mass flow through every ring is equal to the mass flow from the outer ring into the domain. Also shown is the mass flow predicted from theory (red and purple dots). As the theory with gravitational smoothing predicts a too-large mass flow at the outer boundary and the theory without smoothing a too-low value, the surface density adjusts by an increase or decrease at the outer boundary relative to the predicted theoretical value. The too-high / too-low values extend throughout the whole domain as the domain adjusts to the conditions set at the outer boundary. This effect is problematic because the steady state is reached on the viscous timescale, which is long and thus computationally expensive to achieve in standard setups with lower viscosity.

The bottom panel shows the relative deviation of the azimuthal velocity from Eq. (B.2.1). Regardless of the profile prescribed at the outer boundary, both simulations reproduce the theoretical value that considers the effects of gravitational smoothing. This is of little surprise, as the code does solve the equations using a smoothed gravitational potential. The midplane azimuthal velocity (purple dashed line) is also shown for reference.

The second last panel in Fig. B.4.1 shows the relative deviation of the radial velocity from the numerical solution of Eq. (B.4.2). Both simulations develop radial velocities that vary by a few percent around the theoretical value. The deviations likely arise due to a combination of numerical inaccuracies, since the grid resolution is low and the surface density profile is no longer a simple power law. The deviations of the radial velocities are similar to the deviations of the theoretically predicted mass flow rates, since mass flow and radial velocity are closely related. Nevertheless, the numerical prediction is more accurate than the naive formula Eq. (B.4.3).

The conclusions from this section are that when applying gravitational smoothing to the potential of the central star, the equations for equilibrium conditions are no longer analytically solvable. One must resort to numerical methods to find approximate solutions to the steady-state conditions. To initialize a disk in its equilibrium state, one has to prescribe a mass inflow rate at the outer boundary and iteratively solve for a constant mass flow throughout the grid until convergence is reached. Alternatively one has to simulate for a viscous timescale $t_{\text{visc}} \propto \frac{R_{\text{max}}^2}{\nu}$ until a steady state is reached. While the simulations were run only with a smoothed potential, no practical analytical steady-state accretion profile could be found when any form of gravitational smoothing was included.

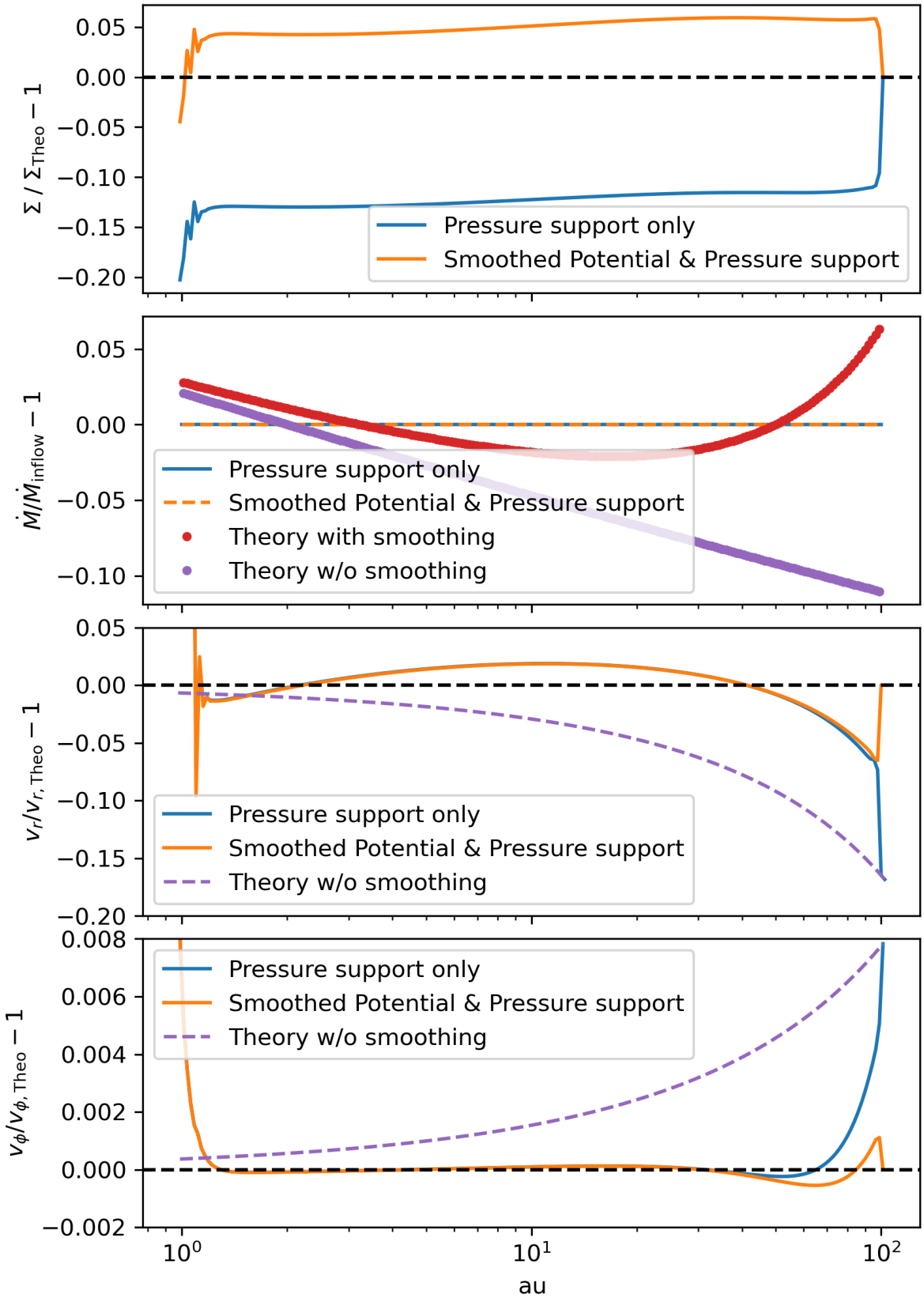

Figure B.4.1. *Surface density, mass flow, and velocity profiles of a steady-state accretion disk using the* FARGOCPT *code (solid lines) compared to the theoretical models (dashed lines) of which one considers the effects of gravitational smoothing and the other does not.*

B.5 Comparing the gravitational force in 3 and 2 dimensions

The effects of the different kinds of gravitational smoothing are compared to the full 3D forces in a simple, locally isothermal model. When the 3D reference force is calculated, the gravity of the star and planet are considered when calculating the scale height in Eq. (B.1.6). The parameters used $G = M_{\rm star} = \Sigma_0 = 1$, $h_0 = 0.05$, $F = 0.3$ and $\Sigma = 1 \cdot r^{-S}$ with $S = 1.1$. The density is constant within a cell and is calculated using Eq. (B.1.4), the position of a cell is its center of mass. An axially symmetric setup in cylindrical coordinates is used. The 3D force is calculated in r, z and the 2D force is calculated in r. The radial cells are logarithmically spaced and the vertical cells are linearly spaced within $[0, 8 \cdot \max(H)]$. The grid resolution is 1500 cells in the radial direction and $5 \cdot 10^5$ cells in the vertical direction. The grid resolution was chosen such that the relative difference between the sum in the vertical direction of all the 3D masses and the 2D mass at the same radius is smaller than 10^{-5}. The 3D force is calculated directly, without any smoothing, and summed over each column to produce the reference force at each radius, which is then compared to the forces produced by Eqs. (B.2.3) to (B.2.5). The acceleration by the gas onto the planet at position $r_p = 1$ is used to compare the forces:

$$a(r_i) = \sum_{j=0}^{j=N_z} \rho(r_i, z_j) V_i \frac{1}{(r_{i,j} - r_p)^2}\,, \tag{B.5.1}$$

where $\rho(r_i, z_j)$ is the density according to Eq. (B.1.4), V_i is the volume of the cell. For the distance $d = \sqrt{(r_i - r_p)^2}$ between the gas cell and the planet, the 2D approximations of the acceleration become:

$$a_{\rm pot}(r_i) = -\Sigma \frac{d + \frac{\partial H}{\partial r} H \epsilon^2}{\sqrt{d^2 + \epsilon^2 H_i^2}^3}\,, \tag{B.5.2}$$

$$a_{\rm f}(r_i) = -\Sigma\, S \frac{1}{d^2 + \epsilon^2 H^2}\,, \tag{B.5.3}$$

$$a_{\rm f3}(r_i) = -\Sigma\, S \frac{d}{\sqrt{d^2 + \epsilon^2 H^2}^3}\,, \tag{B.5.4}$$

where S is the surface area of the cell at position r_i. Note that the position dependency of the cell on the right side has been omitted for better readability and that most constants are set to 1 and not shown.

Potential Smoothing

The top panel in Fig. B.5.1 compares the forces on a moon-sized planet with mass $M_p = 10^{-7}$ from Eq. (B.5.2) when H is computed from the central star only (blue line) and from all objects in the simulation (dashed orange line) for the standard value of $\epsilon = 0.6$. Close to the planet, both methods significantly underestimate the acceleration from the gas onto the planet. Further away from the planet, the force switches from being underestimated to overestimated by a few percent.

Note that what is shown here is the relative deviation of the 2D force from the 3D reference force, not the magnitude of the force. The force depends on how much gas is at a given position which would in turn require modeling the density distribution near the planet which is not done here. This means that large deviations of the force near the planet would be unimportant for massive planets that open a gap and clear out gas from their vicinity.

The brown and red lines are for the same setups as the two previous ones, but the ϵ is used as a fit parameter to reproduce the 3D force. With the additional fit parameter, the 3D force can be reproduced to an accuracy that only depends on the tolerance of the fitting function. When the planet affects the disk scale height, the gradient of the scale height Eq. (B.1.6) near the planet becomes so large that the $\frac{\partial H}{\partial r}$ term flips the sign of the acceleration. With the wrong sign, the fitting method minimizes the error by smoothing the force to zero with very large ϵ values. This can be seen by the weird behavior of the green line close to the planet.

While the drop in scale height near the planet is overestimated in this model, the derivative of the smoothing implies that the gravitational force on a cell depends on the height of the neighboring cell. Such an effect cannot occur in 3D simulations, where the force calculation involves only a single cell and the N-body object. It is questionable whether this effect was intended when the smoothing method was designed.

The middle panel shows the fitting ϵ parameters. The optimal values of ϵ near the planet, from which the torque on the planet arises, are in the range of 0.5-0.8, in agreement with Masset (2002); Müller et al. (2012). Overall, a constant ϵ provides a poor fit as can be seen by the few percent deviation to the reference force over the whole range of the plot. The bottom panel shows the scale height for the cases of primary only and all N-body objects affecting the scale height. At distances further than a few hill radii it does not matter how the scale height is computed; the optimal epsilon and the accuracy with which the 3D force is reproduced are identical.

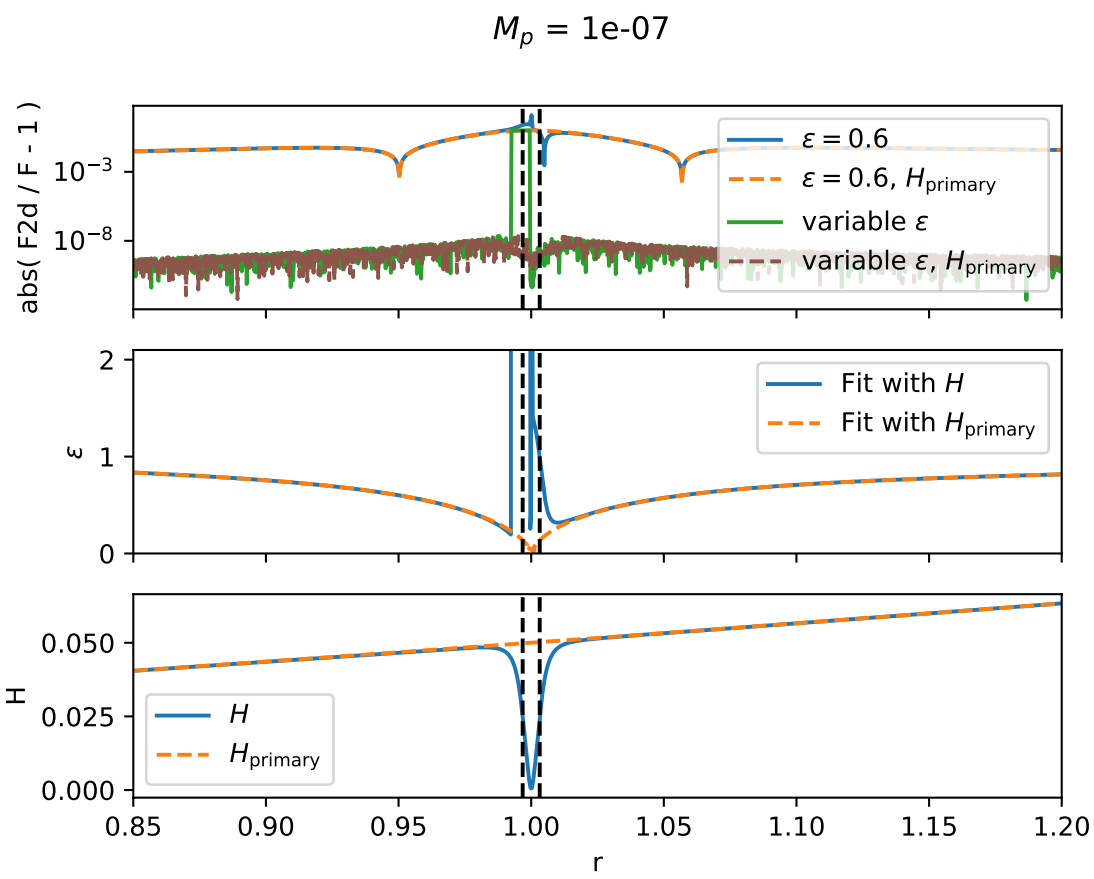

Figure B.5.1. *The Dashed black line in all panels represents the Lagrangian l_1, l_2 points. Top panel: comparing the force derived from a smoothed potential Eq. (B.5.2) to the 3D reference force on a moon-sized planet ($M_p/M_{\text{Star}} = 10^{-7}$). The dashed orange line is from a smoothed potential with $\epsilon = 0.6$, where only the gravity of the central object affects the scale height H_{primary} of the disk. The blue is when the star and planet are considered when computing the scale height H. The green and red lines are fitted when $\epsilon(r)$ is treated as a variable fitting parameter to reproduce the 3D force. The Green line is for the case with H and the red line for H_{primary}. Middle panel: the best-fitting ϵ values to match the 3D force. Bottom panel: dashed orange line is the scale height H_{primary} when only the central star affects the scale height, blue when the star and planet affect the scale height (H).*

Force Smoothing

The previous setup is used again to compare the forces from Eq. (B.5.3) against the 3D force in Fig. B.5.2. When using a constant ϵ, the force near the planet is again severely underestimated (blue and dashed orange lines). The N-body scale height only makes a difference close to the planet. Also plotted is the deviation from the 3D force when using the ϵ prescription in Eq. (B.5.5) with the N-body scale height (green line). While the ϵ prescription could still be improved, it is already better at reproducing the 3D force across the whole domain. It highlights that more accurate planet-disk interactions can be achieved in two dimensions when ϵ is chosen appropriately. The middle panel in Fig. B.5.2 compares Eq. (B.5.5) with the fitted ϵ that reproduces the 3D force. Deviations are visible at distances $d \approx R_{\text{hill}}$, which are not considered further in this work. We repeated the test for a Jupiter mass planet $M_p = 10^{-3}$ in Fig. B.5.3. The more massive planet has a stronger effect on the disk scale height (bottom

plot), and including its effect does improve the accuracy of the force close to the planet (as seen in the top panel). In contrast to the potential smoothing case, the optimal ϵ value for force smoothing has a strong dependence on the planet mass and is close to unity throughout the domain for massive objects (middle plot). As the overall variability of the optimal ϵ is reduced, the relative deviations from the reference force are reduced while using the ϵ function (compare the green lines close to the planet in Fig. B.5.2 and Fig. B.5.3).

$$\epsilon = \frac{1}{1 + \sqrt{0.65 \cdot H/(d_p + H/3.8)}^3} \,. \tag{B.5.5}$$

The function parameters were fitted for a low mass planet with mass $10^{-7}\, M_\odot$. The optimal parameters depend only weakly on the scale height and flaring index of the disk and are relatively constant for planet masses up to Jupiter masses. For stellar masses, the optimal parameters change, but the function is now nearly constant and the precise values of the fitting parameters are less important.

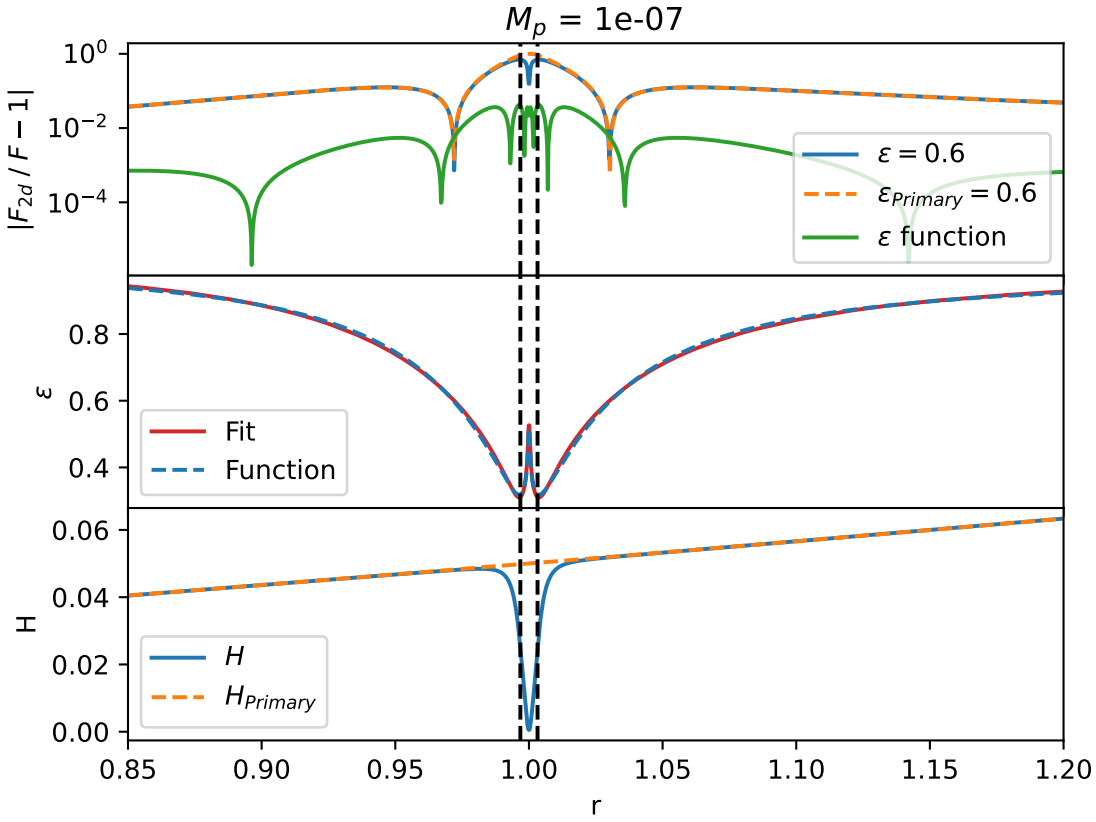

Figure B.5.2. *Similar to the previous plot Fig. B.5.2 but for a smoothed force Eq. (B.5.3). The dashed black lines represent the Lagrangian l_1, l_2 points. Top plot: deviations of the smoothed force prescription to the 3D force for a constant ϵ with the primary star scale height (dashed orange line) and the N-body scale height (blue line). Also shown are the deviations when using a simple prescription for ϵ Eq. (B.5.5). Middle plot: optimal ϵ value to reproduce the 3D force compared to the prescription shown in Eq. (B.5.5). Bottom plot: Same scale heights as in the previous plot, computed by the gravity of the central star only (dashed orange line) and from all N-body objects (blue line).*

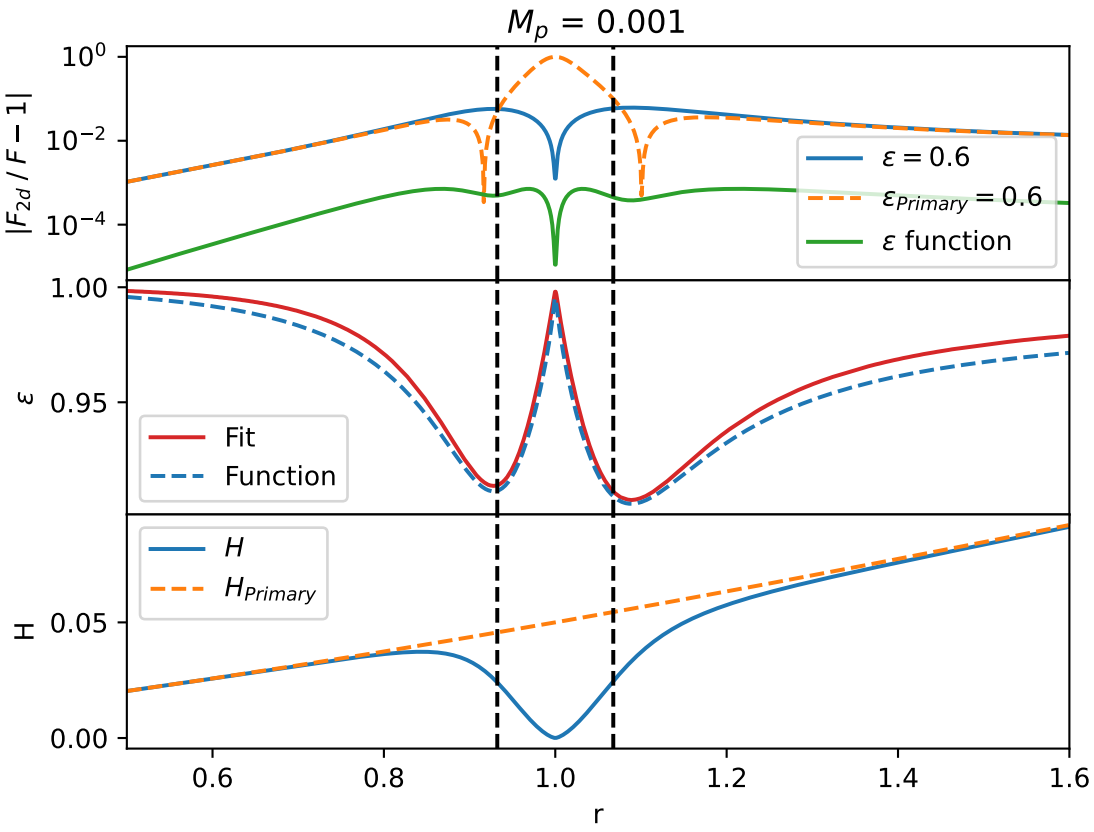

Figure B.5.3. *Same as the previous plot Fig. B.5.2 but for a Jupiter mass planet* $M_p = 10^{-3}$.

When using the force formula that also smooths the direction vector Eq. (B.5.4), the results for the force deviation from 3D are visually identical to Fig. B.5.2 and Fig. B.5.3 and therefore not shown. The only significant difference is that the optimal ϵ converges to 0.8 instead of 1 and the fitted ϵ approximation function for low mass planets becomes:

$$\epsilon = \frac{1}{1.22 + \sqrt{0.77 \cdot H/(d_p + H/4.91)}^3} \,. \tag{B.5.6}$$

Another concern that needs to be addressed is that the small-angle approximation used to derive the scale height in Eq. (B.1.6) does not apply to planets because the disk thickness is comparable to the distance from the planet. Müller et al. (2012) approximated the effect of a small planet on the disk thickness and found that the reduction of the scale height is weaker and contained closer to the planet than predicted by Eq. (B.1.6). Also, the locally isothermal model that was used is missing radiative effects that would support the disk and prevent the scale height from converging to zero near the planet (Montesinos et al. 2021). Therefore, I ran tests with the opposite extreme, where the scale height is not affected by the planet at all.

The effects of the proposed ϵ functions for constant aspect ratios are presented in Fig. B.5.4. Same as before, the 2D forces from Eq. (B.5.4) with constant ϵ and the proposed ϵ function are compared to the direct 3D forces. Outside the hill sphere of the planet, the fitted formula Eq. (B.5.6) is still tracking the optimal ϵ value and brings a significant improvement over a constant ϵ. Inside the hill sphere, the function produces a too-large ϵ and therefore

underestimates the gravitational force in this region, but is still more accurate than a constant ϵ of 0.6. Underestimating the force inside the hill sphere of the planet is not an issue inside a 2D simulation without mesh refinement, because the area cannot be resolved properly and requires more sophisticated physical models and is therefore typically filtered out when computing the disk feedback (Crida et al. 2009).

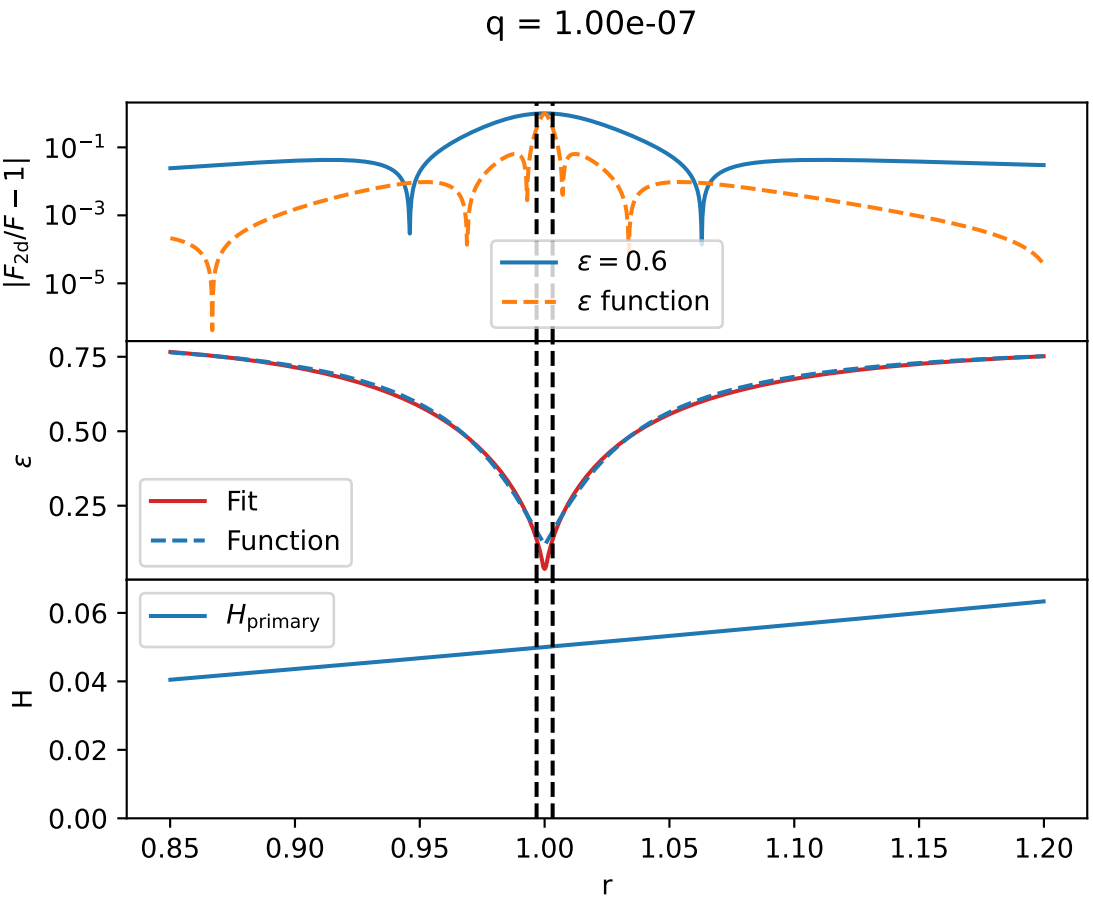

Figure B.5.4. *The Dashed black line in all panels represent the lagrangian l_1, l_2 points. Top panel: comparing the force derived from a smoothed force Eq. (B.5.4) to the 3D reference force on a moon-sized planet ($M_p/M_{\text{Star}} = 10^{-7}$) when only the primary affects the disk scale height. The blue line is from a smoothed force with $\epsilon = 0.6$, the dashed orange line is from the ϵ function Eq. (B.5.6). Middle panel: the best fitting ϵ values to match the 3D force compared to Eq. (B.5.6). Bottom panel: scale height H_{primary} used for computing the smoothing.*

B.6 Smoothing effects on planet torques

The gravitational torques acting on a planet are depicted in Fig. B.6.1 to test the effects of the different ways to compute and smooth the gravitational force. The setup contains a solar mass star and a planet with a reduced mass of $q = 2 \cdot 10^{-5}$ at a distance of 1 au from the star on a

circular orbit. To avoid interactions with the boundaries, the disk is exponentially truncated near the inner and outer boundaries. The surface density of the disk is given by

$$\Sigma = 3341\,\mathrm{g/cm^2}\cdot(r/[\mathrm{au}])^{-1.5}\cdot[1+\exp((r/[\mathrm{au}]-2.75)/0.05)]^{-1}\cdot[1+\exp((0.3-r/[\mathrm{au}])/0.02)]^{-1}, \tag{B.6.1}$$

the disk has an aspect ratio of $h_0 = 0.05$, no flaring ($F = 0$) and is inviscid. The simulation domain spans over $r \times \varphi = [0.1, 4] \times [0, 2\pi]$ and is resolved by $N_r \times N_\varphi = 1182 \times 2010$. The disk mass was kept constant, meaning that if mass left the domain, the densities of all cells were scaled up to restore the initial mass. For numerical stability, the gravitational interaction was smoothed with 1 R_{hill} according to Eq. (B.3.1) or Eq. (B.3.2) in all simulations. However, this has no effect in simulations in which the *epsilon* smoothing length is greater than the hill radius, which is the case for every simulation that only considers the central star when calculating the disk scale height together with a constant *epsilon* parameter.

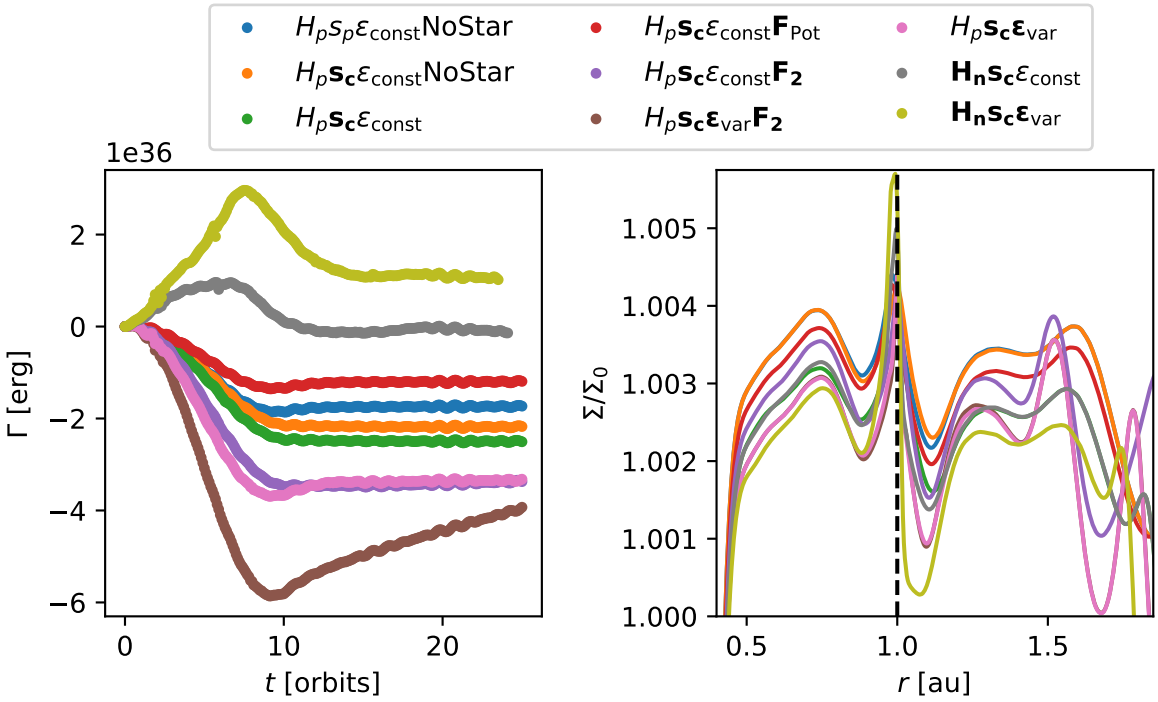

Figure B.6.1. *Planet torques and normalized radial surface density profiles for different combinations smoothing methods, scale height calculations, and force calculations. See text for details.*

In the legend in Fig. B.6.1, H_p means that the scale height is only computed due to the gravity of the central star and H_n due to the gravity of star and planet Eq. (B.1.6). Changes from the fiducial setup are highlighted as bold inside the legend. By default, the force is computed directly and the direction vector is also smoothed, see Eq. (B.5.4). F_2 means that the force on the gas was computed directly as in Eq. (B.5.3) and F_{pot} means that the force was numerically derived from a potential Eq. (B.5.2). NoStar means that the gravity of the star is not smoothed, and s_p means that the smoothing length is calculated using the scale height at the position of the planet. These are the default settings from the original FARGO code (Masset 2000). s_c

means that the smoothing is computed with the scale height of the cell that the planet is interacting with. ϵ_{const} means that the parameter is const $\epsilon = 0.7$ and ϵ_{var} means that it is variable according to Eq. (B.5.5) or Eq. (B.5.6) depending on the force computation. Applying the smoothing to the gravitational force of the star, calculating the smoothing length based on the scale height of the cell, and making the ϵ variable all resulted in higher negative torques acting on the planet, implying faster inward migration. Computing the gravitational force from the planet onto the gas from the smoothed potential resulted in the weakest torque acting on the planet. Calculating the force directly with a smoothed direction vector resulted in a larger negative torque compared to the potential, while calculating the force directly resulted in the largest negative torque. Allowing the planet to influence the scale height is the only change that reduces the negative torques and can even produce positive torques, implying outward migration. The use of the smoothing length at the position of the planet or the position of the gas cell itself are both used in the literature, as are the different ways of calculating the gravitational force. Allowing the planet to influence the disk scale height, as well as the variable ϵ parameter, do not typically appear in literature. But, as argued here, they could make the planet-disk interaction more accurate.

All these options are different ways to model the planet-disk interaction, meaning that one of these must be the most realistic one. To find out which model best approximates planet-disk interactions, comparisons with 3D simulations are required which are not given here.

B.7 Conclusions

The effects of how current 2D hydrodynamic codes compute the gravitational interaction of gas cells with N-body objects have been studied.

In Appendix B.1 it was explained that smoothing the gravitational force in two dimensions simulates the vertical stratification of the gas, so the scale height of the cell should always be used to calculate the smoothing length, and not the scale height at the position of the planet. This also means that the smoothing should be applied to the gravitational force of the central star. Then it was reviewed how the scale height of a disk interacting with multiple N-body objects could be computed.

In Appendix B.2 three methods commonly found in simulation codes for computing the gravitational force from an N-body object onto a gas cell are presented. The effect of these methods on the orbital velocity is then derived, and estimates are given for errors that arise when the vertical stratification of the gas is taken into account but the vertical stratification of the dust particles inside the disk is not.

In Appendix B.3 it was shown that the smoothing developed for 3D simulations by Klahr & Kley (2006) works just as well for ensuring numerical stability in 2D codes.

In Appendix B.4 it was highlighted that the effects of smoothing the gravitational force significantly complicate the initialization of an accretion disk in a viscous steady state and how one could proceed to find a viscous steady state.

In Appendix B.5, a 3D locally isothermal model is compared with the different 2D forces. Empirical formulas for the ϵ parameter are fitted that approximate the 3D force. The $\epsilon \approx 0.6$ parameter for potential smoothing found in (Masset 2002; Müller et al. 2012) is a poor approximation. A more accurate model for ϵ depends on the distance to the N-body object and its mass. For stellar masses, the ϵ parameter becomes nearly constant again. It is also noted that calculating the gravitational force by numerically deriving the potential should be avoided, since the gravitational force of an N-body object on a cell should be independent of the properties of its neighboring cells.

In Appendix B.6 the effects of different ways to calculate the disk scale height, smoothing, and gravitational force on the torque acting on a planet inside the disk are tested. The torques show a large spread from positive to negative depending on the model used. Since the measured torques are an indicator of how the planet is migrating, the planet migration would depend on how the simulation calculates the gravitational force. This is a problem because all these different models for calculating the gravitational force are currently in use, but one of them must be more accurate and should be used over the others. I think that this issue deserves more attention, papers should state more clearly how they model the planet-disk interaction, and studies that focus on the comparisons between 3D simulations and 2D simulations could bring a consensus on how to best to approximate the disk scale height and the planet-disk interaction in 2D.

C The viscously spreading ring as a test setup

When a pressureless ring of gas evolves over time under the influence of viscosity, it will spread, become unstable, and turn into a one-armed spiral (Speith & Kley 2003). Since it has an analytical solution, it provides an excellent test for viscosity implementations in hydrodynamic codes. Speith & Kley (2003) performed a perturbation analysis of the ring and showed that the first-order analysis describes a spiral arm, which they also found in their simulations. They also observed two-armed spiral features in their simulation, which they attributed to the results of the second-order analysis. However, these two-armed spiral features are not found in modern simulations.

My collaborators used the viscously spreading ring to quantify the quality of Cartesian hydrodynamic codes and found that they reproduce the spreading of the ring, but fail to develop the one-armed spiral. They then used an inviscid ring to measure the effects of the numerical viscosity and its magnitude in their codes, which is the main result of the paper. They found that it behaves similarly to the kinematic viscosity used in hydrodynamic codes, whereas before it was a poorly constrained effect.

Because of the similarities between the RH2D code used in Speith & Kley (2003) and the FARGO code, I was tasked to analyze the two-armed spiral features described in Speith & Kley (2003). I was able to reproduce the results from Speith & Kley (2003) and could show that the two-armed spiral features were a numerical artifact caused by an arithmetic grid and low resolution.

A&A, 678, A134 (2023)
https://doi.org/10.1051/0004-6361/202245601
© The Authors 2023

Astronomy & Astrophysics

Measuring the numerical viscosity in simulations of protoplanetary disks in Cartesian grids

The viscously spreading ring revisited

Jibin Joseph[1,3], Alexandros Ziampras[1,2], Lucas Jordan[1], George A. Turpin[2], and Richard P. Nelson[2]

[1] Institut für Astronomie und Astrophysik, Universität Tübingen, Auf der Morgenstelle 10, 72076 Tübingen, Germany
[2] Astronomy Unit, Department of Physics and Astronomy, Queen Mary University of London, London E1 4NS, UK
e-mail: a.ziampras@qmul.ac.uk; r.p.nelson@qmul.ac.uk
[3] Leibniz-Institut für Astrophysik Potsdam (AIP), An der Sternwarte 16, 14482 Potsdam, Germany
e-mail: jjoseph@aip.de

Received 1 December 2022 / Accepted 24 July 2023

ABSTRACT

Context. Hydrodynamical simulations solve the governing equations on a discrete grid of space and time. This discretization causes numerical diffusion similar to a physical viscous diffusion, the magnitude of which is often unknown or poorly constrained. With the current trend of simulating accretion disks with no or very low prescribed physical viscosity, it has become essential to understand and quantify this inherent numerical diffusion in the form of a numerical viscosity.
Aims. We study the behavior of the viscous spreading ring and the spiral instability that develops in it. We aim to use this setup to quantify the numerical viscosity in Cartesian grids and study its properties.
Methods. We simulated the viscous spreading ring and the related instability on a two-dimensional polar grid using PLUTO as well as FARGO, ensuring the convergence of our results with a resolution study. We then repeated our models on a Cartesian grid and measured the numerical viscosity by comparing results to the known analytical solution using PLUTO and Athena++.
Results. We find that the numerical viscosity in a Cartesian grid scales with resolution as approximately $\nu_{\rm num} \propto \Delta x^2$ and is equivalent to an effective $\alpha \sim 10^{-4}$ for a common numerical setup. We also showed that the spiral instability manifests as a single leading spiral throughout the whole domain on polar grids. This is contrary to previous results and indicates that sufficient resolution is necessary in order to correctly resolve the instability.
Conclusions. Our results are relevant in the context of models where the origin should be included in the computational domain, or when polar grids cannot be used. Examples of such cases include models of disk accretion onto a central binary and, inherently, Cartesian codes.

Key words. hydrodynamics – accretion, accretion disks – protoplanetary disks – methods: numerical

1. Introduction

Hydrodynamical simulations are a useful tool for studying a variety of astrophysical processes. An example of such a process is the accretion flow of a protoplanetary disk around a star. Accretion is thought to be achieved via turbulence operating in parts of the disk (Lyra & Umurhan 2019), which transports angular momentum radially outwards similar to a viscosity (Lynden-Bell & Pringle 1974; Balbus & Papaloizou 1999), or via a magnetic torque that is applied on the material close to the surface of the disk as a stellar wind expels gas from the disk surface layers (Bai & Stone 2013) with the bulk of the disk remaining inviscid and laminar. The result, particularly in protoplanetary disks, is a steady radial infall of gas that ultimately depletes the disk over typical timescales of 1–10 Myr (Haisch et al. 2001).

While turbulent angular momentum transport has been the traditional way of modeling accretion, numerous recent observations of disks around T Tauri stars (e.g., the DSHARP survey, Andrews et al. 2018) suggest very low $\alpha \lesssim 10^{-4}$ in order for turbulence to be compatible with the radial width of observed rings (Dullemond et al. 2018), the vertical structure of millimetre (mm) grains (Dullemond et al. 2022), and the formation of rings and gaps by embedded planets (Zhang et al. 2018). As a result, magnetic winds are becoming a favored means of interpreting accretion in protoplanetary disks, and numerical models of such disks tend toward the inviscid limit (e.g., Lega et al. 2022).

However, here we run into a different problem: the numerical schemes used to model protoplanetary disks introduce a certain amount of numerical diffusion. The magnitude of this diffusion is often unknown or poorly constrained. Therefore, calculating an upper limit to this nonphysical diffusion, or equivalently a 'numerical viscosity', is essential in order to ensure that results are not affected by the effects it can induce. This is particularly important for models using Cartesian grids, which are primarily used when the central object should be included in the simulation domain such as when modeling accretion patterns around binary stars (e.g., Tiede et al. 2022), or for certain MHD codes (e.g., Fromang et al. 2006). Analogous issues also appear when an object is not centered on a polar grid, which is often the case for circumplanetary disks (e.g., Crida et al. 2009). Grid noise due to the asymmetric nature of Voronoi-mesh cells has also been identified as a source of numerical diffusion in moving mesh codes (Zier & Springel 2022). In these cases, the geometry of the grid introduces a very high numerical viscosity and as a result

Open Access article, published by EDP Sciences, under the terms of the Creative Commons Attribution License (https://creativecommons.org/licenses/by/4.0), which permits unrestricted use, distribution, and reproduction in any medium, provided the original work is properly cited.
This article is published in open access under the Subscribe to Open model. Subscribe to A&A to support open access publication.

models require the execution of very computationally expensive, high-resolution simulations.

In this work, we revisited the viscously spreading ring problem introduced first by Lüst (1952) and again by Lynden-Bell & Pringle (1974), and analyzed in 2D by Speith & Kley (2003, henceforth SK03). We approached this with numerical hydrodynamics simulations, which we designed to reproduce or improve upon the results of SK03 by reanalyzing the azimuthal instability they reported, and then performed calculations in Cartesian coordinates to quantify the numerical viscosity of the codes PLUTO and Athena++.

The viscous ring problem and our physical and numerical setup are described in Sect. 2. We compare our results with those of SK03 and point out the origin of a numerical artifact in their study through a resolution analysis in Sect. 3. We present our results for Cartesian models and our estimates of the numerical viscosity in Sect. 4. We then discuss our findings in Sect. 5, and conclude in Sect. 6.

2. Model setup

In this section, we revisit the setup for the viscously spreading ring problem and describe our physics and numerical methods. We also provide a list of models that were executed using different codes and in different coordinate systems.

2.1. The viscous ring problem

Starting from an axisymmetric surface density distribution of a pressureless ($P = 0$) ring of gas with mass $M_{\rm ring}$ that is centered at distance R_0 and is infinitely thin in the radial direction,

$$\Sigma_{\rm ring}(t = 0, R) = \frac{M_{\rm ring}}{2\pi R}\delta(R - R_0), \tag{1}$$

the ring will spread along the radial direction R following the analytical solution (e.g., Lynden-Bell & Pringle 1974; Pringle 1981)

$$\Sigma_{\rm ring}(\tau, x) = \frac{M_{\rm ring}}{\pi R_0^2}\frac{1}{\tau x^{1/4}} I_{\frac{1}{4}}\left(\frac{2x}{\tau}\right)\exp\left(-\frac{1+x^2}{\tau}\right), \tag{2}$$

where $x = R/R_0$ and $\tau = 12\nu t R_0^{-2}$ are normalized distance and time quantities, ν is the kinematic viscosity of the gas, and $I_{\frac{1}{4}}$ is the modified Bessel function of the order 1/4. In addition, the radial velocity of the ring is given by the following relation,

$$u_{\rm R,ring} = -\frac{3}{\Sigma_{\rm ring}\sqrt{R}}\frac{\partial}{\partial R}\left[\nu\Sigma_{\rm ring}\sqrt{R}\right]. \tag{3}$$

We note that Eq. (2) is only an approximate solution to the hydrodynamic equations (see Sect. 2.2), and assumes that the disk is massless with highly supersonic and Keplerian azimuthal velocity. Furthermore, one assumes that the kinematic viscosity, ν, is much smaller than the specific angular momentum $R^2\Omega$, an assumption that is violated close to the central object. A time evolution of the viscous ring problem using our fiducial axisymmetric numerical setup (described in Sect. 2.3) is shown in Fig. 1.

The problem was revisited by SK03, who showed that the ring is subject to a viscosity-driven spiral instability in the azimuthal direction that results in the development of a leading spiral arm that covers the full extent of the computational domain. These authors performed a detailed stability analysis and showed that unstable modes with wave-numbers k develop where

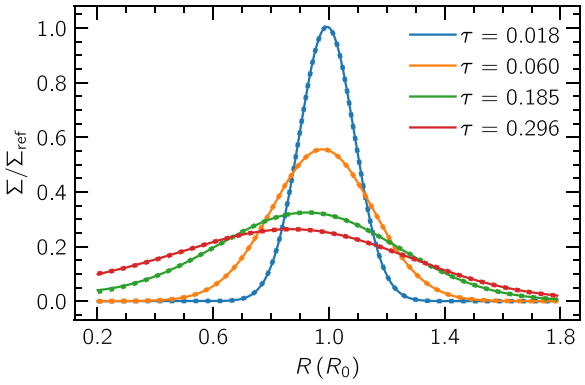

Fig. 1. Evolution of the one-dimensional viscously spreading ring. The colors indicate different time stamps, solid lines represent simulation results, and dots follow the analytical solution at the corresponding time according to Eq. (2).

$$k^2 > \frac{3}{R\Sigma_0}\frac{\partial\Sigma_0}{\partial R}, \tag{4}$$

with Σ_0 being the axisymmetric density profile. SK03 further showed that the spiral arm changes direction from leading to trailing at around the peak of the ring (see second and third panels of Fig. B.3), and verified their results with two fundamentally different codes: the finite-difference upwind grid code RH2D (Kley 1989, 1999), and the smooth particle hydrodynamics (SPH) code used by Flebbe et al. (1994).

2.2. Hydrodynamics

We consider the vertically integrated hydrodynamics equations for a gas with surface density Σ, velocity vector $\boldsymbol{u}$, and nearly zero pressure P at distance R,

$$\begin{aligned}\frac{\partial\Sigma}{\partial t} + \nabla\cdot(\Sigma\boldsymbol{u}) &= 0,\\ \frac{\partial(\Sigma\boldsymbol{u})}{\partial t} + \nabla\cdot(\Sigma\boldsymbol{u}\otimes\boldsymbol{u}) &= -\nabla P - \Sigma\nabla\Phi_\star + \nabla\cdot\overline{\sigma}.\end{aligned} \tag{5}$$

The gas orbits around a star with mass $M_\star$ such that the gravitational potential is given by $\Phi_\star = -GM_\star/R$, with G being the gravitational constant. The viscous stress tensor is represented with $\overline{\sigma}$. We use a locally isothermal equation of state, such that the gas has a (very small) sound speed $c_{\rm s} = \sqrt{P/\Sigma} = h\sqrt{GM_\star/R} = hR\Omega_{\rm K}$, where h is the aspect ratio.

2.3. Numerical setup

For our standard setup, we used PLUTO version 4.3 (Mignone et al. 2007), a finite-volume code with a second-order accurate scheme (HLLC, Toro et al. 1994) and the van Leer flux limiter (van Leer 1977). We followed the setup laid out in SK03 to reproduce the original results. In this section, we provide a detailed description of our model and its differences with the setup in SK03.

To study the viscous ring and the related instability, we used a polar grid with computational domain $R \in [0.2, 2]\,R_0$ and $\phi \in [0, 2\pi)$. We used both logarithmic ($\Delta R \propto R$) and arithmetic (ΔR = const.) scaling in the radial direction for comparison reasons, but focus on logarithmic setups first. We also enabled the FARGO transport scheme (Masset 2000) implemented in PLUTO by Mignone et al. (2012), while the parabolic viscosity term is handled using the explicit time-stepping method in PLUTO. We used a Courant number of 0.4 in all simulations, unless specified otherwise. The system was then evolved for various grid resolutions, the results of which are discussed in Sect. 3.2. The Cartesian setup used to measure the numerical viscosity is described in Sect. 4.2.

To evolve the viscous ring problem, we initialized the surface density using Eq. (2) at $\tau_0 = 0.018$ and added a small, constant surface density floor $\Sigma_{\rm floor} = 10^{-7}\,\Sigma_{\rm ref}$, where $\Sigma_{\rm ref} = \Sigma_{\rm ring}(\tau_0, 1)$. We chose a set of code units where $\bar{G} = \bar{M}_\star = \bar{R}_0 = 1$. This leaves the kinematic viscosity as the only relevant physical constant in this setup, which we chose to be $\bar{\nu} = 10^{-5}$. For this viscosity, we get a viscous ring spreading time (i.e., $\tau = 1$) of 1326 orbital periods (P_0) at $R = R_0$. To facilitate development of the spiral instability, the initial surface density distribution was seeded with a small amount of noise and evolved up to $t = 400\,P_0$, or $\tau = 0.3$.

We chose a strict outflow boundary condition in both radial directions such that $\partial_R \Sigma = 0$, $u_{R,\rm in} = -|u_R(R_{\rm in})|$, $u_{R,\rm out} = |u_R(R_{\rm out})|$. The azimuthal velocity is fixed to the Keplerian speed corrected for pressure support $u_\phi = R\Omega_{\rm K}\sqrt{1-h^2}$ at the boundaries. We explored various values of the aspect ratio, shown in Appendix A, and chose $h = 0.005$ for our simulations, as we find it to be low enough for the gas to act like a pressureless fluid and high enough to ensure numerical stability in our simulations. The RH2D setup in SK03 used a viscosity value of $\bar{\nu} = 4.77 \times 10^{-5}$ and an initial viscous time $\tau_0 = 0.016$, but this has no effect on the subsequent evolution.

To corroborate our results, we used the FARGO code (legacy version; Masset 2000). Similar to the RH2D code used in SK03, FARGO uses a finite difference scheme as described in Stone & Norman (1992) with the second-order upwind algorithm by van Leer (1977). Both codes therefore show a similar behavior and we used FARGO to compare our results to those of SK03.

3. Analysis of the viscous ring problem

In this section, we explore the spiral instability using logarithmically spaced polar grids. In such grids, the radial cell size ΔR increases with distance such that the ratio $\Delta R/H$ remains comparable throughout the domain (in the case of h = const., this ratio is constant as $H = hR$). This makes logarithmically spaced grids highly suitable for general-purpose disk models, where gas dynamics should be resolved over a scale height H using a reasonable number of cells. We briefly describe the general behavior of the viscous spreading ring and show that our fiducial model is numerically converged.

3.1. Time evolution of the viscous ring

We begin our analysis with a 1D model of the viscously spreading ring, using 465 cells logarithmic scaled in the radial direction. This resolution is chosen such that the gas is resolved with at least one cell per scale height $H = hR$. Even though the problem is formally defined for a pressureless fluid ($h = 0$),

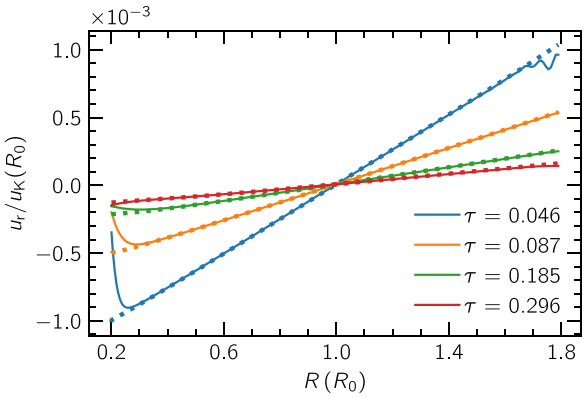

Fig. 2. Similar to Fig. 1 showing the evolution of radial velocity of the ring compared to the analytical solution Eq. (3).

Figs. 1 and 2 show that our model adequately reproduces the analytical equations of Eqs. (2) and (3), respectively.

To assess the robustness of the numerical methods used, we quantified numerical errors in our results by measuring the average density-weighted relative deviation from the analytical solution of both the surface density Σ and radial velocity u_R on the grid, at various times. We find a maximum deviation of 0.74% for Σ and 3.31% for u_R. While these values are largely influenced by regions close to the boundaries, where deviations are the largest, for most of the domain (0.4–1.8 R_0) we find maximum deviations of 0.15 and 0.75% for Σ and u_R respectively. In addition, we find that further reducing the aspect ratio h does not substantially affect the measured errors.

We then expanded to a 2D $\{R, \phi\}$ domain, with a fiducial resolution of $N_R \times N_\phi = 465 \times 256$. Here, we expect the same radial spreading of the ring but also development of the viscosity-driven spiral instability discussed in SK03. Figure 3 shows a time evolution of the ring spreading and of the instability, which manifests in the form of an outward-propagating spiral arm. Weak radial wave-like perturbations are launched immediately after the start of the simulation (see panel a).

The perturbations are not affected by changes to pressure or initial conditions, but they do become weaker and move to smaller wavelengths with lower viscosity. This viscosity dependency is in agreement with the viscous overstability (e.g., Latter & Ogilvie 2006) but a more thorough study of the perturbations is not within the scope of this work.

These initial waves leave the domain through the outer boundary, while the spiral instability begins to develop near the inner boundary, with the spiral becoming apparent at $\tau \approx 0.03$ (panel b). The spiral continues to grow in amplitude and propagate outwards until it eventually spans the entire radial extent of the disk (panels c,d).

In contrast to the results in SK03, we do not see a flip of the direction of the spiral from leading to trailing around the peak of the ring. Instead, we find that this flip is merely a numerical artifact and does not appear in simulations with a sufficiently high radial resolution. We discuss this further in Appendix B.

3.2. Resolution study

To ensure a properly resolved and developed viscous instability, we performed a resolution study by analyzing its growth phase. For this, we measured the largest density deviation from the azimuthally averaged profile at different radii and tracked

Joseph, J., et al.: A&A, 678, A134 (2023)

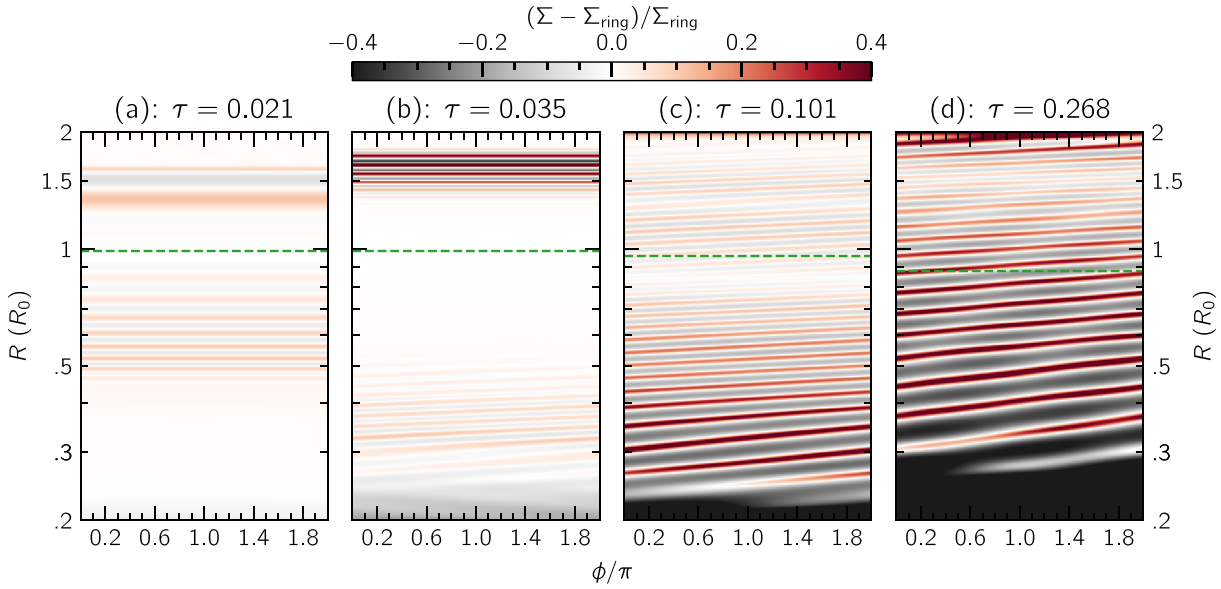

Fig. 3. Snapshots of the normalized deviation from the analytical surface density distribution for our fiducial model at different times. The dashed green line marks the position of maximal surface density, which indicates the peak of the spreading ring. Initial waves (a) are seen as outward-moving rings while the spiral instability develops as a spiral arm at the inner boundary (b) and spreads through the whole domain (c,d).

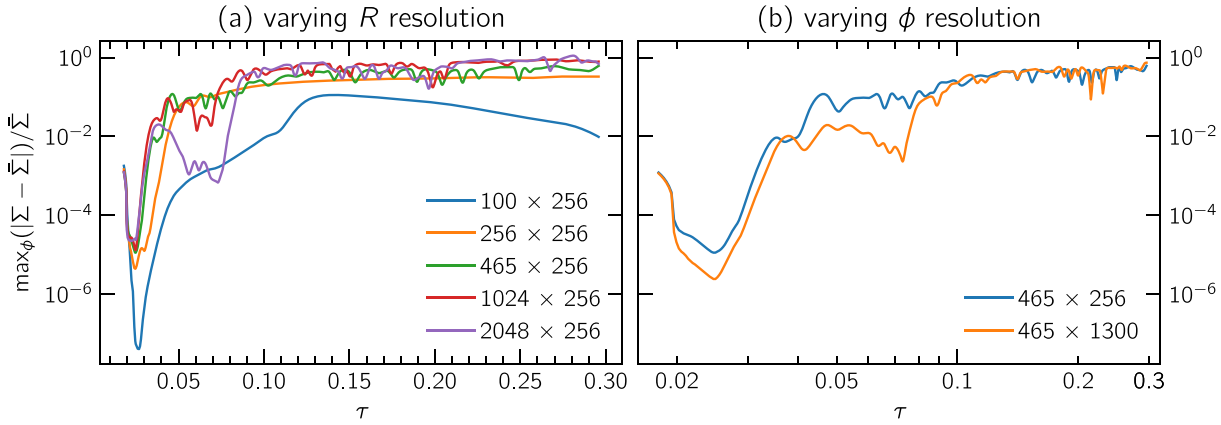

Fig. 4. (a) Time evolution of the normalized maximal deviation from the azimuthally averaged surface density distribution for various numerical configurations. Inadequate resolution in the R-direction can damp the viscous instability, with convergence being achieved for our fiducial model with $N_R = 465$. (b) Comparison of the same quantity for different azimuthal resolutions and $N_R = 465$. The higher resolution of $N_\phi = 1300$ azimuthal cells results in square grid cells but does not influence the growth of the instability.

this quantity over time. In that sense, this quantity acts as a proxy for the time evolution of the amplitude of the strongest spiral at a given radius, which hints at the growth rate of the spiral instability. Figure 4 shows this evolution for various resolutions. Alternatively, we also evaluated the amplitude of the azimuthal Fourier modes of density rings at specific radii over time. The results obtained using this method are similar to those obtained from measuring the density deviations and are therefore not shown here.

After comparing our results against a model with square cells ($N_R \times N_\phi = 465 \times 1300$), we find that increasing the azimuthal resolution beyond 256 cells has no effect on the growth rate of the instability (see Fig. 4b) and therefore fixed the number of azimuthal cells to 256 in our resolution study. In the radial direction we find a resolution of 465 cells to be sufficient.

We confirmed our results using the FARGO code in Appendix B and achieved numerical convergence with both codes at a resolution of 465×256 cells. We conclude that this resolution is sufficient to fully resolve the viscously spreading ring and the development and saturation of spiral arms due to the spiral instability.

4. The viscous ring problem in Cartesian coordinates

Having profiled the viscous ring problem in a polar grid, we now switch to Cartesian coordinates with our ultimate goal being the measurement of the numerical viscosity of PLUTO for such a grid. For this set of models, our computational domain

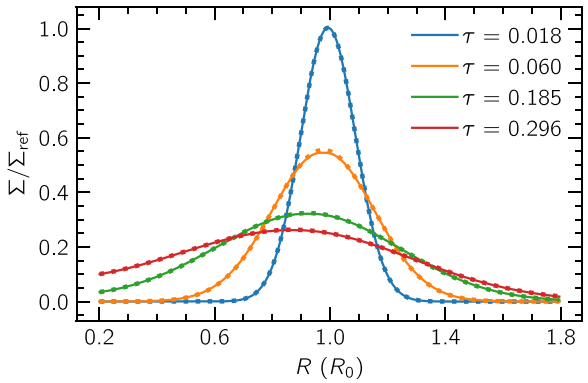

Fig. 5. Snapshots of slices through the $y = 0$ plane showing the evolution of surface density for our fiducial viscous Cartesian simulation. The colors indicate different time stamps, solid lines represent simulation results, and dots follow the analytical solution at the corresponding time according to Eq. (2). Unlike the 2D polar case, no spirals develop.

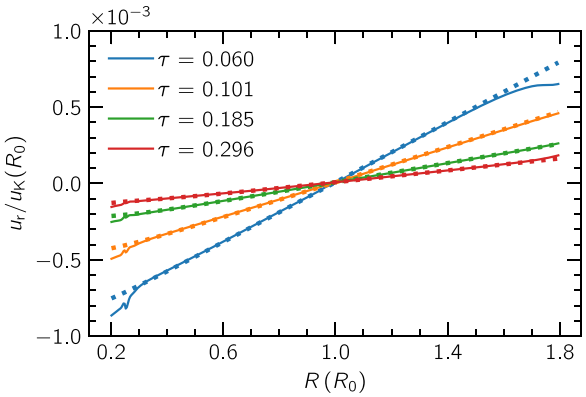

Fig. 6. Similar to Fig. 5, showing the evolution of radial velocity of the ring compared to the analytical solution Eq. (3).

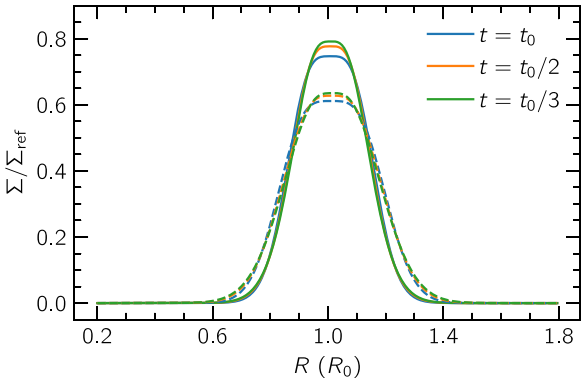

Fig. 7. Slices of surface density profiles for our fiducial inviscid Cartesian model ($\nu = 0$, blue lines) at a given time t_0 against the corresponding viscous models with $\nu = \nu_{\rm num}$ at $t_0/2$ (orange) and $\nu = 2\,\nu_{\rm num}$ at $t_0/3$ (green). Solid and dashed lines correspond to $t_0 = 224$ and 748 orbits at R_0, respectively. The model with $\nu = \nu_{\rm num}$ evolves twice as fast as the inviscid simulation and the $\nu = 2\,\nu_{\rm num}$ model evolves three times as fast, indicating a viscous contribution by the non-negligible numerical viscosity.

extends between $x, y \in [-2, 2]\,R_0$, with a fiducial resolution of $N_x \times N_y = 1024 \times 1024$ cells, which corresponds to approximately one cell per scale height at $R = \sqrt{x^2 + y^2} = R_0$. We note that, $\Delta x = \Delta y = $ const. in these models, and therefore our effective resolution is significantly lower at smaller radii.

For a fair comparison with our models on a polar grid, we retained the second-order accurate HLLC scheme with a linear spatial reconstruction and van Leer flux limiter for all simulations unless otherwise stated. In addition, we emulated the inner radial boundary of a polar grid using a damping region, where we damped Σ to $\Sigma_{\rm ring}$ through Eq. (2) and $u_{\rm R}$ to zero for $R < 0.2\,R_0$. Finally, we set an outflow boundary condition at all domain boundaries. To measure numerical viscosity in `PLUTO`, we used a similar setup but damped Σ to $\Sigma_{\rm floor}$ following (de Val-Borro et al. 2006), and provide a comparison using `Athena++` version 21.0 (Stone et al. 2008).

4.1. Viscous evolution

We first analyze the evolution of the ring with standard viscosity similar to in Sect. 3. The radial ring spreading and the radial velocity evolution can be seen in Figs. 5 and 6, respectively; they match the analytical solution well except for noticeable deviations in $u_{\rm R}$ close to the damping region and boundaries. We again quantified the error by measuring the density-weighted relative deviations in the domain excluding the damping region and find a maximum deviation of 0.71% for Σ and of 15.74% for $u_{\rm R,ring}$. We note that, unlike the polar case, we find no development of spirals in any Cartesian model. We suspect that the spiral instability is suppressed as a result of the highly diffusive grid, which is further discussed in Sect. 5. We see similar results at lower and higher resolutions of 512^2 and 2048^2 cells.

4.2. Inviscid models: Estimates of numerical viscosity

The discretization in space and time inherent in the numerical schemes employed by our codes results in numerical errors when solving the hydrodynamics equations. In our analysis in Appendix C, we show that this error has the form of a numerical viscosity and can lead to ring spreading, even in the absence of any physical viscosity. In this section, we repeat the models shown in Sect. 4.1 with an inviscid prescription ($\nu = 0$), and analyze the subsequent ring spreading in an attempt to quantify the numerical viscosity of the methods in `PLUTO`.

Blue lines in Fig. 7 show the time evolution for our fiducial inviscid model at a resolution of 1024×1024. We find that the ring spreading is indeed quite similar to viscous models, with the exception that the peak of the ring is flatter compared to the analytical solution. We then extracted a global estimate of the numerical viscosity $\nu_{\rm num}$ by fitting the analytical solution Eq. (2) to our data. The fitting method is described in Appendix D.

We repeated the simulation with a prescribed kinematic viscosity equal to the measured numerical viscosity ($\nu = \nu_{\rm num}$) and once again with $\nu = 2\,\nu_{\rm num}$, the time evolution of which is shown as orange and green lines, respectively, in Fig. 7. We find that the $\nu = \nu_{\rm num}$ model evolves twice as fast as our inviscid model, and the $\nu = 2\,\nu_{\rm num}$ model evolves three times as fast. This suggests that all models evolve as if the total viscosity were $\nu_{\rm tot} = \nu + \nu_{\rm num}$. We motivate our approach and rationalize this result in Appendix C.

Table 1. Numerical viscosity $\nu_{\rm num}$ with one standard deviation errors in code units for different grid types and resolutions.

Code	Grid	Resolution	$\bar{\nu}_{\rm num}$	$\alpha_{\rm num}$ at R_0
PLUTO	Cartesian	256×256	$(4.68 \pm 0.19) \times 10^{-6}$	$(1.87 \pm 0.08) \times 10^{-3}$
PLUTO	Cartesian	512×512	$(1.48 \pm 0.01) \times 10^{-6}$	$(5.92 \pm 0.04) \times 10^{-4}$
PLUTO	Cartesian	1024×1024	$(4.16 \pm 0.03) \times 10^{-7}$	$(1.67 \pm 0.01) \times 10^{-4}$
PLUTO	Cartesian	2048×2048	$(9.45 \pm 0.11) \times 10^{-8}$	$(3.78 \pm 0.04) \times 10^{-5}$
PLUTO	Cartesian	4096×4096	$(1.32 \pm 0.08) \times 10^{-8}$	$(5.29 \pm 0.31) \times 10^{-6}$
PLUTO	Polar	465×256	$(3.89 \pm 0.94) \times 10^{-15}$	$(1.56 \pm 0.38) \times 10^{-12}$
Athena++	Cartesian	256×256	$(7.31 \pm 0.22) \times 10^{-6}$	$(2.92 \pm 0.08) \times 10^{-3}$
Athena++	Cartesian	512×512	$(2.04 \pm 0.05) \times 10^{-6}$	$(8.16 \pm 0.19) \times 10^{-4}$
Athena++	Cartesian	1024×1024	$(4.26 \pm 0.11) \times 10^{-7}$	$(1.70 \pm 0.04) \times 10^{-4}$
Athena++	Cartesian	2048×2048	$(1.11 \pm 0.02) \times 10^{-7}$	$(4.44 \pm 0.08) \times 10^{-5}$

Notes. An equivalent $\alpha_{\rm num}$ at R_0 and a realistic $h = 0.05$ is also listed.

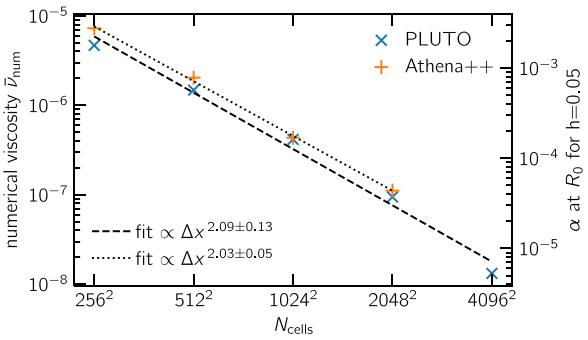

Fig. 8. Numerical viscosity $\bar{\nu}_{\rm num}$ in code units and the corresponding α at R_0 for $h = 0.05$ at different resolutions, extracted by fitting Eq. (2) to our Cartesian grid results for both Athena++ and PLUTO. The two codes agree very well for $N_{\rm cells} \geq 1024^2$. See Appendix E for details on the Athena++ models.

4.2.1. Resolution scaling of the numerical viscosity

In our analysis of the numerical viscosity for a first-order solver in Appendix C, we show that the numerical viscosity scales as $\nu_{\rm num} \propto \Delta x$ for a first-order method. As we used a second-order solver for our tests, we expect the numerical viscosity to scale as $\nu_{\rm num} \propto \Delta x^2$ in our models. To test this, we conducted simulations for grid resolutions of 256^2, 512^2, 1024^2, 2048^2, and 4096^2 cells. The resulting values of $\nu_{\rm num}$ as a function of cell count are listed in Table 1 and shown in Fig. 8. We then fit a power law to the relation $\nu_{\rm num}(\Delta x)$ and find that the numerical viscosity scales as $\nu_{\rm num} \propto \Delta x^{2.09}$. We also find that reducing the maximum Courant number $C_{\rm max} \approx \Delta t / \min\left(\Delta x / u\right)$ from our nominal value of 0.4 had no effect on the numerical viscosity, indicating that the dependence of $\nu_{\rm num}$ on Δx, Δt, and the Courant number is more complicated than it would be for a first-order scheme. While we find our $\nu_{\rm num} \propto \Delta x^2$ estimate to roughly describe the convergence, we also find that the convergence rate is not constant and increases with resolution. We obtain similar results using the code Athena++ (see Appendix E).

For a realistic protoplanetary disk with $h \sim 0.05$, the numerical viscosity $\bar{\nu}_{\rm num} = 4.16 \times 10^{-7} \sqrt{G M_0 R_0}$ extracted from our fiducial Cartesian model translates to an α viscosity parameter (Shakura & Sunyaev 1973) of $\alpha \sim 1.67 \times 10^{-4} / \sqrt{\bar{R}}$. More generally, we can write

$$\alpha = \frac{\nu}{c_s H} \approx 400 \times \bar{\nu} \left(\frac{0.05}{h}\right)^2 \sqrt{\frac{R_0}{R}}. \tag{6}$$

5. Discussion

In this section, we compare our results on the spiral instability to those found in SK03, and comment on the nature of numerical viscosity.

5.1. Comparison to previous results

Analyzing the spreading ring on a polar grid in Sect. 3, we confirm the main findings from SK03 that the viscous pressureless spreading ring is subject to a viscous instability that manifests as a leading spiral arm. On the other hand, we find the flip from a leading to a trailing spiral described by these latter authors to be purely of numerical origin. As shown in Appendix B, we attribute the spiral flip to an under-resolved inner disk; the quantity $\Delta R/R$ increases for small radii in an arithmetic grid like that of SK03, while a constant smoothing length in their SPH simulations results in effectively the same issue. In our adequately resolved models ($N_R \geq 465$), we find many azimuthal spiral modes growing at the beginning of our simulation with their amplitude decaying exponentially with mode number. However, in our arithmetic, low-resolution analog of SK03, the growth of azimuthal Fourier mode amplitudes is delayed and weaker, and their amplitude decays faster with increasing mode number (Fig. B.2). We provide more details in Appendix B, but conclude here that any effects found by SK03 in addition to the leading spiral are due to the lower numerical resolution used by these authors.

5.2. Differences between physical and numerical viscosity

In Sect. 3.1, we show the development of the spiral instability for our fiducial polar model (Fig. 3) and its growth (Fig. 4). Unlike the polar grid, our Cartesian models do not develop this instability, even at comparatively higher resolutions. This can be attributed to the lack of angular momentum conservation, which results in a dramatically high numerical diffusivity. We confirm this by analyzing the growth rates of the instability as in the polar case in Fig. 9, and show that azimuthal wavenumbers in

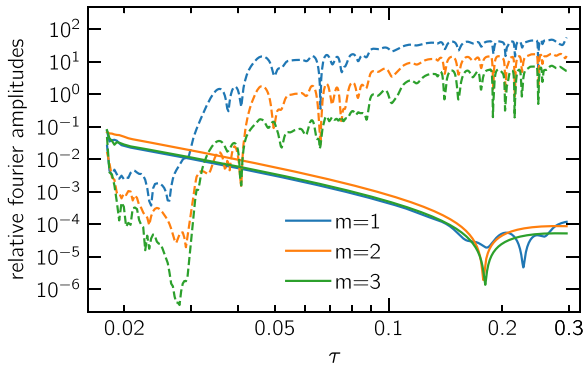

Fig. 9. Fourier amplitude normalized to azimuthally averaged density at $R = 0.5\,R_0$ for $m = 1, 2, 3$ for the fiducial polar simulation (dashed lines) and interpolated fiducial Cartesian simulation (solid lines). The spiral instability does not develop, with amplitudes of up to six orders of magnitude weaker compared to the polar case.

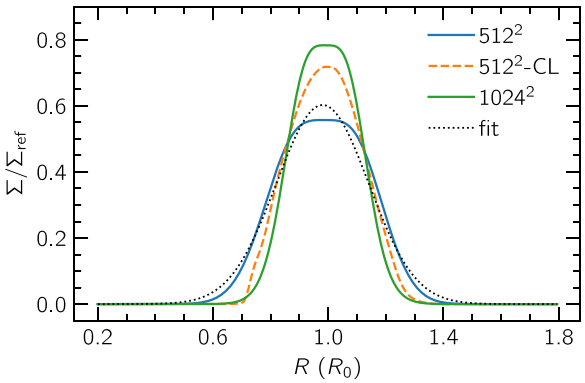

Fig. 10. Inviscid Cartesian 512^2 simulation utilizing characteristic limiting (dashed line) compared to our standard inviscid models at resolutions of 512^2 and 1024^2 (solid lines) after 150 orbits at R_0. Characteristic limiting reduces numerical viscosity by a factor of roughly 2 at 512^2 resolution. A dotted black line shows the fit using the analytical ring profile for the 512^2 simulation.

Cartesian runs saturate at levels that are six orders of magnitude weaker compared to polar runs.

Furthermore, we interpolated our fiducial polar run with a fully developed spiral onto a Cartesian grid and note that the spiral features of the viscous instability completely vanish within a span of 2–4 orbits after continuation. This suggests that even though numerical diffusion causes an effect akin to physical viscosity, the properties of numerical and physical viscosity are not the same. Both physical and numerical viscosity lead to a viscous spreading of the initial ring distribution, whereas a physical viscosity is necessary for the development of the spiral instability. The same effect cannot be replicated by numerical diffusion alone.

5.3. Effect of characteristic limiting on numerical viscosity

A commonly used method to reduce diffusive numerical effects is characteristic limiting (CL; implemented by Mignone et al. 2012), whereby spatial reconstruction is performed on characteristic variables instead of the primitive variables in the system. We assessed the effect of this method by comparing to our inviscid 512×512 Cartesian simulation with otherwise identical parameters. The low resolution was chosen to highlight the substantial difference while using CL. As shown in Fig. 10, the simulation with CL is less diffusive, which is evidenced by the lack of a flattened peak and a more weakly diffused ring overall. On average, the model with CL has roughly half the numerical viscosity of the standard inviscid 512×512 model.

6. Conclusions

We revisited the viscous ring problem in SK03 using the finite-volume codes PLUTO and Athena++ as well as the finite-difference code FARGO in an attempt to measure the numerical viscosity of hydrodynamical codes. We first reproduced the viscous ring spreading in one dimension and the spiral instability in two dimensions on a polar grid. We analyzed the growth of the instability and show that SK03 has insufficient spatial resolution to properly resolve the instability growth.

We then evolved the viscous ring spreading in two dimensions on a Cartesian grid, applying the same viscosity ν as used in the polar grid run. The evolution matches the analytical solution to good accuracy but fails to develop the spiral instability even at higher resolutions. We attributed the absence of spiral development to the lack of angular momentum conservation and subsequently high numerical diffusion inherent to Cartesian grids. Our findings suggest that a high physical viscosity is not the only ingredient to developing the spiral instability, and that a numerical setup is needed with very good angular momentum conservation and low numerical diffusivity.

The viscous spreading ring was then used to measure the numerical viscosity in Cartesian grids. This was done by evolving the viscous ring for an inviscid setup and fitting the simulated ring evolution with the analytical solution in Eq. (2) as a function of time. As the ring evolution depends only on the viscosity ν, this method allows us to extract the viscosity over which the system evolves, which for an inviscid system is the numerical viscosity. We then show a scaling relation between numerical viscosity and resolution that, for second-order methods, corresponds to $\bar{\nu}_{\rm num} \approx 0.63\,\Delta x^2$. Translating our results to a Shakura–Sunyaev α parameter, we find a relation $\alpha \approx 2 \times 10^{-4}/\sqrt{\bar{R}}$ for our fiducial model with $\bar{\nu}_{\rm num} \approx 4 \times 10^{-7}$ and a realistic aspect ratio $h = 0.05$.

We highlight that our models all utilize second-order accurate schemes in both space and time. Even though the effects of numerical viscosity can be mitigated to some degree by using higher order spatial reconstruction and time-marching algorithms, further investigation of this matter is required.

Our results reveal the existence of moderate diffusive effects in Cartesian grids and quantify the resulting numerical viscosity for standard numerical parameters and different grid resolutions. We also lay out a method that can be used to quantify the numerical viscosity to good accuracy. This information can be used to make informed decisions on how to measure and minimize numerical diffusion in hydrodynamics simulations of accretion disks, and is especially useful in the context of low-viscosity or even inviscid configurations of circumbinary or protoplanetary disks on Cartesian grids, as well as for inherently Cartesian codes.

Acknowledgements. We dedicate this paper to the memory of our dear friend and mentor Willy Kley, with whom we developed the idea for this paper. We thank him for his fundamental work, counseling, and kindness. A.Z. and R.P.N. are supported by STFC grant ST/P000592/1, and R.P.N. is supported by the Leverhulme

Trust through grant RPG-2018-418. G.A.T. is supported by an STFC PhD studentship. J.J. is co-funded by the European Union (ERC, EPOCH-OF-TAURUS, 101043302). Views and opinions expressed are however those of the author(s) only and do not necessarily reflect those of the European Union or the European Research Council. Neither the European Union nor the granting authority can be held responsible for them. The authors acknowledge support by the High Performance and Cloud Computing Group at the Zentrum für Datenverarbeitung of the University of Tübingen, the state of Baden-Württemberg through bwHPC and the German Research Foundation (DFG) through grant no INST 37/935-1 FUGG. This research utilised Queen Mary's Apocrita HPC facility, supported by QMUL Research-IT (http://doi.org/10.5281/zenodo.438045). This work was performed using the DiRAC Data Intensive service at Leicester, operated by the University of Leicester IT Services, which forms part of the STFC DiRAC HPC Facility (www.dirac.ac.uk). The equipment was funded by BEIS capital funding via STFC capital grants ST/K000373/1 and ST/R002363/1 and STFC DiRAC Operations grant ST/R001014/1. DiRAC is part of the National e-Infrastructure. The plots in this paper were prepared using the Python library matplotlib (Hunter 2007).

References

Andrews, S. M., Huang, J., Pérez, L. M., et al. 2018, ApJ, 869, L41
Bai, X.-N., & Stone, J. M. 2013, ApJ, 769, 76
Balbus, S. A., & Papaloizou, J. C. B. 1999, ApJ, 521, 650
Courant, R., Isaacson, E., & Rees, M. 1952, Commun. Pure Appl. Math., 5, 243
Crida, A., Baruteau, C., Kley, W., & Masset, F. 2009, A&A, 502, 679
de Val-Borro, M., Edgar, R. G., Artymowicz, P., et al. 2006, MNRAS, 370, 529
Dullemond, C. P., Birnstiel, T., Huang, J., et al. 2018, ApJ, 869, L46
Dullemond, C. P., Ziampras, A., Ostertag, D., & Dominik, C. 2022, A&A, 668, A105
Flebbe, O., Muenzel, S., Herold, H., Riffert, H., & Ruder, H. 1994, ApJ, 431, 754
Fromang, S., Hennebelle, P., & Teyssier, R. 2006, A&A, 457, 371
Haisch, K. E., Jr., Lada, E. A., & Lada, C. J. 2001, ApJ, 553, L153
Hunter, J. D. 2007, Comput. Sci. Eng., 9, 90
Kley, W. 1989, A&A, 208, 98
Kley, W. 1999, MNRAS, 303, 696
Latter, H. N., & Ogilvie, G. I. 2006, MNRAS, 372, 1829
Lega, E., Morbidelli, A., Nelson, R. P., et al. 2022, A&A, 658, A32
Lüst, R. 1952, Zeitschrift Naturforschung Teil A, 7, 87
Lynden-Bell, D., & Pringle, J. E. 1974, MNRAS, 168, 603
Lyra, W., & Umurhan, O. M. 2019, PASP, 131, 072001
Masset, F. 2000, A&AS, 141, 165
Mignone, A., Bodo, G., Massaglia, S., et al. 2007, ApJS, 170, 228
Mignone, A., Zanni, C., Tzeferacos, P., et al. 2012, ApJS, 198, 7
Pringle, J. E. 1981, ARA&A, 19, 137
Shakura, N. I., & Sunyaev, R. A. 1973, A&A, 24, 337
Speith, R., & Kley, W. 2003, A&A, 399, 395
Stone, J. M., & Norman, M. L. 1992, ApJS, 80, 753
Stone, J. M., Gardiner, T. A., Teuben, P., Hawley, J. F., & Simon, J. B. 2008, ApJS, 178, 137
Tiede, C., Zrake, J., MacFadyen, A., & Haiman, Z. 2022, ApJ, 932, 24
Toro, E. F., Spruce, M., & Speares, W. 1994, Shock Waves, 4, 25
van Leer, B. 1977, J. Comput. Phys., 23, 276
Zhang, S., Zhu, Z., Huang, J., et al. 2018, ApJ, 869, L47
Zier, O., & Springel, V. 2022, MNRAS, 515, 525

Appendix A: Effect of pressure scale height on the viscous ring spreading and spiral instability

The analytical solution for the viscous ring spreading and the stability analysis of the spiral instability studied in SK03 assumes a disk without pressure. For a locally isothermal system, this would imply an aspect ratio of $h = 0$ but the PLUTO solver becomes numerically unstable under this condition. To ensure that the pressure in our simulations is small enough to properly simulate the spiral instability, we compared the maximal spiral amplitude time averaged over $\tau = 0.2$–0.3 for different values of aspect ratio h in Fig. A.1.

For aspect ratios $h > 0.006$, the spiral instability is strongly damped and the ring structure deviates substantially from the analytical solution. For aspect ratios $h < 0.006$, the instability becomes stronger, and is fully saturated at our fiducial aspect ratio of $h = 0.005$. We also tested and confirmed (not shown) that the numerical viscosity measured in our Cartesian runs is fully converged for $h = 0.005$. Nevertheless, our fiducial aspect ratio is small enough for the gas to be considered pressureless, and we found that the noise we observed in the amplitude of the instability (see e.g., Fig. 4) fades away for even lower aspect ratios and the time evolution becomes smoother, as is the case in our FARGO simulations (see Fig. B.1).

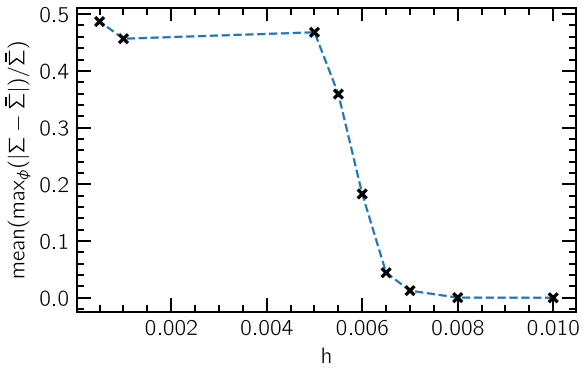

Fig. A.1: Time average of the maximal spiral amplitude at $R = 0.5\,R_0$ between $\tau = 0.2$–0.3 for different values of aspect ratio h. The spiral instability is strongly damped for $h > 0.006$ while spiral amplitudes converge for $h < 0.005$.

Appendix B: Comparison of codes and the spiral flip in SK03

To test the robustness of our results on the spiral instability we performed a similar suite of simulations using the FARGO code. Figure B.1 shows the growth of the spiral instability for different resolutions. We see that a resolution of 465×256 is sufficiently converged, with full convergence at 1024×256 and above. Even though PLUTO achieved convergence at a lower resolution of 465×256, FARGO shows slight improvements in the growth onset and amplitudes for higher resolutions. Regardless, we can conclude that the results are consistent between both codes. We note that just like PLUTO, the spiral flip vanishes before it reaches the ring in FARGO simulations for resolutions with more that 465 radial cells.

To further understand the spiral flip results shown in SK03 we replicated their setup in FARGO, with a 256×256 arithmetically spaced polar grid. Our simulation reproduces their Fig. 6 very well, but is run for longer. The spiral flip pattern emerges after $\tau = 0.04$ and gradually morphs into a single leading spiral for $\tau > 0.43$ (see Fig. B.3). We conducted additional simulations with higher resolutions and also on logarithmic grids. Each time the resolution was increased on an arithmetic grid, the flip occurred further inward and turns into a leading spiral earlier in the simulation. On a logarithmic grid, the inner region is better resolved and the flip always vanishes early in the simulation and never reaches the spreading ring; see Fig. B.3.

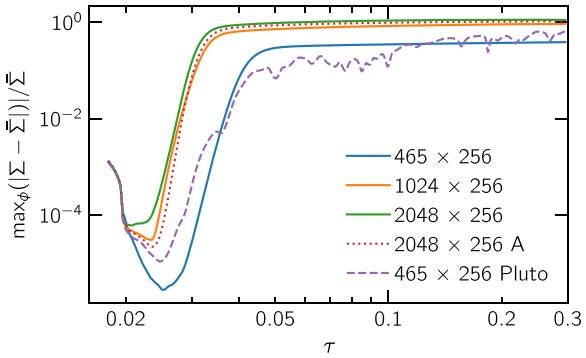

Fig. B.1: Time evolution of the normalized maximal deviation from the initial surface density distribution for different FARGO simulations compared to the fiducial PLUTO simulation.

A comparison of the growth rates between the SK03 setup and a high-resolution FARGO run is shown in Fig. B.2. As the grid is the only difference between the simulations, the flip seems to be a numerical effect that is exacerbated when using an arithmetic grid, which has a lower resolution at the inner boundary. The constant smoothing length used for the SPH code in SK03 has the same resolution effect as an arithmetic grid, which explains why their simulations are in agreement. We conclude that the flipped spiral structure with a trailing spiral observed at the inner domain in SK03 is merely a numerical effect.

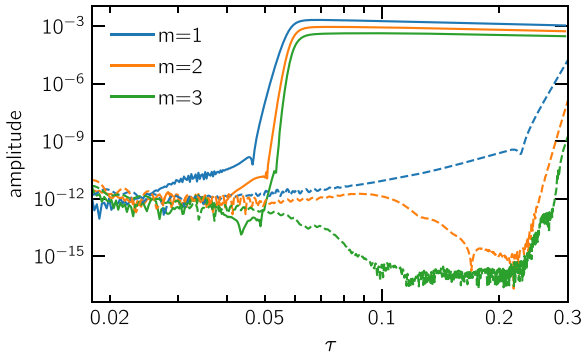

Fig. B.2: Time evolution of the first three Fourier azimuthal modes at $R = R_0$. Solid lines represent a high-resolution (2048×256) simulation using a logarithmic grid, and the dashed lines represent results from an identical setup as in SK03, with a 256×256 arithmetic grid.

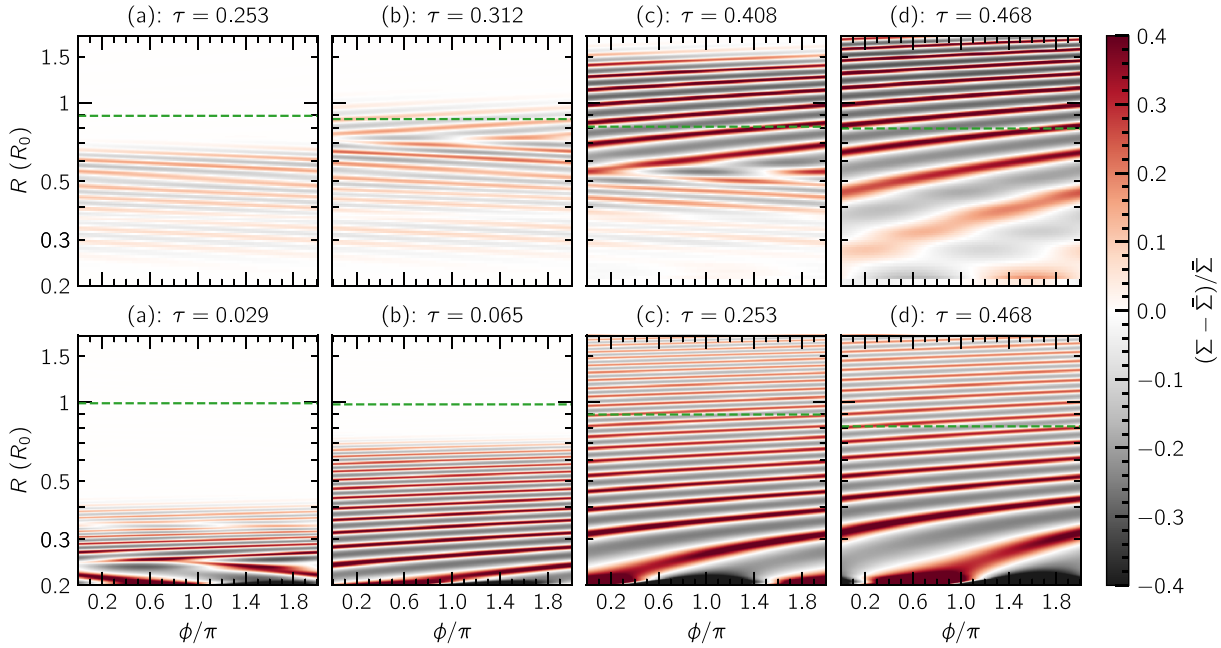

Fig. B.3: Surface density deviation heat maps similar to Fig. 3, but for FARGO simulations at a resolution of 256 × 256 on an arithmetic grid (top) and at 456 × 256 on a logarithmic grid (bottom). Top: Setup that reproduces the results of SK03 (see Fig. 6 therein). The flip from a leading to trailing spiral is visible in the middle two panels, before it disappears into a single leading spiral. Bottom: Setup that is equivalent to our fiducial PLUTO model, and behaves very similar to our results in Fig. 3. Here, spirals develop earlier and the initial flip is short-lived and closer to the inner boundary.

Appendix C: Numerical diffusion as a consequence of advection

We consider the 1D advection equation of a quantity q for a fluid moving at constant velocity $u > 0$

$$\frac{\partial q}{\partial t} + u\frac{\partial q}{\partial x} = 0. \tag{C.1}$$

We can discretize this equation to a first-order upwind scheme (e.g., Courant et al. 1952) where $q' = q(t + \Delta t)$ on a grid where i is the cell index such that $q_{i-1} = q(x_i - \Delta x)$

$$\frac{q'_i - q_i}{\Delta t} + u\frac{q_i - q_{i-1}}{\Delta x} = 0. \tag{C.2}$$

By Taylor-expanding q'_i and q_{i-1} to second order in time and space respectively, and substituting a wave-like solution $q_{tt} = uq_{xx}$, we arrive at a modified upwind equation:

$$\frac{\partial q}{\partial t} + u\frac{\partial q}{\partial x} = D\frac{\partial^2 q}{\partial x^2}, \qquad D = \frac{u\Delta x}{2}(1 - C), \quad C \equiv u\frac{\Delta t}{\Delta x}, \tag{C.3}$$

which corresponds to an advection–diffusion equation with diffusion coefficient D. This term, while not physically motivated, allows the upwind scheme to remain stable for Courant numbers $0 < C < 1$.

This approach does not exactly relate to our results, because the gas velocity is not constant and we further use second-order schemes with PLUTO. Nevertheless, we can expect that our numerical scheme will give rise to a similarly-motivated numerical diffusion term such that Eq. (5) effectively becomes

$$\frac{\partial(\Sigma \boldsymbol{u})}{\partial t} + \nabla \cdot (\Sigma \boldsymbol{u} \otimes \boldsymbol{u}) = -\nabla P - \Sigma \nabla \Phi_\star + \nabla \cdot (\overline{\sigma} + \overline{\sigma}_{\rm num}), \tag{C.4}$$

with $\overline{\sigma} \propto \nu$ and $\overline{\sigma}_{\rm num} \propto \nu_{\rm num}$. Given that our inviscid Cartesian models behave similarly to viscous models with viscosity $\nu_{\rm num}$ as far as ring spreading is concerned, it is therefore unsurprising that a ring in a viscous model with $\nu \sim \nu_{\rm num}$ should spread as if the total viscosity were $\nu_{\rm tot} \approx \nu + \nu_{\rm num}$.

We also note that, for a given Courant number C, the diffusion coefficient in Eq. (C.3) is proportional to Δx for the first-order method we considered, and expect a Δx^2 scaling for a second-order method in 1D. Given that the viscous ring problem evolves on both the x and y directions in 2D, doubling the resolution would require increasing the number of cells in both directions by a factor of 2 (thus increasing grid cell count by a factor of 4). In doing so, we would expect a scaling $\nu_{\rm num} \propto \Delta x^2$, which is verified in Fig. 8.

Finally, we found that doubling the resolution in only one direction (such as $N_x \times N_y = 512 \times 1024$) results in a numerical viscosity estimate that is much closer to the value expected for the low-resolution direction (in this case, N_x) than to an estimate dictated by $\Delta x \times \Delta y$. This rules out that the numerical diffusion we observe depends linearly on Δx and Δy and suggests that it more accurately depends on $\max(\Delta x, \Delta y)^2$, highlighting the second-order accuracy of our solver.

Appendix D: Measuring numerical viscosity

To measure the numerical viscosity in our inviscid simulations we utilize the relation between the viscous timescale τ for the ring spreading and the orbital time t at R_0 given by $\tau = 12\nu t/R_0^2$. We note that for a given viscosity ν, this equation represents the slope–intercept form of an equation for a line with slope $m = 12\nu/R_0^2$ and intercept zero.

To do so, first we fit the analytical solution to a slice of the two-dimensional data at time t to compute τ. Repeating this procedure for all snapshots generates a curve for $\tau(t)$ shown in Fig. D.1. We then fit a straight line to the $\tau(t)$ curve for approximately the last 180 orbits. The slope of this straight line fit gives the numerical viscosity using the above relation for the slope m.

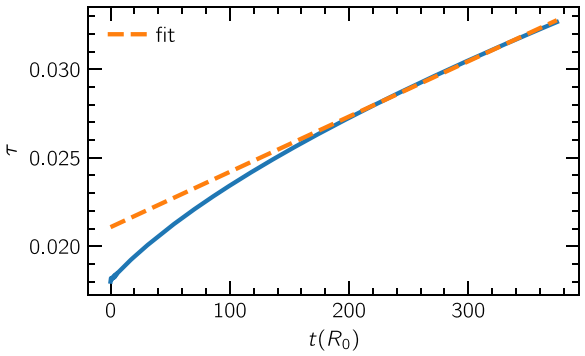

Fig. D.1: The $\tau(t)$ curve for our inviscid 1024 model. The dashed line shows the fit over the last 180 time units. The slope of this line is used to extract the numerical viscosity.

Appendix E: Inviscid Cartesian simulations with Athena++

For the suite of Cartesian models using Athena++, we implement an equivalent setup to the PLUTO runs, as described in Sect. 2. A locally isothermal disk is achieved by using an adiabatic equation of state combined with a thermal relaxation timescale $\tau_{\rm cool} = 0.01\,\Omega_{\rm K}^{-1}$. The viscous ring sits on top of a constant density background with $\Sigma_{\rm bgr} = 10^{-7}\,\Sigma_{\rm ref}$, however the density floor of the domain was set to $\Sigma_{\rm floor} = 10^{-15}\,\Sigma_{\rm ref}$ as interactions with the density floor created numerical instabilities.

Our results are listed in Table 1 and shown in Fig. 8. Both codes agree very well for $N_{\rm cells} \geq 1024^2$, which corresponds to our fiducial resolution. The expected behavior of $\nu_{\rm num} \propto \Delta x^2$ is also found with Athena++.